

Analysis of Atenolol in Rabbit Plasma by HPLC Method

Bilal YILMAZ^{1*}

¹Department of Analytical Chemistry, Faculty of Pharmacy, Ataturk University, 25240, Erzurum, Turkey

Received: 07/03/2022, **Revised:** 27/01/2023, **Accepted:** 24/02/2023, **Published:** 31/03/2023

Abstract

Atenolol is one of the most used drugs today. Therefore, it is important to develop new and simple methods for the determination of atenolol. The goal of this research is to develop a high-performance liquid chromatography method for analyzing atenolol levels in rabbit plasma and apply this method to the pharmacokinetic study. The liquid-liquid extraction technique was used to prepare blood samples from rabbits. Separation of atenolol was achieved on an Ace C₁₈ column. The method's calibration curve was plotted between 5 and 250 ng/mL. The accuracy results were better than 2.97% and the precision results were less than 6.30% in rabbit plasma for atenolol. The method had recovery values >93.1% for all samples in rabbit plasma. In addition, the validated method was used to study atenolol pharmacokinetics in rabbits. The maximum atenolol plasma concentration is 240.1 ± 33.41 ng/mL. The duration to attain the greatest atenolol concentration and the area under the curve from (AUC_{0-12 h}) were 3.0 ± 0.64 h and 1184.1 ± 235.13 ng/mL h, respectively.

Keywords: Atenolol, HPLC, extraction, pharmacokinetic, rabbit

Tavşan Plazmasında Atenololün HPLC Yöntemi ile Analizi

Öz

Atenolol günümüzde en çok kullanılan ilaçlardan biridir. Bu nedenle, atenolol tayini için yeni ve basit yöntemlerin geliştirilmesi önemlidir. Bu araştırmanın amacı tavşan plazmasında atenololün analizi için bir yüksek performanslı sıvı kromatografi yöntemi geliştirmek ve farmakokinetik çalışmaya uygulamaktır. Tavşan kan örnekleri sıvı-sıvı ekstraksiyon yöntemi ile hazırlanmıştır. Atenololün ayırımı Ace C₁₈ kolon ile yapılmıştır. Yöntemin kalibrasyon eğrisi 5 ve 250 ng/ng/ arasında çizildi. Tavşan plazmasında atenololün kesinlik sonuçları %6.30'dan küçüktü ve doğruluk sonuçları %2.97'den daha iyiydi. Yöntemin tavşan plazmasındaki tüm örnekler için geri kazanım değerleri >%93.1'dir. Ayrıca, tavşanlarda atenololün farmakokinetiğini incelemek için valide edilen yöntem uygulanmıştır. Maksimum atenolol plazma konsantrasyonu 240.1 ± 33.41 ng/mL idi. Atenololün maksimum konsantrasyona ulaşma süresi ve eğrinin altındaki alan (AUC_{0-12 h}) sırasıyla 3.0 ± 0.64 h ve 1184.1 ± 235.13 ng/mL h idi.

Anahtar Kelimeler: Atenolol, HPLC, ekstraksiyon, farmakokinetik, tavşan

*Corresponding Author: yilmazb@atauni.edu.tr

1. Introduction

The chemical formula structure of atenolol is 4-(2-hydroxy-3-isopropyl-aminopropoxy) phenylacetamide (Figure 1). It is a type of β -blockers constitute. It has been widely used to angina pectoris, hypertension, myocardial infarction and cardiac arrhythmias (Al-Ghannam, 2006). Therefore, atenolol may be used alone or concomitantly with other antihypertensive agents (Pires de Abreu et al., 2003).

In literature research, UV-Visible spectrophotometry (Saleem, 2019; Antakli et al., 2020; Mohammad et al., 2019; Vaikosen et al., 2020), spectrofluorometry (Tabrizi and Yousefzadeh, 2019), high-performance liquid chromatography (HPLC) (Pires de Abreu et al., 2003; Iha et al., 2002; Chiu et al., 1997; Madhusudhan et al., 2018; El-Alfy et al., 2019; Elkady et al., 2020), gas chromatography-mass spectrometry (GC-MS) (Yilmaz et al., 2009) and capillary electrophoresis (Arias et al., 2001) methods for determining atenolol in invitro conditions and biological materials have been reached.

However, the HPLC method was not available for detecting atenolol in rabbit plasma. Therefore, a new and easy HPLC approach for the analysis of atenolol in rabbit plasma was devised in this study. For this, liquid-liquid extraction technique and fluorescence detection were used to increase sensitivity. The developed method was then validated with respect to the Center for Drug Evaluation and Research guidelines (CDER, 2001).

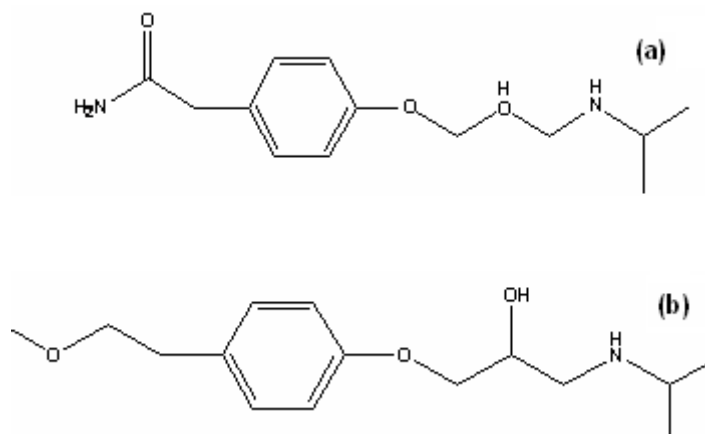


Figure 1. Atenolol (a) and metoprolol (b)

The presented method is based on a simple and single extraction step in a short time using inexpensive chemicals. At the same time, the approach was also used to examine atenolol levels in rabbit plasma. For this, Tensinor tablet containing atenolol was given to six rabbits. Bloods was drawn from the rabbits at different times. The analysis was performed after extraction. From the results obtained, the plasma pharmacokinetic parameters of atenolol were calculated.

2. Materials and Methods

2.1 Chemicals and reagents

Atenolol (99.6% purity) was obtained from Abdi Ibrahim Pharmaceutical Industry. Ethylacetate, chloroform, butanol, methanol, acetonitrile and metoprolol (IS, $\geq 98\%$ purity) were acquired from Sigma-Aldrich. Tensinor tablet that included 50 mg atenolol was purchased.

2.2 HPLC system and chromatographic conditions

HPLC analyses were performed with the Agilent HPLC system. In this work, an Ace C₁₈ column (4.6×250 mm, 5 μ m) was used. 20 μ Ls injection volume was selected for the analysis. As the mobile phase, methanol-water (50:50, v/v) containing 0.1% TFA was employed with a flow rate of 1 mL/min. Fluorescence detector was used employed for HPLC system. Fluorescence detection of atenolol and IS were selected as 276 nm and 296 nm (excitation and emission), respectively.

2.3 Preparation of standard and quality control samples

Methanol was used to make a 1.0 mg/mL atenolol solution. Atenolol standard solutions were diluted with methanol. Standard calibration samples were prepared 05-250 ng/mL (5, 15, 45, 100, 150, 200 and 250 ng/mL). The solutions were all kept at 4 °C. Atenolol quality control standard solutions were produced 10, 125 and 225 ng/mL.

2.4 Extraction procedure

The extraction procedure in rabbit plasma samples was carried out using the liquid-liquid extraction method. Butanol, acetonitrile, hexane, dichloromethane, chloroform and ethylacetate were tried to find the most suitable extraction solvent. In the end, 5 mL chloroform and butanol mixture (4:1, v/v) was chosen.

0.5 mL rabbit plasma was used in the study. 0.1 mL atenolol standard solutions (5, 10, 25, 50, 100, 150 and 250 ng/mL) containing 20 μ L IS solution were added and then 1 M 0.5 mL sodium hydroxide solution was added. The vortex procedure was performed for 30 seconds. 5 mL chloroform and butanol mixture (4:1, v/v) was added in rabbit plasma. The rabbit plasma sample was vortexed for 30 seconds, and the plasma was then centrifuged for 5 minutes at 3000 \times g. The supernatant was transferred into another plastic tube. The supernatant was vaporized under nitrogen gas. The dry residue sample was dissolved in 1 mL methanol and then 20 μ L plasma sample was analyzed in HPLC system.

2.5 Rabbits

Before starting the research, the ethics committee report was obtained from the Ethical Committee for Medical Experimental Research and Application Centre of Ataturk University.

12.5 mg kg⁻¹ of atenolol were six rabbits by oral administration. 2.0 mL blood was taken from the ear vein of six rabbits at 0, 0.5, 1, 2, 3, 4, 6, 8 and 12 h. EDTA tubes were used to collect the bloods. The blood samples were centrifuged. The plasma samples were taken, and samples were extracted. After that, they are analyzed by the HPLC system.

2.6 Statistical analysis

The statistical analyses were done with SPSS V.15.0 version at computer program. Regression analyses were used in the preparation of the atenolol standard line and calculations. The results were given with the mean \pm standard deviation.

3. Results and Discussion

3.1 Method development and optimization

In this work, the reversed-phase column (C₁₈) was used because atenolol is a polar molecule. For the sensitivity of the HPLC method, fluorescence detection was used to atenolol and IS. Several mobile phase components were performed to achieve a good peak shape and resolution in chromatogram. In the end, methanol-water (50:50, v/v) containing 0.1% TFA was employed as the mobile phase. Atenolol retention time was quite short than that studied by Giachetti et al., 1997; Iha et al., 2002). In the proposed HPLC method, the buffer mobile phase system was not used as in the previously published articles (Chatterjee et al., 1995; Giachetti et al., 1997). In this research, there is no column washing after the analysis. This is an advantage of the method. In HPLC chromatogram, atenolol and IS retention times were 2.8 and 4.7 min, respectively. A representative chromatogram of atenolol and IS was given in Figure 2.

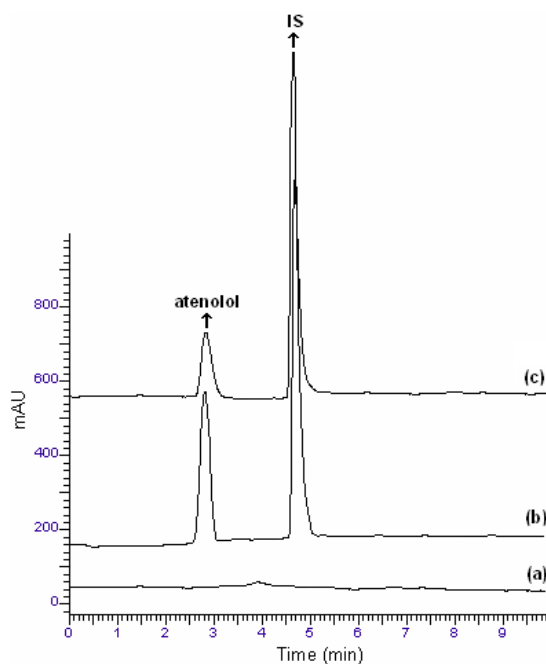


Figure 2. (a) Pre-drug rabbit plasma chromatogram, (b) rabbit plasma chromatogram spiked with 100 ng/mL atenolol, (c) rabbit plasma chromatogram obtained 6h after administration 12.5 mg/kg of atenolol

3.2 Validation of the method

HPLC method was validated with validation parameters according to CDER. These parameters were selectivity, linearity, precision, accuracy, recovery, limits of detection (LOD) and quantification (LOQ), stability and dilution integrity.

i. Selectivity

The selectivity of the developed technique was checked by comparing the chromatograms of spiked rabbit plasma with the blank rabbit plasma. Atenolol and IS retention times were approximately 2.8 and 4.7 min (Figure 2). The symmetry of the peaks and the short retention times are the advantages of the method. In addition, the blank plasma sample was analyzed. Endogenous interferences were not observed.

ii. Linearity

Standards calibration curves were drawn according to peak area ratio (y) of atenolol and IS versus atenolol concentration. It was found to be linear over the 5-250 ng/mL concentration range for atenolol. The mean calibration equation of method is $y=0.1824x + 0.0192$. The correlation coefficient value was higher than 0.99 for the mean calibration curve ($n=3$).

iii. Precision and accuracy

Intra-day and inter-day precision were used to assess the proposed method's precision. Six replicates for each of three different concentrations (7.5, 75, 175 ng/mL) were analyzed to determine intra-day precision. The same samples of plasma were analyzed in three successive days to measure the intermediate precision. The percent relative standard deviation (RSD %) was used to assess precision.

In addition, the percentage relative error was used to assess the method's accuracy. The precision and accuracy were gratifying for atenolol from plasma samples. RSD is obtained as lower than 6.27%. In addition to this, accuracy is detected to be within $\pm 2.97\%$ with relative error. It is understood that both the precision and the accuracy of this method are good in statistical comparison with previously reported methods (Miller et al., 1991; Iha et al., 2002).

iv. Recovery

In order to prepare the samples at rabbit plasma, the extraction technique was used for this work. Therefore, dichloromethane, ethylacetate, butanol and chloroform were tried. In the end, chloroform and butanol mixture (4:1, v/v) was decided to be used as the most suitable solvent for extraction. Atenolol recovery values of rabbit plasma are between 93.1 and 98.6% (Table 1). The mean recovery of atenolol was 96.1% in rabbit plasma.

Table 1. Recovery of atenolol in human plasma

Added (ng/mL)	Found (Mean ± SD ^a)	% Recovery	% RSD ^b
5	4.9 ± 0.23	98.0	4.69
10	9.4 ± 0.47	94.0	5.00
25	24.1 ± 0.63	96.4	2.61
50	48.1 ± 2.32	96.2	4.82
100	98.6 ± 5.59	98.6	5.67
150	145.1 ± 6.49	96.7	4.47
250	232.8 ± 8.62	93.1	3.70

SD^a: Standard deviation of six replicate determinations, RSD: Relative standard deviation

^bAverage of six replicate determinations

In the literature, atenolol was extracted with a solid-phase extraction method from human plasma in previous studies (Chatterjee et al., 1995; Arias et al., 2001; Miller et al. 2002). The solid-phase extraction technique is an expensive method. In our technique, the liquid-liquid method in plasma from rabbits is used as the extraction method. In addition, the extraction technique was very simple, cheap and could be done in one step.

v. Limits of detection (LOD) and quantification (LOQ)

The LOD value was evaluated as the minimum concentration in this work. The reason behind this is the fact that the signal-to-noise ratio of it is found to be 3 for atenolol at HPLC chromatogram. In addition, the LOQ value was evaluated as the minimum concentration of the plasma spiked with atenolol. The LOD and LOQ values were 1.5 and 5.0 ng/mL in the work, respectively. Both precision and accuracy of the LOD and LOQ values were within the criteria (CDER, 2001). In addition, this method is better than reported previously methods (Giachetti et al., 1997; Miller et al., 1991).

vi. Stability

Atenolol stock solution stability was evaluated for at least 72 hours at room temperature. In addition, the stabilities of atenolol in rabbits were investigated under various storage conditions. By analyzing the low and high concentrated samples (15 ng/mL and 225 ng/mL), the method's short-term stability was determined. Therefore, the samples were thawed at room temperature. They were stored in room condition for 24 h. The samples were analyzed at -20 °C for three

days to determine long-term stability. No significant degradation product of atenolol in the storage conditions.

vii. Dilution integrity

The dilution integrity was performed on higher atenolol concentrations above the upper LOQ. The accuracy and precision of atenolol were between 97.9 to 102.1 and 2.46 to 3.27 % for 1/5th and 1/10th dilution.

3.3 Pharmacokinetic analysis

Pharmacokinetic results of atenolol were calculated in rabbit plasma by the linear trapezoidal rule (Yilmaz et al., 2009). In addition, Figure 3 illustrates the average atenolol concentration-time curve for six rabbits.

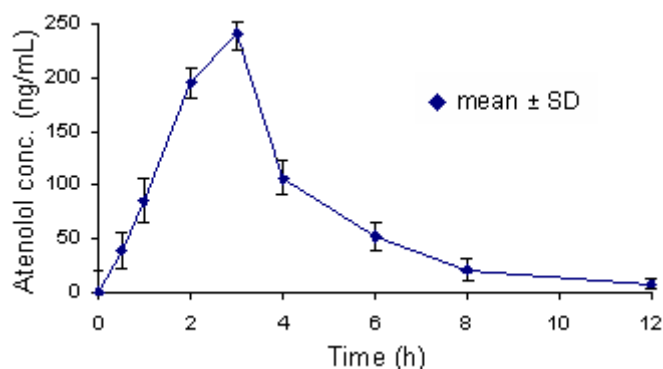


Figure 3. Atenolol concentration-time profile in rabbit plasma (n=6).

The mean AUC_{0-12h} , C_{max} , T_{max} and $t_{1/2}$ of atenolol obtained from six rabbits were $1184.1 \pm 235.13 \mu\text{g/mL h}$, $240.1 \pm 33.41 \text{ ng/mL}$, $3.0 \pm 0.64 \text{ h}$ and $3.18 \pm 0.41 \text{ h}$, respectively. Using this method, the obtained pharmacokinetics results are in agreement with the previously research papers (Giachetti et al., 1997; Iha et al., 2002).

However, in the previously papers especially it has been used with 1.0 mL plasma (Giachetti et al., 1997; Iha et al., 2002). In the proposed method, low plasma volume (0.5 mL) is used This can be advantageous in pharmacokinetic studies. Because, atenolol is one of the most used β -blockers drugs today. Therefore, it is important to develop and validate new and simple methods for the determination of atenolol. In the literature, there are different chromatographic studies on the determination of atenolol in biological materials. Among these, the most used methods are usually HPLC, capillary electrophoresis and GC-MS.

The GC-MS method is a widely used chromatographic method for the analysis of volatile or volatile substances. In this study, atenolol, a polar compound, was volatilized by derivatization. In this way, the sensitivity of the study was increased. With this, it was possible to determine the amount of atenolol in rabbit plasma even at low concentrations. However, the GC-MS

method is not always accessible because it is a very expensive method. Therefore, the HPLC method developed in this study is cheaper than the GC-MS method.

4 Conclusion

In this research, a new and fast HPLC technique has been completely developed in order to analyze atenolol in rabbit plasma. Furthermore, validation parameters were used to validate the procedure. The advantages of the method are that 0.5 mL of plasma is sufficient for the application of the method and that it has an easy extraction method. In addition, the proposed method was applied to six rabbits. Pharmacokinetic parameters were calculated in rabbit plasma. Therefore, the proposed method can be easily used in the plasma of people using atenolol in the clinic.

Ethics in Publishing

Before starting the study, the ethics committee report was obtained from the Ethical Committee for Medical Experimental Research and Application Centre of Ataturk University (2009/4).

Acknowledgements

The author would like to thank Abdi Ibrahim Pharmaceutical Industry for atenolol standard. The author also wishes to thank Semih Yilmaz for expert advice on the use of English.

References

- Al-Ghannam, S.M. 2006. "A simple spectrophotometric method for the determination of β -blockers in dosage forms", *Journal of Pharmaceutical and Biomedical Analysis*, 40, 151-156.
- Antakli, S., Nejem, L., Joumaa, M.A. 2020. "Determination of atenolol in tablet formulation by analytical spectrophotometry". *Research Journal of Pharmacy and Technology*, 13(2), 609-614.
- Arias, R., Jimenez, R.M., Alonso, R.M., Telez, M., Arrieta, I., Flores, P., Ortiz-Lastra, E. 2001. "Determination of the β -blocker atenolol in plasma by capillary zone electrophoresis", *Journal of Chromatography A*, 916, 297-304.
- Chatterjee, D.J., Li, W.Y., Hurst, A.K., Koda, R.T. 1995. "High-performance liquid chromatographic method for determination of atenolol from human plasma and urine: simultaneous fluorescence and ultraviolet detection", *Journal of Liquid Chromatogr*, 18, 791-806.
- Chiu, F.C., Zhang, J.N., Li, R.C., Raymond, K. 1997. "Efficient assay for the determination of atenolol in human plasma and urine by high-performance liquid chromatography with fluorescence detection", *Journal of Chromatography B*, 691, 473-477.

- El-Alfy, W., Ismaiel, O.A., El-Mamml, M.Y., Shalaby, A. 2019. ‘‘Determination of atenolol and trimetazidine in pharmaceutical tablets and human urine using a high-performance liquid chromatography-photo diode array detection method’’, *International Journal of Analytical Chemistry*. Article ID 9625849.
- Elkady, E.F., Fouad, M.A., Faquih, A.A. 2020. ‘‘A versatile stability-indicating liquid chromatographic method for the simultaneous determination of atenolol, hydrochlorothiazide and chlorthalidone’’, *Current Pharmaceutical Analysis*, 16(8):1037-1051.
- Giachetti, C., Tencoti, A., Canali, S., Zanol, G. 1997. ‘‘Simultaneous determination of atenolol and chlorthalidone in plasma by high-performance liquid chromatography Application to pharmacokinetic studies in man’’, *Journal of Chromatography B*, 698, 187-194.
- Guidance for Industry, Bioanalytical Method Validation, US Department of Health and Human Services, Food and Drug Administration, Center for Drug Evaluation and Research (CDER), Rockville, MD, 2001.
- Iha, M.H., Martinez, A.S., Bonato, P.S. 2002. ‘‘Enantioselective analysis of atenolol in biologic fluids: comparison of liquid-liquid and solid-phase extraction methods’’, *Journal of Chromatography B*, 767, 1-9.
- Li, W., Li, Y., Francisco, D.T., Naidong, W. 2005. ‘‘Hydrophilic interaction liquid chromatographic tandem mass spectrometric determination of atenolol in human plasma’’, *Biomedical Chromatography*, 19, 385-393.
- Madhusudhan, P., Reddy, K.V., Singh, S. 2018. ‘‘A novel isocratic RP-HPLC method development and validation for simultaneous determination of atenolol and nifedipine in tablet dosage form’’, *Universal Review* 7(9): 412-421.
- Miller, R.B. 1991. ‘‘A validated high-performance liquid chromatographic method for the determination of atenolol in whole blood’’, *Journal of Pharmaceutical and Biomedical Analysis*, 9, 849-853.
- Mohammad, M.Y., Abdullah, M.S., Sabir, S.S. 2019. ‘‘Simultaneous determination of atenolol and amlodipine using second derivative spectroscopy’’, *Polytechnic Journal*, 9(2), 25-29.
- Morris, R.G., Saccoia, N.C., Sallustio, B.C., Zacest, R. 1991. ‘‘Improved high-performance liquid chromatography assay for atenolol in plasma and urine using fluorescence detection’’, *Therapeutic Drug Monitoring*, 13, 345-349.
- Pires de Abreu, L.R., Calafatti de Castro, S.A., Pedrazzoli Jr, J. 2003. ‘‘Atenolol quantification in human plasma by high-performance liquid chromatography: application to bioequivalence study’’, *AAPS PharmSci*, 5, 1-7.
- Saleem, B.A. 2019. ‘‘Spectrophotometric determination of atenolol using indigo carmine dye’’, *Kirkuk University Journal for Scientific Studies*, 14(2), 15-39.

- Sethi, P.D. 2001. “High Performance Liquid Chromatography-Quantitative Analysis of Pharmaceutical Formulations”, *CBS Publishers & Distributors, Mumbai*, 3-212.
- Tabrizi, A.B., Yousefzadeh, F. 2019. “Spectrofluorimetric determination of atenolol and carvedilol in pharmaceutical preparations after optimization of parameters using response surface methodology”, *Pharmaceutical Sciences*, 25(3), 262-267.
- Vaikosen, E.N., Bioghele, J., Worlu, R.C., Ebeshi, B.U. 2020. “Spectroscopic determination of two beta-blockers—atenolol and propranolol by oxidative derivatization using potassium permanganate in alkaline medium”, *Reviews in Analytical Chemistry*, 39(1): 56-64.
- Yilmaz, B., Arslan, S. 2009. “GC-MS determination of atenolol plasma concentration after derivatization with N-Methyl-N-(trimethylsilyl) trifluoroacetamide”, *Chromatographia*, 70(9-10), 1399-1404.

Determination of Noise Pollution and Noise Dose Level of Kahramanmaraş Sutcu Imam University Medical Faculty Hospital

Ömer SÖĞÜT^{1*}, Büşra Zeytun¹

¹Kahramanmaraş Sütçü İmam University, Science Faculty, Department of Physics, 46100 Kahramanmaraş, Türkiye

Received: 21/07/2022, **Revised:** 01/12/2022, **Accepted:** 06/01/2023, **Published:** 31/03/2023

Abstract

Noise pollution is one of the most important environmental problems waiting to be solved today. For this reason, in this study, to determine the noise level and dose in the hospital environment, which is one of the areas heavily used by society, noise measurement was made in the polyclinic corridors of the KSU Medical Faculty Hospital. In all corridors of the hospital, which has 10 outpatient corridors in total, from Monday to Friday, at 08:00-09:07, 10:00-11:01, 12:00-13:01, 14:00-15:01, 15:01 and 16:00-17:01 at hours noise intensity measurements were made as dB(A) by Testo 815 noise meter. The measurements were averagely performed at each point for 15 minutes, and repeated at least three times. The equivalent noise level (L_{eq}) calculated from the measurement results varies between 27.39 and 50.68 dBA. Most of the L_{eq} values calculated for many corridors are greater than the limit value (35 dB) of the Republic of Turkey Ministry of Environment and Forestry and WHO. But, it was determined that the values of the noise dose calculated for the corridors of the KSU medical faculty hospital (except for ground floor) were smaller than the acceptable noise dose value ($D \leq 1$) defined by the authorized institutions or organizations.

Keywords: Sound, noise dose, noise pollution, dBA and health

Kahramanmaraş Sütçü İmam Üniversitesi Tıp Fakültesi Hastanesi Gürültü Kirliliği ve Gürültü Doz Düzeyinin Belirlenmesi

Öz

Gürültü kirliliği günümüzde çözüm bekleyen en önemli çevre sorunlarından biridir. Bu nedenle bu çalışmada toplumun yoğun olarak kullandığı alanlardan biri olan hastane ortamındaki gürültü seviyesi ve dozunun belirlenmesi amacıyla KSÜ Tıp Fakültesi Hastanesi poliklinik koridorlarında gürültü ölçümü yapılmıştır. Toplam 10 poliklinik koridoru bulunan hastanenin tüm koridorlarında Pazartesi Cumaya kadar 08:00-09:07, 10:00-11:01, 12:00-13:01, 14:00-15:01, 15:01 ve 16:00-17:01 saatlerinde Testo 815 gürültü ölçer ile dB(A) olarak gürültü şiddeti ölçümleri yapılmıştır. Ölçümler ortalama olarak her noktada 15 dakika süreyle yapıldı ve en az üç kez tekrarlandı. Ölçüm sonuçlarından hesaplanan eşdeğer gürültü seviyesi (L_{eq}) 27,39 ile 50,68 dBA arasında değişmektedir. Birçok koridor için hesaplanan L_{eq} değerlerinin çoğu, T.C. Çevre ve Orman Bakanlığının ve DSÖ'nün sınır değerinden (35 dBA) daha büyüktür. Ancak KSÜ tıp fakültesi hastanesinin koridorları için hesaplanan gürültü dozu değerlerinin (zemin kat hariç) yetkili kurum veya kuruluşlar tarafından belirlenen kabul edilebilir gürültü doz değerinden ($D \leq 1$) daha küçük olduğu tespit edilmiştir.

Anahtar Kelimeler: Ses, gürültü dozu, gürültü kirliliği, dBA ve sağlık.

*Corresponding Author: omersogut@gmail.com

Ömer SÖĞÜT, <https://orcid.org/0000-0003-1987-1116>

Büşra ZEYTUN, <https://orcid.org/0000-0002-7779-9928>

1. Introduction

The environment is the area in which people live and carry out all their life-related activities. However, various factors within this field can affect people as positively or negatively. Developments such as rapid population growth due to the development science, industry and technology in recent years have led to the emergence of many environmental problems. Noise pollution still is one of the most important environmental problems today. In the last decade, more and more people are trying to cope with the noise problem in their daily life. The main source of noise is sound waves. The sound is a vibration that can propagate in the air or other medium and can be detected when it reaches the human ear or a suitable receiver (Kara, 2011). If the sound propagates from one point in an enclosure to another observation point, it not only follows the direct path, but also multiple reflections (Kuttruff and Mommertz, 2013). This situation, which is a physical process, causes the sound produced in the environment to be heard for a while after the sound source is turned off (ISO 3382-1, 2009). The noise resulting from human activities is rapidly changing the natural sound balance of the Earth (Connelly et al., 2022; Kight and Swaddle, 2011; Shannon et al., 2016). It has been shown by research that noise pollution can cause serious health effects such as hearing damage, cardiovascular diseases, increased stress, and sleep disturbance in humans (Passchier-Vermeer and Passchier, 2000; Frei et al., 2014; Fyhri and Aasvang, 2010; Basner et al., 2014; Halperin, 2014). The intensity of sound is measured in decibels (dB). The decibel is a ratio of any two of the three components of sound, power, pressure, and intensity. Since the decibel scale is a ratio, a baseline called a filter is used to measure a single sound source. There are three standard filters as called A, B, and C. Filter A is often used to measure ambient noises as it is less sensitive to very high and very low frequencies. Filter B is located between A and C, while filter C is generally used to measure high frequencies. When using a sound meter, it is also very important to choose the filter suitable for the nature of the measuring environment and to determine which filter was used when recording the measurements. It should be noted that the decibel is not an absolute measure of sound pressure, but rather the ratio of the measured sound pressure to the reference sound pressure. However, since this sound scale is exponential, a sound of 10 dB has intensity 10 times greater than a sound of 0 dB, and a sound of 20 dB is 100 times more intense than 0 dB (Field and Long, 2018). Sound is one of the most important communication tools for people. But, when sound turns into noise, it can cause many negative effects on human health. The noise can be defined as unwanted sounds that can adversely affect people's physiological or psychological states, or audible acoustic energy that disturbed and disturbs the peace of any person (Cantrell, 1975). Although sound is an objective concept that can be measured individually and cannot be changed noise is a very subjective concept. Therefore, sounds that are pleasant and beautiful for one person may be disturbing for another. Noise is one of the most common occupational health problems for deafness. Besides the noise-induced hearing loss is generally irreversible. Therefore, to protect from negative consequences of noise exposure, the noise levels should be kept at acceptable levels. The acceptable, that is, safe sound level depends on the severity of the sound, exposure time and frequency of exposure. The medium noise contains all the sounds in an environment. The noise level in an environment can be measured at any time by using a decibel meter. In this sense, a single dBA measurement taken can usage provide a lot of

information about ambient noise, and the most common measurement level of environmental noise is dBA. The investigated noise is measured over a time interval of at least 15 minutes or, if the noise persists for less than 15 minutes, over the duration of the noise to determine that the measured value is adequately representative of the noise in question (WHO, 2019). Exposure to loud sounds, i.e. noise, for any length of time, can cause fatigue of the ear's sensory cells, resulting in temporary hearing loss such as tinnitus or humming in the ear. However, when the exposure time is long, regular, or high, it can cause permanent damage to sensory cells and other structures, resulting in irreversible hearing loss (WHO, 2019). In addition to hearing loss, noise has numerous physical effects on the body. These include pupil dilation, increase production of thyroid hormone, increased heart rate, increased adrenaline production, increases in corticotrophy, increase stomach and abdominal movement, muscle reaction, and constriction of blood vessels. Hearing impairment is typically defined as an increase in the hearing threshold (WHO, 1994). The recommended safe level for daily noise should be below 80 dB and equal to $L_{Aeq, 24h}$ equal to 70 dBA for a maximum of 40 hours per week (WHO, 2018, 2019; Neitzel and Filgor, 2017). Noise pollution is one of the important environmental pollutions that can cause hearing health problems in people in developed and developing countries. In recent years, while the number of people living in apartments has been increasing, the noise level caused by the technological devices used in most modern houses with poor sound insulation are affected the quality of life of people negatively (Peterso, 1980).

The aim of this study is to measure the noise level in dBA of Kahramanmaraş Sütçü İmam University (KSU) Medical Faculty Hospital for five days from Monday to Friday, and to calculate the equivalent noise level and noise dose. In addition, it is to draw attention to noise pollution which is one of the most important environmental problems of today and to the negative health effects caused by this pollution.

2. Material and Method

2.1. Testo 815 Sound Intensity Meter

The Testo 815 is the ideal instrument for measuring noise or sound intensity. The testo 815 sound meter (decibelmeter) used for measuring sound frequencies has sound level measurement ranges of 32-80 dB, 50-100 dB and 80-130 dB, two time and frequency ranges, maximum/minimum function and a tripod screw. The device, which has slow and fast time intervals, can collect incoming audio signals in the range of 1s to 125 ms. The Testo 815 noise meter has an accuracy of ± 1.0 dB and a resolution of 0.1dB. The device is especially used to measure sound levels with A-weighted frequency standards. The photographs of the Testo 815 decibel meter (a) and CEM SC-05 sound level calibrator devices (b) used are given in Figure 1. Before starting the measurements, the Testo 815 sound level or noise meter was calibrated with the CEM SC-05 sound level calibrator, which has ± 0.5 dB sensitivity.



Figure 1. (a) The photographs of the Testo 815 decibelmeter, and (b) CEM SC-05 sound level calibrator devices.

2.2. Measurement of the Sound Intensity

The first stage of noise control is the sound level measurement, and determination of the frequency and intensity of the affecting noise. There are 10 different polyclinic corridors in total in KSU Medical Faculty Hospital. Since the corridors were so long, three points were determined in each corridor for measurements, and the sound pressure levels of the noise in the outpatient corridors were measured on the A-weighted (dBA) decibel scale. The measurements were made at 08-09, 10-11, 12-13, 14-15 and 16-17 hours every day of the week at selected points. Measurements were started on 14 April 2019 and finished on 12 July 2019. That is, it took three months to complete measurements in all corridors of the hospital. Testo 815 decibelmeter was used to measure sound intensity in hospital corridors. The probabilities of reflection of sound waves from walls, ceilings and other objects were taken into account while making the measurements, and therefore the measurements were made 1.5 m away from the walls and at a height of 1m from the ground. If the measurements were made more than one meter away from the person's, measurement errors could occur. The measurements were made at a distance of at least 30 cm and 50 cm from the body in order to avoid similar errors. Measurements were made at each measurement point for at least 15 minutes or during the noise period, and each measurement was repeated three times. A photo of the moment of measuring in one of the corridors is given in Figure 2. The list of outpatient clinics located in the corridors is given in Table 1.



Figure 2. Photograph of one of the hospital corridors where measurements were made

Table 1. Lists of polyclinics in the corridors of KSU Medical Faculty Hospital

Ground floor	
Corridor A	Physical Medicine and Rehabilitation, Urology and Nephrology
Corridor B	Child Health and Diseases, Newborn and Healthy Child, Pediatric Endocrinology, and Pediatric Neurology
Corridor C	Internal Medicine, Nutrition and Dietetics, and Gastroenterology
Corridor D	Cardiology, Cardiovascular Surgery, Infectious Diseases and Clinical Microbiology, and Endocrinology and Metabolism
Corridor E	Brain and Nerve Surgery, Neurology, Orthopedics and Traumatology, and Rheumatology
First floor	
Corridor A	Ear, Nose and Throat Diseases
Corridor B	Chest Diseases, Thoracic Surgery, Plastic, Reconstructive and Aesthetic Surgery, General Surgery, Child and Adolescent Psychiatry and Diseases, and Forensic Medicine
Corridor C	Skin and Venereal Diseases, Gynaecology and Obstetrics
Corridor D	Eye Diseases, Mental Health and Diseases
Radiology corridor	Radiology polyclinic

2.3. Calculation of Equivalent Noise Level (L_{eq})

Equivalent noise level (L_{eq}) should be calculated in sound intensity or noise measurements. Because in many measurement situations, the widely fluctuating display data of a conventional sound level meter can make it extremely difficult to detect the correct sound level. The equivalent noise level, L_{eq} , is a noise scale in dB(A) that gives the average value of sound energy or sound pressures continued over a given period, and can be calculated by the following equation (Ministry of Environment and Forestry, 2008),

$$L_{eq} = 10 \log \text{ dB(A)} \tag{1}$$

where L_{eq} is the equivalent noise level, n is the number of sample data noise measurements, L_i is the noise value over the specified measurement time interval, and its unit is dB(A). Equivalent continuous level L_{eq} can also be defined as the level of a constant level sound that has the same total energy as the corresponding sound in a given time interval. The noise dose can be calculated in two ways, depending on whether the noise level is constant or consist of periods of different noise levels:

If the sound level L is constant over the entire working time (shift), the noise dose D, in percent, is calculated as follows:

$$D = 100x \frac{C}{T} \tag{2}$$

where D is the dose level as in percent, C is the total length of the working day (hours), and T is the reference time level corresponding to the measured sound level (L).

But, if the daily noise exposure consists of periods of different noise levels, the daily dose D , in percent, is calculated according to the formula given below, and D equals or cannot exceed 100 (NIOSH, 1998; Field and Long, 2018).

$$D = \left[\frac{C_1}{T_1} + \frac{C_2}{T_2} + \dots + \frac{C_n}{T_n} \right] \times 100 \quad (3)$$

where C_n is the total exposure time at a given noise level, and T_n is the exposure time at which noise at that level becomes dangerous (the reference duration for that level). The first equation determines the dose for those exposed as a percentage, and the maximum allowable dose is 100%. The reference duration level, T , is calculated using the following equation (Field and Long, 2018);

$$T = \frac{8}{2^{(L-90)/5}} \quad (4)$$

where T is reference duration, and L is dBA exposure which is the measured sound level. The daily dose, on the other hand, can be converted to an 8-hour time-weighted average (TWA) according to the formula (NIOSH, 1998):

$$TWA = 10 \times \log(D/100) + 85 \quad (5)$$

where 85 dBA is the recommended exposure limit, and exposures above this level are considered hazardous. However, continuous, variable, intermittent or impulsive noise exposure should not exceed 140 dBA (NIOSH, 1998; Field and Long, 2018).

3. Results and Discussion

The noise measurement values made with the Testo 815 decibelmeter on the dBA scale in the corridors where the polyclinics of Kahramanmaraş Sütçü İmam University Medical Faculty Hospital are located are given in Tables 2 and 3. The equivalent noise levels calculated for all corridors are given in Tables 4 and 5. The calculated percentages of noise dose are given in Tables 6 and 7. As seen from Table 4 and Figure 3, the highest equivalent noise level in corridor A of the ground floor was measured as 31.03 dBA on Monday, while the lowest noise level was measured as 27.39 dBA on Thursday. For the ground floor B corridor, the highest equivalent noise level was calculated as 50.68 dBA on Monday, while the lowest equivalent noise level was calculated as 41.48 dB on Thursday. While the highest equivalent noise level calculated from the sound intensity measurements made in the ground floor C corridor was 47.72 dBA on Wednesday, the lowest equivalent noise level was calculated as 43.08 dBA on Monday. In the calculations made using sound intensity measurements made in the ground floor D corridor, the lowest equivalent noise level was calculated as 41.58 dBA on Thursday, while the highest equivalent noise level was calculated as 47.12 dBA on

Wednesday. The highest equivalent noise level for the ground floor E corridor was calculated as 43.33 dBA on Friday, while the lowest equivalent noise level was calculated as 39.90 dBA on Wednesday.

As seen from Table 4 and Figure 4, the highest equivalent noise level was found as 47.80 dBA on Thursday, and the lowest equivalent noise level was found at 32.99 dBA on Friday, from the calculations made using the sound intensity data made in the radiology corridor on the minus first floor. As seen from Table 5 and Figure 5, the average equivalent noise level achieved from the calculations for the ground floor corridors was found to be 29.09 dBA for corridor A, 45.55 dBA for corridor B, 45.04 dBA for corridor C, 44.91 dBA for corridor D and 41.39 dBA for corridor E, respectively. Similarly, the average equivalent noise level for the minus first-floor radiology corridor was 41.80 dBA. The limit value of the equivalent noise level (L_{eq}) in health institutions has been accepted as 35 dB by national and international institutions and organizations (Republic of Turkey Ministry of Environment and Urbanization, 2017; NESREA, 2007).

As seen from Table 4, in the radiology corridor on the minus first floor, the equivalent noise level calculated for all of the other days except Friday is greater than the limit value of 35 dBA. The value of the equivalent noise level calculated for all days in corridor A on the ground floor is smaller than the 35 dBA limit value. The values of the equivalent noise level calculated for all days in corridors B, C, D, and E on the ground floor are bigger than the 35 dBA limit value.

Table 2. The values of the sound intensity measured in dBA in the corridors on the first floor of KSU Faculty of Medicine in between Monday and Friday, April 15-19, 2019.

Hours	Monday	Tuesday	Wednesday	Thursday	Friday	
08:00-09:01	68±2.12	72.65±1.34	69.45±0.91	72.80±2.54	72.65±1.13	A Block
10:00-11:01	77.40±5.37	74.20±0.84	82.2±3.11	79.55±10.81	81.1±4.94	
12:00-13:01	64.40±5.93	72.45±1.76	78.10±8.48	66.70±10.18	65.30±6.08	
14:00-15:01	81.55±8.69	74.65±5.02	75.40±3.11	83.95±0.35	75.70±4.38	
16:00-17:01	61.45±0.35	62.50±0.56	78.10±17.11	64.85±8.83	72.70±2.12	
Mean	70.56±4.50	71.29±1.90	76.65±6.54	73.57±6.54	73.49±3.75	
08:00-09:01	71.90±0.15	69.20±3.22	78.87±4.95	77.43±2.75	70.00±3.15	B Block
10:00-11:01	80.83±1.05	80.97±1.20	77.30±4.45	79.83±4.73	81.00±4.90	
12:00-13:01	70.63±9.26	70.60±3.43	71.00±0.51	68.93±5.55	74.53±1.78	
14:00-15:01	71.17±2.10	77.73±3.44	78.73±3.15	63.17±5.64	78.77±6.26	
16:00-17:01	67.94±5.16	58.17±2.19	61.50±3.61	75.00±4.43	61.27±6.36	
Mean	72.52±3.54	71.33±2.70	72.45±3.33	72.81±4.62	72.40±4.50	
08:00-09:01	73.50±1.67	64.73±3.94	72.6±5.54	73.2±5.23	79.9±12.32	C Block
10:00-11:01	79.60±4.01	72.06±3.07	66.06±8.76	77±2.81	67.9±8.69	
12:00-13:01	70.50±10.67	71.56±7.26	65.66±7.03	67.4±7.23	60.43±0.92	
14:00-15:01	79.43±7.87	74.26±1.94	74.26±3.70	79.1±3.67	70.20±1.47	
16:00-17:01	60.13±7.48	56.3±5.18	60.7±6.29	62.93±12.36	63.10±4.46	
Mean	72.63±6.34	67.79±4.28	67.85±6.26	71.92±6.26	68.30±5.57	
08:00-09:01	71.90±1.40	71.91±4.01	73.06±0.57	68.73±0.72	72.76±4.17	D Block
10:00-11:01	80.86±8.85	77.93±4.36	78.43±4.40	71.13±1.13	75.63±10.65	
12:00-13:01	70.20±6.58	67.50±0.90	77.46±10.37	67.10±6.78	59.80±2.86	
14:00-15:01	70.90±2.55	75.66±4.57	77.80±5.65	78.70±7.56	76.10±3.89	
16:00-17:01	65.73±5.51	65±7.86	60.66±1.25	67.56±3.04	60.90±1.11	
Mean	71.91±4.98	71.60±4.34	73.48±4.45	70.64±3.85	69.03±4.54	
08:00-09:01	72.46±6.65	71.9±1.47	71.66±3.70	76.33±5.39	68.13±6.50	Radiology floor
10:00-11:01	74.7±5.28	80.23±4.82	78.33±3.83	76±1.47	72.6±0.21	
12:00-13:01	70.6±6.32	73.66±4.64	78.56±1.40	76.9±4.71	69.1±0.96	
14:00-15:01	70.83±3.67	76.2±2.68	76.96±7.80	73.7±6.23	68.6±2.10	
16:00-17:01	62.83±3.30	61.9±3.76	59.33±1.47	63.23±4.89	63.83±4.53	
Mean	70.28±5.04	72.77±3.47	73.56±3.64	73.23±5.54	68.45±2.86	

Table 3. The values of the sound intensity measured in dBA in the corridors on the ground floor of KSU Faculty of Medicine in between Monday and Friday, April 15-19, 2019

Hours	Monday	Tuesday	Wednesday	Thursday	Friday	
08:00-09:01	63.56±2.20	99.25±0.98	62.60±2.86	66.13±3.18	64.46±4.86	A Block
10:00-11:01	63.70±2.07	66.73±4.47	71.56±7.26	68.70±4.60	71.16±2.18	
12:00-13:01	75.73±0.29	61.93±5.16	62.30±5.03	59.00±1.31	67.56±2.23	
14:00-15:01	112.80±1.49	67.10±6.78	73.00±2.95	64.16±5.42	67.66±7.35	
16:00-17:01	62.43±2.40	66.40±2.50	55.63±3.36	60.70±6.29	63.53±2.17	
Mean	75.64±1.69	72.28±4.00	65.01±4.29	63.73±4.16	66.87±3.86	
08:00-09:01	74.60±2.64	69.73±4.13	76.8±6.84	74.26±3.70	72.70±3.12	B Block
10:00-11:01	77.06±5.04	77.13±4.31	76.9±4.55	71.63±1.50	75.13±0.64	
12:00-13:01	76.00±1.48	74.26±12.73	74.53±2.94	70.63±2.51	76.53±3.69	
14:00-15:01	81.33±7.91	81.66±10.27	71.90±7.35	72.66±3.07	75.00±1.14	
16:00-17:01	64.86±4.74	61.66±3.32	63.16±6.15	59.50±0.62	64.86±4.31	
Mean	74.77±4.36	72.88±6.95	72.65±5.57	69.73±11.40	72.84±2.58	
08:00-09:01	72.64±3.59	72.15±3.07	69.42±4.11	69.56±3.85	68.96±1.72	C Block
10:00-11:01	70.43±6.25	73.75±2.31	71.75±0.70	71.03±6.33	69.03±3.88	
12:00-13:01	51.76±5.47	61.24±3.30	63.73± 5.79	67.34±40.04	59.56±34.62	
14:00-15:01	71.55±3.91	70.25±2.27	70.99± 5.06	71.09±5.42	70.39±1.17	
16:00-17:01	41.36±35.59	44.24±37.53	52.78±37.07	42.07±36.85	42.20±35.26	
Mean	61.54±10.96	64.37±9.70	65.73±10.56	64.218±12.50	62.02±15.33	
08:00-09:01	73.43±3.63	73.10±3.01	74.30±3.81	74.23±8.21	71.00±2.40	D Block
10:00-11:01	71.97±0.80	53.40±4.12	74.80±2.49	78.00±0.75	71.70±2.34	
12:00-13:01	72.27±1.48	68.27±7.23	76.60±5.40	68.07±5.77	72.20±3.13	
14:00-15:01	70.07±3.18	70.43±0.55	75.40±0.77	73.67±3.62	73.40±0.75	
16:00-17:01	66.93±5.38	93.25±1.60	67.37±7.77	78.83±10.12	71.07±2.16	
Mean	70.91±2.89	69.67±3.30	73.69±16.76	73.00±5.70	71.85±2.16	
08:00-09:01	72.46±2.89	69.33±0.51	69.53±2.90	68.6±2.27	71.56±6.40	E Block
10:00-11:01	75.16±0.66	75.16±5.25	75.63±4.98	76.13±2.60	74.7±1.64	
12:00-13:01	68.36±7.31	77.8±5.65	70.66±2.49	68.53±4.53	76.46±3.70	
14:00-15:01	76.56±2.25	75.8±4.57	78.86±9.60	70.06±0.32	75±1.13	
16:00-17:01	63.53±1.90	65.13±6.75	65.23±3.98	63.1±5.89	58.86±1.70	
Mean	71.21±6.42	72.64±5.55	71.98±4.79	69.28±3.12	71.31±2.90	

Table 4. The equivalent noise level calculated for the ground floor and minus the first-floor corridors (dBA)

Corridors/Days	Monday	Tuesday	Wednesday	Thursday	Friday	Mean
Corridor A	31.03	29.27	28.39	27.39	29.38	29.09
Corridor B	50.68	43.87	47.74	41.48	44.00	45.55
Corridor C	43.08	44.36	47.72	46.51	43.54	45.04
Corridor D	45.77	46.80	47.12	41.58	43.30	44.91
Corridor E	40.06	42.37	39.90	41.30	43.33	41.39
Minus the first floor*	41.57	42.80	43.68	47.80	32.99	41.80

*The corridor of the radiology polyclinic

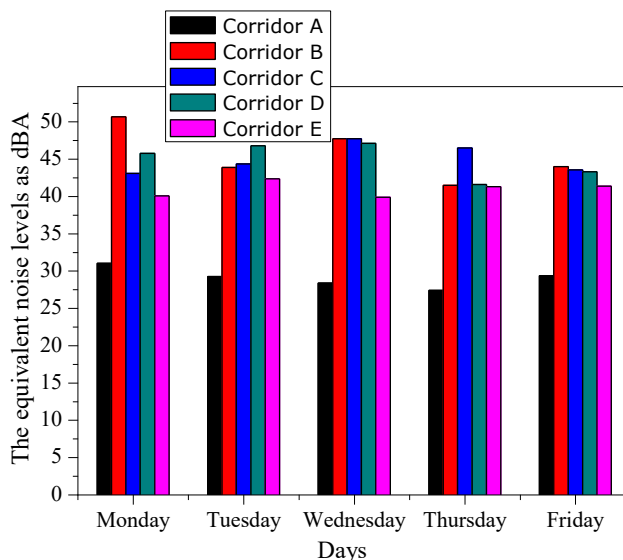


Figure 3. Variation of equivalent noise level calculated as dBA for ground floor corridors according to days

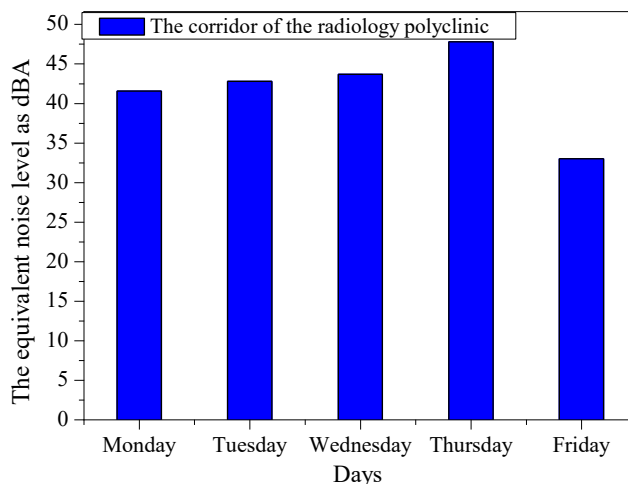


Figure 4. Variation of the equivalent noise level calculated in dBA for the corridor of the radiology polyclinic on the minus first floor, according to days

As seen from Table 5 and Figure 5, in the calculations made for the corridors on the first floor, the highest equivalent noise level was calculated as 44.38 dBA on Tuesday in corridor A, 47.22 dBA on Monday in corridor B, 53.57 dBA on Monday in corridor C and 46.80 dBA on Thursday in corridor D. Similarly, again, in the calculations made for the corridors on the

first floor, the smallest equivalent noise level was calculated as 34.68 dBA on Monday and Friday in corridor A, 38.70 dBA on Friday in corridor B, 44.90 dBA on Friday in corridor C and 36.92dBA on Friday in corridor D. The average equivalent noise levels for these corridors was calculated as 39.18 dBA for A corridor, 43.09 dBA for B corridor, 48.60 dBA for corridor C and 43.27 dBA for corridor D, respectively. As seen from Table 5, the value of the equivalent noise level calculated for all of the other days, except for Monday and Friday, in corridor A on the first floor is bigger than the 35 dBA limit value. The value of the equivalent noise level calculated for all days in B, C and D corridors on the first floor are greater than the 35 dBA limit value. In addition, to determine the average equivalent noise level of each floor, when take the average of all corridors on each floor, the mean equivalent noise levels were calculated as 41.80 dBA for minus the first floor (radiology corridor), 41.20 dBA for the ground floor and 43.54 dBA for the first floor, respectively. All of these calculated values are bigger than the 35 dBA limit value determined by national and international institutions and organizations.

Table 5. The equivalent noise level calculated for first-floor corridors (dBA)

Corridors/Days	Monday	Tuesday	Wednesday	Thursday	Friday	Mean
Corridor A	34.68	44.38	40.00	42.18	34.68	39.18
Corridor B	47.22	43.41	42.40	43.70	38.70	43.09
Corridor C	53.57	46.03	47.18	51.27	44.90	48.60
Corridor D	41.70	44.80	46.12	46.80	36.92	43.27

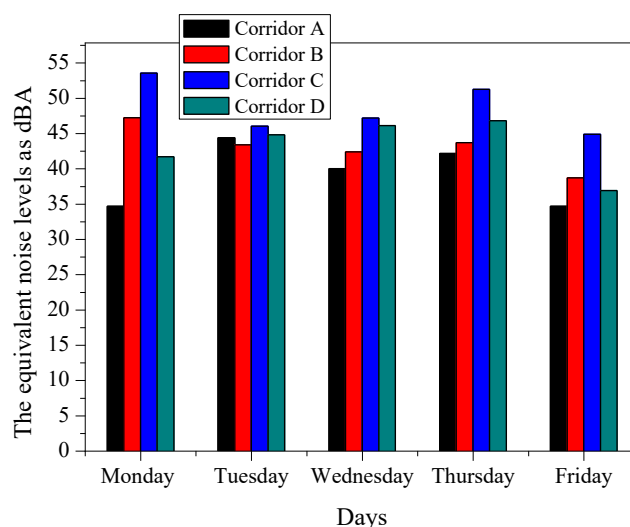


Figure 5. Variation of equivalent noise level calculated as dBA for the first floor corridors according to days.

As seen from Table 6 and Figure 6, the percentage of noise dose was also calculated for the ground floor corridors where sound intensity measurement was made. The highest noise dose percentage calculated for corridors on the ground floor was 0.00% for corridor A, 0.23% for corridor B, 0.12% for corridor C, 0.10% for corridor D and 0.03% for corridor E, respectively. As seen from Table 6 and Figure 7, the maximum percentage of noise dose

calculated according to the measured data in the corridor of the radiology outpatient clinic on the minus first floor is 0.12.

Table 6. The calculated the percentage of noise dose for the ground floor and minus the first-floor corridors

Corridors/Days	Monday	Tuesday	Wednesday	Thursday	Friday
Corridor A	0.00	0.00	0.00	0.00	0.00
Corridor B	0.23	0.05	0.12	0.13	0.05
Corridor C	0.05	0.05	0.12	0.09	0.05
Corridor D	0.07	0.10	0.10	0.03	0.04
Corridor E	0.02	0.03	0.02	0.03	0.02
The minus the first floor*	0.03	0.04	0.05	0.12	0.00

*The corridor of the radiology polyclinic

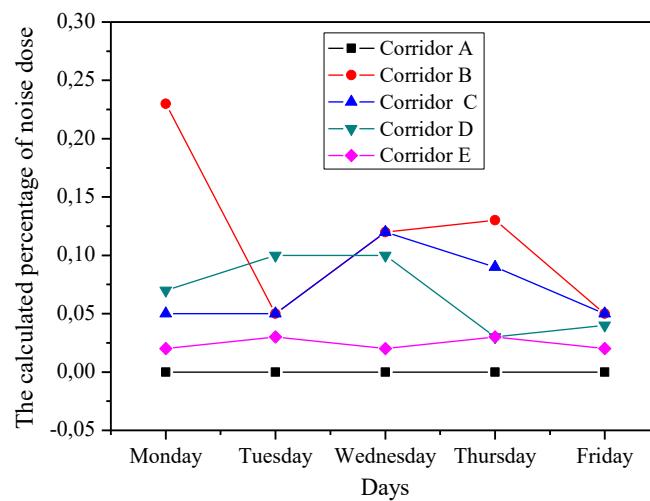


Figure 6. The variation of the calculated percentage of noise dose for the ground floor corridors according to days

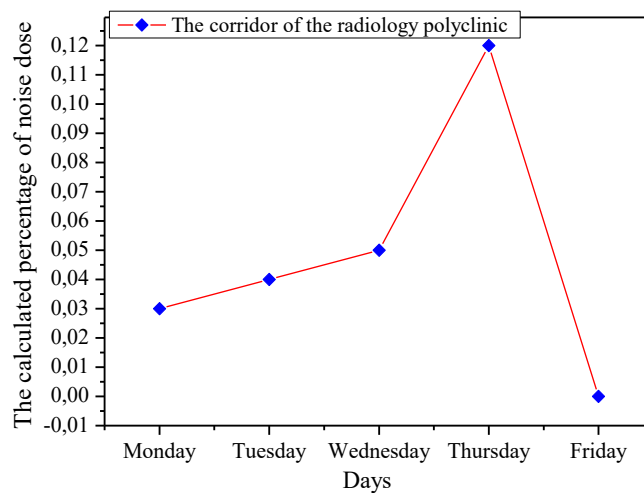


Figure 7. The variation of the calculated percentage of noise dose for the minus the first floor (the corridor of radiology polyclinic) corridors according to days.

As seen from Table 7 and Figure 8, the highest noise dose percentage calculated for the first-floor corridors was 0.06 for corridor A, 0.11 for corridor B, 0.04 for corridor C and 0.08 for corridor D, respectively. As seen from Table 6 and Figure 8, in the radiology polyclinic corridor on the minus first floor, the highest noise dose percentage was calculated as 0.12 on Thursday, and the lowest noise dose percentage was also 0.00 on Friday.

Table 7. The calculated the percentage of noise dose for the first-floor corridors

Corridors/Days	Monday	Tuesday	Wednesday	Thursday	Friday
Corridor A	0.01	0.06	0.02	0.03	0.02
Corridor B	0.11	0.04	0.03	0.05	0.01
Corridor C	0.04	0.01	0.01	0.03	0.01
Corridor D	0.03	0.06	0.08	0.02	0.01

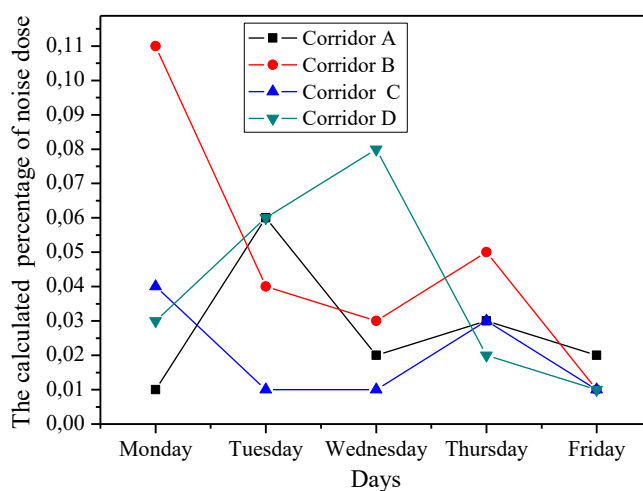


Figure 8. The variation of the calculated the percentage of noise dose for the first floor corridors according to days

The acceptable equivalent noise level (L_{eq}) for health buildings and hospitals was accepted as 35 dBA in the noise control directive of the Ministry of Environment and Forestry of the Republic of Turkey, which was published in the Official Gazette dated 11.12.1986 and numbered 19308. The World Health Organization Guidelines for Community Noise and the National Environmental Standards and Regulations Enforcement Agency have defined the equivalent noise level for indoor and outdoor noise levels in health institutions as 35 and 55 dBA, respectively (Berglund et al., 1999; NESREA, 2007). As seen from Table 4 and Figure 3, the equivalent noise levels calculated for the ground floor corridors vary between 27.39 dBA and 50.68 dBA. Again, as seen from Table 4 and Figure 4, the equivalent noise levels calculated for the minus first-floor corridor vary between 32.99 dBA and 47.80 dBA. As seen from Table 5 and Figure 5, the equivalent noise levels calculated for the first-floor corridors vary also between 34.68 dBA and 53.57 dBA. But, the values of the equivalent noise level calculated for all corridors were generally found to be greater than 35 dBA, which is the acceptable limit value for health facilities (hospitals). Noise pollution in hospitals is an important problem that needs to be solved for both healthcare professionals and patients.

Because the noise ruins performance, and it can be created some physiological responses mediated by the autonomic nervous system (increased heart rate and blood pressure), nausea, headache, argumentativeness, and mood and anxiety changes that can affect the patient-physician relationship (Gültekin et al., 2013). In a study conducted by Tijunelis et al. in 2005, they determined that there is an excessive noise level that can vary and is regular in the emergency room of a hospital. In a study conducted in 2011, it was reported that the noise level in intensive care units and emergency services was above the limit values (Khademi et al., 2011). Mohamed et al., in 2021, have prepared a book chapter titled Noise Pollution and its impact on human health and the environment, and in this chapter they have given very important basic information about sound, noise and the environment. A study was conducted on the noise pollution caused by vehicles in the province of Tokat, Turkiye, and the measurement values were found to be much larger than the limit values in most of the measurement points (Ozer et al., 2009). In a study conducted in Australia in 2021 has been investigated the impact of environmental noise from road traffic, airplanes, trains and industry on mental health and psychological distress by 31,387 participants using a 19-year longitudinal data set. In the study, it was concluded that perceived residential noise has a negative effect on mental health (Li et al., 2022). According to the findings of the World Health Organization (WHO), noise pollution is the second biggest environmental problem for human health after air pollution. Because the World Health Organization defines the state of being healthy as a state of complete physical, mental and social well-being in the absence of disease or infirmity. The noise should be considered an environmental pollutant that negatively affects human health and should be evaluated accordingly. Regarding its properties, it should be classified as a physical and atmospheric pollutant. The noise can harm human health and well-being; adversely can affect ecosystems and ecological services. With this, when long-term exposure to noise pollution can also occurs serious health problems such as hearing impairment, cardiovascular diseases, sleep disorders and negative social behaviours. Extreme emerged noise in hospitals reduces the intelligibility of speech, disrupts communication, causing discomfort, irritation, and tiredness, and reduces the quality and safety of healthcare services. In addition, it has been reported to play a role in the development of intensive care psychosis (mental balance disorder), stress caused by hospitalization, increased pain sensitivity, high blood pressure, and poor mental health (Xyrichis et al., 2018; Grumet,1993; Choiniere, 2010; Buxton et al., 2012).

Conclusions

This study was carried out to determine the noise level in the outpatient clinic corridors of the KSU Medical Faculty Hospital and to raise awareness about the negative effects of noise on human health. As seen in Table 2, the average sound intensity level measured on the first floor was calculated as 71.61 dBA. The average sound intensity measured on the minus first floor, that is, in the corridor where the radiology outpatient clinic is located, was calculated as 71.66 dBA. As can be seen from Table 3, the average sound intensity measured on the ground floor was also calculated as 69.72 dBA. As can be seen from Table 4, while the average equivalent noise level of the ground floor was calculated as 41.20 dBA, the average equivalent noise level of the radiology polyclinic corridor, that is, minus the first-floor, was

calculated as 41.80 dBA. As can be seen from Table 5, the average equivalent noise level of the first floor was calculated as 43.54 dBA. As a result, the measured sound intensity level and the calculated equivalent noise level in approximately all corridors and floors of the KSU Medical Faculty hospital are above the limit value of 35 dBA.

As can be seen in Tables 6 and 7, on average, the noise dose percentage-calculated for the floors is 0.057 for the ground floor, 0.048 for minus the first floor (the corridor of the radiology outpatient clinic), and 0.034 for the first floor. As a result, since the acceptable noise dose percentage is $D \leq 1$, it can be seen that the values of all corridors and days meet this condition and the noise dose in all the areas is not exceeded. But, since the calculated total noise dose percentage in the ground floor corridors is 1.40, it is greater than the limit value of $D \leq 1$. For all that, the percentages of the total noise dose calculated for the corridors on the other floor are less than the limit value of $D \leq 1$.

Noise pollution is an intense, common anthropogenic discomfort that can have highly damaging effects on natural populations, societies and ecosystems around the world. Therefore, research on noise and its health effects should be done locally and solutions should be made locally. That is, it should be investigated by considering where (such as educational institutions, business environment, health institutions and so on) and in which groups the noise is effective. In particular, the building standards and public-policies should focus on both reinforcing areas with weak noise profiles and having consistent and stable standards for urban planning and substructure design (Li et al., 2022). The noise levels above the standard values defined by national and international organizations can seriously affect the treatment of patients and the quality of staff services. For this reason, noise reduction measures should be taken in corridors and even floors where the noise levels are above the limit values. For this, first of all, devices and instruments with low noise levels should be purchased to reduce noise levels in Hospitals. Secondly, if possible, only one polyclinic should be left in the corridors on the hospital floors instead of more than one. Thus, since the patient density in the corridors is reduced, human-induced noise is reduced. Thirdly, the hospital building should be built to absorb sound waves, especially when constructing corridor walls and ceilings. In conclusion, a multidisciplinary approach should be applied to hospital management, academic, administrative, and all other ancillary services along with all personnel in order to reduce noise in the hospital in general.

Ethics in Publishing

This study was planned as a master's thesis in 2019, and since the measurements will take about three months, ethics committee approval was obtained from the institutional ethics committee (dated: 12/03/2019, number: E.10619 and decision no:2019-3).

Author Contributions

The authors did not declare any contribution.

Acknowledgment

This research was supported by Kahramanmaraş Sütçü İmam University (KSU) Scientific Research Projects Coordination Unit (Project No: 2019/2-1 YLS), and the authors thank KSU BAP unit for this support.

References

- Buxton OM, Ellenbogen JM, Wang W, Carballeira A, O'Connor S, Cooper D, Gordhandas AJ, McKinney SM, Solet JM, 2012. Sleep disruption due to hospital noises: a prospective evaluation. *Ann Intern Med* 157: 170-9.
- Basner M, Babisch W, Davis A, Brink M, Clark C, Janssen S, and Stansfeld S, 2014. Auditory and non-auditory effects of noise on health. *The Lancet* 383(9925): 1325-1332.
- Berglund B, Lindvall T, Schwela DH, (1999) Guidelines for community Noise. Participant list of The WHO expert task force meeting on guidelines for community noise, 26-30 April, MARC, London, UK.
- Choiniere DB, 2010. The effects of hospital noise. *Nursing Administration Quarterly* 34: 327-33.
- Cantrell RW, 1975. The Effects of Noise Exposure', AGARD Conference Proceedings No. 171, Effects of Long Duration Noise Exposure on Hearing and Health, NATO.
- Connelly F, Hall ML, Johnsson R.D, Elliot-Kerr S, Dow BR, Lesku JA, Mulder RA, 2022. Noise caused by human activity is rapidly changing Earth's natural soundscapes, *Animal Behaviour* 188: 35-44.
- Gültekin E, Develioğlu ÖN N, Yener M, Şenay N, Külekçi M, 2013. Noise Pollution in Different Hospital Polyclinics of İstanbul/Turkey, *Turk Arch Otolaryngol* 51: 101-105.
- Grumet GW, 1993. Pandemonium in the modern hospital. *N Engl J Med* 328: 433-7.
- Field HL, Long JM, 2018. *Sound and Noise In: Introduction to Agricultural Engineering Technology*. Springer, Cham.
- Fyhri A, and Aasvang GM, 2010. Noise, sleep and poor health: Modeling the relationship between road traffic noise and cardiovascular problems. *The Science of the Total Environment* 408(21): 4935-4942.
- Frei P, Mohler E, and Rösli M, 2014. Effect of nocturnal road traffic noise exposure and annoyance on objective and subjective sleep quality. *International Journal of Hygiene and Environmental Health* 217(2-3): 188-195.
- Halperin D, 2014. Environmental noise and sleep disturbances: A threat to health? *Sleep Science* 7(4): 209-212.
- ISO 3382-1, 2009. *Acoustics—Measurement of Room Acoustic Parameters—Part1: Performance Spaces*, International Standard Organization, Geneva, Switzerland. <https://www.iso.org/standard/40979.html>.
- Kara OK, 2011. Determination of voice similarities and differences between siblings using automatic speaker recognition software in forensic voice analysis. Master Thesis. Istanbul University Forensic Medicine Institute. Istanbul. p.96s.

- Khademi G, Roudi M, Farhat AS, Shahabian M, 2011. Noise Pollution in Intensive Care Units and Emergency Wards, *Iranian Journal of Otorhinolaryngology* 23 (4): 141-148.
- Kuttruff H, Mommertz E, 2013. Roomacoustics in: *Handbook of Engineering Acoustics*. Springer 239–267.
- Kight CR and Swaddle JP, 2011. How and why environmental noise impacts animals: An integrative, mechanistic review. *Ecology Letters* 14(10): 1052-1061.
- Mohamed AMO, Paleologos EK, Howari FM, 2021. Pollution Assessment for Sustainable Practices in Applied Sciences and Engineering. Chapter 19 -Noise pollution and its impact on human health and the environment 975-1026.
- Ministry of Environment and Forestry, 2010. Regulation on Evaluation and Management of Environmental Noise. 2002/49/EC/2008. Ankara.
- National Environmental Standards and Regulations Enforcement Agency (NESREA), 2007. No 25, 30 July 2007. http://www.ilo.org/dyn/natlex/natlex4.detail?p_lang=en&p_isn=87618.
- Neitzel R, Filgor B, 2017. Determination of risk of noise-induced hearing loss due to recreational sound: Review. Geneva: World Health Organization.
- NIOSH, 1998. Occupational Noise Exposure Revised Criteria, U.S. Department of Health and Human Services, Public Health Service Centers for Disease Control and Prevention National Institute for Occupational Safety and Health Cincinnati, OH 45226, DHHS (NIOSH) Publication No. 98-126.
- Ozer S, Yilmaz H, Yeşil M, Yeşil P, 2009. Evaluation of noise pollution caused by vehicles in the city of Tokat, Turkey, *Scientific Research and Essay* 4 (11): 1205-1212.
- Peterson APG, 1980. *Handbook of Noise Measurement*, GenRad; 9th edition, ASIN :B000B647H0, p.394.
- Passchier-Vermeer W and Passchier WF, 2000. Noise exposure and public health. *Environmental Health Perspectives* 108(1): 123-131.
- Shannon G, McKenna MF, Angeloni LM, Crooks KR, Fristrup KM, Brown E, Warner KA, Nelson MD, White C, Briggs J, McFarland S, and Wittemyer G, 2016. A synthesis of two decades of research documenting the effects of noise on wildlife. *Biological reviews of the Cambridge Philosophical Society* 91(4): 982-1005
- Shield BM, Dockrell JE, 2003. The effects of noise on children at school: a review, *Building Acoustics* 10(2): 97- 116.
- Tijunelis MA, Fitzsullivan E, Henderson SO, 2005. Noise in the Emergency Department, *The American Journal of Emergency Medicine* 23: 332-5.
- WHO, 2019. Safe listening devices and systems: a WHO-ITU global standard. Geneva: World Health Organization and International Telecommunication Union, 2019. Licence: CC BY-NC-SA 3.0 IGO.
- WHO, 1994. Assessing human health risks of chemicals. Derivation of guidance values for health based exposure limits. World Health Organization, Geneva.
- WHO, 2018. Environmental noise guidelines for the European Region. WHO Regional Office for Europe, UN City, Marmorvej 51 DK-2100 Copenhagen Ø, Denmark.
- Xyrichis A, Wynne J, Mackrill J, Rafferty AM, Carlyle A, 2018. Noise pollution in hospitals, *BMJ* 363, k4808. 10.1136/bmj.k4808.

Chamotte Clay: A Natural Adsorbent for Separation and Preconcentration of Aluminium

Raif İLKTAÇ 

Application and Research Center for Testing and Analysis, University of Ege, 35100 Bornova, İzmir, Türkiye

Received: 25/08/2022, **Revised:** 26/01/2023, **Accepted:** 01/03/2023, **Published:** 31/03/2023

Abstract

The adsorption behavior of aluminium ions on chamotte clay has been studied in this study. Chamotte clay has been used for the first time for determination of trace levels of aluminium in aqueous solutions. Quantitative adsorption and recovery of aluminium were both rapid and reached an equilibrium in 30 minutes. Aluminium was detected based on the formation of the highly fluorescent Al(III)-morin complex. Two linear calibration graphs were obtained in the range of 0.5-10 $\mu\text{g L}^{-1}$ and 10-100 $\mu\text{g L}^{-1}$ with the detection limits of 0.12 $\mu\text{g L}^{-1}$ and 1.12 $\mu\text{g L}^{-1}$, respectively. Chamotte clay was characterized by scanning electron microscope coupled with energy-dispersive X-ray spectroscopy, energy dispersive X-ray fluorescence and X-ray photoelectron spectroscopy techniques. Different isotherm models were evaluated and the results showed that the adsorption study was fitted to Freundlich isotherm and a favorable and multilayer adsorption of aluminium was occurred on the heterogeneous surface of the chamotte clay. Thermodynamic and kinetic parameters of aluminium adsorption were also investigated. Various experimental parameters were optimized and the method has been applied to tap and bottled drinking water samples and quantitative recoveries were obtained. The results demonstrated that the chamotte clay, as a natural clay, was expected to be a promising adsorbent for the determination and preconcentration of the trace levels of analyte in real samples.

Keywords: aluminium, separation, clay, adsorption, fluorescence

Şamot Kili: Alüminyumun Ayrılması ve Önderiştirilmesi için Doğal Bir Adsorban

Öz

Bu çalışmada alüminyum iyonlarının şamot kili üzerine olan adsorpsiyon davranışı incelenmiştir. Şamot kili, sulu çözeltilerde eser miktarda alüminyumun tayini için ilk kez kullanılmıştır. Alüminyumun kantitatif adsorpsiyonu ve geri kazanımı hızlı olup 30 dakikada dengeye ulaşmıştır. Alüminyum, floresan özellik gösteren Al(III)-morin kompleksinin oluşumuna dayalı olarak tespit edilmiştir. Çalışmada, 0.5-10 $\mu\text{g L}^{-1}$ ve 10-100 $\mu\text{g L}^{-1}$ aralığında, sırasıyla 0.12 $\mu\text{g L}^{-1}$ ve 1.12 $\mu\text{g L}^{-1}$ belirlenme sınırları ile iki ayrı lineer kalibrasyon grafiği elde edilmiştir. Şamot kili, taramalı elektron mikroskobu-enerji dağılım spektroskopisi, enerji dağılımlı X-ışını floresans ve X-ışını fotoelektron spektroskopisi teknikleri ile karakterize edilmiştir. Farklı izoterm modelleri incelenmiş ve sonuçlar adsorpsiyonun Freundlich izotermine uyduğunu ve şamot kilinin heterojen yüzeyinde alüminyumun çok katmanlı adsorpsiyonunun gerçekleştiğini göstermiştir. Alüminyum adsorpsiyonuna ilişkin termodinamik ve kinetik parametreler de incelenmiştir. Çeşitli deneysel parametreler optimize edilmiş ve yöntem musluk ve şişelenmiş içme suyu numunelerine uygulanmış ve nicel geri kazanımlar elde edilmiştir. Sonuçlar, doğal bir kil olarak şamot kilinin, gerçek örneklerde eser miktarda analitin belirlenmesi ve önderiştirilmesi için umut verici bir adsorban olmasının beklendiğini göstermiştir.

Anahtar Kelimeler: alüminyum, ayırma, kil, adsorpsiyon, floresans

1. Introduction

Aluminium is the most abundant metal and the third most abundant element after oxygen and silicon in the Earth's crust [1,2]. Aluminium has a wide range of applications such as food packaging and drinking materials, electrical wires and metal equipments, construction and machinery [3,4]. The excessive use of aluminium has resulted in contamination of food, environmental or biological samples. Aluminium mainly enters the human body through the consumption of food and water [5] whereas WHO set the tolerable value of aluminium in drinking water to 0.2 mg L^{-1} [6]. Studies over the last decade reveal that aluminium accumulates in internal organs and excessive levels can cause harmful effects to lungs and kidneys [7,8]. Parkinson's and Alzheimer's diseases are also linked to overdose of aluminium in the human body [9-11]. Thus, separation and quantitative determination of trace levels of aluminium in aqueous samples is crucial.

Several instrumental methods including atomic absorption spectrometry (AAS) [12] inductively coupled plasma-mass spectrometry (ICP-MS) [13] and inductively coupled plasma atomic emission spectrometry (ICP-AES) [14] have been used for the determination of aluminium in different types of samples. Aluminium can also be determined by electrochemical [15] and spectroscopic methods such as spectrophotometry [16] and spectrofluorimetry [17].

Fluorimetric sensing systems have been widely used for the determination of different metal ions due to their high sensitivity, selectivity, rapidity and simplicity [18,19]. Highly sensitive fluorimetric analysis of aluminium is mainly based on the formation of fluorescent complexes with different reagents including morin [20,21], lumogallion [22], 8-hydroxyquinoline [23] and different Schiff bases synthesized in the laboratory [24,25]. However, determination of trace levels of analyte in real samples is very difficult due to matrix effects and the lack of detection limits of instruments. Therefore, preconcentration of aluminium before its determination is essential and necessary.

Numerous of organic and inorganic adsorbents have been used for the separation and preconcentration of metal ions [26-29]. Especially over the last decade, natural adsorbents have been widely used in metal ion analysis [30,31]. Among the natural adsorbents, different types of natural clay are attracting attention, for their non-toxicity, stability, low-cost and abundance [32]. Kaolinite [33,34], montmorillonite [35,36], vermiculite [37] and bentonite [38-39] are some of the natural clays which were used as adsorbents for the separation and detection of different metal ions. In the literature, it was reported that chamotte clay was used for the palm kernel biodiesel purification [40] and adsorption of lead(II) [41]. However, to the best of my knowledge, a method based on the usage of chamotte clay for separation, preconcentration and determination of aluminium has not been proposed yet.

This study focuses on the development of a method based on the preconcentration and determination of aluminium using chamotte clay. Chamotte clay was used in this study for the first time for separation and determination of aluminium in aqueous samples. Separation and preconcentration of aluminium with the usage of chamotte clay was combined with spectrofluorimetric detection based on the highly fluorescent aluminium(III)-morin complex

which provides high sensitivity for the detection of aluminium. The adsorbent was characterized using energy dispersive X-ray fluorescence spectroscopy (EDXRF), scanning electron microscopy-energy dispersive X-ray spectroscopy (SEM-EDX) and X-ray photoelectron spectroscopy (XPS). Kinetics and the thermodynamic parameters of the adsorption were also evaluated. Various experimental parameters were optimized and the developed method has been successfully applied to aqueous samples for determination of trace levels of aluminium.

2. Materials and Methods

2.1. Materials

$\text{Al}(\text{NO})_3 \cdot 9\text{H}_2\text{O}$, $\text{FeCl}_2 \cdot 4\text{H}_2\text{O}$, $\text{FeCl}_3 \cdot 6\text{H}_2\text{O}$, HCl, HNO_3 , CH_3COOH , NaOH and absolute ethanol were purchased from Merck (St. Louis, MO, USA). Chamotte clay was obtained from a local company (Desmark, Izmir, Turkey). Morin hydrate were purchased from Fluka (Portland, OR, USA). Ultrapure water was used in all studies (Millipore, Bedford, MA, USA).

1000 mg L⁻¹ stock standard solution of aluminium was prepared by dissolving the appropriate amount of $\text{Al}(\text{NO})_3 \cdot 9\text{H}_2\text{O}$ in 10 mL ultrapure water. 100 mg L⁻¹ morin solution was prepared by dissolving appropriate amount of morin hydrate in 50 mL absolute ethanol. Working standard solutions were prepared daily by diluting the stock standard solution with ultrapure water. All solutions were stored at 4°C in refrigerator.

2.2. Instrumentation

Fluorimetric determination of aluminium was carried out with a RF-5301 PC spectrofluorometer (Shimadzu, Japan). Energy dispersive X-ray fluorescence (EDXRF) spectrometer was used for determining the elemental composition of chamotte clay (Rigaku, Japan). Apreo S LoVac model scanning electron microscope (SEM) coupled with energy-dispersive X-ray spectroscopy (EDX) was used for determining the morphology and elemental analysis of the adsorbent (Thermoscientific, USA). For SEM analysis, the sample surfaces were coated with gold and the surface was made conductive under vacuum. SEM images were taken at different magnification rates with an acceleration voltage of 20 kV. X-ray photoelectron spectra (XPS) were recorded on a Thermo Scientific K-alpha X-ray photoelectron spectrometer (ThermoFisher, E. Grinstead, UK). A AV264 model balance was used for weight measurements (Ohaus, USA). pH meter was used for measuring and adjusting the pH of the solutions (Hanna Instruments, Woonsocket, RI, USA). All experiments were carried out in a shaking incubator (Wisd Laboratory Instruments, Wertheim, Germany) at a shaking speed of 150 rpm. Sigma 3 - 18 KS model centrifuge was used for the separation of the phases (Sigma, Germany). Visual Minteq program version 3.0 (Stockholm, Sweden) was used for the determination of the dominant chemical form of aluminium.

2.3. Adsorption and recovery procedures for aluminium

For adsorption of aluminium, 5 mL, 1 mg L⁻¹ aluminium solution in ultrapure water (with pH values in the range of 2.0-10.0) was added onto 25 mg of chamotte clay. The mixture was

shaken for 30 minutes at 25°C. After adsorption, chamotte clay was separated from the solution by centrifuging at 10,000 rpm for 5 minutes and aluminium in the solution was measured with spectrofluorometer.

For recovery of aluminium, in the first step, adsorption procedure was applied as explained above. HCl, HNO₃ and CH₃COOH with the concentrations of 0.1, 0.5 and 1 mol L⁻¹ were used for determining the quantitative recovery of the analyte. However, unexpectedly high signal was measured in 1 mol L⁻¹ acidic medium, possibly due to the partial dissolution of the clay. 0.1 mol L⁻¹ HCl supplies the highest recovery value and selected as the recovery agent. Thus, after adsorption, separation of chamotte clay was performed and 5 mL, 0.1 mol L⁻¹ HCl was added onto adsorbent and shaken for 30 minutes for recovery of the adsorbed aluminium. Aluminium in the solution was measured with spectrofluorometer.

2.4. Fluorimetric determination of aluminium

Fluorimetric determination of aluminium was based on the formation of the highly fluorescent Al(III)-morin complex. In order to obtain the highly fluorescent compound, firstly, pH of Al(III) solution was adjusted to 3.5 with HCl-NaOH. Then, 0.8 mL of 100 mg L⁻¹ morin solution was added onto 2.5 mL of Al(III) solution and the solution was diluted to 5 mL with absolute ethanol. The emission spectra of the solutions were recorded after 15 minutes in the wavelength range from 440 nm up to 600 nm, using 420 nm as the excitation wavelength and 498 nm as the maximum emission wavelength. Fluorescence spectrum of Al(III)-morin complex is shown in Fig. S1.

3. Results and Discussion

3.1. Characterization of chamotte clay

Chamotte clay was characterized with XPS, SEM-EDX and EDXRF analysis. As shown in the SEM image in Fig. 1, chamotte clay has a porous layered structure with irregular shapes and various sizes. Elemental composition of chamotte clay was determined using XPS, EDXRF and EDX. XPS gives the atomic percentage, EDXRF gives the weight percentage and EDX gives both of the data for the amount of the elements. EDX analysis gathers the chemical information that refers to the surface of the material and may differ from the original bulk composition. However, the similar values were obtained from the analyses and the results are shown in Table 1. Only for XPS analysis, carbon was detected on the surface of the adsorbent which may be due to the atmospheric contamination [42]. According to the results, chamotte clay was mainly composed of Si, Al and O which were attributed to SiO₂ and Al₂O₃ with the trace amounts of Fe, Ca, Ti, Mg, Na and K.

Table 1. Elemental composition of chamotte clay.

Method	Al	Si	O	Fe	Ca	Ti	Mg	Na	K
EDXRF (weight %)	5.1	22.3	70.2	0.8	0.3	0.5	0.2	-	0.7
XPS (atomic %)	12.8	18.5	58.6	0.4	0.4	0.1	0.7	0.3	0.5
EDX (atomic- weight %)	12.3-8.8	26.9-18.5	58.6-70.7	0.7-0.3	0.2-0.1	0.2-0.1	0.8-0.6	0.7-0.6	0.9-0.5

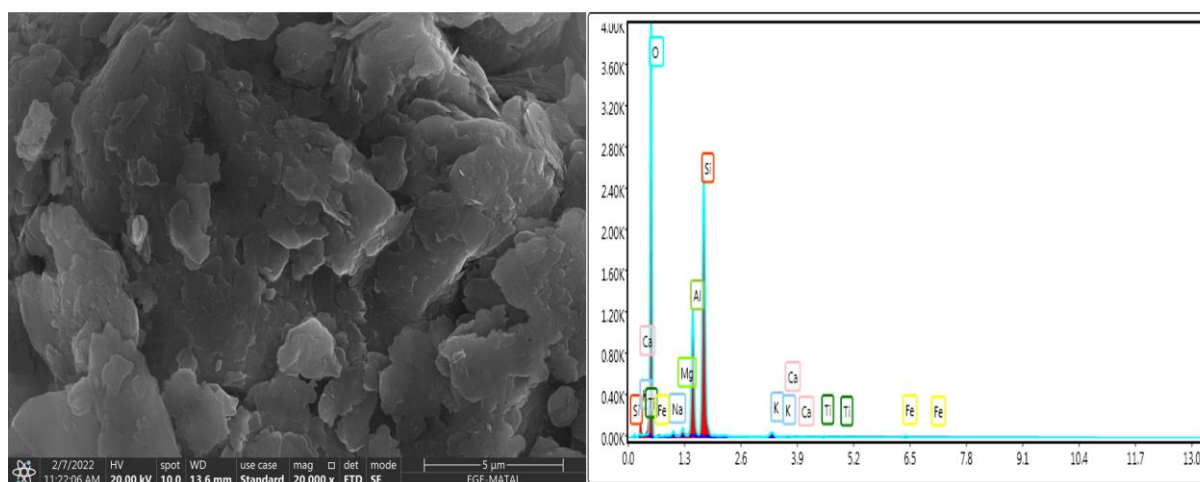


Figure 1. SEM-EDX analysis of chamotte clay (applied voltage: 20 kV, working distance: 13.6 mm, magnification: 20000x).

3.2 Effect of initial pH on the adsorption of Aluminium

The efficiency of aluminium adsorption was affected by the initial pH of the solution as pH not only determines the surface charge of the sorbent but also influences chemical speciation in the solution. In order to investigate the effect of pH on the adsorption efficiency of aluminium, the pH of the water solutions were adjusted in the range of 2.0 to 10.0 using hydrochloric acid (HCl) or sodium hydroxide (NaOH) solutions at various concentrations. As shown in Fig. 2, the maximum adsorption efficiency for Al(III) was observed at pH 7.5. At lower pH values (pH<4, acidic pH values), the adsorption efficiency decreases due to the competitive sorption with proton ions. With increasing pH (4<pH<7), the amount of proton ions decreases which favours the adsorption of aluminium ions. In higher pH values (pH>8), aluminium not only exists in the form of hydroxides which may precipitate depending its concentration but also exists ions with negative charge which cause an electronic repulsion with the adsorbent which has a negative surface charge as stated below. Thus, in alkaline pH values, there is a decrease

in the adsorption efficiency. Using the Visual Minteq software, it was found that the dominant chemical form of aluminium at pH 7.5 is $\text{Al}(\text{OH})_4^-$. Thus, it was concluded that the quantitative adsorption of aluminium at pH 7.5 can be proceeded in the form of $\text{Al}(\text{OH})_4^-$.

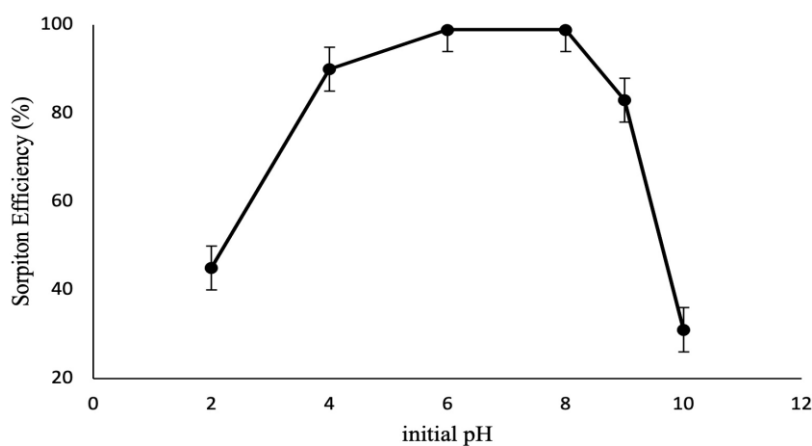


Figure 2. Effect of initial pH on aluminium adsorption (amount of clay: 25 mg, sample volume: 5 mL, initial aluminium(III) concentration: 1 mg L^{-1} , contact time: 30 minutes, pH: 2-10).

The surface charge of the adsorbent was also investigated to identify the sorption mechanism of aluminium. The pH of the point of zero charge (pH_{pzc}) of chamotte clay was determined using the pH drift method [43]. As stated in the literature [44], the point of zero charge (pH_{pzc}) can be defined as the pH of the solution at which charge of the positive surface sites is equal to that of the negative ones, thus, the sorbent surface charge has zero value. The surface charge is negative at $\text{pH} > \text{pH}_{\text{pzc}}$ and positive at $\text{pH} < \text{pH}_{\text{pzc}}$ [45].

For the determination of pH_{pzc} , the pH of a solution of 0.01 M NaCl was adjusted in the range of 2-12 with the addition of either HCl or NaOH. The initial and final pH (after 24 h) values were recorded and the graph of final pH versus initial pH was used to determine the point at which the initial pH and final pH values were equal which was taken as pH_{pzc} . The Fig. S2 shows the pH_{pzc} of the chamotte clay determined with the pH drift method. As shown from the Fig. S2, the pH_{pzc} of the chamotte clay was determined as 7.8. In acidic pH values, both dominant species of aluminium and chamotte clay has a positive charge and in alkaline pH values ($\text{pH} > 8$) both dominant species of aluminium and chamotte clay has a negative charge, for both cases, an electronic repulsion occurs and adsorption efficiency decreases. However, for pH between 7 and 7.8, dominant species of aluminium, $\text{Al}(\text{OH})_4^-$, is negatively charged and chamotte clay is positively charged thus, attractive interaction occurs and adsorption efficiency increases and reaches its maximum. Thus, pH 7.5 was selected as the optimum pH for the determination and preconcentration of trace levels of aluminium.

3.3 Effect of time on adsorption and recovery of aluminium

Contact time is an important parameter that affects the diffusion of metal ions onto adsorbent which determines the sorption/removal efficiency and recovery values.

Fig. 3 shows the effect of time on adsorption and recovery of aluminium. According to Fig. 3, quantitative adsorption and recovery of aluminium were both rapid and reached an equilibrium in 30 minutes. It can be concluded that the rapid adsorption was observed due to the abundant availability of the active sites on the surface of the chamotte clay.

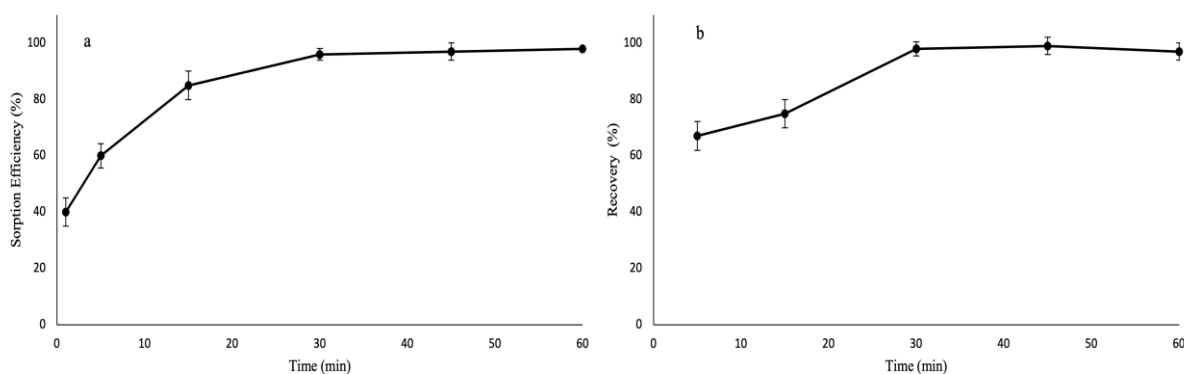


Figure 3. Effect of time on a) adsorption and b) recovery (amount of clay: 25 mg, sample volume: 5 mL, time: 0-60 minutes).

3.4 Effect of adsorbent dosage

In order to ensure the quantitative adsorption of aluminium in different sample volumes, usage of the minimum adsorbent dosage is very important. As shown in Fig. 4, 5 g L⁻¹ is the required adsorbent dosage for the quantitative adsorption of aluminium. It can be concluded that the number of active sites increases as the amount of clay increases up to 5 g L⁻¹ which supplies an increase in the adsorption efficiency. Increasing the adsorbent dosage had no effect on adsorption efficiency above 5 g L⁻¹ and in order to use the minimum amount of sorbent and provide more economical method 5 g L⁻¹ was used in the study.

Table 2. Isotherm models for aluminium adsorption.

Adsorption model	Equation	Parameters of the Equation
Freundlich	$\ln q_e = \ln K_F + \frac{1}{n} \ln C_e$	$K_F = 0.53 \text{ mg g}^{-1}$ $n = 2.64$ $R^2 = 0.9917$
Langmuir	$\frac{C_e}{q_e} = \frac{1}{K_L Q_m} + \frac{C_e}{Q_m}$	$Q_m = 2.66 \text{ mg g}^{-1}$ $K_L = 0.13 \text{ L mg}^{-1}$ $R^2 = 0.9323$
Dubinin–Radushkevich	$\ln q_e = \ln q_m - k\varepsilon^2$ $\varepsilon = (2k)^{-0.5}$	$k = 0.018 \text{ mol}^2 \text{ kJ}^{-2}$ $q_m = 0.00036 \text{ mol g}^{-1}$ $E = 5.24 \text{ kJ mol}^{-1}$ $R^2 = 0.9577$

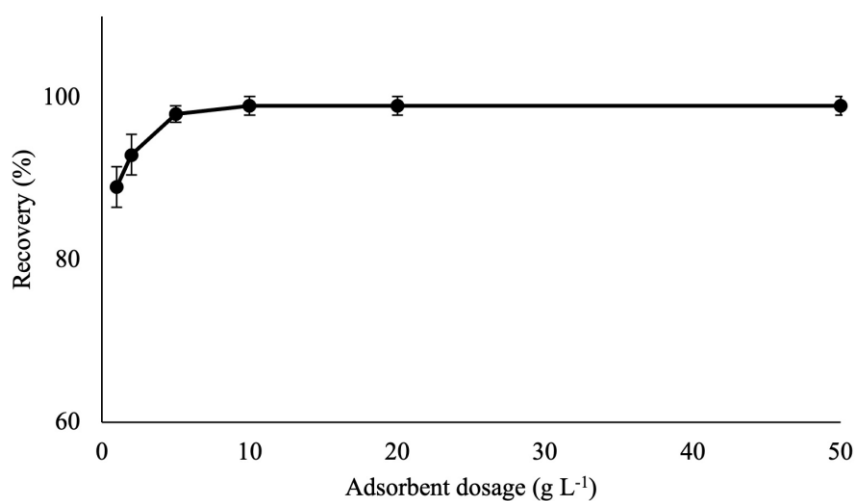


Figure 4. Effect of adsorbent dose (amount of clay: 5-250 mg, sample volume: 5 mL, contact time: 30 minutes, pH: 7.5).

3.5 Sorption isotherm models

The type of the adsorption was determined using Freundlich, Langmuir and Dubinin–Radushkevich (D-R) isotherm models. In order to determine the type of the interaction of the adsorbents with the adsorbate; 10 mg chamotte clay was shaken with 5 mL of various initial concentration of aluminium solution (1-50 mg L⁻¹) in ultrapure water (pH~7.5) for 24 hours. After sorption, clay was separated from the solution with the aid of centrifugation and the amount of aluminium in the solution was determined with spectrofluorometer.

The equations of the isotherm models can be seen at Table 2. In Freundlich isotherm model, q_e is the amount of aluminium adsorbed by the clay (mg g⁻¹), C_e is the equilibrium concentration of aluminium (mg L⁻¹), K_F (mg g⁻¹) and n (dimensionless) are Freundlich constants related to the adsorption capacity and intensity of adsorption, respectively. Freundlich isotherm was obtained by plotting $\ln C_e$ versus $\ln q_e$.

In Langmuir isotherm model, C_e is the equilibrium concentration of aluminium (mg L⁻¹), q_e is the adsorption capacity adsorbed at equilibrium (mg g⁻¹), Q_m is maximum adsorption capacity (mg g⁻¹) and K_L is the Langmuir adsorption constant (L mg⁻¹). Langmuir isotherm was obtained by plotting C_e/q_e versus C_e .

For D-R isotherm model, q_e is the amount of aluminium adsorbed by the clay (mg g⁻¹), q_m is the maximum sorption capacity (mol g⁻¹), k is the activity coefficient related to sorption energy, R is the gas constant (J mol⁻¹K⁻¹), T is the temperature (K), ϵ is the Polanyi potential (mol² J⁻²), C_e is the equilibrium concentration of aluminium (mol L⁻¹) and E is the sorption energy represents the energy required for moving one mole of the solute from infinity to the surface of the adsorbent (kJ mol⁻¹). D-R isotherm was obtained by plotting $\ln q_e$ versus ϵ^2 .

Parameters of the equations were calculated using the slope and intercept of the plots and the results are shown in Table 2. The most suitable isotherm is determined by the correlation coefficient (R^2). The R^2 value closest to 1 indicates the best fit model.

Among the isotherm models, Freundlich isotherm is commonly used to describe the multilayer adsorption and adsorption on heterogeneous surfaces [46-48] whereas Langmuir isotherm represents a monolayer adsorption at specific homogenous sites [49-50]. On the other hand, D-R isotherm both assumes that the adsorption is multilayered and depends on a pore-filling mechanism [51-52]. Considering the correlation coefficients, it can be seen that the sorption process fits to Freundlich isotherm very well. A value of 2.64 obtained for n with the Freundlich isotherm represents that the adsorption is favorable, as it is greater than 1 [53]. Thus, it can be concluded that a favorable and multilayer adsorption of aluminium was occurred on the heterogeneous surface of the chamotte clay.

3.6 Kinetic of aluminium adsorption

10 mL of 5 mg L⁻¹ aluminium solution (pH 7.5) was shaken with 200 mg chamotte clay for different periods of time (from 5 to 1440 min) at 25°C using shaking incubator in order to determine the kinetic parameters of aluminium adsorption. After sorption, clay was separated from the solution using centrifugation and the amount of aluminium in the solution was determined with spectrofluorometer.

The linear pseudo-first-order, pseudo-second-order kinetic and intra-particle diffusion models were applied using the following equations [54,55]:

where q_e is the amount of aluminium adsorbed ($\mu\text{g g}^{-1}$) at equilibrium, q_t is the amount of aluminium adsorbed ($\mu\text{g g}^{-1}$) at time t , k_1 , k_2 and k_{id} are the pseudo-first-order rate constant (min^{-1}), pseudo-second-order rate constant ($\text{g } \mu\text{g}^{-1} \text{ min}^{-1}$) and the intraparticle diffusion rate constant ($\mu\text{g g}^{-1} \text{ min}^{-1/2}$), respectively, t is the time (min) and C ($\mu\text{g g}^{-1}$) represents the boundary layer thickness. Kinetic parameters for the adsorption of aluminium can be shown in Table 3. As shown in Table 3, considering the correlation coefficients, pseudo-second-order model is more suitable to describe the adsorption of aluminium onto chamotte clay. As the adsorption of aluminium fits to pseudo second-order kinetic reaction model, it can be concluded that the chemisorption is the rate-limiting mechanism through sharing or exchange of electrons between adsorbent and adsorbate [56].

$$\log(q_e - q_t) = \log q_e - \frac{k_1}{2.303} t \quad (1)$$

$$\frac{t}{q_t} = \frac{1}{k_2 q_e^2} + \frac{t}{q_e} \quad (2)$$

$$q_t = k_{id} t^{\frac{1}{2}} + C \quad (3)$$

Table 3. Kinetic parameters of different models for the sorption of aluminium.

Kinetic model	Parameters
pseudo-first-order	$q_e = 64.18 \mu\text{g g}^{-1}$ $k_1 = 0.004 \text{ min}^{-1}$ $R^2 = 0.4704$
pseudo-second-order	$q_e = 43.5 \mu\text{g g}^{-1}$ $k_2 = 0.025 \text{ g } \mu\text{g}^{-1} \text{ min}^{-1}$ $R^2 = 0.9996$
intra-particle diffusion	$C = 40.47 \mu\text{g g}^{-1}$ $k_{id} = 0.1995 \mu\text{g g}^{-1} \text{ min}^{-1/2}$ $R^2 = 0.9764$

3.7 Thermodynamics of aluminium adsorption

In order to determine the thermodynamic parameters of the aluminium adsorption, experiments were carried out at three different temperatures. 10 mL of 5 mg L⁻¹ aluminium solution (pH 7.5) was shaken with 200 mg chamotte clay for 30 minutes at 25°C, 35°C and 45°C using temperature controlled shaking incubator. After sorption, chamotte clay was separated from the solution using centrifugation and the amount of aluminium in the solution was determined with spectrofluorometer. Gibbs free energy change (ΔG^0), enthalpy (ΔH^0) and entropy (ΔS^0) were calculated from the following equations [57-58]:

$$\Delta G^0 = -RT \ln K_C, \quad K_C = \frac{C_s}{C_e} \quad (4)$$

$$\ln K_C = \frac{\Delta S^0}{R} - \frac{\Delta H^0}{RT} \quad (5)$$

$$\Delta G^0 = \Delta H^0 - T\Delta S^0 \quad (6)$$

where K_C is the equilibrium constant, C_s is the amount of analyte adsorbed by adsorbent (mg g⁻¹), C_e is the equilibrium concentration of aluminium (mg L⁻¹), R is the gas constant (8.314 J mol⁻¹ K⁻¹) and T is the temperature (K). Parameters change in enthalpy (ΔH^0) and change in entropy (ΔS^0) were calculated from the slope and the intercept of the linear plot of $\ln K_C$ versus $1/T$. The calculated thermodynamic parameters are summarized in Table 4.

As mentioned in the literature, ΔG value lower than 20 kJ mol^{-1} states physical adsorption while values above 40 kJ mol^{-1} indicates the chemical adsorption and the negative values indicate the spontaneous nature of the sorption [59]. Negative ΔH^0 values emphasize that the adsorption is exothermic and the adsorption capacity decreases with an increase in the temperature [60]. If the value of ΔH^0 is lower than 40 kJ mol^{-1} the adsorption process is physisorption while the value is more than 100 kJ mol^{-1} the type of adsorption is chemisorption [61]. A negative ΔS^0 value denotes the decreased randomness at the solid–solution interface during the adsorption process [62]. When the thermodynamic parameters evaluated, it is evaluated that the aluminium adsorption is exothermic due to the negative value of ΔH^0 , spontaneous and favorable due to the negative value of ΔG^0 and the degree of freedom decreased at the liquid-solid interface due to the negative value of ΔS^0 .

Table 4. Thermodynamic parameters for aluminium adsorption.

Temperature (K)	ΔG^0 (kJ mol ⁻¹)	ΔH^0 (kJ mol ⁻¹)	ΔS^0 (kJ mol ⁻¹ K ⁻¹)
298	-6.73	-16.13	-0.03
308	-6.42		
318	-6.10		

3.8 Analytical figures of merit

The aluminium content in the solution was determined via the formation of the highly fluorescent aluminium(III)-morin complex in acidic medium. As stated in the literature [21], the addition of ethanol into aqueous system increases the fluorescence signal of the complex. Two calibration graphs were obtained for two different range of aluminium. Using a slit width of 5 nm, the calibration graph (calibration graph #1) was linear within the range of $0.5\text{-}10 \mu\text{g L}^{-1}$ with an equation of $y = 82993x + 149625$ and a correlation coefficient (R^2) of 0.9991 ($n=3$). When the slit width set to 3 nm, the calibration graph (calibration graph #2) was linear within the range of $10\text{-}100 \mu\text{g L}^{-1}$ with an equation of $y = 9777.5x + 33040$ and a correlation coefficient (R^2) of 0.9971 ($n=3$).

Limit of detection (LOD) and limit of quantification (LOQ) were calculated using the equations;

$$LOD = \frac{\sigma}{S} \times 3 \quad (7)$$

and

$$LOQ = \frac{\sigma}{S} \times 10 \quad (8)$$

where σ is the standard deviation of the responses of the blank solution and S is the slope of the calibration curve [63,64].

For the calibration graph #1, LOD and LOQ were calculated as 0.12 $\mu\text{g L}^{-1}$ and 0.39 $\mu\text{g L}^{-1}$, respectively, whereas LOD and LOQ were calculated as 1.18 $\mu\text{g L}^{-1}$ and 3.95 $\mu\text{g L}^{-1}$, respectively, for the calibration graph #2.

In order to determine the precision of the method, relative standard deviations (RSDs) of intra-day and inter-day precisions of three different concentration levels of aluminium were determined for the obtained calibration graphs. 2.5, 5.0 and 7.5 $\mu\text{g L}^{-1}$ aluminium(III) solutions were used for the precision study for calibration graph #1 where 25, 50 and 75 $\mu\text{g L}^{-1}$ aluminium(III) solutions were used for the precision study for calibration graph #2. The intra-day precision was determined with the five repeated measurements of the samples on the same day and the inter-day precision was determined by measuring the sample once a day for five consecutive days. RSD values of intra-day and inter-day studies were found to be in the range of 0.8 - 1.4 % and 1.2 - 1.5 % for calibration graph #1 and 1.2 - 1.8 % and 1.5 - 2.2 % for calibration graph #2, respectively.

Table 5 summarizes a comparison of the general performance parameters for the published methods used for the determination and preconcentration of aluminium. When the parameters were compared, the developed method based on the preconcentration of aluminium using chamotte clay was expected to be a promising method for the determination and preconcentration of the trace levels of analyte in real samples.

Table 5. Comparison of the analytical performance of published methods with the present work for the determination of aluminium.

Working range	Limit Detection	of	Method	Reference
1–50 $\mu\text{g L}^{-1}$	1.7 $\mu\text{g L}^{-1}$		fabric phase sorptive extraction-high performance liquid chromatography-UV detection	[65]
5-1600 $\mu\text{g L}^{-1}$	1.5 $\mu\text{g L}^{-1}$		graphene oxide modified (4-phenyl) methanethiol nanomagnetic composite-atom trap flame atomic absorption spectrometer	[11]
-	0.2 $\mu\text{g L}^{-1}$		8-hydroxyquinoline–cobalt(II) coprecipitation system- UV–vis spectrophotometry	[66]
27 $\mu\text{g L}^{-1}$ - 270 mg L^{-1}	6.6 $\mu\text{g L}^{-1}$		all-solid-state potentiometric detection	[8]
0.5-10 $\mu\text{g L}^{-1}$ and 10-100 $\mu\text{g L}^{-1}$	0.12 $\mu\text{g L}^{-1}$ and 1.12 $\mu\text{g L}^{-1}$	and	chamotte clay-fluorescence detection	This study

3.9 Reusability of the adsorbent

Reusability of the same chamotte clay was investigated since the reusability of the same adsorbent affects the cost of the developed method. Ten cycles of sorption-recovery procedures were applied to the same adsorbent and according to the recovery values 98.9 ± 1.3 ($n=10$), it was observed that same adsorbent can be used for ten times for the determination of aluminium.

3.10 Interference effects

The interference effects of other cations, such as Na(I), K(I), Mg(II), Ca(II), Co(II), Fe(II), Fe(III), Mn(II), Co(II), Ni(II), Zn(II), Cd(II), and Pb(II) and anions such as chloride, nitrate, sulphate and phosphate on the recovery of aluminium(III) were investigated. The interference effect was studied independently for each of the ions. 5 mL of $10 \mu\text{g L}^{-1}$ aluminium solution

(pH 7.5) with different concentrations of ions was shaken with 25 mg chamotte clay for 30 minutes. After sorption, chamotte clay was separated from the solution using centrifugation and 5 mL 0.1 M HCl was added onto adsorbent and shaken for 30 minutes for recovery of aluminium. Then, the fluorimetric determination procedure was applied. The tolerable ratios of all investigated ions were investigated up to 1 mg L⁻¹ (100-fold) and it was found that the investigated ions did not exhibit any remarkable change (> ±5%) on the recovery of aluminium.

3.11 Analytical application

The developed method was applied to both tap and bottled drinking water samples. Before the analysis, water samples were first filtered through a filter paper. After adjusting the pH values to 7.5, 50 mL of water samples were shaken with 250 mg chamotte clay for 30 minutes for the adsorption of aluminium. After sorption of aluminium, chamotte clay was separated from the solution with centrifugation. 5.0 mL 0.1 M HCl was added onto chamotte clay and shaken for 30 minutes for the recovery of aluminium. After centrifugation, the phases were separated and the pH of the solution was adjusted to 3.5. Then, 0.8 mL of 100 mg L⁻¹ morin solution was added onto 2.5 mL of the solution and the solution was diluted to 5 mL with absolute ethanol. The preconcentration factor for both analyses was 10. The amount of aluminium in the solution was measured with spectrofluorometer ($\lambda_{ex}=420$ nm and $\lambda_{em}=498$ nm). Spike addition was also applied to the samples and the results of the sample applications are shown in Table 6. The quantitative recovery values revealed that the developed method can be applied to aqueous samples for the determination of aluminium.

Table 6. Sample application of the method.

Sample	Added ($\mu\text{g L}^{-1}$)*	Found ($\mu\text{g L}^{-1}$)*	Recovery (%)
Tap water	-	0.39±0.07	-
	10	10.68±0.18	102.82±1.69
	25	25.40±0.56	100.04±2.19
	50	50.87±0.61	100.95±1.21
Bottled drinking water	-	<LOD**	-
	10	9.83±0.25	98.33±2.52
	25	25.03±0.32	100.13±1.29
	50	49.83±1.27	99.67±2.53

*(n=3)

**LOD = Limit of Detection

4. Conclusion

The present work involves the development of a method for determination of aluminium in aqueous samples based on the usage of chamotte clay. Chamotte clay has been used for the first time for determination of trace levels of aluminium. Quantitative adsorption and recovery of aluminium were both rapid and reached an equilibrium in 30 minutes. The adsorption study was fitted to Freundlich isotherm and multilayer adsorption of aluminium was occurred on the heterogeneous surface of the chamotte clay. Thermodynamic parameters revealed that the aluminium adsorption is exothermic, spontaneous and favorable. The method is applied to tap and bottled drinking water samples and the recoveries were found to be in the range of 98.3 and 102.8 %. The preconcentration factor of both analyses was determined as 10 and same adsorbent can be used for ten times for the determination of aluminium. Upon the evaluation of the analytical parameters, the developed method was expected to be a promising method for the determination and preconcentration of the trace levels of analyte in real samples.

Acknowledgment

The author would like to thank Dr. Ece Bayır for her great support and valuable comments on this paper.

Ethics in Publishing

There are no ethical issues regarding the publication of this study.

References

- [1]. Arunakumara, K. K. I. U. Walpola, B. C. Yoon, M. H. (2013) Aluminum toxicity and tolerance mechanism in cereals and legumes – a review. *J. Korean Soc. Appl. Biol. Chem.*, 56, 1–9.
- [2]. Sidqi, M. E. Aziz, A. A. A. Abolehasan, A. E. Sayed, M. A. (2022) Photochemical processing potential of a novel Schiff base as a fluorescent probe for selective monitoring of Al³⁺ ions and bioimaging in human cervical cancer HeLa cells. *J. Photochem. Photobiol.*, 424, 113616.
- [3]. Gupta, V. K. Shoor, S. K. Kumawat, L. K. Jain, A. K. (2015) A highly selective colorimetric and turn-on fluorescent chemosensor based on 1-(2-pyridylazo)-2-naphthol for the detection of aluminium(III) ions. *Sens. Actuators B Chem.*, 209, 15-24.
- [4]. Abbaspour, A. Refahi, M. Khalafinezhad, A. Rad, M. N. S. Behrouz, S. (2010) A selective and sensitive carbon composite coated platinum electrode for aluminium determination in pharmaceutical and mineral water samples. *Anal. Chim. Acta.*, 662, 76–81.
- [5]. Loeschner, K. Correia, M. Chaves, C. L. Rokkjær, I. Sloth, J. J. (2018) Detection and characterisation of aluminium-containing nanoparticles in Chinese noodles by single particle ICP-MS. *Food Addit. Contam. Part A.*, 35, 6-93.

- [6]. WHO, (2011) Aluminium, guidelines for drinking water quality. 4th ed., World Health Organization, Geneva.
- [7]. Kejík, Z. Kapláne, R. Havlík, M. Bříza, T. Vavřinová, D. Dolenský, B. Martásek, P. Král, V. (2016) Aluminium(III) sensing by pyridoxal hydrazone utilising the chelation enhanced fluorescence effect. *J. Lumin.*, 180, 269-277.
- [8]. Ying, K. S. Heng, L. Y. Hassan, N. I. Hasbullah, S. A. (2020) A new and all-solid-state potentiometric aluminium ion sensor for water analysis. *Sensors.*, 20, 6898.
- [9]. Suherman, A. L. Tanner, E. E. L. Kuss, S. Sokolov, S. V. Holter, J. Young, N. P. Compton, R. G. (2018) Voltammetric determination of aluminium(III) at tannic acidcapped-gold nanoparticle modified electrodes. *Sens. Actuators B Chem.*, 265, 682-690.
- [10]. Youssef, H. M. Azzam, M. A. (2021) Efficient removal of aluminium(III) from aqueous solutions via ion-flotation technique using aluminon as a chelating agent and oleic acid as a surfactant. *Int. J. Environ. Anal. Chem.*, 1-18.
- [11]. Shirkhanloo, H. Abbasabadi, M. K. Hosseini, F. Zarandi, A. F. (2021) Nanographene oxide modified phenyl methanethiol nanomagnetic composite for rapid separation of aluminum in wastewaters, foods, and vegetable samples by microwave dispersive magnetic micro solid-phase extraction. *Food Chem.*, 347, 129042.
- [12]. Komarek, J. Cervenka, R. Ruzicka, T. Kuban, T. (2007) ET-AAS determination of aluminium in dialysis concentrates after continuous flow solvent extraction. *J. Pharmaceut. Biomed.*, 45, 504-509.
- [13]. Eroglu, E. I. Gulec, A. Ayaz, A. (2018) Determination of aluminium leaching into various baked meats with different types of foils by ICP-MS. *J. Food Process. Preserv.*, 42, e13771.
- [14]. Samarina, T. O. Volkov, D. S. Mikheev, I. V. Proskurnin, M. A. (2018) High-sensitivity and high-performance determination of trace aluminum in water for pharmaceutical purposes by microwave plasma and inductively coupled plasma-atomic emission spectrometry. *Anal. Lett.*, 51, 659-672.
- [15]. Thomas, S. D. Davey, D. E. Mulcahy, D. E. Chow, C. W. K. (2005) Indirect amperometric detection of aluminium by flow injection analysis using DASA as ligand. *Anal. Lett.*, 38, 133-147.
- [16]. Elečková, L. Alexovič, M. Kuchár, J. Balogh, I. S. Andruch, V. (2015) Visual detection and sequential injection determination of aluminium using acinnamoyl derivative. *Talanta.*, 133, 27-33.
- [17]. Anwar, Z. M. Ibrahim, I. A. Kamel, R. M. Salam, E. T. A. Asfoury, M. H. E. (2018) New highly sensitive and selective fluorescent terbium complex for the detection of aluminium ions. *J. Mol. Struct.*, 1154, 272-279.
- [18]. Kamel, R. M. Sakka, S. S. E. Bahgat, K. Monir, M. R. Soliman, M. H. A. (2021) New turn on fluorimetric sensor for direct detection of ultra-trace ferric ions in industrial wastewater and its application by test strips. *J. Photochem. Photobiol.*, 411, 113218.
- [19]. Pomal, N. C. Bhatt, K. D. Modi, K. M. Desai, A. L. Patel, N. P. Kongor, A. Kolivoška, V. (2021) Functionalized silver nanoparticles as colorimetric and fluorimetric sensor for environmentally toxic mercury ions: an overview. *J. Fluoresc.*, 31, 635-649.

- [20]. Renedo, O. D. Cuñado, A. M. N. Romaya, E. V. Lomillo, M. A. A. (2019) Determination of aluminium using different techniques based on the Al(III)-morin complex. *Talanta.*, 196, 131-136.
- [21]. Mateos, A. A. Parra, M. J. A. Serrano, Y. C. Martín, F. J. R. (2008) Online monitoring of aluminium in drinking water with fluorimetric detection. *J. Fluoresc.*, 18, 183-192.
- [22]. Chu, F. Han, P. Feng, S. Wei, S. Ma, H. Bian, Z. (2021) Hydrogel optical fibers functionalized with lumogallion as aluminum ions sensing platform. *Optik.*, 240, 166875.
- [23]. Yamaguchi, S. Matusi, K. (2016) Formation and entrapment of tris(8-hydroxyquinoline)aluminum from 8-hydroxyquinoline in anodic porous alumina. *Materials.*, 9, 715.
- [24]. Peng, H. Han, Y. Lin, N. Liu, H. (2019) Two pyridine-derived Schiff-bases as turn-on fluorescent sensor for detection of aluminium ion. *Opt. Mater.*, 95, 109210.
- [25]. Samanta, S. Nath, B. Baruah, J. B. (2012) Hydrolytically stable Schiff base as highly sensitive aluminium sensor. *Inorg. Chem. Commun.*, 22, 98-100.
- [26]. Kayan, A. (2019) Inorganic-organic hybrid materials and their adsorbent properties. *Adv. Compos. Mater.*, 2, 34-45.
- [27]. Saltan, F. Saltan, G. M. (2022) Synthesis of a new adsorbent poly(allylisothiocyanate-co- hydroxyethylmethacrylate-co-vinylimidazole) via photopolymerization: Characterization and investigation of heavy metal adsorption capacity. *J. Appl. Polym. Sci.*, 139, e52639.
- [28]. Karimi, F. Ayati, A. Tanhaei, B. Sanati, A. L. Afshar, S. Kardan, A. Dabirifar, Z. Karaman, C. (2022) Removal of metal ions using a new magnetic chitosan nano-bio-adsorbent; A powerful approach in water treatment. *Environ. Res.*, 203, 111753.
- [29]. Usman, M. Ahmed, A. Yu, B. Wang, S. Shen, Y. Cong, H. (2021) Simultaneous adsorption of heavy metals and organic dyes by β -cyclodextrin-chitosan based cross-linked adsorbent. *Carbohydr. Polym.*, 255, 117486.
- [30]. Chakraborty, R. Asthana, A. Singh, A. K. Jain, B. Susan, A. B. H. (2022) Adsorption of heavy metal ions by various low-cost adsorbents: a review. *Int. J. Environ. Anal. Chem.*, 102, 342-379.
- [31]. Sdiri, A. T. Higashi, T. Jamoussi, F. (2014) Adsorption of copper and zinc onto natural clay in single and binary systems. *Int. J. Environ. Sci. Technol.*, 11, 1081-1092.
- [32]. Gu, S. Kang, X. Wang, L. Lichtfouse, E. Wang, C. (2019) Clay mineral adsorbents for heavy metal removal from wastewater: a review. *Environ. Chem. Lett.*, 17, 629-654.
- [33]. Doi, A. Khosravi, M. Ejtemaei, M. Nguyen, T. A. H. Nguyen, A. V. (2020) Specificity and affinity of multivalent ions adsorption to kaolinite surface. *Appl. Clay Sci.*, 190, 105557.
- [34]. Fijałkowska, G. Wiśniewska, M. Karpisz, K. S. (2020) Adsorption and electrokinetic studies in kaolinite/anionic polyacrylamide/chromate ions system. *Colloids Surf. A Physicochem. Eng. Asp.*, 603, 125232.

- [35]. Ijagbemi, C. O. Baek, M. H. Kim, D. S. (2009) Montmorillonite surface properties and sorption characteristics for heavy metal removal from aqueous solutions. *J. Hazard. Mater.*, 1, 538-546.
- [36]. Akpomie, K. G. Dawodu, F. A. (2016) Acid-modified montmorillonite for sorption of heavy metals from automobile effluent. *Beni-Seuf Univ. J. Appl.*, 1, 1-16.
- [37]. Brião, G. D. V. Silva, M. G. C. D. Vieira, M. G. A. (2021) Efficient and selective adsorption of neodymium on expanded vermiculite. *Ind. Eng. Chem. Res.*, 60, 4962-4974.
- [38]. Manohar, D. M. Noeline, B. F. Anirudhan, T. S. (2006) Adsorption performance of Al-pillared bentonite clay for the removal of cobalt(II) from aqueous phase. *Appl. Clay Sci.*, 31, 194-206.
- [39]. Bertagnolli, C. Kleinübing, S. J. Silva, M. G. C. D. (2011) Preparation and characterization of a Brazilian bentonite clay for removal of copper in porous beds. *Appl. Clay Sci.*, 53, 73-79.
- [40]. Santos, F. D. Conceição, L. R. V. D. Ceron, A. Castro, H. F. D. (2017) Chamotte clay as potential low cost adsorbent to be used in the palm kernel biodiesel purification. *Appl. Clay Sci.*, 149, 41-50.
- [41]. Rakhym, A. B. Seilkhanova, G. A. Kurmanbayeva, T. S. (2020) Adsorption of lead (II) ions from water solutions with natural zeolite and chamotte clay. *Mater. Today: Proc.*, 31, 482-485.
- [42]. Nita, C. Fullenwarth, J. Monconduit, L. Meins, J. M. L. Fioux, P. Parmentier, J. Ghimbeu, C. M. (2019) Eco-friendly synthesis of SiO₂ nanoparticles confined in hard carbon: a promising material with unexpected mechanism for Li-ion batteries. *Carbon.*, 143, 598-609.
- [43]. Zhang, Z. Moghaddam, L. O'Hara, I. M. Doherty, W. O. S. (2011) Congo red adsorption by ball-milled sugarcane bagasse. *Chem. Eng. J.*, 178, 122-128.
- [44]. Fiol, N. Villaescusa, I. 2009. Determination of sorbent point zero charge: usefulness in sorption studies. *Environ. Chem. Lett.*, 7, 79-84.
- [45]. Kragović, M. Stojmenović, M. Petrović, J. Loredó, J. Pašalić, S. Nedeljković, A. Ristović, I. (2019) Influence of alginate encapsulation on point of zero charge (pHpzc) and thermodynamic properties of the natural and Fe(III) - modified zeolite. *Procedia Manuf.*, 32, 286-293.
- [46]. Syafiqah, M. S. I. Yussof, H. W. (2018) Kinetics, isotherms, and thermodynamic studies on the adsorption of mercury (II) ion from aqueous solution using modified palm oil fuel ash. *Mater. Today Proc.*, 5, 21690-21697.
- [47]. Ayawei, N. Ebelegi, A. N. Wankasi, D. (2017) Modelling and interpretation of adsorption isotherms. *J. Chem.*, 1-11.
- [48]. Wang, J. Liu, G. Li, T. Zhou, C. (2015) Physicochemical studies toward the removal of Zn(II) and Pb(II) ions through adsorption on montmorillonite-supported zero-valent iron nanoparticles. *RSC Adv.*, 5, 29859-29871.
- [49]. Gai, W. Z. Deng, Z. Y. Shi, Y. (2015) Fluoride removal from water using high-activity aluminum hydroxide prepared by the ultrasonic method. *RSC Adv.*, 5, 84223-84231.

- [50]. Rajahmundry, G. K. Garlapati, C. Kumar, P. S. Alwi, R. S. Vod, D. V. N. (2021) Statistical analysis of adsorption isotherm models and its appropriate selection. *Chemosphere.*, 276, 130176.
- [51]. Nnaji, C. C. Agim, A. E. Mama, C. N. Emenike, P. G. C. Ogarekpe, N. M. (2021) Equilibrium and thermodynamic investigation of biosorption of nickel from water by activated carbon made from palm kernel chaff. *Sci. Rep.*, 11, 7808.
- [52]. Roby, R. B. Gagnon, J. Deschênes, J. S. Chabot, B. (2018) Development and treatment procedure of arsenic-contaminated water using a new and green chitosan sorbent: kinetic, isotherm, thermodynamic and dynamic studies. *Pure Appl. Chem.*, 90, 63-77.
- [53]. Hameed, B. M. (2009) Spent tea leaves: a new non-conventional and low-cost adsorbent for removal of basic dye from aqueous solutions. *J. Hazard. Mater.*, 161, 753-759.
- [54]. Fei, F. Gao, Z. Wu, H. Wurendaodi, W. Zhao, S. Asuha, S. (2020) Facile solid-state synthesis of Fe₃O₄/kaolinite nanocomposites for enhanced dye adsorption. *J. Solid State Chem.*, 291, 121655.
- [55]. Kassimi, A. E. Achour, Y. Himri, M. E. Laamari, M. Haddad, M. E. (2021) High efficiency of natural safiot clay to remove industrial dyes from aqueous media: kinetic, isotherm adsorption and thermodynamic studies. *Biointerface Res. Appl. Chem.*, 11, 12717-12731.
- [56]. Shafey, E. S. I. E. Lawati, H. A. Sumri, A. S. A. (2012) Ciprofloxacin adsorption from aqueous solution onto chemically prepared carbon from date palm leaflets. *J. Environ. Sci.*, 24, 1579-1586.
- [57]. Alorabi, A. Q. Hassan, M. S. Alam, M. M. Zabin, S. A. Alsenani, N. I. Baghdadi, N. E. (2021) Natural clay as a low-cost adsorbent for crystal violet dye removal and antimicrobial activity. *Nanomaterial.*, 11, 2789.
- [58]. Okorie, H. O. C. Ekemezie, P. N. Akpomie, K. G. Olikagu, C. S. (2018) Calcined corncob-kaolinite combo as new sorbent for sequestration of toxic metal ions from polluted aqua media and desorption. *Front. Chem.*, 6, 273.
- [59]. Akinbulumo, O. A. Odejobi, O. J. Odekanle, E. L. (2020) Thermodynamics and adsorption study of the corrosion inhibition of mild steel by Euphorbia heterophylla L. extract in 1.5 M HCl. *Results Mat.*, 5, 10074.
- [60]. Ramesh, A. Lee, D. J. Wong, J. W. C. (2005) Thermodynamic parameters for adsorption equilibrium of heavy metals and dyes from wastewater with low-cost adsorbents. *J. Colloid Interface Sci.*, 291, 588-592.
- [61]. Shukla, S. K. Ebenso, E. E. (2011) Corrosion inhibition, adsorption behavior and thermodynamic properties of streptomycin on mild steel in hydrochloric acid medium. *Int. J. Electrochem. Sci.*, 6, 3277-3291.
- [62]. Sahmoune, M. N. (2019) Evaluation of thermodynamic parameters for adsorption of heavy metals by green adsorbents. *Environ. Chem. Lett.*, 17, 697-704.
- [63]. Chen, L. Liu, J. Zeng, Q. Wang, H. Yu, A. Zhang, H. Ding, L. (2009) Preparation of magnetic molecularly imprinted polymer for the separation of tetracycline antibiotics from egg and tissue samples. *J. Chromatogr. A.*, 1216, 3710-3719.

- [64]. Wang, J. Pan, J. Yin, Y. Wu, R. Dai, X. Dai, J. Gao, L. Ou, H. (2015) Thermo-responsive and magnetic molecularly imprinted Fe₃O₄@ carbon nanospheres for selective adsorption and controlled release of 2,4,5-trichlorophenol. *J. Ind. Eng. Chem.*, 25, 321–328.
- [65]. Rekhi, H. Kaur, R. Rani, S. Malik, A. K. Kabir, A. K. G. (2018) Direct rapid determination of trace aluminum in various water samples with quercetin by reverse phase high-performance liquid chromatography based on fabric phase sorptive extraction technique. *J. Chromatogr. Sci.*, 56, 452-460.
- [66]. Bulut, V. N. Arslan, D. Ozdes, D. Soylak, M. Tufekci, M. (2010) Preconcentration, separation and spectrophotometric determination of aluminium(III) in water samples and dialysis concentrates at trace levels with 8-hydroxyquinoline–cobalt(II) coprecipitation system. *J. Hazard. Mater.*, 182, 331-336.

A Survey on Timelike-Spacelike Involute-Evolute Curve Pair

Mustafa BİLİCİ^{1*}

¹ Department of Mathematics, Ondokuz Mayıs University, Samsun, TURKEY

Received: 12/06/2022, **Revised:** 28/10/2022, **Accepted:** 07/11/2022, **Published:** 31/03/2023

Abstract

This paper concentrates on the requirements of being an integral curve for the geodesic spray of the natural lift curves (n.l.c) of spherical indicatrices of the timelike-spacelike involute-evolute curve pair in Lorentz 3-space. In addition, the obtained results were supported by one example.

Keywords: Involute-evolute curve pair, Lorentz space, geodesic spray, spherical indicatrix, natural lift curve.

Zamansı-Uzaysı İnvölüt-Evolüt Eğri Çifti Üzerine Bir Araştırma

Öz

Bu makale, Lorentz 3-uzayında zamansı-uzaysı involüt-evolüt eğri çiftinin küresel göstergelerinin tabii lift eğrilerinin jeodezik spray için bir integral eğri olma gerekliliklerine odaklanır. Ayrıca elde edilen sonuçlar bir örnekle desteklenmiştir.

Anahtar Kelimeler: İnvölüt-evolüt eğri çifti, Lorentz uzayı, jeodezik spray, küresel gösterge, tabii lift eğrisi

1. Introduction

One of the exciting curves derived with the help of a curve is the involute curve. C. Huygens discovered the involute curve for the first time in 1673. The curve whose tangent vectors form right angles at each point of a given curve is called the involute curve, and these two curves are called the involute-evolute curve pair. For example, the involute of a circle is a spiral. In particular, a circle and its involute are significant in gear technology. For the characteristic properties and the more detailed information on the involute-evolute curve pair in classical differential geometry, see [1-3]. This article will focus more on n.l.c and geodesic sprays. See [4] for basic information on these concepts. In [5], authors have examined these concepts in the three dimensional space of Euclidean geometry. In [6], Bilici et al. generalized this problem to spherical indicatrices of the involute-evolute curve pair. Later, the authors adapted this problem for a non-null curves in the three dimensional Lorentz spaces [7, 8]. Moreover, there are also many studies on spherical indicatrix curves and the n.l.c in Euclidean space and Lorentz space [9-15]. Recently, authors have found the relations between the Frenet vectors of the curve pair in the Lorentz 3-space [16]. These relationships were the source of inspiration for this study. In this sense, in the present paper, firstly, we defined the spherical indicatrices of the involute curve on the hyperbolic unit sphere and Lorentzian unit sphere. Then, we investigated the n.l.c and geodesic sprays for these indicatrices in Lorentz 3-space, and obtained some significant results.

2. Preliminaries

The space E^3 with the metric tensor

$$\langle A, B \rangle = -a_1b_1 + a_2b_2 + a_3b_3$$

is called Lorentz 3-spaces and denoted by E_1^3 . There can be three states for a vector $A \in E_1^3$:

$$\begin{cases} \text{spacelike, } \langle A, A \rangle > 0 \text{ or } A = 0 \\ \text{timelike, } \langle A, A \rangle < 0 \\ \text{null(lightlike), } \langle A, A \rangle = 0 \text{ and } A \neq 0 \end{cases}$$

Similarly, a curve $\gamma = \gamma(s)$ in E_1^3 can be spacelike, timelike or null, if all of its velocity vectors $\gamma'(s)$ are spacelike, timelike or null respectively, [17]. The cross product of two vectors can be defined as follows:

$$A \times B = (a_3b_2 - a_2b_3, a_1b_3 - a_3b_1, a_1b_2 - a_2b_1).$$

Let denote the moving Frenet frame along the curve γ by $\{E_1, E_2, E_3\}$. In this trihedron, E_1 and E_3 are spacelike vectors, E_2 is timelike vector. From [18], definition of Lorentzian cross product we can write

$$E_1 \times E_2 = -E_3, \quad E_2 \times E_3 = -E_1, \quad E_3 \times E_1 = E_2.$$

Then the following Frenet formulas hold between these three vectors [19]:

$$\begin{cases} E_1' = p E_2, \\ E_2' = p E_1 + q E_3, \\ E_3' = q E_2. \end{cases}$$

The Darboux vector is expressed by

$$\omega = -q E_1 + p E_3,$$

where $p = \|\omega\| \cos \theta$, $q = \|\omega\| \sin \theta$.

On the other hand, from [16] the unit Darboux vector C can be given as follows

$$C = \frac{\omega}{\|\omega\|} = -\sin \theta E_1 + \cos \theta E_3.$$

Theorem 1. γ is a general helix if and only if $f = \frac{q}{p} = \tan \theta = \text{constant}$.

We can generalize the conception of integral curve to the hypersurface $M \subset E_1^3$ easily as follows:

A smooth curve $\gamma : I \rightarrow M$ is an integral curve of a smooth vector field $W \in \chi(M)$ if

$$\gamma'(t) = W(\gamma(t)) \tag{1}$$

for all $t \in I$, [18].

For a curve γ , the parametrized curve $\gamma : I \rightarrow TM$ is defined as the n.l.c given by the equation

$$\gamma(t) = (\gamma(t), \gamma'(t)) = \gamma'(t)|_{\gamma(t)}, \tag{2}$$

where $TM = \bigcup_{m \in M} T_m(M)$ is the set of all tangent vectors to M .

The Lorentzian and hyperbolic unit sphere of radius 1 and center 0 in E_1^3 are given by

$$S_1^2(H_0^2) = \{A = (a_1, a_2, a_3) \in E_1^3 : \langle A, A \rangle = 1 (\langle A, A \rangle = -1)\}$$

respectively, [18].

For $u \in TM$, the smooth vector field $W \in \chi(TM)$ defined by

$$W(u) = \varepsilon \langle u, S(u) \rangle \xi|_{\gamma(t)} \tag{3}$$

is called the geodesic spray on TM .

We know from [7] that "The n.l.c γ of the curve γ is an integral curve of the geodesic spray W if and only if γ is a geodesic on M ".

Theorem 2. Let (η, γ) be the involute-evolute curve pair. The following equality [16] gives the Frenet vectors of the curve pair:

$$\begin{cases} T^* = E_2 \\ N^* = -\cos \theta E_1 - \sin \theta E_3 \\ B^* = -\sin \theta E_1 - \cos \theta E_3 \end{cases} \tag{4}$$

3. Main Theorems and Proofs

In this section, we investigate the n.l.c η_{T^*} , η_{N^*} , η_{B^*} derived from spherical indicatrices of the involute curve η in E_1^3 . For this purpose, we seek an answer to the following question. What type of curve must the evolute curve γ be for the n.l.c of the spherical indicatrix curve to be an integral curve for geodesic spray?

3.1. The curve η_{T^*} for the first indicatrix of η

Let η_{T^*} be n.l.c of the tangent indicatrix $\eta_{T^*} = T^*$. If η_{T^*} is an integral curve of the geodesic spray, then by means of Lemma 1. we can write

$$\overline{D}_{\eta_{T^*}'} \eta_{T^*}' = 0, \quad (5)$$

where $\overline{D} = \frac{d}{ds_{T^*}}$ is the differential operator of H_0^2 . Thus from Theorem 2. and (5) we have

$$-\frac{\theta'}{\|\omega\|} \sin \theta E_1 + \frac{\theta'}{\|\omega\|} \cos \theta E_3 = 0.$$

Because of $\{E_1, E_2, E_3\}$ are linear independent, we get

$$\theta = \text{constant}.$$

Thus, from Theorem 1. we obtain

$$f = \text{constant}.$$

Result 3.1.1. If the curve γ is a general helix, then η_{T^*} is a geodesic on H_0^2 .

3.2. The curve η_{N^*} for the second indicatrix of η

Let η_{N^*} be the n.l.c of the principal normal indicatrix $\eta_{N^*} = N^*$. If η_{N^*} is an integral curve of the geodesic spray, then from Lemma 1. we can write

$$\overline{D}_{\eta_{N^*}'} \eta_{N^*}' = 0. \quad (6)$$

From the Theorem 2. and (6) we get,

$$\begin{aligned} \overline{D}_{\eta_{N^*}'} \eta_{N^*}' = & \left[(-\sigma' \sin \theta - \sigma \theta' \cos \theta + \frac{\kappa}{k_N} + \|\omega\| k_N \cos \theta) E_1 + \left(-\frac{k_N'}{k_N^2}\right) E_2 \right. \\ & \left. + (\sigma' \cos \theta - \theta' \sigma \sin \theta + \frac{\tau}{k_N} - \|\omega\| k_N \sinh \theta) E_3 \right] \frac{1}{\|\omega\| k_N}, \end{aligned}$$

where $\bar{D} = \frac{d}{ds_{N^*}}$ is the differential operator of S_1^2 and $\sigma = \frac{g_N}{k_N}$. From [20], $g_N = \frac{\theta'}{\|\omega\|}$ and $k_N = \frac{1}{\|\omega\|} \sqrt{|\theta'^2 - \|\omega\|^2|}$ are the geodesic curvatures of the principal normal indicatrix $\alpha_N = N$ with respect to S_1^2 and E_1^3 , respectively. Since $\{E_1, E_2, E_3\}$ are linear independent, we can write

$$\begin{cases} \sigma' \sin \theta + \theta' \sigma \cos \theta - \frac{\kappa}{k_N} - \|\omega\| k_N \cos \theta = 0, \\ \frac{k'_N}{k_N^2} = 0, \\ \sigma' \cos \theta - \theta' \sigma \sin \theta + \frac{\tau}{k_N} + \|\omega\| k_N \sin \theta = 0, \end{cases}$$

then we have

$$k_N = \text{constant}, \quad g_N = \text{constant}.$$

Result 3.2.1. If $k_N = \text{constant}$, $g_N = \text{constant}$, then η_{N^*} is a geodesic line on S_1^2 .

3.3. The curve η_{B^*} for the third indicatrix of η

Let η_{B^*} be the n.l.c of the binormal indicatrix $\eta_{B^*} = B^*$. If η_{B^*} is an integral curve of the geodesic spray, then we can write

$$\bar{D}_{\eta_{B^*}} \eta'_{B^*} = 0,$$

that is,

$$\frac{\|\omega\|}{\theta'} E_2 = 0.$$

Since $\{E_1, E_2, E_3\}$ are linear independent, we have

$$\|\omega\| = 0.$$

Thus we get

$$\kappa = 0, \quad \tau = 0.$$

Thus, we can say that γ is a line and know its involute is a circle segment. Thus we can give the following result.

Result 3.3.1. If the curve γ is a line, then η_{B^*} is a geodesic on S_1^2 .

Example 3.3.2. Let $\gamma(s) = \left(\frac{\sqrt{3}}{2} \cosh s, \frac{\sqrt{3}}{2} \sinh s, \frac{s}{2} \right)$ be a unit speed spacelike helix. For the curve γ we obtain

$$\begin{cases} E_1 = \left(\frac{\sqrt{3}}{2} \sinh s, \frac{\sqrt{3}}{2} \cosh s, \frac{1}{2} \right) \\ E_2 = (\cosh s, \sinh s, 0) \\ E_3 = \left(\frac{1}{2} \sinh s, \frac{1}{2} \cosh s, \frac{\sqrt{3}}{2} \right) \end{cases}, \quad \kappa = \frac{\sqrt{3}}{2}, \quad \tau = \frac{1}{2}.$$

Then we get the timelike involute curve η of γ such that

$$\eta(s) = \left(\frac{\sqrt{3}}{2} (\cosh s + (\sigma - s) \sinh s), \frac{\sqrt{3}}{2} (\sinh s + (\sigma - s) \cosh s), \frac{\sigma}{2} \right),$$

The following figures show the spacelike evolute curve γ (Fig. 1) and timelike involute curve η (Fig. 2) for $\sigma = 2$ and $s \in [-5, 5]$.

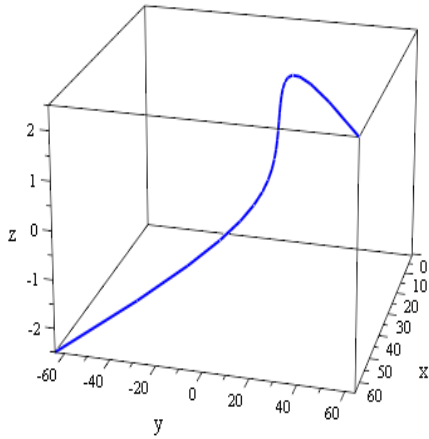


Figure 1. Evolute curve γ

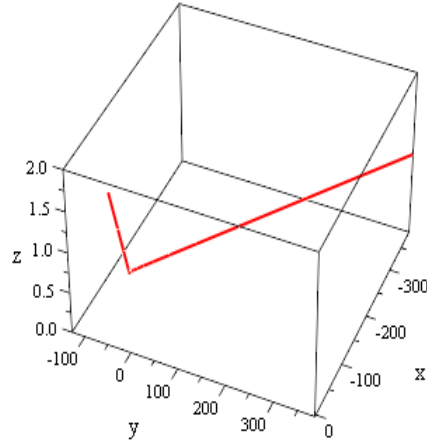


Figure 2. Involute curve η

Then we can give the spherical indicatrices and the n.l.c of η as follow:

$$\begin{cases} \eta_{T^*} = (\cosh s, \sinh s, 0), \\ \eta_{N^*} = (\sinh s, \cosh s, 0), \\ \eta_{B^*} = (0, 0, 1), \end{cases} \quad \begin{cases} \eta_{T^*} = (\sinh s, \cosh s, 0), \\ \eta_{N^*} = (\cosh s, \sinh s, 0), \\ \eta_{B^*} = (0, 0, 0). \end{cases}$$

Since $\langle \eta_{T^*}', \eta_{T^*}' \rangle = 1$, η_{T^*} is a spacelike curve. For being η_{T^*} is a spacelike, its tangent indicatrix which is a geodesic line on H_0^2 and the n.l.c of this spherical curve are as Fig.3. On the other hand, the normal indicatrix which is a geodesic on S_1^2 and its n.l.c are as Fig.4. It is also obvious that the third spherical indicatrix (binormal indicatrix) and its n.l.c is a point. Furthermore, we can say that (η, γ) is timelike-spacelike involute-evolute curve pair, and the condition $g(E_1, T^*) = 0$ is satisfied.

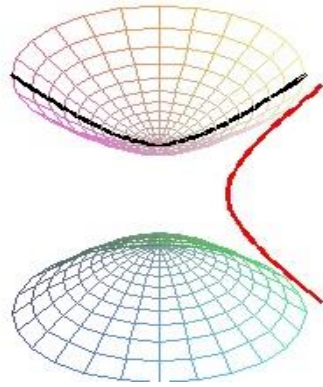


Figure 3. Tangent indicatrix curve η_{T^*}
and its n.l.c η_{T^*} (red color)

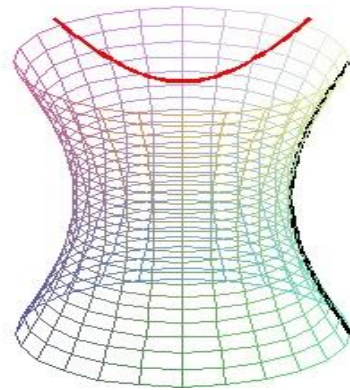


Figure 4. Normal indicatrix curve η_{N^*}
and its n.l.c η_{N^*} (red color)

Ethics in Publishing

There are no ethical issues regarding the publication of this study.

References

- [1] Millman, R. S., Parker, G. D., (1977) Elements of Differential Geometry, Prentice-Hall Inc., Englewood Cliffs Press, New Jersey.
- [2] Hacısalihoğlu H. H., (2000) Differential Geometry, Ankara University Faculty of Science Press, Ankara.
- [3] Çalışkan, M., Bilici, M., (2002) Some characterizations for the pair of involute-evolute curves in Euclidean space E^3 , *Bulletin of Pure and Applied Sciences*, 21(2), pp. 289-294.
- [4] Thorpe, J. A., (1979) Elementary Topics In Differential Geometry, Springer-Verlag, New York, Heidelberg-Berlin.

- [5] Çalışkan, M., Sivridağ, A.İ., (1984) Hacısalihoğlu. H. H., Some characterizations for the natural lift curves and the geodesic spray, *Communications Faculty of Sciences University of Ankara Series A1: Mathematics and Statistics*, 33, pp. 235-242.
- [6] Bilici, M., Çalışkan, M., Aydemir, İ., (2003) The natural lift curves and the geodesic sprays for the spherical indicatrices of the pair of evolute-involute curves, *International Journal of Applied Mathematics*, 11(4), pp. 415-420.
- [7] Bilici, M., (2011) Natural lift curves and the geodesic sprays for the spherical indicatrices of the involutes of a timelike curve in Minkowski 3- space. *International Journal of the Physical Sciences*, 6(20), pp. 4706-4711.
- [8] Bilici, M., Ahmad, T. A., (2017) On the natural lift curves for the involute spherical indicatrices in Minkowski 3-space. *Malaya Journal of Matematik*, 5(2), pp. 407-415.
- [9] Şenyurt, S., (2012) Natural lifts and the geodesic sprays for the spherical indicatrices of the Mannheim partner curves in E^3 , *International Journal of the Physical Sciences*, 7(16), pp. 2414-2421.
- [10] Ali, A.T., (2012) New special curves and their spherical indicatrix, *Global Journal of Advanced Research Clasical and Modern Geometries*, 1(2), pp. 28-38.
- [11] İyigün, E., (2013) The tangent spherical image and ccr-curve of a time-like curve in L^3 , *Jornal of Inequalities and Applications*, 55, pp. 1-5.
- [12] Bilici, M., Ergün, E., Çalışkan, M., (2014) The natural lift curves for the spherical indicatrices of spacelike Bertrand couple in Minkowski 3-space, *Journal of Mathematical and Computational Science* 4(1), pp. 85-104.
- [13] Bilici, M., Çalışkan, M., (2014) Some geometrical calculations for the spherical indicatrices of involutes of a timelike curve in Minkowski 3-Space, *Journal of Advances in Mathematics* 5(2), pp. 668-677.
- [14] Bilici, M., Ergün, E., Çalışkan, M., (2015) A new approach to natural lift curves of the spherical indicatrices of timelike Bertrand mate of a spacelike curve in Minkowski 3-space, *International Journal of Mathematical Combinatorics*, 1, pp. 35-48.
- [15] Bilici, M., Çalışkan, M., (2019) Some new results on the curvatures of the spherical indicatrices of the involutes of a spacelike curve with a spacelike binormal in Minkowski 3-space, *MathLAB Journal*, 2(1), pp. 110-119.
- [16] Bilici, M., Çalışkan, (2018) M., A new perspective on the involutes of the spacelike curve with a spacelike binormal in Minkowski 3-space, *Journal of Science and Arts*, 18(3), 573-582.

- [17] Ali, A. T., Lopez, R., (2011) Slant helices in Minkowski space E_1^3 . *Journal of the Korean Mathematical Society*, 48(1), pp. 159–167.
- [18] O’neill, B., (1983) *Semi Riemann Geometry*, Academic Press, New York, London.
- [19] Woestijne, V. D. I., (1990) *Minimal surfaces of the 3-dimensional Minkowski space*, World Scientific Publishing. Singapore, pp 344-369.
- [20] Bilici, M., (2009) *On the timelike or spacelike involute-evolute curve couples*, Ph.D. thesis, Ondokuz Mayıs University, Samsun, Turkey.

Digitized and Automated a University Process with Robotic Process Automation

Müge OLUÇOĞLU¹, Onur DOĞAN^{2*}, Ekin AKKOL², Burak KESKİN²

¹Izmir Bakircay University, Department of Computer Engineering, 35665, Izmir, Turkey

²Izmir Bakircay University, Department of Management Information Systems, 35665, Izmir, Turkey

Received: 01/07/2022, **Revised:** 09/10/2022, **Accepted:** 17/10/2022, **Published:** 31/03/2023

Abstract

Due to the changing student demographics and technological advances in research and teaching, both public and private higher education institutions offer services in an increasingly competitive environment. At the same time, the service quality expectations of the stakeholders continue to rise. For these reasons, technology solutions are needed for cost savings, efficiency gains, and improved service delivery. Like many other industries, higher education institutions have processes that can benefit from robotic process automation (RPA). RPA can be used to run student/staff jobs that manage back-office functions. It enables to ease the workload of their employees charged with doing these tasks and improve the user experience for students. This study examines an administrative process carried out at İzmir Bakırçay University. At least one administrative personnel assigned for the business process at the beginning of the research. The process consists of repetitive activities defined by specific rules. It was recommended to improve the process, considering the multitude of human errors and the length of the processing time. At the end of the study, the same process was completed within 16 minutes for 240 students without making mistakes, which means 96.97% of the time was saved. Moreover, 75% of personnel needs were reduced, and a 98.51% saving rate.

Keywords: Robotic process automation, Digital transformation, Process analysis and Digital robot

Robotik Süreç Otomasyonu ile Dijitalleştirilmiş ve Otomatikleştirilmiş Üniversite Süreci

Öz

Araştırma ve eğitimdeki teknolojik gelişmeler ve öğrencilerin sürekli değişen demografik özellikleri nedeniyle hem kamu hem de özel yükseköğretim kurumları artan rekabet ortamında hizmet sunmaktadırlar. Aynı zamanda paydaşların hizmet kalitesi beklentileri de yükselmeye devam etmektedir. Bu sebeplerden dolayı, maliyet tasarrufu, verimlilik kazanımları ve iyileştirilmiş hizmet sunumu için teknoloji çözümlerine ihtiyaç vardır. Diğer birçok sektör gibi yükseköğretim kurumlarının da robotik süreç otomasyonundan (RSO) yararlanabilecek süreçleri bulunmaktadır. RSO, yönetsel süreçler olan öğrenci/personel işlerinde kullanılabilir. Bu süreçleri yürütmekle görevli çalışanların iş yükünü hafifletmeyi ve öğrencilerin kullanıcı deneyimini iyileştirmeyi sağlar. Bu çalışma, İzmir Bakırçay Üniversitesi'nde yürütülen bir idari süreci incelemektedir. Bu sürecin başında iş süreci için en az bir idari personel görevlendirilir. Süreç, belirli kurallarla tanımlanan ve tekrarlayan faaliyetlerden oluşur. Bu çalışma ile çok sayıda insan hatası ve işlem süresinin uzunluğu göz önünde bulundurularak sürecin iyileştirilmesi önerilmiştir. Çalışma sonunda 240 öğrenci için aynı işlem 16 dakikada hatasız tamamlanarak %96,97 oranında zaman tasarrufu sağlanmıştır. Ayrıca personel ihtiyacı %75 azaltılmış ve %98,51 tasarruf oranı sağlanmıştır.

Anahtar Kelimeler: Robotik süreç otomasyonu, Dijital dönüşüm, Süreç analizi ve Dijital robot

*Corresponding Author: onur.dogan@bakircay.edu.tr

Müge OLUÇOĞLU, <https://orcid.org/0000-0002-0137-5854>

Onur DOĞAN, <https://orcid.org/0000-0003-3543-4012>

Ekin AKKOL, <https://orcid.org/0000-0003-2924-8758>

Burak KESKİN, <https://orcid.org/0000-0002-0560-2225>

1. Introduction

According to the [8], Robotic Process Automation (RPA) is a technology application that enables to execute operations in existing applications, select data, interpret, manipulate, and communicate with other digital systems with computer software or a digital “robot” configuration in the company.

RPA is not only the fastest way to digital transformation but also the most efficient way for organizations to increase their operational efficiency [16]. RPA robots can collect data, run applications, trigger responses, make decisions based on the defined rules, and interact with other systems [9]. It is primarily used to automate highly manual, repetitive, rule-based procedures with low exception rates and standard electronic readable input [2]. Like a human workforce, RPA solutions can be thought of as a virtual robotic workforce whose operational management is handled by the pipeline (supported only by IT). It combines well-understood technical skills with the ability to swiftly understand business processes in terms of inputs, outputs, and decision points while developing a RPA project. RPA provides firms with improved process documentation, lower error rates, and better report quality in addition to cost reductions [10].

RPA, which allows for the easy completion of repetitive and complicated processes, can also be used in university processes. Performing repetitive work by the personnel in the units causes time and cost losses. Furthermore, human-caused mistakes might obstruct effective process management. Including RPA in university processes and executing relevant tasks by robots can reduce human-induced errors while also saving time and cost [13]. This study focuses on the use of RPA in university processes. The study aims to digitize and automate a process at İzmir Bakırçay University. Students require the internship obligation document prepared by the departments. The problem is that the preparation process of the internship obligation document is regularly done for around 240 students in the Faculty of Engineering in each semester, and it wastes time and resources. As part of the process, the internship obligation document, which is a work that is regularly repeated and demands labor, was digitalized and automatically completed, signed, and delivered to the relevant student. Thus, it will be possible to save time and cost, especially in the repetitive operations at the operational level. The motivation of this study is to use the limited human resources of the university more efficiently and to ensure that repeated tasks may be completed more quickly and autonomously. This study achieved 75% of labour force, 96.67% of time savings and 98.51% of saving rate.

The rest of the article begins by explaining the studies in Section 2 and revealing the connections between them. The flow chart of the study is presented in Section 3, and all steps are explained in detail. Section 4 gives the results of the RPA implementation and discusses them. Finally, Section 5 concludes the study.

RPA tools are designed to relieve employees of the burden of repetitive and/or uncomplicated activities in a wide range of areas [1]. Each sector has its own set of processes. The automation of internal administrative procedures related to the delivery of public services is highlighted as part of the progression toward a more digitized, efficient, and thriving local government. However, this progress is frequently founded on unrealistic expectations about digital technology' revolutionary ability [11]. RPA seems to have the potential to benefit municipalities by performing organized activities and decreasing the need for workers to undertake repetitive and monotonous work, hence reducing cost and reducing lead times [12,14]. A study of federal and state agencies found [6]:

- RPA has already been embraced by 65% of federal agencies and 41% of state agencies to facilitate work.
- RPA is viewed as a building block for exploiting AI and ML capabilities by 61% of federal agencies and 49% of state agencies.
- 26% of agencies have 51-100 robots deployed, while 15% have 101-200 robots deployed.
- RPA success is measured by government agencies by:
 - Increased speed of service delivery (46%)
 - Cost avoidance/savings (41%)
 - Reduction in data processing errors (37%)
- RPA was expected to save 5,000 to 50,000 hours of annual work time by 34% of respondents.

According to the 2021 Gartner Digital Transformation Divergence Across Government Sectors Survey [7], 19% of government respondents had already used RPA, with another 33% planning to do so in the next two years. The popularity of RPA stems mainly from the operational efficiency it provides and its ability to bring benefits fast and its application in automating old system activities.

There are various examples of the applications of RPA in public institutions. In their study, [18] focused on the methodology of RPA in administrative business processes. The usage of RPA in public administration administrative processes is investigated using the example of subject accreditation for scientific and technical activities. Through the introduction of elements of robotization business processes, the proposed methodology takes into account the unique characteristics of government processes, meets the needs of government agencies, and will significantly improve government agency performance and citizen satisfaction, as well as reduce costs in automating the functions and processes of government agencies. In another study, [3] conducted an in-depth case study at the Finnish government shared services center during their implementation of an Artificial Intelligence (AI) centric RPA technology. They used a theory of knowledge embodiment to explain how people and machines interact. They wanted to add to the theory by conceptualizing the knowledge embodying process in the future of work while expanding the knowledge embodiment theory. They contribute to practice by elucidating the consequences of how people and computers collaborate on knowledge work in organizations that have adopted AI technology.

RPA is increasingly being used to develop more modern, complex administrative operations in universities. [4] mentioned the use of RPA by an Australian university. According to the study, the institution reaped significant benefits from its RPA adoption. By automating student document uploads, the university was able to cut processing time in half, eliminate manual procedures, and reduce process touch points from 40 to one, saving the institution 1,330 hours of manual labor per year while also enhancing service time and eliminating mistakes. [17] explored the adoption of RPA technology within higher education. This article provided an overview of the possibilities for RPA technology to improve the functionality and efficiency of higher education institutions. They studied numerous prospective beneficiaries of this technology to address RPA in the context of higher education. They offered just a few use cases, but some with tremendous value and specific benefits. [15] focused on automating the entry of student information into the University portal. They claim that this robotization will help the organization use fewer human resources for such automated measures, resulting in successful, efficient, and error-free investigations.

Although the benefits of using RPA technology in public institutions have been clearly demonstrated in the literature, there are relatively few studies on the issue. This study aims to contribute to the literature by creating and discussing the benefits of an example digital robot at the university.

2. Material and Methods

RPA consists of software of robots that work instead of humans, without human involvement. From the development of robots to their implementation, the robot must pass through several stages in the automation process. Figure 1 shows the flowchart representation of the methodology used in this study. RPA studies are generally carried out using the methodology described below, consisting of six steps [5].

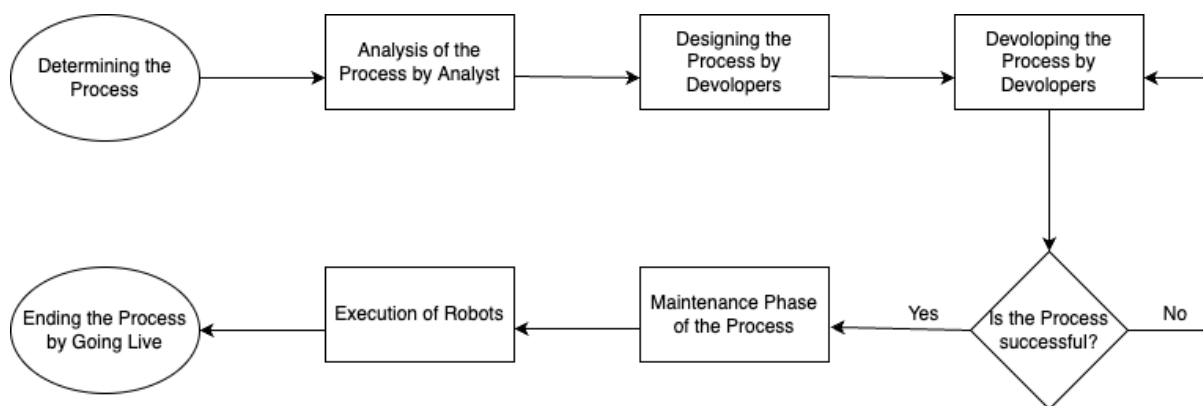


Figure 1. Flowchart of RPA methodology

2.1 Analysis Phase:

The RPA life cycle begins with the analysis phase. The customer's requirements are examined at this point. The next step is to determine whether or not the process can be automated. If the process can be automated, the RPA analyst team and the developer team collaborate to examine the process.

2.2 Design Phase:

Automation of tasks occurs during the design phase. The RPA development team collaborates with the analyst team to prepare a "Process Description Document" (PDD) that contains details about the entire process. The analyst team then creates a flowchart to visualize the process flow. After the design is complete, the RPA tool is used to initiate the development of the RPA software and automate the tasks. RPA employs both human path and robot path ideas. The human path is the step-by-step processing of all procedures using just human power and no robots. The user completes all the job's steps without any assistance. Robot path is the automatic execution of steps defined by a user.

2.3 Development Phase:

With the help of the PDD tool, the developer constructs bots-commands to automate processes. The created robots can run on the entire operating system without any restrictions.

2.4 Control and Monitoring Phase:

The RPA development team tests the robots developed at this step. If the tests fail, the robots are sent to development to fix bugs found during testing. The next phase begins after the test phase has been completed.

2.5 Support and Maintenance Phase:

If software errors are discovered after the control and monitoring phase, the process is sent back to the RPA development and testing team. The development team reanalyzes the robots and works to fix the issues.

2.6 Execution of Robots:

Robots are examined to ensure that the implementation fits the requirements. At this stage, the software is sent back to the testing and development team to correct any errors—the robots whose fixed errors are finally run in the production system.

3. Results and Discussion

RPA applications can be applied in various areas within universities, particularly in operational procedures. It is feasible to reduce the requirement for personnel and use it more efficiently in repetitive routine applications thanks to RPA applications. In this study, as an example case, a robot was developed that automatically generates the internship obligation document required

by the students studying at İzmir Bakırçay University who must complete an internship to graduate. This job is regularly done for around 240 students in four departments in each semester, and it wastes time and resources. Figure 2 presents the human path of the process. If this task is to be completed utilizing just human resources and no robots, the steps in Figure 2 must be followed step by step. First, an excel file should be opened. Then, the word document should be opened and filled in all necessary places on the document until all students' documents are completed. Then, the documents should be sent to the students one by one by e-mail.

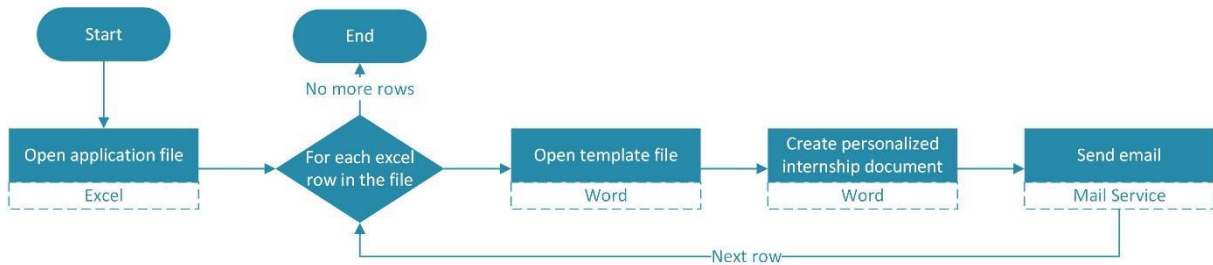


Figure 2. Human path of the selected process

The study aims to use RPA to avoid wasting time and resources. Figure 3 shows the robot path that summarizes the followed flow.

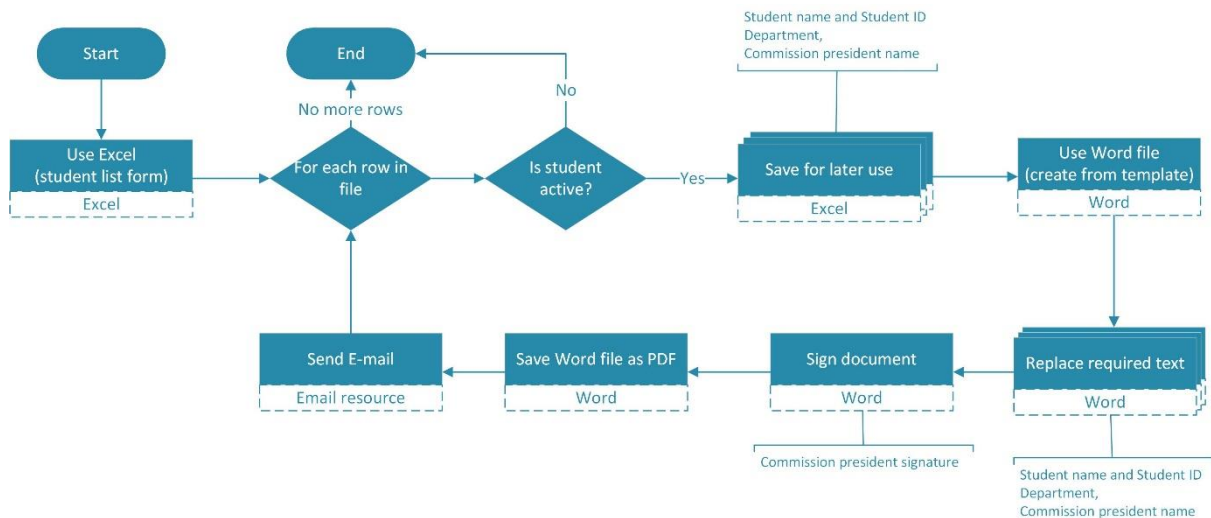


Figure 3. Robot path of the selected process

During the development of the robot, the UiPath StudioX application was used. Currently, there is an excel file containing the details of the students (Student Number, Department, Name and Surname, Student Status, Internship Commission President) and a draft of the internship obligation document. The study's goal is to automatically transfer each student's details from excel to the internship obligation document one by one. Once the robot is designed, the excel file containing the student's information is automatically opened, and the student's status is checked. If the student status is active, the robot transfers the Student Number, Department, Name, Surname, and Internship Commission President sections of the excel sheet to each student's internship obligation document. The chairman of the commission's signature, which

is saved as a picture file, is also added as a picture to the relevant field, and each student's signed documents are saved as PDF. The process is completed by sending the documents saved as PDFs to the students' email address. Since the automated process is rule-based, consists of digital and structured data, and is a static process that will not change much, it was deemed appropriate to be done by the robot. The robot can quickly complete a process that requires a person to spend 2 minutes for each student (totally $2 \times 240 = 480$ minutes), especially given the university's high student density, in minutes and without human assistance. With RPA, the work of four people (one from each of the four departments) who had been working for more than a day was finished in 16 minutes with only one person. 75% of personnel and 96.67% of the time were saved in total.

4. Conclusion

RPA is a type of automation that may be repeated continuously, is prone to human error, and is employed in tasks that could result in avoidable labor loss. It provides secure and fast transactions in data cleaning, data extraction, and data transfer procedures. In addition to all of this, RPA technology allows employees' performance and productivity to improve and cost savings. Although RPA is used in various areas, the automatic internship obligation document is created with an example study, which focuses on its usage in universities. It is usually an iterative and static procedure that involves a considerable number of people and requires the production of hundreds of documents at once. Considering these process features, it is very suitable for RPA technology, as it provides savings in terms of both labor, cost, and time.

The automatic creation of the internship obligation document, a routine job that must be completed every semester for about one thousand students, was completed and made available at İzmir Bakırçay University. In this approach, a process involving many people, including students, civil servants, and the heads of the internship commission, that would generally take four and a half days to complete can be finished in 16 minutes. The entire process takes place in a digital environment, and once done, the required document is produced and sent to the students' email addresses. The workforce loss of all people involved in the process is reduced by 97%, and the risk of human error is eliminated. Table 1 summarizes the values in the current situation where the works are conducted without the use of a robot, and Table 2 summarizes the improved values seen with the developed robot.

Table 1. Current situation analysis

Metrics	Values
Frequency	Once per semester
Repetition	240
Cycle time (min)	2
Duration (min)	480
Number of employees	4
Cost (TL)	80600

Table 2. Improved situation analysis

Metrics	Values	Improvement
Frequency	Once per semester	
Repetition	240	
Cycle time (min)	0.06	96.67%
Duration (min)	16	
Number of employees	1	75%
Cost (TL)	1200	98.51%

In terms of universities, there are numerous RPA-related works available. In future studies, the development of robots related to other jobs can be allowed the university to save money on labor and other expenses. Considering RPA's contribution to digitalization universities are expected to benefit significantly from a valuable automation system.

Acknowledgement

This work has been supported by İzmir Bakırçay University Scientific Research Projects Coordination Unit, under grant number KBP.2022.004.

Ethics in Publishing

There are no ethical issues regarding the publication of this study.

Author Contributions

All authors contributed equally.

References

- [1] Aguirre, S., & Rodriguez, A. (2017, September). Automation of a business process using robotic process automation (RPA): A case study. In *Workshop on engineering applications* (pp. 65-71). Springer, Cham.
- [2] Cohen, M., & Rozario, A. (2019). Exploring the use of robotic process automation (RPA) in substantive audit procedures. *The CPA Journal*, 89(7), 49-53.
- [3] Dias, M., Pan, S., & Tim, Y. (2019). Knowledge embodiment of human and machine interactions: Robotic-process-automation at the Finland government.
- [4] Duncan, B., Lundy, K., How universities are using robotic process automation, Available: https://www.ey.com/en_us/government-public-sector/how-universities-are-using-robotic-process-automation, April 19, 2022.
- [5] Enríquez, J. G., Jiménez-Ramírez, A., Domínguez-Mayo, F. J., & Garcia-Garcia, J. A. (2020). Robotic process automation: a scientific and industrial systematic mapping study. *IEEE Access*, 8, 39113-39129.
- [6] Fedscoop., RPA's Expanding Role In Government, Available: <https://cdn.fedscoop.com/robotic-process-automation-in-government-report.pdf>, April 19, 2022.

- [7] How Government CIOs Can Realize the True Potential of Robotic Process Automation, Available: <https://www.gartner.com/en/articles/3-ways-for-government-cios-to-realize-the-true-potential-of-robotic-process-automation>, April 19, 2022.
- [8] Institute For Robotic Process Automation & Artificial Intelligence IRSOAI., What is Robotic Process Automation?, Available: <https://irpaai.com/what-is-robotic-process-automation>, April 19, 2022.
- [9] Kaya, C. T., Türkyılmaz, M., & Birol, B. (2019). Impact of RPA technologies on accounting systems. *Muhasebe ve Finansman Dergisi*, (82).
- [10] Kokina, J., & Blanchette, S. (2019). Early evidence of digital labor in accounting: Innovation with Robotic Process Automation. *International Journal of Accounting Information Systems*, 35, 100431.
- [11] Lindgren, I., Åkesson, M., Thomsen, M., & Toll, D. (2022). Organizing for Robotic Process Automation in Local Government: Observations from Two Case Studies of Robotic Process Automation Implementation in Swedish Municipalities. In *Service Automation in the Public Sector* (pp. 189-203). Springer, Cham.
- [12] Lacity, M. C., & Willcocks, L. P. (2016). A new approach to automating services. *MIT Sloan Management Review*, 58(1), 41-49.
- [13] Rutschi, C., & Dibbern, J. (2020). Towards a framework of implementing software robots: Transforming human-executed routines into machines. *ACM SIGMIS Database: the DATABASE for Advances in Information Systems*, 51(1), 104-128.
- [14] Madakam, S., Holmukhe, R. M., & Jaiswal, D. K. (2019). The future digital work force: robotic process automation (RPA). *JISTEM-Journal of Information Systems and Technology Management*, 16.
- [15] Nandwani, T., Sharma, M., & Verma, T. (2021). Robotic Process Automation–Automation of Data Entry for Student Information in University Portal. In *Proceedings of the International Conference on Innovative Computing & Communication (ICICC)*.
- [16] Syed, R., Suriadi, S., Adams, M., Bandara, W., Leemans, S. J., Ouyang, C., ... & Reijers, H. A. (2020). Robotic process automation: contemporary themes and challenges. *Computers in Industry*, 115, 103162.
- [17] Turcu, C., & Turcu, C. (2018). On robotic process automation and its integration in higher education.
- [18] Uskenbayeva, R., Kalpeyeva, Z., Satybaldiyeva, R., Moldagulova, A., & Kassymova, A. (2019, July). Applying of RPA in administrative processes of public administration. In *2019 IEEE 21st Conference on Business Informatics (CBI)* (Vol. 2, pp. 9-12). IEEE.

Some Fixed Point Theorems in Extended Fuzzy Metric Spaces

Meryem ŞENOCAK^{1*}, Erdal GÜNER²

¹ Turkish Grain Board, Head of Poppy and Alkaloid Affairs Department, Ankara, TURKEY

² Department of Mathematics, Faculty of Sciences, Ankara University, Ankara, TURKEY

Received: 20/07/2022, **Revised:** 19/09/2022, **Accepted:** 10/10/2022, **Published:** 31/03/2023

Abstract

In this article, we present a newly fuzzy contraction mapping and using it we prove a fixed point theorem. In fact, we transfer this contraction mapping, first defined in metric spaces, and then transferred to fuzzy metric spaces with modification, to extended fuzzy metric spaces. And so we prove some fixed point theorems existing in the literature in the new space.

Keywords: Fixed-point, extended fuzzy metric space, fuzzy contraction.

Genişletilmiş Bulanık Metrik Uzaylarda Bazı Sabit Nokta Teoremleri

Öz

Bu makalede, yeni bir bulanık büzülme dönüşümü sunuyoruz ve bunu kullanarak bir sabit nokta teoremi ispatlıyoruz. Aslında, önce metrik uzaylarda tanımlanan ve daha sonra modifiye edilerek bulanık metrik uzaylara aktarılan bu büzülme dönüşümünü, genişletilmiş bulanık metrik uzaylara aktarıyoruz. Ve böylece yeni uzaylarda literatürde var olan bazı sabit nokta teoremlerini ispatlıyoruz.

Anahtar Kelimeler: Sabit nokta, genişletilmiş bulanık metrik uzay, bulanık büzülme.

*Corresponding Author : meryemsnc@gmail.com

Meryem ŞENOCAK, <https://orcid.org/0000-0002-2988-9419>

Erdal GÜNER, , <https://orcid.org/0000-0003-4749-1321>

1. Introduction

The idea of fuzzy was first defined by Zadeh [4]. It has used and attracted attention not only in mathematics but also in many fields. Kramosil and Michalek [5] contributed to the literature fuzzy metric spaces generalizing probabilistic metric spaces, and then George and Veeramani [6] made slight modification in this concept and V. Gregori et al. [3] introduced a kind of generalized version this concept called extended fuzzy metric spaces. Recently, it is a paramount development that defining the concept of contractive mapping in some fuzzy spaces. After the remarkable Banach [7] contractivity, a large amount of mathematicians studied some contractive mappings to proof a fixed point exists such as Grabiec [8], Gregori and his coauthors ([9], [10]), Mihet ([11], [12]). And numerous authors studied different versions contractive mappings in the different spaces ([13], [14], [15]). Concepts, properties and especially some contraction mappings defined in metric spaces in the literature have been transferred to fuzzy metric spaces. For example Wardowski [1] manifested a special contraction and using it he demonstrated theorems in metric spaces. And then inspiring by him, H. Huang and coauthors [2] presented the fuzzy version with simplification. They made slight modification on it and then they indicated some theorems via this contraction in fuzzy metric spaces [2].

In this paper, we define a new fuzzy contraction. Using this newly concept, we verify some theorems [2] in the extended fuzzy metric spaces. And so we get "t=0", versions which are exist in the literature.

While proving theorems in extended novel spaces, we considered two cases. First one is "t>0", which expresses fuzzy metric spaces. The second is the case of "t=0", which is an important point. This situation corresponds to stationary fuzzy metric spaces. This is why we consider the study we obtained by adding the "t=0", point to the existing one in the literature more comprehensive.

2. Preliminaries

In this section, we remember some descriptions and results that will be used later.

Definition 2.1: [16] A binary operation $T: [0,1] \times [0,1] \rightarrow [0,1]$ is t-norm, if the subsequent circumstances hold:

- (TN₁) $T(\rho, \varphi) = T(\varphi, \rho)$;
- (TN₂) $T(\rho, \varphi) \leq T(\gamma, \delta)$ if $\rho \leq \gamma$ and $\varphi \leq \delta$;
- (TN₃) $T(\rho, T(\varphi, \gamma)) = T(T(\rho, \varphi), \gamma)$;
- (TN₄) $T(\rho, 1) = \rho$.

Now we present definitions of fuzzy metric space (FMS), stationary fuzzy metric space (SFMS) and extended fuzzy metric space (EFMS), each of which is a trio $(Y, A, *)$, where $Y \neq \emptyset$ is a set, $*$ is a continuous t-norm and A is a fuzzy set on $Y \times Y \times (0, \infty)$, $Y \times Y$ and $Y \times Y \times [0, \infty)$ respectively.

Definition 2.2: [6] It is FMS, ensuring $\forall u, v, w \in Y$ and $\forall t, s > 0$ the next items:

- (FMS₁) $A(u, v, t) > 0$;

- (FMS₂) $A(u, v, t) = 1 \Leftrightarrow u = v$;
- (FMS₃) $A(u, v, t) = A(v, u, t)$;
- (FMS₄) $A(u, v, t) * A(v, w, s) \leq A(u, w, t + s)$;
- (FMS₅) $A(u, v, \cdot): (0, \infty) \rightarrow (0, 1]$ is continuous.

Definition 2.3: [9] It is SFMS, ensuring $\forall u, v, w \in Y$ the next items:

- (SFMS₁) $A(u, v) > 0$;
- (SFMS₂) $A(u, v) = 1 \Leftrightarrow u = v$;
- (SFMS₃) $A(u, v) = A(v, u)$;
- (SFMS₄) $A(u, v) * A(v, w) \leq A(u, w)$.

$\{u_i\}$ named Cauchy, if $\lim_{i,j \rightarrow \infty} A(u_i, u_j) = 1$; $u_i \rightarrow u$, if $\lim_{i \rightarrow \infty} A(u_i, u) = 1$

Definition 2.4: [3] It is EFMS, ensuring $\forall u, v, w \in Y$ and $\forall t, s \geq 0$, the next items:

- (EFMS₁) $A^0(u, v, t) > 0$;
- (EFMS₂) $A^0(u, v, t) = 1 \Leftrightarrow u = v$;
- (EFMS₃) $A^0(u, v, t) = A^0(v, u, t)$;
- (EFMS₄) $A^0(u, v, t) * A^0(v, w, s) \leq A^0(u, w, t + s)$;
- (EFMS₅) $A^0_{u,v}: [0, \infty) \rightarrow (0, 1]$ is continuous; $A^0_{u,v}(t) = A^0(u, v, t)$.

There are different completeness and Cauchy sequence definitions in FMS ([6],[8]). The authors adapted the M-Cauchy in [3] from FMS to EFMS. As follows;

Definition 2.5: [3] A sequence $\{u_n\}$ in Y is named Cauchy if, given $\varepsilon \in (0, 1)$, it can be find $n_\varepsilon \in \mathbb{N}$ such that $A^0(u_n, u_m, 0) > 1 - \varepsilon$ for all $n, m \geq n_\varepsilon$.

$$\{u_n\} \text{ is a Cauchy} \Leftrightarrow \lim_{m,n} A^0(u_n, u_m, 0) = 1.$$

An EFMS is called complete if every Cauchy sequence is convergent.

EFMS, defined in [3] and chosen as the study space in our article, is separated from FMS by the "t=0" point. This is the difference between Definition 2.2 and Definition 2.4 given above. For this reason, we examine the proof of theorems in EFMS in two cases; the first is "t>0", which denotes fuzzy metric spaces, the second is "t=0", which represents stationary fuzzy metric spaces.

We continue with theorems and propositions about EFMS.

Theorem 2.1: [3] Let be a fuzzy set on $Y \times Y \times (0, \infty)$, and its extension A^0 is on $Y \times Y \times [0, \infty)$ given by $\forall u, v \in Y$

$$A^0(u, v, t) = A(u, v, t), \quad t > 0 \text{ and } A^0(u, v, 0) = \bigwedge_{t>0} A(u, v, t).$$

Then, $(Y, A^0, *)$ is an EFMS $\Leftrightarrow (Y, A, *)$ is a FMS, A is called extendable ensuring

$$\forall u, v \in Y, \text{ the condition } \bigwedge_{t>0} A(u, v, t) > 0.$$

Proposition 2.1: [3] Let $(Y, A, *)$ be a FMS, given by $N_A(u, v) = \bigwedge_{t>0} A(u, v, t)$

Then, $(N_A, *)$ is a SFMS on $Y \Leftrightarrow \bigwedge_{t>0} A(u, v, t) > 0; \forall u, v \in Y$.

It is clear that;

$$N_A(u, v) = A^0(u, v, 0) = \bigwedge_{t>0} A(u, v, t) \tag{1}$$

Proposition 2.2: [3] Let $(Y, A^0, *)$ is complete $\Leftrightarrow (Y, N_A, *)$ is complete.

H. Huang and coauthors [2] presented a new concept and they verified some fixed point theorems using it in FMS. And so, they modified and generalized some notions in the literature ones [1].

The class of $F_H: [0,1] \rightarrow (0, \infty)$ mappings is \mathcal{F}_H , ensuring $\forall u, v [0,1]$,

$u < v$ implies $F_H(u) < F_H(v)$. That is F_H is strictly increasing.

Definition 2.6: [2] Let $(Y, A, *)$ be a FMS and $F_H \in \mathcal{F}_H$. $\mathfrak{S}: Y \rightarrow Y$ is called a fuzzy F_H -contraction if $\exists \tau \in (0,1)$ such that

$$\tau \cdot F_H(A(\mathfrak{S}u, \mathfrak{S}v, t)) \geq F_H(A(u, v, t)) \quad (2)$$

for all $u, v \in Y$ ($u \neq v$) and $t > 0$.

3. Main Theorems and Proofs

We present F_H -fuzzy contraction. This new notion can be consider as extended version of the contraction which introduced by H. Huang and his coauthors [2]. In addition, we prove their theorems in the extended fuzzy metric space. And so, we obtain new results which are generalizations of ones exist in the literature.

Definition 3.1: Let $(Y, A^0, *)$ be an EFMS, $F_H \in \mathcal{F}_H$ and an injective mapping $\mathfrak{S}: Y \rightarrow Y$ is named F_H -fuzzy contraction, if (2) is ensured for $\forall u, v \in Y$ and $t \geq 0$.

Theorem 3.1: Let $(Y, A^0, *)$ be a complete EFMS and $\lim_{t \rightarrow 0^+} A(u, v, t) > 0$. If the sequel items hold:

- i. \mathfrak{S} is continuous,
- ii. \mathfrak{S} is a F_H -fuzzy contraction,

then \mathfrak{S} has a unique fixed point in Y .

Proof : The proof will be examine in two parts.

I. $t > 0$;

This case was proved in Theorem1's proof [2]. Because,

$$A^0_{u,v}(t) = A_{u,v}(t) \quad \forall u, v \in Y \text{ and } t > 0, \text{ it is similar in FMS.}$$

II. $t = 0$;

$$\{u_n\} \text{ is a Cauchy} \Leftrightarrow \lim_{m,n} A^0(u_n, u_m, 0) = 1$$

Let $u_0 \in Y$ and the sequence $\{u_n\}$ in Y with $u_{n+1} = \mathfrak{S}u_n, \forall n \in \mathbb{N}$.

Provided that $u_{n+1} = u_n = \mathfrak{S}u_n$, for some $n \in \mathbb{N}$, then $u^* = u_n$ is fixed point of \mathfrak{S} .

We presume that, $u_{n+1} \neq u_n; \forall n \in \mathbb{N}$.

From (ii), using (1) and implementing (2) with $u = u_{n-1}, v = u_n, t = 0$, we obtain;

$$\begin{aligned} F_H(A^0(\mathfrak{S}u_{n-1}, \mathfrak{S}u_n, 0)) &= F_H(N_A(\mathfrak{S}u_{n-1}, \mathfrak{S}u_n)) \\ &> \tau \cdot F_H(N_A(\mathfrak{S}u_{n-1}, \mathfrak{S}u_n)) \\ &\geq F_H(N_A(u_{n-1}, u_n)) \end{aligned}$$

So, we have;

$$F_H(N_A(\mathfrak{S}u_{n-1}, \mathfrak{S}u_n)) > F_H(N_A(u_{n-1}, u_n))$$

Since F_H is strictly increasing, we get;

$$N_A(u_n, u_{n+1}) > N_A(u_{n-1}, u_n)$$

$\{N_A(u_n, u_{n+1})\}$ is a strictly increasing sequence. Also, since it is bounded from above, the sequence is convergent.

And so, as $n \rightarrow \infty$,

$$N_A(u_n, u_{n+1}) = \mu, \quad \mu \in [0,1] \text{ and } n \in \mathbb{N}.$$

It is obviously that,

$$N_A(u_n, u_{n+1}) < \mu, \quad \text{for } n \in \mathbb{N}.$$

As $n \rightarrow \infty$,

$$F_H(N_A(u_n, u_{n+1})) = F_H(\mu)$$

We assume that $\mu < 1$,

From (2) with $u = u_n, v = u_{n+1}, t = 0$,

$$F_H(N_A(\mathfrak{I}u_n, \mathfrak{I}u_{n+1})) > \tau. F_H(N_A(\mathfrak{I}u_n, \mathfrak{I}u_{n+1})) \geq F_H(N_A(u_n, u_{n+1}))$$

as $n \rightarrow \infty$,

$$F_H(\mu) > \tau. F_H(\mu) \geq F_H(\mu)$$

Then $F_H(\mu) = 0$. It is a contradiction.

So, as $n \rightarrow \infty$,

$$N_A(u_n, u_{n+1}) = 1, n \in \mathbb{N}.$$

Whether the sequence $\{u_n\}$ is Cauchy or not is very important the proof. Assume that $\{u_n\}$ is not Cauchy sequence.

$\exists \varepsilon \in (0,1)$ and $\{u_{m_k}\}$ and $\{u_{n_k}\}$ such that $\forall k \in \mathbb{N}$ and $m_k > n_k \geq k$, we obtain

$$N_A(u_{m_k}, u_{n_k}) \leq (1 - \varepsilon)$$

$$N_A(u_{m_{k-1}}, u_{n_{k-1}}) > 1 - \varepsilon \text{ and } N_A(u_{m_{k-1}}, u_{n_k}) > (1 - \varepsilon)$$

And so using (SFMS₄), we have

$$(1 - \varepsilon) \geq N_A(u_{m_k}, u_{n_k}) \geq N_A(u_{m_{k-1}}, u_{n_{k-1}}) * N_A(u_{n_{k-1}}, u_{n_k})$$

As $k \rightarrow \infty$,

$$\lim_{k \rightarrow \infty} (1 - \varepsilon) \geq \lim_{k \rightarrow \infty} N_A(u_{m_k}, u_{n_k}) \geq \lim_{k \rightarrow \infty} N_A(u_{m_{k-1}}, u_{n_{k-1}}) * \lim_{k \rightarrow \infty} N_A(u_{n_{k-1}}, u_{n_k})$$

And so,

$$(1 - \varepsilon) \geq \lim_{k \rightarrow \infty} N_A(u_{m_k}, u_{n_k}) > (1 - \varepsilon)$$

We get,

$$\lim_{k \rightarrow \infty} N_A(u_{m_k}, u_{n_k}) = (1 - \varepsilon).$$

In addition to, by (2) with implementing $u = u_{m_{k-1}}, v = u_{n_{k-1}}, t = 0$, we obtain

$$F_H(N_A(\mathfrak{I}u_{m_{k-1}}, \mathfrak{I}u_{n_{k-1}})) > \tau. F_H(N_A(\mathfrak{I}u_{m_{k-1}}, \mathfrak{I}u_{n_{k-1}})) \geq F_H(N_A(u_{m_{k-1}}, u_{n_{k-1}}))$$

Since F_H is strictly increasing on $[0,1]$,

$$(1 - \varepsilon) \geq N_A(u_{m_k}, u_{n_k}) > N_A(u_{m_{k-1}}, u_{n_{k-1}}) > (1 - \varepsilon)$$

It is a contradiction. So, we get that $\{u_n\}$ is a Cauchy. Because, Y is complete, $\exists u^* \in Y$: as $n \rightarrow \infty$ and $u_n \rightarrow u^*$.

Now we will prove that $\mathfrak{S}u^* = u^*$.

From the continuity of \mathfrak{S} ,

$$u^* = \lim_{n \rightarrow \infty} u_{n+1} = \mathfrak{S}(\lim_{n \rightarrow \infty} u_n) = \mathfrak{S}u^*.$$

Now we want to show that whether u^* is unique or not. Presume that u^* and v^* are two different fixed points of \mathfrak{S} ; we get*,

$$F_H(N_A(\mathfrak{S}u^*, \mathfrak{S}v^*)) > \tau. F_H(N_A(\mathfrak{S}u^*, \mathfrak{S}v^*)) \geq F_H(N_A(u^*, v^*))$$

And so, we obtain

$$N_A(\mathfrak{S}u^*, \mathfrak{S}v^*) > N_A(u^*, v^*) = N_A(\mathfrak{S}u^*, \mathfrak{S}v^*).$$

It is a contradiction. That is u^* is unique.

So, we complete the proof. ■

Now we want to introduce and prove a new theorem. In fact, this theorem can be consider as a modified version proved in [2] (Theorem 3).

Theorem 3.2: Let $(Y, A^0, *)$ be a complete EFMS and $\lim_{t \rightarrow 0^+} A(u, v, t) > 0$, $\mathfrak{S}: Y \rightarrow Y$ be a mapping, $F_H \in \mathcal{F}_H$ and $\forall u, v \in Y (u \neq v), t \geq 0$ there exists $\tau \in (0, 1)$ such that

$$\tau. F_H(A^0(\mathfrak{S}u, \mathfrak{S}v, t)) \geq F_H(\min\{A^0(u, v, t), A^0(v, \mathfrak{S}v, t), A^0(u, \mathfrak{S}u, t)\}) \quad (3)$$

If F_H or \mathfrak{S} is continuous, \mathfrak{S} has a unique fixed point in Y .

Proof : The proof will be examine in two parts.

I. $t > 0$;

This case was proved in Theorem3's proof [2].

Because, $A^0_{u,v}(t) = A_{u,v}(t) \forall u, v \in Y$, it is similar in FMS.

II. $t = 0$;

Let $u_0 \in Y$ and the sequence $\{u_n\}$ in Y with $u_{n+1} = \mathfrak{S}u_n, \forall n \in \mathbb{N}$.

Provided that $u_{n+1} = u_n = \mathfrak{S}u_n$, for some $n \in \mathbb{N}$, then $u^* = u_n$ is fixed point of \mathfrak{S} .

If $u_{n+1} \neq u_n, \forall n \in \mathbb{N}$;

Using (1) and (3) with $u = u_{n-1}, v = u_n, t = 0$, we obtain

$$\begin{aligned} F_H(A^0(\mathfrak{S}u_{n-1}, \mathfrak{S}u_n, 0)) &= F_H(N_A(\mathfrak{S}u_{n-1}, \mathfrak{S}u_n)) \\ &> \tau. F_H(N_A(\mathfrak{S}u_{n-1}, \mathfrak{S}u_n)) \\ &\geq F_H(\min\{N_A(u_{n-1}, u_n), N_A(u_n, \mathfrak{S}u_n), N_A(u_{n-1}, \mathfrak{S}u_{n-1})\}) \\ &\geq F_H(\min\{N_A(u_{n-1}, u_n), N_A(u_n, u_{n+1}), N_A(u_{n-1}, u_n)\}) \\ &\geq F_H(\min\{N_A(u_{n-1}, u_n), N_A(u_n, u_{n+1})\}) \end{aligned}$$

And so, we get,

$$F_H(N_A(\mathfrak{S}u_{n-1}, \mathfrak{S}u_n)) = F_H(N_A(u_n, u_{n+1})) > F_H(\min\{N_A(u_{n-1}, u_n), N_A(u_n, u_{n+1})\})$$

If $\min\{N_A(u_{n-1}, u_n), N_A(u_n, u_{n+1})\} = N_A(u_n, u_{n+1})$,

$$N_A(u_n, u_{n+1}) > N_A(u_n, u_{n+1}).$$

It is a contradiction.

If $\min\{N_A(u_{n-1}, u_n), N_A(u_n, u_{n+1})\} = N_A(u_{n-1}, u_n)$,
 $N_A(u_n, u_{n+1}) > N_A(u_{n-1}, u_n)$.

We know that $\lim_{n \rightarrow \infty} u_n = u^*$, $u^* \in Y$ by the proof of Theorem 3.1.

Assume that F_H is continuous;

Using (3) with $u = u_{n+1}, v = u_n, t = 0$, we obtain

$$\begin{aligned} F_H(A^0(\mathfrak{I}u_{n+1}, \mathfrak{I}u_n, 0)) &= F_H(N_A(\mathfrak{I}u_{n+1}, \mathfrak{I}u_n)) \\ &> \tau \cdot F_H(N_A(\mathfrak{I}u_{n+1}, \mathfrak{I}u_n)) \\ &\geq F_H(\min\{N_A(u_{n+1}, u_n), N_A(u_n, \mathfrak{I}u_n), N_A(u_{n+1}, \mathfrak{I}u_{n+1})\}) \end{aligned}$$

For all $n \in \mathbb{N}$ and $t = 0$.

If $\mathfrak{I}u^* \neq u^*$ and as $n \rightarrow \infty$,

$$\begin{aligned} F_H(N_A(u_{n+1}, \mathfrak{I}u^*)) &> \tau \cdot F_H(N_A(u_{n+1}, \mathfrak{I}u^*)) \\ &\geq F_H(\min\{N_A(u_n, u^*), N_A(u_n, u_{n+1}), N_A(u^*, \mathfrak{I}u^*)\}) \end{aligned}$$

And we obtain,

$$\begin{aligned} F_H(N_A(u^*, \mathfrak{I}u^*)) &> \tau \cdot F_H(N_A(u^*, \mathfrak{I}u^*)) \\ &\geq F_H(\min\{N_A(u^*, u^*), N_A(u^*, u^*), N_A(u^*, \mathfrak{I}u^*)\}) \\ &= F_H(\min\{1, 1, N_A(u^*, \mathfrak{I}u^*)\}) \\ &= F_H(N_A(u^*, \mathfrak{I}u^*)) \end{aligned}$$

So we obtain,

$$F_H(N_A(u^*, \mathfrak{I}u^*)) = 0.$$

It is a contradiction. Therefore $\mathfrak{I}u^* = u^*$, that is u^* is a fixed point of \mathfrak{I} .

Presume that \mathfrak{I} is continuous;

Since $\{u_n\}$ is a sequence in Y with $u_{n+1} = \mathfrak{I}u_n$ and $\lim_{n \rightarrow \infty} u_n = u^*$, we obtain $\mathfrak{I}u^* = u^*$.

That is u^* is a fixed point of \mathfrak{I} .

Now we prove the uniqueness of u^* .

Presume that \mathfrak{I} have two different fixed points; u^* and v^* .

Using (1) and (3) implementing with $u = u^*$ and $v = v^*$, $t=0$ we obtain,

$$\begin{aligned} F_H(A^0(\mathfrak{I}u^*, \mathfrak{I}v^*, 0)) &= F_H(N_A(\mathfrak{I}u^*, \mathfrak{I}v^*)) \\ &> \tau \cdot F_H(N_A(\mathfrak{I}u^*, \mathfrak{I}v^*)) \\ &\geq F_H(\min\{N_A(u^*, v^*), N_A(v^*, \mathfrak{I}v^*), N_A(u^*, \mathfrak{I}u^*)\}) \\ &\geq F_H(\min\{N_A(u^*, v^*), N_A(v^*, v^*), N_A(u^*, u^*)\}) \end{aligned}$$

$$\begin{aligned}
 &= F_H(\min\{N_A(u^*, v^*), 1, 1\}) \\
 &= F_H(\min\{N_A(u^*, v^*)\})
 \end{aligned}$$

And so, we get,

$$F_H(N_A(u^*, v^*)) > F_H(N_A(u^*, v^*)).$$

It is a contradiction. Therefore \mathfrak{F} has a unique fixed point.

The proof is completed. ■

4. Conclusion

In this article, we proved some fixed point theorems in the literature, in extended fuzzy metric spaces, using new concepts. In the proofs, we specifically examined for "t=0", in which case we worked with stationary fuzzy metrics. The difference between fuzzy metrics and extended fuzzy metrics comes from "t=0" point. The case of F "t>0" is already the same as fuzzy metrics. So, we provide some methods to the researchers who want to work on fixed point theorems via various contractive mappings in the extended fuzzy metrics. If we can inspire researchers, it will be a source of happiness for us.

Ethics in Publishing

There are no ethical issues regarding the publication of this study.

Authors' Contributions

All authors contributed equally to the writing of this paper and they read and approved the final of it.

Acknowledgements



The authors thank the reviewers and editor for their precious proposals which made this paper much advanced.

References

- [1] Wardowski, D., 2012. Fixed points of a new type of contractive mappings in complete metric spaces, *Fixed Point Theory Appl.*, 2012, 94.
- [2] Huang, H., Caric, B., Dosenovic, T., Rakic, D. and Brdar, M., 2021. Fixed point theorems in fuzzy metric spaces via fuzzy F-contraction, *Mathematics Journal*, 9, 641.10
- [3] Gregori, V., Minana, J. J. and Miravet, D., 2019. Extended fuzzy metrics and fixed point theorems, *Mathematics Journal*, 7, 303.
- [4] Zadeh, L.A., 1965. Fuzzy sets, *Inform. Control*, 8, 338-353.
- [5] Kramosil, I., Michalek, J., 1975. Fuzzy metrics and statistical metric spaces, *Kybernetika*, 11, 336-344.

- [6] George, A., Veeramani, P., 1994. On some results in fuzzy metric spaces, *Fuzzy Sets and Systems*, 64, 395-399.
- [7] Banach, S., 1922. Sur les opérations dans les ensembles abstraits et leur application aux équations intégrales, *Fund Math.*, vol. 3, 133-181.
- [8] Grabiec, M., 1988. Fixed points in fuzzy metric spaces, *Fuzzy Sets and Systems*, 27, 385-389.
- [9] Gregori, V., Romaguera, S., 2014. Characterizing completable fuzzy metric spaces, *Fuzzy Sets and Systems*, 144, 411-420.
- [10] Gregori, V., Sapena, A., 2002. On fixed point theorems in fuzzy metric spaces, *Fuzzy Sets and Systems*, 125, 245-252.
- [11] Mihet, D., 2008. Fuzzy ψ - contractive mappings in non-Archimedean fuzzy metric space, *Fuzzy Sets and Systems*, 159, 739-744. 10.
- [12] Mihet, D., 2014. A note on fuzzy contractive mappings in fuzzy metric spaces, *Fuzzy Set. Syst.*, 251, 83-91,16.
- [13] Di Bari, C., Vetro, C., 2005. Fixed points, attractors and weak fuzzy contractive mappings in a fuzzy metric space, *J. Fuzzy Math.*, 13(4), 973-982.
- [14] Gopal, D. and Vetro, C., 2014. Some new fixed point theorems in fuzzy metric spaces, *Iranian Journal of Fuzzy Systems*, Vol.11, No.3, 95-107.
- [15] Samet, B. Vetro, C. Vetro, P., 2012. Fixed point theorems for α - ψ contractive type mappings, *Nonlinear Analysis Theory, Methods and Applications*, 75, 2154-2165.
- [16] Schwizer, B., Sklar, A., 1960. Statistical metric spaces, *Pacific Journal of Mathematics* 10, 315-367.

Isolated MPPT, CC, CV Solar Battery Charger Design and Application

Görkem ÖZKUR¹ , Hüseyin YEŞİLYURT^{1*} 

¹Izmir Katip Celebi University, Department of Electrical and Electronics Engineering, Izmir/Turkey

Received:18/04/2022, **Revised:** 06/07/2022, **Accepted:** 06/07/2022, **Published:** 31/03/2023

Abstract

With the rapid increase in energy consumption, the production and storage of solar energy from renewable energy sources has become an important subject. The problem of low-efficiency energy transfer from the solar panel has been overcome with the maximum power point tracking (MPPT) methods and algorithms. In this study, an isolated MPPT, constant current (CC), constant voltage (CV) solar battery charging circuit with perturb and observe (P&O) algorithm is proposed. Three different modes (MPPT, CC, CV) work together in the proposed solar battery charging circuit. Panel and battery current and voltage values are constantly measured by the microcontroller, and according to these values, the algorithm determines which mode the circuit will operate in. The converter is constantly trying to transfer maximum power to the battery in every mode it operates. The CC and CV modes in the converter also try to achieve maximum power continuously and quickly, and their algorithms are much easier and simpler than traditional PID controls. Another advantage of the algorithm is that it has a direct transition between modes, thanks to its fast response in terms of efficiency and protection. After changing the duty (D) in any mode, it is checked whether it is necessary to switch to the other two modes without returning to the beginning. Theoretical analyses have been verified by the application of a battery charging circuit with 120 W output power, 12 V output voltage and 10 A output current.

Keywords: Maximum Power Point Tracking, Solar Energy, Constant Current, Constant Voltage, Battery Charger

İzoleli MPPT, CC, CV Solar Akü Şarj Devresi Tasarımı ve Uygulaması

Öz

Enerji tüketiminin hızla artması ile birlikte yenilenebilir enerji kaynaklarından güneş enerjisinin üretimi ve depolanması önemli bir konu haline gelmiştir. Güneş panelinden düşük verimle enerji aktarımı sorunu ise maksimum güç noktası takip (MPPT) yöntemi ve algoritmaları ile birlikte aşılmaya başlanmıştır. Bu çalışmada değişir ve gözle (P&O) algoritmaları, izoleli, MPPT, sabit akım (CC), sabit gerilim (CV) solar akü şarj devresi sunulmuştur. Sunulan solar akü şarj devresinde 3 farklı mod (MPPT, CC, CV) birlikte çalışmaktadır. MPPT yöntemi olarak sade yapılı, değişir ve gözle (P&O) algoritması kullanılmaktadır. Panel ve akü akım – gerilim değerleri sürekli olarak mikroişlemci tarafından ölçülmektedir ve bu değerlere göre algoritma, devrenin hangi modda çalışacağını belirlemektedir. Dönüştürücü çalıştığı her modda sürekli olarak maksimum gücü aküye aktarmaya çalışmaktadır. Dönüştürücüde bulunan CC ve CV modları da sürekli ve hızlı bir şekilde maksimum gücü elde etmeye çalışmaktadır ve algoritmaları geleneksel PID kontrollere göre çok daha kolay ve sadedir. Algoritmanın bir diğer avantajı ise verimlilik ve koruma açısından hızlı tepki vermesi sayesinde modlar arasında direkt geçiş bulundurmasıdır. Herhangi bir modda doluluk oranı (D) değiştirildikten hemen sonra başa dönmeyen diğer iki moda geçilip geçilmemesi gerektiğine bakılmaktadır. Teorik analizler, 120 W çıkış gücü, 12 V çıkış gerilimi ve 10 A çıkış akımı değerlerine sahip akü şarj devresi uygulaması ile doğrulanmıştır.

Anahtar Kelimeler: Maksimum Güç Noktası Takibi, Solar Enerji, Sabit Gerilim, Sabit Akım, Akü Şarj Cihazı

*Corresponding Author: huseyin.yesilyurt@ikcu.edu.tr

Görkem Özkur, <https://orcid.org/0000-0002-6265-8452>

Hüseyin Yeşilyurt, <https://orcid.org/0000-0002-8969-1893>

1. Introduction

With the development of technology, the demand for electrical energy is increasing rapidly, however, many reasons such as the danger of exhaustion of resources like oil and natural gas, non-renewable and harmful to human health encourage people to produce electricity from renewable energy sources [1]. Solar panels are used to generate electricity from the sun, which is an endless source of energy. The biggest problem with electricity generation from solar panels is that low efficiency electricity that can be produced due to variables such as light and temperature [2]. In recent years, maximum power point tracking (MPPT) techniques have been used for higher efficiency electricity generation and storage. MPPT techniques aim to provide the maximum power that can be obtained from the panel according to variable conditions [3].

To implement the MPPT technique, many different methods are used, mainly perturb and observe algorithm (P&O), incremental conductance algorithm (INC), fuzzy logic (FL) [4]. On the other hand, in conventional battery charging systems, constant voltage (CV) and constant current (CC) methods are generally used [5].

DC-DC converters are divided into two groups as isolated and non-isolated. Isolated converters provide isolation by transferring the input power to the output through the transformer. Although isolated converters seem to be disadvantageous due to their higher cost, preference is of great importance in terms of system and human health, and making an isolated design increases the usability and usage areas of the design [6-7].

In this study, P&O algorithm, isolated, MPPT, CC, CV solar battery charging circuit design and application is proposed. In the proposed battery charging circuit, 3 different modes (MPPT, CC, CV) work together. As the MPPT method, the simple structured perturb and observe (P&O) algorithm is used. Thanks to the designed algorithm, the panel and battery current and voltage values are constantly measured, and it determines which mode of the circuit will operate. The circuit is constantly trying to transfer maximum power to the battery in every mode it works. CC and CV modes in the circuit also try to achieve maximum power continuously and quickly, and their algorithms are much easier and simpler than the pre-designed PID controls [8-9-10]. In addition, the proposed battery charging circuit algorithm includes overvoltage protection (OVP), undervoltage protection (UVP), overcurrent protection (OCP) and soft start (SS). The proposed P&O algorithm design has been verified by the application of the battery charging circuit with 120 W output power, 12 V output voltage and 10 A output current.

2. Material and Methods

The proposed isolated MPPT, CC, CV solar battery circuit with P&O algorithm converts the energy from the sun into electrical energy with the help of the solar panel. The electrical energy obtained from the solar panel is charged by an isolated DC-DC converter to the battery at the output. While the energy obtained from the solar panel is transferred to the battery, the MPPT algorithm is used, while the MPPT algorithm is provided by the microcontroller. The general scheme of the circuit's operation is shown in Figure 1.

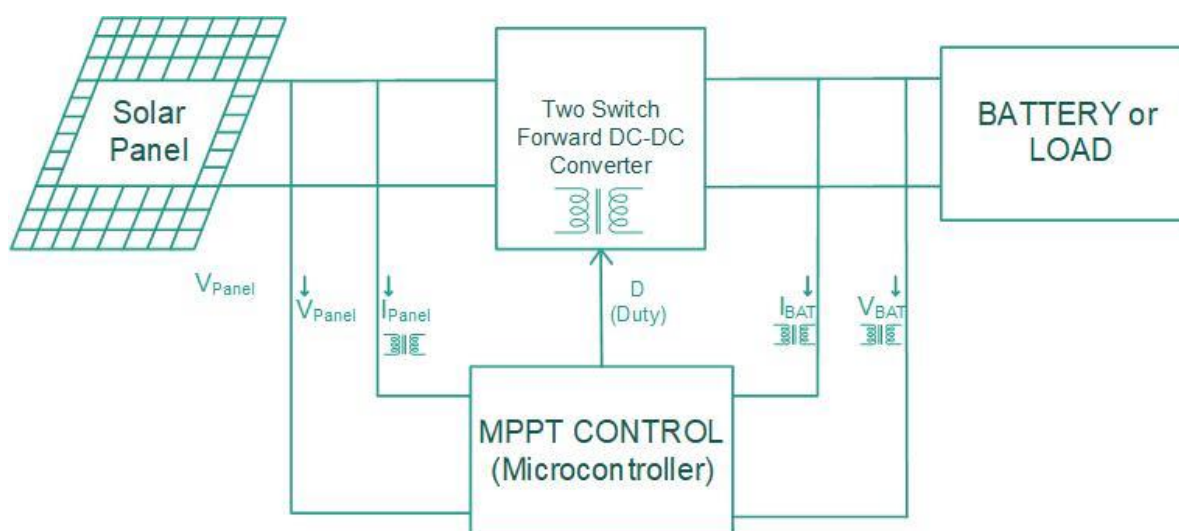


Figure 1. General Scheme of Circuit's Opeation.

2.1 Solar Panel

Solar panel formed by parallel and series connection of solar cells; it converts the rays coming from the solar energy into electrical energy. There are two types of solar panels, monocrystalline and polycrystalline, and monocrystalline panels have higher efficiency [11].

A monocrystalline solar panel with a power of 150 W is used in the proposed battery charging circuit. The electrical properties of the selected solar panel shared in Table 1.

Table 1. Electrical Charecteristics of Proposed Circuit's Solar Panel.

Panel Power	150 W
Max. Open Circuit Voltage	23.8 V
Maximum Point Voltage	20.7 V
Max. Short Circuit Current	7.61 A
Maximum Point Current	7.25 A
Max. System Voltage	1000 V

2.2 DC-DC Converter Circuit

The DC electrical energy obtained from the sun is transferred to the battery by isolating it via a two-switch forward DC-DC converter and the battery is charged. In this study, an isolated MPPT, CC, CV solar battery circuit with P&O algorithm by using a two-switch forward converter which is an isolated converter is proposed. The aim of using an isolated converter in the design; to consider system and human health, to make the usage areas of design wider.

Two-switch forward (TSF) DC-DC converters are more advantageous in terms of cost and ease of control than other isolated converters such as half-bridge and full-bridge. TSF converters are known for their durability and they are often used at medium power levels [12].

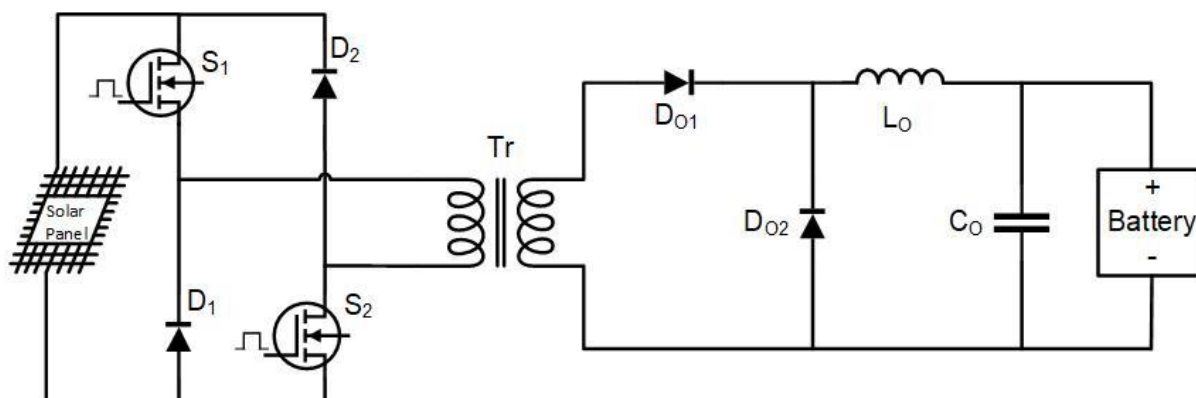


Figure 2. Two Switch Forward DC-DC Converter Schematic.

The schematic of the proposed DC-DC converter circuit is shown in Figure 2. DC-DC converter is designed to operate at 16 – 30 V input voltages, considering protection, solar panel electrical properties and cost issues. The converter works up to 120 W power and its control is provided by a microcontroller.

2.3 Control – Feedback Circuit

The proposed battery charging circuit is controlled by a microcontroller. In the battery charging circuit, continuous voltage is obtained from the solar panel, but the battery is not charged at low and high panel voltages.

In Figure 3, the electrical characteristic graph of the solar panel is shared. As can be seen from the graph, the panel power takes its maximum value at the point where the panel voltage and current multiply at the maximum.

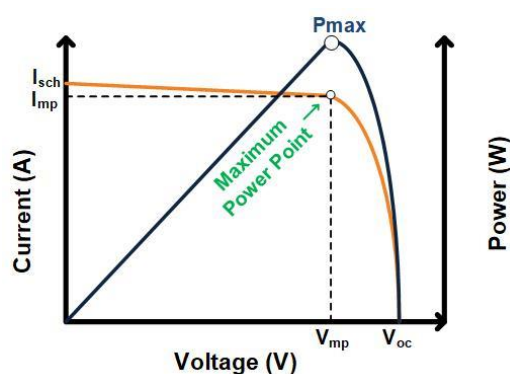


Figure 3. Electrical Characteristics of the Solar Panel.

In order to transfer the maximum value of the panel power to the output, the panel current and voltage must be constantly observed. The panel voltage is read in the ADC channel of the microcontroller with the classical voltage divider method. The panel current is read with an isolated hall current sensor considering situations such as short circuit and high current.

Batteries have maximum charge voltage and current values. The proposed solar battery charging circuit has constant current (CC) and constant voltage (CV) modes. In order to use these modes, the battery charging voltage and current must be constantly checked. In the proposed solar battery charging circuit, the battery voltage is transmitted to the microcontroller with isolation by using an optocoupler. The battery charging current is read with isolation by using hall current sensor, just like the panel current.

The solar panel current and voltage and battery charging current and voltage values are continuously read by the microcontroller and the microcontroller generates the PWM signal through the algorithm inside according to the these values and the duty (D) is constantly updated.

2.4 Battery

Lead-Acid batteries are the most common types of batteries used from the past to present, due to their low cost and rechargeable nature. Since they give high current, they can be used in projects that require high power and are widely used in solar energy systems, automobiles, etc. [13-14].

The proposed solar battery charging circuit is designed to charge a 12 V – 10 A lead-acid battery. In addition, the circuit is suitable for charging batteries as Li-Ion and LiFePO₄.

3. Control Methodology

The proposed solar battery charging circuit works in 3 different modes with the MPPT method. The microcontroller constantly measures the panel and battery voltage and current values, and takes the average of 50 analog to digital conversion (ADC) readings for each value to reach a clearer result and operates according to the average values. The basic flow diagram of the proposed solar battery charging circuit shown in Figure 4.

According to the flowchart shown in Figure 4, the algorithm has high and low voltage protections, if the solar panel voltage value is outside the determined minimum and maximum values, it does not produce a PWM signal and continues to measure continuously. If the voltage value is within the specified range, which goes to the next step, mode selection.

For the mode selection process, the predetermined CV_{limit} and CC_{limit} values are checked. CV_{limit} value indicates battery charge voltage limit value and CC_{limit} value indicates battery charge current limit value. If the measured battery voltage is less than the determined CV_{limit} value and the measured battery current is less than the determined CC_{limit} value, the MPPT mode works. If the measured battery voltage value is greater than CV_{limit} , CV mode works. And if the measured battery value is greater than CC_{limit} , CC mode works.

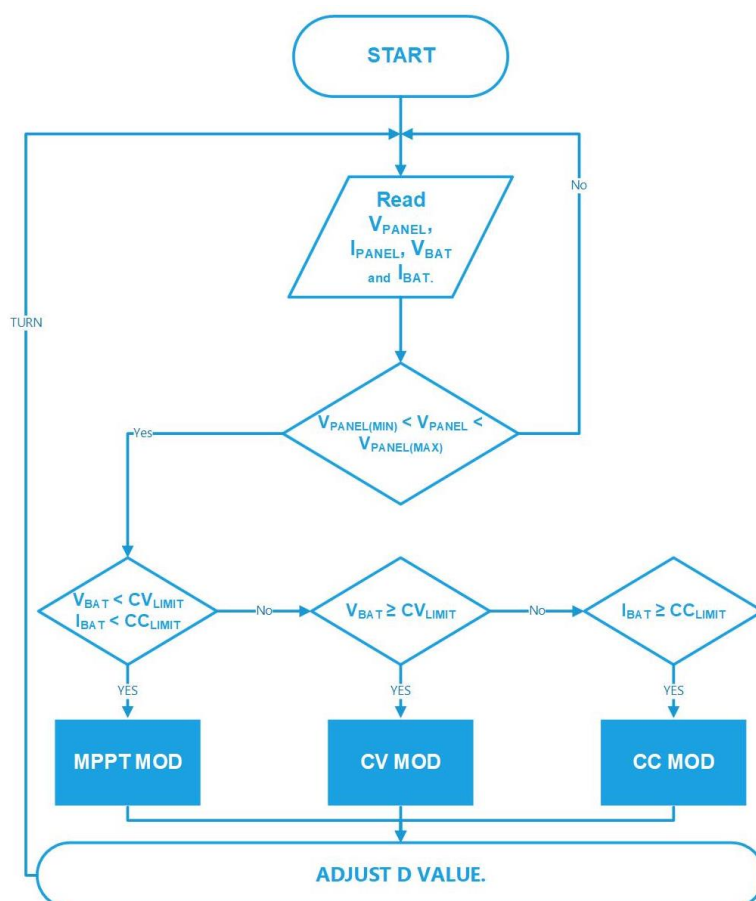


Figure 4. Basic Flowchart of the Circuit.

PWM signal is generated according to the D value determined in the operating mode and these signals are transferred to the switches of the two-switch forward DC-DC converter via the isolated drive circuit. And by going back to the beginning, it is checked in which mode the algorithm will work. This process continues continuously until the solar panel is disconnected.

3.1 MPPT Mode

If the battery voltage and battery current values are lower than the limit values, it works in MPPT mode. The simple structured P&O algorithm is used as the MPPT method. The basic flowchart of the MPPT mode is shown in figure 5.

The panel power is calculated by multiplying the solar panel voltage V_{panel} and current I_{panel} values, which are measured and averaged at the start of the MPPT mode. The calculated power value is compared with the previous power value. If the power has increased, the D value is increased, if the power has decreased, the D value is decreased, and if the power has not changed, the D value remains constant.

Immediately after changing the D value in MPPT mode, it is checked whether the battery voltage and current exceed the CV and CC limit values before the code returns. In such a case, CV or CC mode algorithms are activated directly without returning the code to the beginning.

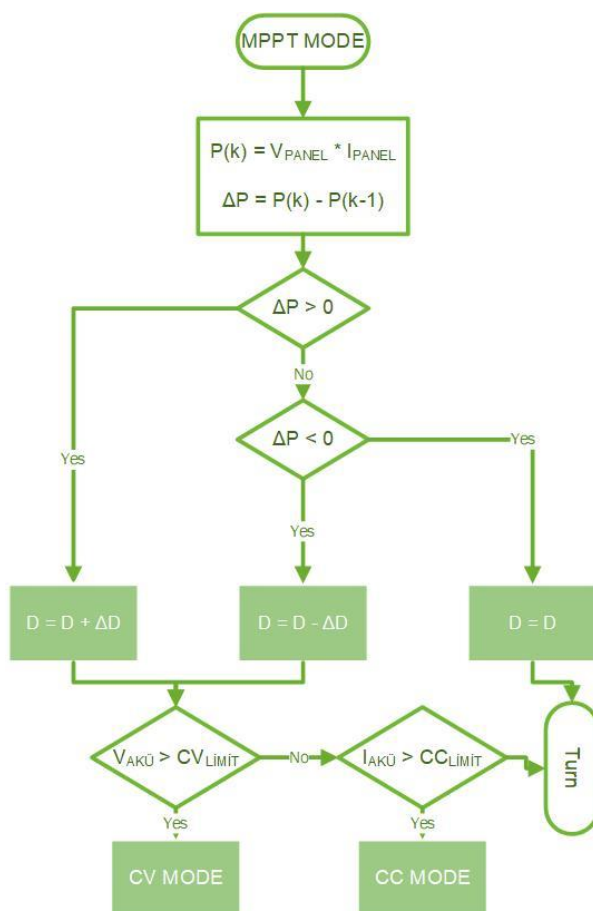


Figure 5. Basic Flowchart of MPPT Mode.

3.2 CV Mode

In case the battery voltage is higher than the determined battery charge voltage limit value, the CV mode algorithm starts to work. The basic flow diagram of CV mode operation is shown in figure 6.

When the CV mode starts, the battery voltage is checked again, if it is between the determined minimum and maximum limits, D is increased and the maximum power is tried to be obtained continuously, in line with the MPPT logic. If the battery voltage value is higher than the determined maximum limit, the D value is reduced to prevent damage to the battery and the voltage is reduced to the CV value range.

Just like in MPPT mode, the battery voltage and current values are checked immediately after PWM signal is applied to the switches in CV mode, and if the battery charge current value is greater than CC_{limit} , the CC mode is started, if the battery charge current value is lower than CC_{limit} and the battery If the charging voltage value is lower than CV_{limit} , MPPT mode is started.

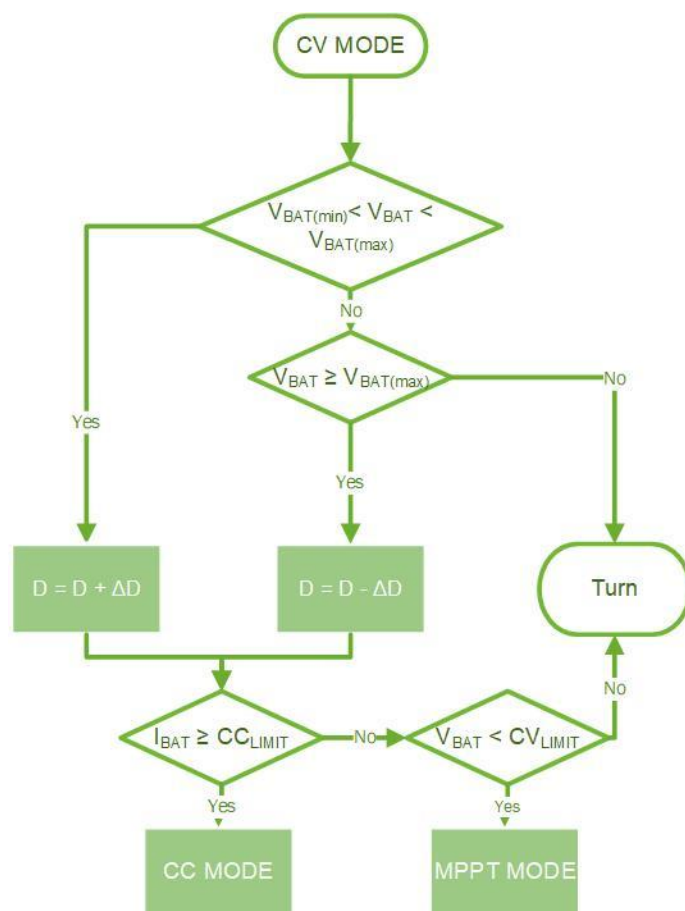


Figure 6. Basic Flowchart of CV Mode.

3.3 CC Mode

When the battery charging current is above the specified limit value, the CC mode algorithm starts to work. The basic flow diagram of the CC mode algorithm is shown in Figure 7.

CC mode stages and CV mode stages are similar. When the battery charging current is between the determined limits, the D value is continuously increased to obtain maximum power. If the battery charging current exceeds the maximum limit value, D is reduced.

As in MPPT mode and CV mode, battery charge and voltage values are checked immediately after D value is changed and PWM signal is applied to the switches. If the battery charging voltage is above the CV_{limit} value, the CV mode, if the battery charging voltage is below the CV_{limit} value and the charging current is below the CC_{limit} value, the MPPT mode algorithms start to work.

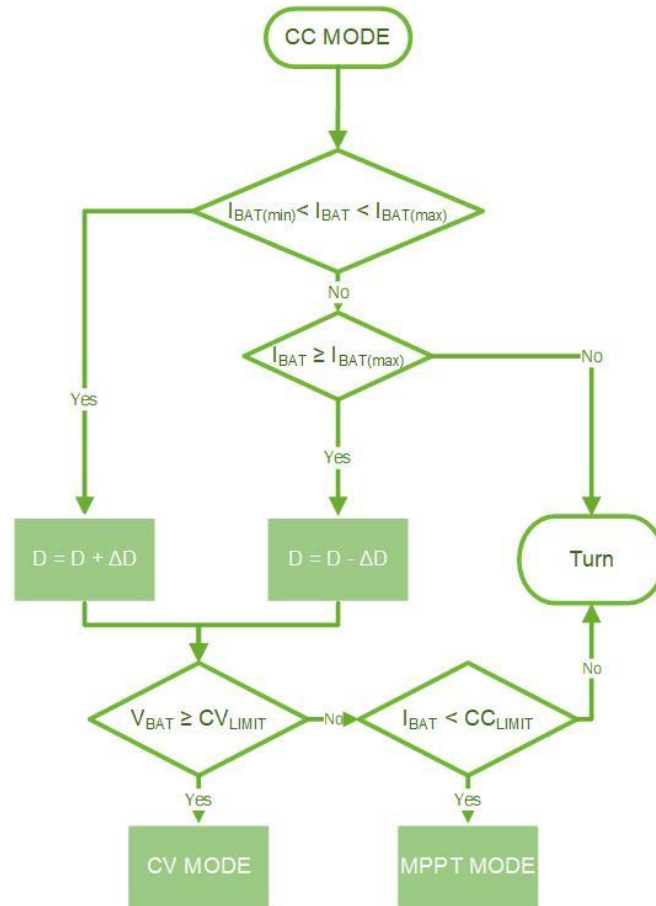


Figure 7. Basic Flowchart of CC Mode.

4. Application and Results

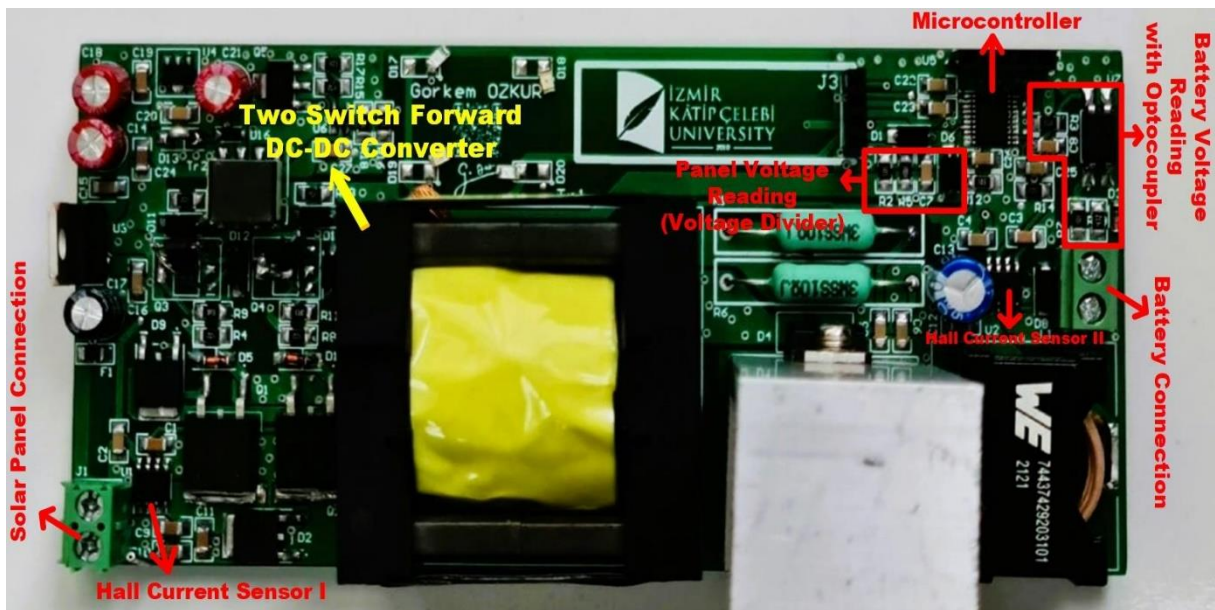


Figure 8. Proposed Solar Battery Charger Circuit.

The PCB design of the presented P&O algorithm, isolated MPPT, CC, CV solar battery circuit is shown in Figure 8. The two-switch forward DC-DC converter of the battery charging circuit presented in Figure 8, the circuits and components of the panel and battery voltage reading methods, solar panel and battery connections, microprocessor location are shown by marking.

The proposed solar charging battery circuit has been connected and tested with the algorithm designed for the circuit. Operating states, output current and voltage signals, PWM signal D change and other signals have been observed in MPPT, CC and CV modes, which are 3 different modes included in the algorithm. The signals were observed as instant value readings together with the program of the application in which the microcontroller was coded.

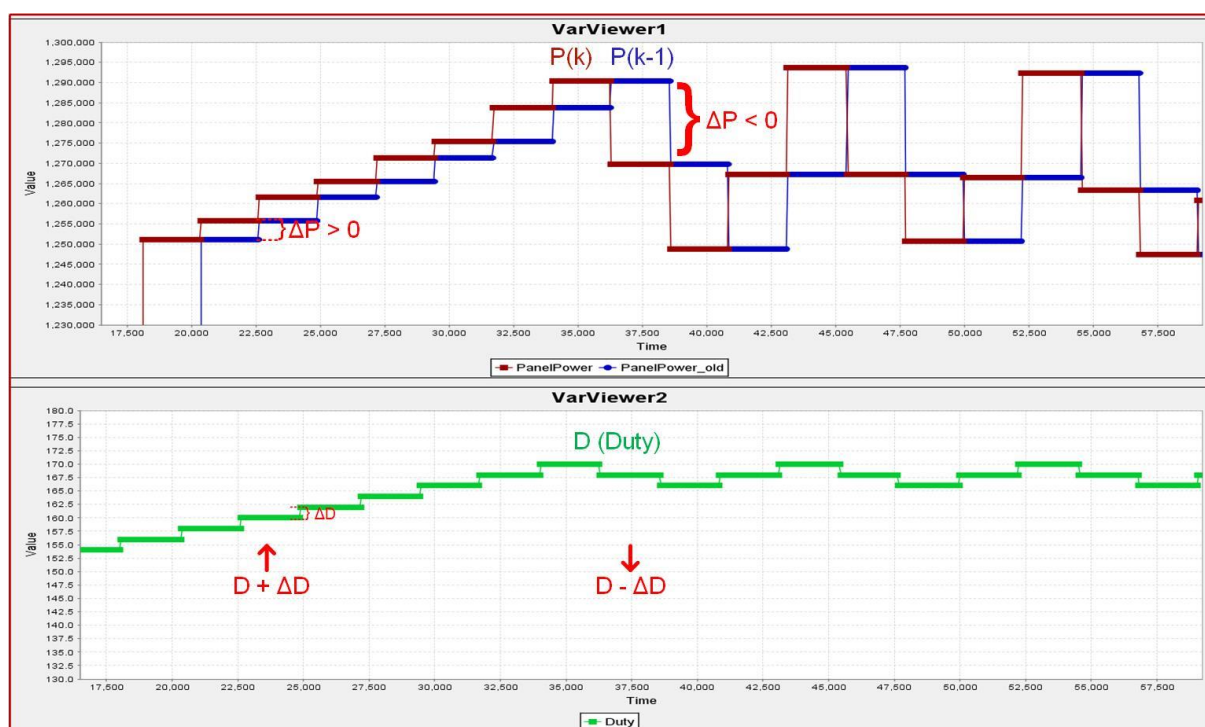


Figure 9. MPPT Mode Operating Graphs of Proposed Design.

In Figure 9, the graph of the circuit working in MPPT mode is shared. At the top of the graph, the panel power old value $P(k-1)$ and the new measured value $P(k)$ signals are seen. The lower part of the graph shows the variation of D in the same range.

Figure 9 shows the change in power with ΔP and the change in value with ΔD . As explained in the algorithm, D value increases when $\Delta P > 0$, D value decreases when $\Delta P < 0$, and D remains constant where power variation is zero.

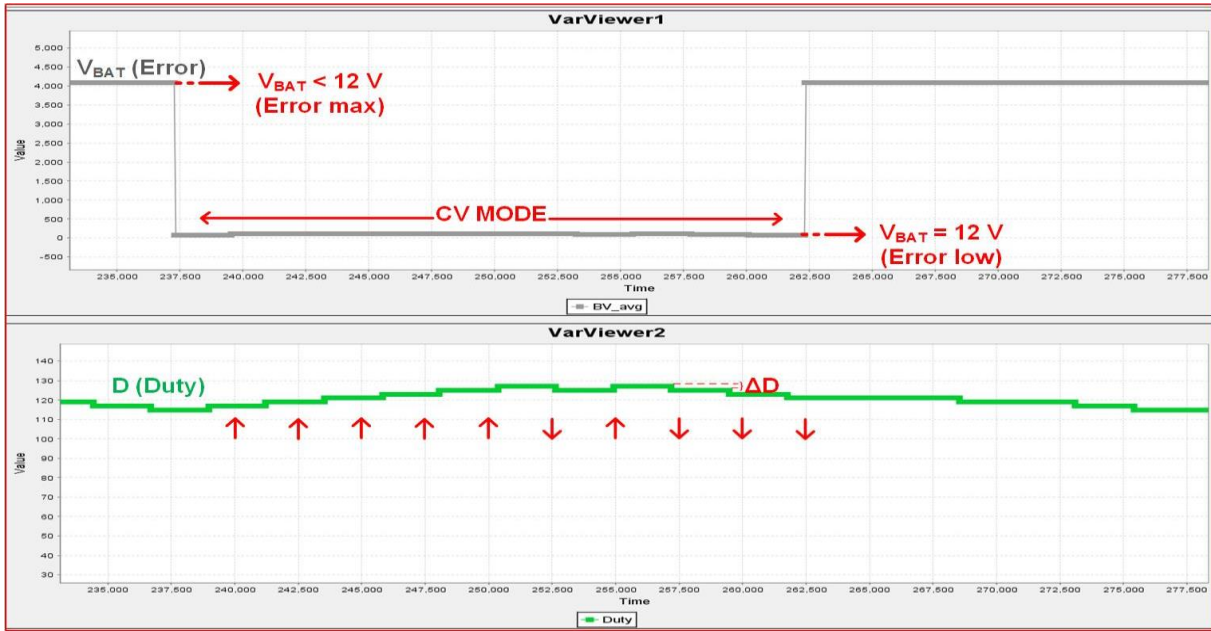


Figure 10. CV Mode Operating Graphs of Proposed Design.

The CV mode operating graph is shown in Figure 10. On the upper part of the graph, there is the battery charge voltage error reading waveform, and on the lower part, there is the D change graph. In the circuit, the battery voltage is read by generating an error signal over the optocoupler. When the battery voltage is less than 12 V, the error is maximum, and when the battery charge voltage is 12 V, the error takes a determined minimum value.

As can be seen from the graph in Figure 10 in CV mode, while trying to keep the battery voltage constant within a certain range, the D value is constantly increased within this range and maximum power is utilized. As soon as the battery charge voltage exceeds the determined maximum value, D is reduced and put into range again.

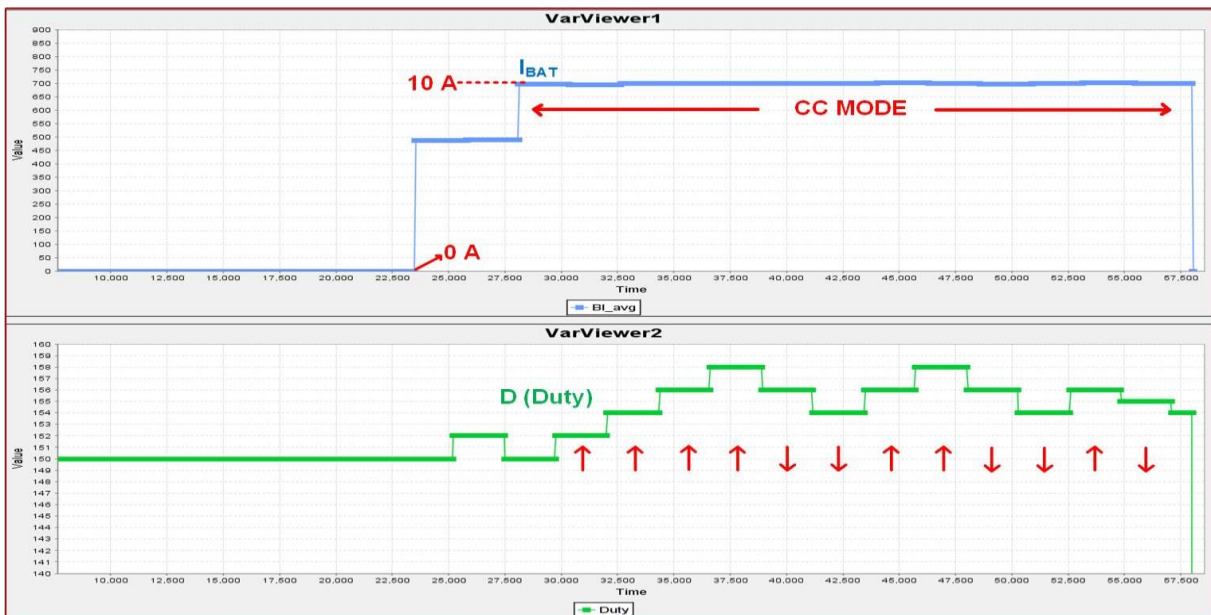


Figure 11. CC Mode Operating Graphs of Proposed Design.

Figure 11 shows the signals of the CC mode application of the solar battery charging circuit. The battery charging current is shown at the top and the D change at the bottom.

CC mod and CV mod work with similar logic. As seen in Figure 11, when the battery charging current is within the determined constant current range, the D value is constantly increasing, and when it exceeds the maximum limit value, it is decreased. Maximum power has been achieved continuously and the protection of the battery has been taken into account. Also, it is seen in the graph that the battery current is 0 for a certain period of time at the beginning, this indicates undervoltage protection, the battery is not charged because the panel voltage is lower than the specified limit value.

5. Conclusion

In this study, the design and application of isolated MPPT, CC, CV solar battery charging circuits for solar panels, the use of which is constantly increasing, is proposed. All components of the proposed solar battery charging circuit; solar panel, DC-DC converter, battery and P&O MPPT control algorithm) are explained in detail. The designed algorithm for the proposed solar battery charging circuit and the algorithms of 3 different (MPPT, CC and CV) modes are explained separately. The solar battery charging circuit designed to implement the proposed method and the control connections of the circuit are shared. The proposed method is validated with a solar battery charging circuit with 120 W output power, 12 V – 10 A output voltage and current. In practice, signals belonging to MPPT, CC and CV modes have been examined. Along with the reviews, it has been seen that the algorithms of all three modes are designed to achieve maximum power at all times. It has been seen that the proposed P&O algorithm method, together with the signals and results, can be easily applied for MPPT solar battery charging circuits compared to other algorithms such as its equivalent PID.

Ethics in Publishing

There are no ethical issues regarding the publication of this study.

Acknowledgements

Solar Battery Charger with MPPT Algorithm project is supported by TUBITAK within the scope of TUBITAK 2209-A programme.

References

- [1] Bodur, H., Yesilyurt, H., Ting, N.S., Sahin, Y., (2021), " Zero-voltage switching half-bridge pulse width modulation DC–DC converter with switched capacitor active snubber cell for renewable energy applications", *Int J Circ Theor Appl*, Volume 49, Pages 2686–2698.
- [2] Manokar, A.M., Winston, D.P., Mondol, J.D., Sathyamurthy, R., Kabeel, A.E, Panchal, H., (2018), "Comparative study of an inclined solar panel basin solar still in passive and active mode", *Solar Energy*, Volume 169, Pages 206-216.

- [3] Brito, M. A. G., Galotto, L., Sampaio, L.P., Melo, G.D.A., and Canesin, C.A., (2013), "Evaluation of the Main MPPT Techniques for Photovoltaic Applications," in IEEE Transactions on Industrial Electronics, Volume 60, No 3, Pages 1156-1167.
- [4] Karami, N., Moubayed, N., Outbib, R., (2017) "General review and classification of different MPPT Techniques", Renewable and Sustainable Energy Reviews, Volume 68, Part 1, Pages 1-18.
- [5] Schaefer, F. and Boucsein, W. (2000), "Comparison of electrodermal constant voltage and constant current recording techniques using the phase angle between alternating voltage and current." Psychophysiology, Volume 37, Pages 85-91.
- [6] Tan, N. M. L., Abe T., and Akagi, H., (2012) "Design and Performance of a Bidirectional Isolated DC–DC Converter for a Battery Energy Storage System," in IEEE Transactions on Power Electronics, Volume 27, No 3, Pages 1237-1248.
- [7] Baçoğlu, M.E., Çakır, B., (2016), "Comparisons of MPPT performances of isolated and non-isolated DC–DC converters by using a new approach", Renewable and Sustainable Energy Reviews, Volume 60, Pages 1100-1113.
- [8] Pareek S., and Kaur, T., (2021), "Hybrid ANFIS-PID Based MPPT Controller for a Solar PV System with Electric Vehicle Load", IOP Conference Series. Materials Science and Engineering, Volume 1033, (1).
- [9] Elbaksawi O., (2019), "Design of Photovoltaic System Using Buck-Boost Converter based on MPPT with PID Controller." Universal Journal of Electrical and Electronic Engineering, Volume 6, Part 5, Pages 314 - 322.
- [10] Nasir, A., Rasool, I., Sibtain, D., (2020), "Adaptive Fractional Order PID Controller Based MPPT for PV Connected Grid System Under Changing Weather Conditions." J. Electr. Eng. Technol. Volume 16, Pages 2599–2610.
- [11] Nogueira, C.E.C., Bedin, J., Niedzialkoski, R.K., Souza, S.N.M., Neves, J.C.M., (2015), "Performance of monocrystalline and polycrystalline solar panels in a water pumping system in Brazil." Renewable and Sustainable Energy Reviews, Volume 51, Pages 1610-1616.
- [12] Lin, B.-R. and Wan, J.-F., (2008), "Analysis of the ZVS two-switch forward converter with synchronous current doubler rectifier." Int. J. Circ. Theor. Appl., Volume 36, Pages 311-325.
- [13] Silva, G.de.O., Hendrick, P., (2016), "Lead–acid batteries coupled with photovoltaics for increased electricity self-sufficiency in households." Applied Energy, Volume 178, Pages 856-867.
- [14] Moseley, P.T., Rand, D.A.J., Peters, K., (2015), "Enhancing the performance of lead–acid batteries with carbon – In pursuit of an understanding," Journal of Power Sources, Volume 295, Pages 268-274.

On Neutrosophic Soft Multisets and Neutrosophic Soft Multi Topological Spaces

Adem Yolcu^{1*}, Büşra Aka¹

¹Department of Mathematics, Kafkas University, Kars, Turkey

Received: 11/05/2022, **Revised:** 30/01/2023, **Accepted:** 13/03/2023, **Published:** 31/03/2023

Abstract

In this paper, a new hybrid system, neutrosophic soft multisets is introduced. Also, we studied some basic properties such as subset, equal set, null set, absolute set, union, intersection, different on these concept. Furthermore, we introduced neutrosophic soft multi topological spaces. Some important notions such as open set, closed set, interior, closure on these topological spaces have investigated. The important properties of all studied concepts have been examined, some theorems have been proved and various examples have been presented.

Keywords: multisets, neutrosophic soft multisets, neutrosophic soft multi topology

Neutrosophic Esnek Çoklu Kümeler ve Neutrosophic Esnek Çoklu Topolojik Uzaylar Üzerine

Öz

Bu çalışma da, yeni bir hibrit sistem olan neutrosophic esnek çoklu kümeler tanıtılmaktadır. Ayrıca, alt küme, eşit küme, boş küme, mutlak küme, birleşim, kesişim, farklı gibi bazı temel özellikleri bu kavramlar üzerinde çalıştık. Dahası, neutrosophic esnek çoklu topolojik uzayları tanıttık. Bu topolojik uzaylar üzerinde açık küme, kapalı küme, iç, kapanış gibi bazı önemli kavramlar araştırılmıştır. İncelenen tüm kavramların önemli özellikleri araştırılmış, bazı önemli teoremler ispatlanmış ve konu ile ilgili çeşitli örnekler sunulmuştur.

Anahtar Kelimeler: çoklu kümeler, neutrosophic esnek çoklu kümeler, neutrosophic esnek çoklu topoloji.

1. Introduction

A number of research on generalizations of fuzzy set (FS) notions have been conducted since the invention of the fuzzy set [47]. The theory of FSs is a generalization of the traditional theory of sets, in the sense that the theory of sets should have been a special instance of the theory of FSs. Following the generalisation of FSs, several researchers used the notion of generalised FSs to a wide range of scientific and technological domains. Chang [6] was the first to develop fuzzy topology (FT), while Coker [7] defined intuitionistic fuzzy topological space. Lupianez [16-18] and Salama et al. [36] are two scholars that explored topology using neutrosophic sets (NS). In 1963, Kelly [14] introduced the notion of bitopological space (BTS). The concept of fuzzy bitopological space (FBTS) was investigated by Kandil et al. [13]. Lee et al. [15] looked

*Corresponding Author: yolcu.adem@gmail.com

Adem Yolcu, <https://orcid.org/0000-0002-4317-652X>

Büşra Aka, <https://orcid.org/0000-0003-3654-1004>

at some of the properties of Intuitionistic Fuzzy Bitopological Space (IFBTS). Garg [11] used a modified scoring function to study how to rank interval-valued Pythagorean FSs. The TOPSIS approach based on Pythagorean FSs was addressed as a Pythagorean fuzzy method for order of preference by similarity to ideal solution (TOPSIS), which accepted the experts' preferences in the form of interval-valued Pythagorean fuzzy decision matrices. In addition, [1,5,41,48] contains several investigations of the notion of Pythagorean FSs. The q-rung orthopair FSs were proposed by Yager [43], in which the sum of the qth powers of the membership (MS) and non-MS degrees is limited to one [44]. For q-rung orthopair FSs, Peng and Liu [32] investigated the systematic transformation for information measures. Pinar and Boran [33] used a q-rung orthopair fuzzy multi-criteria group decision-making technique based on a unique distance measure to pick suppliers. As Molodtsov [25] points out, each of these hypotheses has its own set of problems. Molodtsov [24] proposed an entirely new advanced soft sets theory methodology for modeling ambiguity and uncertainty that is devoid of the complexities that plague current methods. The challenge of determining the membership function, as well as other related issues, does not arise in soft set theory. Soft sets are a subset of context-dependent fuzzy sets and are referred to as neighbourhood systems. By applying the knowledge reduction approach to the information table created by the soft set, Maji et al. [19] functionalized soft sets in multicriteria decision-making issues. They defined and investigated some basic concepts in soft set theory in [20]. Ozkan studied soft multi generalized regular set and soft multi generalized closed sets [26-27].

Smarandache [37] proposed a neutrosophic set and logic in 1999, in which neutrosophic sets are defined by the truth membership function (T), indeterminacy membership function (I), and falsity membership function (F). Classical sets, fuzzy sets, and intuitionistic fuzzy sets are all generalized in neutrosophic set theory. The theory is a strong tool for dealing with knowledge that is imperfect, uncertain, and inconsistent in the actual world. Bera and Mahapatra [3] explored several important conclusions while introducing the notion of neutrosophic soft topology. New notions in neutrosophic soft topological spaces were developed by Ozturk in [29]. The terms boundary, dense set, and neutrosophic soft basis are used to describe these notions. The notion of soft subspace on neutrosophic soft topological spaces is also discussed. With regard to soft points, several intriguing results are discussed. The greatest examples are used to obtain some difficult outcomes. Yolcu et al. [46] examined the images and inverse images of neutrosophic soft sets and redefined neutrosophic soft mapping. The authors went on to trace the core activities of neutrosophic soft mapping as well as other related features. The authors did an excellent job of applying neutrosophic soft mapping to decision-making challenges. Ozturk et al. [30, 31] are pioneers of innovative neutrosophic soft set procedures. On the basis of the operation outlined in [29]. Some of the outcomes are backed up by the most easily accessible instances. New notions of neutrosophic soft sets were presented by Gunduz et al. [12]. With respect to soft points, they developed new separation axioms in neutrosophic soft topological spaces. The link between these neutrosophic soft axioms has also been discussed. Also examined are the inside and closer of neutrosophic soft settings. Other structures are addressed using these notions as a foundation. The best examples are used to secure the majority of the tough results. Also Ozturk et. al. [28] investigated neutrosophic soft compact spaces.

Blizard [4] claimed that multisets go all the way back to the beginning of numbers, claiming that the number was typically represented as a group of n strokes, tally marks, or units in ancient times. Yager [42] first proposed the concept of fuzzy multiset (FMS) as fuzzy bags. We consider our focus to the core notions such as an open fuzzy multiset, closed fuzzy multiset, interior, closure, and continuity of fuzzy multiset in the purpose of brevity. In [42], Yager introduced the idea of FMS (fuzzy bag) to generalize the FS, and in [42], he presented a calculus for them. An FMS element can appear more than once, with the same or distinct MS values. There has been some research on the multi fuzzy set [22,23,35], the intuitionistic fuzzy multiset [10,34,32,39], and the neutrosophic multiset [2,8,38,40,45]. The set theories discussed above have been applied to a variety of situations, including real-life decision-making difficulties.

In this paper, we introduced a new hybrid system neutrosophic soft multisets and neutrosophic soft multi topological spaces as an update for the research in neutrosophic multisets. Furthermore, we attempted to prove several of these features and provided instances. The neutrosophic multi almost topological group was defined using the notion of neutrosophic multi nearly continuous mapping, and several features and theorems of the neutrosophic multi almost topological group were investigated. In the section 3, we present and investigated neutrosophic soft multiset structure and some notions such as complement, union, intersection, different, subset, equal set, null set, absolute set on these set structure. We have proved important theorems about these concepts and presented various examples. In the section 4, we introduced neutrosophic soft multi topological spaces. Furthermore, we investigated some properties such as open set, closed set, interior, closure on these topological structure. Also, We have proved important theorems about these notions and presented various examples.

2. Preliminaries

Definition 2.1 [37] Let ζ be an initial universe. Then a neutrosophic set N on ζ is defined as follows:

$$N = \{ \langle h, T_N(h), I_N(h), F_N(h) \rangle : h \in \zeta \},$$

where $T, I, F : \zeta \rightarrow]0, 1+[$ and $^-0 \leq T_N(h) + I_N(h) + F_N(h) \leq 3^+$.

Definition 2.2 [24] Let ζ be an initial universe, Υ be a set of all parameters and $P(\zeta)$ denotes the power set of ζ . A pair (H, Υ) is called a soft set over ζ , where H is a mapping given by $H : \Upsilon \rightarrow P(\zeta)$.

In other words, the soft set is a parameterized family of subsets of the set ζ . For $\sigma \in \Upsilon$, $H(\sigma)$ may be considered as the set of σ -elements of the soft set (H, Υ) , or as the set of σ -approximate elements of the soft set, i.e.,

$$(H, E) = \{ (e, H(e)) : e \in E, H : E \rightarrow P(X) \}.$$

Firstly, neutrosophic soft set defined by Maji [21] and later this concept has been modified by Deli and Bromi [9] as given below:

Definition 2.3 Let ζ be an initial universe set and Υ be a set of parameters. Let $P(\zeta)$ denote the set of all neutrosophic sets of ζ . Then, a neutrosophic soft set (H, Υ) over ζ is a set defined by a set valued function H representing a mapping $H: \Upsilon \rightarrow P(\zeta)$ where H is called approximate function of the neutrosophic soft set (H, Υ) . In other words, the neutrosophic soft set is a parameterized family of some elements of the set $P(\zeta)$ and therefore it can be written as a set of ordered pairs,

$$(H, \Upsilon) = \left\{ \left(\sigma, \langle h, T_{H(\sigma)}(h), I_{H(\sigma)}(h), F_{H(\sigma)}(h) \rangle : h \in \zeta \right) : \sigma \in E \right\}$$

where $T_{H(\sigma)}(h), I_{H(\sigma)}(h), F_{H(\sigma)}(h) \in [0, 1]$, respectively called the truth-membership, indeterminacy-membership, falsity-membership function of $H(\sigma)$. Since supremum of each T, I, F is 1 so the inequality $0 \leq T_{H(\sigma)}(h) + I_{H(\sigma)}(h) + F_{H(\sigma)}(h) \leq 3$ is obvious.

Definition 2.4 [38] A neutrosophic multiset is a type of neutrosophic set in which one or more elements with the same or different neutrosophic components are repeated several times.

3. Main Theorem and Proof

Definition 3.1 Let ζ be a universe, Υ be a set of parameters. Let $P(\zeta)$ denote the all neutrosophic multisets of ζ . Then a neutrosophic soft multiset (H^{nm}, Υ) over ζ is a set valued function H^{nm} representing a mapping $H^{nm}: \Upsilon \rightarrow P(\zeta)$ where H^{nm} is called approximate function of the neutrosophic soft multiset (H^{nm}, Υ) . A neutrosophic soft multiset (H^{nm}, Υ) on ζ can be defined as follows:

$$(H^{nm}, \Upsilon) = \left\{ \left(\sigma, \langle h, \left(T_{H^{nm}(\sigma)}^1(h), T_{H^{nm}(\sigma)}^2(h), \dots, T_{H^{nm}(\sigma)}^i(h) \right), \right. \right. \\ \left. \left. \left(I_{H^{nm}(\sigma)}^1(h), I_{H^{nm}(\sigma)}^2(h), \dots, I_{H^{nm}(\sigma)}^i(h) \right), \right. \right. \\ \left. \left. \left(F_{H^{nm}(\sigma)}^1(h), F_{H^{nm}(\sigma)}^2(h), \dots, F_{H^{nm}(\sigma)}^i(h) \right) \rangle : h \in \zeta \right) \right. \\ \left. : \sigma \in \Upsilon, i = 1, 2, \dots, k \right\}$$

where truth-membership sequence $\left(T_{H^{nm}(\sigma)}^1(h), T_{H^{nm}(\sigma)}^2(h), \dots, T_{H^{nm}(\sigma)}^i(h) \right)$, the indeterminacy-membership sequence $\left(I_{H^{nm}(\sigma)}^1(h), I_{H^{nm}(\sigma)}^2(h), \dots, I_{H^{nm}(\sigma)}^i(h) \right)$ and the falsity membership

sequence $\left(F_{H^{nm}(\sigma)}^1(h), F_{H^{nm}(\sigma)}^2(h), \dots, F_{H^{nm}(\sigma)}^i(h)\right)$ and the sum of $T_{H^{nm}(\sigma)}^i(h), I_{H^{nm}(\sigma)}^i(h), F_{H^{nm}(\sigma)}^i(h) \in [0,1]$ satisfies the condition $0 \leq T_{H^{nm}(\sigma)}^i(h) + I_{H^{nm}(\sigma)}^i(h) + F_{H^{nm}(\sigma)}^i(h) \leq 3$ for $i = 1, 2, \dots, k$. Here, the element $h \in \zeta$ is repeated k times for each parameter using in set.

Example 3.1 Let $\zeta = \{h_1, h_2\}$ be universe set and $\Upsilon = \{\sigma_1, \sigma_2\}$ be a parameters. Let consider the neutrosophic soft multisets (H^{nm}, Υ) as follows;

$$(H^{nm}, \Upsilon) = \left\{ \begin{array}{l} \sigma_1, \left(\langle h_1, (0.4, 0.6, 0.8), (0.4, 0.5, 0.7), (0.5, 0.6, 0.2) \rangle \right) \\ \langle h_2, (0.3, 0.7, 0.2), (0.5, 0.5, 0.3), (0.2, 0.4, 0.4) \rangle \\ \sigma_2, \left(\langle h_1, (0.2, 0.4, 0.3), (0.4, 0.5, 0.7), (0.5, 0.6, 0.2) \rangle \right) \\ \langle h_2, (0.7, 0.4, 0.7), (0.5, 0.5, 0.3), (0.2, 0.4, 0.4) \rangle \end{array} \right\}$$

It is clear that above, $k = 3$ for the neutrosophic soft multiset (H^{nm}, Υ) . So $\forall h_i \in \zeta, i = 1, 2$ is repeated 3 times for each parameters using in set. This set can be written more clearly as follows.

$$(H^{nm}, \Upsilon) = \left\{ \begin{array}{l} \sigma_1, \left(\langle h_1, (0.4, 0.4, 0.5) \rangle, \langle h_1, (0.6, 0.5, 0.6) \rangle, \langle h_1, (0.8, 0.7, 0.2) \rangle \right) \\ \langle h_2, (0.3, 0.5, 0.2) \rangle, \langle h_2, (0.7, 0.5, 0.4) \rangle, \langle h_2, (0.2, 0.3, 0.4) \rangle \\ \sigma_2, \left(\langle h_1, (0.2, 0.4, 0.5) \rangle, \langle h_1, (0.4, 0.5, 0.6) \rangle, \langle h_1, (0.3, 0.7, 0.2) \rangle \right) \\ \langle h_2, (0.7, 0.5, 0.2) \rangle, \langle h_2, (0.4, 0.5, 0.4) \rangle, \langle h_2, (0.7, 0.3, 0.4) \rangle \end{array} \right\}$$

Definition 3.2 Let $(H_1^{nm}, \Upsilon) = \left\{ \left(\sigma, \langle h, T_{H_1^{nm}(\sigma)}^i(h), I_{H_1^{nm}(\sigma)}^i(h), F_{H_1^{nm}(\sigma)}^i(h) \rangle : h \in \zeta \right) \right\}$ and $: \sigma \in \Upsilon, i = 1, 2, \dots, k$

$(H_2^{nm}, \Upsilon) = \left\{ \left(\sigma, \langle h, T_{H_2^{nm}(\sigma)}^i(h), I_{H_2^{nm}(\sigma)}^i(h), F_{H_2^{nm}(\sigma)}^i(h) \rangle : h \in \zeta \right) \right\}$ be two neutrosophic soft multiset over the ζ . Then, there are the following relations:

1. (H_1^{nm}, Υ) is called to be neutrosophic soft multi-subset of (H_2^{nm}, Υ) is denoted by $(H_1^{nm}, \Upsilon) \subseteq (H_2^{nm}, \Upsilon)$ if $T_{H_1^{nm}(\sigma)}^i(h) \leq T_{H_2^{nm}(\sigma)}^i(h), I_{H_1^{nm}(\sigma)}^i(h) \leq I_{H_2^{nm}(\sigma)}^i(h), F_{H_1^{nm}(\sigma)}^i(h) \geq F_{H_2^{nm}(\sigma)}^i(h)$ for all $\sigma \in \Upsilon$ and for all $h \in \zeta, i = 1, 2, \dots, k$.
2. (H_1^{nm}, Υ) is called to be neutrosophic soft multi-equal of (H_2^{nm}, Υ) is denoted by $(H_1^{nm}, \Upsilon) = (H_2^{nm}, \Upsilon)$ if $T_{H_1^{nm}(\sigma)}^i(h) = T_{H_2^{nm}(\sigma)}^i(h), I_{H_1^{nm}(\sigma)}^i(h) = I_{H_2^{nm}(\sigma)}^i(h), F_{H_1^{nm}(\sigma)}^i(h) = F_{H_2^{nm}(\sigma)}^i(h)$ for all $\sigma \in \Upsilon$ and for all $h \in \zeta, i = 1, 2, \dots, k$.
3. The complement of (H_1^{nm}, Υ) is denoted by $(H_1^{nm}, \Upsilon)^c$ and defined as follows:

$$(H_1^{nm}, \Upsilon) = \left\{ \left(\sigma, \langle h, F_{H_1^{nm}(\sigma)}^i(h), 1 - I_{H_1^{nm}(\sigma)}^i(h), T_{H_1^{nm}(\sigma)}^i(h) \rangle : h \in \zeta \right) : \sigma \in \Upsilon, i = 1, 2, \dots, k \right\}$$

4. The union of (H_1^{nm}, Υ) and (H_2^{nm}, Υ) is denoted by $(H_1^{nm}, \Upsilon) \cup (H_2^{nm}, \Upsilon) = (H_3^{nm}, \Upsilon)$ and is defined as follows

$$(H_3^{nm}, \Upsilon) = \left\{ \left(\sigma, \langle h, T_{H_3^{nm}(\sigma)}^i(h), I_{H_3^{nm}(\sigma)}^i(h), F_{H_3^{nm}(\sigma)}^i(h) \rangle : h \in \zeta \right) : \sigma \in \Upsilon, i = 1, 2, \dots, k \right\}$$

where

$$T_{H_3^{nm}(\sigma)}^i(h) = \max \left\{ T_{H_1^{nm}(\sigma)}^i(h), T_{H_2^{nm}(\sigma)}^i(h) \right\}$$

$$I_{H_3^{nm}(\sigma)}^i(h) = \max \left\{ I_{H_1^{nm}(\sigma)}^i(h), I_{H_2^{nm}(\sigma)}^i(h) \right\}$$

$$F_{H_3^{nm}(\sigma)}^i(h) = \min \left\{ F_{H_1^{nm}(\sigma)}^i(h), F_{H_2^{nm}(\sigma)}^i(h) \right\}$$

5. The intersection of (H_1^{nm}, Υ) and (H_2^{nm}, Υ) is denoted by $(H_1^{nm}, \Upsilon) \cap (H_2^{nm}, \Upsilon) = (H_3^{nm}, \Upsilon)$ and is defined as follows

$$(H_3^{nm}, \Upsilon) = \left\{ \left(\sigma, \langle h, T_{H_3^{nm}(\sigma)}^i(h), I_{H_3^{nm}(\sigma)}^i(h), F_{H_3^{nm}(\sigma)}^i(h) \rangle : h \in \zeta \right) : \sigma \in \Upsilon, i = 1, 2, \dots, k \right\}$$

where

$$T_{H_3^{nm}(\sigma)}^i(h) = \min \left\{ T_{H_1^{nm}(\sigma)}^i(h), T_{H_2^{nm}(\sigma)}^i(h) \right\}$$

$$I_{H_3^{nm}(\sigma)}^i(h) = \min \left\{ I_{H_1^{nm}(\sigma)}^i(h), I_{H_2^{nm}(\sigma)}^i(h) \right\}$$

$$F_{H_3^{nm}(\sigma)}^i(h) = \max \left\{ F_{H_1^{nm}(\sigma)}^i(h), F_{H_2^{nm}(\sigma)}^i(h) \right\}$$

Definition 3.3 Let (H_1^{nm}, Υ) and (H_2^{nm}, Υ) be neutrosophic soft multiset over the ζ . The difference of (H_1^{nm}, Υ) and (H_2^{nm}, Υ) is denoted by $(H_1^{nm}, \Upsilon) \setminus (H_2^{nm}, \Upsilon) = (H_3^{nm}, \Upsilon)$ and is defined as follows;

$$(H_3^{nm}, \Upsilon) = (H_1^{nm}, \Upsilon) \cap (H_2^{nm}, \Upsilon)^c$$

$$(H_3^{nm}, \Upsilon) = \left\{ \left(\sigma, \langle h, T_{H_3^{nm}(\sigma)}^i(h), I_{H_3^{nm}(\sigma)}^i(h), F_{H_3^{nm}(\sigma)}^i(h) \rangle : h \in \zeta \right) : \sigma \in \Upsilon, i = 1, 2, \dots, k \right\}$$

where

$$T_{H_3^{nm}(\sigma)}^i(h) = \min \left\{ T_{H_1^{nm}(\sigma)}^i(h), F_{H_2^{nm}(\sigma)}^i(h) \right\}$$

$$I_{H_3^{nm}(\sigma)}^i(h) = \min \left\{ I_{H_1^{nm}(\sigma)}^i(h), 1 - I_{H_2^{nm}(\sigma)}^i(h) \right\}$$

$$F_{H_3^{nm}(\sigma)}^i(h) = \max \left\{ F_{H_1^{nm}(\sigma)}^i(h), T_{H_2^{nm}(\sigma)}^i(h) \right\}$$

Definition 3.4 Let $\{(H_p^{nm}, \Upsilon) \mid p \in I\}$ be a family of neutrosophic soft multisets over the ζ .

Then

$$\bigcup_{i \in I} (H_p^{nm}, \Upsilon) = \left\{ \left(\sigma, \langle h, \sup_{p \in I} \left[T_{H_p^{nm}(\sigma)}^i(h) \right], \sup_{p \in I} \left[I_{H_p^{nm}(\sigma)}^i(h) \right], \inf_{p \in I} \left[F_{H_p^{nm}(\sigma)}^i(h) \right] \rangle : h \in \zeta \right) \right\},$$

$$: \sigma \in \Upsilon, i = 1, 2, \dots, k$$

$$\bigcap_{i \in I} (H_p^{nm}, \Upsilon) = \left\{ \left(\sigma, \langle h, \inf_{p \in I} \left[T_{H_p^{nm}(\sigma)}^i(h) \right], \inf_{p \in I} \left[I_{H_p^{nm}(\sigma)}^i(h) \right], \sup_{p \in I} \left[F_{H_p^{nm}(\sigma)}^i(h) \right] \rangle : h \in \zeta \right) \right\}.$$

$$: \sigma \in \Upsilon, i = 1, 2, \dots, k$$

Definition 3.5

1. A null neutrosophic soft multiset over the ζ is denoted by $0_{(\zeta^{nm}, \Upsilon)}$ and defined as

$$0_{(\zeta^{nm}, \Upsilon)} = \left\{ \left(\sigma, \langle h, T_{\zeta^{nm}(\sigma)}^i(h), I_{\zeta^{nm}(\sigma)}^i(h), F_{\zeta^{nm}(\sigma)}^i(h) \rangle : h \in \zeta \right) : \sigma \in \Upsilon, i = 1, 2, \dots, k \right\}$$

where $T_{\zeta^{nm}(\sigma)}^i(h) = 0, I_{\zeta^{nm}(\sigma)}^i(h) = 0$ and $F_{\zeta^{nm}(\sigma)}^i(h) = 1$.

2. A absolute neutrosophic soft multiset over the ζ is denoted by $1_{(\zeta^{nm}, \Upsilon)}$ and defined as

$$1_{(\zeta^{nm}, \Upsilon)} = \left\{ \left(\sigma, \langle h, T_{\zeta^{nm}(\sigma)}^i(h), I_{\zeta^{nm}(\sigma)}^i(h), F_{\zeta^{nm}(\sigma)}^i(h) \rangle : h \in \zeta \right) : \sigma \in \Upsilon, i = 1, 2, \dots, k \right\}$$

where $T_{\zeta^{nm}(\sigma)}^i(h) = 1, I_{\zeta^{nm}(\sigma)}^i(h) = 1$ and $F_{\zeta^{nm}(\sigma)}^i(h) = 0$.

It is clear that $\left(0_{(\zeta^{nm}, \Upsilon)} \right)^c = 1_{(\zeta^{nm}, \Upsilon)}$ and $\left(1_{(\zeta^{nm}, \Upsilon)} \right)^c = 0_{(\zeta^{nm}, \Upsilon)}$.

Proposition 3.1 Let $(H_1^{nm}, \Upsilon), (H_2^{nm}, \Upsilon)$ and (H_3^{nm}, Υ) be neutrosophic soft multi sets over the universe set ζ . Then,

1. $(H_1^{nm}, \Upsilon) \cup \left[(H_2^{nm}, \Upsilon) \cup (H_3^{nm}, \Upsilon) \right] = \left[(H_1^{nm}, \Upsilon) \cup (H_2^{nm}, \Upsilon) \right] \cup (H_3^{nm}, \Upsilon)$ and

$$(H_1^{nm}, \Upsilon) \cap \left[(H_2^{nm}, \Upsilon) \cap (H_3^{nm}, \Upsilon) \right] = \left[(H_1^{nm}, \Upsilon) \cap (H_2^{nm}, \Upsilon) \right] \cap (H_3^{nm}, \Upsilon);$$

2. $(H_1^{nm}, \Upsilon) \cup \left[(H_2^{nm}, \Upsilon) \cap (H_3^{nm}, \Upsilon) \right] = \left[(H_1^{nm}, \Upsilon) \cup (H_2^{nm}, \Upsilon) \right] \cap \left[(H_1^{nm}, \Upsilon) \cup (H_3^{nm}, \Upsilon) \right]$ and

$$(H_1^{nm}, \Upsilon) \cap \left[(H_2^{nm}, \Upsilon) \cup (H_3^{nm}, \Upsilon) \right] = \left[(H_1^{nm}, \Upsilon) \cap (H_2^{nm}, \Upsilon) \right] \cup \left[(H_1^{nm}, \Upsilon) \cap (H_3^{nm}, \Upsilon) \right];$$

3. $(H_1^{nm}, \Upsilon) \cup 0_{(\zeta^{nm}, \Upsilon)} = (H_1^{nm}, \Upsilon)$ and $(H_1^{nm}, \Upsilon) \cap 0_{(\zeta^{nm}, \Upsilon)} = 0_{(\zeta^{nm}, \Upsilon)}$;

$$4. (H_1^{nm}, \Upsilon) \cup_{(\zeta^{nm}, \Upsilon)} 1_{(\zeta^{nm}, \Upsilon)} = 1_{(\zeta^{nm}, \Upsilon)} \text{ and } (H_1^{nm}, \Upsilon) \cap_{(\zeta^{nm}, \Upsilon)} 1_{(\zeta^{nm}, \Upsilon)} = (H_1^{nm}, \Upsilon).$$

Proof. Straightforward.

Proposition 3.2 Let (H_1^{nm}, Υ) and (H_2^{nm}, Υ) be two neutrosophic soft multi sets over the universe set ζ . Then,

1. $\left[(H_1^{nm}, \Upsilon) \cup (H_2^{nm}, \Upsilon) \right]^c = (H_1^{nm}, \Upsilon)^c \cap (H_2^{nm}, \Upsilon)^c$;
2. $\left[(H_1^{nm}, \Upsilon) \cap (H_2^{nm}, \Upsilon) \right]^c = (H_1^{nm}, \Upsilon)^c \cup (H_2^{nm}, \Upsilon)^c$.

Proof. 1. For all $e \in \Upsilon$ and $x \in \zeta$,

$$(H_1^{nm}, \Upsilon) \cup (H_2^{nm}, \Upsilon) = \left\langle \left\langle x, \max \left\{ T_{H_1^{nm}(\sigma)}^i(x), T_{H_2^{nm}(\sigma)}^i(x) \right\}, \max \left\{ I_{H_1^{nm}(\sigma)}^i(x), I_{H_2^{nm}(\sigma)}^i(x) \right\} \right\rangle, \min \left\{ F_{H_1^{nm}(\sigma)}^i(x), F_{H_2^{nm}(\sigma)}^i(x) \right\} \right\rangle$$

$$\left[(H_1^{nm}, \Upsilon) \cup (H_2^{nm}, \Upsilon) \right]^c = \left\langle \left\langle x, \min \left\{ F_{H_1^{nm}(\sigma)}^i(x), F_{H_2^{nm}(\sigma)}^i(x) \right\}, 1 - \max \left\{ I_{H_1^{nm}(\sigma)}^i(x), I_{H_2^{nm}(\sigma)}^i(x) \right\} \right\rangle, \max \left\{ T_{H_1^{nm}(\sigma)}^i(x), T_{H_2^{nm}(\sigma)}^i(x) \right\} \right\rangle.$$

Now,

$$(H_1^{nm}, \Upsilon)^c = \left\langle \left\langle x, F_{H_1^{nm}(\sigma)}^i(x), 1 - I_{H_1^{nm}(\sigma)}^i(x), T_{H_1^{nm}(\sigma)}^i(x) \right\rangle \right\rangle,$$

$$(H_2^{nm}, \Upsilon)^c = \left\langle \left\langle x, F_{H_2^{nm}(\sigma)}^i(x), 1 - I_{H_2^{nm}(\sigma)}^i(x), T_{H_2^{nm}(\sigma)}^i(x) \right\rangle \right\rangle.$$

Then,

$$(H_1^{nm}, \Upsilon)^c \cap (H_2^{nm}, \Upsilon)^c = \left\langle \left\langle x, \min \left\{ F_{H_1^{nm}(\sigma)}^i(x), F_{H_2^{nm}(\sigma)}^i(x) \right\}, \min \left\{ (1 - I_{H_1^{nm}(\sigma)}^i(x)), (1 - I_{H_2^{nm}(\sigma)}^i(x)) \right\} \right\rangle, \max \left\{ T_{H_1^{nm}(\sigma)}^i(x), T_{H_2^{nm}(\sigma)}^i(x) \right\} \right\rangle$$

$$= \left\langle \left\langle x, \min \left\{ F_{H_1^{nm}(\sigma)}^i(x), F_{H_2^{nm}(\sigma)}^i(x) \right\}, 1 - \max \left\{ I_{H_1^{nm}(\sigma)}^i(x), I_{H_2^{nm}(\sigma)}^i(x) \right\} \right\rangle, \max \left\{ T_{H_1^{nm}(\sigma)}^i(x), T_{H_2^{nm}(\sigma)}^i(x) \right\} \right\rangle.$$

Therefore, $\left[(H_1^{nm}, \Upsilon) \cup (H_2^{nm}, \Upsilon) \right]^c = (H_1^{nm}, \Upsilon)^c \cap (H_2^{nm}, \Upsilon)^c$.

2. It is obtained in a similar way.

Example 3.2 Let $\zeta = \{h_1, h_2, h_3\}$ be universe set and $\Upsilon = \{\sigma_1, \sigma_2\}$ be a parameters. Let consider two neutrosophic soft multisets (H_1^{nm}, Υ) and (H_2^{nm}, Υ) as follows:

$$(H_1^{nm}, Y) = \left\{ \begin{array}{l} \sigma_1, \left(\begin{array}{l} \langle h_1, (0.4, 0.6, 0.8, 0.3), (0.4, 0.5, 0.7, 0.6), (0.5, 0.6, 0.2, 0.8) \rangle \\ \langle h_2, (0.3, 0.7, 0.2, 0.4), (0.5, 0.5, 0.3, 0.8), (0.2, 0.4, 0.4, 0.5) \rangle \\ \langle h_3, (0.4, 0.6, 0.8, 0.3), (0.4, 0.5, 0.8, 0.2), (0.7, 0.5, 0.3, 0.6) \rangle \end{array} \right) \\ \sigma_2, \left(\begin{array}{l} \langle h_1, (0.2, 0.4, 0.3, 0.6), (0.4, 0.5, 0.7, 0.6), (0.5, 0.6, 0.2, 0.8) \rangle \\ \langle h_2, (0.7, 0.4, 0.7, 0.5), (0.5, 0.5, 0.3, 0.8), (0.2, 0.4, 0.4, 0.5) \rangle \\ \langle h_3, (0.8, 0.5, 0.3, 0.2), (0.6, 0.4, 0.3, 0.4), (0.5, 0.3, 0.2, 0.7) \rangle \end{array} \right) \end{array} \right\}$$

$$(H_2^{nm}, Y) = \left\{ \begin{array}{l} \sigma_1, \left(\begin{array}{l} \langle h_1, (0.2, 0.3, 0.6, 0.4), (0.2, 0.3, 0.2, 0.2), (0.4, 0.6, 0.1, 0.4) \rangle \\ \langle h_2, (0.5, 0.4, 0.6, 0.3), (0.6, 0.7, 0.4, 0.4), (0.8, 0.4, 0.3, 0.2) \rangle \\ \langle h_3, (0.5, 0.5, 0.7, 0.4), (0.7, 0.3, 0.6, 0.7), (0.4, 0.4, 0.5, 0.6) \rangle \end{array} \right) \\ \sigma_2, \left(\begin{array}{l} \langle h_1, (0.8, 0.5, 0.2, 0.7), (0.6, 0.3, 0.4, 0.3), (0.6, 0.2, 0.4, 0.2) \rangle \\ \langle h_2, (0.6, 0.5, 0.4, 0.3), (0.6, 0.4, 0.2, 0.1), (0.4, 0.5, 0.8, 0.6) \rangle \\ \langle h_3, (0.8, 0.6, 0.4, 0.5), (0.5, 0.3, 0.4, 0.2), (0.3, 0.5, 0.4, 0.4) \rangle \end{array} \right) \end{array} \right\}$$

Then;

$$(H_1^{nm}, Y) \cup (H_2^{nm}, Y) = \left\{ \begin{array}{l} \sigma_1, \left(\begin{array}{l} \langle h_1, (0.4, 0.6, 0.8, 0.4), (0.4, 0.5, 0.7, 0.6), (0.4, 0.6, 0.1, 0.4) \rangle \\ \langle h_2, (0.5, 0.7, 0.6, 0.4), (0.6, 0.7, 0.4, 0.8), (0.2, 0.4, 0.3, 0.2) \rangle \\ \langle h_3, (0.5, 0.6, 0.8, 0.4), (0.7, 0.5, 0.8, 0.7), (0.4, 0.4, 0.3, 0.6) \rangle \end{array} \right) \\ \sigma_2, \left(\begin{array}{l} \langle h_1, (0.8, 0.5, 0.3, 0.7), (0.6, 0.5, 0.7, 0.6), (0.5, 0.2, 0.2, 0.2) \rangle \\ \langle h_2, (0.7, 0.5, 0.7, 0.5), (0.6, 0.5, 0.3, 0.8), (0.2, 0.4, 0.4, 0.5) \rangle \\ \langle h_3, (0.8, 0.6, 0.4, 0.5), (0.6, 0.4, 0.4, 0.4), (0.3, 0.3, 0.2, 0.4) \rangle \end{array} \right) \end{array} \right\}$$

$$(H_1^{nm}, Y) \cap (H_2^{nm}, Y) = \left\{ \begin{array}{l} \sigma_1, \left(\begin{array}{l} \langle h_1, (0.2, 0.3, 0.6, 0.4), (0.2, 0.3, 0.2, 0.2), (0.4, 0.6, 0.1, 0.4) \rangle \\ \langle h_2, (0.5, 0.4, 0.6, 0.3), (0.6, 0.7, 0.4, 0.4), (0.8, 0.4, 0.3, 0.2) \rangle \\ \langle h_3, (0.5, 0.5, 0.7, 0.4), (0.7, 0.3, 0.6, 0.7), (0.4, 0.4, 0.5, 0.6) \rangle \end{array} \right) \\ \sigma_2, \left(\begin{array}{l} \langle h_1, (0.8, 0.5, 0.2, 0.7), (0.6, 0.3, 0.4, 0.3), (0.6, 0.2, 0.4, 0.2) \rangle \\ \langle h_2, (0.6, 0.5, 0.4, 0.3), (0.6, 0.4, 0.2, 0.1), (0.4, 0.5, 0.8, 0.6) \rangle \\ \langle h_3, (0.8, 0.6, 0.4, 0.5), (0.5, 0.3, 0.4, 0.2), (0.3, 0.5, 0.4, 0.4) \rangle \end{array} \right) \end{array} \right\}$$

$$(H_1^{nm}, Y) \setminus (H_2^{nm}, Y) = \left\{ \begin{array}{l} \sigma_1, \left(\begin{array}{l} \langle h_1, (0.4, 0.6, 0.1, 0.3), (0.4, 0.5, 0.7, 0.6), (0.5, 0.6, 0.6, 0.8) \rangle \\ \langle h_2, (0.3, 0.4, 0.2, 0.2), (0.4, 0.3, 0.3, 0.6), (0.5, 0.4, 0.6, 0.5) \rangle \\ \langle h_3, (0.3, 0.4, 0.5, 0.3), (0.3, 0.5, 0.4, 0.2), (0.7, 0.5, 0.7, 0.6) \rangle \end{array} \right) \\ \sigma_2, \left(\begin{array}{l} \langle h_1, (0.2, 0.2, 0.3, 0.2), (0.4, 0.5, 0.6, 0.6), (0.8, 0.6, 0.2, 0.8) \rangle \\ \langle h_2, (0.4, 0.4, 0.7, 0.5), (0.4, 0.5, 0.3, 0.8), (0.6, 0.5, 0.4, 0.5) \rangle \\ \langle h_3, (0.3, 0.5, 0.3, 0.2), (0.5, 0.4, 0.3, 0.4), (0.8, 0.6, 0.4, 0.7) \rangle \end{array} \right) \end{array} \right\}$$

Definition 3.6 Let $NSMS(\zeta^{nm}, Y)$ be the family of all neutrosophic soft multi sets over the universe set ζ and τ^{nm} be a subfamily of $NSMS(\zeta^{nm}, Y)$. Then τ^{nm} is known as neutrosophic soft multi topology on ζ if the given conditions are satisfied:

1. $0_{(\zeta^{nm}, Y)}, 1_{(\zeta^{nm}, Y)} \in \tau^{nm}$
2. The union of any number of neutrosophic soft multi sets in τ^{nm} belongs to τ^{nm}
3. The intersection of finite number of neutrosophic soft multi sets in τ^{nm} belongs to τ^{nm} .

Then (ζ, τ, Y) is said to be a neutrosophic soft multi topological space over ζ . Each members of τ^{nm} is said to be neutrosophic soft multi open set.

Definition 3.7 Let (ζ, τ, Y) be a neutrosophic soft multi topological space over ζ and (H^{nm}, Y) be a neutrosophic soft multi set over ζ . Then (H^{nm}, Y) is said to be neutrosophic soft multi closed set iff its complement is a neutrosophic soft multi open set.

Proposition 3.3 Let (ζ, τ, Y) be a neutrosophic soft multi topological space over ζ . Then

1. $0_{(\zeta^{nm}, Y)}$ and $1_{(\zeta^{nm}, Y)}$ are neutrosophic soft multi closed sets over ζ
2. the intersection of any number of neutrosophic soft multi closed sets is a neutrosophic soft multi closed set over ζ
3. the union of finite number of neutrosophic soft multi closed sets is a neutrosophic soft multi closed set over ζ .

Proof. It is easily obtained from the definition neutrosophic soft topological space and Proposition 3.2.

Definition 3.8 Let $NSMS(\zeta^{nm}, Y)$ be the family of all neutrosophic soft multisets over the universe set ζ .

1. If $\tau^{nm} = \left\{ 0_{(\zeta^{nm}, Y)}, 1_{(\zeta^{nm}, Y)} \right\}$, then τ^{nm} is said to be the neutrosophic soft multi indiscrete topology and (ζ, τ, Y) is said to be a neutrosophic soft multi indiscrete topological space over ζ .
2. If $\tau^{nm} = NSMS(\zeta^{nm}, Y)$, then τ^{nm} is said to be the neutrosophic soft multi discrete topology and (ζ, τ, Y) is said to be a neutrosophic soft multi discrete topological space over ζ .

Proposition 3.4 Let (ζ, τ_1, Y) and (ζ, τ_2, Y) be two neutrosophic soft multi topological spaces over the same universe set ζ . Then $(\zeta, \tau_1 \cap \tau_2, Y)$ is neutrosophic soft multi topological space over ζ .

Proof. 1. Since $0_{(\zeta^{nm}, \Upsilon)}, 1_{(\zeta^{nm}, \Upsilon)} \in \tau_1$ and $0_{(\zeta^{nm}, \Upsilon)}, 1_{(\zeta^{nm}, \Upsilon)} \in \tau_2$, then $0_{(\zeta^{nm}, \Upsilon)}, 1_{(\zeta^{nm}, \Upsilon)} \in \tau_1 \cap \tau_2$.

2. Suppose that $\left\{ \left(H_i^{nm}, \Upsilon \right) \middle| i \in I \right\}$ be a family of neutrosophic soft multisets in $\tau_1 \cap \tau_2$.

Then $\left(H_i^{nm}, \Upsilon \right) \in \tau_1$ and $\left(H_i^{nm}, \Upsilon \right) \in \tau_2$ for all $i \in I$, so $\bigcup_{i \in I} \left(H_i^{nm}, \Upsilon \right) \in \tau_1$ and $\bigcup_{i \in I} \left(H_i^{nm}, \Upsilon \right) \in \tau_2$.

Thus $\bigcup_{i \in I} \left(H_i^{nm}, \Upsilon \right) \in \tau_1 \cap \tau_2$.

3. Let $\left\{ \left(H_i^{nm}, \Upsilon \right) \middle| i = \overline{1, n} \right\}$ be a family of the finite number of neutrosophic soft multisets in $\tau_1 \cap \tau_2$. Then $\left(H_i^{nm}, \Upsilon \right) \in \tau_1$ and $\left(H_i^{nm}, \Upsilon \right) \in \tau_2$ for $i = \overline{1, n}$, so $\bigcap_{i=1}^n \left(H_i^{nm}, \Upsilon \right) \in \tau_1$ and $\bigcap_{i=1}^n \left(H_i^{nm}, \Upsilon \right) \in \tau_2$. Thus $\bigcap_{i=1}^n \left(H_i^{nm}, \Upsilon \right) \in \tau_1 \cap \tau_2$.

Remark 3.1 The union of two neutrosophic soft multi topologies over ζ may not be a neutrosophic soft multi topology on ζ .

Example 3.3 Let $\zeta = \{h_1, h_2, h_3\}$ be universe set and $\Upsilon = \{\sigma_1, \sigma_2\}$ be a parameters. Let consider neutrosophic soft multisets (H_1^{nm}, Υ) , (H_2^{nm}, Υ) , (H_3^{nm}, Υ) and (H_4^{nm}, Υ) as follows:

$$(H_1^{nm}, \Upsilon) = \left\{ \begin{array}{l} \sigma_1, \left(\begin{array}{l} \langle h_1, (0.8, 0.6, 0.7, 0.4), (0.6, 0.8, 0.5, 0.3), (0.4, 0.5, 0.3, 0.2) \rangle \\ \langle h_2, (0.7, 0.8, 0.6, 0.5), (0.9, 0.5, 0.6, 0.5), (0.2, 0.4, 0.4, 0.5) \rangle \\ \langle h_3, (0.6, 0.7, 0.5, 0.6), (0.7, 0.6, 0.8, 0.7), (0.5, 0.3, 0.4, 0.4) \rangle \end{array} \right) \\ \sigma_2, \left(\begin{array}{l} \langle h_1, (0.7, 0.7, 0.6, 0.6), (0.5, 0.6, 0.6, 0.9), (0.5, 0.4, 0.6, 0.2) \rangle \\ \langle h_2, (0.8, 0.9, 0.4, 0.6), (0.7, 0.8, 0.8, 0.5), (0.3, 0.2, 0.4, 0.6) \rangle \\ \langle h_3, (0.7, 0.7, 0.8, 0.6), (0.9, 0.8, 0.6, 0.7), (0.5, 0.1, 0.6, 0.3) \rangle \end{array} \right) \end{array} \right\}$$

$$(H_2^{nm}, \Upsilon) = \left\{ \begin{array}{l} \sigma_1, \left(\begin{array}{l} \langle h_1, (0.6, 0.5, 0.7, 0.3), (0.6, 0.7, 0.4, 0.3), (0.6, 0.6, 0.4, 0.4) \rangle \\ \langle h_2, (0.7, 0.6, 0.4, 0.4), (0.8, 0.3, 0.4, 0.2), (0.5, 0.6, 0.7, 0.6) \rangle \\ \langle h_3, (0.5, 0.6, 0.3, 0.5), (0.5, 0.4, 0.6, 0.5), (0.6, 0.5, 0.5, 0.7) \rangle \end{array} \right) \\ \sigma_2, \left(\begin{array}{l} \langle h_1, (0.5, 0.6, 0.4, 0.4), (0.4, 0.5, 0.3, 0.7), (0.7, 0.6, 0.7, 0.5) \rangle \\ \langle h_2, (0.7, 0.6, 0.4, 0.5), (0.5, 0.7, 0.6, 0.3), (0.4, 0.4, 0.6, 0.4) \rangle \\ \langle h_3, (0.5, 0.4, 0.7, 0.6), (0.6, 0.7, 0.3, 0.5), (0.6, 0.3, 0.7, 0.4) \rangle \end{array} \right) \end{array} \right\}$$

$$(H_3^{nm}, \Upsilon) = \left\{ \begin{array}{l} \sigma_1, \left(\begin{array}{l} \langle h_1, (0.4, 0.3, 0.5, 0.3), (0.4, 0.3, 0.2, 0.1), (0.7, 0.8, 0.5, 0.6) \rangle \\ \langle h_2, (0.6, 0.5, 0.3, 0.2), (0.5, 0.2, 0.3, 0.2), (0.6, 0.8, 0.9, 0.8) \rangle \\ \langle h_3, (0.3, 0.4, 0.2, 0.3), (0.4, 0.3, 0.5, 0.2), (0.7, 0.6, 0.5, 0.8) \rangle \end{array} \right) \\ \sigma_2, \left(\begin{array}{l} \langle h_1, (0.4, 0.3, 0.2, 0.3), (0.2, 0.4, 0.2, 0.5), (0.8, 0.7, 0.9, 0.9) \rangle \\ \langle h_2, (0.6, 0.5, 0.2, 0.4), (0.4, 0.3, 0.2, 0.2), (0.5, 0.6, 0.6, 0.7) \rangle \\ \langle h_3, (0.4, 0.3, 0.6, 0.6), (0.5, 0.6, 0.4, 0.3), (0.7, 0.5, 0.8, 0.6) \rangle \end{array} \right) \end{array} \right\}$$

$$(H_4^{nm}, \Upsilon) = \left\{ \begin{array}{l} \sigma_1, \left(\begin{array}{l} \langle h_1, (0.7, 0.8, 0.8, 0.5), (0.8, 0.7, 0.7, 0.4), (0.5, 0.3, 0.2, 0.3) \rangle \\ \langle h_2, (0.8, 0.7, 0.5, 0.6), (0.8, 0.6, 0.5, 0.3), (0.1, 0.5, 0.6, 0.4) \rangle \\ \langle h_3, (0.7, 0.9, 0.4, 0.7), (0.6, 0.7, 0.7, 0.6), (0.4, 0.3, 0.2, 0.4) \rangle \end{array} \right) \\ \sigma_2, \left(\begin{array}{l} \langle h_1, (0.6, 0.8, 0.5, 0.8), (0.7, 0.8, 0.5, 0.8), (0.4, 0.5, 0.3, 0.2) \rangle \\ \langle h_2, (0.8, 0.8, 0.5, 0.5), (0.7, 0.8, 0.7, 0.8), (0.2, 0.2, 0.4, 0.3) \rangle \\ \langle h_3, (0.6, 0.5, 0.8, 0.8), (0.7, 0.8, 0.6, 0.6), (0.3, 0.2, 0.5, 0.2) \rangle \end{array} \right) \end{array} \right\}$$

Then

$$\tau_1^{nm} = \{0_{(\zeta^{nm}, \Upsilon)}, 1_{(\zeta^{nm}, \Upsilon)}, (H_1^{nm}, \Upsilon), (H_2^{nm}, \Upsilon), (H_3^{nm}, \Upsilon)\}$$

and

$$\tau_2^{nm} = \{0_{(\zeta^{nm}, \Upsilon)}, 1_{(\zeta^{nm}, \Upsilon)}, (H_2^{nm}, \Upsilon), (H_4^{nm}, \Upsilon)\}$$

are neutrosophic soft multi topological spaces over ζ . Since $(H_1^{nm}, \Upsilon) \cup (H_4^{nm}, \Upsilon) \notin \tau_1^{nm} \cup \tau_2^{nm}$, then $\tau_1^{nm} \cup \tau_2^{nm}$ is not a neutrosophic soft multi topology on ζ .

Definition 3.9 Let (ζ, τ, Υ) be a neutrosophic soft multi topological space over ζ and $(H^{nm}, \Upsilon) \in NSMS(\zeta^{nm}, \Upsilon)$ be a neutrosophic soft multiset. Then, the neutrosophic soft multi interior of (H^{nm}, Υ) , denoted $(H^{nm}, \Upsilon)^\circ$, is defined as the neutrosophic soft multi union of all neutrosophic soft multi open subsets of (H^{nm}, Υ) .

Clearly, $(H^{nm}, \Upsilon)^\circ$ is the biggest neutrosophic soft multi open set that is contained by (H^{nm}, Υ) .

Example 3.4 Let $\zeta = \{h_1, h_2, h_3\}$ be universe set and $\Upsilon = \{\sigma_1, \sigma_2\}$ be a parameters. Let consider neutrosophic soft multisets (H_1^{nm}, Υ) and (H_2^{nm}, Υ) as follows:

$$(H_1^{nm}, \Upsilon) = \left\{ \begin{array}{l} \sigma_1, \left(\begin{array}{l} \langle h_1, (0.6, 0.5, 0.7, 0.3), (0.6, 0.7, 0.4, 0.3), (0.6, 0.6, 0.4, 0.4) \rangle \\ \langle h_2, (0.7, 0.6, 0.4, 0.4), (0.8, 0.3, 0.4, 0.2), (0.5, 0.6, 0.7, 0.6) \rangle \\ \langle h_3, (0.5, 0.6, 0.3, 0.5), (0.5, 0.4, 0.6, 0.5), (0.6, 0.5, 0.5, 0.7) \rangle \end{array} \right) \\ \sigma_2, \left(\begin{array}{l} \langle h_1, (0.5, 0.6, 0.4, 0.4), (0.4, 0.5, 0.3, 0.7), (0.7, 0.6, 0.7, 0.5) \rangle \\ \langle h_2, (0.7, 0.6, 0.4, 0.5), (0.5, 0.7, 0.6, 0.3), (0.4, 0.4, 0.6, 0.4) \rangle \\ \langle h_3, (0.5, 0.4, 0.7, 0.6), (0.6, 0.7, 0.3, 0.5), (0.6, 0.3, 0.7, 0.4) \rangle \end{array} \right) \end{array} \right\}$$

$$(H_2^{nm}, Y) = \left\{ \begin{array}{l} \sigma_1, \left(\begin{array}{l} \langle h_1, (0.7, 0.8, 0.8, 0.5), (0.8, 0.7, 0.7, 0.4), (0.5, 0.3, 0.2, 0.3) \rangle \\ \langle h_2, (0.8, 0.7, 0.5, 0.6), (0.8, 0.6, 0.5, 0.3), (0.1, 0.5, 0.6, 0.4) \rangle \\ \langle h_3, (0.7, 0.9, 0.4, 0.7), (0.6, 0.7, 0.7, 0.6), (0.4, 0.3, 0.2, 0.4) \rangle \end{array} \right) \\ \sigma_2, \left(\begin{array}{l} \langle h_1, (0.6, 0.8, 0.5, 0.8), (0.7, 0.8, 0.5, 0.8), (0.4, 0.5, 0.3, 0.2) \rangle \\ \langle h_2, (0.8, 0.8, 0.5, 0.5), (0.7, 0.8, 0.7, 0.8), (0.2, 0.2, 0.4, 0.3) \rangle \\ \langle h_3, (0.6, 0.5, 0.8, 0.8), (0.7, 0.8, 0.6, 0.6), (0.3, 0.2, 0.5, 0.2) \rangle \end{array} \right) \end{array} \right\}$$

then $\tau_1^{nm} = \{0_{(\zeta^{nm}, Y)}, 1_{(\zeta^{nm}, Y)}, (H_1^{nm}, Y), (H_2^{nm}, Y)\}$ is a neutrosophic soft multi topology on ζ .

Suppose that any $(H_3^{nm}, Y) \in NSMS(\zeta^{nm}, Y)$ is defined as follows:

$$(H_3^{nm}, Y) = \left\{ \begin{array}{l} \sigma_1, \left(\begin{array}{l} \langle h_1, (0.8, 0.6, 0.7, 0.4), (0.6, 0.8, 0.5, 0.3), (0.4, 0.5, 0.3, 0.2) \rangle \\ \langle h_2, (0.7, 0.8, 0.6, 0.5), (0.9, 0.5, 0.6, 0.5), (0.2, 0.4, 0.4, 0.5) \rangle \\ \langle h_3, (0.6, 0.7, 0.5, 0.6), (0.7, 0.6, 0.8, 0.7), (0.5, 0.3, 0.4, 0.4) \rangle \end{array} \right) \\ \sigma_2, \left(\begin{array}{l} \langle h_1, (0.7, 0.7, 0.6, 0.6), (0.5, 0.6, 0.6, 0.9), (0.5, 0.4, 0.6, 0.2) \rangle \\ \langle h_2, (0.8, 0.9, 0.4, 0.6), (0.7, 0.8, 0.8, 0.5), (0.3, 0.2, 0.4, 0.6) \rangle \\ \langle h_3, (0.7, 0.7, 0.8, 0.6), (0.9, 0.8, 0.6, 0.7), (0.5, 0.1, 0.6, 0.3) \rangle \end{array} \right) \end{array} \right\}$$

Then $0_{(\zeta^{nm}, Y)}, (H_1^{nm}, Y) \subseteq (H_3^{nm}, Y)$. Therefore, $(H_3^{nm}, Y)^\circ = 0_{(\zeta^{nm}, Y)} \cup (H_1^{nm}, Y) = (H_1^{nm}, Y)$.

Theorem 3.1 Let (ζ, τ, Y) be a neutrosophic soft multi topological space over ζ and $(H^{nm}, Y) \in NSMS(\zeta^{nm}, Y)$. (H^{nm}, Y) is a neutrosophic soft multi open set iff $(H^{nm}, Y) = (H^{nm}, Y)^\circ$.

Proof. Let (H^{nm}, Y) be a neutrosophic soft multi open set. Then the biggest neutrosophic soft multi open set that is contained by (H^{nm}, Y) is equal to (H^{nm}, Y) . Hence, $(H^{nm}, Y) = (H^{nm}, Y)^\circ$.
 Conversely, it is known that $(H^{nm}, Y)^\circ$ is a neutrosophic soft multi open set and if $(H^{nm}, Y) = (H^{nm}, Y)^\circ$, then (H^{nm}, Y) is a neutrosophic soft multi open set.

Theorem 3.2 Let (ζ, τ, Y) be a neutrosophic soft multi topological space over ζ and $(H_1^{nm}, Y), (H_2^{nm}, Y) \in NSMS(\zeta^{nm}, Y)$. Then,

1. $\left[(H_1^{nm}, Y)^\circ \right]^\circ = (H_1^{nm}, Y)^\circ$,

2. $\left(0_{(\zeta^{nm}, \Upsilon)}\right)^\circ = 0_{(\zeta^{nm}, \Upsilon)}$ and $\left(1_{(\zeta^{nm}, \Upsilon)}\right)^\circ = 1_{(\zeta^{nm}, \Upsilon)}$,
3. $\left(H_1^{nm}, \Upsilon\right) \subseteq \left(H_2^{nm}, \Upsilon\right) \Rightarrow \left(H_1^{nm}, \Upsilon\right)^\circ \subseteq \left(H_2^{nm}, \Upsilon\right)^\circ$,
4. $\left[\left(H_1^{nm}, \Upsilon\right) \cap \left(H_2^{nm}, \Upsilon\right)\right]^\circ = \left(H_1^{nm}, \Upsilon\right)^\circ \cap \left(H_2^{nm}, \Upsilon\right)^\circ$,
5. $\left(H_1^{nm}, \Upsilon\right)^\circ \cup \left(H_2^{nm}, \Upsilon\right)^\circ \subseteq \left[\left(H_1^{nm}, \Upsilon\right) \cup \left(H_2^{nm}, \Upsilon\right)\right]^\circ$.

Proof. 1. Let $\left(H_1^{nm}, \Upsilon\right)^\circ = \left(H_2^{nm}, \Upsilon\right)$. Then $\left(H_2^{nm}, \Upsilon\right) \in \tau$ iff $\left(H_2^{nm}, \Upsilon\right) = \left(H_2^{nm}, \Upsilon\right)^\circ$. So,

$$\left[\left(H_1^{nm}, \Upsilon\right)^\circ\right]^\circ = \left(H_1^{nm}, \Upsilon\right)^\circ.$$

2. Straightforward.

3. It is known that $\left(H_1^{nm}, \Upsilon\right)^\circ \subseteq \left(H_1^{nm}, \Upsilon\right) \subseteq \left(H_2^{nm}, \Upsilon\right)$ and $\left(H_2^{nm}, \Upsilon\right)^\circ \subseteq \left(H_2^{nm}, \Upsilon\right)$. Since $\left(H_2^{nm}, \Upsilon\right)^\circ$ is the biggest neutrosophic soft multi open set contained in $\left(H_2^{nm}, \Upsilon\right)$ and so, $\left(H_1^{nm}, \Upsilon\right)^\circ \subseteq \left(H_2^{nm}, \Upsilon\right)^\circ$.

4. Since $\left(H_1^{nm}, \Upsilon\right) \cap \left(H_2^{nm}, \Upsilon\right) \subseteq \left(H_1^{nm}, \Upsilon\right)$ and $\left(H_1^{nm}, \Upsilon\right) \cap \left(H_2^{nm}, \Upsilon\right) \subseteq \left(H_2^{nm}, \Upsilon\right)$, then $\left[\left(H_1^{nm}, \Upsilon\right) \cap \left(H_2^{nm}, \Upsilon\right)\right]^\circ \subseteq \left(H_1^{nm}, \Upsilon\right)^\circ$ and $\left[\left(H_1^{nm}, \Upsilon\right) \cap \left(H_2^{nm}, \Upsilon\right)\right]^\circ \subseteq \left(H_2^{nm}, \Upsilon\right)^\circ$ and so, $\left[\left(H_1^{nm}, \Upsilon\right) \cap \left(H_2^{nm}, \Upsilon\right)\right]^\circ \subseteq \left(H_1^{nm}, \Upsilon\right)^\circ \cap \left(H_2^{nm}, \Upsilon\right)^\circ$.

On the other hand, since $\left(H_1^{nm}, \Upsilon\right)^\circ \subseteq \left(H_1^{nm}, \Upsilon\right)$ and $\left(H_2^{nm}, \Upsilon\right)^\circ \subseteq \left(H_2^{nm}, \Upsilon\right)$, then $\left(H_1^{nm}, \Upsilon\right)^\circ \cap \left(H_2^{nm}, \Upsilon\right)^\circ \subseteq \left(H_1^{nm}, \Upsilon\right) \cap \left(H_2^{nm}, \Upsilon\right)$. Besides,

$\left[\left(H_1^{nm}, \Upsilon\right) \cap \left(H_2^{nm}, \Upsilon\right)\right]^\circ \subseteq \left(H_1^{nm}, \Upsilon\right) \cap \left(H_2^{nm}, \Upsilon\right)$ and it is the biggest neutrosophic soft multi

open set. Therefore, $\left(H_1^{nm}, \Upsilon\right)^\circ \cap \left(H_2^{nm}, \Upsilon\right)^\circ \subseteq \left[\left(H_1^{nm}, \Upsilon\right) \cap \left(H_2^{nm}, \Upsilon\right)\right]^\circ$. Thus,

$$\left[\left(H_1^{nm}, \Upsilon\right) \cap \left(H_2^{nm}, \Upsilon\right)\right]^\circ = \left(H_1^{nm}, \Upsilon\right)^\circ \cap \left(H_2^{nm}, \Upsilon\right)^\circ.$$

5. Since $\left(H_1^{nm}, \Upsilon\right) \subseteq \left(H_1^{nm}, \Upsilon\right) \cup \left(H_2^{nm}, \Upsilon\right)$ and $\left(H_2^{nm}, \Upsilon\right) \subseteq \left(H_1^{nm}, \Upsilon\right) \cup \left(H_2^{nm}, \Upsilon\right)$, then $\left(H_1^{nm}, \Upsilon\right)^\circ \subseteq \left[\left(H_1^{nm}, \Upsilon\right) \cup \left(H_2^{nm}, \Upsilon\right)\right]^\circ$ and $\left(H_2^{nm}, \Upsilon\right)^\circ \subseteq \left[\left(H_1^{nm}, \Upsilon\right) \cup \left(H_2^{nm}, \Upsilon\right)\right]^\circ$. Therefore, $\left(H_1^{nm}, \Upsilon\right)^\circ \cup \left(H_2^{nm}, \Upsilon\right)^\circ \subseteq \left[\left(H_1^{nm}, \Upsilon\right) \cup \left(H_2^{nm}, \Upsilon\right)\right]^\circ$.

Definition 3.10 Let (ζ, τ, Υ) be a neutrosophic soft multi topological space over ζ and $(H^{nm}, \Upsilon) \in NSMS(\zeta^{nm}, \Upsilon)$ be a neutrosophic soft multiset. Then, the neutrosophic soft multi closure of (H^{nm}, Υ) , denoted $\overline{(H^{nm}, \Upsilon)}$, is defined as the neutrosophic soft multi intersection of all neutrosophic soft multi closed supersets of (H^{nm}, Υ) .

Clearly, $\overline{(H^{nm}, \Upsilon)}$ is the smallest neutrosophic soft multi closed set that containing (H^{nm}, Υ) .

Example 3.5 Let $\zeta = \{h_1, h_2, h_3\}$ be universe set and $\Upsilon = \{\sigma_1, \sigma_2\}$ be a parameters. Let consider neutrosophic soft multisets (H_1^{nm}, Υ) and (H_2^{nm}, Υ) as follows:

$$(H_1^{nm}, \Upsilon) = \left\{ \begin{array}{l} \sigma_1, \left(\begin{array}{l} \langle h_1, (0.6, 0.5, 0.7, 0.3), (0.6, 0.7, 0.4, 0.3), (0.6, 0.6, 0.4, 0.4) \rangle \\ \langle h_2, (0.7, 0.6, 0.4, 0.4), (0.8, 0.3, 0.4, 0.2), (0.5, 0.6, 0.7, 0.6) \rangle \\ \langle h_3, (0.5, 0.6, 0.3, 0.5), (0.5, 0.4, 0.6, 0.5), (0.6, 0.5, 0.5, 0.7) \rangle \end{array} \right) \\ \sigma_2, \left(\begin{array}{l} \langle h_1, (0.5, 0.6, 0.4, 0.4), (0.4, 0.5, 0.3, 0.7), (0.7, 0.6, 0.7, 0.5) \rangle \\ \langle h_2, (0.7, 0.6, 0.4, 0.5), (0.5, 0.7, 0.6, 0.3), (0.4, 0.4, 0.6, 0.4) \rangle \\ \langle h_3, (0.5, 0.4, 0.7, 0.6), (0.6, 0.7, 0.3, 0.5), (0.6, 0.3, 0.7, 0.4) \rangle \end{array} \right) \end{array} \right\}$$

$$(H_2^{nm}, \Upsilon) = \left\{ \begin{array}{l} \sigma_1, \left(\begin{array}{l} \langle h_1, (0.7, 0.8, 0.8, 0.5), (0.8, 0.7, 0.7, 0.4), (0.5, 0.3, 0.2, 0.3) \rangle \\ \langle h_2, (0.8, 0.7, 0.5, 0.6), (0.8, 0.6, 0.5, 0.3), (0.1, 0.5, 0.6, 0.4) \rangle \\ \langle h_3, (0.7, 0.9, 0.4, 0.7), (0.6, 0.7, 0.7, 0.6), (0.4, 0.3, 0.2, 0.4) \rangle \end{array} \right) \\ \sigma_2, \left(\begin{array}{l} \langle h_1, (0.6, 0.8, 0.5, 0.8), (0.7, 0.8, 0.5, 0.8), (0.4, 0.5, 0.3, 0.2) \rangle \\ \langle h_2, (0.8, 0.8, 0.5, 0.5), (0.7, 0.8, 0.7, 0.8), (0.2, 0.2, 0.4, 0.3) \rangle \\ \langle h_3, (0.6, 0.5, 0.8, 0.8), (0.7, 0.8, 0.6, 0.6), (0.3, 0.2, 0.5, 0.2) \rangle \end{array} \right) \end{array} \right\}$$

then $\tau_1 = \{0_{(\zeta^{nm}, \Upsilon)}, 1_{(\zeta^{nm}, \Upsilon)}, (H_1^{nm}, \Upsilon), (H_2^{nm}, \Upsilon)\}$ is a neutrosophic soft multi topology on ζ .

Now, we will find neutrosophic soft multi closed sets as follows:

$$(H_1^{nm}, \Upsilon)^c = \left\{ \begin{array}{l} \sigma_1, \left(\begin{array}{l} \langle h_1, (0.6, 0.6, 0.4, 0.4), (0.4, 0.3, 0.6, 0.7), (0.6, 0.5, 0.7, 0.3) \rangle \\ \langle h_2, (0.5, 0.6, 0.7, 0.6), (0.2, 0.7, 0.6, 0.8), (0.7, 0.6, 0.4, 0.4) \rangle \\ \langle h_3, (0.6, 0.5, 0.5, 0.7), (0.5, 0.6, 0.4, 0.5), (0.5, 0.6, 0.3, 0.5) \rangle \end{array} \right) \\ \sigma_2, \left(\begin{array}{l} \langle h_1, (0.7, 0.6, 0.7, 0.5), (0.6, 0.5, 0.7, 0.3), (0.5, 0.6, 0.4, 0.4) \rangle \\ \langle h_2, (0.4, 0.4, 0.6, 0.4), (0.5, 0.3, 0.4, 0.7), (0.7, 0.6, 0.4, 0.5) \rangle \\ \langle h_3, (0.6, 0.3, 0.7, 0.4), (0.4, 0.3, 0.7, 0.5), (0.5, 0.4, 0.7, 0.6) \rangle \end{array} \right) \end{array} \right\}$$

$$(H_2^{nm}, Y)^c = \left\{ \begin{array}{l} \sigma_1, \left(\begin{array}{l} \langle h_1, (0.5, 0.3, 0.2, 0.3), (0.2, 0.3, 0.3, 0.6), (0.7, 0.8, 0.8, 0.5) \rangle \\ \langle h_2, (0.1, 0.5, 0.6, 0.4), (0.2, 0.4, 0.5, 0.7), (0.8, 0.7, 0.5, 0.6) \rangle \\ \langle h_3, (0.4, 0.3, 0.2, 0.4), (0.4, 0.3, 0.3, 0.4), (0.7, 0.9, 0.4, 0.7) \rangle \end{array} \right) \\ \sigma_2, \left(\begin{array}{l} \langle h_1, (0.4, 0.5, 0.3, 0.2), (0.3, 0.2, 0.5, 0.2), (0.6, 0.8, 0.5, 0.8) \rangle \\ \langle h_2, (0.2, 0.2, 0.4, 0.3), (0.3, 0.2, 0.3, 0.2), (0.8, 0.8, 0.5, 0.5) \rangle \\ \langle h_3, (0.3, 0.2, 0.5, 0.2), (0.3, 0.2, 0.4, 0.4), (0.6, 0.5, 0.8, 0.8) \rangle \end{array} \right) \end{array} \right\}$$

Suppose that any $(H_3^{nm}, Y) \in NSMS(\zeta^{nm}, Y)$ is defined as follows:

$$(H_3^{nm}, Y) = \left\{ \begin{array}{l} \sigma_1, \left(\begin{array}{l} \langle h_1, (0.4, 0.2, 0.2, 0.2), (0.1, 0.2, 0.1, 0.5), (0.8, 0.9, 0.8, 0.7) \rangle \\ \langle h_2, (0.1, 0.3, 0.4, 0.2), (0.2, 0.3, 0.2, 0.5), (0.8, 0.8, 0.7, 0.8) \rangle \\ \langle h_3, (0.3, 0.1, 0.2, 0.3), (0.2, 0.2, 0.1, 0.3), (0.8, 0.9, 0.5, 0.8) \rangle \end{array} \right) \\ \sigma_2, \left(\begin{array}{l} \langle h_1, (0.2, 0.4, 0.3, 0.2), (0.2, 0.1, 0.3, 0.2), (0.7, 0.8, 0.6, 0.9) \rangle \\ \langle h_2, (0.1, 0.1, 0.2, 0.3), (0.2, 0.2, 0.1, 0.1), (0.8, 0.9, 0.6, 0.7) \rangle \\ \langle h_3, (0.2, 0.1, 0.4, 0.1), (0.2, 0.2, 0.3, 0.2), (0.6, 0.8, 0.8, 0.9) \rangle \end{array} \right) \end{array} \right\}$$

Then $1_{(\zeta^{nm}, Y)}, (H_1^{nm}, Y)^c, (H_2^{nm}, Y)^c \supseteq (H_3^{nm}, Y)$. Therefore,

$$\overline{(H_3^{nm}, Y)} = 1_{(\zeta^{nm}, Y)} \cap (H_1^{nm}, Y)^c \cap (H_2^{nm}, Y)^c = (H_2^{nm}, Y)^c.$$

Theorem 3.3 Let (ζ, τ, Y) be a neutrosophic soft multi topological space over ζ and $(H^{nm}, Y) \in NSMS(\zeta^{nm}, Y)$. (H^{nm}, Y) is neutrosophic soft multi closed set iff $(H^{nm}, Y) = \overline{(H^{nm}, Y)}$.

Proof. Straightforward.

Theorem 3.4 Let (ζ, τ, Y) be a neutrosophic soft multi topological space over ζ and $(H_1^{nm}, Y), (H_2^{nm}, Y) \in NSMS(\zeta^{nm}, Y)$. Then,

1. $\overline{\overline{(H_1^{nm}, Y)}} = \overline{(H_1^{nm}, Y)}$,
2. $\overline{0_{(\zeta^{nm}, Y)}} = 0_{(\zeta^{nm}, Y)}$ and $\overline{1_{(\zeta^{nm}, Y)}} = 1_{(\zeta^{nm}, Y)}$
3. $(H_1^{nm}, Y) \subseteq (H_2^{nm}, Y) \Rightarrow \overline{(H_1^{nm}, Y)} \subseteq \overline{(H_2^{nm}, Y)}$,
4. $\overline{\overline{(H_1^{nm}, Y)} \cup \overline{(H_2^{nm}, Y)}} = \overline{(H_1^{nm}, Y)} \cup \overline{(H_2^{nm}, Y)}$,
5. $\overline{\overline{(H_1^{nm}, Y)} \cap \overline{(H_2^{nm}, Y)}} \subseteq \overline{(H_1^{nm}, Y)} \cap \overline{(H_2^{nm}, Y)}$.

Proof. 1. Let $\overline{(H_1^{nm}, \Upsilon)} = (H_2^{nm}, \Upsilon)$. Then, (H_2^{nm}, Υ) is a neutrosophic soft multi closed set. Hence, (H_2^{nm}, Υ) and $\overline{(H_2^{nm}, \Upsilon)}$ are equal. Therefore, $\overline{\overline{(H_1^{nm}, \Upsilon)}} = \overline{(H_1^{nm}, \Upsilon)}$.

2. Straightforward.

3. It is known that $(H_1^{nm}, \Upsilon) \subseteq \overline{(H_1^{nm}, \Upsilon)}$ and $(H_2^{nm}, \Upsilon) \subseteq \overline{(H_2^{nm}, \Upsilon)}$ and so, $(H_1^{nm}, \Upsilon) \subseteq (H_2^{nm}, \Upsilon) \subseteq \overline{(H_2^{nm}, \Upsilon)}$. Since $\overline{(H_1^{nm}, \Upsilon)}$ is the smallest neutrosophic soft multi closed set containing (H_1^{nm}, Υ) , then $\overline{(H_1^{nm}, \Upsilon)} \subseteq \overline{(H_2^{nm}, \Upsilon)}$.

4. Since $(H_1^{nm}, \Upsilon) \subseteq (H_1^{nm}, \Upsilon) \cup (H_2^{nm}, \Upsilon)$ and $(H_2^{nm}, \Upsilon) \subseteq (H_1^{nm}, \Upsilon) \cup (H_2^{nm}, \Upsilon)$, then $\overline{(H_1^{nm}, \Upsilon)} \subseteq \overline{(H_1^{nm}, \Upsilon) \cup (H_2^{nm}, \Upsilon)}$ and $\overline{(H_2^{nm}, \Upsilon)} \subseteq \overline{(H_1^{nm}, \Upsilon) \cup (H_2^{nm}, \Upsilon)}$ and so, $\overline{(H_1^{nm}, \Upsilon)} \cup \overline{(H_2^{nm}, \Upsilon)} \subseteq \overline{(H_1^{nm}, \Upsilon) \cup (H_2^{nm}, \Upsilon)}$.

Conversely, since $(H_1^{nm}, \Upsilon) \subseteq \overline{(H_1^{nm}, \Upsilon)}$ and $(H_2^{nm}, \Upsilon) \subseteq \overline{(H_2^{nm}, \Upsilon)}$, then $(H_1^{nm}, \Upsilon) \cup (H_2^{nm}, \Upsilon) \subseteq \overline{(H_1^{nm}, \Upsilon)} \cup \overline{(H_2^{nm}, \Upsilon)}$. Besides, $\overline{(H_1^{nm}, \Upsilon) \cup (H_2^{nm}, \Upsilon)}$ is the smallest neutrosophic soft multi closed set that containing $(H_1^{nm}, \Upsilon) \cup (H_2^{nm}, \Upsilon)$. Therefore,

$$\overline{(H_1^{nm}, \Upsilon) \cup (H_2^{nm}, \Upsilon)} \subseteq \overline{(H_1^{nm}, \Upsilon)} \cup \overline{(H_2^{nm}, \Upsilon)}. \quad \text{Thus,}$$

$$\overline{(H_1^{nm}, \Upsilon) \cup (H_2^{nm}, \Upsilon)} = \overline{(H_1^{nm}, \Upsilon)} \cup \overline{(H_2^{nm}, \Upsilon)}.$$

5. Since $(H_1^{nm}, \Upsilon) \cap (H_2^{nm}, \Upsilon) \subseteq \overline{(H_1^{nm}, \Upsilon)} \cap \overline{(H_2^{nm}, \Upsilon)}$ and $\overline{(H_1^{nm}, \Upsilon) \cap (H_2^{nm}, \Upsilon)}$ is the smallest neutrosophic soft multi closed set that containing $(H_1^{nm}, \Upsilon) \cap (H_2^{nm}, \Upsilon)$, then $\overline{(H_1^{nm}, \Upsilon) \cap (H_2^{nm}, \Upsilon)} \subseteq \overline{(H_1^{nm}, \Upsilon)} \cap \overline{(H_2^{nm}, \Upsilon)}$.

Theorem 3.5 Let (ζ, τ, Υ) be a neutrosophic soft multi topological space over ζ and $(H^{nm}, \Upsilon) \in NSMS(\zeta^{nm}, \Upsilon)$. Then,

$$1. \left[\overline{(H^{nm}, \Upsilon)} \right]^c = \left[(H^{nm}, \Upsilon)^c \right]^c,$$

$$2. \left[\left(H^{nm}, \Upsilon \right)^\circ \right]^c = \overline{\left[\left(H^{nm}, \Upsilon \right)^c \right]}.$$

Proof. 1.

$$\begin{aligned} \overline{\left(H^{nm}, \Upsilon \right)} &= \cap \left\{ (G, \Upsilon) \in \tau^c : (G, \Upsilon) \supseteq \left(H^{nm}, \Upsilon \right) \right\} \\ &\Rightarrow \left[\overline{\left(H^{nm}, \Upsilon \right)} \right]^c = \left[\cap \left\{ (G, \Upsilon) \in \tau^c : (G, \Upsilon) \supseteq \left(H^{nm}, \Upsilon \right) \right\} \right]^c \\ &= \cup \left\{ (G, \Upsilon)^c \in \tau : (G, \Upsilon)^c \subseteq \left(H^{nm}, \Upsilon \right)^c \right\} = \left[\left(H^{nm}, \Upsilon \right)^c \right]^\circ. \end{aligned}$$

$$\begin{aligned} 2. \left(H^{nm}, \Upsilon \right)^\circ &= \cup \left\{ (G, \Upsilon) \in \tau : (G, \Upsilon) \subseteq \left(H^{nm}, \Upsilon \right) \right\} \\ &\Rightarrow \left[\left(H^{nm}, \Upsilon \right)^\circ \right]^c = \left[\cup \left\{ (G, \Upsilon) \in \tau : (G, \Upsilon) \subseteq \left(H^{nm}, \Upsilon \right) \right\} \right]^c \\ &= \cap \left\{ (G, \Upsilon)^c \in \tau^c : (G, \Upsilon)^c \supseteq \left(H^{nm}, \Upsilon \right)^c \right\} = \overline{\left[\left(H^{nm}, \Upsilon \right)^c \right]}. \end{aligned}$$

4. CONCLUSION

In this paper, we defined basic concept of neutrosophic soft multisets and neutrosophic soft multi topological spaces. The basic operations of neutrosophic soft multisets, namely, subset, equal set, null set, equal set, complement, union, intersection different and some basic properties of neutrosophic soft multi topological spaces, namely, open set, closed set, interior, closure have investigated. Novel numerical examples are given for definitions. Neutrosophic soft sets have an important place in the solution of decision making problems. We hope that with the newly defined neutrosophic soft multiset structure, important studies will be conducted on decision making processes. It is possible that this work will be extended in the future for: 1. Dealing neutrosophic soft multiset and topology with multi-criteria decision-making techniques. 2. Various topological concepts such as separation axioms, connectivity, compactness, using this structure. 3. All concepts studied on NSS can be carried in accordance with this structure.

Ethics in Publishing

There are no ethical issues regarding the publication of this study

Author Contributions

Authors did not declare any contributions.

References

- [1] Bakioglu, G. and Atahan, A. O., (2021) AHP integrated TOPSIS and VIKOR methods with Pythagorean fuzzy sets to prioritize risks in self-driving vehicles, *Applied Soft Computing*, 99, 106948.
- [2] Basumatary, B., Wary, N., Mwchahary, D.D., Brahma, A.K., Moshahary, J., Basumatary, U.R. and Basumatary, J., (2021) A Study on Some Properties of Neutrosophic Multi Topological Group, *Symmetry*, 13(9), 1689.
- [3] Bera T. and Mahapatra N. K., (2017) Introduction to neutrosophic soft topological space, *Opsearch*, 54(4), 841–867.
- [4] Blizard, W., (1989) Multiset theory, *Notre Dame J. Form. Logic*, 30, 36–66.
- [5] Boyacı, A.Ç., and Şişman, A., (2022). Pandemic hospital site selection: a GIS-based MCDM approach employing Pythagorean fuzzy sets. *Environmental Science and Pollution Research*, 29(2), 1985-1997.
- [6] Chang, C. L., (1968) Fuzzy topological spaces, *J. Math. Anal. Appl.* 24(1), 182–190.
- [7] Coker D., (1996) A note on intuitionistic sets and intuitionistic points, *Tr. J. of Mathematics*, 20, 343-351.
- [8] Das, R., and Tripathy, B.C., (2020) Neutrosophic multiset topological space, *Neutrosophic sets and systems*, 35, 142-152.
- [9] Deli I. and Broumi S., (2015) Neutrosophic soft relations and some properties, *Ann. Fuzzy Math. Inform.*, 9(1), 169–182.
- [10] Ejegwa, P.A., (2015) New operations on intuitionistic fuzzy multisets. *J. of Mathematics and Informatics*, 3, 17-23.
- [11] Garg, H., (2017) A new improved score function of an interval-valued Pythagorean fuzzy set based TOPSIS method, *Int. J. Uncertain. Quantif.*, 7, 463–474.
- [12] Gunduz Aras, C., Ozturk, T.Y. and Bayramov, S., (2019) Separation axioms on neutrosophic soft topological spaces, *Turkish Journal of Mathematics*, 43(1), 498–510.
- [13] Kandil, A., Nouth, A.A., El-Sheikh, S.A., (1995) On fuzzy bitopological spaces, *Fuzzy Sets Syst.*, 74, 353–363.
- [14] Kelly, J.C. (1963) Bitopological spaces, *Proc. Lond. Math. Soc.*, 3, 71–89.
- [15] Lee, S.J. and Kim, J.T., (2012) Some Properties of Intuitionistic Fuzzy Bitopological Spaces. In *Proceedings of the 6th International Conference on Soft Computing and Intelligent Systems, and The 13th IEEE International Symposium on Advanced Intelligence Systems*, Kobe, Japan, pp. 20–24
- [16] Lupianez, F.G., (2008) On neutrosophic topology, *Int. J. Syst. Cybern.*, 37, 797–800.
- [17] Lupianez, F.G., (2009) Interval neutrosophic sets and topology, *Int. J. Syst. Cybern.*, 38, 621–624.
- [18] Lupianez, F.G. (2010) On neutrosophic paraconsistent topology, *Int. J. Syst. Cybern.*, 39, 598–601.
- [19] Maji, P.K., Roy, A.R. and Biswas, R., (2002) An application of soft sets in a decision making problem, *Computers & Mathematics with Applications*, 44(8-9), 1077–1083.

- [20] Maji, P.K., Biswas, R. and Roy, A.R., (2003) Soft set theory, *Computers & Mathematics with Applications*, 45(4-5), 555–562.
- [21] Maji, P. K., (2013) Neutrosophic soft set, *Ann. Fuzzy Math. Inform.* 5(1), 157–168.
- [22] Miyamoto, S., (2001) Fuzzy Multisets and Their Generalizations. In *Multiset Processing*; Springer: Berlin, Germany, pp. 225–235.
- [23] Miyamoto, S., (2000) Multisets and fuzzy multisets. In *Soft computing and human-centered machines*, pp. 9-33, Springer, Tokyo.
- [24] Molodtsov, D., (1999) Soft Set Theory-First Results, *Comput. Math. Appl.*, 37, 19-31.
- [25] Molodtsov, D., Leonov, V.Y. and Kovkov, D.V. (2006) Soft sets technique and its application, *Nechetkie Sistemy Myagkie Vychisleniya*, 1, 8–39.
- [26] Ozkan, A., (2018) On Soft Multi Generalized Closed Sets. *Asian Journal of Mathematics and Computer Research*, 25(6), 353-366.
- [27] Ozkan, A., (2017). Soft multi generalized regular sets in soft multi topological spaces. *Journal of Advanced Studies in Topology*, 8(1), 9-20.
- [28] Ozturk, T. Y., Benek, A. and Ozkan, A. (2021). Neutrosophic soft compact spaces, *Afrika Matematika*, 32(1), 301-316.
- [29] Ozturk, T.Y., (2021) Some structures on neutrosophic topological spaces. *Applied Mathematics and Nonlinear Sciences*, 6(1), 467-478.
- [30] Ozturk, T. Y., Aras, C. G. and Bayramov, S., (2019) A New Approach to Operations on Neutrosophic Soft Sets and to Neutrosophic Soft Topological Spaces, *Communications in Mathematics and Applications*, 10(3), 481-493.
- [31] Ozturk, T.Y., Karataş, E. and Yolcu, A., (2021) On neutrosophic soft continuous mappings, *Turkish Journal of Mathematics*, 45(1), 81-95.
- [32] Peng, X. and Liu, L. (2019) Information measures for q-rung orthopair fuzzy sets, *Int. J. Intell. Syst.*, 34, 1795–1834.
- [33] Pinar, A., Boran, F.E., (2020) A q-rung orthopair fuzzy multi-criteria group decision making method for supplier selection based on a novel distance measure, *Int. J. Mach. Learn. Cybern.*, 11, 1749–1780.
- [34] Rajarajeswari, P. and Uma, N., (2014) Normalized hamming similarity measure for intuitionistic fuzzy multi sets and its application in medical diagnosis, *International Journal of Mathematics Trends and Technology*, 5(3), 219-225.
- [35] Riesgo, Á., Alonso, P., Díaz, I. and Montes, S. (2018) Basic operations for fuzzy multisets. *International Journal of Approximate Reasoning*, 101, 107-118.
- [36] Salama, A.A.; Smarandache, F.; Kroumov, V., (2014) Closed sets and Neutrosophic Continuous Functions. *Neutrosophic Sets Syst.* 2014, 4, 4–8.
- [37] Smarandache, F., (2005) Neutrosophic set, a generalisation of the intuitionistic fuzzy sets, *Int. J. Pure Appl. Math.*, 24, 287–297.
- [38] Smarandache, F., (2007) Neutrosophic Perspectives: Triplets, Duplets, Multisets, Hybrid Operators, Modal Logic, Hedge Algebras and Applications; p. 323, Pons Publishing House Brussels: Brussels, Belgium.
- [39] Shinoj, T. K. and John, S. J., (2012) Intuitionistic fuzzy multisets and its application in medical diagnosis, *World Academy of Science, Engineering and Technology*, 6(1), 1418-1421.

- [40] Uluçay, V. and Şahin, M., (2019) Neutrosophic multigroups and applications. *Mathematics*, 7(1), 95.
- [41] Ullah, K., Mahmood, T., Ali, Z. and Jan, N., (2020) On some distance measures of complex Pythagorean fuzzy sets and their applications in pattern recognition. *Complex & Intelligent Systems*, 6(1), 15-27.
- [42] Yager, R.R., (1986) On the theory of bags, *Int. J. Gen Syst.*, 13, 23-37.
- [43] Yager, R.R., (2017) Generalized orthopair fuzzy sets. *IEEE Trans. Fuzzy Syst.*, 25, 1222–1230.
- [44] Yager, R.R. and Alajlan, N., (2017) Approximate reasoning with generalized orthopair fuzzy sets, *Inf. Fusion*, 38, 65–73
- [45] Ye, S. and Ye, J., (2014) Dice similarity measure between single valued neutrosophic multisets and its application in medical diagnosis, *Neutrosophic sets and systems*, 6(1), 9.
- [46] Yolcu, A., Karatas, E. and Ozturk, T.Y., (2021) A new approach to neutrosophic soft mappings and application in decision making, in *Neutrosophic Operational Research*, F. Smarandache and M. Abdel-Basset, Eds pp. 291–313, ., Springer, Cham.
- [47] Zadeh, L.A., (1965) Fuzzy Sets, *Inform. Control*, 8, 338-353.
- [48] Zhou, Q., Mo, H. and Deng, Y., (2020) A new divergence measure of pythagorean fuzzy sets based on belief function and its application in medical diagnosis, *Mathematics*, 8(1), 142.

Programming the Measurement System by using VEE Pro to Determine Cyclic I-V Characteristics: Resistive Switching Device Application

Ersin TEMEL¹, Abdullah AKKAYA^{2*}

¹ Giresun University, Technical Sciences Vocational High School, Department of Electric and Energy, Giresun, Turkey

² Kırşehir Ahi Evran University, Mucur Vocational High School, Department of Chemistry and Chemical Processing Technology, 40500 Mucur/Kırşehir, Turkey

Received:31/08/2022, **Revised:** 23/11/2022, **Accepted:** 25/11/2022, **Published:** 31/03/2023

Abstract

In this study we introduce a simple program for cyclic current–voltage (I–V) measurements for bipolar and unipolar resistive switching devices. This cyclic I-V measurement (CYC-IV) program was developed under the Keysight VEE Pro (Visual Engineering Environment Program) software and has a graphical interface. CYC-IV was developed for programming the Keysight B2912 Precision Source/Measure Unit (SMU) for I-V measurement of resistive switching devices in sweep mode. CYC-IV can be used in six different sweep modes. Moreover, the ramp rate, upper and lower limits of bias, cycle delay time and number of cycles easily define by user. Measurement results were visualized in three graphs that can be viewed simultaneously with the measurements.

Keywords: Cyclic I-V, Sweep mode, VEE Pro, Resistive switching devices, SMU

Döngüsel I-V Karakteristiklerinin Belirlenmesi için Ölçüm Sisteminin VEE Pro kullanarak Programlanması: Dirençli Anahtarlama Aygıtları Uygulaması

Öz

Bu çalışmada, iki kutuplu ve tek kutuplu dirençli anahtarlama aygıtları için döngüsel akım-gerilim (I–V) ölçümleri için basit bir program hazırlanmıştır. Bu döngüsel akım-gerilim ölçüm programı (CYC-IV) Keysight VEE Pro (Visual Engineering Environment Program) yazılımı altında geliştirilmiştir ve grafik arayüze sahiptir. CYC-IV, tarama modunda dirençli anahtarlama cihazlarının I-V ölçümü için Keysight B2912 Hassas Kaynak/Ölçüm Birimi'ni (SMU) programlamak üzere geliştirilmiştir. CYC-IV altı farklı tarama modunda kullanılabilir. Ayrıca gerilim artış hızı, üst ve alt gerilimin limitleri, döngü gecikme süresi ve döngü sayısı kullanıcı tarafından kolaylıkla tanımlanabilir. Ölçüm sonuçları, ölçümlerle aynı anda görüntülenebilen üç grafikte görselleştirildi.

Anahtar Kelimeler: Döngüsel I-V, Tarama modu, VEE Pro, Dirençli anahtarlama aygıtları, SMU

1. Introduction

Today, research laboratories are places where researchers from many disciplines work together and multi-tasks are carried out together. For this reason, researchers have to gain different abilities for different tasks, rather than specializing in a particular subject. For example, in a study on thin films, one or more of the thin film production techniques and basic characterization techniques should be known and easily applied by researchers. In addition, it is expected that the produced films will carry out studies on the possible application area. Such as, performance measurements of a film produced using metal-oxides for solar panel applications, applications to determine possible sensor properties or electrical characterization to be used as a possible electronic device. Due to the requirements mentioned above, researchers need to buy a new equipment or rearrange their basic equipment to measure the desired parameter in order to realize some specific applications. In its simplest form, this arrangement can be in the form of purchasing a new software package or making basic modifications as appropriate for the purpose [1-4].

Researchers generally uses a measurement setup, which has a software package that, come with this hardware. For this reason, studies for new applications of measurement setup are limited to this software. Many measurement devices can be reprogrammed for the purpose of the researcher using different programming languages and common command systems such as Standard Commands for Programmable Instruments (SCPI). However, in order to do this, the researcher needs to know programming languages such as C+, XML and/or Python [2, 5-7]. However, some manufacturers also offer the main software packages to the users in order to allow more flexible use of their devices [8]. Programs, such as VEE Pro and LabView, allow users to make appropriate measurements and calculations without the need to know any programming language [9-11]. In these type of interfaces, visual objects are used instead of command lines, variables and data can be defined with pre-defined programming objects instead of codes (see Figure 1.). So, this software packages allows the user for data recording, visualization, and basic calculations. VEE Pro is one of the most important graphical programming environment and generally used for building test systems and computation for researcher's specific demands [1, 2, 7, 11-14].

Non-volatile memories built on semiconductor substrate make an impressive progress and successfully scaled down to achieve large-capacity memories through improvements in photolithography technique [15]. However that they come up against technical and physical limits in the near future, so, three-dimensional structures and new materials are presented as alternatives. In this context, some metal oxides and polymers have attracted a great deal of attention for use as next-generation nonvolatile memories due to their resistive switching (RS) behavior. RS devices are cyclically changing their electrical resistivity values between different stable voltage levels under some certain electrical stresses conditions. These resistive states could be controlled and used to represent logic states in memories and computations [15, 16]. In this study, a program is introduced to make a programmable current-voltage measuring device used for current-voltage measurements of transistors and Schottky diodes suitable for multiple cyclic current-voltage measurements of RS devices using VEE Pro. Thus we create a

program can perform cyclic I-V measurements (when the equipped with SMU such as Agilent B2912), basic calculations, saving and visualizing the measurement results synchronously (Cyclic I-V measurement program, CYC-IV). Also our program allows users to control the electrical measurement processes of devices, which it's not possible for many commercially available programs. It provides flexible measurement solutions and offers a new approach for user requirements in the electrical measurement process of RS devices.

2. Material and Methods

Basic electrical characterization of RS devices is based on cycled I-V data. Thus, electrical measurements are important for device fabrications and have to be performed with the high-precision source-measure units under the certain conditions. Controlling the measurement environment and conditions is essential. In addition, it is necessary to define the measurement parameters flexibly in the program, to following the measurement process closely, and automatically save the data that emerges at the end of the process. All these requirements have been taken into account in the preparation of our program using VEE Pro. The prepared program (CYC-IV) contains more than 30 types VEE Pro objects in total. These objects includes instrument control transactions for B2912, loop elements, graphical interface, test data display elements, variables, program flow modifiers, some subscripts required for data logging, components that allow the user to input data, etc. (Figure 1.) [17].

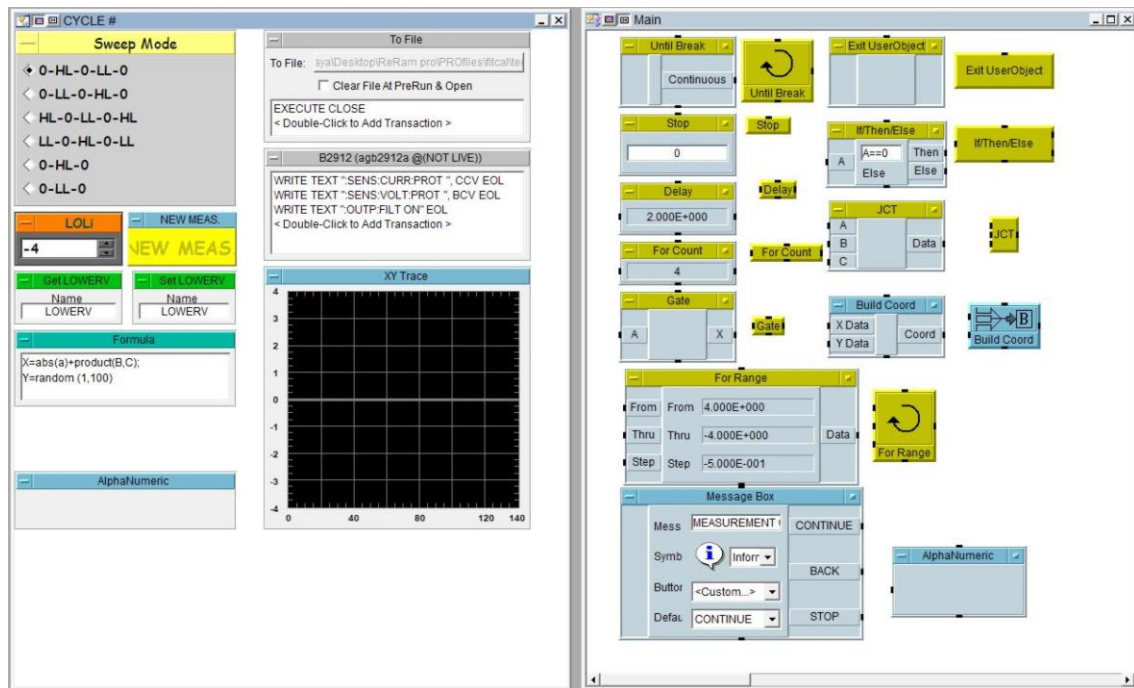


Figure 1. Some of programming elements of VEE Pro used in CYC-IV.

The components included here are combined using appropriate variable definition and data transmission paths. The basic steps of programming are as follows (Figure 2.);

- i. Creating of basic files
- ii. Defining variables and assigning values to some variables by the user
- iii. Defining process (measurement) parameters

- iv. Measurement start, new variable assignments, temporary recording of results
- v. Completion of data permanently recording at the end of the measurement

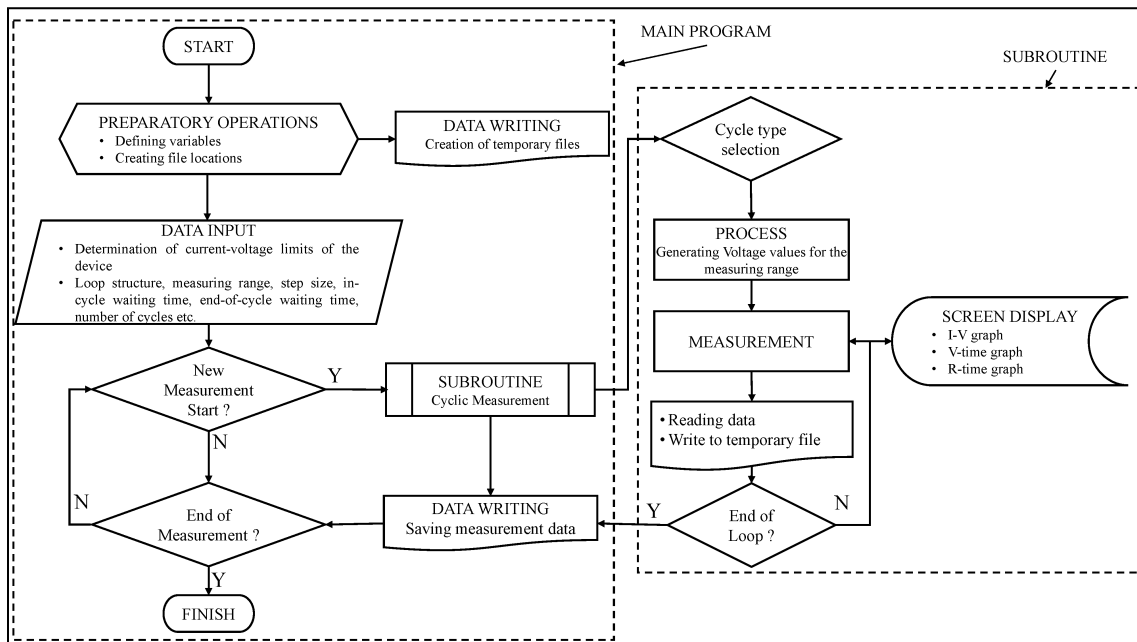


Figure 2. Main flow diagram and measurement subroutines of CYC-IV.

3. Results and Discussion

3.1. RS Devices Characteristics and Cyclic I-V Measurements

RS devices usually represent their switching characteristic parameters such as resistance value of high-resistance state (RHRS or R_{ON}) and resistance value of low-resistance state (RLRS or R_{OFF}) and their ratio (R_{ON} / R_{OFF}), which could be used to calculate the energies set and reset condition (E_{SET} and E_{RESET}) can be easily found with the cyclic I-V measurements method. Typical I-V plots were obtained during the applied ramped voltage stresses (RVS) and current vs time (I-t) plots were obtained during the applied pulsed voltage stresses (PVS). In this method, RS behavior can be detected by applying RVS, which current raises and transitions occurs between the HRS-to-LRS (called a SET) and current drops and transitions occurs between the LRS-to-HRS (called a RESET) (Figure 3.). So, the current values in the forward and backward sweep directions are different for a given certain voltage (typically ~ 0.1 V), and their resistances (RHRS and RLRS) can be calculated [16].

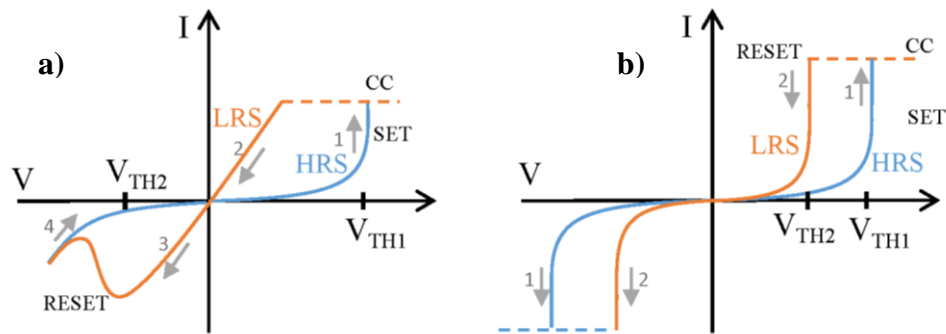


Figure 3. a) Typical I–V sweeps showing one cycle of bipolar RS device and b) unipolar RS device.

3.2. Programming Details of CYC-IV

CYC-IV was developed for cyclic I-V measurements of some devices by using the VEE Pro (v7.5). This program is focused on automation of Agilent B2912 SMU to help measure the cyclic switching behavior of RS devices. Throughout the programming steps, five programming stages are considered and applied on our flow diagram. Firstly, some requirements such as control the B2912A SMU for output status, bias/current compliance values, bias travel range and directions, certain increment rates for bias etc.) are defined. Also, all measurement data are could record without user command and sweep parameters can be described by user before the measurement. Secondly, basic programming task was created and virtual instrument components were used in process. In addition, a subroutine has been developed that will take place under the main loop of the program and will actually performs I-V measurements cyclically according to the parameters defined by the user

Thirdly, Graphical User Interface (GUI) based development environment of VEE Pro was used for creating a task and some communication objects (instrument–computer), variables, data input objects for user, data display objects, loop/flow elements and file management components etc. in accordance with the flow chart. After that, start screen objects were placed in main user panel (user welcome screen) (Figure 4a.) and then, subroutine for the measurement task is arranged to sequentially run by user command (Figure 4b.). Also in here, “Current Directory Settings” button allows the user for file directory selection of measurement results. User can be select file names and their location on computer.

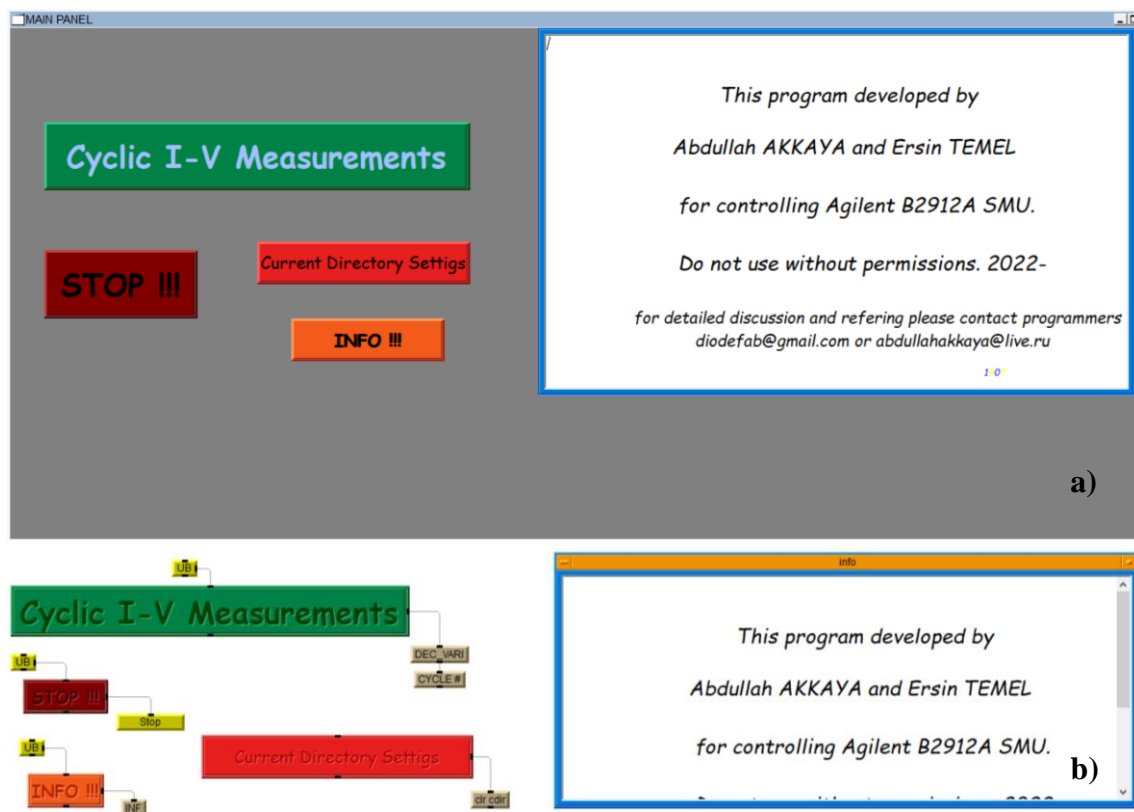


Figure 4. a) Main user panel view and b) arrangement of programming objects and user-defined functions in the main panel.

Subroutine part of our program allows the user for entering some measurement parameters and starting cyclic measurements (Figure 5.). Also, this subroutine was prepared to perform six different types of cyclic I-V measurements (sweep mode) and work with a user command (sweep mode) in Figure 5a.). Each type of f sweep mode has its own loop for generating a bias data (see on Figure 5b.). First four sweep mode scans both direction positive and negative biases and can be used bipolar RS device characterization. Last two mode performs voltage sweeps only one direction (semi-cycle) and belongs to unipolar RS device characterization.

Panel view of subroutine can be seen in Figure 5a. In this panel, top-left side contains subroutine control buttons such as error clear for B2912A, cancel, back, polarity/connection control (Check Connection/Polarity - CCP). Bottom-left side of panel view contains user parameter define/select objects for measurement conditions such as compliance values for current and voltage of B2912 SMU, upper, lower and step size of bias cycle, cycle number, delay time for internal measurements and between the each cycles, and bias status graph for cycles. Right side of panel consist of two real-time graph, upper graph is I-V (logarithmic or linear scale can be chosen by user) and bottom graph is R versus time.

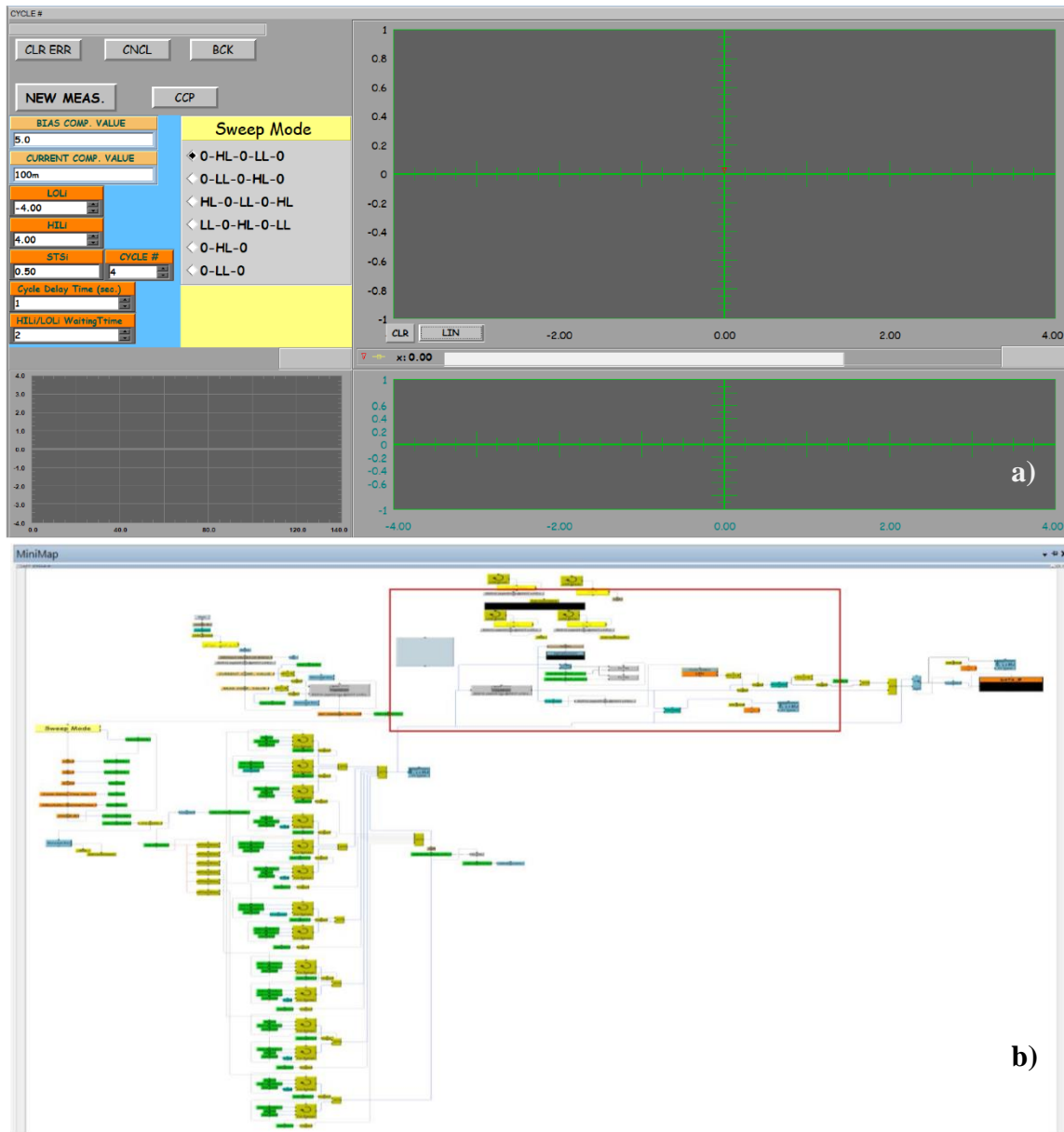


Figure 5. a) Subroutine's panel view and b) objects of the program and their flow routine.

Finally, each cycle was tested for stability under the different measurement parameters and data record options (dry run), and all program was documented.

3.3. User Manual and Features of CYC-IV

CYC-IV only runs under the VEE Pro software packages. Installing the VEE Pro or creating a RunTime version (see on user manual) of CYC-IV measurements can perform. After the run command main panel elements appears and clicking "Cyclic I-V Measurements" button starts the subroutine and its panel view. In here, user can select the measurement mode and define cyclic measurement parameters. For example, first mode for cyclic structure (sweep mode) is (0-HL-0-LL-0) starts with the applying 0 V on device via B2912 and continue with the increment (increment value equals the step size) up to the higher voltage limit (ramped voltage), then reaches the higher voltage limit and returns the 0 V by decreasing the bias (first half of

cycle). After that, bias voltage is carried out the lower limit of cycle then bias returns the 0 V similarly of first half (second half of cycle). The subroutine repeats this loops up to the number of cycles defined by the user. When the measurement completed all data files (*.dat) saved to "DATAS" folder, can be found in same directory with CYC-IV, with the time stamped and cycle numbered file name (Figure 6.). A "new measurement" or "stop" is selected in the pop-up window that opens after all cycles are completed.



Figure 6. a) Typical data folder and b) data file.

4. Conclusion

Unlike its commercial equivalents, this program can be arranged to perform cyclic I-V measurements and make basic calculations. This allows the measurement system to be rearranged in line with user requirements in laboratories where different processes are carried out simultaneously and multidisciplinary studies are carried out. The program interface was GUI-based, allowing users to create programs without the need to write code. The CYC-IV program was successfully applicable to the cyclic I-V measurements of RS devices and re-design for easily expand other similar applications such as sensors. Also, our program was still open to development and can be carried out to simulation and calculation of some specific parameters (e.g. set and reset times) of RS devices.

Ethics in Publishing

There are no ethical issues regarding the publication of this study.

Author Contributions

Abdullah AKKAYA performed writing-original draft, software, validation and conceptualization. Ersin TEMEL performed writing-review and editing; conceptualization.

Acknowledgements

The authors declare that they have no known competing financial interests or personal relationships that could have appeared to influence the work reported in this paper.

References

- [1] A. Akkaya, E. Ayyıldız, Automation Software for Semiconductor Research Laboratories: Electrical Parameter Calculation Program (SeCLaS-PC), *Journal of Circuits, Systems and Computers*, 29 (2020) 2050215.
- [2] A. Akkaya, E. Ayyıldız, Automation Software for Semiconductor Research Laboratories: Measurement System and Instrument Control Program (SeCLaS-IC), *MAPAN*, 35 (2020) 343-350.
- [3] K. Jeyadheepan, P. Palanichamy, P. Kalyanasundaram, M. Jayaprakasam, C. Sanjeeviraja, K. Ramachandran, Automation of photoacoustic spectrometer using VEE Pro software, *Measurement*, 43 (2010) 1336-1344.
- [4] V.M. Srivastava, K. Yadav, G. Singh, Application of VEE Pro software for measurement of MOS device parameters using CV curve, *International Journal of Computer Applications*, 1 (2010) 43-46.
- [5] A. Cabrini, L. Gobbi, D. Baderna, G. Torelli, A compact low-cost test equipment for thermal and electrical characterization of integrated circuits, *Measurement*, 42 (2009) 281-289.
- [6] P. Visconti, P. Costantini, C. Orlando, A. Lay-Ekuakille, G. Cavalera, Software solution implemented on hardware system to manage and drive multiple bi-axial solar trackers by PC in photovoltaic solar plants, *Measurement*, 76 (2015) 80-92.
- [7] S. Wu, Electrical Automation Control System Based on Brovey Algorithm, in: 2022 IEEE Asia-Pacific Conference on Image Processing, Electronics and Computers (IPEC), 2022, pp. 1304-1308.
- [8] O. KAHVECİ, M.F. KAYA, Farklı Metal/n-Si Kontakların Sayısal Olarak Modellenmesi ve Simülasyonu, *Karadeniz Fen Bilimleri Dergisi*, 12 (2022) 398-413.
- [9] E. Garzón, F. Sanchez, L.M. Procel, L. Trojman, Remote control of VNA and parameter analyzer for RFCV measurements using Python, in: 2016 IEEE ANDESCON, 2016, pp. 1-4.
- [10] S.H. Bayes, S. Shukri, R.S. Balog, Low Cost, Stand-Alone, In-situ PV Curve Trace, in: 2020 2nd International Conference on Photovoltaic Science and Technologies (PVCon), 2020, pp. 1-6.
- [11] D. Ursutiu, C. Samoila, P. Cotfas, D.T. Cotfas, D.V. Pop, M.E. Auer, D.G. Zutin, Multifunction iLab implemented laboratory, in: 2011 IEEE Global Engineering Education Conference (EDUCON), 2011, pp. 185-190.
- [12] A. Haleem, M. Javaid, R.P. Singh, S. Rab, R. Suman, Hyperautomation for the enhancement of automation in industries, *Sensors International*, 2 (2021) 100124.
- [13] V.M. Srivastava, K.S. Yadav, G. Singh, Measurement Process of MOSFET Device Parameters with VEE Pro Software for DP4T RF Switch, *International Journal of Communications, Network and System Sciences*, 4 (2011) 590.
- [14] S. Costinas, R. Dobra, C. Zoller, I. Zoller, Wind power plant condition monitoring using HP VEE Pro Software, in: Environment and Electrical Engineering (EEEIC), 2011 10th International Conference on, IEEE, 2011, pp. 1-4.
- [15] Y. Chen, ReRAM: History, Status, and Future, *Ieee T Electron Dev*, 67 (2020) 1420-1433.

- [16] M. Lanza, H.-S.P. Wong, E. Pop, D. Ielmini, D. Strukov, B.C. Regan, L. Larcher, M.A. Villena, J.J. Yang, L. Goux, A. Belmonte, Y. Yang, F.M. Puglisi, J. Kang, B. Magyari-Köpe, E. Yalon, A. Kenyon, M. Buckwell, A. Mehonic, A. Shluger, H. Li, T.-H. Hou, B. Hudec, D. Akinwande, R. Ge, S. Ambrogio, J.B. Roldan, E. Miranda, J. Suñe, K.L. Pey, X. Wu, N. Raghavan, E. Wu, W.D. Lu, G. Navarro, W. Zhang, H. Wu, R. Li, A. Holleitner, U. Wurstbauer, M.C. Lemme, M. Liu, S. Long, Q. Liu, H. Lv, A. Padovani, P. Pavan, I. Valov, X. Jing, T. Han, K. Zhu, S. Chen, F. Hui, Y. Shi, Recommended Methods to Study Resistive Switching Devices, *Advanced Electronic Materials*, 5 (2019) 1800143.
- [17] Keysight, VEE Pro v9.33 User Manual in.

Numerical Solution for Time-Fractional Murray Reaction-Diffusion Equations via Reduced Differential Transform Method

Serkan OKUR¹, Muhammed YİĞİDER^{2*}

¹ Erzurum Technical University, Faculty of Science, Department of Mathematics, Erzurum, Turkey

² Erzurum Technical University, Faculty of Science, Department of Mathematics, Erzurum, Turkey

Received: 17/12/2022, **Revised:** 09/02/2023, **Accepted:** 22/02/2023, **Published:** 31/03/2023

Abstract

In this study, solutions of time-fractional differential equations that emerge from science and engineering have been investigated by employing reduced differential transform method. Initially, the definition of the derivatives with fractional order and their important features are given. Afterwards, by employing the Caputo derivative, reduced differential transform method has been introduced. Finally, the semi-analytical and numerical solutions of the fractional order Murray equation have been obtained by utilizing reduced differential transform method and results have been compared through graphs and tables.

Keywords: Time-fractional differential equations, reduced differential transform methods, murray equations, caputo fractional derivative.

Zaman-Kesirli Murray Reaksiyon-Difüzyon Denklemlerinin İndirgenmiş Diferansiyel Dönüşüm Yöntemiyle Sayısal Çözümü

Öz

Bu çalışmada mühendislik ve fen bilimlerinde ortaya çıkan zaman-kesirli diferansiyel denklemin yarı analitik ve sayısal çözümleri indirgenmiş diferansiyel dönüşüm metodu kullanılarak incelenmiştir. Öncelikle kesirli mertebeden türevlerin tanımı ve önemli özellikler verilmiştir. Daha sonra Caputo kesirli türev tanımı kullanılarak indirgenmiş diferansiyel metodu sunulmuştur. Son olarak, kesirli mertebeden Murray diferansiyel denkleminin yarı analitik ve sayısal çözümleri İndirgenmiş diferansiyel metodu kullanılarak elde edilmiştir. Elde edilen çözümler tablo ve grafik üzerinde gösterilerek karşılaştırılma yapılmıştır.

Anahtar Kelimeler: Zaman-kesirli diferansiyel denklemler, indirgenmiş diferansiyel dönüşüm metodu, murray denklemleri, caputo kesirli türevi.

1. Introduction

The mathematical modelling is highly important for defining and creating solutions for problems, which are encountered in science and engineering. As we know that there is no exact solution for most partial differential equations. The fact that these differential equations have fractional derivatives and non-linearity makes it difficult to produce analytical solutions. At this juncture, numerical methods come to the aid. Firstly, Zhou used the differential transformation method for solving linear and nonlinear initial value problems in electrical circuit analysis [1]. In 1980, Adomian introduced some definitions and theorems about the Adomian decomposition method which he named after himself, also he demonstrated how to apply this method to some differential equations [2]. Chen and Ho used the transform method to obtain eigen-values and eigen-functions [3]. He introduced a new analytical solution called the method of variational iterations for the solution of nonlinear problems. Initial value problems are solved with the help of Lagrange multiplier in variational theory via this method. This method converges faster to the analytical solutions compared to the Adomian method [4]. Chen and Ho introduced the novel two-dimensional differential transform method to solve Partial Differential Equations (PDE) and for the first-time differential transform method was applied to partial differential equations [5]. Two-dimensional differential transform method for solving the initial value problems for partial differential equations have been studied by Ayaz. Novel theorems have been introduced and some linear and non-linear PDEs solved by employing this method [6]. The Reduced Differential Transform Method (RDTM), which was first proposed by the Keskin [7], has received much attention due to its applications to solve a wide variety of problems. In this study, RDTM and Homotopy Perturbation Method (HPM) are successfully applied to the fractional Benney-Lin equation and solutions are obtained [8]. In the Srivastava's study, the solution of two- and three-dimensional time-fractional telegraph equation with RDTM is presented. As a result, it has been observed that RDTM technique is efficient and, by this method, the numerical solution quickly convergences to the analytical solution [9].

In this study, the solution of time-fractional differential Murray equation is tackled. The Burgers' equation, which is a member of the reaction-diffusion equation is defined as:

$$u_t = u_{xx} + \lambda_1 uu_x .$$

The Burgers' equation has many applications in applied mathematics, modeling fluid dynamics, modeling of gas dynamics, boundary layer behavior, turbulence and shock wave formation [10]. Fisher's equation, another member of the reaction diffusion equation, is defined as:

$$u_t = u_{xx} + \lambda_2 u - \lambda_3 u^2 .$$

It was introduced by Fisher to describe the dynamics of the spread of a mutant gene. The Fisher equation has wide applications in many fields. They explain the spread of biological populations, branching Brownian motion processes, logistic population growth, neurophysiology, flame propagation, neutron population in a nuclear reaction, chemical kinetics, autocatalytic chemical reactions and nuclear reactor theory. Murray equation is the generalized form of the Fisher and Burgers equations. Nonlinear reaction-diffusion equations

are very important due to their ease of use in various fields in engineering and science [10]. The Murray equation, which is a member of the reaction-diffusion equation family, is as follows;

$$u_t = u_{xx} + \lambda_1 u u_x + \lambda_2 u - \lambda_3 u^2, \quad 0 \leq x < 1, \quad 0 \leq t < 1 \quad [11,12].$$

Reaction-Diffusion equations have a wide range of applications in science and engineering and have gained attention in recent years due to their interesting properties and rich variety of solutions. The fractional version of Murray equation defines as

$$D_t^\alpha u = u_{xx} + \lambda_1 u u_x + \lambda_2 u - \lambda_3 u^2, \quad 0 \leq x < 1, \quad 0 \leq t < 1.$$

In this study, we apply reduced differential transform method to obtain the numerical solution of fractional Murray differential equation.

The paper is organized as follows; in section 2, we present some essential definitions of the fractional calculus theory. In section 3, we demonstrate the definition and some features of fractional reduced differential transform method. Also, we define the time-fractional Murray equation with initial condition. In section 4, we illustrate a numerical example and we apply the numerical method to solve the test problem. The tables and graphs are created for this example. Finally, in section 5 the data obtained in the previous sections are compared and comments are made on the method.

2. Preliminaries

In this section, some notations and definitions, which are necessary for the solution of the problem, are given. Fractional analysis theory is as old as classical analysis theory and interest in fractional analysis has increased in the last two decades. In addition, more than one definition has emerged. In this study, Riemann-Liouville fractional integral, Riemann-Liouville fractional derivative and Caputo derivative are given.

2.1. Fractional Derivative Definitions

Definition 2.1. [13] A real valued function $f(x)$, $x > 0$, is said to be in the space C_μ , $\mu \in \mathbb{R}$ if there exists a real number $p > \mu$, such that $f(x) = x^p f_1(x)$ where $f_1(x) \in C[0, \infty)$ and a function $f(x)$, $x > 0$ is said to be in the space C_μ^m , $m \in \mathbb{N} \cup \{0\}$, if $f^{(m)} \in C_\mu$.

Definition 2.2. The Riemann-Liouville fractional integral operator [14] of order $\alpha \geq 0$, of a function $f \in C_\mu$, $\mu \geq -1$ is defined as

$$(J_a^\alpha f)(x) = \frac{1}{\Gamma(\alpha)} \int_a^x (x - \tau)^{\alpha-1} f(\tau) d\tau, \quad x > a, x > 0.$$

The properties of the operator J^α can be found in [15], and here we only mention the following (in case, $f \in C_\mu$, $\mu \geq -1$, $\alpha, \beta \geq 0$ and $v > -1$):

$$(J_a^0 f)(x) = f(x)$$

$$\begin{aligned} (J_a^\alpha J_a^\beta f)(x) &= (J_a^{\alpha+\beta} f)(x) \\ J_a^\alpha x^v &= \frac{\Gamma(v+1)}{\Gamma(\alpha+v+1)} x^{\alpha+v} \end{aligned}$$

where $\alpha, \beta \geq 0, x > 0$ and $v > -1$.

Definition 2.3. Let the function f be continuous and integrable in every finite (a, x) range. Let $m \in \mathbb{N}, m-1 < \alpha \leq m$ and $x > a, a \in \mathbb{R}$. Therefore, the Riemann-Liouville fractional derivative [15] of the function f is defined as

$$\begin{aligned} D^\alpha f(x) &= D^m J^{m-\alpha} f(x) \\ (D_a^\alpha f)(x) &= \frac{d^m}{dx^m} \left[\frac{1}{\Gamma(m-\alpha)} \int_a^x (x-\tau)^{m-\alpha-1} f(\tau) d\tau \right]. \end{aligned}$$

Definition 2.4 The fractional derivative of $f(x)$ in the Caputo sense [16,17] is defined as

$$\begin{aligned} D^\alpha f(x) &= J^{m-\alpha} D^m f(x) \\ (D_a^\alpha f)(x) &= \frac{1}{\Gamma(m-\alpha)} \int_a^x (x-\tau)^{m-\alpha-1} f^{(m)}(\tau) d\tau \end{aligned}$$

for $m-1 < \alpha \leq m, m \in \mathbb{N}, x > 0, f \in C_{-1}^m$.

The following two properties of this operator will be used in what follows.

Lemma: If $m-1 < \alpha \leq m, m \in \mathbb{N}$ and $f \in C_\mu^m, \mu \geq -1$, then

$$\begin{aligned} (D_a^\alpha J_a^\alpha f)(x) &= f(x) \\ (J_a^\alpha D_a^\alpha f)(x) &= f(x) - \sum_{k=0}^{m-1} f^{(k)}(a) \frac{(x-a)^k}{k!}, a \geq 0. \end{aligned}$$

The Caputo fractional derivative is considered here, because it allows traditional initial and boundary conditions to be included in the formulation of the problem.

3. 2-dimensional fractional reduced differential transform method

In this section, reduced differential transform method will be given for the solution of fractional partial differential equations. By using the reduced differential transform method, we can decrease the processes density of the generalized differential transform method. Therefore, it will be possible to obtain solutions of fractional differential equations quickly.

Let us consider a function of two individual variables $u(x, t)$, and suppose that it can be represented as a product of two single-variable functions, i.e., $u(x, t) = \phi(x)\psi(t)$. On the basis of the properties of the one-dimensional differential transformation, the function $u(x, t)$ can be represented as [18]

$$u(x, t) = \sum_{k=0}^{\infty} \Phi(k)x^k \sum_{h=0}^{\infty} \Psi_{\alpha}(h)t^{\alpha h} = \sum_{h=0}^{\infty} U_{\alpha h}(x)t^{\alpha h}$$

where $0 < \alpha \leq 1$, $U_{\alpha h}(x) = \Psi_{\alpha}(h)\Phi(k)$ is called spectrum function of $u(x, t)$. The basic definitions and operations of the reduced differential transform are introduced as follows

Definition 3.1 [19,20] Let $u(x, t)$ be an analytic function that continuously differentiable with respect to time t and space x in domain of interest. Define

$$U_h(x) = \frac{1}{\Gamma(\alpha h + 1)} [D_t^{\alpha h} u(x, t)]_{t=t_0} \quad (3.1)$$

where α is the parameter that describes the order of time fractional derivative in the Caputo sense and t -dimensional spectrum function $U_h(x)$ is defined as

$$u(x, t) = \sum_{h=0}^{\infty} U_h(x) (t - t_0)^{\alpha h} \quad (3.2)$$

combining equation (3.1) and (3.2), we have

$$u(x, t) = \sum_{h=0}^{\infty} \frac{1}{\Gamma(\alpha h + 1)} [D_t^{\alpha h} u(x, t)]_{t=t_0} (t - t_0)^{\alpha h} \quad (3.3)$$

when $t_0 = 0$, Eqs. (3.3) reduces to

$$u(x, t) = \sum_{h=0}^{\infty} \frac{1}{\Gamma(\alpha h + 1)} [D_t^{\alpha h} u(x, t)]_{t=t_0} t^{\alpha h}$$

from the above definition, it can be found that the concept of the reduced differential transform is derived from the power series expansion of a function.

Table 1. Reduced fractional differential Transformations [7,21]

Original function	Transformed function
$u(x, t)$	$U_h(x) = \frac{1}{\Gamma(1 + h\alpha)} \left[\frac{\partial^{h\alpha}}{\partial t^{h\alpha}} u(x, t) \right]_{t=0}$
$u(x, t) = \ell_1 w(x, t) \pm \ell_2 v(x, t)$	$U_k(x) = \ell_1 W_h(x) \pm \ell_2 V_h(x) \quad \ell_1, \ell_2 \in \mathbb{R}$
$u(x, t) = cw(x, t) \quad (c \in \mathbb{R})$	$U_h(x) = cW_h(x) \quad (c \in \mathbb{R})$

$$\begin{aligned}
 u(x, t) &= \frac{\partial^r}{\partial x^r} w(x, t) & U_h(x) &= \frac{\partial^r}{\partial x^r} W_h(x) \\
 u(x, t) &= \frac{\partial^{N\alpha}}{\partial t^{N\alpha}} w(x, t) & U_h(x) &= \frac{\Gamma(h\alpha + N\alpha + 1)}{\Gamma(h\alpha + 1)} W_{h+N}(x) \\
 u(x, t) &= w(x, t)v(x, t) & U_h(x) &= \sum_{s=0}^h V_s(x) W_{h-s}(x) \\
 \psi(x, t) &= u(x, t)w(x, t)v(x, t) & \Psi_k &= \sum_{r=0}^k \sum_{i=0}^r U_i(x)V_{r-i}(x)W_{k-r}(x)
 \end{aligned}$$

We illustrate the reduced differential transform method by employing the fractional Murray equation in standard form,

$$L(u(x, t)) + R(u(x, t)) + N(u(x, t)) + F(u(x, t)) = 0 \quad (3.4)$$

with initial condition

$$u(x, 0) = f(x) \quad (3.5)$$

where $L = \frac{\partial^\alpha}{\partial t^\alpha}$, $R = \frac{\partial^2}{\partial x^2}$, $F = u$ and $N = u \frac{\partial u}{\partial x}$ are the linear operators which has partial derivatives.

According to RDTM formulas in [Table 1](#), we can derive the following iteration formulas;

$$\frac{\Gamma(\alpha(h + N) + 1)}{\Gamma(\alpha h + 1)} U_{h+1}(x) = -N(U_h(x)) - R(U_h(x)) - U_h(x) \quad (3.6)$$

where $N(U_h(x))$, $R(U_h(x))$ and $U_h(x)$ are the transformations of $N(u(x, t))$, $R(u(x, t))$ and $F(u(x, t))$, respectively. From the initial condition, we write

$$U_0(x) = f(x) \quad (3.7)$$

substituting eqs. (3.7) into (3.6) and by a straight forward iterative formula, we get the following $U_h(x)$ values. Then, we apply the inverse transformation to all the values $\{U_h(x)\}_{h=0}^n$ to obtain the approximation solution as

$$\tilde{u}_n(x, t) = \sum_{h=0}^n U_h(x) t^{\alpha h} \quad (3.8)$$

where n is order of approximation solution. Thus, the exact solution of the problem is obtained by

$$u(x, t) = \lim_{n \rightarrow \infty} \tilde{u}_n(x, t).$$

4. Main Theorem and Proof

4.1 Numerical Example

Example The Murray equation with initial condition and analytical solution is given by

$$D_t^\alpha u = u_{xx} + \lambda_1 u u_x + \lambda_2 u - \lambda_3 u^2, \quad 0 \leq x < 1, \quad 0 \leq t < 1 \quad (4.1)$$

$$u(x, 0) = \frac{1}{2} \left(1 + \tanh \left(\frac{x}{4} \right) \right) \quad (4.2)$$

$$u(x, t) = \frac{\lambda_2}{2\lambda_3} \left(1 + \tanh \left[\frac{\lambda_2}{8\lambda_3^2} (2\lambda_1\lambda_3 x + (\lambda_1^2 + 4\lambda_3^2)t) \right] \right) \quad (4.3)$$

[10]

If $\lambda_1 = 1, \lambda_2 = 1$ ve $\lambda_3 = 1$ ($\lambda_1, \lambda_2, \lambda_3 \in \mathbb{R}$) in equation (4.1), the time-fractional partial differential equation turns into

$$D_t^\alpha u = u_{xx} + u u_x + u - u^2, \quad 0 \leq x < 1, \quad 0 \leq t < 1. \quad (4.4)$$

Using the initial condition at (4.2), we apply the reduced differential transform method to (4.4) Murray equation and obtained:

$$\begin{aligned} \frac{\Gamma(\alpha(h+1)+1)}{\Gamma(\alpha h+1)} U_{h+1}(x) = \\ \frac{\partial^2}{\partial x^2} U_h(x) + \sum_{s=0}^h U_s(x) \frac{\partial}{\partial x} U_{h-s}(x) + U_h(x) - \sum_{s=0}^h U_s(x) U_{h-s}(x). \end{aligned} \quad (4.5)$$

If we iterate for $h = 0, 1, 2, 3 \dots$;

$$U_0(x) = \frac{1}{2} \left(1 + \tanh \left(\frac{x}{4} \right) \right)$$

$$U_1 = \frac{4 + \operatorname{sech}^2 \left(\frac{x}{4} \right) - 4 \tanh^2 \left(\frac{x}{4} \right)}{16\Gamma(\alpha+1)}$$

$$\begin{aligned} U_2 = \frac{1}{64\Gamma(2\alpha+1)} [2\operatorname{sech}^2 \left(\frac{x}{4} \right) - 2\operatorname{sech}^4 \left(\frac{x}{4} \right) - 16\tanh \left(\frac{x}{4} \right) - 9\operatorname{sech}^2 \left(\frac{x}{4} \right) \tanh \left(\frac{x}{4} \right) \\ - 2\operatorname{sech}^2 \left(\frac{x}{4} \right) \tanh^2 \left(\frac{x}{4} \right) + 16\tanh^3 \left(\frac{x}{4} \right)] \end{aligned}$$

$$\begin{aligned} U_3 = \frac{-1}{512\Gamma(3\alpha+1)\Gamma^2(\alpha+1)} [32\Gamma(2\alpha+1) + 16\Gamma^2(\alpha+1)\operatorname{sech}^2 \left(\frac{x}{4} \right) \\ + 16\Gamma(2\alpha+1)\operatorname{sech}^2 \left(\frac{x}{4} \right) + 9\Gamma^2(\alpha+1)\operatorname{sech}^4 \left(\frac{x}{4} \right) + 2\Gamma(2\alpha+1)\operatorname{sech}^4 \left(\frac{x}{4} \right) \end{aligned}$$

$$\begin{aligned}
 &+36\Gamma^2(\alpha+1)\operatorname{sech}^2\left(\frac{x}{4}\right)\tanh\left(\frac{x}{4}\right)+20\Gamma(2\alpha+1)\operatorname{sech}^2\left(\frac{x}{4}\right)\tanh\left(\frac{x}{4}\right) \\
 &-86\Gamma^2(\alpha+1)\operatorname{sech}^4\left(\frac{x}{4}\right)\tanh\left(\frac{x}{4}\right)+5\Gamma(2\alpha+1)\operatorname{sech}^4\left(\frac{x}{4}\right)\tanh\left(\frac{x}{4}\right) \\
 &-128\Gamma^2(\alpha+1)\tanh^2\left(\frac{x}{4}\right)-64\Gamma(2\alpha+1)\tanh^2\left(\frac{x}{4}\right) \\
 &-138\Gamma^2(\alpha+1)\operatorname{sech}^2\left(\frac{x}{4}\right)\tanh^2\left(\frac{x}{4}\right)-16\Gamma(2\alpha+1)\operatorname{sech}^2\left(\frac{x}{4}\right)\tanh^2\left(\frac{x}{4}\right) \\
 &-36\Gamma^2(\alpha+1)\operatorname{sech}^2\left(\frac{x}{4}\right)\tanh^3\left(\frac{x}{4}\right)-20\Gamma(2\alpha+1)\operatorname{sech}^2\left(\frac{x}{4}\right)\tanh^3\left(\frac{x}{4}\right) \\
 &+128\Gamma^2(\alpha+1)\tanh^4\left(\frac{x}{4}\right)+32\Gamma(2\alpha+1)\tanh^4\left(\frac{x}{4}\right)] \\
 U_4 = &\frac{-1}{4096\Gamma(4\alpha+1)\Gamma(2\alpha+1)\Gamma^2(\alpha+1)} [32\Gamma^2(2\alpha+1)\operatorname{sech}^2\left(\frac{x}{4}\right) \\
 &+128\Gamma(3\alpha+1)\Gamma(\alpha+1)\operatorname{sech}^2\left(\frac{x}{4}\right)-92\Gamma(2\alpha+1)\Gamma^2(\alpha+1)\operatorname{sech}^4\left(\frac{x}{4}\right) \\
 &-44\Gamma^2(2\alpha+1)\operatorname{sech}^4\left(\frac{x}{4}\right)+4\Gamma(3\alpha+1)\Gamma(\alpha+1)\operatorname{sech}^4\left(\frac{x}{4}\right) \\
 &-233\Gamma(2\alpha+1)\Gamma^2(\alpha+1)\operatorname{sech}^6\left(\frac{x}{4}\right)-13\Gamma^2(\alpha+1)\operatorname{sech}^6\left(\frac{x}{4}\right) \\
 &-7\Gamma(3\alpha+1)\Gamma(\alpha+1)\operatorname{sech}^6\left(\frac{x}{4}\right)-256\Gamma^2(2\alpha+1)\tanh\left(\frac{x}{4}\right) \\
 &-512\Gamma(3\alpha+1)\Gamma(\alpha+1)\tanh\left(\frac{x}{4}\right)-416\Gamma(2\alpha+1)\Gamma^2(\alpha+1)\operatorname{sech}^2\left(\frac{x}{4}\right)\tanh\left(\frac{x}{4}\right) \\
 &-288\Gamma^2(2\alpha+1)\operatorname{sech}^2\left(\frac{x}{4}\right)\tanh\left(\frac{x}{4}\right)-400\Gamma(3\alpha+1)\Gamma(\alpha+1)\operatorname{sech}^2\left(\frac{x}{4}\right)\tanh\left(\frac{x}{4}\right) \\
 &-456\Gamma(2\alpha+1)\Gamma^2(\alpha+1)\operatorname{sech}^4\left(\frac{x}{4}\right)\tanh\left(\frac{x}{4}\right)-96\Gamma^2(2\alpha+1)\operatorname{sech}^4\left(\frac{x}{4}\right)\tanh\left(\frac{x}{4}\right) \\
 &-64\Gamma(3\alpha+1)\Gamma(\alpha+1)\operatorname{sech}^4\left(\frac{x}{4}\right)\tanh\left(\frac{x}{4}\right) \\
 &+322\Gamma(2\alpha+1)\Gamma^2(\alpha+1)\operatorname{sech}^6\left(\frac{x}{4}\right)\tanh\left(\frac{x}{4}\right)-85\Gamma^2(2\alpha+1)\operatorname{sech}^6\left(\frac{x}{4}\right)\tanh\left(\frac{x}{4}\right) \\
 &-24\Gamma(3\alpha+1)\Gamma(\alpha+1)\operatorname{sech}^6\left(\frac{x}{4}\right)\tanh\left(\frac{x}{4}\right) \\
 &-488\Gamma(2\alpha+1)\Gamma^2(\alpha+1)\operatorname{sech}^2\left(\frac{x}{4}\right)\tanh^2\left(\frac{x}{4}\right) \\
 &-264\Gamma^2(2\alpha+1)\operatorname{sech}^2\left(\frac{x}{4}\right)\tanh^2\left(\frac{x}{4}\right)-616\Gamma(3\alpha+1)\Gamma(\alpha+1)\operatorname{sech}^2\left(\frac{x}{4}\right)\tanh^2\left(\frac{x}{4}\right) \\
 &+2280\Gamma(2\alpha+1)\Gamma^2(\alpha+1)\operatorname{sech}^4\left(\frac{x}{4}\right)\tanh^2\left(\frac{x}{4}\right) \\
 &+2280\Gamma(2\alpha+1)\Gamma^2(\alpha+1)\operatorname{sech}^4\left(\frac{x}{4}\right)\tanh^2\left(\frac{x}{4}\right) \\
 &+144\Gamma^2(2\alpha+1)\operatorname{sech}^4\left(\frac{x}{4}\right)\tanh^2\left(\frac{x}{4}\right)-144\Gamma(3\alpha+1)\Gamma(\alpha+1)\operatorname{sech}^4\left(\frac{x}{4}\right)\tanh^2\left(\frac{x}{4}\right) \\
 &+1024\Gamma(2\alpha+1)\Gamma^2(\alpha+1)\tanh^3\left(\frac{x}{4}\right)+512\Gamma^2(2\alpha+1)\tanh^3\left(\frac{x}{4}\right) \\
 &+1024\Gamma(3\alpha+1)\Gamma(\alpha+1)\tanh^3\left(\frac{x}{4}\right) \\
 &+1892\Gamma(2\alpha+1)\Gamma^2(\alpha+1)\operatorname{sech}^2\left(\frac{x}{4}\right)\tanh^3\left(\frac{x}{4}\right) \\
 &+288\Gamma^2(2\alpha+1)\operatorname{sech}^2\left(\frac{x}{4}\right)\tanh^3\left(\frac{x}{4}\right)+384\Gamma(3\alpha+1)\Gamma(\alpha+1)\operatorname{sech}^2\left(\frac{x}{4}\right)\tanh^3\left(\frac{x}{4}\right)
 \end{aligned}$$

$$\begin{aligned}
 & -128\Gamma(2\alpha + 1)\Gamma^2(\alpha + 1)\operatorname{sech}^4\left(\frac{x}{4}\right)\tanh^3\left(\frac{x}{4}\right) \\
 & +140\Gamma^2(2\alpha + 1)\operatorname{sech}^4\left(\frac{x}{4}\right)\tanh^3\left(\frac{x}{4}\right) - 8\Gamma(3\alpha + 1)\Gamma(\alpha + 1)\operatorname{sech}^4\left(\frac{x}{4}\right)\tanh^3\left(\frac{x}{4}\right) \\
 & +488\Gamma(2\alpha + 1)\Gamma^2(\alpha + 1)\operatorname{sech}^2\left(\frac{x}{4}\right)\tanh^4\left(\frac{x}{4}\right) \\
 & +232\Gamma^2(2\alpha + 1)\operatorname{sech}^2\left(\frac{x}{4}\right)\tanh^4\left(\frac{x}{4}\right) + 488\Gamma(3\alpha + 1)\Gamma(\alpha + 1)\operatorname{sech}^2\left(\frac{x}{4}\right)\tanh^4\left(\frac{x}{4}\right) \\
 & -1024\Gamma(2\alpha + 1)\Gamma^2(\alpha + 1)\tanh^5\left(\frac{x}{4}\right) - 256\Gamma^2(2\alpha + 1)\tanh^5\left(\frac{x}{4}\right) \\
 & -512\Gamma(3\alpha + 1)\Gamma(\alpha + 1)\tanh^5\left(\frac{x}{4}\right) + 16\Gamma(3\alpha + 1)\Gamma(\alpha + 1)\operatorname{sech}^2\left(\frac{x}{4}\right)\tanh^5\left(\frac{x}{4}\right)].
 \end{aligned}$$

From here, the approximate solution is found from the inverse transformation of the values of the set $\{U_k(x)\}_{k=0}^4$.

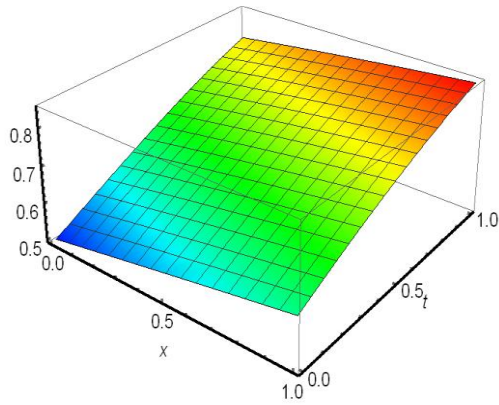
In order to obtain the approximate solution of this equation, if the below terms are written on the total series,

$$\tilde{u}_n(x, t) = \sum_{h=0}^n U_h(x)t^{\alpha h}$$

and we then arrive at the following solution:

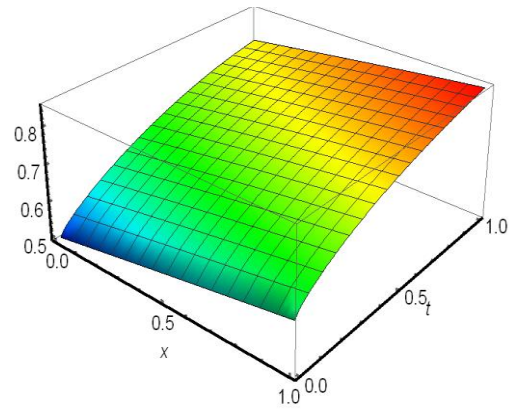
$$\begin{aligned}
 \tilde{u}_4(x, t) &= \sum_{h=0}^4 U_h(x)t^{\alpha h} = \frac{1}{2}\left(1 + \tanh\left(\frac{x}{4}\right)\right) + \frac{4 + \operatorname{sech}^2\left(\frac{x}{4}\right) - 4\tanh^2\left(\frac{x}{4}\right)}{16\Gamma(\alpha + 1)}t^\alpha \\
 &+ \frac{1}{64\Gamma(2\alpha + 1)}\left[2\operatorname{sech}^2\left(\frac{x}{4}\right) - 2\operatorname{sech}^4\left(\frac{x}{4}\right) - 16\tanh\left(\frac{x}{4}\right) - 9\operatorname{sech}^2\left(\frac{x}{4}\right)\tanh\left(\frac{x}{4}\right) \right. \\
 &\left. - 2\operatorname{sech}^2\left(\frac{x}{4}\right)\tanh^2\left(\frac{x}{4}\right) + 16\tanh^3\left(\frac{x}{4}\right)\right]t^{2\alpha} \\
 &+ \frac{-1}{512\Gamma(3\alpha + 1)\Gamma^2(\alpha + 1)}\left[32\Gamma(2\alpha + 1) + 16\Gamma^2(\alpha + 1)\operatorname{sech}^2\left(\frac{x}{4}\right) \right. \\
 &+ 16\Gamma(2\alpha + 1)\operatorname{sech}^2\left(\frac{x}{4}\right) + 9\Gamma^2(\alpha + 1)\operatorname{sech}^4\left(\frac{x}{4}\right) + 2\Gamma(2\alpha + 1)\operatorname{sech}^4\left(\frac{x}{4}\right) \\
 &+ 36\Gamma^2(\alpha + 1)\operatorname{sech}^2\left(\frac{x}{4}\right)\tanh\left(\frac{x}{4}\right) + 20\Gamma(2\alpha + 1)\operatorname{sech}^2\left(\frac{x}{4}\right)\tanh\left(\frac{x}{4}\right) \\
 &- 86\Gamma^2(\alpha + 1)\operatorname{sech}^4\left(\frac{x}{4}\right)\tanh\left(\frac{x}{4}\right) + 5\Gamma(2\alpha + 1)\operatorname{sech}^4\left(\frac{x}{4}\right)\tanh\left(\frac{x}{4}\right) \\
 &- 128\Gamma^2(\alpha + 1)\tanh^2\left(\frac{x}{4}\right) - 64\Gamma(2\alpha + 1)\tanh^2\left(\frac{x}{4}\right) \\
 &- 138\Gamma^2(\alpha + 1)\operatorname{sech}^2\left(\frac{x}{4}\right)\tanh^2\left(\frac{x}{4}\right) - 16\Gamma(2\alpha + 1)\operatorname{sech}^2\left(\frac{x}{4}\right)\tanh^2\left(\frac{x}{4}\right) \\
 &- 36\Gamma^2(\alpha + 1)\operatorname{sech}^2\left(\frac{x}{4}\right)\tanh^3\left(\frac{x}{4}\right) - 20\Gamma(2\alpha + 1)\operatorname{sech}^2\left(\frac{x}{4}\right)\tanh^3\left(\frac{x}{4}\right) \\
 &\left. + 128\Gamma^2(\alpha + 1)\tanh^4\left(\frac{x}{4}\right) + 32\Gamma(2\alpha + 1)\tanh^4\left(\frac{x}{4}\right)\right]t^{3\alpha} \\
 &+ \frac{-1}{4096\Gamma(4\alpha + 1)\Gamma(2\alpha + 1)\Gamma^2(\alpha + 1)}\left[32\Gamma^2(2\alpha + 1)\operatorname{sech}^2\left(\frac{x}{4}\right) \right. \\
 &\left. + 128\Gamma(3\alpha + 1)\Gamma(\alpha + 1)\operatorname{sech}^2\left(\frac{x}{4}\right) - 92\Gamma(2\alpha + 1)\Gamma^2(\alpha + 1)\operatorname{sech}^4\left(\frac{x}{4}\right) \right]
 \end{aligned}$$

$$\begin{aligned}
 & -44\Gamma^2(2\alpha + 1)\operatorname{sech}^4\left(\frac{x}{4}\right) + 4\Gamma(3\alpha + 1)\Gamma(\alpha + 1)\operatorname{sech}^4\left(\frac{x}{4}\right) \\
 & -233\Gamma(2\alpha + 1)\Gamma^2(\alpha + 1)\operatorname{sech}^6\left(\frac{x}{4}\right) - 13\Gamma^2(\alpha + 1)\operatorname{sech}^6\left(\frac{x}{4}\right) \\
 & -7\Gamma(3\alpha + 1)\Gamma(\alpha + 1)\operatorname{sech}^6\left(\frac{x}{4}\right) - 256\Gamma^2(2\alpha + 1)\tanh\left(\frac{x}{4}\right) \\
 & -512\Gamma(3\alpha + 1)\Gamma(\alpha + 1)\tanh\left(\frac{x}{4}\right) - 416\Gamma(2\alpha + 1)\Gamma^2(\alpha + 1)\operatorname{sech}^2\left(\frac{x}{4}\right)\tanh\left(\frac{x}{4}\right) \\
 & -288\Gamma^2(2\alpha + 1)\operatorname{sech}^2\left(\frac{x}{4}\right)\tanh\left(\frac{x}{4}\right) - 400\Gamma(3\alpha + 1)\Gamma(\alpha + 1)\operatorname{sech}^2\left(\frac{x}{4}\right)\tanh\left(\frac{x}{4}\right) \\
 & -456\Gamma(2\alpha + 1)\Gamma^2(\alpha + 1)\operatorname{sech}^4\left(\frac{x}{4}\right)\tanh\left(\frac{x}{4}\right) - 96\Gamma^2(2\alpha + 1)\operatorname{sech}^4\left(\frac{x}{4}\right)\tanh\left(\frac{x}{4}\right) \\
 & -64\Gamma(3\alpha + 1)\Gamma(\alpha + 1)\operatorname{sech}^4\left(\frac{x}{4}\right)\tanh\left(\frac{x}{4}\right) \\
 & +322\Gamma(2\alpha + 1)\Gamma^2(\alpha + 1)\operatorname{sech}^6\left(\frac{x}{4}\right)\tanh\left(\frac{x}{4}\right) - 85\Gamma^2(2\alpha + 1)\operatorname{sech}^6\left(\frac{x}{4}\right)\tanh\left(\frac{x}{4}\right) \\
 & -24\Gamma(3\alpha + 1)\Gamma(\alpha + 1)\operatorname{sech}^6\left(\frac{x}{4}\right)\tanh\left(\frac{x}{4}\right) \\
 & -488\Gamma(2\alpha + 1)\Gamma^2(\alpha + 1)\operatorname{sech}^2\left(\frac{x}{4}\right)\tanh^2\left(\frac{x}{4}\right) \\
 & -264\Gamma^2(2\alpha + 1)\operatorname{sech}^2\left(\frac{x}{4}\right)\tanh^2\left(\frac{x}{4}\right) - 616\Gamma(3\alpha + 1)\Gamma(\alpha + 1)\operatorname{sech}^2\left(\frac{x}{4}\right)\tanh^2\left(\frac{x}{4}\right) \\
 & +2280\Gamma(2\alpha + 1)\Gamma^2(\alpha + 1)\operatorname{sech}^4\left(\frac{x}{4}\right)\tanh^2\left(\frac{x}{4}\right) \\
 & +2280\Gamma(2\alpha + 1)\Gamma^2(\alpha + 1)\operatorname{sech}^4\left(\frac{x}{4}\right)\tanh^2\left(\frac{x}{4}\right) \\
 & +144\Gamma^2(2\alpha + 1)\operatorname{sech}^4\left(\frac{x}{4}\right)\tanh^2\left(\frac{x}{4}\right) - 144\Gamma(3\alpha + 1)\Gamma(\alpha + 1)\operatorname{sech}^4\left(\frac{x}{4}\right)\tanh^2\left(\frac{x}{4}\right) \\
 & +1024\Gamma(2\alpha + 1)\Gamma^2(\alpha + 1)\tanh^3\left(\frac{x}{4}\right) + 512\Gamma^2(2\alpha + 1)\tanh^3\left(\frac{x}{4}\right) \\
 & +1024\Gamma(3\alpha + 1)\Gamma(\alpha + 1)\tanh^3\left(\frac{x}{4}\right) \\
 & +1892\Gamma(2\alpha + 1)\Gamma^2(\alpha + 1)\operatorname{sech}^2\left(\frac{x}{4}\right)\tanh^3\left(\frac{x}{4}\right) \\
 & +288\Gamma^2(2\alpha + 1)\operatorname{sech}^2\left(\frac{x}{4}\right)\tanh^3\left(\frac{x}{4}\right) + 384\Gamma(3\alpha + 1)\Gamma(\alpha + 1)\operatorname{sech}^2\left(\frac{x}{4}\right)\tanh^3\left(\frac{x}{4}\right) \\
 & -128\Gamma(2\alpha + 1)\Gamma^2(\alpha + 1)\operatorname{sech}^4\left(\frac{x}{4}\right)\tanh^3\left(\frac{x}{4}\right) \\
 & +140\Gamma^2(2\alpha + 1)\operatorname{sech}^4\left(\frac{x}{4}\right)\tanh^3\left(\frac{x}{4}\right) - 8\Gamma(3\alpha + 1)\Gamma(\alpha + 1)\operatorname{sech}^4\left(\frac{x}{4}\right)\tanh^3\left(\frac{x}{4}\right) \\
 & +488\Gamma(2\alpha + 1)\Gamma^2(\alpha + 1)\operatorname{sech}^2\left(\frac{x}{4}\right)\tanh^4\left(\frac{x}{4}\right) \\
 & +232\Gamma^2(2\alpha + 1)\operatorname{sech}^2\left(\frac{x}{4}\right)\tanh^4\left(\frac{x}{4}\right) + 488\Gamma(3\alpha + 1)\Gamma(\alpha + 1)\operatorname{sech}^2\left(\frac{x}{4}\right)\tanh^4\left(\frac{x}{4}\right) \\
 & -1024\Gamma(2\alpha + 1)\Gamma^2(\alpha + 1)\tanh^5\left(\frac{x}{4}\right) - 256\Gamma^2(2\alpha + 1)\tanh^5\left(\frac{x}{4}\right) \\
 & -512\Gamma(3\alpha + 1)\Gamma(\alpha + 1)\tanh^5\left(\frac{x}{4}\right) + 16\Gamma(3\alpha + 1)\Gamma(\alpha + 1)\operatorname{sech}^2\left(\frac{x}{4}\right)\tanh^5\left(\frac{x}{4}\right)t^{4\alpha}.
 \end{aligned}$$



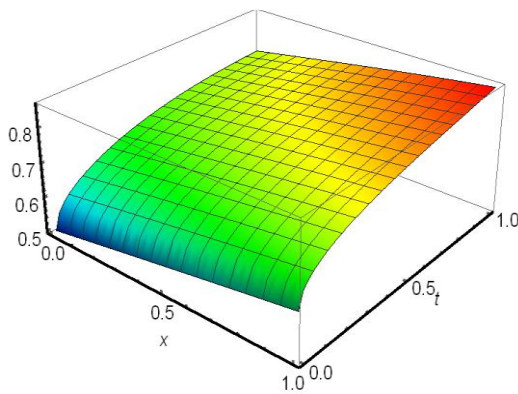
$\alpha = 1$

(a)



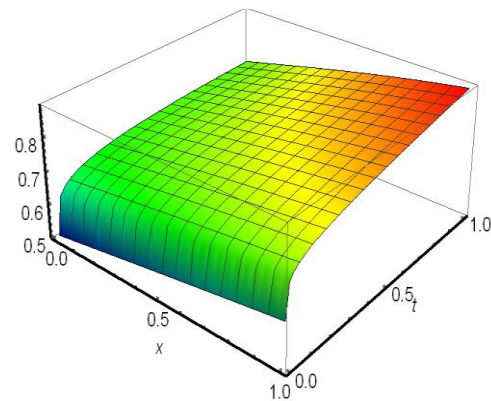
$\alpha = 0,75$

(b)



$\alpha = 0,50$

(c)



$\alpha = 0,25$

(d)

Figure 1. (a) Murray equation graph for $\alpha = 1$, (b) Murray equation graph for $\alpha = 0,75$, (c) Murray equation graph for $\alpha = 0,50$, (d) Murray equation graph for $\alpha = 0,25$.

Table 2. When $\alpha = 1$ and $t = 0,125$, the $u(x, t)$ numerical solution of time-fractional differential equation (4.4)

x value	t value	Numerical solution	Analytical solution	Absolute error
0,125	0,125	0,5544702743	0,5544704649	$1,9 \times 10^{-7}$
0,225	0,125	0,5667858200	0,5667860060	$1,8 \times 10^{-7}$
0,325	0,125	0,5790194078	0,5790195874	$1,7 \times 10^{-7}$
0,425	0,125	0,5911567286	0,5911568998	$1,7 \times 10^{-7}$
0,525	0,125	0,6031839359	0,6031840971	$1,6 \times 10^{-7}$
0,625	0,125	0,6150877057	0,6150878555	$1,4 \times 10^{-7}$
0,725	0,125	0,6268552909	0,6268554280	$1,3 \times 10^{-7}$
0,825	0,125	0,6384745708	0,6384746941	$1,2 \times 10^{-7}$
0,925	0,125	0,6499340935	0,6499342022	$1,0 \times 10^{-7}$

Table 3. When $t = 0,125$ and $\alpha = 1, \alpha = 0,75, \alpha = 0,50, \alpha = 0,25$, the $u(x, t)$ numerical solution of time-fractional differential equation (4.4)

x	t	$\alpha = 1$	$\alpha = 0,75$	$\alpha = 0,50$	$\alpha = 0,25$
0,125	0,125	0,5544702743	0,5859103286	0,6334478288	0,6894731167
0,225	0,125	0,5667858200	0,5979239246	0,6446632874	0,7000300566
0,325	0,125	0,5790194078	0,6098216121	0,6557299695	0,7104476486
0,425	0,125	0,5911567286	0,6215906289	0,6666378629	0,7207052979
0,525	0,125	0,6031839359	0,6332187959	0,6773775486	0,7307833264
0,625	0,125	0,6150877057	0,6446945618	0,6879402342	0,7406632610
0,725	0,125	0,6268552909	0,6560070412	0,6983177834	0,7503280899

0,825	0,125	0,6384745708	0,6671460477	0,7085022739	0,7597624789
0,925	0,125	0,6499340935	0,6781021211	0,7184883430	0,7689529449

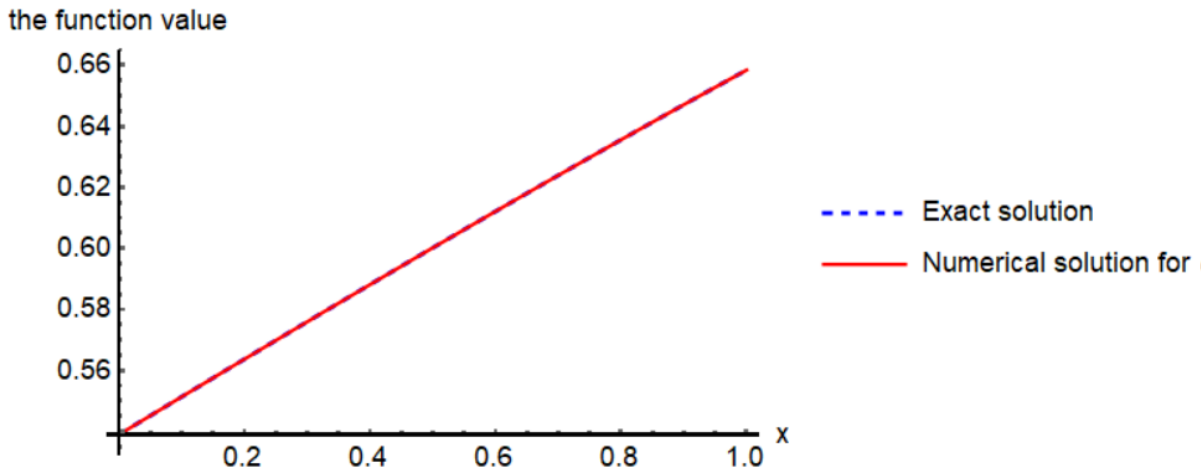


Figure 2. 2D graphic of the exact and numerical solution of $u(x, 0.125)$ of the (4.4) time-fractional differential equation for $\alpha = 1$.

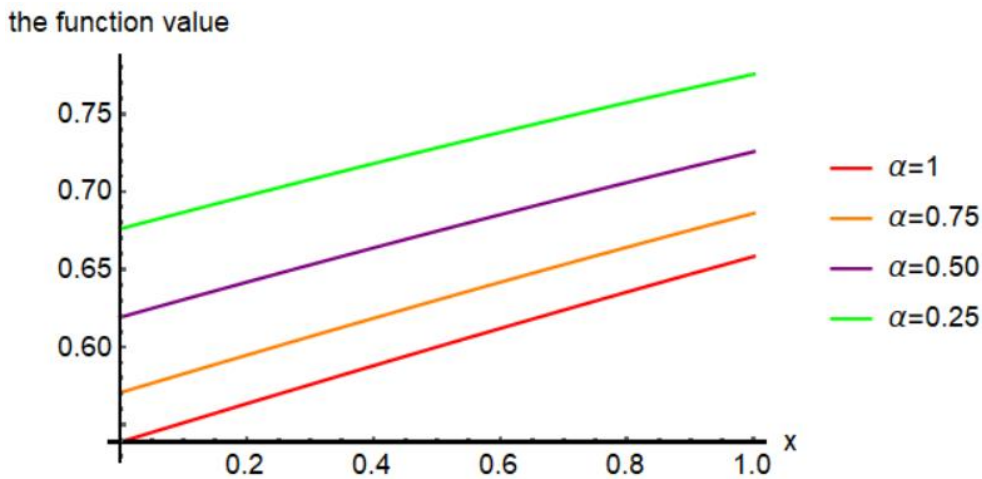


Figure 3. 2D graphic of the numerical solution of $u(x, 0.125)$ of the (4.4) time-fractional differential equation for $\alpha = 1, \alpha = 0,75, \alpha = 0,50, \alpha = 0,25$ of the (4.4) time fractional differential equation.

Table 4. When $\alpha = 1$ and $t = 0,325$, the $u(x, t)$ numerical solution of time-fractional differential equation (4.4)

x value	t value	Numerical solution	Analytical solution	Absolute error
0,125	0,325	0,6150657708	0,6150878555	0,0000220847
0,225	0,325	0,6268340714	0,6268554281	0,0000213566
0,325	0,325	0,6384542799	0,6384746942	0,0000204143
0,425	0,325	0,6499149279	0,6499342022	0,0000192743
0,525	0,325	0,6612052504	0,6612232068	0,0000179564
0,625	0,325	0,6723152161	0,6723316992	0,0000164831
0,725	0,325	0,6832355529	0,6832504316	0,0000148788
0,825	0,325	0,6939577659	0,6939709354	0,0000131695
0,925	0,325	0,7044741505	0,7044855324	0,0000113819

Table 5. When $t = 0,325$ and $\alpha = 1, \alpha = 0,75, \alpha = 0,50, \alpha = 0,25$, the $u(x, t)$ numerical solution of time-fractional differential equation (4.4)

x	t	$\alpha = 1$	$\alpha = 0,75$	$\alpha = 0,50$	$\alpha = 0,25$
0,125	0,325	0,6150657708	0,6541561282	0,6919781039	0,7192267946
0,225	0,325	0,6268340714	0,6651658729	0,7021446159	0,7307671602
0,325	0,325	0,6384542799	0,6760042568	0,7121570774	0,7421752989
0,425	0,325	0,6499149279	0,6866625171	0,7220040752	0,7534040021
0,525	0,325	0,6612052504	0,6971325471	0,7316746799	0,7644082702
0,625	0,325	0,6723152161	0,7074069155	0,7411585762	0,7751460837

0,725	0,325	0,6832355529	0,7174788827	0,7504461818	0,7855790777
0,825	0,325	0,6939577659	0,7273424109	0,7595287530	0,7956731036
0,925	0,325	0,7044741505	0,7369921707	0,7683984747	0,8053986682

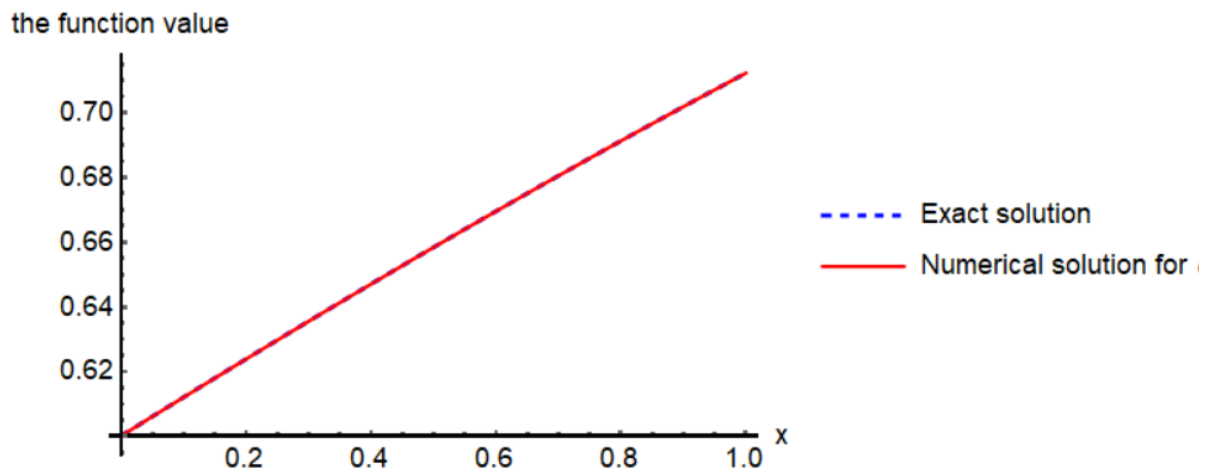


Figure 4. 2D graphic of the exact and numerical solution of $u(x, 0.325)$ of the (4.4) time-fractional differential equation for $\alpha = 1$.

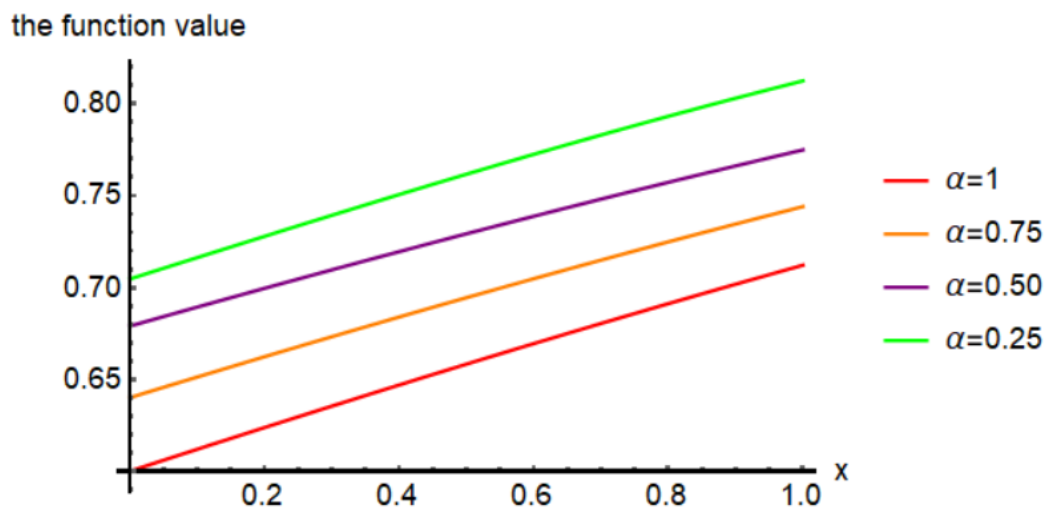


Figure 5. 2D graphic of the numerical solution of $u(x, 0.325)$ of the (4.4) time-fractional differential equation for $\alpha = 1, \alpha = 0,75, \alpha = 0,50, \alpha = 0,25$ of the (4.4) time fractional differential equation.

It was observed that the acquired for $t=0,125$ taken in tables [2](#) and [3](#) are consistent with the 2D plots in figures [2](#) and [3](#). At the same time, for the $t=0,325$ value taken in tables [4](#) and [5](#), it was acquired that it is consistent with the 2D plots in figures [4](#) and [5](#) in our studies, it has been observed that there is a convergence for the other values of t in the table and the variable values of x , as in the above graphs.

3. Conclusion

In this study, the reduced differential transform method was applied to the time-fractional Murray equation, which is a member of reaction-diffusion equation family. A series solution for the problem was obtained by using the initial condition. These solutions were compared with tables and graphs. For $\alpha = 1$ these solutions were compared with the analytical solutions. As a result, this method was found to be very useful for solving nonlinear equations. Reduced differential transform method converges to the solution faster than classical or generalized differential transform methods. Furthermore, this method eliminates the intensive processing load.

Ethics in Publishing

There are no ethical issues regarding the publication of this study.

Author Contributions

The authors contributed equally.

References

- [1] Zhou J.K., (1986) Differential transformation and its applications for electrical circuits, Huazhong University Press. Wuhan, China
- [2] Adomian G., (1994) Solving frontier problems of physics: The Decomposition Method, Kluwer Academic Publishers, Boston, Usa
- [3] Chen C.K., Ho S.H., (1996) Application of differential transformation to eigenvalue problems, Applied Mathematics and Computation, 79(2-3), 173-188. [https://doi.org/10.1016/0096-3003\(95\)00253-7](https://doi.org/10.1016/0096-3003(95)00253-7).
- [4] He J.H., (1999) Variational iteration method-a kind of non-linear analytical technique: some examples, International Journal of Non-Linear Mechanics, 34(4), 699-708. [https://doi.org/10.1016/S0020-7462\(98\)00048-1](https://doi.org/10.1016/S0020-7462(98)00048-1).
- [5] Chen C.K., Ho S.H., (1999) Solving partial differential equations by two dimensional differential transform method, Applied Mathematics and Computation, 106(2-3), 171-179. [https://doi.org/10.1016/S0096-3003\(98\)10115-7](https://doi.org/10.1016/S0096-3003(98)10115-7).

- [6] Ayaz F., (2003) On the two-dimensional differential transform method, *Applied Mathematics and computation*, 143(2-3), 361-374. [https://doi.org/10.1016/S0096-3003\(02\)00368-5](https://doi.org/10.1016/S0096-3003(02)00368-5).
- [7] Keskin Y., Oturanç G., (2009) Reduced differential transform method for partial differential equations. *International Journal of Nonlinear Sciences and Numerical Simulation*, 10(6), 741-749. <https://doi.org/10.1515/IJNSNS.2009.10.6.741>.
- [8] Gupta P.K., (2011) Approximate analytical solutions of fractional Benney-lin equation by reduced differential transform method and the homotopy perturbation method. *Computers and Mathematics with Applications*, 61(9), 2829-2842. <https://doi.org/10.1016/j.camwa.2011.03.057>.
- [9] Srivastava V.K., (2014) Analytical approximations of two and three dimensional time-fractional telegraphic equation by reduced differential transform method, *Egyptian Journal of Basic and Applied Sciences*, 1(1):60-66. <https://doi.org/10.1016/j.ejbas.2014.01.002>.
- [10] Bhrawy A.H., Doha E.H., Abdelkawy M.A., Van Gorder R.A., (2016) Jacobi gauss lobatto collocation method for solving nonlinear reaction-diffusion equations subject to dirichlet boundary conditions, *Applied Mathematical Modelling*, 40(3), 1703-1716. <https://doi.org/10.1016/j.apm.2015.09.009>.
- [11] Murray J.D., (1977) *Nonlinear differential equation models in biology*, Clarendon Press, Oxford, England
- [12] Murray J.D., (1989) *Mathematical biology*, Springer, Berlin, Germany
- [13] Luckho Y., Gorenflo R., (1999) An Operational Method for Solving Fractional Differential Equations with The Caputo Derivatives, *Acta Mathematica Vietnamica*, Vol. 24, 207-233.
- [14] Oldham K.B., Spainer J., (1974) *The Fractional calculus: theory and applications of differentiation and integration to arbitrary order*, Academic Press, California, USA
- [15] Podlubny I., (1999) *Fractional differential equations*, Academic Press, San Diego, USA
- [16] Caputo M., (1976) Linear models of dissipation whose Q is almost frequency independent-II, *Geophysical Journal of The Royal Astronomical Society*, 13(5), 529-539. <https://doi.org/10.1111/j.1365-246X.1967.tb02303.x>.
- [17] Kılıbas A.A., Srivastava H.M., Trujillo J.J., (2006) *Theory and applications of fractional differential equations*, Vol. 204, Elsevier, Amsterdam, Holland
- [18] Arshad M., Lu D., Wang J., (2017) (N+1)-dimensional fractional reduced differential transform method for fractional order partial differential equations, *Commun Nonlinear Sci Numer Simulat*, 48, 509-519. <https://doi.org/10.1016/j.cnsns.2017.01.018>.

- [19] Momani S., Odibat Z., Erturk V.S., (2007) Generalized differential transform method for solving a space and time- fractional diffusion-wave equation, *Physics Letters A.*, 370(5-6), 379-387. <https://doi.org/10.1016/j.physleta.2007.05.083>.
- [20] Keskin Y., (2010) Kısmi türevli diferansiyel denklemlerin indirgenmiş diferansiyel dönüşüm yöntemiyle çözülmesi, Ph.D. Thesis, Selcuk University, Konya, TR
- [21] Srivastava V.K., Awasthi M.K., Tamsir M., (2013) RDTM solution of Caputo time fractional-order hyperbolic telegraph equation, *AIP Advances*, Vol.3., <https://doi.org/10.1063/1.4799548>.

Agonistic Effects of Deinoxanthin on Tamoxifen Antiproliferative Activity on HER2 Positive Breast Cancer: An In vitro Study on MDA-MB-453

Nihan GÜNAY¹, Mehmet KUZUCU^{1*}

¹ Department of Biology, Graduate School of Natural and Applied Sciences, Erzincan Binali Yıldırım University, Erzincan, Türkiye

Received: 26/12/2022, Revised: 03/03/2023, Accepted: 15/03/2023, Published: 31/03/2023

Abstract

Tamoxifen, an estrogen receptor competitive and nonsteroidal drug, has been used for nearly 20 years to treat patients with hormone receptor-positive breast cancer. Deinoxanthin is a xanthophyll derivative purified from the cell wall of a radiation-resistant bacterium, *Deinococcus radiodurans*, has been shown in some studies to have proapoptotic and antiproliferative effects on some types of cancer.

Within the study's scope, it aimed to increase the effectiveness of Tamoxifen with deinoxanthin. The combination of 4.21 µM tamoxifen (TMX) and 3.125 µM deinoxanthin showed the best synergistic effect (CI:0.052) at 24 h incubation in MDA-MB-453 cells according to calculation of XTT findings using CompuSyn software. In this concentration combination, gene expression levels and protein levels of BCL2 Associated X protein (BAX), Caspase 3 (CASP-3), B cell leukemia/lymphoma 2 protein (BCL-2) and Human Epidermal Growth Factor Receptor 2 (HER2) were determined by RT-qPCR and ELISA method, respectively, and according to the results, it is thought that the intrinsic apoptotic pathway is activated.

Keywords: Breast cancer, Deinoxanthin, Tamoxifen, MDA-MB-453.

Deinoksantinin HER2 Pozitif Meme Kanseri Tamoksifenin Antiproliferatif Aktivitesi Üzerindeki Agonistik Etkileri: MDA-MB-453 Üzerine Bir In vitro Çalışma

Öz

Östrojen reseptörü yarışmalı ve steroid olmayan bir bileşik olan Tamoksifen, hormon reseptör pozitif meme kanseri olan hastaları tedavi etmek için yaklaşık 20 yıldır kullanılmaktadır. Deinoxanthin, radyasyona dirençli bir bakteri olan *Deinococcus radiodurans*'ın hücre duvarından saflaştırılan bir ksantofil türevidir ve bazı kanser türleri üzerinde proapoptotik ve antiproliferatif etkilere sahip olduğu bazı çalışmalarda gösterilmiştir.

Çalışma kapsamında Tamoksifenin (TMX) deinoksantin (DNX) ile etkinliğinin artırılması hedeflendi. 4.21 µM TMX ve 3.125 µM DNX kombinasyonu, CompuSyn yazılımı kullanılarak XTT bulgularının hesaplanmasına göre MDA-MB-453 hücrelerinde 24 saatlik inkübasyonda en iyi sinerjistik etkiyi (CI:0.052) gösterdi. Bu konsantrasyon kombinasyonunda BCL-2 ilişkili X proteini (BAX), Kaspaz 3 (CASP-3), B hücreli lösemi/lenfoma 2 proteini (BCL-2) ve İnsan Epidermal Büyüme Faktörü Reseptörü 2'nin (HER2) gen ifade seviyeleri ve protein düzeyleri sırasıyla RT-qPCR ve ELISA yöntemi ile belirlenmiş olup sonuçlara göre intrinsek apoptotik yolağın aktifleştiği olduğu düşünülmektedir.

Anahtar Kelimeler: Meme Kanseri, Deinoksantin, Tamoksifen, MDA-MB-453.

1. Introduction

Cancer, which has become a global threat and causes millions of deaths, is among the causes of mortality after heart diseases [1]. Breast cancer, which is the most common type of cancer in women, is malignant and metastatic tumors. Hormone receptor-positive breast cancer accounts for 80% of all breast cancers [2].

Cancer caused an estimated 9.6 million deaths in 2018. About 1 out of 6 deaths in the world and 1 out of every 5 deaths in Türkiye are caused by cancer [3]. According to 2013 data, breast cancer is the most common type of cancer in women in our country, and it is known that approximately 25% of women with this disease have HER2 positive breast cancer [4].

The exact cause of the onset of cancer is not known. In addition, studies are carried out to characterize cancer and prevent its formation and progression [5]. Since the determination of the type of treatment is of great importance, scientists have used different parameters to define the types of breast cancer. Rare breast cancers, special type; the common breast cancers were named as non-specific types. There are cells with specific characteristics in rare special types of breast cancers.

Combination therapy has also gained momentum in oncology in recent years, with higher response rates with drug combinations compared to monotherapy in several studies, the FDA has recently approved therapeutic combination regimens that show superior safety and efficacy to monotherapy [6,7].

In therapeutic agent development research, the identification of membrane receptors and the creation of ligands with high affinity for them have been identified as the most important end goal. Advances in molecular biology and genetics have brought along important innovations in drug development. As a result of the joint studies of these fields with the science of bioinformatics, it has been an important step in the discovery of new therapeutic targets by investigating the genetic causes of many diseases [8].

Tamoxifen is a non-steroidal antiestrogen drug commonly used in the treatment of hormone-sensitive breast cancer. More than 70% of all breast cancer patients are estrogen receptor-positive breast cancer patients [9]. Tamoxifen is used in the prevention and treatment of ER+ breast cancer in pre- and post-menopausal women [10]. It reduces breast cancer recurrence by 50% and the annual death rate by 31%. Despite this success, approximately 25% of tumors develop resistance to Tamoxifen treatment within a few years in addition to its side effects [11].

Estrogen hormone, which is a growth factor, binds to the estrogen receptor on the cell surface, also called its name, and ensures the growth of normal breast cells. In the case of breast cancer, estrogen receptors work for the growth and proliferation of cancer cells. It has been determined that in the majority of breast cancer types, tumor cells become dependent on estrogen for growth by significantly increasing the number of estrogen receptors in their membranes. Tamoxifen, designed to block estrogen receptors on the breast cancer cell surface, exerts its anti-proliferative effect by competitively binding to the estrogen receptor, thereby blocking the mitogenic effect of estrogen [12].

Evidence is presented that Tamoxifen induces a response in tumors lacking *ER* gene expression [13,14]. Adjuvant Tamoxifen treatment has been shown to reduce the risk of recurrence even in lesions without *ER* gene expression [15].

These clinical findings propose that Tamoxifen may have some ER-independent anticancer properties. Additionally, Blackwell et al. (2000) found that Tamoxifen was able to inhibit angiogenesis in the ER-negative fibrosarcoma model [16].

Liu et al., in a study they conducted on five different ER-negative human breast cancer cell lines to understand the antiproliferative effect of Tamoxifen on ER-negative breast cancer cells; a dose- and time-dependent induction of apoptosis was observed in MDA-MB-468, MDA-MB-231, MDA-MB-453, and SK-BR3 cells, while no significant apoptotic effect was observed in HCC-1937 cell line [17, 18].

There are more than 600 different carotenoids in nature, and they are common natural pigments [19]. Although some natural carotenoids, such as astraxanthin, β -carotene, and lycopene have been used as food coloring for many years, it has recently been an area of intense study in investigating its potential to prevent epithelial cancer and chronic diseases, with the discovery of antioxidant activity [20, 21]. Carotenoids are found in many bacteria and are found in a wide variety of phyla, not only photosynthetic but also non-photosynthetic species [19].

Deinococcus radiodurans is a red-pigmented, non-sporeforming, non-pathogenic bacteria species 1.5-3.5 μm in diameter, in clusters of two or four cells, highly resistant to stress and UV rays [19, 22, 23, 24, 29]. *D. radiodurans* synthesizes a unique ketocarotenoid, deinoxanthin (DNX) [25, 26]. Deinoxanthin has a much higher antioxidant effect than other xanthine derivatives and therefore shows a stronger ROS scavenging ability [27, 28].

Some carotenoids such as fucoxanthin, lycopene, lutein, and β -carotene suppress carcinogenesis in animals and cause apoptosis of various cancer cell lines [29]. Also, some studies show that taking carotenoids reduces the risk of cancer. It protects against DNA damage as deinoxanthin is a more effective reactive oxygen species scavenger than lutein, lycopene, or β -carotene [30, 31]. Therefore, it is noteworthy to investigate the effect of deinoxanthin on cancer cells.

Deinoxanthin has a pro-oxidative effect as well as an antioxidant effect under certain conditions. Many studies have shown that oxidative stress plays an important role in the process of inducing apoptosis. [32, 33, 34, 35]

Studies have shown that this pigment inhibits the growth of cancer cells by inducing apoptosis in various cancer cells. Within the scope of the study, it was aimed to increase the antiproliferative activity of Tamoxifen with deinoxanthin on MDA-MB-453, a HER-2 positive breast cancer cell line.

Deinoxanthin is a carotenoid derivative that has a pro-oxidant effect against cancer cells, on which studies have not been fully deepened. This xanthine derivative, which helps *Deinococcus radiodurans* survive in the highly oxidative environments it is exposed to, also plays an

antioxidant role. In the study, it was aimed that tamoxifen, which is used against ER-positive cancer types, with deinoxanthin at lower doses, has a better anti-cancer effect against ER-negative breast cancer. Deinoxanthin, which makes tamoxifen more effective in vitro with lower IC₅₀ values than known, can also reduce side effects with its antioxidant property in healthy cells.

2. Materials and Methods

2.1. Materials

The MDA-MB-453 (HTB-131) breast cancer cell line was purchased commercially from ATCC.

Dulbecco's modified Eagle's medium (DMEM), L-glutamine, heat-inactivated fetal bovine serum, penicillin-streptomycin, trypsin-EDTA, phosphate buffer saline (PBS), and XTT (2,3-Bis-(2-Methoxy-4-Nitro-5-Sulfophenyl)-2H-Tetrazolium-5-Carboxanilide) cell proliferation kit was obtained from Biological Industries Ltd (Catalog number:20-300-1000).

TMX was obtained from Sigma Aldrich.

DNX was supplied from the purified stock of Seda KILINÇ, produced in the joint venture of Erzincan Binali Yıldırım University and Marmara University, Türkiye.

RNA isolation (Catalog number:K0732) and cDNA synthesis (Catalog number:4368814) were performed according to the manufacturer's instructions (Thermo Scientific, US). Human BAX (Catalog number: E-EL-H0562), CASP-3 (Catalog number: E-EL-H0017), BCL-2 (Catalog number: E-EL-H0114), and HER2 (Catalog number: E-EL-H6083) ELISA kits were purchased from Elabscience Biotechnology Co. (Wuhan, China). All other chemical reagents were purchased from Merck and Sigma Aldrich.

2.2. Cell line and culture

MDA-MB-453 breast cancer cell line; was cultured in DMEM containing 1% penicillin-streptomycin, 1% L-glutamine, and 10% FBS. Incubation was carried out in an incubator at 37° C and 5% CO₂ sterile air.

2.3. Cell proliferation assay

Cell cultivation was inoculated into each well of 96-well TC-treated plates in 200 µl DMEM at 5x10⁴ cells and incubated for 24 hours at 37° C, 5% CO₂, and 95% humidity.

To determine the cytotoxic effects depending on time and concentration, a study was conducted to determine the combined and separate concentrations of TMX and DNX.

Table 1. Application concentrations of TMX and DNX.

Concentration Sets	TMX (μM)	DNX (μM)	TMX (μM) + DNX (μM)
1	270	200	270+200
2	135	100	135+100
3	67,5	50	67,5+50
4	33,75	25	33,75+25
5	16,87	12,5	16,87+12,5
6	8,43	6,25	8,43+6,25
7	4,21	3,125	4,21+3,125

At the end of the incubation periods, 50 μl of XTT reagent was added to each well to determine cell viability. After 3 hours, the absorbance was measured at 450 nm with a microplate reader to calculate the percent cell viability versus negative control.

2.4. Combinational Index Value

TMX and DNX interactions and combination index (CI) values were determined with the CompuSyn program.

2.5. RT-qPCR Analysis

In study, It was determined that the best synergistic effect in the calculated CI values was the 24 hours incubation period and the combination of 4.21 μM TMX and 3.125 μM DNX. RNA isolation and cDNA synthesis were performed by culturing the MDA-MB-453 breast cancer cell line applied with these parameters. The expression levels of *BAX*, *CASP-3*, *BCL2*, and *HER2* genes of the MDA-MB-453 cell line were determined. The *ACTB* gene was used as the reference gene. Real-time PCR with SYBR green was performed using Bio-rad iTaq™ universal SYBR® Green supermix (Catalog number: 1725125) and a Qiagen Rotor-Gene Q 6plex Real-Time PCR System. Primers designed by using NCBI Primer-BLAST program were synthesized by Metabion Company according to the sequences specified in (Table 2.).

Table 2. Primer sequences.

Gene	Primer sequence	Accession Number
<i>BAX</i>	F: 5-AGCAGATCATGAAGACAGGG R: 5-GAAGTTGCCGTCAGAAAACA	NM 138764
<i>CASP-3</i>	F: 5-GCGCTCTGGTTTTTCGTTAAT R: 5-ACCCATCTCAGGATAATCCATTT	NM 004346
<i>BCL2</i>	F: 5-TATCTGGGCCACAAGTGAAG R: 5-ATTCGACGTTTTGCCTGAAG	NM 000657
<i>HER2</i>	F: 5-GTGAAGCTGAGATTCCCCTC R: 5-GCAGCTTCATGTCTGTGC	NM 001005862
<i>ACTB</i>	F: 5-CACCATGGATGATGATATCGC R: 5-GAATCCTTCTGACCCATGCC	NM 001101

2.6. Protein extraction

TMX (4.21 μ M), DNX (3.125 μ M), and TMX + DNX (4.21 μ M + 3.125 μ M) drug applications, which were the lowest CI values obtained in the study, levels of BAX, CASP-3, BCL-2 and HER2, on MDA-MB-453 cell line and to determine the expression proteins, commercial ELISA kits were used. Also, the total protein concentration in the sample was measured using the Bradford protein assay.

2.7. Statistical analysis

BAX, *CASP-3*, *BCL-2*, and *HER2* genes expression levels were determined using the primary normalization $2^{-\Delta\Delta CT}$ method developed by Livak and Schmittgen using *ACTB* as the reference gene (Livak & Schmittgen, 2001). Statistical analysis was evaluated using SPSS 17.0 program. The significant percentage of the results is $p < 0.05$.

3. Results and Discussion

3.1. Cell Viability Test

XTT studies were carried out on MDA-MB-453 cells at 24 and 48 hours incubation times where the indicated concentrations of TMX and DNX were applied separately and in combination. With the absorbance data obtained at 450 nm, "cell survival percentages" were calculated and as a result of these calculations, the findings in the graphs shown in (Figure 1) and (Figure 2) were obtained.

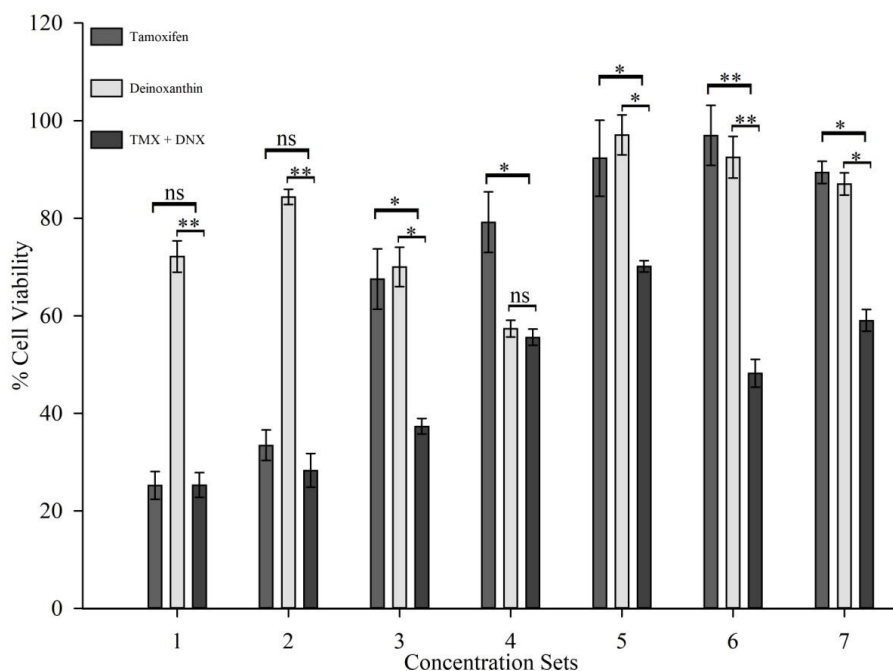


Figure 1. Antiproliferative activity of TMX, DNX and TMX + DNX on MDA-MB-453 at 24 hours. Values are represented as the mean \pm standard error of mean. "ns" indicates not significant ($p > 0.05$); * $p < 0.05$; ** $p < 0.01$.

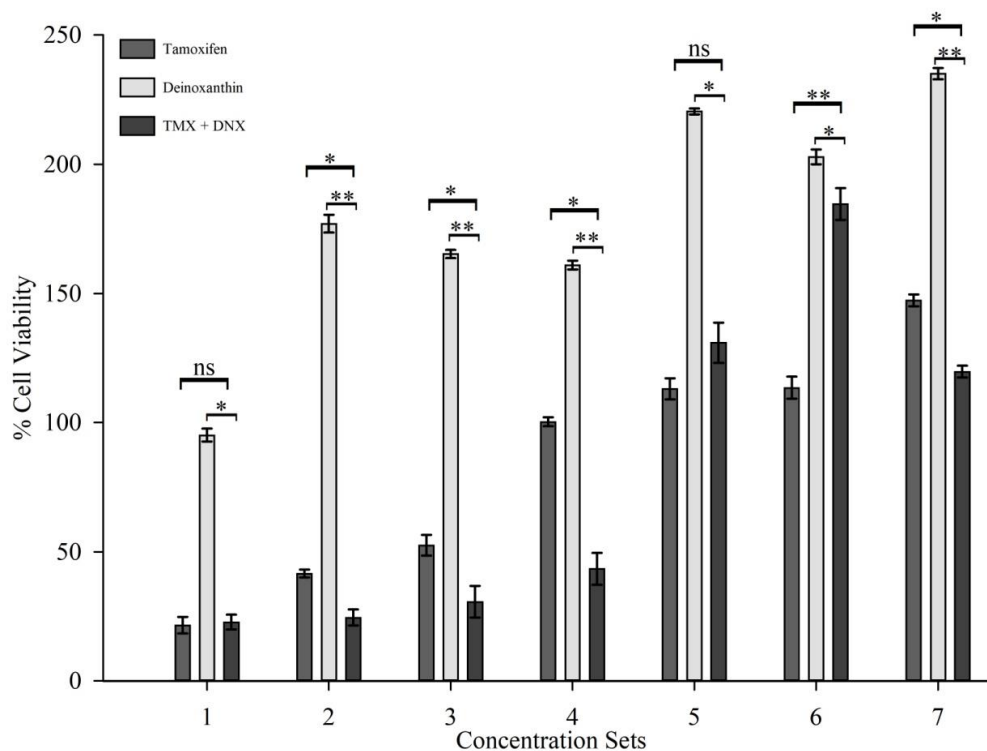


Figure 2. Antiproliferative activity of TMX, DNX and TMX + DNX on MDA-MB-453 at 48 hours. Values are represented as the mean \pm standard error of mean. “ns” indicates not significant ($p > 0.05$); * $p < 0.05$; ** $p < 0.01$.

The combination effect value (CI) was calculated using the CompuSyn program using the absorbance values measured at the 24 and 48 hours in the MDA-MB-453 cell line where TMX, DNX and their combinations were administered.

Table 3. CI values calculated after the application of TMX, DNX and TMX + DNX on MDA-MB-453 at the 24 hours.

TMX+DNX (μ M)	CI	Effect
270+200	1,048	Medium Antagonistic
135+100	0,589	Synergistic
67,5+50	0,407	Synergistic
33,75+25	0,373	Synergistic
16,87+12,5	0,327	Synergistic
8,43+6,25	0,072	Very strong synergistic
4,21+3,125	0,052	Very strong synergistic

Table 4. CI values calculated after the application of TMX, DNX and TMX + DNX on MDA-MB-453 at the 48 hours.

TMX+DNX (μ M)	CI	Effect
270+200	1,228	Medium Antagonistic
135+100	0,652	Synergistic
67,5+50	0,394	Synergistic
33,75+25	0,286	Strong synergistic
16,87+12,5	0,943	Additive
8,43+6,25	9,033	Strong Antagonistic
4,21+3,125	0,159	Strong synergistic

Within the scope of the studies carried out, as a result of 24 and 48 hours incubation on MDA-MB-453 cell line; according to the results of XTT studies conducted with the application of TMX, DNX and their combinations at the determined concentrations; it has been determined that TMX has a higher antiproliferative effect than DNX, except for the 4th, 6th and 7th concentrations of the 24 hours, and when applied together at all concentrations, it has a better antiproliferative effect than when applied separately.

It was observed that at the 48th hour, compared to the 24th hour, TMX, DNX, or both lost their half-lives because they were present in a longer period or fluctuations in the vitality rates were observed due to probabilities such as deterioration of their molecular structure.

3.2.RT-qPCR Analysis and ELISA

The expression levels of *BAX*, *CASP-3*, *BCL-2*, and *HER2* genes of the MDA-MB-453 cell line were determined at the lowest CI value determined in the study. *ACTB* (beta-actin) gene was used as the reference gene. Graphics of the results obtained; (Figure 3, Figure 4, Figure 5, and Figure 6.

When looking at the findings, it was observed that TMX applied alone on the MDA-MB-453 breast cancer cell line did not have a very high effect on the expression level of *BAX* and *CASP-3* genes, but when applied together with DNX, it was observed that it caused a significant increase in the expression levels of *BAX* and *CASP-3* genes.

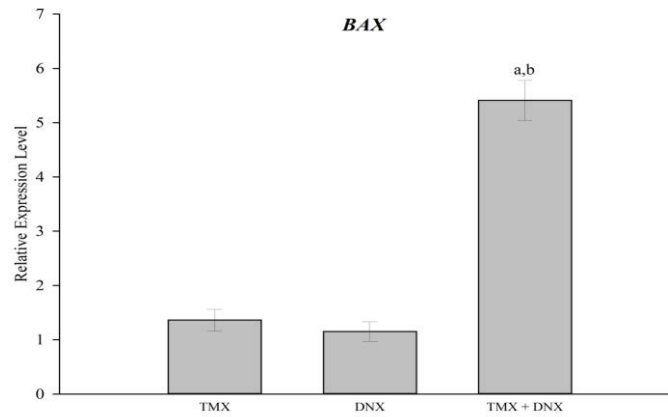


Figure 3. The effect of TMX, DNX, and their combinations on *BAX* gene expression level. Values are represented as the mean \pm standard error of mean. ^a $p < 0.05$ versus TMX-treated group. ^b $p < 0.05$ versus DNX-treated group.

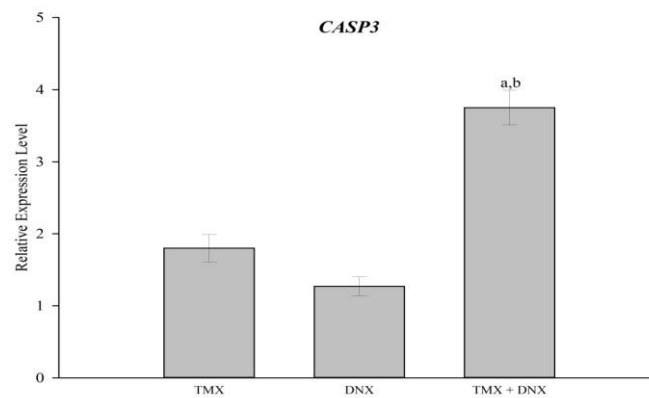


Figure 4. The effect of TMX, DNX, and their combinations on *CASP-3* gene expression level. Values are represented as the mean \pm standard error of mean. ^a $p < 0.05$ versus TMX-treated group. ^b $p < 0.05$ versus DNX-treated group.

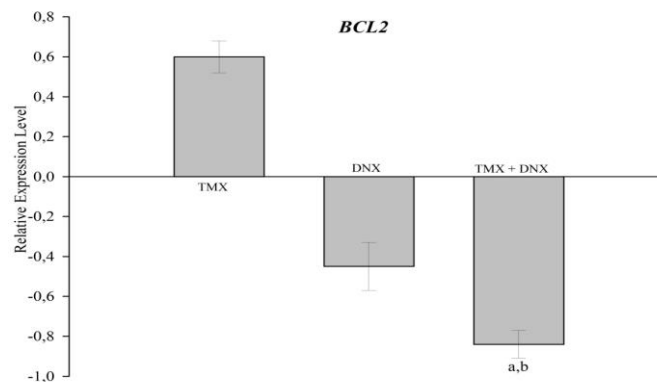


Figure 5. The effect of TMX, DNX, and their combinations on *BCL2* gene expression level. Values are represented as the mean \pm standard error of mean. ^a $p < 0.05$ versus TMX-treated group. ^b $p < 0.05$ versus DNX-treated group.

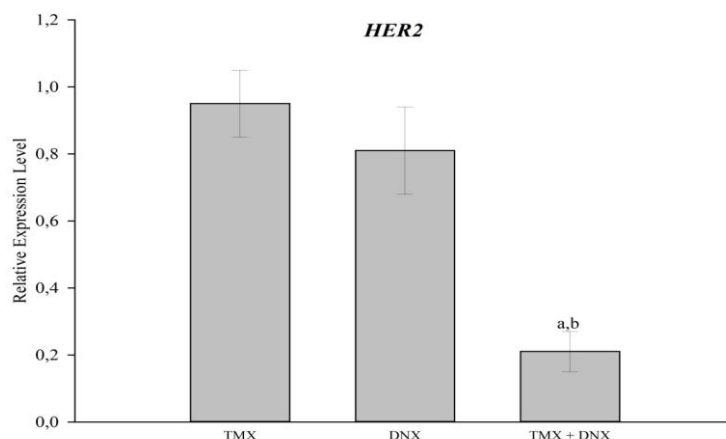


Figure 6. TMX, DNX, and their combination effects on *HER2* gene expression. Values are represented as the mean \pm standard error of mean. ^a $p < 0.05$ versus TMX-treated group. ^b $p < 0.05$ versus DNX-treated group.

The expression level of BAX and CASP-3 genes in the DNX-group did not increase at a very high rate, and had less effect on *BCL-2* and *HER2* alone. It is not considered to have a greater effect as an intrinsic apoptotic stimulus alone.

According to the results of RT-qPCR in all samples where 4,21 μM TMX + 3,125 μM DNX combination was applied; *BAX* and *CASP3* genes; It was observed that higher expression levels were reached compared to the control group and TMX-group. In determining the expression levels of *BCL-2* and *HER2* genes, it was revealed that the combination of drugs was more effective than individual drugs on MDA-MB-453.

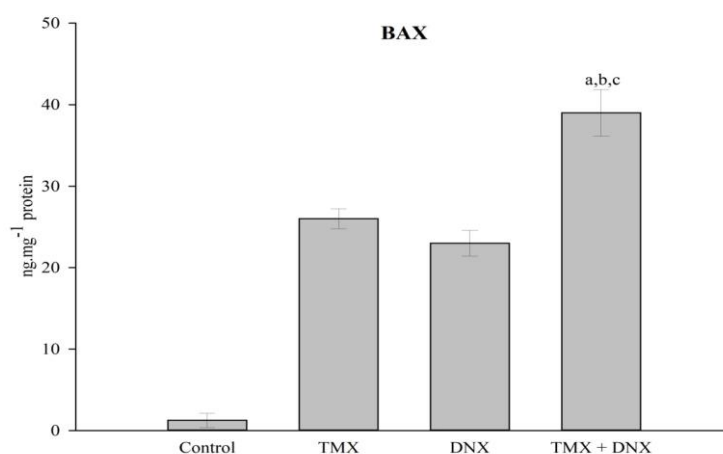


Figure 7. The effect of TMX, DNX, and their combinations on BAX protein expression level. Values are represented as the mean \pm standard error of mean. ^a $p < 0.05$ versus TMX-treated group. ^b $p < 0.05$ versus DNX-treated group.

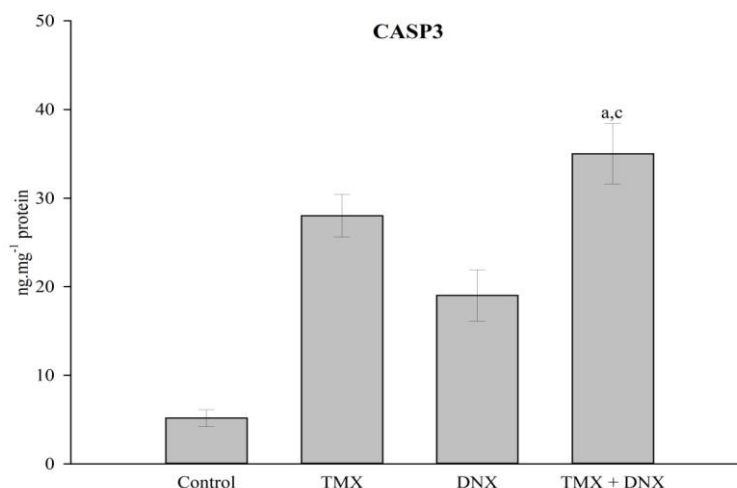


Figure 8. The effect of TMX, DNX, and their combinations on CASP-3 protein expression level. Values are represented as the mean \pm standard error of mean. ^a $p < 0.05$ versus TMX-treated group. ^b $p < 0.05$ versus DNX-treated group.

In many cancer types, while pro-apoptotic protein levels such as BAX and CASP-3 decrease, anti-apoptotic protein levels such as BCL-2 increase. It was determined that BAX and CASP-3 protein levels differed significantly in the drug concentration administered in combination compared to the control and separately administered drug concentrations. This significant increase in BAX and CASP-3 protein levels suggests that apoptosis was induced in cancer cells.

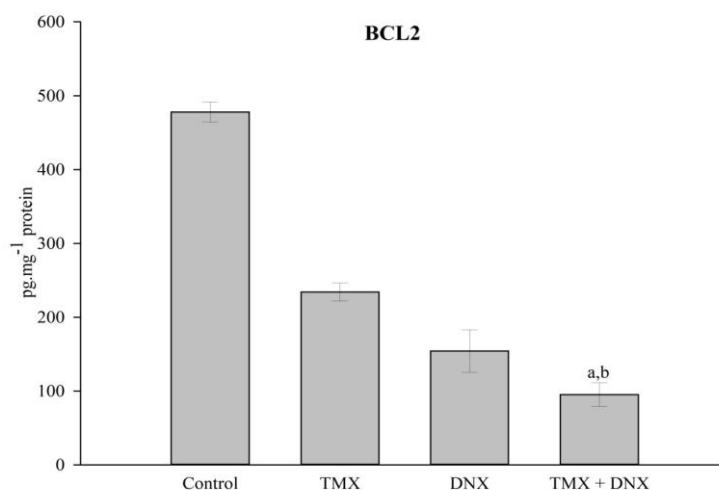


Figure 9. The effect of TMX, DNX and their combinations on BCL-2 protein expression level. Values are represented as the mean \pm standard error of mean. ^a $p < 0.05$ versus TMX-treated group. ^b $p < 0.05$ versus DNX-treated group.

The Bcl-2 family plays an important role in the regulation of apoptosis. The intensity of Bcl-2 production in various cancer cells shows a positive correlation with the lifespan of the cell [36]. In addition to BAX and CASP-3 protein levels, a significant decrease was observed in the determined BCL-2 and HER-2 protein levels, and the suppression of apoptosis in cells decreased. And it is thought that the cell is more easily dragged into apoptosis.

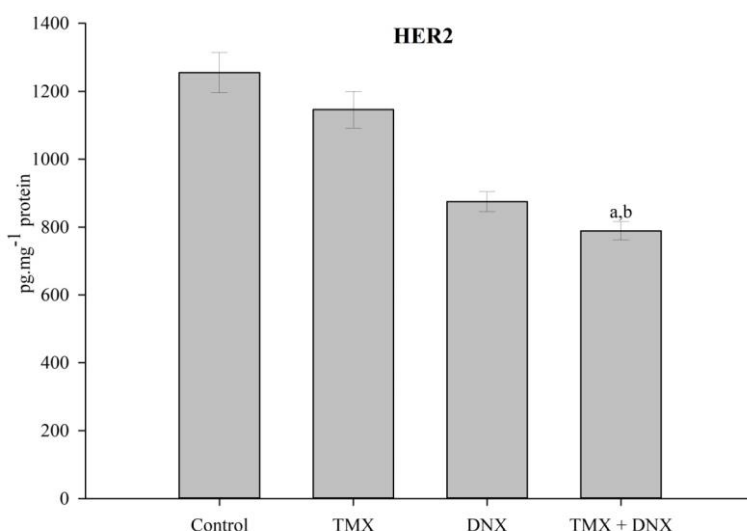


Figure 10. The effect of TMX, DNX and their combinations on HER-2 protein expression level. Values are represented as the mean \pm standard error of mean. ^a $p < 0.05$ versus TMX-treated group. ^b $p < 0.05$ versus DNX-treated group.

Table 5. The amount of BAX, BCL-2, CASP-3, and HER2 in MDA-MB-453 cell line exposed to DNX (3,125 μ M), TMX (4,21 μ M) separately and also in combination (4,21 μ M+3,125 μ M) for 24 h.

	BAX (ng/mg protein)		BCL2 (pg/mg protein)		CASP3 (ng/mg protein)		HER2 (pg/mg protein)	
Control	1,25	\pm 0,87 ^{b,c,d,*}	478	\pm 13,5 ^{b,c,d}	5,16	\pm 0,96 ^{b,c,d}	1255	\pm 59 ^{c,d}
TMX	26,1	\pm 1,23 ^{a,d}	234	\pm 12 ^{a,c,d}	28	\pm 2,4 ^{a,c}	1146	\pm 54 ^{c,d}
DNX	22,6	\pm 1,58 ^{a,d}	154	\pm 29 ^{a,b}	19	\pm 2,9 ^{a,b,d}	875	\pm 29 ^{a,b}
TMX+DNX	39,2	\pm 2,87 ^{a,b,c}	95	\pm 16 ^{a,b}	35	\pm 3,4 ^{a,c}	789	\pm 27 ^{a,b}

*:Results given as the mean \pm SD. One-way ANOVA with post-hoc LSD test. Different letters show statistical differences. $P < 0.05$ is the level of significance.

The results were as follows BAX protein was found to be increased 31 times more compared to control and 1.5 and 1.7 times more compared to TMX-group and DNX-group, respectively; CASP-3 protein was found to be increased approximately 7 times compared to control and 1.25; 1.8 times more compared to TMX-group and DNX-group, respectively.

The combination of 4.21 μ M TMX + 3.125 μ M DNX at the *BCL2* expression level decreased 5 times compared to the control and approximately 2.5 and 1.5 times, respectively, compared to TMX-group and DNX-group; In the expression level of HER2, it was determined that the

combination of 4.21 μM TMX + 3.125 μM DNX decreased 1.6 times compared to the control and 1.4; 1.1 times more compared to TMX-group and DNX-group.

In a 2020 study by Maqbool et al., they showed that the synergistic combination of tamoxifen with the novel synthesis product di-2-pyridylketone4-cyclohexyl-4-methyl-3-thiosemicarbazone (DpC), a thiosemicarbazone derivative, could be a promising new therapeutic strategy to overcome tamoxifen resistance in ER-positive breast cancer. Using a tamoxifen-resistant cell line, MDA-MB-453 and MDA-MB-231, in the study creates the potential to provide a different treatment strategy with a similar combinatorial approach. As a matter of fact, in previous bioinformatic studies, it was determined that deinoxanthin's ability to bind to testosterone and estrogen receptors may be high. In addition, studies are continuing that deinoxanthin increases the expression levels of estrogen and testosterone receptors.

Tamoxifen, a selective ER modulator, can drive cancer cells into apoptosis through mechanisms other than ER antagonism. In a study by Liu et al. in 2014, the drug mechanism was examined by testing the efficacy of tamoxifen by testing the ER-negative breast cancer cell lines HCC-1937, MDA-MB-231, MDA-MB-468, MDA-MB-453 and SK-BR-3. As a result, it was determined that Tamoxifen significantly induced apoptosis in MDA-MB-231, MDA-MB-468, MDA-MB-453 and SK-BR-3 cells, but was not effective in HCC-1937 cells. They suggested that tamoxifen-induced induction of apoptosis is associated with tamoxifen dose-dependent inhibition of protein phosphatase 2A (CIP2A) and phospho-Akt (p-Akt).

According to the research conducted by Ibrahim et al. in 2019, the combination of Tamoxifen and Simvastatin was treated with different concentrations of TAM and/or SIM for 72 hours in the estrogen receptor positive (ER+) breast cancer cell line T47D. In the study, cytotoxicity, oxidative stress markers, apoptosis, angiogenesis and metastasis analyzes were performed and as a result, higher BAX/BCL-2 ratio and CASP3 activity were observed in the combination groups compared to the others.

In the study, it was observed that the apoptotic pathway was more active in the combination of deinoxanthin with tamoxifen than when tamoxifen was administered alone. Although the MDA-MB-453 cell line is estrogen receptor-negative, it became more sensitive to tamoxifen by triggering inhibition of CIP2A and p-Akt or by a different pathway. More detailed metabolomic analysis of the effect of deinoxanthin with tamoxifen is planned in future studies.

4. Conclusion

In line with these results, it has been shown that Tamoxifen may be to combined with deinoxanthin, which has high antioxidant properties, to increase its effectiveness and further strengthen its antiproliferative activity. In addition, Tamoxifen, which is used in hormone receptor sensitive breast cancer treatments, has also been reported to have a significant effect on cell lines that also show triple negative breast cancer characteristics [37]. We aimed to obtain a more effective combination therapy that can be used in Tamoxifen treatment by using this cell line that can show both features.

Significant antiproliferative activity was found in our study as a result of the combination of Tamoxifen, which was confirmed to have a strong effect on breast cancer, by benefiting from the strong antioxidant effect of deinoxanthin and its ability to drive cancer cells to apoptosis. It is planned to increase the effectiveness of this cure by making much more detailed analyzes in future studies.

Ethics in Publishing

There are no ethical issues regarding the publication of this study.

Author Contributions

With the joint contribution of Nihan GÜNAY and Mehmet KUZUCU, the literature was searched, the study was designed, the experiments were carried out, the study was analyzed and interpreted, the results were determined and interpreted and the article was written.

Acknowledgments - This study was supported by Erzincan Binali Yıldırım University Scientific Research Projects Coordinator ship, project no. FLY-2019-643. We also thank to Seda KILINÇ for providing pure deinoxanthin.

References

- [1] Merey, S. (2002). “Breast cancer screening behavior in women”. *University of Istanbul, Istanbul*.
- [2] Hart, C. D., Migliaccio, I., Malorni, L., Guarducci, C., Biganzoli, L., Di Leo, A. (2015). “Challenges in the management of advanced, ER-positive, HER2-negative breast cancer”. *Nature reviews Clinical oncology*, 12(9), 541-552.
- [3] <https://www.who.int/news-room/fact-sheets/detail/cancer> Access Date: (2020)
- [4] Gültekin, M., Boztaş, G. (2014). “Türkiye kanser istatistikleri”. *Sağlık Bakanlığı, Türkiye Halk Sağlığı Kurumu*, 43, 12-32.
- [5] Harbeck, N., Penault-Llorca, F., Cortes, J., Gnant, M., Houssami, N., Poortmans, P., ... & Cardoso, F. (2019). “Breast cancer (Primer)”. *Nat. Rev. Dis. Primers*, 66.
- [6] Janku, F., Hong, D. S., Fu, S., Piha-Paul, S. A., Naing, A., Falchook, G. S., ... & Kurzrock, R. (2014). “Assessing PIK3CA and PTEN in early-phase trials with PI3K/AKT/mTOR inhibitors”. *Cell reports*, 6(2), 377-387.
- [7] Musgrove, E. A., Caldon, C. E., Barraclough, J., Stone, A., & Sutherland, R. L. (2011). “Cyclin D as a therapeutic target in cancer”. *Nature Reviews Cancer*, 11(8), 558-572.
- [8] Tutun, H., Baydan, E. (2019). “İlaç geliştirmede reseptör analizinin önemi”. *Mehmet Akif Ersoy Üniversitesi Sağlık Bilimleri Enstitüsü Dergisi*, 4(1).

- [9] Ibrahim, A. B., Zaki, H. F., Ibrahim, W. W., Omran, M. M., Shouman, S. A. (2019). "Evaluation of Tamoxifen and simvastatin as the combination therapy for the treatment of hormonal dependent breast cancer cells". *Toxicology Reports*, 6, 1114-1126.
- [10] Subramani, T., Yeap, S. K., Ho, W. Y., Ho, C. L., Omar, A. R., Aziz, S. A., ... & Alitheen, N. B. (2014). "Vitamin C suppresses cell death in MCF-7 human breast cancer cells induced by Tamoxifen". *Journal of cellular and molecular medicine*, 18(2), 305-313.
- [11] Zhang, M. H., Man, H. T., Zhao, X. D., Dong, N., Ma, S. L. (2014). "Estrogen receptor-positive breast cancer molecular signatures and therapeutic potentials". *Biomedical reports*, 2(1), 41-52.
- [12] Aesoy, R., Sanchez, B. C., Norum, J. H., Lewensohn, R., Viktorsson, K., Linderholm, B. (2008). "An autocrine VEGF/VEGFR2 and p38 signaling loop confers resistance to 4-hydroxyTamoxifen in MCF-7 breast cancer cells". *Molecular Cancer Research*, 6(10), 1630-1638.
- [13] Osborne, C. K., Yochmowitz, M. G., Knight III, W. A., McGuire, W. L. (1980). "The value of estrogen and progesterone receptors in the treatment of breast cancer". *Cancer*, 46(S12), 2884-2888.
- [14] Osborne, C. K. (1998). "Tamoxifen in the treatment of breast cancer". *New England Journal of Medicine*, 339(22), 1609-1618.
- [15] Theriault, R. L., Carlson, R. W., Allred, C., Anderson, B. O., Burstein, H. J., Edge, S. B., ... & Kumar, R. (2013). "Breast cancer, version 3.2013". *Journal of the National Comprehensive Cancer Network*, 11(7), 753-761.
- [16] Blackwell, K. L., Haroon, Z. A., Shan, S., Saito, W., Broadwater, G., Greenberg, C. S., Dewhirst, M. W. (2000). "Tamoxifen inhibits angiogenesis in estrogen receptor-negative animal models". *Clinical cancer research*, 6(11), 4359-4364.
- [17] Liu, C. Y., Hung, M. H., Wang, D. S., Chu, P. Y., Su, J. C., Teng, T. H., ... & Chen, K. F. (2014). "Tamoxifen induces apoptosis through cancerous inhibitor of protein phosphatase 2A-dependent phospho-Akt inactivation in estrogen receptor-negative human breast cancer cells". *Breast cancer research*, 16(5), 1-15.
- [18] Ibrahim, A. B., Zaki, H. F., Ibrahim, W. W., Omran, M. M., Shouman, S. A. (2019). "Evaluation of Tamoxifen and simvastatin as the combination therapy for the treatment of hormonal dependent breast cancer cells". *Toxicology Reports*, 6, 1114-1126.
- [19] Choi, Y. J., Hur, J. M., Lim, S., Jo, M., Kim, D. H., Choi, J. I. (2014). "Induction of apoptosis by deinoxanthin in human cancer cells". *Anticancer research*, 34(4), 1829-1835.
- [20] Sharoni, Y., Danilenko, M., Walfisch, S., Amir, H., Nahum, A., Ben-Dor, A., ... & Levy, J. (2002). "Role of gene regulation in the anticancer activity of carotenoids". *Pure and applied chemistry*, 74(8), 1469-1477.
- [21] Rao, A. V., Rao, L. G. (2007). "Carotenoids and human health". *Pharmacological research*, 55(3), 207-216.

- [22] Krinsky, N. I., Johnson, E. J. (2005). "Carotenoid actions and their relation to health and disease". *Molecular aspects of medicine*, 26(6), 459-516.
- [23] Cheng, J., Zhang, Z., Zheng, Z., Lv, G., Wang, L., Tian, B., Hua, Y. (2014). "Antioxidative and hepatoprotective activities of deinoxanthin-rich extract from *Deinococcus radiodurans* R1 against carbon tetrachloride-induced liver injury in mice". *Tropical Journal of Pharmaceutical Research*, 13(4), 581-586.
- [24] Zhou, Z., Zhang, W., Su, S., Chen, M., Lu, W., Lin, M., ... & Xu, Y. (2015). "CYP287A1 is a carotenoid 2- β -hydroxylase required for deinoxanthin biosynthesis in *Deinococcus radiodurans* R1". *Applied microbiology and biotechnology*, 99(24), 10539-10546.
- [25] Lemee, L., Peuchant, E., Clerc, M., Brunner, M., Pfander, H. (1997). "Deinoxanthin: a new carotenoid isolated from *Deinococcus radiodurans*". *Tetrahedron*, 53(3), 919-926.
- [26] Ji, H., (2010) "Insight into the strong antioxidant activity of deinoxanthin, a unique carotenoid in *Deinococcus radiodurans*", *International Journal of Molecular Sciences* 11:4506-4510
- [27] Tian, B., Xu, Z., Sun, Z., Lin, J., Hua, Y. (2007). "Evaluation of the antioxidant effects of carotenoids from *Deinococcus radiodurans* through targeted mutagenesis, chemiluminescence, and DNA damage analyses". *Biochimica et Biophysica Acta (BBA)-General Subjects*, 1770(6), 902-911.
- [28] Apel, K., Hirt, H. (2004). "Reactive oxygen species: metabolism, oxidative stress, and signaling transduction". *Annual review of plant biology*, 55, 373.
- [29] Tanaka, T., Shnimizu, M., Moriwaki, H. (2012). "Cancer chemoprevention by caroteno". *Molecules*, 17(3), 3202-3242.
- [30] Sun, Z., Shen, S., Tian, B., Wang, H., Xu, Z., Wang, L., Hua, Y. (2009). "Functional analysis of γ -carotene ketolase involved in the carotenoid biosynthesis of *Deinococcus radiodurans*". *FEMS microbiology letters*, 301(1), 21-27.
- [31] Tian, B., Xu, Z., Sun, Z., Lin, J., Hua, Y. (2007). "Evaluation of the antioxidant effects of carotenoids from *Deinococcus radiodurans* through targeted mutagenesis, chemiluminescence, and DNA damage analyses". *Biochimica et Biophysica Acta (BBA)-General Subjects*, 1770(6), 902-911.
- [32] Muller, K., Carpenter, K. L., Challis, I. R., Skepper, J. N., Arends, M. J. (2002). Carotenoids induce apoptosis in the T-lymphoblast cell line Jurkat E6.1". *Free radical research*, 36(7), 791-802.
- [33] Kotake-Nara, E., Terasaki, M., Nagao, A. (2005). "Characterization of apoptosis induced by fucoxanthin in human promyelocytic leukemia cells". *Bioscience, biotechnology, and biochemistry*, 69(1), 224-227.

- [34] Özcan, O., Erdal, H., Çakırca, G., Yönden, Z. (2015). "Oxidative stress and its impacts on intracellular lipids, proteins and DNA". *J Clin Exp Invest*, 6(3), 331-336.
- [35] Rahal, A., Kumar, A., Singh, V., Yadav, B., Tiwari, R., Chakraborty, S., Dhama, K. (2014). "Oxidative stress, prooxidants, and antioxidants: the interplay". *BioMed research international*, 2014.
- [36] Vranic, S., Gatalica, Z., Wang, Z. Y. (2011). Update on the molecular profile of the MDA-MB-453 cell line as a model for apocrine breast carcinoma studies. *Oncology letters*, 2(6), 1131-1137.
- [37] Chen, J., Xiong, W. B., Xiong, Y., Wu, Y. Y., Chen, X. J., Shao, Z. J., ... & Zhou, L. M. (2011). Calycosin Stimulates Proliferation of Estrogen Receptor-Positive Human Breast Cancer Cells Through Downregulation of Bax Gene Expression and Upregulation of Bcl-2 Gene Expression at Low Concentrations. *Journal of Parenteral and Enteral Nutrition*, 35(6), 763-769.
- [38] Maqbool, S. N., Lim, S. C., Park, K. C., Hanif, R., Richardson, D. R., Jansson, P. J., & Kovacevic, Z. (2020). Overcoming tamoxifen resistance in oestrogen receptor-positive breast cancer using the novel thiosemicarbazone anti-cancer agent, DpC. *British journal of pharmacology*, 177(10), 2365-2380.

Synthesis and Characterization of Poly(lactic-co-glycolic acid) Derived with *L*-Glutamic Acid and *L*-Aspartic Acid

Gülce TAŞKOR ÖNEL *

Erzincan Binali Yıldırım University, Faculty of Pharmacy, Department of Analytical Chemistry,
Yalnızbağ 24002, Erzincan, TÜRKİYE

Received: 15/01/2023, **Revised:** 19/03/2023, **Accepted:** 22/03/2023, **Published:** 31/03/2023

Abstract

Poly(lactic-co-glycolic acid) (PLGA) is a biodegradable and biocompatible polymer approved by the FDA and EMA, which is the most widely used in the field of health. In this study, PLGA was synthesized primarily from lactide and glycolide by polycondensation and ring-opening polymerization. Then, amino acid derivatives of PLGA were synthesized by the reaction of PLGA and amino acids in the existence of 1-ethyl-3-(3-dimethylaminopropyl)carbodiimide (EDC). The polymers synthesized were PLGA, PLGA-*L*-glutamic acid (PLGA-G), and PLGA-*L*-aspartic acid (PLGA-A). The chemical structure of these polymers was verified by ¹H and ¹³C Nuclear Magnetic Resonance (¹H NMR and ¹³C NMR), Fourier Transform Infrared Spectroscopy (FTIR), Differential Scanning Calorimetry (DSC), and Gel Permeation Chromatography (GPC). When the ¹³C NMR analyses of PLGA-amino acid derivatives were observed, an increase in the number of carbonyl carbons around 170 ppm was found and the structure accuracy was supported. In addition, when the FTIR analyses of PLGA-amino acid derivatives were examined, the structure was confirmed by observing the signal of the amide bond carbonyl vibration at 1700 cm⁻¹. While the typical endothermic thermogram of the PLGA-amino acid derivative structures was observed by DSC analysis, it was found that the structures were low molecular weight polymers [~5000-6000 Da] by GPC analysis.

Keywords: PLGA, amino acid, biodegradable polymer.

L-Glutamik Asit ve *L*-Aspartik Asit ile Türevlendirilen Poli(laktik-ko-glikolik asit)'in Sentezi ve Karakterizasyonu

Öz

Poli(laktik-ko-glikolik asit) sağlık alanında en çok kullanılan biyobozunur ve biyoyumlu özellikte FDA ve EMA onaylı bir polimerdir. Bu çalışmada öncelikle polikondenzasyon ve halka açılma polimerizasyonu ile laktid ve glikolidden PLGA sentezlenmiştir. Daha sonra PLGA ve amino asitlerin 1-etil-3-(3-dimetilaminopropil)karbodiimid (EDC) varlığında reaksiyonu ile PLGA'nın amino asit türevleri sentezlenmiştir. Sentezlenen polimerler PLGA, PLGA-*L*-glutamik asit (PLGA-G) ve PLGA-*L*-aspartik asit (PLGA-A)'dir. Bu polimerlerin kimyasal yapısı ¹H ve ¹³C Nükleer Manyetik Rezonans (¹H NMR ve ¹³C NMR), Fourier Dönüşümlü Kızılötesi Spektroskopisi (FTIR), Diferansiyel Taramalı Kalorimetri (DSC) ve Jel Geçirgenlik Kromatografisi (GPC) ile doğrulandı. PLGA-amino asit türevlerinin ¹³C NMR analizleri incelendiğinde 170 ppm yakınlarında karbonil karbonlarının sayısında artış gözlenerek yapı doğruluğu desteklenmiştir. Ayrıca yine PLGA-amino asit türevlerinin FTIR analizleri incelendiğinde amid bağı karbonil titreşimine ait sinyal 1700 cm⁻¹'de gözlenerek yapı doğrulanmıştır. PLGA-aminoasit türev yapılarının DSC analizi ile tipik endotermik termogram gözlenirken, GPC analizleri ile yapıların düşük molekül ağırlıklı polimerler [~5000-6000 Da] olduğu bulunmuştur.

Anahtar Kelimeler: PLGA, amino asit, biyobozunur polimer.

1. Introduction

Researchers have frequently investigated novel biomolecule-derived poly(lactic-co-glycolic acid)s (PLGAs) [1], polyurethanes (PUs) [2], and poly(ethylene glycol)s (PEGs) [3], biopolymers because of increasing attention to their biocompatibility, biodegradability superior mechanical properties, and chemical versatility. PLGA is biodegradable and biocompatible, displays different degradation times with chemical versatility has adjustable mechanical properties, and is an FDA and EMA-approved polymer [4, 5]. There are many studies where PLGA is used for new-generation drug carrier systems and biomaterials. For example, Ansari et al. have reported in their studies that the flexibility and biodegradability properties of amino acid-based polyester amides provide unique thermomechanical properties. They stated that the addition of amino acids to the structure of polyester amides increases the H-bond capacity of the structure and affects cell interaction well [6].

Zhao et al. reported which is an example of the bonding of peptide structures such as Arg-Gly-Asp tripeptide (RGD) and Tyr-Ile-Gly-Ser-Arg (YIGSR) with PLGA, indicated adjusting that the distribution, density, and bioactive regions of amino acid or peptide structures in PLGA [7]. In a different study where PLGA-mucin nanoparticles had the dual role of resistance to biofouling and, molecular recognition was reported reducing plasma protein adsorption, and subsequent dampening of complement and platelet activation [8]. It is observed that amino acid structures bonding with PLGA provide positive enhancement to biological interaction.

In the study of Takeuchi et al. reported that PLGA microparticles derived from leucine and aspartic acid significantly improved the thin particle fraction and the phagocytotic ratio of alveolar macrophages [9]. pH-sensitive nanoparticle system containing charge reversible pullulan-based (CAPL) shell and poly(β -amino ester)/PLGA structure were designed for potential novel carriers of paclitaxel (PTX) and combretastatin A4 (CA4) for combining chemotherapy and anti-angiogenesis to treat hepatocellular carcinoma (HCC) [10]. PLGA amino acid derivative structures are ideal polymer systems for micro/nanoparticulate drug carriers.

Also in tissue engineering applications PLGA microparticles were combined with poly(β -amino ester) particles to create new crossbred scaffolds capable of the both release of drug and growth factor. PLGA microsphere with poly(β -amino ester) particles containing a quick-degrading porogen was observed to release two drugs while establishing a porous microarchitecture for cell ingrowth within a matrix capable of maintaining a compressive modulus applicable for soft tissue grafts [11]. Cui et al. studied that a synthetic polypeptide poly(N_ϵ -Cbz-*L*-lysine) (PZL) with PLGA having relatively high strength and osteoinductive bioglass (BG) particles, and manufactured foamy PZL/PLGA/BG composite scaffolds using a negative NaCl-templating method. The results exhibited that the composite scaffolds allowed the ingrowth of tissue and microvessels and exhibited reduced inflammation response as compared to other scaffolds after 8 weeks of implantation [12]. In summary, the PLGA amino acid composite structures demonstrated that had good comprehensive performances and would meet the needs of tissue or bone regeneration.

In this study, alternative biopolymers were produced for biomedical applications such as sustained release systems and tissue engineering by synthesizing PLGA's amino acid derivative structures.

2. Material and Methods

2.1. Chemistry

All reagents were of commercial quality and reagent-quality solvents were used without further purification. 3,6-Dimethyl-1,4-dioxane-2,5-dione (99%) (CAS number 95-96-5), 1,4-dioxane-2,5-dione ($\geq 99\%$) (CAS number 502-97-6), 1-dodecanol for synthesis (CAS number 112-53-8) were obtained from Sigma-Aldrich Co. Stannous 2-ethylhexanoate (95%) (CAS number 301-10-0) was purchased from Aber GmbH Co. 1-Ethyl-3-(3-dimethylaminopropyl)carbodiimide-hydrochloride (EDC-HCl) ($\geq 99\%$) (CAS number 25952-53-8) was obtained from Carl Roth GmbH+ Co. The solvents, dichloromethane (DCM) (CAS number 75-09-2) and methanol (MeOH) (CAS number 67-56-1) were supplied from Sigma-Aldrich Co. Before use DCM was stored in the presence of a 4 Å molecular sieves. The reaction was assessed by thin-layer chromatography (TLC) (Merck silica gel plates, type 60 F₂₅₄) and the spots were visualized using a UV lamp.

2.2. Synthesis of Poly(lactic-co-glycolic acid) (PLGA)

PLGA copolymer is synthesized by polycondensation and ring-opening polymerization (ROP) reaction of different ratios with lactide and glycolide monomers [13]. The reaction was carried out under a nitrogen atmosphere. To prepare [L]:[G] 75:25 PLGA by mass proportions, 0.015 mol (2.16 g) of DL-lactide, and 0.005 mol (0.58 g) of glycolide were added to a dried reaction flask. The reaction flask was sealed and purged with N₂. After solutions containing initiator and co-initiator tin(II) 2-ethylhexanoate and 1-dodecanol (0.02% over the total mass of monomers) in anhydrous toluene were added to the reaction flask and a vacuum was applied to remove the toluene. The reaction mixture was put in an inert atmosphere, placed in an oil bath at 160°C, and magnetically stirred at 400 rpm for 2.5h. After cooling to room temperature, the crude PLGA was dissolved in DCM. This PLGA solution was poured into a beaker containing anhydrous MeOH and fiber-like PLGAs were obtained for precipitation. After the solvents were removed with a rotary evaporator, the PLGA was dried for 24h at 35-40°C in a vacuum oven to prevent moisture absorption [14, 15] (Fig 1.).

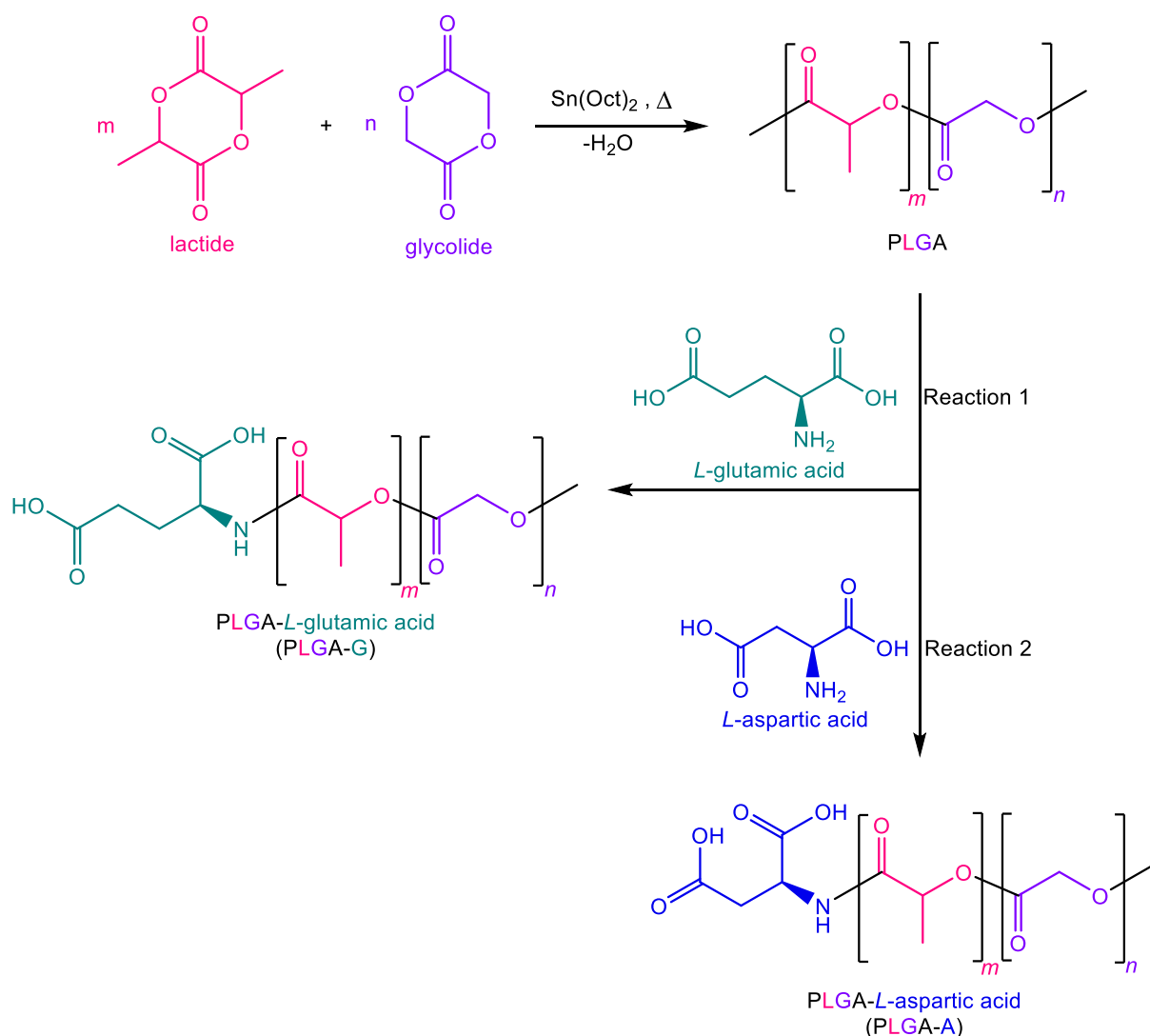


Figure 1. Schematic representation of the PLGA and PLGA derived with amino acids synthesis steps.

2.3. Synthesis of PLGA derived with amino acids

The carboxylic acid functional group of synthesized PLGA and amino functional group of amino acid reacted forming an amide bond in the presence of EDC and a suitable solvent [16]. *L*-Glutamic acid (Reaction 1) and *L*-aspartic acid (Reaction 2) were selected as amino acids to react with PLGA (Fig 1.). In a round-bottom flask equipped with a magnetic stirrer, PLGA (100 mg) dissolved in anhydrous DCM (15 mL) was reacted with EDC (48 mg). To the mixture, amino acid (10 mg) was added and stirred at room temperature for 48 h. The reaction was monitored by TLC (DCM: MeOH/9:1). When the reaction was completed, the solvent was removed by rotary evaporation and dried in a vacuum. The product was stored at 8°C.

2.4. Characterizations

PLGA chemical identifications were done in terms of an explanation of the NMR and IR spectra, determination of molecular weight, and thermal properties. NMR spectra were followed on the Bruker Avance 300 MHz spectroscopy for ^1H NMR and ^{13}C NMR, with the chemical shifts (δ s) reported in parts per million and with tetramethylsilane as an internal

standard with CDCl_3 as the solvent. IR spectra were acquired in reflectance mode using a Nicolet 6700 FT-IR Spectrometer from Thermo Fisher Scientific, using the ATR accessory. The spectral range was $4000\text{--}40\text{ cm}^{-1}$; each spectrum was the result of 16 scans. DSC experiments were recorded on a Hitachi Exstar X-DSC7000 SII NanoTechnology Inc.). Samples were scanned over a temperature range of $25\text{--}400^\circ\text{C}$ and at a heating rate of $10^\circ\text{C min}^{-1}$ under an N_2 flow. Samples of a mass of 5 mg were used. The molecular weight determination of PLGA was studied by Gel Permeation Chromatography (METU PAL Laboratories), Malvern OmniSEC with THF column). The Universal Calibration method was used during the GPC analysis.

3. Results and Discussion

3.1. Nuclear Magnetic Resonance Spectroscopy (NMR)

PLGA, white solid, $R_f=0.51$ ($\text{CH}_3\text{OH}:\text{CHCl}_3$, 9:1), ^1H NMR (300 MHz, CDCl_3) δ_{H} 5.23-5.15 (-CH-), 4.91-4.60 (- CH_2 -), 1.56 (- CH_3), ^{13}C NMR (125 MHz, CDCl_3) δ_{C} 175.13 (CO), 169.38 (CO), 71.46 (-CH-), 60.78 (- CH_2 -), 16.75 (- CH_3). (Fig. 2&3).

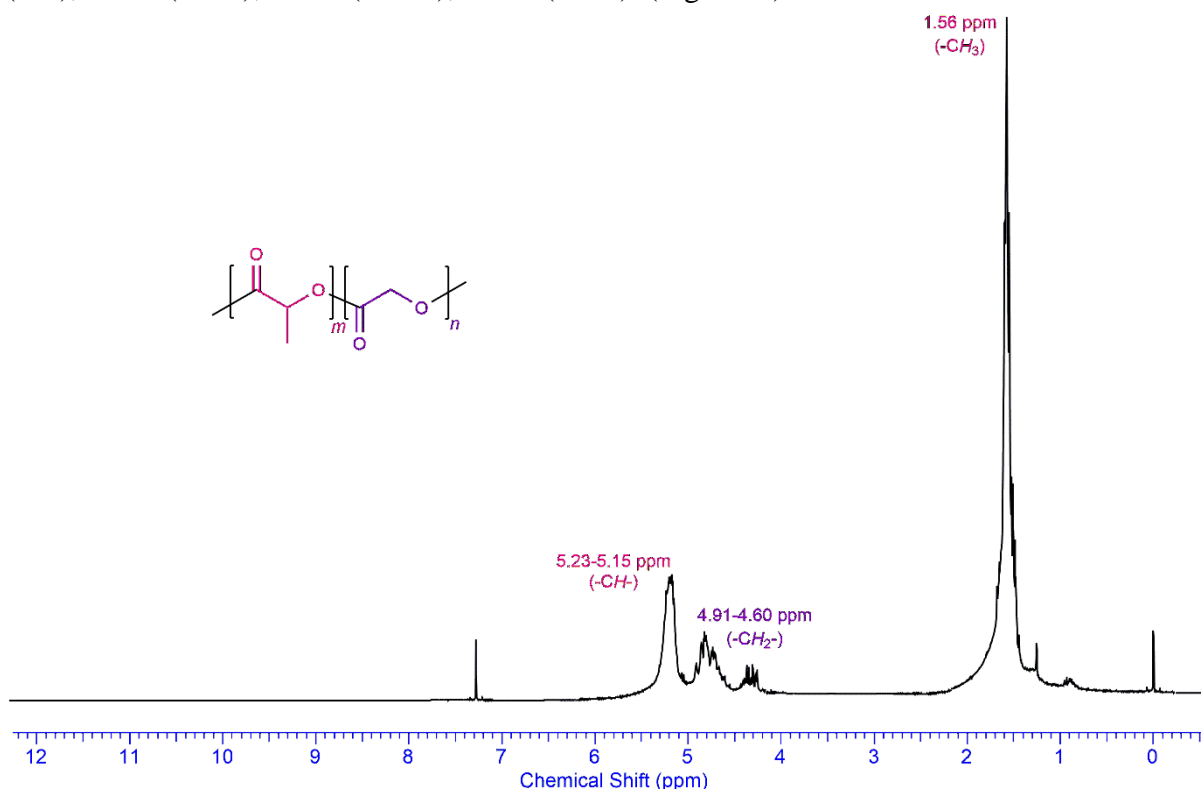


Figure 2. ^1H NMR spectra of PLGA.

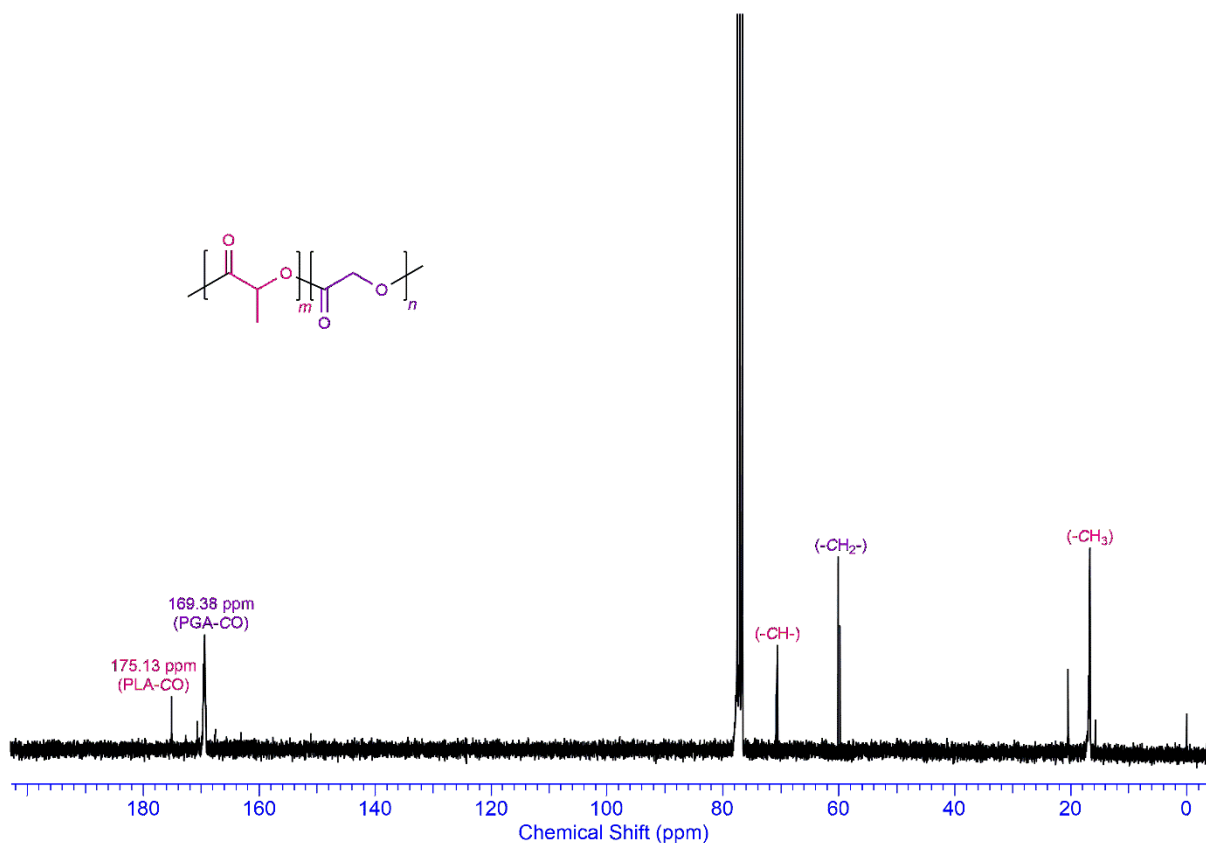


Figure 3. ¹³C NMR spectra of PLGA.

PLGA-L-glutamic acid, white viscous solid, $R_f = 0.59$ (CH₃OH:CHCl₃, 9:1), ¹H NMR (300 MHz, CDCl₃) δ_H 7.74 (-OH), 5.24-5.14 (-CH-), 4.92-4.61 (-CH₂-), 3.76 (*L*-glutamic acid-CH-), 2.91-2.77 (*L*-glutamic acid-CH₂-), 1.57 (-CH₃), ¹³C NMR (125 MHz, CDCl₃) δ_C 175.13 (CO), 170.78 (CO), 169.33 (CO), 166.43 (CO), 69.26 (-CH-), 66.68 (-CH₂-), 60.78 (-CH-), 32.01 (-CH₂-), 26.49 (-CH₂-), 16.76 (-CH₃). (Fig. 4&5)

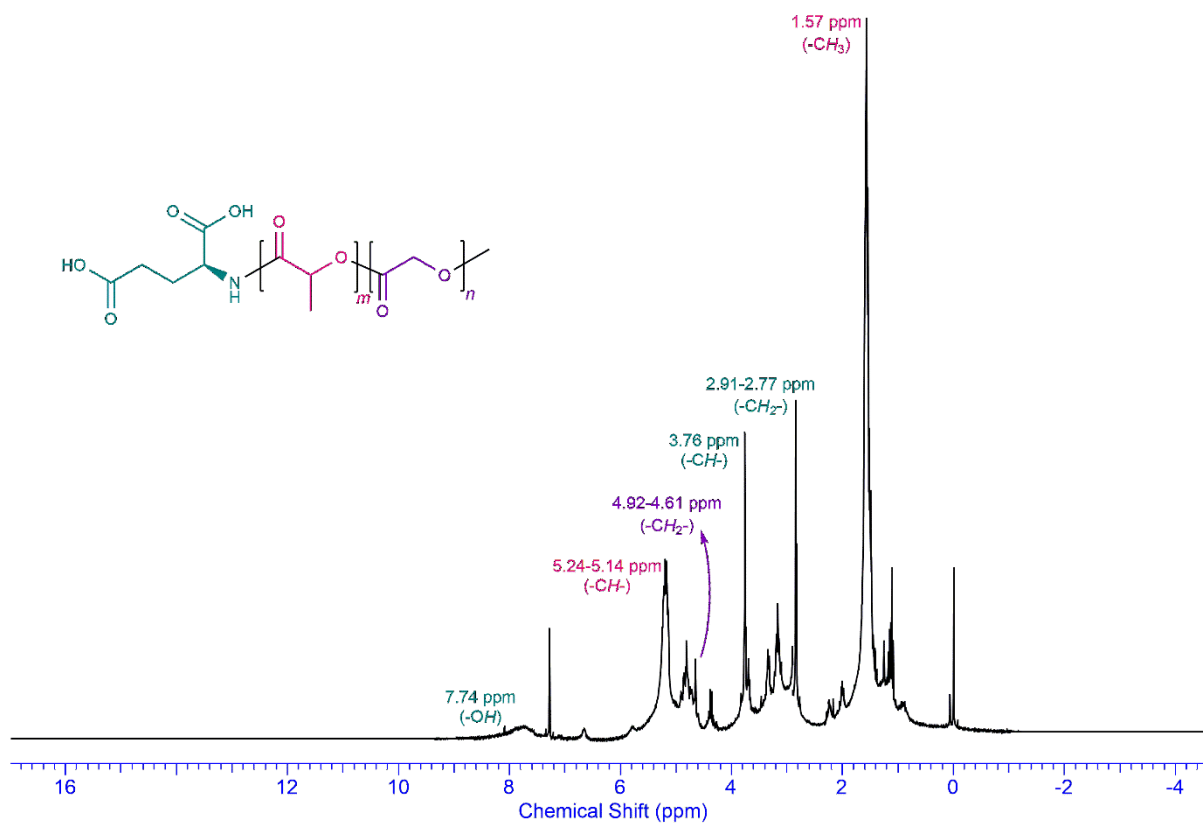


Figure 4. ¹H NMR spectrum of PLGA-*L*-glutamic acid.

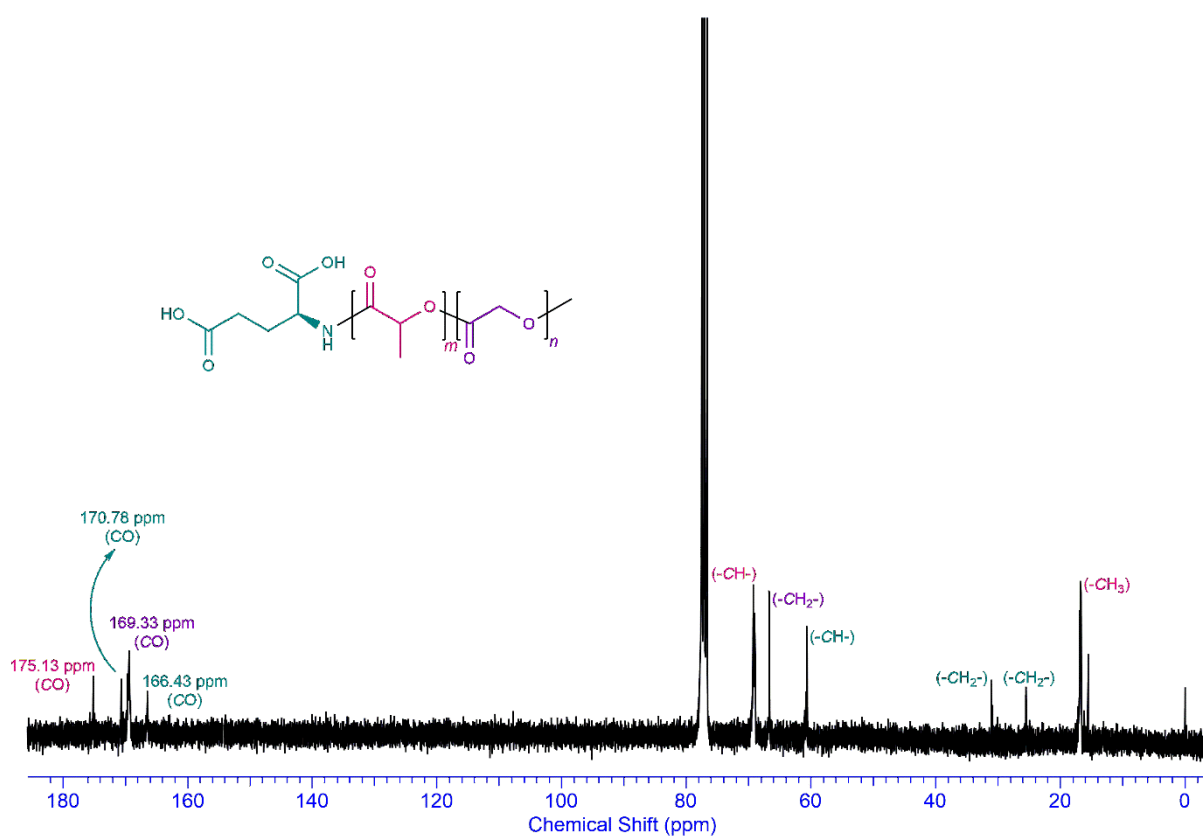


Figure 5. ¹³C NMR spectrum of PLGA-*L*-glutamic acid.

PLGA-L-aspartic acid, white viscose solid, $R_f=0.61$ ($\text{CH}_3\text{OH}:\text{CHCl}_3$, 9:1), ^1H NMR (300 MHz, CDCl_3) δ_{H} 7.72 (-OH), 5.22-5.14 (-CH-), 4.90-4.58 (-CH₂-), 4.41-4.31 (*L*-aspartic acid-CH-), 3.77-3.73 (*L*-aspartic acid-CH₂-), 1.56 (-CH₃), ^{13}C NMR (125 MHz, CDCl_3) δ_{C} 175.15 (CO), 170.71 (CO), 170.37 (CO), 169.37 (CO), 69.23 (-CH-), 66.65 (-CH₂-), 52.59 (-CH-), 34.99 (-CH₂-), 16.64 (-CH₃). (Fig. 6&7)

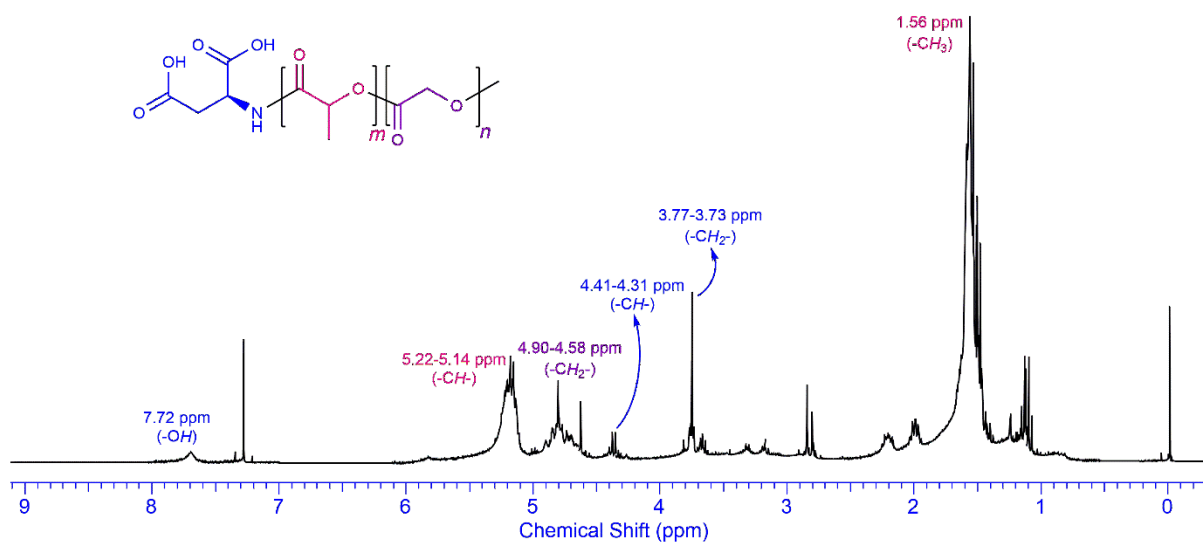


Figure 6. ^1H NMR spectrum of PLGA-*L*-aspartic acid.

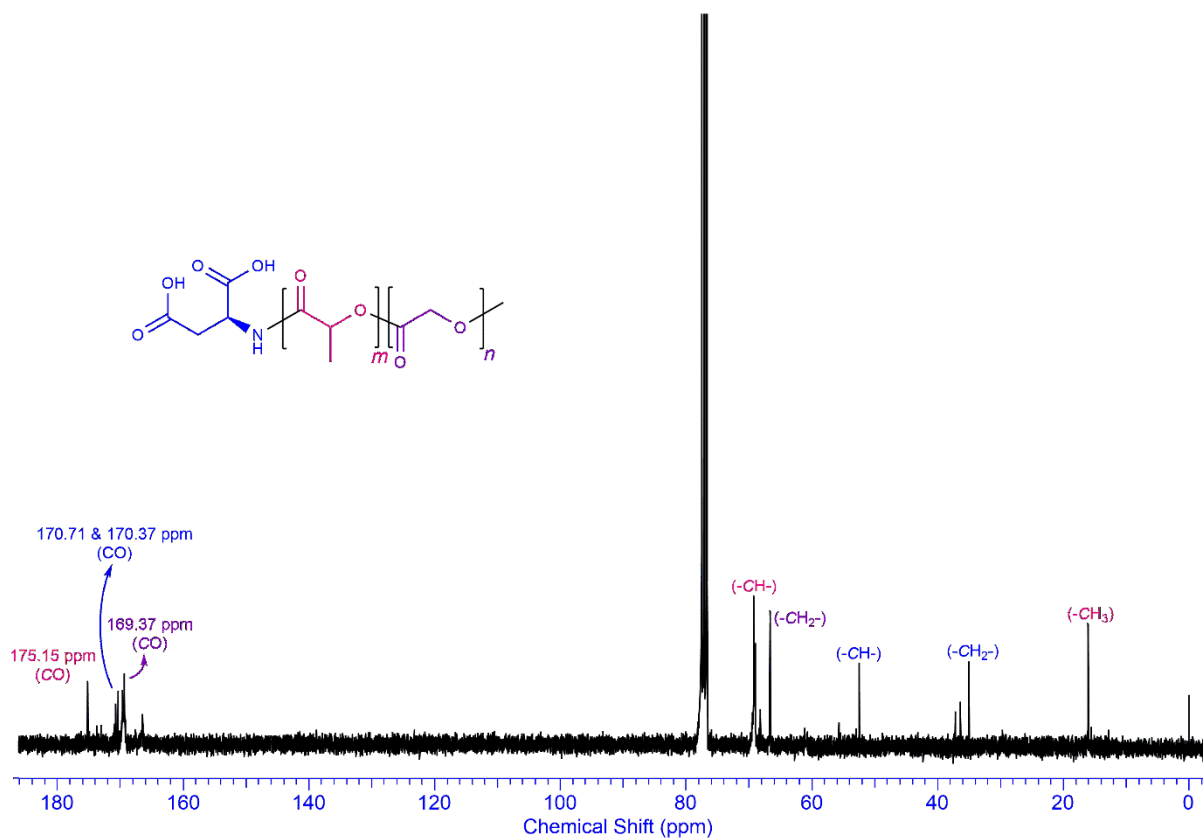


Figure 7. ^{13}C NMR spectrum of PLGA-*L*-aspartic acid.

In the ^1H NMR spectrum of PLGA, the *CH* proton belonging to the lactic acid chain was observed at 5.23-5.15 ppm and the CH_3 protons were also observed at 1.56 ppm, while the CH_2 protons belonging to the glycolic acid chain were observed at 4.91-4.60 ppm similarly to the literature [17]. The *CH* proton at 3.76 ppm and CH_2 protons at 2.91-2.77 ppm from the *L*-glutamic acid side observed in the ^1H NMR spectrum of the derivative of *L*-glutamic acid of PLGA confirm the structure. In addition, the *CH* proton at 4.41-4.31 ppm and CH_2 protons at 3.77-3.73 ppm confirm the structure of *L*-aspartic acid-derived PLGA in the ^1H NMR spectrum. When the ^{13}C NMR spectrum of the amino acid derivatives of PLGA were observed, their structure accuracy was supported by the characteristic carbonyl carbons at 170 ppm.

3.2. Fourier Transform Infrared Spectroscopy (FTIR)

PLGA, FT-IR (neat, cm^{-1}) 3003.58 (νCH_3), 2925.08 (νCH_3), 1750.72 ($\nu\text{C}=\text{O}$), 1445.06 (δCH_2), 1385.24 (δCH_3), 1249.21 (τCH_2), 1087.55 ($\nu\text{C}-\text{O}-\text{C}$).

PLGA-L-glutamic acid, FT-IR (neat, cm^{-1}) 3298.84 (OH), 2989.57 (νCH_3), 1746.04 ($\nu\text{C}=\text{O}$), 1700.91 ($\nu\text{C}=\text{O}$), 1449.55 (δCH_2), 1384.05 (δCH_3), 1267.51 (τCH_2), 1179.74 ($\nu=\text{C}-\text{O}$), 1082.65 ($\nu\text{C}-\text{O}-\text{C}$).

PLGA-L-aspartic acid, FT-IR (neat, cm^{-1}) 3298.75 (OH), 2978.03 (νCH_3), 1745.99 ($\nu\text{C}=\text{O}$), 1700.84 ($\nu\text{C}=\text{O}$), 1449.31 (δCH_2), 1384.27 (δCH_3), 1267.85 (τCH_2), 1179.66 ($\nu=\text{C}-\text{O}$), 1082.38 ($\nu\text{C}-\text{O}-\text{C}$).

For the determination of vibration, rotation, and stretching movements of IR signals of PLGA, PLGA-G, and PLGA-A structures, Xiao et al. and Anamaria T.C.R. Silva et al. works were got referenced [18, 19].

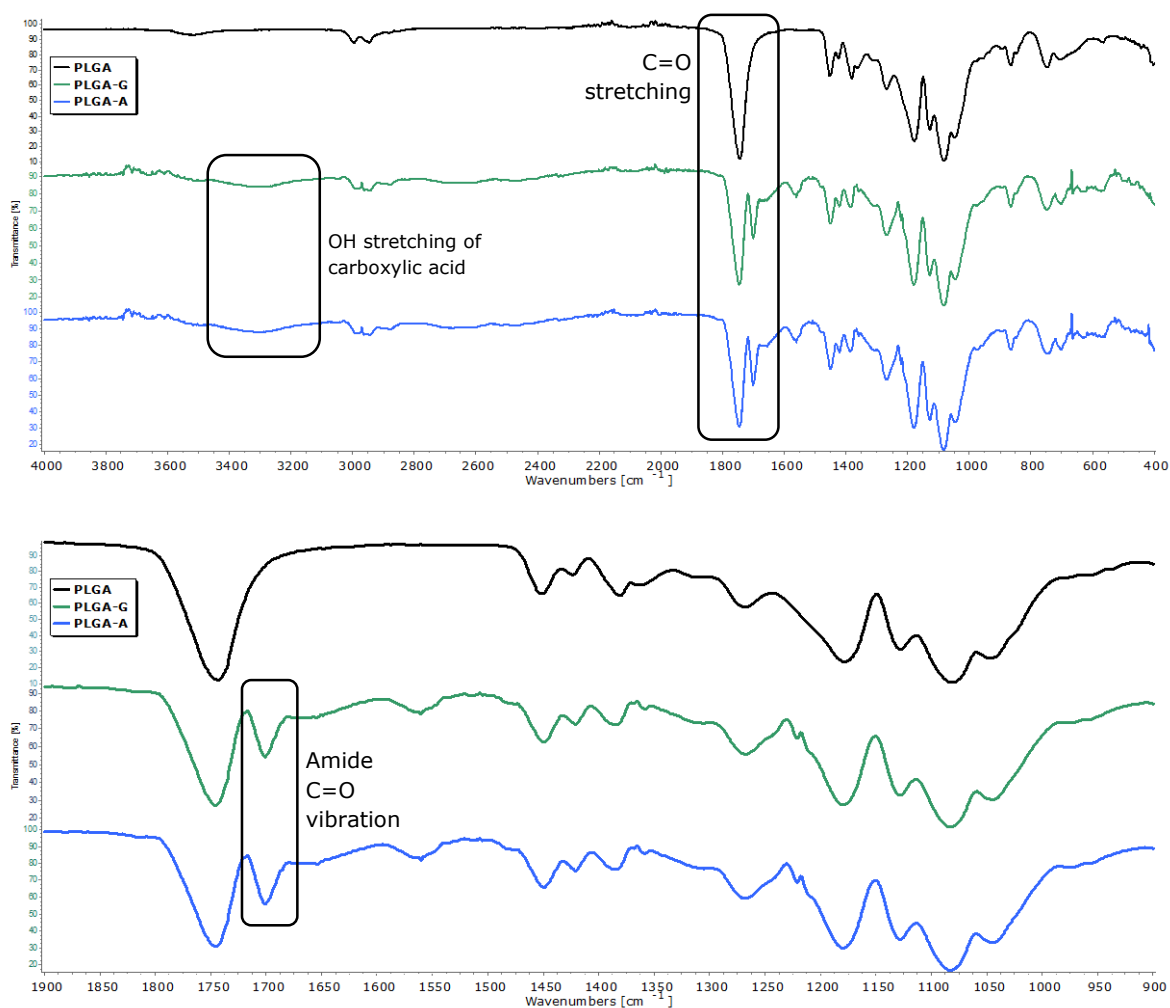


Figure 8. IR spectra of PLGA, PLGA-G, and PLGA-A.

In the IR spectra of PLGA amino acid derivative samples were observed the two typical stretching vibrations at 1745 cm^{-1} and 1700 cm^{-1} were for ester and amide carbonyl absorptions. (Fig. 8) In literature, Manoochehri et al. proved that the amide bond or conjugation of PLGA and the amino acid group HSA was formed [20]. It was noteworthy that the amide signal at 1713.4 cm^{-1} was not observed when the IR spectrum of the PLGA and HSA mixture was taken. When conjugation between PLGA and HSA occurred, the increased peak intensity in the signal belonging to the spectrum carbonyl carbon supported the structure accuracy. Similarly, for PLGA-G and PLGA-A, signals of the amide bond were observed at about 1700 cm^{-1} with a sharp peak.

For PLGA-G and PLGA-A, signals at close to 170 ppm in the ^{13}C NMR spectrums and signals at 1700 cm^{-1} in the IR spectrum indicated amino acid carbonyls and support the accuracy of the structures. In addition, the signals of all protons and carbons belonging to PLGA-G and PLGA-A structures were observed in ^1H NMR and ^{13}C NMR spectrum.

3.3. Thermal Analysis

The thermal transitions of the PLGA derivatives were conducted by differential scanning calorimetry (DSC).

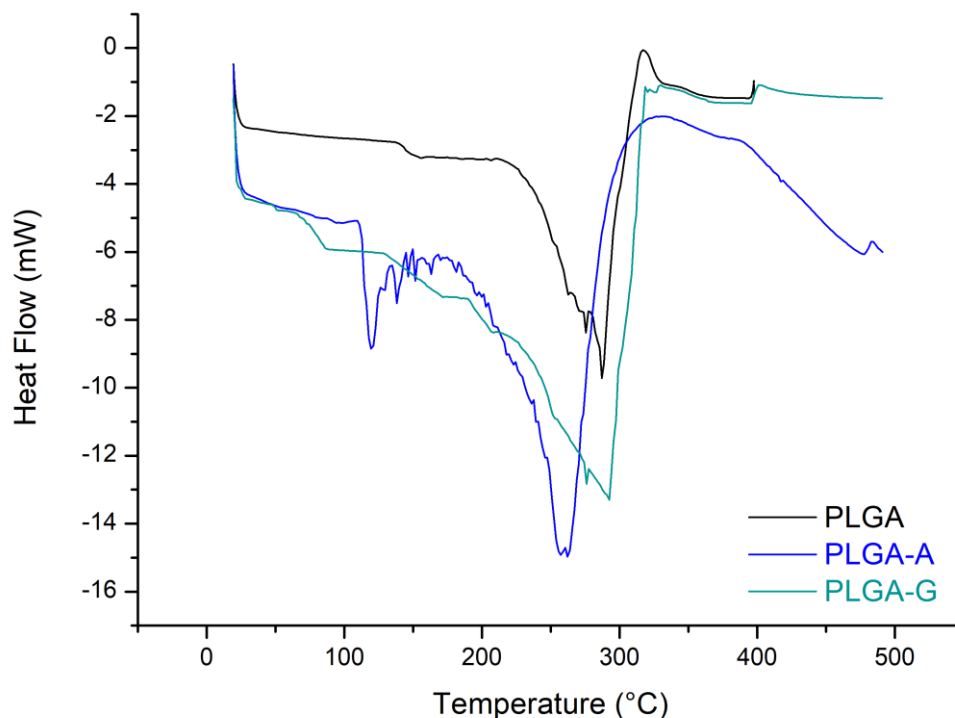


Figure 9. DSC thermograms of PLGA, PLGA-G and PLGA-A.

DSC analysis results in an order with PLGA, PLGA-G, and PLGA-A were exhibited typical endothermic peaks with an onset of melting at 288.75°C, 289.14°C, 265.49°C. (Fig. 9) Also, in Fig. 9, it was seen that the thermal behavior of PLGA and amino acid derivative PLGAs was similar. The glass transition temperature of PLGA-A and PLGA-G in both derivatives were observed differently from PLGA. It was concluded that all derivatives were amorphous and were compatible with the literature [20].

3.4. Molecular Weight Analysis

Table 1. Average molecular weights and PDI values of PLGA, PLGA-G, and PLGA-A.

<i>Sample</i>	<i>Mn (kDa)</i>	<i>Mw (kDa)</i>	<i>PDI</i>
<i>PLGA</i>	3.019	4.251	1.408
<i>PLGA-G</i>	3.710	5.027	1.355
<i>PLGA-A</i>	3.945	5.607	1.421

The compositions and properties of the molecular weight of PLGA and the derivatives were shown in **Table 1** and analyzed with GPC.

Synthesized PLGA had an average molecular weight value of 4251 g/mol, and with the presence of L-glutamic acid, the average molecular weight increased by 5027 g/mol, and also with the presence of L-aspartic acid, the average molecular weight increased by 5607 g/mol. The reason for this increase was that amino acids covalently bond with PLGA. PLGAs with lower molecular masses degrade more easily than those with higher molecular masses [20]. PLGA's amino acid derivatives could be good alternative polymers for controlled drug release systems where slow degradation is advantageous which were determined low molecular weight polymers [~5000-6000 Da] by GPC analysis [21].

4. Conclusion

It is very crucial to synthesize novel biocompatible and biodegradable derivatives of PLGA polymer, which are often needed in drug carriers and medical applications, and to complete the chemical characterizations. In this study, PLGA, PLGA-G, and PLGA-A were successfully synthesized and their chemical structure was characterized. Chemical characterizations proved the covalent bonding between amino acid and PLGA. The amide bond, indicating the formation of the PLGA-amino acid bond, was demonstrated by both ¹³C NMR and FTIR analysis. PLGA-amino acid derivatives, which were low molecular weight [~ 5000-6000] determined by GPC analysis, were observed in DSC thermograms where thermal properties were the endothermic character.

Ethics in Publishing

There are no ethical issues regarding the publication of this study.

Acknowledgments

This research was supported by Erzincan Binali Yıldırım University Scientific Research Projects Coordination Unit with Grant Number [TSA-2021-7769].

References

- [1] Wang, H., Zhang, Y., Liu, Y., Ren, Y., Wang, J, Niu, B., Li, W., (2022) Preparation of curcumin loaded hyaluronic acid-poly (lactic-co-glycolic acid) micelles with pH response and tumor targeting, *European Polymer Journal*, 177, 111450, <https://doi.org/10.1016/j.eurpolymj.2022.111450>.
- [2] Aksoy, E. A., Taskor, G., Gultekinoglu, M., Kara, F., Ulubayram, K., (2018) Synthesis of biodegradable polyurethanes chain-extended with (2S)-bis(2-hydroxypropyl) 2-aminopentane dioate, *Journal of applied polymer science*, 135(5) 45764, <https://doi.org/10.1002/app.45764>.
- [3] Paula, C. T. B, Madeira, A. B, Pereira, P., Branco, R., Morais, P. V., Coelho, J. F. J., Fonseca, A. C., Serra, A. C., (2022) ROS-degradable PEG-based wound dressing films

- with drug release and antibacterial properties, *European Polymer Journal*, 177, 111447, <https://doi.org/10.1016/j.eurpolymj.2022.111447>.
- [4] Makadia, H. K., Siegel, S. J., (2011) Poly Lactic-co-Glycolic Acid (PLGA) as Biodegradable Controlled Drug Delivery Carrier, *Polymers*, 3(3) 1377-1397, <https://www.mdpi.com/2073-4360/3/3/1377>.
- [5] Taşkor Önel, G., (2022) Poly(lactic-co-glycolic acid): FDA and EMA-approved biodegradable elastomeric copolymer, in *Recent Approaches in Mathematics and Natural Science*, P. Ç. SAYIL (Ed.) Chapter 2, pp. 9-17, Livre De Lyon, Lyon France.
- [6] Ansari, V, Calore, A., Zonderland, J., Harings, J. A. W., Moroni, L., Bernaerts, K. V., (2022) Additive Manufacturing of α -Amino Acid Based Poly(ester amide)s for Biomedical Applications, *Biomacromolecules*, 23(3) 1083-1100, <https://doi.org/10.1021/acs.biomac.1c01417>.
- [7] Zhao, J., Quan, D., Liao, K., Wu, Q., (2005) PLGA-(L-Asp-alt-diol)x-PLGAs with Different Contents of Pendant Amino Groups: Synthesis and Characterization, *Macromolecular Bioscience*, 5(7), 636-643, <https://doi.org/10.1002/mabi.200500043>.
- [8] Thasneem, Y. M., Rekha, M. R., Sajeesh, S., Sharma, C. P., (2013) Biomimetic mucin modified PLGA nanoparticles for enhanced blood compatibility, *Journal of Colloid and Interface Science*, 409, 237-244, <https://doi.org/10.1016/j.jcis.2013.07.004>.
- [9] Takeuchi, I., Taniguchi, Y., Tamura, Y., Ochiai, K., Makino, K. (2018) Effects of l-leucine on PLGA microparticles for pulmonary administration prepared using spray drying: Fine particle fraction and phagocytotic ratio of alveolar macrophages, *Colloids and Surfaces A: Physicochemical and Engineering Aspects*, 537, 411-417, <https://doi.org/10.1016/j.colsurfa.2017.10.047>.
- [10] Zhang, C., An, T., Wang, D., Wan, G., Zhang, M., Wang, H., Zhang, S., Li, R., Yang, X., Wang, Y., (2016) Stepwise pH-responsive nanoparticles containing charge-reversible pullulan-based shells and poly(β -amino ester)/poly(lactic-co-glycolic acid) cores as carriers of anticancer drugs for combination therapy on hepatocellular carcinoma, *Journal of Controlled Release*, 226, 193-204, <https://doi.org/10.1016/j.jconrel.2016.02.030>.
- [11] Clark, A., Milbrandt, T. A., Hilt, J. Z., Puleo, D. A., (2014) Mechanical properties and dual drug delivery application of poly(lactic-co-glycolic acid) scaffolds fabricated with a poly(β -amino ester) porogen, *Acta Biomaterialia*, 10(5) 2125-2132, <https://doi.org/10.1016/j.actbio.2013.12.061>.
- [12] Cui, N., Qian, J., Wang, J., Wang, Y., Xu, W., Wang, H., (2016) Physicochemical properties and biocompatibility of PZL/PLGA/bioglass composite scaffolds for bone tissue engineering, *RSC Advances*, 6(99) 97096-97106, <https://doi.org/10.1039/C6RA20781B>.
- [13] Liu, G., McEnnis, K., (2022) Glass Transition Temperature of PLGA Particles and the Influence on Drug Delivery Applications, *Polymers*, 14(5) 993, <https://doi.org/10.3390/polym14050993>.

- [14] Little, A., Wemyss, A. M., Haddleton, D. M., Tan, B., Sun, Z., Ji, Y., Wan, C.. (2021) Synthesis of Poly(Lactic Acid-co-Glycolic Acid) Copolymers with High Glycolide Ratio by Ring-Opening Polymerisation, *Polymers*, 13(15) 2458, <https://www.mdpi.com/2073-4360/13/15/2458>.
- [15] Yildırım, Y., (2021) Synthesis and Characterization of Poly(lactic-co-glycolic acid) (PLGA)/Oil Composites, Master, Graduate School of Natural and Applied Sciences Department of Chemical Engineering, Ankara University, 686593, <https://dspace.ankara.edu.tr/xmlui/bitstream/handle/20.500.12575/73798/10408913.pdf?sequence=1&isAllowed=y>
- [16] Singh, A., Thotakura, N., Singh, B., Lohan, S., Negi, P., Chitkara, D., Raza, K.. (2019) Delivery of Docetaxel to Brain Employing Piperine-Tagged PLGA-Aspartic Acid Polymeric Micelles: Improved Cytotoxic and Pharmacokinetic Profiles, *AAPS PharmSciTech*, 20(6) 220, <https://doi.org/10.1208/s12249-019-1426-8>.
- [17] Pereira, E. D., Cerruti, R., Fernandes, E., Peña, L., Saez, V., Pinto, J. C., Ramón, J. A., Oliveira, G. E., Gomes de Souza Júnior, F., (2016) Influence of PLGA and PLGA-PEG on the dissolution profile of oxaliplatin, *Polímeros*, 26, <https://doi.org/10.1590/0104-1428.2323>.
- [18] Xiao, H., Wang, L., (2015) Effects of X-shaped reduction-sensitive amphiphilic block copolymer on drug delivery, *International journal of nanomedicine*, 10, 5309-5325, <https://doi.org/10.2147/IJN.S85230>.
- [19] Silva, A. T. C. R., Cardoso, B. C. O., Silva, M. E. S. R. e., Freitas, R. F. S., Sousa, R. G., (2015) Synthesis, Characterization, and Study of PLGA Copolymer in Vitro Degradation, *Journal of Biomaterials and Nanobiotechnology*, 6(1) 12, 52929, <https://doi.org/10.4236/jbnb.2015.61002>.
- [20] Erbetta, C. D. A. C., Alves, R. J., Resende, J. M. e., Freitas, R. F. d. S., Sousa, R. G. d., (2012) Synthesis and Characterization of Poly(D, L-Lactide-co-Glycolide) Copolymer, *Journal of Biomaterials and Nanobiotechnology*, 3(2) 18, 18940, <https://doi.org/10.4236/jbnb.2012.32027>.
- [21] Brauner, B., Schuster, C., Wirth, M., Gabor, F., (2020) Trimethoprim-Loaded Microspheres Prepared from Low-Molecular-Weight PLGA as a Potential Drug Delivery System for the Treatment of Urinary Tract Infections, *ACS Omega*, 5(15) 9013-9022, <https://doi.org/10.1021/acsomega.0c00981>.

Quantum Chemical Calculations of m-Toluidine and Investigation of Its Adsorption on Eggshells

Taner Kalaycı¹, Deniz Türköz Altuğ², Neslihan Kaya Kınaytürk^{3*}, Belgin Tunalı³

¹Bandırma Onyedi Eylül University, Vocational School of Health Services, Bandırma, Balıkesir, Turkey

²Süleyman Demirel University, Faculty of Education, Department of Science Education, East Campus, 32260, Isparta, Turkey

³Burdur Mehmet Akif Ersoy University, Faculty of Arts and Sciences, Department of Nanoscience and Nanotechnology, Burdur, Turkey

Received: 25/11/2022, **Revised:** 28/03/2023, **Accepted:** 29/03/2023, **Published:** 31/03/2023

Abstract

Aromatic nitro compounds, which have good water solubility, are one of the essential industrial pollutants, highly toxic and non-biodegradable, and adversely affect human health, aquatic life, and the environment. In this study, we have investigated the adsorption of m-toluidine on three types of eggshells characterized by FT-IR and FT-Raman spectroscopy. Also, the theoretical analysis of this harmful organic was determined using density functional theory on GAUSSIAN 09W software program. Molecular electrostatic analysis, Infrared and Raman vibrational bands, frontier molecular orbitals, and molecular geometry were investigated for this purpose. After the adsorption process, the NH₂ groups were observed at 3423-3347 cm⁻¹ and 3433- 3350 cm⁻¹ in CCJ-mT and C-CCJ/mT samples, respectively in FTIR spectrum. While these bands were not seen in CCJ-mT in the Raman spectrum, they were observed in C-CCJ-mT at 3429 and 3375 cm⁻¹. After adsorption, C-H bands were observed at 3216, 3036, 3013, 2978, 2919, 2865 cm⁻¹ in CCJ/mT sample and at 3216, 3034, 3011, 2978, 2947, 2917, 2856 cm⁻¹ in C-CCJ/mT sample. The C-C bands in the FTIR spectra of CCJ/mT and C-CCJ/mT samples were observed at 1591 and 1590 cm⁻¹, respectively, but they were not seen in the Raman spectrum after the adsorption process.

Keywords: m-Toluidine, Quantum Chemical Calculations, Adsorption, Molecular Electrostatic Potential

m-Toluidin'in Kuantum Kimyasal Hesapları ve Yumurta Kabuklarına Adsorpsiyonunun İncelenmesi

Öz

Suda çözünürlüğü iyi olan aromatik nitro bileşikleri, temel endüstriyel kirleticilerden biridir, oldukça toksiktir ve biyolojik olarak parçalanamaz ve insan sağlığını, su yaşamını ve çevreyi olumsuz etkiler. Bu çalışmada, FT-IR ve FT-Raman spektroskopisi ile karakterize edilen üç tip yumurta kabuğu üzerinde m-toluidinin adsorpsiyonu nu araştırdık. Ayrıca GAUSSIAN 09W yazılım programında yoğunluk fonksiyonel teorisi kullanılarak bu zararlı organik teorik analizi yapılmıştır. Bu amaçla moleküler elektrostatik analiz, Kızılötesi ve Raman titreşim bantları, sınır moleküler orbitalleri ve moleküler geometri incelenmiştir. Adsorpsiyon işlemi sonrasında FTIR spektrumunda CCJ-mT ve C-CCJ/mT örneklerinde NH₂ grupları sırasıyla 3423-3347 cm⁻¹ ve 3433- 3350 cm⁻¹'de gözlemlendi. Bu bantlar CCJ-mT nin Raman spektrumunda de görülmezken C-CCJ-mT' nin Raman spektrumunda 3429 ve 3375 cm⁻¹'de gözlemlendi. Adsorpsiyon sonrası CCJ/mT örneğinde 3216, 3036, 3013, 2978, 2919, 2865 cm⁻¹'de ve C-CCJ/'de 3216, 3034, 3011, 2978, 2947, 2917, 2856 cm⁻¹'de C-H bantları gözlemlendi. CCJ/mT ve C-CCJ/mT örneklerinin FTIR spektrumundaki C-C bantları sırasıyla 1591 ve 1590 cm⁻¹'de gözlemlenmiş, ancak adsorpsiyon işlemi nedeniyle Raman spektrumunda görülmemiştir.

Anahtar Kelimeler: m-toluidin, Kuantum Kimyasal Hesaplamalar, Adsorpsiyon, Moleküler Elektrostatik Potansiyel

*Corresponding Author: nkinayturk@mehmetakif.edu.tr

1. Introduction

Today, recycling waste materials in the economy is a topic that attracts much attention and is being studied. The main reason why this subject attracts attention is that it is low cost and high gain. In addition, using natural waste material in any work also ensures minimized damage to the environment. Eggshells are a solid waste material, especially in the food industry. After the inner part of the egg is used, the shell parts are usually thrown away. However, these eggshells can now be used in many areas. On the one hand, it is used as a supplement due to the rich Ca content in its structure [1] [2] [3]; on the other hand, it is used as a biodiesel [4] [5]. It can even be used as a molecular adsorbent [6] [7] [8] while allowing it to adsorb heavy metals that cause environmental pollution due to the pores in its structure [9] [10]. There are studies in the literature about eggshells can be calcined and their ability to adsorb heavy metals or molecules can be increased [11] [12] [13] [14].

Three types of eggshells were used in this study. These were *Anser anser* (AA), *Denizli Hen* (DH), and *Coturnix Coturnix Japonica* (CCJ) eggshells. The reason for choosing these three samples is that the AA eggshell is very thick, the DH eggshell is of medium thickness, and the CCJ eggshell is thin. Figure 1 shows the consistency of these eggshells.

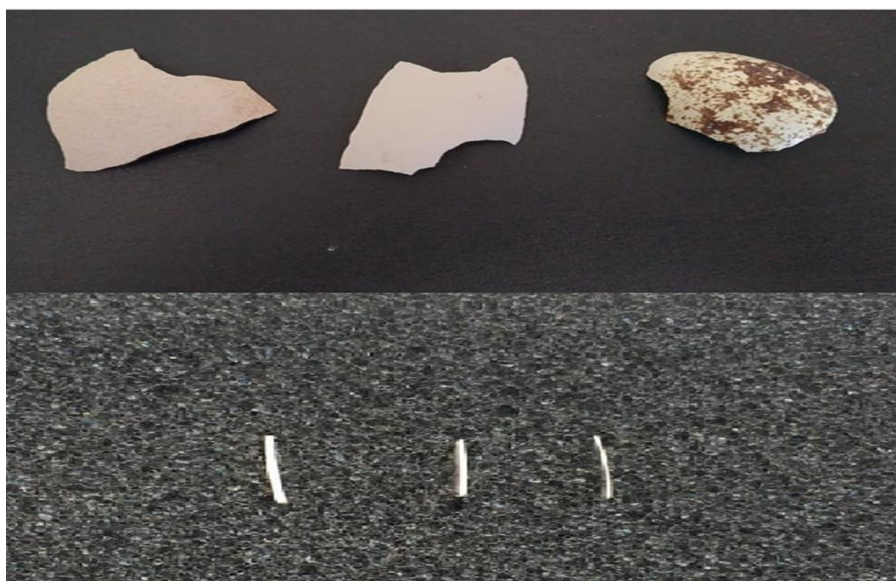


Figure 1. Photograph of the thickness of the eggshells (From left to right AA, DH, and CCJ)

m-Toluidine (m-methylaniline) is a simple aromatic amine compound bonded to the 1st carbon atom of the benzene ring with NH_2 (amine) and the 3rd carbon atom CH_3 (methyl) [15]. Its chemical formula is $\text{C}_7\text{H}_9\text{N}$. Its molecular structure is shown in Figure 2. m-Toluidine is used in dyestuffs, photochemicals, and antioxidants [16] [17]. In addition, an increase in m-toluidine was observed in smoking environments [17]. Aromatic amine group compounds are considered a compound in the severely destructive group for environmental and ecological balance [17, 18]. In addition, aniline and its derivatives can have a toxic and carcinogenic effect on human health, even if exposed in very low amounts [17] [19] [20].

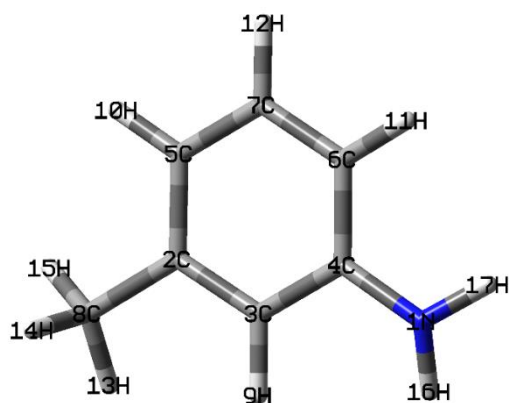


Figure 2. Molecular structure of m-Toluidine.

Apart from that, aromatic amine groups can easily mix with soil and water by decomposition of various insecticides, pesticides, and paint polyurethane classes. Thus, it can pose a threat to both the environment and human health [21]. Furthermore, in national and international environmental platforms, m-Toluidine is defined as a chemical threatening the environment and human life [22].

These aromatic amine groups can be easily analyzed by gas chromatography or liquid chromatography, but since high amounts of organic solvents will be used, they will be environmentally unfriendly methods [21]. Therefore, we used Raman and FTIR spectroscopic analysis in this study and obtained excellent results. These were also low cost, high analysis speed, low sample requirement, and environmentally friendly methods.

In this study, the adsorption properties of the m-toluidine molecule, which is densely present in the environment and may cause harm to human health on the one hand and environmental pollution on the other, were demonstrated by Raman and FTIR spectroscopy and theoretical calculations.

2. Materials and Methods

Eggshell samples *AA*, *DH*, and *CCJ* were obtained from Isparta University of Applied Sciences, Educational Research, and Application Farm. Eggshell samples were taken from the incubation wastes of the farm. m-Toluidine (mT) in liquid phase was bought from MERCK company. And they were used without purification. FTIR spectroscopic analysis was taken by JASCO FTIR 4700 Spectrometer.

2.1. Experimental Procedure

The cleaning procedure for eggshells was applied like the previous study, as in our last study [13]. They were put in a mortar. We used pure and calcinated powdered shells of each sample. The calcination process was performed by heating at 900°C for 2 hours. In the rest of the study, the calcination process is shown abbreviated with the letter “C.” 0.5 gram of each sample treated

by 10 mL mT was used. They were shaken for 48 hours on stirring magnetic equipment. The samples were filtered and dried. It was then analyzed by FTIR spectroscopy.

2.2. Theoretical Details

Theoretical calculations had been done before another study [23].

3. Results and Discussion

3.1. Molecular Geometry

In this part of this work, bond lengths and angles for mT molecules were calculated to explain the molecular geometry. The optimized parameters of mT are presented in Table 1. The N1 atom in the amine molecule attached to the C4 atom in the benzene ring, which shows the characteristic geometry of the molecule, forms bonds with the H16 and H17 atoms, respectively. The bond length between N1-C4 is 1.411 Å. The bond lengths between N1-H16 and N1-H17 are 1.011 Å.

Table 1. Optimized parameters for mT

Atoms	Bond length (Å)	Atoms	Angle (°)	Atoms	Angle (°)
N1-C4	1.411	C4-N1-H16	120.04	C7-C6-H11	119.30
N1-H16	1.011	C4-N1-H17	120.04	C5-C7-C6	120.01
N1-H17	1.011	H16-N1-H17	119.93	C5-C7-H12	120.00
C2-C3	1.395	C3-C2-C5	120.00	C6-C7-H12	120.00
C2-C5	1.395	C3-C2-C8	120.02	C2-C8-H13	111.09
C2-C8	1.491	C5-C2-C8	119.98	C2-C8-H14	110.07
C3-C4	1.395	C2-C3-C4	120.00	C2-C8-H15	111.23
C3-H9	1.088	C2-C3-H9	119.98	H13-C8-H14	108.73
C4-C6	1.395	C4-C3-H9	120.02	H13-C8-H15	106.97
C5-C7	1.395	N1-C4-C3	120.02	H14-C8-H15	108.64
C5-H10	1.087	N1-C4-C6	119.98		
C6-C7	1.395	C3-C4-C6	120.00		
C6-H11	1.087	C2-C5-C7	120.00		
C7-H12	1.086	C2-C5-H10	120.72		
C8-H13	1.096	C7-C5-H10	119.29		
C8-H14	1.095	C4-C6-C7	120.00		
C8-H15	1.095	C4-C6-H11	120.71		

At the same time, the bond length of the N1 atom with both H16 and H17 forms the shortest bond in the molecule. In addition, the bond length between the C2 atom in benzene to which the methyl group is attached is 1.491Å, and this bond is the longest in the m-toluidine molecule. The bond lengths of H13, H14, and H15 atoms in the methyl group with C8 are equal and

1.095Å. The bond lengths between C3-H9, C5-H10, C6-H11, and C7-H12 atoms are 1.088, 1.087, 1.087, and 1.086Å, respectively. There are slight differences in the bond lengths between the carbon and hydrogen atoms. The reason for this can be explained as adding an amine molecule and methyl molecule to the benzene ring affects the C-H bond lengths in the benzene ring. The C-C bond lengths in the benzene ring are equal. Even though methyl and amine groups were added to the benzene molecule, it was observed that these additions did not disrupt the hexagonal structure of the benzene molecule.

When the CH₃ substitution was added to the C2 atom in the benzene ring, the angle between C3-C2-C5 was calculated to be 120.00°. The grades between the C8 atom attached to the C2 atom and the H13, H14, and H15 atoms were calculated as 111.09, 110.07, and 111.23°, respectively. The computed values here differ from each other. This difference is thought to be due to the geometry of the methyl group. The bond angles between the N1 atom attached to the C4 atom of the benzene ring and H16 and H17 were calculated as 120.04°. The angles between C-C-H in the benzene ring were estimated to be approximately 120° for each. When the C-C-C curves in the benzene ring were compared, it was seen that the angles in all the benzene rings had the same value. According to this result, it was seen that the angles between the carbon atoms in the ring were not affected even if methyl and amine groups were added to the benzene ring, just like the bond lengths.

3.2. Vibrational Analysis

In the first stage of this study, the %PED distributions of the theoretical vibrational bands of the mT molecule were calculated in detail. FTIR analysis was done experimentally, and the work of Puranik and Ramiah was used for the assignment of the Raman vibration bands [24]. Three eggshells were selected in the second stage (CCJ, AA, DH). Each of these eggshells was divided into two parts. While no treatment was applied to one part, calcination was applied to the other. mT adsorption was performed on untreated and treated eggshell samples, and then the vibration bands were reconsidered to prove the adsorption process. The intensities and detailed %PED assignments of the IR and Raman bands calculated by the B3LYP/6-311++G(d,p) method are given in Table 2. Since B3LYP vibrational wavenumbers are known to be higher than the experimental wavenumbers, they were scaled down by a uniform scaling factor of 0.983 for wavenumbers up to 1700 cm⁻¹ and of 0.958 for wavenumbers greater than 1700 cm⁻¹ [23]. The experimental FTIR and Raman vibrational bands of CCJ, mT/CCJ are presented in Figure 3.

3.2.1. NH₂ Vibration

Characteristic N-H vibrational bands are observed at 3500-3300 cm⁻¹ [25]. The N-H asymmetric and symmetric vibration bands for mT were theoretically calculated at 3536 and 3443 cm⁻¹, respectively. These vibration bands were observed at 3450 and 3349 cm⁻¹ in the experimental FTIR spectrum and 3455 and 3370 cm⁻¹ in the Raman spectrum. N-H vibration bands were observed at 3423-3347 cm⁻¹ and 3433-3350 cm⁻¹ in the FTIR spectra of CCJ-mT

and C-CCJ/mT samples after the adsorption process. While these bands were not seen in CCJ-mT in the Raman spectrum, they were kept in C-CCJ-mT at 3429 and 3375 cm^{-1} .

3.2.2. C-H Vibration

C-H vibrational bands are observed at 3200-3000 cm^{-1} in aromatic and heteroatomic structures [26]. The C-H vibration bands of the investigated molecule were calculated as pure modes at 3069, 3055, 3044, 3033, 2991, 2967, and 2915 cm^{-1} with PED values of 93-97%. While these bands are observed at 3215, 3036, 3013, 2978, 2917, and 2857 in the IR spectrum, they are attributed to 3036, 2919, and 2865 cm^{-1} in the Raman spectrum. After adsorption, these bands were observed at 3216, 3036, 3013, 2978, 2919, and 2865 cm^{-1} in the CCJ/mT sample and at 3216, 3034, 3011, 2978, respectively 2947, 2917, 2856 cm^{-1} in C-CCJ/mT sample.

In-plane aromatic C-H bending vibrations occur as weak to moderate bands in the range of 1400-1000 cm^{-1} (C-H in the plane). In this study, these bands for mT were calculated at 1474, 1439, 1363, 1301, and 1150 cm^{-1} . It is assigned to 1467, 1432, 1376, 1311, 1170, and 1076 cm^{-1} in the experimental FTIR spectrum and 1431, 1377, 1157, 1077 cm^{-1} in the Raman spectrum. After adsorption, these bands are in the FTIR spectrum of the CCJ/mT sample at 1379, 1310, 1169, and 1080 cm^{-1} , and in the Raman spectrum at 1364, 1294, and 1154 cm^{-1} . It was observed at 1469, 1364, 1312, 1292, 1170, 1090, and 1467, 1430, 1360, 1156 cm^{-1} in the FTIR and Raman spectrum, respectively of the C-CCJ/mT sample.

The out-of-plane C-H vibration bands are assigned to the 984-971 cm^{-1} range [27]. For the mT molecule, these vibration bands were observed at 995 and 928 cm^{-1} in the FTIR spectrum, while they were observed at 996-926 and 996-927 cm^{-1} in CCJ/mT and C-CCJ/mT samples, respectively.

3.2.3. C-C Vibration

In FTIR/ Raman Spectra, C=C and C-C vibration bands are observed in the range of 1650-1430 and 1614-1352 cm^{-1} , respectively [28]. While these bands were observed at 1588, 1491 cm^{-1} in the FTIR spectrum of the mT molecule, they were kept at 1585 cm^{-1} in the Raman spectrum. After adsorption, it was observed in the FTIR spectra of CCJ/mT and C-CCJ/mT samples at 1591 and 1590 cm^{-1} , respectively, but not in the Raman spectrum.

Similar assignments were made in AA/mT, DH/mT, C-AA/mT, C-DH/mT samples. Details are presented in the attached file.

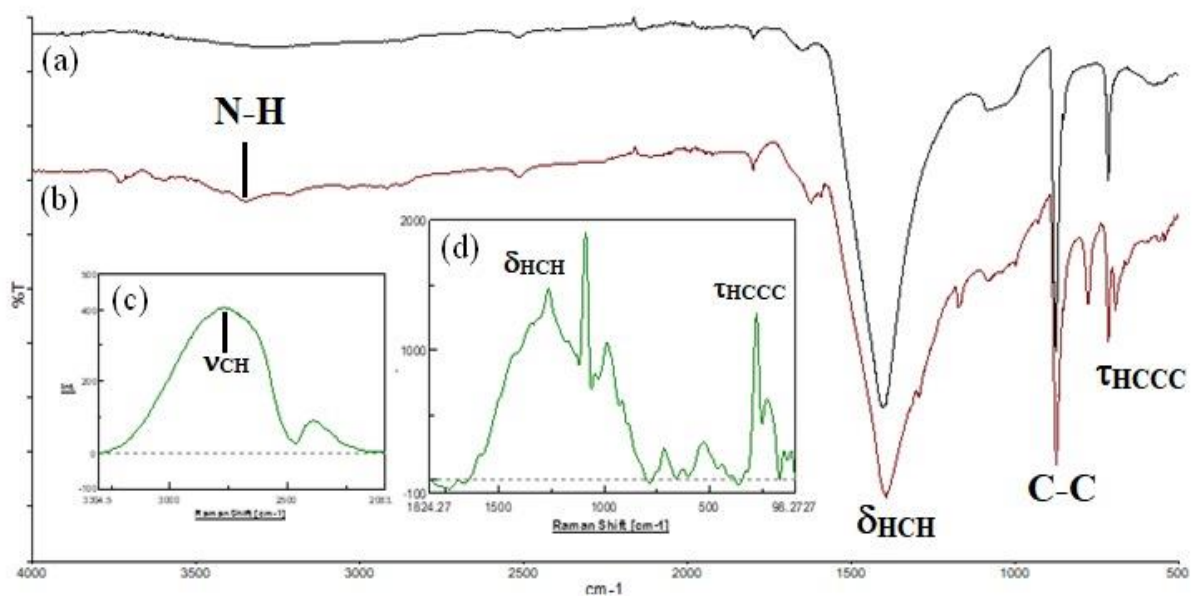


Figure 3. (a) FTIR spectrum of CCJ (b) FTIR spectrum of mT/CCJ (c) Raman spectrum of mT/CCJ in the range of 3500-2080 cm^{-1} (d) Raman spectrum of mT/CCJ in the range of 1800-96 cm^{-1}

Table 2. Detailed assignments of experimental and theoretical wavenumbers (cm^{-1}) of mT, CCJ/mT, C-CCJ/mT, along with potential energy distribution.

mT DFT	Scaled	I_{IR}	I_{R}	Exp. mT		CCJ/mT		C-CCJ/mT		Assignment
				IR	Raman *	IR	Raman	IR	Raman	
3664	3536	15.01	57.89	3450	3455	3423w		3433 w	3429 w	ν_{NH} (100)
3567	3443	16.74	205.88	3349	3370	3347w		3350 w	3375 w	ν_{NH} (100)
3180	3069	17.34	215.7	3215		3216w		3216		ν_{CH} (93)
3165	3055	21.36	65.35	3032		3036w		3034 w		ν_{CH} (93)
3154	3044	4.93	72.89	3017	3011	3013 vw		3011 w		ν_{CH} (93)
3143	3033	20.92	80.18	2982		2978 vw		2978 vw		ν_{CH} (99)
3099	2991	17.65	62.20	2950				2947 vw		ν_{CH} (96)
3074	2967	20.36	83.03	2917	2915	2919w		2917 w		ν_{CH} (95)
3020	2915	31.41	242.30	2857	2869	2865w	2807	2856 w	2810 s	ν_{CH} (97)
1662	1604	152.59	22.35	1628	1612			1621 m		δ_{HNH} (70)+ τ_{HNCC} (10)
1646	1589	53.67	17.85	1588	1585	1591sh	1583 w	1590sh		ν_{CC} (41)+ δ_{HNH} (12)
1627	1570	25.45	9.09	1491	1480			1493 m		ν_{CC} (41)+ δ_{CCC} (28)
1527	1474	38.28	1.64	1467				1469 m	1467sh	δ_{HCC} (47)+ δ_{CCC} (15)
1491	1439	6.95	9.97	1432	1431		1429sh		1430 w	δ_{HCH} (71)+ τ_{HCCC} (21)
1412	1363	1.04	14.39	1376	1377	1379 sh	1364 s	1364sh	1360	δ_{HCH} (91)
1348	1301	4.58	1.19	1311		1310 vw		1312 sh		δ_{HCC} (49)+ ν_{CC} (30)
1339	1292	9.42	2.15	1292	1295	1291 m	1294 sh	1292 m	1291 sh	ν_{CC} (32)+ δ_{HNC} (25)
1192	1150	2.14	1.91	1170	1157 w	1169w	1154 s	1170 m	1156 s	δ_{HCC} (63)+ ν_{CC} (12)
1131	1092	2.13	3.62	1076	1077 s	1080		1090	1085 s	δ_{HCC} (30)+ δ_{HNC} (25)+ ν_{CC} (19)
1092	1054	1.98	1.34	1036		1038	1035	1053		δ_{HNC} (34)+ ν_{CC} (26)+ δ_{HCC} (10)
1058	1021	8.33	1.69	995		996 w		996 w		τ_{HCCC} (62)
1009	974	2.22	42.71		968 s	963 sh		961 sh		δ_{CCC} (57)+ ν_{CC} (35)
973	939	0.03	0.22	928	927 sh	926 w		927 w		τ_{HCCC} (88)
860	830	6.94	0.33	773	776	773 m		774 m	775 w	τ_{HCCC} (64)
747	721	0.54	19.15		736	711 m		712 m	735 w	δ_{CCC} (48)+ ν_{CC} (26)
702	678	18.84	0.19	663		669 sh		666 sh		τ_{HCCC} (63)+ γ_{CCCC} (12)

v=stretching; δ =deformation (bending); τ =torsion; vs= very strong; s=strong; m=medium; w=weak; vw= very weak; sh=shoulder, PED: Potential energy distribution

3.3. Molecular electrostatic potential surface (MEP) analysis

Molecular electrostatic potential surface maps (MEP) reveal the charge distribution of molecules along with different charge regions. It is convenient to guess the charge distribution, electrophilic feature, molecular behavior, activity, and details of hydrogen bonding [29]. In addition, MEP maps pave the way for new chemical synthesis methods by clarifying active sites between intramolecular bonds. The color codes of the electrostatic potential surface map are depicted in Figure 4. The decrease in potential continues in the order of blue>green>yellow>orange>red [30] [31].

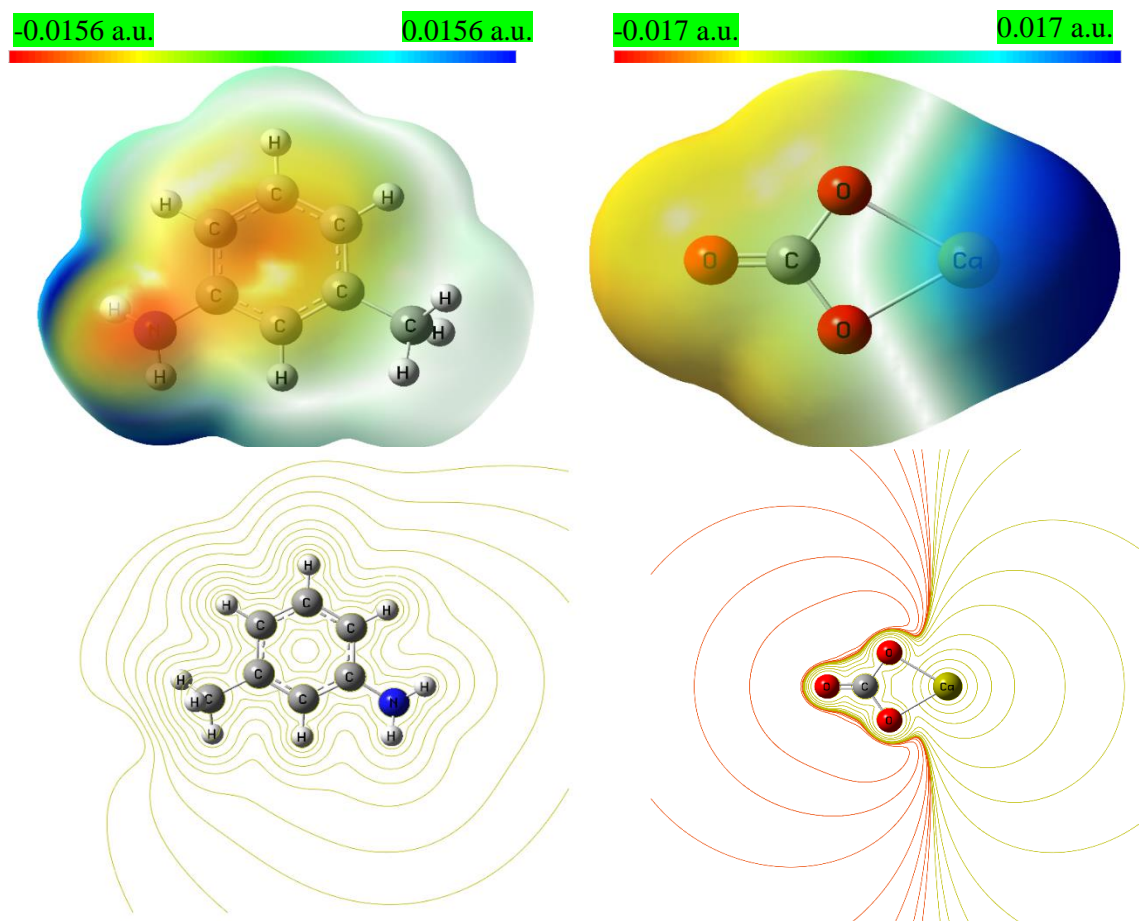


Figure 4. Molecular electrostatic potential mapped of m-Toluidine and CaCO_3

In the MEP map of the molecule, the electron deficient region is coded in blue, and the region with high electron density is coded in red. Regions with the most positive and negative potential for m-Toluidine are 0.156 to -0.156 a.u. The relatively red region in the center of the ring is the most electronegative but is localized to the N atom. Blue region is the most nucleophilic region, a concentrated Hydrogen atom in NH_2 . On the other hand, the region with the most positive to most negative potential is between 0.017 to -0.017 a.u. for CaCO_3 . The most nucleophilic region is concentrated on the Calcium atom and is coded in blue, while the most electronegative region is coded in red and located on the O atoms. The graph of Mulliken's atomic charges is given in Figure 5.



Figure 5. Mulliken Atomic Charges of m-Toluidine

Mulliken population analysis supplements MEP analysis in identifying electronegative sites within a molecule. MEP and Mulliken population analysis are very convenient methods to explain the reactive behavior of all chemical systems in electrophilic and nucleophilic reactions. Detailed Mulliken population analysis for the title molecule is shown in Figure 5. It is seen that the results are in good agreement with the MEP results and among themselves.

3.4. Frontier molecular orbitals (FMOs) and chemical activity

HOMO (Highest Occupied Molecular Orbital) and LUMO (Lowest Unoccupied Molecular Orbital) energies are essential properties in theoretical calculations. HOMO and LUMO surface images and the calculated parameters are given in Figure 6 and Table 3, respectively.

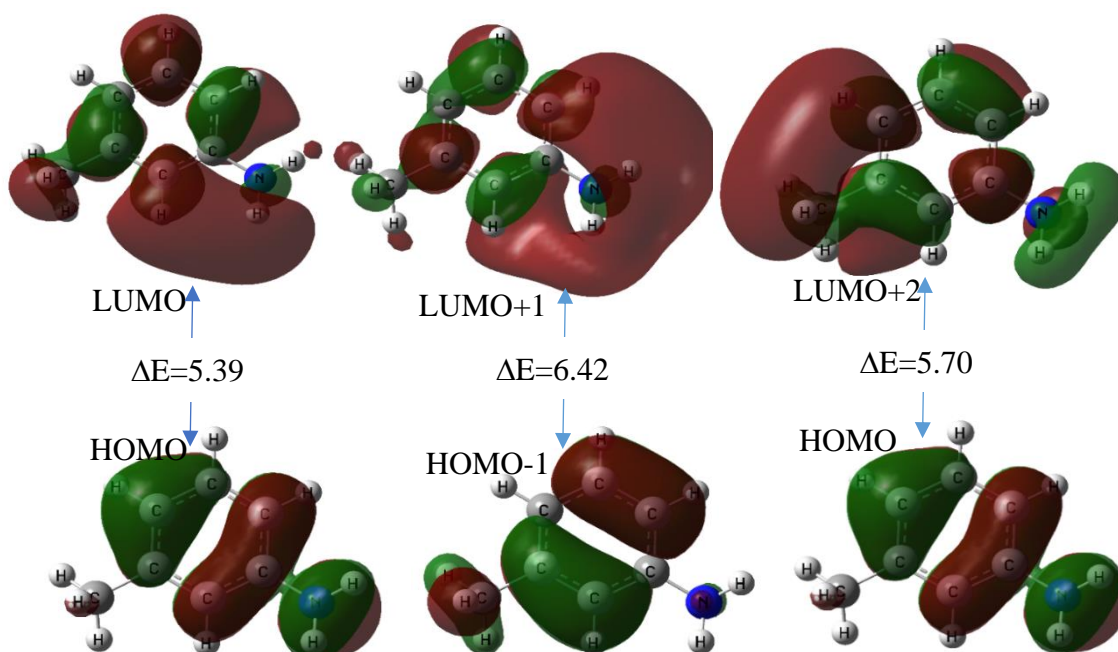


Figure 6. Highest occupied molecular orbital and lowest unoccupied molecular orbital plot of mT

Table 3. Calculated energy values of mT

Parameters	mT (eV)
E_{HOMO}	-5.670
E_{LUMO}	-0.280
ΔE	5.390
Ionization potential (I)	5.670
Electron affinity (A)	0.280
Electronegativity (χ)	2.980
Chemical potential (μ)	-2.980
Chemical hardness (η)	2.700
Chemical softness (s)	0.180
Electrophilic index (w)	1.640
Maximum load transfer parameter (ΔN_{max})	0.550

m: meta form of toluidine; eV: electron-Volt; E_{HOMO} : highest occupied molecular orbital energy; E_{LUMO} : lowest unoccupied molecular orbital energy; ΔE : energy differences between HOMO and LUMO

Results show that mT has high hardness and low softness parameters due to increased energy gaps. These show that this molecule has low chemical activity and high kinetic stability, and it can therefore be concluded that it is pretty stable. High hardness and common softness values indicate less intermolecular charge transfer and low polarity. HOMO energy is calculated as -5.670 eV for mT. LUMO energy is calculated as -0.280. Also, the energy gap is calculated as 5.390 eV. This low HOMO–LUMO energy gap shows that the charge transfer occurs in mT. Electronegativity (χ) and chemical hardness (η) can be calculated as used in the frontier molecular orbital energies [32]. In a molecule, the electron will be transferred from low w to high w (electrons flow from high chemical potential to low chemical potential). In the molecule, χ value is obtained as 2.980 eV. From the HOMO and LUMO energies, the η value is defined as 2.700 eV for mT.

3.5.AFM Analyses

When the eggshells of CCJ, DH and AA are compared to each other, AFM images reveal that the pore sizes are different. When Figure 7 is examined, it is seen that CCJ has a small circular pore structure and AA has a channel-shaped pore structure. AFM images show that the CCJ eggshell has the maximum number of pores per unit surface. Since the mT molecule is a relatively small molecule, it can be said that it easily settles into these small pores. For this reason, it was thought that adsorption was positively affected.

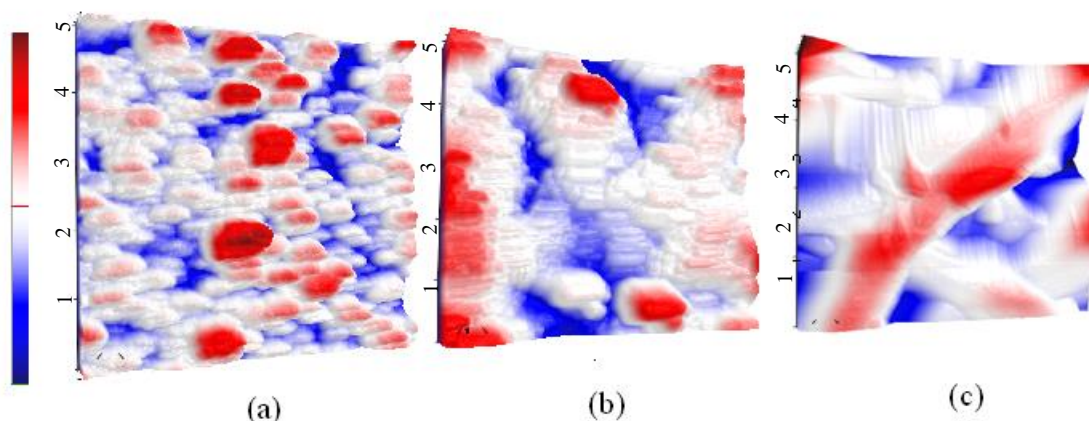


Figure 7. AFM Images and region histogram of Eggshell Sample (a) CCJ (b) DH (c) AA

4. Conclusion

Theoretical calculations give valuable information about bond lengths. mT molecule shows slight differences in bond lengths between C and H atoms. Even though methyl and amine groups were added to the benzene molecule, it was observed that these additions did not disrupt the hexagonal structure of the benzene molecule. According to this result, it was seen that the angles between the carbon atoms in the ring were not affected even if methyl and amine groups were added to the benzene ring, just like the bond lengths. It can be concluded that the adsorption was noticed more strongly in the CCJ type among the three eggshell types. The most distinctive feature of CCJ is its thin crust and small pores. mT molecule is a relatively small molecule. For mT, it is possible to say that as the results, mT settles in tiny pores comfortably. Another conclusion, the adsorption process can be viewed on carbonized eggshells dominantly. The vibrational frequencies were almost the same in FTIR spectra after adsorption on eggshells; these results indicated that physical adsorption had taken place. 2C has a positive Mulliken atomic charge compared to other Carbon atoms in mT. The substitute CH_3 group is linked at 2C in mT. This indicates that the 2C has a more nucleophilic behavior. mT has high hardness and low softness parameters due to its high energy gaps. These indicate that this molecule has low chemical activity and high kinetic stability; therefore, it can be concluded that it is pretty stable. The high stability feature of the mT molecule shows the unwillingness of any chemical reaction. This property is the demonstration of physical adsorption on eggshells. In addition, CaCO_3 , the eggshell's primary content, affects the electrical charge attraction on the surface to adsorb the mT molecule. Mulliken's atomic charge distribution supports the idea.

Author Contributions

Taner Kalaycı; Investigation, Original Draft Writing, Material/Instrument Supply

Deniz Türköz Altuğ; Investigation, Original Draft Writing, Material Supply

Neslihan Kaya Kınaytürk; Investigation, Computational and Experimental Analyses, Original Draft Writing, Visualization, Review and Editing,

Belgin Tunalı: Investigation, Experimental Analyses, Original Draft Writing, Material/Instrument Supply, Supervisor.

Ethics in Publishing

There are no ethical issues regarding the publication of this study.

Acknowledgments

The present work is supported by Research Projects with Foundation Number BAP-22-1003-006, Bandırma Onyedü Eylül University, Scientific Research Commission, Turkey.

References

- [1] Waheed, M., Butt, M. S., Shehzad, A., Adzahan, N. M., Shabbir, M. A., Suleria, H. A. R., Aadil, R. M. (2019). "Eggshell calcium: A cheap alternative to expensive supplements", *Trends in Food Science & Technology*, 91, 219-230.
- [2] Gaonkar, M., Chakraborty, A. P. (2014) "Application of eggshell as fertilizer and calcium supplement tablet", *International journal of innovative research in science, engineering and technology*, 5(3), 3520-3525.
- [3] Schaafsma, A., Van Doormaal, J. J., Muskiet, F. A., Hofstede, G. J., Pakan, I., Van der Veer, E., (2002). "Positive effects of a chicken eggshell powder-enriched vitamin–mineral supplement on femoral neck bone mineral density in healthy late post-menopausal Dutch women", *British Journal of Nutrition*, 87(3), 267-275..
- [4] Kirubakaran, M., Selvan, V. A. M. (2021). "Experimental investigation on the effects of micro eggshell and nano-eggshell catalysts on biodiesel optimization from waste chicken fat", *Bioresource Technology Reports*, 14(100658), 1-10.
- [5] Kavitha, V., Geetha V., Jacqueline, P. J. (2019). "Production of biodiesel from dairy waste scum using eggshell waste", *Process Safety and Environmental Protection*, 125, 279-287.
- [6] Kınaytürk, N. K., Tunalı, B., Türköz Altuğ, D. (2021). "Eggshell as a biomaterial can have a sorption capability on its surface: A spectroscopic research", *Royal Society Open Science*, 8(6), 1-14.
- [7] Muhammad, I. M., El-Nafaty, U. A., Abdulsalam, S., Makarfi, Y. I. (2012). "Removal of oil from oil produced water using eggshell", *Civil and Environmental Research*, 2(8), 52-63.
- [8] Jendia, A. H., Hamzah, S., Abuhabib, A. A. El-Ashgar, N. M. (2020) "Removal of nitrate from groundwater by eggshell biowaste", *Water Supply*, 20(7), 2514-2529.
- [9] Rahmani-Sani, A., Singh, P. Raizada, P. E. Lima, C. Anastopoulos, I. D., Giannakoudakis, A., Sivamani, S., Dontsova T., Hosseini-Bandegharai, A. (2020). "Use of chicken feather and eggshell to synthesize a novel magnetized activated carbon for sorption of heavy metal ions", *Bioresource Technology*, 297(122452), 1-9.
- [10] Lin, T. Y., Chai, W. S. Chen, S. J., Shih, J. Y., Koyande, A. K., Liu, B. L., Chang, Y. K. (2021). "Removal of soluble microbial products and dyes using heavy metal wastes decorated on eggshell", *Chemosphere*, 270(128615), 1-12.

- [11] Lee, J. I., Kim, J. M., Yoo, S. C., Jho, E. H., Lee, C. G., Park, S. J. (2022). "Restoring phosphorus from water to soil: Using calcined eggshells for P adsorption and subsequent application of the adsorbent as a P fertilizer", *Chemosphere*, 287(132267), 1-10.
- [12] Eletta, O. A. A., Ajayi, O. A., Ogunleye, O. O., Akpan, I. C. (2016). "Adsorption of cyanide from aqueous solution using calcinated eggshells: Equilibrium and optimisation studies", *Journal of Environmental Chemical Engineering*, 4(1), 1367-1375.
- [13] Türköz Altuğ, D. Kaya Kınaytürk, N., Kalaycı, T., Tunalı, B. (2022). "Heavy Metal Adsorption with Eggshell of Phasianus Colchicus", *Süleyman Demirel Üniversitesi Fen Edebiyat Fakültesi Fen Dergisi=Süleyman Demirel University Faculty of Arts and Science*, 17(1), 230-241.
- [14] Eskikaya, O., Gun, M., Bouchareb, R., Bilici, Z., Dizge, N., Ramaraj, R., and Balakrishnan, D. (2022). "Photocatalytic activity of calcined chicken eggshells for Basic Red 2 and Reactive Red 180 decolorization", *Chemosphere*, 304(135210), 1-10.
- [15] Allan, J. R., Paton, A. D. (1993). "Preparation, structural characterisation, thermal and electrical studies of complexes of cobalt, nickel and copper with m-toluidine", *Thermochimica acta*, 214(2), 235-241.
- [16] [Online]. Available: https://www.chemicalbook.com/ChemicalProductProperty_EN_CB4277541.htm.
- [17] Palmiotto, G., Pieraccini, G., Moneti, G., Dolara, P. (2001). "Determination of the levels of aromatic amines in indoor and outdoor air in Italy". *Chemosphere*, 43(3), 355-361.
- [18] Thippeswamy, MS, Naik L., Maridevarmath, C. V., Malimath G. H. (2022). "Interactions of Environmental Pollutant Aromatic Amines With Photo Excited States of Thiophene Substituted 1, 3, 4-Oxadiazole Derivative: Fluorescence Quenching Studies", *Journal of Fluorescence*, 32, 1543–1556.
- [19] Aktaş Şüküroğlu, A., Burgaz, S. (2018). "Occupational Exposure to the Chemicals in Hairdressing Salons and Health Risk", *Turkish Bulletin of Hygiene and Experimental Biology*, 75(2), 195-212.
- [20] Johansson, G. M., Jönsson, B. A., Axmon, A. C., Lindh, H., Lind, M. L., Gustavsson, M., Broberg, K., Boman, A., Meding, B., Lidén, C., Albin, M. (2015). "Exposure of hairdressers to ortho-and meta-toluidine in hair dyes" *Occupational and Environmental Medicine*, 72(1), 57-63.
- [21] Zhou, Q., Jiang, G., Liu, J., Cai, Y. (2004). "Combination of microporous membrane liquid–liquid extraction and capillary electrophoresis for the analysis of aromatic amines in water samples", *Analytica chimica acta*, 509(1), 55-62.
- [22] Pinheiro, H. M., Touraud, E., Thomas, O. (2004). "Aromatic amines from azo dye reduction: status review with emphasis on direct UV spectrophotometric detection in textile industry wastewaters", *Dyes and pigments*, 61(2), 121-139.
- [23] Kaya Kınaytürk, N., Oturak, H. (2016). "Identification of Structural and Spectral Features of 2-Amino 4-Chlorobenzoic Acid and 4-Amino 2-Chlorobenzoic Acid: A Comparative Experimental and DFT Study", *Acta Physica Polonica Series a*, 130(1), 276-281.
- [24] Puranik, P., Ramiah, K. (1961). "Raman and infra-red spectra of amines, Toluidines and para-amino-acetophenone", *Proceedings of the Indian Academy of Sciences - Section A*, 54, 146–154.
- [25] Mohammed, T., Soliman, U., Hanafy, A., Hassan, A. M. (2008). "Conformational stability, barriers to internal rotation of 2-aminothiophenol (d0 and d3): A combined

- vibrational and theoretical approach", *Journal of Molecular Structure: THEOCHEM*, 865(1-3), 14-24.
- [26] Zochedh, A., Priya, M., Shunmuganarayanan, A., Thandavarayan, K., Sultan, A. (2022). "Investigation on structural, spectroscopic, DFT, biological activity and molecular docking simulation of essential oil Gamma-Terpinene", *Journal of Molecular Structure*, 1268, 133651.
- [27] Hony, S., Van Kerckhoven, C., Peeters, E., Tielend, A., Hudgins, D., Allamandola, L. (2001). "The CH out-of-plane bending modes of PAH molecules in astrophysical environments", *Astronomy and Astrophysics*, 370(3), 1030 -1043.
- [28] Altun, A., Gölcük, K., Kumru, M. (2003), "Theoretical and experimental studies of the vibrational spectra of m-methylaniline", *Journal of Molecular Structure: THEOCHEM*, 625(1-3), 17-24.
- [29] Berrah, F., Boursas, F., Bouacida, S., Ouannassi, F. (2020). "Structural, Spectroscopic and Thermal Characterizations Combined with DFT Calculations and Hirshfeld Analysis of a Novel Hydrogen-Bonded Complex: P-Phenylenediammonium Dinitrate", *Journal of Molecular Structure*, 1205, 127624.
- [30] Chaudhary, J., Mittal, V., Mishra, S., Daiya, A., Chowdhury, R., Laskar, I. R., Roy, R. K." (2020). A New Aggregation Induced Emission Active Halochromic White Light Emissive Molecule: Combined Experimental and Theoretical Study", *The Journal of Physical Chemistry*, 124(28), 15406-15417.
- [31] Kaya Kınaytürk, N., Kalaycı, T. Tunalı, B. (2021). "Experimental and computational investigations on the molecular structure, vibrational spectra, electronic properties, and molecular electrostatic potential analysis of phenylenediamine isomers" *Spectroscopy Letters*, 54(9), 693-706.
- [32] Keçel-Gündüz, S., Bıçak, B., Çelik, S., Akyüz, S., Özel, A. (2017) "Structural and spectroscopic investigation on antioxidant dipeptide, l-methionyl-l-serine: A combined experimental and DFT study". *Journal of Molecular Structure*, 1137, 756-770.

The Effect Of Urban Areas On Human Bioclimatic Comfort Conditions; Sample Of Amasya City

Savaş ÇAĞLAK^{1*}, Süleyman TOY²

¹Milli Eğitim Bakanlığı, Amasya

²Atatürk Üniversitesi, Mimarlık ve Tasarım Fakültesi, Şehir ve Bölge Planlama Bölümü, Erzurum

Received: 15/04/2022, **Revised:** 22/05/2022, **Accepted:** 28/08/2022, **Published:** 30/03/2023

Abstract

Urban settlements, one of the most important developments in the history of humanity, expanded due to the migration movements from rural to urban areas and turned into high density built environments with high-rise buildings. This situation has caused urban areas to have different climatic conditions from the suburban and rural areas around them. Bioclimatic comfort is the state of people to feel comfortable, happy and fit in the atmospheric environment they are in. Uncomfortable conditions cause much negativity such as decrease in people's work efficiency, health conditions and increase in energy consumption. Amasya is a small Anatolian city in the Central Black Sea Region of the Black Sea Region, where industrialization has not developed. In this study, hourly data of the year 2021 of two meteorology stations, which are considered as urban and suburban, were used in order to examine the effects of urban areas on bioclimatic comfort conditions in Amasya. As a method, the PET (Physiological Equivalent Temperature) index obtained from the RayMan model, which calculates many factors together, was used. As a result of the study, suburban is 2.1 °C cooler than urban at the general PET average; 3.4°C cooler at the maximum average and 2.8°C cooler at the minimum average. The urban area is exposed to heat stress by 8.1% more throughout the year than the suburban area. In order to reduce the negative bioclimatic comfort conditions of cities and for sustainable urbanization, it is necessary to make urban design and planning that takes into account human, ecological and physical conditions.

Keywords: Amasya, Bioclimatic Comfort, Urban Climate, Urbanization, PET.

Kentsel Alanların İnsan Biyoklimatik Konfor Koşullarına Etkisi; Amasya Kenti Örneği

Öz

İnsanlık tarihinin en önemli gelişmelerinden biri olan kent yerleşmeleri, kırdan kente yaşanan göç hareketlerine bağlı olarak genişlemiş, yoğun ve yüksek yapıli yerleşmelere dönüşmüştür. Bu durum kentlerin çevrelerindeki yarı kentsel ve kırsal alanlardan farklı iklim koşullarına sahip olmalarına neden olmuştur. Biyoklimatik konfor, insanların buldukları atmosferik ortamda kendilerini rahat, mutlu ve zinde hissetme durumudur. Konforsuz şartlar insanların iş verimlerinde azalma, sağlık koşulları ve enerji tüketiminde artış gibi birçok olumsuzluklara neden olmaktadır. Amasya, Karadeniz Bölgesi'nin Orta Karadeniz Bölümünde sanayileşmenin gelişmediği küçük bir Anadolu kentidir. Bu çalışmada Amasya'da kentsel alanların biyoklimatik konfor koşullarına etkisinin incelenmesi amacıyla çalışmada kent ve yarı kent olarak kabul edilen iki meteoroloji istasyonunun 2021 yılı saatlik verileri kullanılmıştır. Yöntem olarak birçok etkeni bir arada hesaplayan RayMan modelinden elde edilen PET (Physiological Equivalent Temperature) indisinden yararlanılmıştır. Çalışma sonucunda genel PET ortalamasında yarı kent; kente göre 2,1 °C, maksimum ortalamasına göre 3,4°C ve minimum ortalama ise 2,8°C daha serindir. Kentsel alan yarı kent alanına göre tüm yıl boyunca % 8,1 daha fazla sıcak stresine maruz kalmaktadır. Kentlerin olumsuz biyoklimatik konfor koşullarını azaltmak ve sürdürülebilir kentleşme için, beşeri, ekolojik ve fiziksel koşulları dikkate alan kentsel tasarım ve planlamaların yapılması gerekmektedir.

Anahtar Kelimeler: Amasya, Biyoklimatik Konfor, Kent İklimi, Kentleşme, PET.

1. Introduction

Cities are places where many sectors such as social, health, education, economic and trade develop and have many service branches. In this respect, cities are more attractive to people than rural areas. As a result of the increasing world population and technological developments due to the developments in medicine, the destruction of the natural environment has increased with the increase in the power of human beings to intervene in nature. Changes, especially with the industrial revolution, changes in human habits and philosophy of life, and the increase in production and consumption have increased the number and size of cities [1, 2].

Rapid migration from rural to urban areas causes an increase in housing, transportation and infrastructure services in the city. Besides increased artificial surfaces and reduced evaporation, one group of factors is anthropogenic effects including transportation, production activities, and air pollution. This situation causes the destruction of the natural environment in urban areas, the increase of impermeable surfaces such as asphalt and concrete, the increase of multi-storey structures and the dense settlements. As a result of these changes, urban areas have different climatic conditions from the rural and sub-urban areas around them. In many studies in the world and in Turkey, it has been explained that adverse climatic conditions are observed in urban areas due to the destruction of natural surfaces and the decrease in the amount of green areas [3-11].

In parallel with the population and construction density in the cities, heat islands are formed, and changes occur in the microclimatic structures of the cities. The cumulative effects of these microclimatic changes on each other can negatively affect the lives of humans and other living things on a global scale. This effect on humans can be explained by the concept of bioclimatic comfort. Bioclimatic comfort is when people feel comfortable, happy and fit in the thermal environment they are in [12, 13]. In other words, it is the state where there is no discomfort between an uncomfortable temperature and an uncomfortable cold [14]. Uncomfortable conditions can lead to physiological and psychological health conditions of people, decreased work efficiency, more energy use, heat-related symptoms and an increase in death rates [13, 15-18].

In this study, it is aimed to examine the effects of urbanization on bioclimatic comfort conditions in Amasya, a small Anatolian city where industrialization has not developed. For this purpose, hourly data of 2021, in which the city meteorology station in the city of Amasya, representing the urban area, and the meteorology stations in Amasya University, representing the sub-urban area, made simultaneous measurements, were used. Bioclimatic comfort conditions were compared according to PET (Physiological Equivalent Temperature) index by using RayMan software. Significant differences were determined between the two stations in terms of bioclimatic comfort. Amasya, according to NUTS it is located in the Samsun sub-region of the Western Black Sea Region (TR83 Level). The city center is located in the Central Black Sea Region of the Black Sea Region (between 35°46' - 35°51' east longitudes and 40°40' - 40°37' northern latitudes, in the back region of the Canik Mountains. Established

along the Yeşilirmak valley, the city of Amasya developed at elevations between 390 and 500 meters. Yeşilirmak River, an important river of Turkey, passes through the city. Yeşilirmak has been decisive in the establishment and development of the city [19]. The city is surrounded by mountains from the north and south. In the city of Amasya, where industrialization has not developed, it has a dense settlement due to topographic conditions (it is located at the bottom of the valley) (Figure 1). The suburban weather station is located in a loosely structured area, while the urban weather station is located in a densely built urban area.

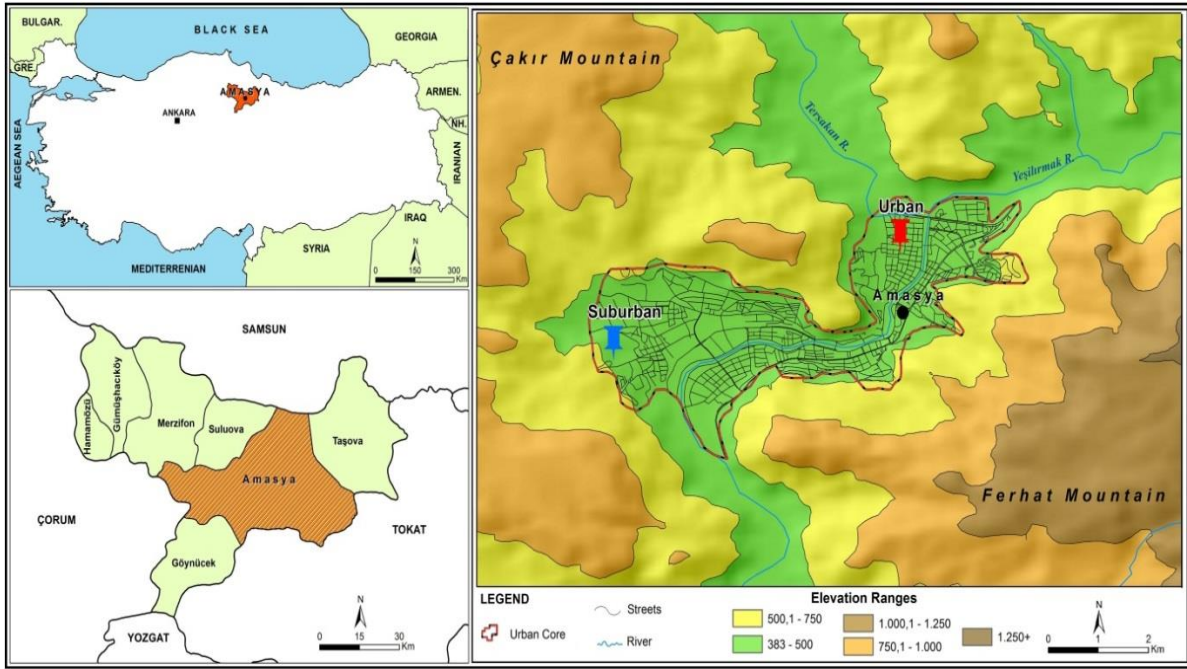


Figure 1. Location of map Amasya city

The city of Amasya has a transitional climate between the Black Sea climate and the continental climate. When evaluated according to climate classifications, in Amasya, according to Köppen-Geiger; (Csa) climate with mild winter, very hot summer and dry climate; according to Erinç; steppe-semi-arid; according to de martonne; steppe-damp, according to Thornthwaite; D,B'2,d,b'3 (D: semi-arid, B'2: mesothermal, d: little or no excess water, b'3: summer evaporation rate: 53%) [20].

2. Material and Methods

In the study, the Amasya meteorology station with the number 17085 representing the urban area and the Amasya University meteorology station with the sub-urban feature number 19911 in 2021; air temperature (°C), relative humidity (%), wind velocity (m/s) and cloud cover (octa) hourly data were used. Table 1 represents the features of the meteorological measurement stations (Table 1, Figure 2).










Table 1. Meteorology stations used in the study

Represented Area	Location	Altitude (m)	Surface
Urban	40°39'59.87"N; 35°50'6.64"E	409	Dense structured
Sub-urban	40°39'0.08"N; 35°47'28.41"E	495	Loosely structured

**Figure 2.** Meteorology stations used in the study

PET index was used through the RayMan model, which is widely used to determine bioclimatic comfort conditions. PET (Physiological Equivalent Temperature) [21-23] index calculates human bioclimatic comfort according to body heat energy balance. The index calculates all the effects of the thermal environment on people (short and long wave solar radiation, air temperature, relative humidity and wind velocity) and the thermo-physiological conditions of the human body (clothing type and activity) [22-24]. Human temperature sensation levels and physiological stress levels on humans in each value range of the PET index; 35 years old, 175 cm height, 75 kg weight, male, 0.9 clo clothing load and 80 W workload were taken into consideration [25-27] (Table 2).

Table 2. Human thermal sensation and stress ranges for PET [22,23].

PET [°C]	Thermal sensation	Level of thermal stress	Colors
< 4°C	very cold	extreme cold stress	
4.1 - 8°C	cold	strong cold stress	
8.1 - 13°C	cool	moderate cold stress	
13.1 - 18°C	slightly cool	slight cold stress	
18.1 - 23°C	neutral (comfortable)	no thermal stress	
23.1 - 29°C	slightly warm	slight heat stress	
29.1 - 35°C	warm	moderate heat stress	
35.1 - 41°C	hot	strong heat stress	
41°C >	very hot	extreme heat stress	

The values obtained by using the hourly data of 2021, which meteorology stations made joint measurements, were calculated as daily averages and hourly numbers. In total, 8760 hours (365 x 24) of data were calculated for each station.

3. Results and Discussion

Among the environmental factors that cause global warming or climate change, the most important factor is urbanization. With the industrial revolution, many families who were unemployed in the countryside had to migrate to the city. Especially in urban areas, the increasing need for labor and the development of the city's service functions such as education and health have made migration from rural to urban attractive. Population growth in cities with migrations has created a need for more housing. Both the increase in the number of residences and the development of infrastructure and transportation services have caused the expansion and concentration of urban areas. This situation has led to the destruction of natural areas in urban areas, the destruction of green areas, the increase in air pollution with the increase in the use of motor vehicles, and the increase in asphalt and concrete surfaces. Due to such anthropogenic factors, cities have different climatic conditions from the suburban or rural areas around them. This situation caused the bioclimatic comfort conditions of the cities to be negatively affected. Many studies in the world and in Turkey reveal that urban areas cause climate change.

In the study, it was seen that the suburban area had more positive results than the urban area. On the general PET average, suburban is 2.1°C cooler, with a maximum average of 3.4°C and a minimum average of 2.8°C cooler than a city (Figure 3). Although urban land use differences are effective in the emergence of such a difference, the altitude difference (86 meters) between the two stations is also effective.

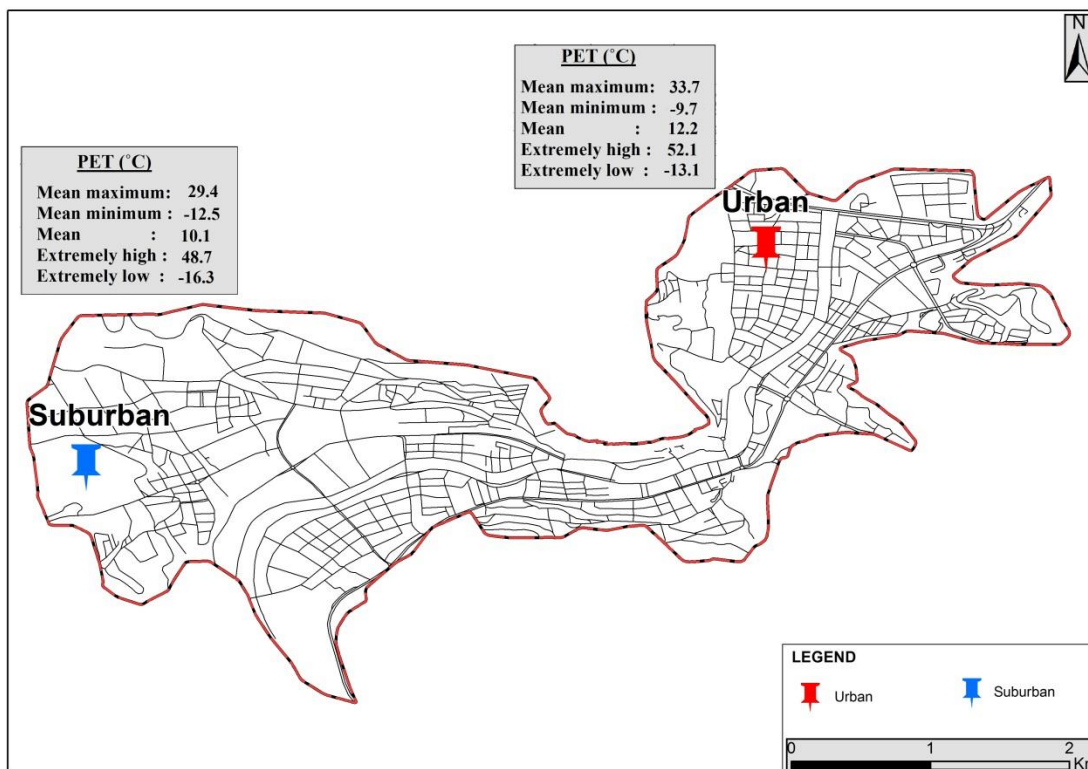


Figure 3. Urban and suburban meteorological stations

According to these findings, it is expected that those living in suburban areas will feel more comfortable than those living in urban areas. In heat stresses, it is possible for those living in urban areas to be exposed to higher thermal stresses.

Hourly suburban and urban comparisons of the whole working period and the hot months (June, July, August and September) were made. According to hourly comparisons; suburban has higher “comfortable” conditions (general; 7.9% and summer 13.1%) than urban, both in summer and all year round. Cold stresses (< 18.1 °C) are perceived as 72.1% in suburban and 64.8% in urban areas. Suburban is 7.2% colder than the city. In heat stresses; “slightly warm” stress is in suburban in the whole period, at a rate of 0.9% compared to the city (7.3% and 6.4%, respectively) and 1.7% in the summer period (7.3% and 6.4%, respectively) (respectively 13.1% and 11.4%) are more common. In the "warm", "hot" and "very hot" stresses, the city is exposed to 0.5%, 4.1% and 5.4% more exposure than the suburban, respectively. On the other hand, in the summer period, the city has more stressful conditions in the "hot", "very hot" and "extremely hot" stresses, respectively, by 1.1%, 8.7% and 13.6% compared to the suburban (Table 3).

Table 3. Hourly suburban and urban comparison

Annual Values						
PET (°C)	Thermal sensation	Level of thermal stress	Suburban (hour)	Suburban (%)	Urban (hour)	Urban (%)
<4	Very cold	Extreme cold stress	2689	30,7	2541	29,0
4,1–8,0	Cold	Strong cold stress	984	11,2	995	11,4
8,1–13,0	Cool	Moderate cold stress	1308	14,9	1122	12,8
13,1–18,0	Slightly cool	Slightly cold stress	1341	15,3	1014	11,6
18,1–23,0	Comfortable	No thermal stress	695	7,9	631	7,2
23,1–29,0	Slightly warm	Slightly heat stress	640	7,3	564	6,4
29,1–35,0	Warm	Moderate heat stress	612	7,0	657	7,5
35,1–41,0	Hot	Strong heat stress	411	4,7	683	7,8
>41,0	Very Hot	Extreme heat stress	80	0,9	553	6,3
		Total	8760	100	8760	100
Summer Months						
PET (°C)	Thermal sensation	Level of thermal stress	Suburban (hour)	Suburban (%)	Urban (hour)	Urban (%)
<4	Very cold	Extreme cold stress	20	0,7	8	0,3
4,1–8,0	Cold	Strong cold stress	28	1,0	24	0,8
8,1–13,0	Cool	Moderate cold stress	436	15,7	219	7,6
13,1–18,0	Slightly cool	Slightly cold stress	776	26,9	439	15,2
18,1–23,0	Comfortable	No thermal stress	376	13,1	327	11,4
23,1–29,0	Slightly warm	Slightly heat stress	403	14,0	348	12,1
29,1–35,0	Warm	Moderate heat stress	440	15,3	473	16,4
35,1–41,0	Hot	Strong heat stress	321	11,1	571	19,8
>41,0	Very Hot	Extreme heat stress	80	2,8	471	16,4

It has been determined that comfortable conditions are less experienced in the city station during the whole time period and in the summer period than in the sub-urban, and cold thermal conditions are experienced more frequently in the suburban. In heat stresses, it has been observed that the city is exposed to more heat stresses than the suburban in the whole time period and especially in the summer period. It has been determined that suburban areas are more advantageous than urban areas according to thermal conditions. According to the daily percentage distribution of bioclimatic comfort conditions in the study; in the winter season it is seen that colder conditions are experienced in the suburban. In the summer season, especially in July and August, "very hot" and "hot" stresses are effective in the city, while "warm" and "slightly warm" stresses are effective in the suburban. "Comfortable" conditions are perceived more in sub-urban than urban (Figure 4, Figure 5).

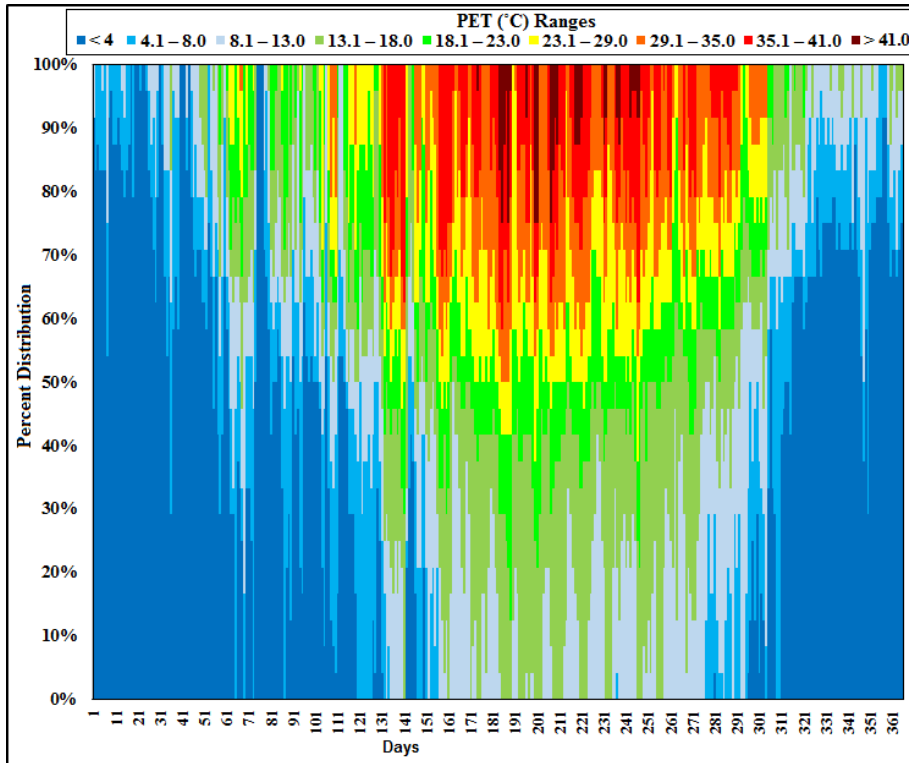


Figure 4. Temporal distribution of bioclimatic comfort conditions in sub-urban area

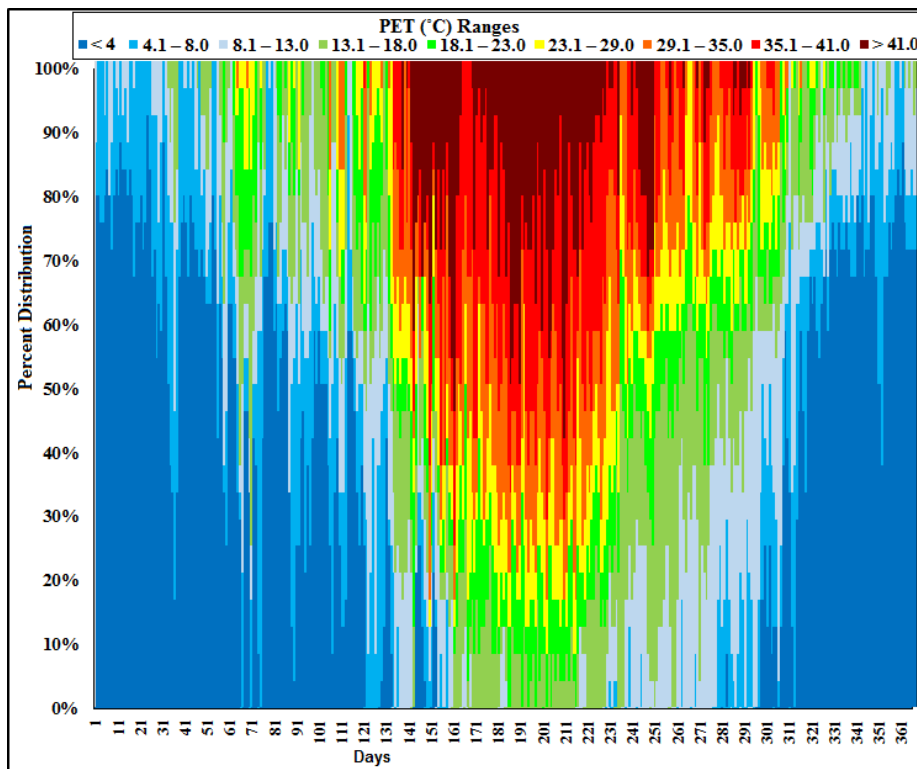


Figure 5. Temporal distribution of bioclimatic comfort conditions in the urban area

In this study, the effects of urbanization movements in the world and in Turkey on bioclimatic comfort conditions were examined in Amasya, a small city where industrialization was not

developed. As a result of the study, it was seen that the suburban area had more positive results than the urban area. Suburban is 2.1 °C cooler than urban at the general PET average; 3.4°C cooler at the maximum average and 2.8°C cooler at the minimum average. In addition, suburban area has higher “comfortable” conditions (7.9%) all year round than the city. It has been observed that the urban area is exposed to heat stresses 8.1% more throughout the year and 21.5% more in summer than the suburban area. Although urban land use differences are effective in the emergence of such a difference, the altitude difference (86 meters) between the two stations is also effective. When the results obtained are compared with other studies, the difference between the city and the suburban was found as; 1,4 – 2,2 °C in Ankara, the capital of Turkey [28], 8,7 °C in Atina [7], 1,5 °C in Belgrade [29], 1,4 °C in Eskişehir [10] and 2,5-5,5 °C in Kolkata , India [11]. The results of the study are similar to the results of the studies in the literature.

4. Conclusion

Even in Amasya, a small Anatolian city where industrialization has not developed, it has been revealed that urban areas have more negative comfort conditions than the suburban areas around them. It has also been explained in many studies that bioclimatic comfort conditions have negative effects in urban centers where more than half of the world's population and more than 90% of Turkey's population live. The fact that the city of Amasya was established on the valley floor and accordingly the limited expansion area caused the settlements to become dense. This situation caused a decrease in wind speed in the city, excessive concreting and asphaltting.

Depending on climate change, it is possible to experience more adverse bioclimatic comfort conditions in the city in the future. Therefore, the climate and bioclimatic comfort conditions of the city should be considered in the planning and designs to be made in urban areas. The amount of green areas in cities should be increased and these green areas should be distributed in a balanced way. In addition, afforestation to be made by choosing suitable species on streets will improve bioclimatic comfort conditions. Green buildings should be preferred in building designs. It is recommended to make urban design and planning from a geographical perspective to reduce the negative effects of bioclimatic comfort conditions and for sustainable cities.

Ethics in Publishing

There are no ethical issues regarding the publication of this study.

Author Contributions

The collection and calculation of the data and the writing of the article were made by Savaş ÇAĞLAK. The evaluation and general design of the results of the study was made by Süleyman TOY.

References

- [1] Rossi, U. (2004) The Multiplex City. The Process Of Urban Change in The Historic Centre District of Naples. *European Urban and Regional Studies*, 11 (2), 156-169.
- [2] Gonzalez, M. J., De Lazora, M.L. (2011) Urban Development and Sustainability. *European Journal of Geography*, 1, 1- 12.
- [3] Oke, TR. (1973) City Size and The Urban Heat Island. *Atmospheric Environment*, 7 (8), 769-779.
- [4] Mayer, H. (1993) Urban Bioclimatology. *Experientia*, 49, 957-963.
- [5] Unger J. (1999) Urban–rural Air Humidity Differences in Szeged, Hungary. *International Journal of Climatology*, 19 (13), 1509-15015.
- [6] Çiçek, İ., Doğan, U. (2005) Investigation of the Urban Heat Island in Ankara. *Journal of Geographic Sciences*, 3 (1), 57-72.
- [7] Charalampopoulos, I., Tsiros, I., Sereli, A., Matzarakis, A. (2013) Analysis of Thermal Bioclimate in Various Urban Configurations in Athens, Greece, *Urban Ecosyst*, 16, 217-233.
- [8] Çağlak, S. (2017) Investigation of Samsun's Bioclimatic Comfort Conditions and the Effect of Urbanization on Bioclimatic Comfort Conditions.(Unpublished Master's Thesis) Ondokuz Mayıs University / Social Sciences Institute, Department of Geography, Samsun.
- [9] Çağlak, S., Aydemir, KPK., Kazancı, G. (2021) Effects of Urbanization on Bioclimatic Comfort Conditions; Bolu Example. *City Health Journal*, 2(2), 47-55.
- [10] Toy, S., Çağlak, S., Esrigü, A. (2022) Assessment of Bioclimatic Sensitive Spatial Planning in a Turkish City, Eskisehir. *Atmosfera*, 35(4), 719-735.
- [11] Bal, S., Matzarakis, A. (2022) Temporal Analysis of Thermal Bioclimate Conditions Between Kolkata (India) and its Three Neighbouring Suburban Sites. *Theoretical and Applied Climatology*, 148, 1545-1562.
- [12] Toy, S. (2010) Investigation of Eastern Anatolia Region Recreational Areas in Terms of Bioclimatic Comfort Values. (Unpublished PhD Thesis), Atatürk University / Institute of Science and Technology, Department of Landscape Architecture, Erzurum.
- [13] Çağlak, S. (2021) Effects and Possible Consequences of Climate Change on Bioclimatic Comfort Conditions. Doctoral Thesis. Ondokuz Mayıs University.

- [14] Parsons, K.C. (2003) *Human Thermal Environments: The Effects of Hot, Moderate, and Cold Environments on Human Health, Comfort And Performance*. Taylor & Francis, London, New York.
- [15] Vanoz, J.K., Warland, J.S., Gillespie, T.J., Kenny, N.A. (2010) Review of the Physiology of Human Thermal Comfort While Exercising in Urban Landscapes and Implications for Bioclimatic Design. *International Journal of Biometeorology*, 54, 319-334.
- [16] Nastos, P. T., Giaouzaki, K. N., Kampanis, N. A., Matzarakis, A. (2013) Acute Coronary Syndromes Related to Bio-Climate in a Mediterranean Area. The case of IeraTHIra, Crete Island, Greece. *International Journal of Environmental Health Research*, 23 (1), 76-90.
- [17] Blazejczyk, K., Baranowski, J., Blazejczyk, A. (2018) Climate Related Diseases. Current Regional Variability and Projections to The Year 2100. *Quaestiones Geographicae*, 37(1), 23-36.
- [18] Schlegel, I., Muthers, S., Mücke, H.-G., Matzarakis, A. (2020) Comparison of Respiratory and Ischemic Heart Mortalities and Their Relationship to the Thermal Environment. *Atmosphere*, 11(8), 811-826.
- [19] Zeybek, H.İ. (1998). *Physical Geography of Amasya Plain and Its Neighborhood*. Doctoral Thesis. Ondokuz Mayıs University.
- [20] Bölük, E. (2016) *Turkish Climate According to Köppen Climate Classification*. MGM. Publications, Ankara.
https://www.mgm.gov.tr/FILES/iklim/iklim_siniflandirmalari/koppen.pdf
- [21] Höppe, P. (1993) Heat Balance Modelling. *Experientia*, 49, 741-746.
- [22] Höppe, P. (1999) The Physiological Equivalent Temperature - a Universal Index for the Biometeorological Assessment of The Thermal Environment. *International Journal of Biometeorology*, 43, 71-75.
- [23] Matzarakis, A., Mayer, H., Iziomon, M. G. (1999) Applications of a Universal Thermal Index: Physiological Equivalent Temperature. *International Journal of Biometeorology*, 43, 76-84.
- [24] Gulyas, A., Unger, J., Matzarakis, A. (2006) Assessment of The Micro Climatic and Human Comfort Conditions in A Complex Urban Environment: Modelling And Measurements. *Building and Environment*, 4, 1713-1722.
- [25] Fanger, P.O. (1970) *Thermal Comfort*. Copenhagen, Danish Technical Press, 244.
- [26] Mayer, H. (1993). Urban Bioclimatology, *Experientia* 49, 957-963.
- [27] Matzarakis, A., Mayer, H. (1996) Another Kind of Environmental Stress: Thermal Stress. *WHO Newsletters*, 18, 7-10.

[28] Türkoğlu, N., Çalışkan, O., Çiçek, İ., Yılmaz, E. (2012) An Investigation of the Effect of Urbanization on Bioclimatic Conditions in Ankara Scale. *International Journal of Human Sciences*, 9(1), 932-955.

[29] Pecelj, M., Matzarakis, A., Vujadinović, M., Radovanović, M., Vagić, N., Đurić, D., Cvetkovic, M. (2021) Temporal Analysis of Urban-Suburban PET, mPET and UTCI Indices in Belgrade (Serbia). *Atmosphere*, 12, 916.

Smart Contract Security Vulnerabilities

Ruhi Taş^{1*}

¹ Turkish Radio Television Co.

Received: 18/04/2022, **Revised:** 14/09/2022, **Accepted:** 15/09/2022, **Published:** 30/03/2023

Abstract

A smart contract is a concept of computer protocols that helps to facilitate blockchain technology. This blockchain-based smart contract is a public ledger of all participating transactions. It is considered a self-executable application and contains predetermined rules. It also operates by decentralizing networks that are shared between all parties, and this execution of contracts between parties could be securely done without a middleman or a third party. With blockchain technology, developers could provide an efficient framework and ensure security issues. While the new blockchain has successfully been developed to prevent the problems of fraud and hacking, there is still a considerable risk concerning security and confidentiality. Therefore, we should not underestimate this matter. This study aims to review the potential risks that may take place on blockchain-based smart contracts. In addition, the options that may assist application developers in order to provide viable guidance, and to avoiding these security vulnerabilities.

Keywords: Blockchain, Smart Contract, Vulnerability, Ethereum, Solidity

Akıllı Sözleşme Güvenlik Zaafiyetleri

Öz

Akıllı sözleşme, blok zinciri teknolojisini kolaylaştırmaya yardımcı olan bir bilgisayar protokolleri kavramıdır. Bu blok zinciri tabanlı akıllı sözleşme, katılan tüm işlemlerin halka açık bir defteridir. Kendi kendine çalıştırılabilir bir uygulama olarak kabul edilir ve önceden belirlenmiş kurallar içerir. Ayrıca, tüm taraflar arasında paylaşılan ağları merkezi olmayan hale getirerek çalışır ve taraflar arasındaki bu sözleşmelerin yürütülmesi, bir aracı veya üçüncü bir taraf olmadan güvenli bir şekilde yapılabilir. Blockchain teknolojisi ile geliştiriciler verimli bir çerçeve sağlayabilir ve güvenlik sorunlarını sağlayabilir. Yeni blok zinciri, dolandırıcılık ve bilgisayar korsanlığı sorunlarını önlemek için başarıyla geliştirilmiş olsa da, güvenlik ve gizlilik konusunda hala önemli bir risk var. Bu nedenle bu konuyu hafife almamalıyız. Bu çalışma, blockchain tabanlı akıllı sözleşmelerde yer alabilecek potansiyel risklerin incelenmesi amaçlamaktadır. Ayrıca geliştiricilere rehberlik ederek, olası güvenlik açıklarından kaçınmak için uygulama geliştiricilere yardımcı olunması sağlanmıştır.

Anahtar Kelimeler: Blok zinciri, Akıllı sözleşmeler, Zaafiyet, Ethereum, Solidity

1. Introduction

Satoshi Nakamoto proposed a system with several rules to build the blockchain infrastructure in 2008. In particular, he created the first cryptocurrency, a form of digital money based on cryptography, which prioritizes the level of security [1]. In 2009, Bitcoin cryptocurrency was created and started to be traded on the market. It gained popularity as a result of the use of the Bitcoin blockchain infrastructure. Bitcoin is the first application that managed to disable central control [2]. Blockchain, which uses a decentralized structure, offers a reliable system thanks to its immutability and distributed record structure. Particularly, participants who do not know each other confirm the accuracy of the transactions within the framework of certain rules and keep them [3]. The blockchain provides an unalterable permanent record of transactions on a network. The system uses a decentralized ledger similar to a database. In this system, the people involved in the system can see the records of all transactions, if they wish. This feature causes it to differentiate from traditional databases [4]. In the following process, their usability in alternative areas has emerged. It has spread to a wide area such as supply chain [5], agricultural practices, insurance [6], health [7] to secure digital rights management [8], pharmaceuticals [9], financial transactions, and trade and commerce [10].

A smart contract is a leading product of Ethereum blockchain; and it is one of the most useful cryptocurrencies. Ethereum [11] allows other blockchain applications to be built on it [12]. With the use of smart contracts in blockchain systems, special applications have started to be developed within contract-based privatized sectors [13]. It is stated that blockchain technology provides security and a stable working environment, especially in online transactions. However, the lack of standards and weaknesses in application development can pose serious risks. These vulnerabilities could take place at different levels: the blockchain framework level, the peer-to-peer network level, and the blockchain application at the reasonable contract level. In this study, we primarily focus on security matters and how to prevent these vulnerabilities which may take place on the blockchain-based smart contracts.

2. What is Smart Contract?

A smart contract is code developed as a script that is pinned to a blockchain or similar distributed infrastructure. Triggered by the blockchain transaction and verified over the network, it is used to execute predefined actions. Since the terms of a smart contract are transparently stored on the blockchain, it can always be checked whether all parties are working as intended. In this way, trust problems between the related parties are reduced. Smart contracts can be written as software scripts, just like scripts running in non-blockchain applications. The term smart contract and the underlying idea predates the emergence of Bitcoin. Szabo [14] defined the smart contract as a piece of computerized transaction. The protocol, which meets the terms of payment, contract terms such as confidentiality or execution, enables the realization of transactions in accordance with the criteria by making the necessary transactions. Solidity, Ethereum The design of such systems has legal, economic and technical bases. Therefore, smart contracts require interdisciplinary analysis.

3. Potential Risks of Smart Contract Implementations on Blockchain

The Smart Contract definition was first proposed by Nick Szabo in 1994 [14]. According to the structure defined by Szabo, it has been stated that the contracts that have to be used in some cases can be converted into codes that computers can process. In this way, it will be able to be stored and copied in the system. When applied to the blockchain, it can be activated as a control mechanism in the nodes on the network [15]. Smart contracts are the writing of a contract on the lines of code, and the transactions are executed according to the terms of this contract [16]. Contracts developed to provide the necessary controls are uploaded to the nodes. Later, other nodes in the blockchain will be enabled to communicate with the same mechanism. Smart contracts ensure that transactions between nodes are carried out securely.

Smart contract programming requires different features from the standard application development methods. If there is any failure of the applications, the cost for defective software could be high. The expected changes could also be difficult, which can be compared to a hardware design and programming. It is usually written in a simple language of smart contract languages, expressions, operators, functions, and variables. Although they are already quite abstract and difficult to understand, the components of a smart contract can be expressed in part by name from anywhere in the program; sometimes it is almost impossible to see how different parts interact and fit.

Smart contracts are self-distributed computer programs which are executed on the blockchain framework. Popular applications of smart contracts include cryptocurrencies and online gambling; those applications often involve financial transactions which consider as a part of the contract. Similar to conventional programs, smart contracts are written in Solidity [9], and can contain security vulnerabilities which could potentially lead to attacks. Unlike ordinary programs, the problem is overcome by an inability to correct smart contracts.

In recent years, some studies have demonstrated that all blockchain-based smart contracts contain some security vulnerabilities [17] and could encounter the attacks which can potentially lead to devastating losses [18, 19]. For example, structure attacks; such as forks [20], DDoS attacks [18], majority attacks [21], and double spending [22]. There is an increasing number of occurrences in smart contracts, and financial losses have been reported [18]. These attacks have been found to exploit the vulnerabilities in smart contracts. To give an example, there is an incident of a DAO attack, and this is considered as a result of a minor error in the DAO contract [23]. Moreover, on June 17, 2016, there were over 3.5 million of Ether have been stolen from the DAO smart contract [24].

According to a report published in 2018, the smart contract contains approximately 4.4 million dollars with an Ethereum value at that time, this could be a potential vulnerability for hackers to exploit it [25, 26]. Currently, 4,008 DApps and 7.16K smart contracts are executing on the blockchain networks (Figure 1) [27]. The most widespread blockchain networks have several security concerns that could be exploited by hackers.

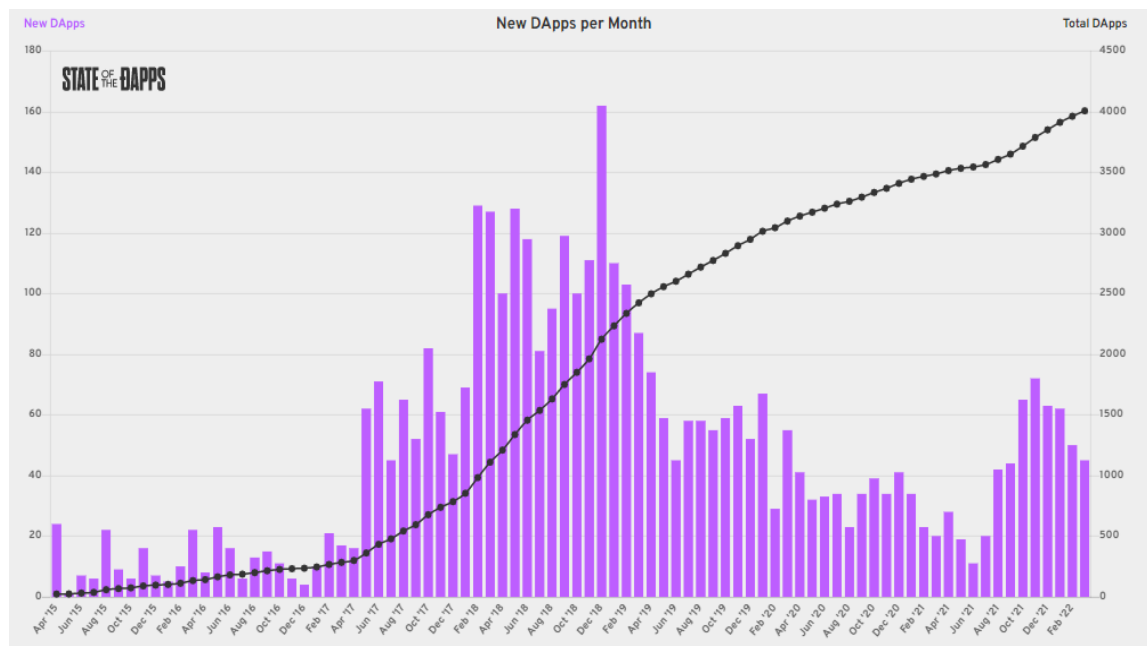


Figure 1. DApps per Month [27].

4. Material and Methods

In order to obtain the articles on this topic, we first establish a possibility of the following search criterias: search queries “smart contract vulnerabilities”, “contract vulnerabilities”, “smart contract attacks” applied to Arxiv [28] (143 article), and IEEEExplore [29] (443 article) digital library and general search. We will then obtain search results by reviewing title and abstracts. Non-English articles and those with different topics will also be eliminated.

5. Conclusions

As a result of the examination of the articles that meet the criteria, vulnerabilities in smart contracts that can easily be mistaken have been identified.

Reentrancy Attacks

Reentrancy attack on the smart contracts is a well-known vulnerability because this kind of attack allows attackers to take control of the flow on smart contracts. It is also known as an “unknown call,” or a “recursive call” vulnerability. Multiple parallel external initializations are possible using the structures call family. If the global state is not managed suitably, a contract may be vulnerable to delay attacks [30]. Hackers can take over the control flow, and make changes to your data that the calling function is not expected [31]. When the linked cross-function is in a racing state, two different functions will then operate on the same global state [30]. Smart contracts have found the opportunity to be used with Blockchain 2.0. In particular, Ethereum has started to be used in the infrastructure of crypto money. The particularly risky situation is when one contract calls another, the current execution has to wait for the call to finish. This can cause a problem especially when the recipient of the call is using the intermediate state the caller is in [32, 33]. An attacker can perform a parallel attack by using two different functions that share at the same state [34]. It is advised to use a built-in transfer() function, specifically when we make external calls to another untrusted contracts.

We also need to confirm all logics that could change the state variables that could happen before it sent out of the contract [35].

A code written in this way can be easily exploited by an attacker. Line 15 contains a bypassable vulnerability that can be recalled by the attacker (Figure 2).

```

1  contract Bank {
2      uint256 public paraCekmeLimiti = 1 ether;
3      mapping(address => uint256) public sonParaCekmeZamani;
4      mapping(address => uint256) public kalanPara;
5
6      function mevduat() public payable {
7          mevduatlar[msg.sender] += msg.value;
8      }
9
10     function paraCekmeFonu (uint256 _miktar) public {
11         require(mevduatlar[msg.sender] >= _miktar);
12         require(_miktar <= paraCekmeLimiti);
13         require(now >= sonParaCekmeZamani[msg.sender] + 1 weeks);
14         require(msg.sender.call.value(_miktar)());
15         mevduatlar[msg.sender] -= _miktar;
16         sonParaCekmeZamani[msg.sender] = now;
17     }
18 }
19

```

Figure 2. Reentry sample code

```

24  function Attacker() public payable {
25
26      require(msg.value >= 1 ether);
27      // send eth to the mevduat() function
28      Bank.mevduat.value(1 ether)();
29      // start the attack
30      Bank.paraCekmeFonu(1 ether);
31  }
32  function () payable {
33      if (etherStore.balance > 1 ether) {
34          bank.paraCekmeFonu(1 ether);
35      }
36  }

```

Figure 3. Reentry Attacker sample code

In cases where the necessary control is not performed by calling the same function again on the 30th and 34th lines, the transactions in the other expenditure can be started before the expenditure transaction is concluded (Figure 3).

Gas Limit Attacks

This attack is possible in a contract that accepts basic data and uses it to make another contract through the low-level `address.call ()` function, as is often the case in multi-signed and transactional situations [31]. It is claimed that we could avoid this potential vulnerability by looping over arrays of unknown length, setting an upper limit for the array length, and controlling the loop by inspecting the gas limit [36].

```
1  struct Payment {
2      address paymentAddress;
3      uint256 value;
4  }
5
6  Payment[] payments;
7  uint256 nextPaymentI;
8
9  function paymentOut() {
10     uint256 i = nextPaymentI;
11     while (i < payments.length && msg.gas > 200000) {
12         payments[i].paymentAddress.send(payments[i].value);
13         i++;
14     }
15     nextPaymentI = i;
16 }
```

Figure 4. Gas Limit sample code

It is necessary to ensure that there are no undesirable consequences if other transactions are processed while waiting for the next iteration of the `PaymentOut()` function. Therefore, this pattern should only be used if absolutely necessary (Figure 4).

Arithmetic Issues (Integer Overflow)

Integer overflow is a type of errors that can be found in many programming languages. It could cause a serious security vulnerability in blockchain applications. For example, if a loop counter overflow and creates an infinite loop, the contract then can be completely frozen. This overflow can be used by an attacker, especially when there is an increasing number of iterations in the loop which has been registered by new users of the agreement [30, 37]. Therefore, when writing contracts, we need to utilize a secure math libraries for all arithmetic operations, such as OpenZeppelin's `SafeMath` library [38].

Even the “solidity” library used in the example below has a great influence on whether the system malfunctions or not. When version 0.8.0 is used, the system works properly as a result of compilation (Figure 5, Figure 6).

```
1 pragma solidity 0.7.0;
2
3 contract ChangeBalance {
4     uint8 public balance;
5
6     function decrease() public {
7         balance--;
8     }
9
10    function increase() public {
11        balance++;
12    }
13 }
```

```
1 pragma solidity 0.8.0;
2
3 contract ChangeBalance {
4     uint8 public balance;
5
6     function decrease() public {
7         balance--;
8     }
9
10    function increase() public {
11        balance++;
12    }
13 }
```

Figure 5. Overflow sample code

```
[vm] from: 0x5B3...eddC4 to: ChangeBalance.decrease() 0x7EF...8CB47 value: 0 wei data: 0xd73...2d955 log: 0 hash: 0xa14...7259f

```

```
transact to ChangeBalance.decrease errored: VM error: revert.

```

```
revert

```

```
The transaction has been reverted to the initial state.
Note: The called function should be payable if you send value and the value you send should be less than your current balance.
Debug the transaction to get more information.
```

Figure 6. Overflow compile error

Delegatecall

A message except that the calls DELEGATECALL offered under the contract is the same as the destination address in the code calls. The destination address in the code call contract (Jiang et al., 2018) is carried out under a separate message call from the same DELEGATECALL called the message there are certain types of calls. When using DELEGATECALL, both the library contract and the possible negotiating conditions of the interview contract should be considered [30].

```
Delegatcall.sol
1  pragma solidity ^0.8.10;
2
3  contract Lib {
4      address public owner;
5
6      function pwn() public {
7          owner = msg.sender;
8      }
9  }
10
11 contract HackMe {
12     address public owner;
13     Lib public lib;
14
15     constructor(Lib _lib) {
16         owner = msg.sender;
17         lib = Lib(_lib);
18     }
19
20     fallback() external payable {
21         address(lib).delegatecall(msg.data);
22     }
23 }
24
25 contract Attack {
26     address public hackMe;
27
28     constructor(address _hackMe) {
29         hackMe = _hackMe;
30     }
31
32     function attack() public {
33         hackMe.call(abi.encodeWithSignature("pwn()"));
34     }
35 }
```

Figure 7. Delegatecall sample code

At first, HackMe works according to whether the pwn function is present in the Contract (Figure 7). Since there is no pwn function, HackMe's fallback function is triggered, which calls the Lib contract with the pwn function's signature. That the lib contract has the pwn function definition and the owner is set to msg.sender. With context protection msg.sender can now be used as owner of HackMe contract.

State Variable Visibility

Visibility is used to determine whether the functions should be invoked by users internally or externally from different contracts [30]. Variables or functions can be defined as public, private, or internal [27]. Private variables can only be accessed by a declaring contract itself, and internal variables can be accessed by defining contracts and the contracts derived from them [38]. It is obligatory to determine a visibility of all functions that are used in a contract in a controlled manner.

It is important to define public, internal and private accessibility in the example so that it does not cause clarity (Figure 8).

```
16  contract Accessibility {
17      uint public publicInt; //public
18      uint internal internalInt; //internal
19      uint private privateInt; //private
20  }
21  // can get and set from other smart contracts
22  contract AccessPublic {
23      Accessibility accessibility = new Accessibility();
24      function accessPublicInt() public view returns(uint) {
25          uint publicInt = accessibility.publicInt();
26          return publicInt;
27      }
28  }
```

Figure 8. State variable sample code

Bad Randomness

Ethereum has been exploited as a platform for a variety of blockchain applications, especially the ones that relate to random numbers, for instance the lottery and timestamps. Generating random numbers on the blockchain is technically difficult, and these numbers can simply be manipulated by attackers. `Block.timestamp` is one of the methods that has been adopted, but it is considered as a perilous tool, because Miners have an opportunity to select, modify, and manipulate those random numbers. Therefore, the utilize of block variables as a source should be avoided [38]. The following function can be used as the simplest random method (Figure 9).

```
30
31  // Randomness provided by this is predicatable. Use with care!
32  function randomNum() internal view returns (uint) {
33      uint random = uint(keccak256(_seed, blockhash(block.number - 1)));
34      return random;
35  }
```

Figure 9. Randomness sample code

External Contract Referencing

Reusing codes developed in Ethereum systems and interacting with other smart contracts in the network can provide plus benefits. Basically, many contracts call for a relationship with each other. Allowing such calls can help attackers use it as an attack surface. Any address in this state can be unintentionally used as a contract, the code in the address represents the type of

contract being issued. This can be dangerous, especially if the person who wrote the code is hiding something malicious in the code [32]. Avoid using external contracts for sensitive operations is an imperative safety measure, and if an external contract is required, the incoming data must be checked.

In the example below (Figure 10), the attacker was able to disable Line 77. In order to prevent this, It should be defined in the constructor section. `encryptionLibrary = new Rot13Encryption();`

```
71 import "Rot13Encryption.sol";
72 // encrypt your top-secret info
73 contract EncryptionContract {
74     // library for encryption
75     Rot13Encryption encryptionLibrary;
76     // constructor - initialize the library
77     encryptionLibrary = _encryptionLibrary;
78 }
79 function encryptPrivateData(string privateInfo) {
80     // potentially do some operations here
81     encryptionLibrary.rot13Encrypt(privateInfo);
82 }
83
```

Figure 10. External Contract sample code

Short Address/Parameter Attack

Parameter attack is considered as a classical SQL injection attack. As an attack method; If the EVM detects a substream when dealing with data types up to 256 bits, it adds 0 to the end of the address. The attacker is able to create this attack by removing the last zeros from an Ether address ending with 0 or multiple 0s at addresses in this situation [39].

If the necessary checks are not made, the system accepts both in the use made without the address below and the 00s at the end.

```
0xc3DC35818d54FDA1C4943bA98938cb6F46A91700
```

If the code in Figure 11 is checked for `msg.data.length` on line 88, it will not be accepted with `ashortaddress`.

```
85
86 contract NonPayloadAttackableToken {
87     modifier onlyPayloadSize(uint size) {
88         assert(msg.data.length >= size + 4);
89         _;
90     }
91     function transfer(address _to, uint256 _value) onlyPayloadSize(2 * 32) {
92         // todo
93     }
94 }
95
```

Figure 11. Short address sample code

Timestamp Dependency/Manipulation

Miners are generally considered as nodes that can interfere with transactions as an attacker. Potential danger is recognized if they have the opportunity to manipulate environmental variables and can profit from it. A miner can control the timestamp and gain an unfair advantage. They can use block numbers and the average time between blocks to estimate the current time [32], [40]. In the article published in 2019 by Mei et al. [41] Timestamp dependency was found to be the most common vulnerability [40].

In the simple roulette game below (Figure 12), miner spin can play with 1 Ether and then win for the next block. The 15 second rule should be applied. This rule is that the timestamp between two blocks within 15 seconds should not be more than 15 seconds. If the difference is phase, it should be rejected.

```
100 contract Roulette {
101     uint public pastBlockTime;
102     constructor() payable {}
103
104
105     function spin() external payable {
106         require(msg.value == 1 ether);
107         require(block.timestamp != pastBlockTime);
108         pastBlockTime = block.timestamp;
109
110         if(block.timestamp % 7 == 0) {
111             (bool sent, ) = msg.sender.call{value: address(this).balance}("");
112             require(sent, "Failed to send Ether");
113         }
114     }
115 }
116
```

Figure 12. Timestamp sample code

Denial Of Service (DOS)

DOS attacks are attacks that all internet-connected digital systems have to deal with from time to time. As a result of such an attack, it may be possible that the contracts become unusable for a while. This attack can freeze these contracts for an indefinite period or even indefinitely [32], [42].

In the example below, an attacker could repeatedly attack a new account, stressing the system unusable (Figure 13).

```
52 contract DistributeTokens {
53     address public owner; // gets set somewhere
54     address[] investors; // array of investors
55     uint[] investorTokens; // the amount of tokens each investor gets
56     // ... extra functionality, including transfertoken()
57     function invest() external payable {
58         investors.push(msg.sender);
59         investorTokens.push(msg.value * 5); // 5 times the wei sent
60     }
61     function distribute() public {
62         require(msg.sender == owner); // only owner
63         for(uint i = 0; i < investors.length; i++) {
64             // here transferToken(to,amount) transfers "amount" of
65             // tokens to the address "to"
66             transferToken(investors[i],investorTokens[i]);
67         }
68     }
69 }
70
```

Figure 13. DOS sample code

In order to avoid this attack, gas must be used in every account creation. It will also help in checking `require(msg.sender == owner || now > unlockTime)` for account.

tx.origin Authentication

Solidity has a distinctive method to check who is calling by using a function `msg.sender` [43]. We may use `tx.origin` to test who is calling as an alternative to `msg.sender`. As a result, an attack can be formed. A transactional attack is a form of phishing attack that can simply drain a contract of all funds [44].

```
38 contract PhishabletxOrigin {
39     address public owner;
40     constructor (address _owner) {
41         owner = _owner;
42     }
43     function () external payable {} |
44     function withdrawAll(address _recipient) public {
45         require(tx.origin == owner);
46         _recipient.transfer(this.balance);
47     }
48 }
```

Figure 14. tx.origin sample code

If the control is not performed on line 45 of the code shown in Figure 14, the attacker can show himself in the state of ownership. For this reason, it should be edited as `require (tx.origin == msg.sender)`.

6. Discussion

Several testing tools have recently emerged. Applications must be automatically checked for common security vulnerabilities from static analysis tool platforms, especially before a deployment of applications. [45], Chainsecurity [46], and Smartcheck [47] are some of them. The first written smart contract must be loaded on these systems, and a detailed result report must be examined by the system. A single application cannot detect all vulnerabilities (Table 1). Therefore, it will be efficacious to exploit different testing tools. It has been shown that while reentry attacks can be caught by all scanning programs, different results are obtained in different applications of other vulnerable parts.

When starting a new project, the first of the latest version should be preferred. Never use tx.origin for authorization checks [44]. In cases where randomness is needed, using an external source of randomness is a mandatory. Do not use the status check as the block timestamp may cause weaknesses. In addition to a frequent examination, we need to avoid a looping over especially when there is an unknown size of data structure. Using a safe library for arithmetic operations is another imperative safety measure that we must follow [38]. We should cautiously pay attention to the use of different contracts, and also avoid the codes that are obtained from untrusted sources [30].

Oyente was developed by researchers from the National University of Singapore in January 2016. Oyente can be defined as a symbolic execution tool that works directly with the Ethereum virtual machine (EVM) bytecode. Oyente is able to detect many vulnerabilities of Ethereum, especially the TheDAO bug. Currently, Oyente is available as a Docker image for easy testing and installation. It is available at <https://github.com/melonproject/oyente> and can be downloaded and tested [48].

Table 1. Tools matrix

Tool	Analysis Method	Source	Reentry	Timespend Manipulation	Tx.origin
<i>Ovente</i>	Heuristic	source code(.sol)	yes	yes	yes
<i>Chainsecurity</i>	Formal	Byte code and source code(.sol)	yes	no	no
<i>Smartcheck</i>	Analytic and Heuristic	source code(.sol)	yes	yes	yes

Unlike other examples, SmartCheck is a tool developed as a static analysis tool. SmartCheck translates Solidity source code into an XML-based intermediate representation and checks it against XPath patterns. Smartcheck is designed based on current knowledge of Solidity vulnerabilities. It has been noted that SmartCheck has limitations, as some error detection requires more sophisticated techniques such as defect analysis or even manual inspection [49].

7. Conclusion

We have done extensive research on vulnerability articles and online websites. This study identified several security vulnerabilities in the new blockchain-based smart contracts that are frequently used by many sectors. In this study, application developers have been advised to minimize their weaknesses. To improve smart contract security and its performance, we strongly suggest all users to employ safe practices and procedures. Nonetheless, in order to ensure the highest level of security, additional testings and repeating security audits on the blockchain-based smart contracts are required. Further research could be implemented if there is any present of unascertained vulnerabilities and practicable prevention.

Ethics in Publishing

There are no ethical issues regarding the publication of this study.

Conflict of Interest

The authors have no conflicts of interest to declare.

References

- [1] <https://bitcoin.org/bitcoin.pdf>, [Accessed]: 01.07.2022.
- [2] <https://bitcoin.org/en/> [Accessed]: 13.10.2022.
- [3] Lauslahti, K., Mattila, J. , Seppala, T. (2017) Smart Contracts How Will Blockchain Technology Affect Contractual Practices?. ETLA Reports, 1-27.
- [4] Dorri, A. , Kanhere, S. S., Jurdak, R., Gauravaram, P. (2017) Blockchain for IoT security and privacy: The case study of a smart home. IEEE. International Conference on Pervasive Computing and Communications Workshops (PerCom) Workshops, 618-623.

- [5] Leng, K., Bi, Y., Jing, L., Fu, H. C., Van Nieuwenhuysse, I. (2018) Research on agricultural supply chain system with double chain architecture based on blockchain technology. *Future Generation Computer Systems*, 86, 641-649.
- [6] Raikwar, M., Mazumdar, S., Ruj, S., Sen Gupta, S., Chattopadhyay, A., Lam, K.Y. (2018) A Blockchain Framework for Insurance Processes. *IFIP International Conference on New Technologies, Mobility and Security (NTMS)*, 1-4.
- [7] Amofa, S., Sifah, E. B., Kwame O. Agyekum, B. Abia, S., Xia, Q., Gao, J. (2018) A Blockchain-based Architecture Framework for Secure Sharing of Personal Health Data. *IEEE. International Conference on e-Health Networking, Applications and Services (Healthcom)*, 1-6.
- [8] Ma, Z., Huang, W., Gao, H. (2018) Secure DRM Scheme Based on Blockchain with High Credibility. *Chinese Journal of Electronic*, 27(5), 1025-1036.
- [9] Azaria, A., Ekblaw, A., Vieira, T., Lippman, A. (2016) MedRec: Using Blockchain for Medical Data Access and Permission Management. *International Conference on Open and Big Data*, 25-30.
- [10] Chen, B., Tan, Z., Fang, W. (2018) Blockchain-Based Implementation for Financial Product Management. *International Telecommunication Networks and Applications Conference*, 1-3.
- [11] <http://arxiv.org/abs/2007.00286> [Accessed]: 01.07.2022.
- [12] Kemmoe, V. Y., Stone, W., Kim, J., Kim, D., Son, J. (2020) Recent Advances in Smart Contracts: A Technical Overview and State of the Art. *IEEE Access*, 8, 117782-117801.
- [13] Li, X., Jiang, P., Chen, T., Luo, X., Wen, Q. (2020) A survey on the security of blockchain systems. *Future Generation Computer Systems*, 107, 841-853.
- [14] <https://nakamotoinstitute.org/static/docs/micropayments-and-mental-transaction-costs.pdf> [Accessed]: 01.07.2022.
- [15] <https://www.investopedia.com/terms/s/smart-contracts.asp> [Accessed]: 12.07.2022.
- [16] <https://ordina-jworks.github.io/blockchain/2017/05/10/Blockchain-Introduction.html#smart-contracts> [Accessed]: 13.09.2022.
- [17] Ribeiro, S. L.I., Barbosa, A. P. (2020) Risk Analysis Methodology to Blockchain-based Solutions. *Conference on Blockchain Research & Applications for Innovative Networks and Services (BRAINS)*, 59-60.
- [18] <http://arxiv.org/abs/1904.03487> [Accessed]: 13.11.2022.
- [19] Xu, J. J. (2016) Are blockchains immune to all malicious attacks?. *Financ Innovation*, 2(1), 25.
- [20] Wang, S., Wang, C., Hu, Q. (2019) Corking by Forking: Vulnerability Analysis of Blockchain. *IEEE Conference on Computer Communications*, 829-837.
- [21] Dey, S. (2018) Securing Majority-Attack in Blockchain Using Machine Learning and Algorithmic Game Theory: A Proof of Work. *Computer Science and Electronic Engineering*, 7-10.
- [22] Ramezan, G., Leung, C., Wang, J. Z. (2018) A Strong Adaptive, Strategic Double-Spending Attack on Blockchains. *International Conference on Internet of Things and IEEE Green Computing and Communications and IEEE Cyber, Physical and Social Computing and IEEE Smart Data*, 1219-1227.
- [23] Zhao, X., Chen, Z., Chen, X., Wang, Y., Tang, C. (2017) The DAO attack paradoxes in propositional logic. *International Conference on Systems and Informatics*, 1743-1746.
- [24] <https://www.wired.com/2016/06/50-million-hack-just-showed-dao-human/> [Accessed]: 23.10.2022.
- [25] <https://www.investopedia.com/news/ethereum-smart-contracts-vulnerable-hacks-4-million-ether-risk/> [Accessed]: 13.10.2022..

-
- [26] <https://www.findlaw.com/legalblogs/technologist/reports-ethereum-smart-contracts-are-far-from-secure/> [Accessed]: 14.10.2022.
- [27] <https://www.stateofthedapps.com/stats> [Accessed]: 14.10.2022.
- [28] <https://arxiv.org/> [Accessed]: 13.10.2022..
- [29] <https://ieeexplore.ieee.org/Xplore/home.jsp> [Accessed]: 13.10.2022.
- [30] <https://blog.sigmaprime.io/solidity-security.html#reentrancy> [Accessed]: 14.10.2022.
- [31] Atzei, N., Bartoletti, M., Cimoli, T. (2017) A Survey of Attacks on Ethereum Smart Contracts (SoK). Principles of Security and Trust, 164-186.
- [32] Dika, A., Nowostawski, M. (2018) Security Vulnerabilities in Ethereum Smart Contracts. IEEE International Conference on Internet of Things and IEEE Green Computing and Communications and IEEE Cyber, Physical and Social Computing and IEEE Smart Data, 955-962.
- [33] Luu, L., Chu, D.H., Olickel, H., Saxena, P., Hobor, A. (2016) Making Smart Contracts Smarter. ACM SIGSAC Conference on Computer and Communications Security, 254-269.
- [34] <https://consensys.github.io/smart-contract-best-practices/attacks/> [Accessed]: 13.10.2022.
- [35] <http://arxiv.org/abs/1902.06710> [Accessed]: 15.07.2022.
- [36] Grech, N., Kong, M., Jurisevic, A., Brent, L., Scholz, B., Smaragdakis, Y. (2018) MadMax: surviving out-of-gas conditions in Ethereum smart contracts. ACM Programming Language, 1-27.
- [37] Nan, Y., Yang, Z., Wang, X., Zhang, Y., Zhu, D., Yang, M. (2018) Finding Clues for Your Secrets: Semantics-Driven, Learning-Based Privacy Discovery in Mobile Apps. Network and Distributed System Security Symposium.
- [38] <https://yos.io/2018/10/20/smart-contract-vulnerabilities-and-how-to-mitigate-them/#vulnerability-all-data-is-public/> [Accessed]: 14.10.2022.
- [39] <https://medium.com/huzzle/ico-smart-contract-vulnerability-short-address-attack-31ac9177eb6b> [Accessed]: 13.10.2022.
- [40] Tikhomirov, S., Voskresenskaya, E., Ivanitskiy, I., Takhaviev, R., Marchenko, E., Alexandrov, Y. (2018) SmartCheck: Static Analysis of Ethereum Smart Contracts. IEEE/ACM 1st International Workshop on Emerging Trends in Software Engineering for Blockchain, 9-16.
- [41] Mei, X., Ashraf, I., Jiang, B., Chan, W. K. (2019) A Fuzz Testing Service for Assuring Smart Contracts. IEEE International Conference on Software Quality, Reliability and Security Companion, 544-545.
- [42] Saad, M., Njilla, L., Kamhoua, C., Kim, J., Nyang, D., Mohaisen, A. (2019) Mempool optimization for Defending Against DDoS Attacks in PoW-based Blockchain Systems. IEEE International Conference on Blockchain and Cryptocurrency, 285-292.
- [43] <https://consensys.github.io/smart-contract-best-practices/development-recommendations/solidity-specific/tx-origin/> [Accessed]: 14.10.2022.
- [44] <https://medium.com/coinmonks/solidity-tx-origin-attacks-58211ad95514>[Accessed]: 14.10.2022.
- [45] <https://github.com/enzymefinance/oyente> [Accessed]: 14.10.2022.
- [46] <https://chainsecurity.com/audits/> [Accessed]: 14.10.2022.
- [47] <https://smartdec.net/> [Accessed]: 14.10.2022.
- [48] <https://medium.com/haloblock/how-to-use-oyente-a-smart-contract-security-analyzer-solidity-tutorial-86671be93c4b> [Accessed]: 14.10.2022.
- [49] Tikhomirov, S., Voskresenskaya, E., Ivanitskiy, I., Takhaviev, R., Marchenko, E., Alexandrov, Y. (2018) SmartCheck: Static Analysis of Ethereum Smart Contracts. IEEE/ACM 1st International Workshop on Emerging Trends in Software Engineering for Blockchain, 9-16.

On Hybrid numbers with Gaussian Mersenne Coefficients

Serhat YILDIRIM¹, Fatih YILMAZ^{1*}

¹ Ankara Hacı Bayram Veli University, Department of Mathematics, 06900, Ankara/ Türkiye

Received: 15/08/2022, **Revised:** 30/11/2022, **Accepted:** 02/12/2022, **Published:** 30/03/2023

Abstract

In this paper, we consider hybrid numbers with Gaussian Mersenne coefficients and investigate their interesting properties such as the Generating function, Binet formula, Cassini, Catalan, Vajda, D'Ocagne and Honsberger identities. Moreover, we illustrate the results with some examples.

Keywords: generating function, binet formula, cassini identity, catalan identity, vajda identity.

Gauss Mersenne Katsayılı Hibrit Sayılar

Öz

Bu çalışmada, Gauss Mersenne katsayılı hibrit sayıların tanımı ve bazı karakteristik özellikleri incelendi. Bu bağlamda, Üreteç Fonksiyonu, Binet formülü, Cassini, Catalan, Vajda, D'Ocagne ve Honsberger eşitlikleri elde edildi.

Anahtar Kelimeler: üreteç fonksiyonu, binet formülü, cassini özelliği, catalan özelliği, vajda özelliği

*Corresponding Author: fatih.yilmaz@hbv.edu.tr

Serhat Yıldırım, <https://orcid.org/0000-0002-8398-1670>

Fatih Yılmaz, <https://orcid.org/0000-0001-7873-1979>

1. Introduction

Recently, there has been a huge amount of interest to hybrid numbers which can be considered as a generalization of the complex numbers and composed of a combination of the complex ($i^2 = -1$), hyperbolic ($h^2 = 1$) and dual numbers ($\varepsilon^2 = 0$). The set of hybrid numbers, for details see [1], are defined as below:

$$\mathbb{K} = \{a + bi + c\varepsilon + dh : a, b, c, d \in \mathbb{R}, i^2 = -1, \varepsilon^2 = 0, h^2 = 1, ih = -hi = \varepsilon + i\}.$$

Here, we want to take your attention that the product of any two hybrid numbers is done by exploiting the following table, please see [1]:

Table 1. Multiplication rule

•	1	i	ε	h
1	1	i	ε	h
i	i	-1	$1 - h$	$\varepsilon + i$
ε	ε	$h + 1$	0	$-\varepsilon$
h	h	$-\varepsilon - i$	ε	1

The Gaussian Mersenne sequence, denoted by GM_n , is defined by the recurrence relation

$$GM_n = 3GM_{n-1} - 2GM_{n-2}, \quad \text{for } n \geq 2$$

with the initial conditions $GM_0 = -i/2, GM_1 = 1$. Note that the recurrence relation of Gaussian Mersenne sequence [2] can be rewritten as follows:

$$GM_n = M_n + iM_{n-1}$$

where $M_0 = 0$ and $M_1 = 1$. Some values of the Gaussian Mersenne numbers are given in

Table 2. Gaussian Mersenne numbers

n	0	1	2	3	4	5	6	7
GM_n	$-i/2$	1	$3 + i$	$7 + 3i$	$15 + 7i$	$31 + 15i$	$63 + 31i$	$127 + 63i$

In literature, many researchers investigate some remarkable properties of some well-known sequences. For example, in [3], the authors get some properties for the Mersenne-Lucas hybrid numbers. In [4], the authors scrutinize some identities for the Mersenne, Jacobsthal and Jacobsthal-Lucas hybrid numbers. The authors obtain some results for the generalized

tetranacci hybrid numbers, in [5]. For some similar studies, please see the references [6, 7, 8, 9, 10, 11, 12] and the references therein.

In this paper, we consider the hybrid numbers with Gaussian Mersenne coefficients. Then we get some characteristic relations of them.

2. Preliminaries

At this section, we give the definition of hybrid numbers with Gaussian Mersenne coefficients, denoted by HGM_n .

Definition 2.1. : Let us define the hybrid numbers with Gaussian Mersenne coefficients as below:

$$HGM_n = GM_n + GM_{n+1}i + GM_{n+2}\varepsilon + GM_{n+3}h; \quad n \geq 0,$$

where HGM_n denotes the n th hybrid numbers with Gaussian Mersenne coefficients.

By using the definition of the HGM_n , we can write:

$$\begin{aligned} HGM_n &= GM_n + GM_{n+1}i + GM_{n+2}\varepsilon + GM_{n+3}h \\ &= 3GM_{n-1} - 2GM_{n-2} \\ &\quad + (3GM_n - 2GM_{n-1})i \\ &\quad + (3GM_{n+1} - 2GM_n)\varepsilon \\ &\quad + (3GM_{n+2} - 2GM_{n+1})h \end{aligned}$$

and

$$\begin{aligned} HGM_{n-1} &= GM_{n-1} + GM_n i + GM_{n+1} \varepsilon + GM_{n+2} h \\ HGM_{n-2} &= GM_{n-2} + GM_{n-1} i + GM_n \varepsilon + GM_{n+1} h \end{aligned}$$

In other words, for $n \geq 2$, the hybrid numbers with Gaussian Mersenne coefficients can be rewritten by following recurrence

$$HGM_n = 3HGM_{n-1} - 2HGM_{n-2},$$

with initial conditions $HGM_0 = 1 + \frac{7}{2}i + 6\varepsilon + 6h$ and $HGM_1 = 3 + 10i + 14\varepsilon + 12h$.

Table 3. Some Gaussian Mersenne hybrid numbers

n	HGM_n
0	$1 + \frac{7}{2}i + 6\varepsilon + 6h$
1	$3 + 10i + 14\varepsilon + 12h$
2	$7 + 23i + 30\varepsilon + 24h$
3	$15 + 49i + 62\varepsilon + 48h$
4	$31 + 101i + 126\varepsilon + 96h$
5	$63 + 205i + 254\varepsilon + 192h$
6	$127 + 413i + 510\varepsilon + 384h$
7	$255 + 829i + 1022\varepsilon + 768h$
8	$511 + 1661i + 2046\varepsilon + 1536h$

In order to find the generating function for the hybrid numbers with Gaussian Mersenne coefficients, we have to write the sequence as a power series where each term of the sequence corresponds to the coefficients of the series. For more details, please see [13].

Lemma 2.1. :

$$HGM_n = 2HGM_{n-1} + (1 + 3i + 2\varepsilon)$$

Proof. For $n \geq 0$, by exploiting $GM_{n+1} = 2GM_n + 1 + i$, please see [2];

$$\begin{aligned} HGM_n &= GM_n + GM_{n+1}i + GM_{n+2}\varepsilon + GM_{n+3}h \\ &= 2HGM_{n-1} + (1 + 3i + 2\varepsilon). \end{aligned}$$

3. Main Theorem and Proof

Theorem 3.1. : (Generating Function) The generating function for the hybrid numbers with Gaussian Mersenne coefficients is given by

$$g(x) = \sum_{n=0}^{\infty} (HGM_n)x^n = \frac{\left(1 + \frac{7}{2}i + 6\varepsilon + 6h\right) + \left(\frac{-i}{2} - 4\varepsilon - 6h\right)x}{1 - 3x + 2x^2}.$$

Proof. We first write

$$g(x) = HGM_0 + HGM_1x + HGM_2x^2 + \dots + HGM_nx^n + \dots$$

and compute

$$\begin{aligned} -3xg(x) &= -3HGM_0x - HGM_1x^2 - 3HGM_2x^3 - \dots - 3HGM_{n-1}x^n - \dots \\ 2x^2g(x) &= 2HGM_0x^2 + 2HGM_1x^3 + 2HGM_2x^4 + \dots + 2HGM_{n-2}x^n + \dots \end{aligned}$$

From the above it follows that

$$\begin{aligned} (1 - 3x + 2x^2)g(x) &= HGM_0 + (HGM_1 - 3HGM_0)x \\ &\quad + (HGM_2 - 3HGM_1 + 2HGM_0)x^2 \\ &\quad + (HGM_3 - 3HGM_2 + 2HGM_1)x^3 \\ &\quad \vdots \\ &\quad + (HGM_n - 3HGM_{n-1} + 2HGM_{n-2})x^n + \dots \end{aligned}$$

As a result, we find

$$\begin{aligned} g(x) &= \frac{HGM_0 + (HGM_1 - 3HGM_0)x}{1 - 3x + 2x^2} \\ &= \frac{\left(1 + \frac{7}{2}i + 6\varepsilon + 6h\right) + \left(\frac{-i}{2} - 4\varepsilon - 6h\right)x}{1 - 3x + 2x^2}. \end{aligned}$$

So, the proof is completed.

The Binet formula is obtained by the following result.

Theorem 3.2. (Binet Formula): For $n \geq 0$, the Binet formula for the hybrid numbers with Gaussian Mersenne coefficients is given by

$$HGM_n = A2^n + B,$$

$$\text{where } A = 2 + \frac{13}{2}i + 8\varepsilon + 6h \text{ and } B = -1 - 3i - 2\varepsilon. \tag{2.1}$$

Proof. By exploiting the generating function and the definition of the hybrid numbers with Gaussian Mersenne coefficients, we get

$$\begin{aligned}
 g(x) &= \frac{HGM_0 + (HGM_1 - 3HGM_0)x}{1 - 3x + 2x^2} \\
 &= \frac{\left(1 + \frac{7}{2}i + 6\varepsilon + 6h\right) + \left(\frac{-i}{2} - 4\varepsilon - 6h\right)x}{1 - 3x + 2x^2} \\
 &= \frac{A}{(1 - 2x)} + \frac{B}{(1 - x)},
 \end{aligned}$$

where

$$A = \left(2 + \frac{13}{2}i + 8\varepsilon + 6h\right) \text{ and } B = (-1 - 3i - 2\varepsilon).$$

It can be rewritten

$$\begin{aligned}
 \frac{\left(1 + \frac{7}{2}i + 6\varepsilon + 6h\right) + \left(\frac{-i}{2} - 4\varepsilon - 6h\right)x}{1 - 3x + 2x^2} &= \frac{\left(2 + \frac{13}{2}i + 8\varepsilon + 6h\right)}{1 - 2x} + \frac{(-1 - 3i - 2\varepsilon)}{1 - x} \\
 &= \left(\sum_{n=0}^{\infty} A2^n x^n\right) + \left(\sum_{n=0}^{\infty} Bx^n\right) \\
 &= \sum_{n=0}^{\infty} (A2^n + B)x^n
 \end{aligned}$$

where:

$$g(x) = \sum_{n=0}^{\infty} (A2^n + B)x^n.$$

i.e.;

$$HGM_n = A2^n + B.$$

So, the proof is completed.

Example 3.1. : For $n = 3$, the hybrid numbers with Gaussian Mersenne coefficients HGM_3 , with the Binet formula is

$$\begin{aligned}
 HGM_3 &= A2^3 + B \\
 &= \left(2 + \frac{13}{2}i + 8\varepsilon + 6h\right)2^3 - 1 - 3i - 2\varepsilon \\
 &= 15 + 49i + 62\varepsilon + 48h.
 \end{aligned}$$

Theorem 3.3. (Cassini Identity): For $n > 0$, the Cassini identity for the hybrid numbers with Gaussian Mersenne coefficients is given by

$$HGM_{n-1}HGM_{n+1} - HGM_n^2 = 2^n BA - 2^{n-1} AB,$$

where A and B are given in the equation (2.1).

Proof. From the Binet formula, we get;

$$\begin{aligned} HGM_{n-1}HGM_{n+1} - HGM_n^2 &= (A2^{n-1} + B)(A2^{n+1} + B) - (A2^n + B)(A2^n + B) \\ &= 2^{2n}A^2 + 2^{n-1}AB + 2^{n+1}BA + B^2 \\ &\quad - 2^{2n}A^2 - 2^nAB - 2^nBA - B^2 \\ &= 2^{n-1}AB + 2^{n+1}BA - 2^nAB - 2^nBA \\ &= AB(2^{n-1} - 2^n) + BA(2^{n+1} - 2^n) \\ &= 2^n BA - 2^{n-1} AB. \end{aligned}$$

So, the proof is completed.

Example 3.2. : For $n = 3$, the Cassini identity is

$$\begin{aligned} HGM_2HGM_4 - HGM_3^2 &= 2^3 BA - 2^2 AB \\ &= 2^3 \left(-\frac{39}{2} - \frac{61}{2}i - 18\varepsilon + 5h \right) \\ &\quad - 2^2 \left(-\frac{39}{2} + \frac{11}{2}i - 6\varepsilon - 17h \right) \\ &= -78 - 266i - 120\varepsilon + 108h. \end{aligned}$$

Theorem 3.4. (Catalan Identity): For $n, r \geq 0$, the Catalan identity for the hybrid numbers with Gaussian Mersenne coefficients is given by

$$HGM_{n-r}HGM_{n+r} - HGM_n^2 = 2^{n-r}(1 - 2^r)[AB - 2^r BA],$$

where A and B are given in the equation (2.1).

Proof. By considering the Binet formula, we have;

$$\begin{aligned} HGM_{n-r}HGM_{n+r} - HGM_n^2 &= (A2^{n-r} + B)(A2^{n+r} + B) - (A2^n + B)(A2^n + B) \\ &= 2^{2n}A^2 + 2^{n-r}AB + 2^{n+r}BA + B^2 \\ &\quad - 2^{2n}A^2 - 2^nAB - 2^nBA - B^2 \\ &= 2^{n-r}AB + 2^{n+r}BA - 2^nAB - 2^nBA \\ &= AB(2^{n-r}(1 - 2^r)) + BA(2^n(2^r - 1)) \end{aligned}$$

$$= 2^{n-r}(1 - 2^r)[AB - 2^r BA].$$

So, the proof is completed.

Example 3.3. : For $n = 3$, $r = 1$, the Catalan identity is

$$\begin{aligned} HGM_2 HGM_4 - HGM_3^2 &= 2^2(1 - 2)[AB - 2BA] \\ &= -2^2 AB + 2^3 BA \\ &= 2^3 BA - 2^2 AB \\ &= 2^3 \left(-\frac{39}{2} - \frac{61}{2}i - 18\varepsilon + 5h \right) \\ &\quad - 2^2 \left(-\frac{39}{2} + \frac{11}{2}i - 6\varepsilon - 17h \right) \\ &= -78 - 266i - 120\varepsilon + 108h. \end{aligned}$$

Theorem 3.5. (Vajda Identity): For $n, m, r \geq 0$, the Vajda identity for the hybrid numbers with Gaussian Mersenne coefficients is given by

$$HGM_{n+r} HGM_{n+k} - HGM_n HGM_{n+r+k} = 2^n(2^r - 1)[AB - 2^k BA],$$

where A and B are given in the equation (2.1).

Proof. We conclude from the Binet formula that

$$\begin{aligned} HGM_{n+r} HGM_{n+k} - HGM_n HGM_{n+r+k} &= (A2^{n+r} + B)(A2^{n+k} + B) - (A2^n + B)(A2^{n+r+k} + B) \\ &= 2^{2n+r+k} A^2 + 2^{n+r} AB + 2^{n+k} BA + B^2 \\ &\quad - 2^{2n+r+k} A^2 - 2^n AB - 2^{n+r+k} BA - B^2 \\ &= 2^{n+r} AB + 2^{n+k} BA - 2^n AB - 2^{n+r+k} BA \\ &= 2^n(2^r - 1)AB - 2^{n+k}(2^r - 1)BA \\ &= 2^n(2^r - 1)[AB - 2^k BA]. \end{aligned}$$

So, the proof is completed.

Example 3.4. : For $n = 2$, $r = 1$, $k = 1$, the Vajda identity is

$$HGM_3 HGM_3 - HGM_2 HGM_4 = 2^2(2 - 1)[AB - 2BA]$$

$$\begin{aligned}
 &= 2^2 AB - 2^3 BA \\
 &= -(2^3 BA - 2^2 AB) \\
 &= -\left[2^3 \left(-\frac{39}{2} - \frac{61}{2}i - 18\varepsilon + 5h\right) \right. \\
 &\quad \left. - 2^2 \left(-\frac{39}{2} + \frac{11}{2}i - 6\varepsilon - 17h\right)\right] \\
 &= -(-78 - 266i - 120\varepsilon + 108h) \\
 &= 78 + 266i + 120\varepsilon - 108h .
 \end{aligned}$$

Theorem 3.6. (D’Ocagne Identity): For $n, m \geq 0$, the D’Ocagne identity for the Gaussian Mersenne hybrid numbers is given by

$$HGM_m HGM_{n+1} - HGM_n HGM_{m+1} = (2^n - 2^m)[2BA - AB],$$

where A and B are given in the equation (2.1).

Proof. From the Binet formula, we see that

$$\begin{aligned}
 HGM_m HGM_{n+1} - HGM_n HGM_{m+1} &= (A2^m + B)(A2^{n+1} + B) \\
 &\quad - (A2^n + B)(A2^{m+1} + B) \\
 &= 2^{n+m+1}A^2 + 2^m AB + 2^{n+1}BA + B^2 \\
 &\quad - 2^{n+m+1}A^2 - 2^n AB - 2^{m+1}BA - B^2 \\
 &= 2^m AB + 2^{n+1}BA - 2^n AB - 2^{m+1}BA \\
 &= (2^m - 2^n)AB + (2^{n+1} - 2^{m+1})BA \\
 &= (2^n - 2^m)[2BA - AB].
 \end{aligned}$$

So, the proof is completed.

Example 3.5. : For $n = 3, m = 2$, the D’Ocagne identity is

$$\begin{aligned}
 HGM_2 HGM_4 - HGM_3 HGM_3 &= (2^3 - 2^2)[2BA - AB] \\
 &= (2^2)[2BA - AB] \\
 &= 2^3 BA - 2^2 AB
 \end{aligned}$$

$$\begin{aligned}
 &= 2^3 \left(-\frac{39}{2} - \frac{61}{2}i - 18\varepsilon + 5h \right) \\
 &\quad - 2^2 \left(-\frac{39}{2} + \frac{11}{2}i - 6\varepsilon - 17h \right) \\
 &= -78 - 266i - 120\varepsilon + 108h.
 \end{aligned}$$

Theorem 3.7. (Honsberger Identity): For $n, m \geq 0$, the Honsberger identity for the hybrid numbers with Gaussian Mersenne coefficients is given by

$$HGM_n HGM_m + HGM_{n+1} HGM_{m+1} = 2^{n+m}(5A^2) + 2^n(3AB) + 2^m(3BA) + 2B^2,$$

where A and B are given in the equation (2.1).

Proof. According to the Binet formula, we see that

$$\begin{aligned}
 HGM_n HGM_m + HGM_{n+1} HGM_{m+1} &= (A2^n + B)(A2^m + B) \\
 &\quad + (A2^{n+1} + B)(A2^{m+1} + B) \\
 &= 2^{n+m}A^2 + 2^nAB + 2^mBA + B^2 \\
 &\quad + 2^{n+m+2}A^2 + 2^{n+1}AB + 2^{m+1}BA + B^2 \\
 &= 2^{n+m}(5A^2) + 2^n(3AB) + 2^m(3BA) + 2B^2.
 \end{aligned}$$

So, the proof is completed.

Theorem 3.8. (Summation Formula):

$$\sum_{k=0}^n HGM_k = HGM_{n+1} - (n+1)(1+3i+2\varepsilon) - \left(1 + \frac{7}{2}i + 6\varepsilon + 6h\right).$$

Proof. By using the Lemma 2.1. ;

$$HGM_1 = 2HGM_0 + (1 + 3i + 2\varepsilon)$$

$$HGM_2 = 2HGM_1 + (1 + 3i + 2\varepsilon)$$

$$HGM_3 = 2HGM_2 + (1 + 3i + 2\varepsilon)$$

⋮

$$HGM_{n+1} = 2HGM_n + (1 + 3i + 2\varepsilon)$$

$$2 \sum_{k=0}^n HGM_k = \sum_{k=1}^{n+1} HGM_k - (n+1)(1+3i+2\varepsilon)$$

$$= \sum_{k=0}^n HGM_k - (n+1)(1+3i+2\varepsilon) - HGM_0 + HGM_{n+1}$$

i.e.;

$$\sum_{k=0}^n HGM_k = HGM_{n+1} - (n+1)(1+3i+2\varepsilon) - \left(1 + \frac{7}{2}i + 6\varepsilon + 6h\right).$$

So, the proof is completed.

4. Conclusion

In this study, we initially present the hybrid numbers with Gaussian Mersenne coefficients. Then, we investigate some interesting properties for them. At this content, we obtain the Binet formula by exploiting the generating function. Moreover, we get the Generating function, Cassini identity, Catalan identity, Vajda identity, D’Ocagne identity and Honsberger identity for the hybrid numbers with Gaussian Mersenne coefficients. Also, we illustrate the obtained results with some examples.

Ethics in Publishing

There are no ethical issues regarding the publication of this study.

Author Contributions

The authors contributed equally.

References

- [1] Özdemir, M. (2018) Introduction to Hybrid Numbers. *Adv. Appl. Clifford Algebras*, 28, 1-32.
- [2] Taşcı, D. (2021) On Gaussian Mersenne Numbers. *Journal of Science and Arts*, 21, 1021-1028.
- [3] Özkan, E. and Uysal, M. (2021) Mersenne-Lucas Hybrid Numbers. *Mathematica Montisnigri*, 52, 17-29.
- [4] Taşcı, D. and Sevgi, E. (2021) Some Properties between Mersenne, Jacobsthal and Jacobsthal-Lucas Hybrid Numbers. *Chaos, Solitons and Fractals*, 146, 1-4.
- [5] Soykan, Y. and Taşdemir, E. (2021) Generalized Tetranacci Hybrid Numbers. *Annales Mathematicae Silesianae*, 35, 113-130.

- [6] Alp, Y. and Koçer, E.G. (2021) Hybrid Leonardo numbers. *Chaos, Solitons and Fractals*, 150, 1-5.
- [7] İşbilir, Z. and Gürses, N. (2021) Pentanacci and Pentanacci-Lucas hybrid numbers. *Journal of Discrete Mathematical Sciences and Cryptography*, 1-21.
- [8] Kocer, E.G. and Alsan, H. (2021) Generalized Hybrid Fibonacci and Lucas p-numbers. *Indian Journal of Pure and Applied Mathematics*, 53(4), 948-955.
- [9] Kızılates, C. (2020) A new generalization of Fibonacci hybrid and Lucas hybrid numbers. *Chaos, Solitons and Fractals*, 130, 1-5.
- [10] Szynal-Liana, A. (2018) The Horadam hybrid numbers. *Discussiones Mathematicae—General Algebra and Applications*, 38, 91-98.
- [11] Uysal, M. and Özkan, E. (2022) Padovan Hybrid Quaternions and Some Properties. *Journal of Science and Arts*, 22(1), 121-132.
- [12] Szynal-Liana, A. and Włoch, I. (2020) On generalized Mersenne hybrid numbers. *Annales Universitatis Mariae Curie-Skłodowska, sectio A – Mathematica*, 74(1), 77-84.
- [13] Srivastava, H. M. and Manocha, H. L. (1984) *A Treatise on Generating Functions*, Halsted Press (Ellis Horwood Limited, Chichester), John Wiley and Sons, New York.

Biosynthesis of Zirconium dioxide Nanoparticles by *Streptomyces sp. HC1*: Characterization and Bioactivity

Gözde KOŞARSOY AĞÇELİ^{1*}, Hamideh HAMMAMCHİ¹, Nilüfer CİHANGİR¹,
Zümriye AKSU²

¹Hacettepe University, Department of Biology, Beytepe 06800, Ankara, TURKEY

²Hacettepe University, Department of Chemical Engineering, Ankara, Turkey

Received:20/10/2022, **Revised:** 02/02/2023, **Accepted:** 23/02/2023, **Published:** 30/03/2023

Abstract

Nanoparticles can be synthesized in many different ways. However, synthesis methods that are except of biosynthesis are very expensive and environmentally hazardous processes. Nanoparticles with various morphologies and shapes are frequently used in biosynthesis studies due to the advantages of their small size. Bio-synthesized nanoparticles gain great importance for reasons such as prevention of environmental pollution and being economical. Zirconium dioxide nanoparticles(ZrO₂ NPs) are prominent especially in dental coatings and photocatalytic applications. With this study, for the first time, zirconium dioxide nanoparticles biologically synthesized with *Streptomyces sp. HC1* strain were produced. The bio-synthesized ZrO₂ NPs were characterized different methods and instruments. Then the nanoparticles were studied their bioactivity especially antimicrobial and antibiofilm. The results confirmed the efficient antimicrobial effect of zirconium dioxide nanoparticles as well as efficient antibiofilm effect. The synthesis of ZrO₂ nanoparticles from *Streptomyces sp. HC1* by biological synthesis and determination of the bioactivity of these nanoparticles were reported for the first time in this work.

Keywords: zirconia nanoparticle, biosynthesis, antimicrobial, antibiofilm, *Streptomyces sp. HC1*

Zirkonyum dioksit Nanopartiküllerinin *Streptomyces sp. HC1* Tarafından Biyosentezi: Karakterizasyon ve Biyoaktivite

Öz

Nanopartiküller birçok farklı şekilde sentezlenebilir ancak biyosentez dışındaki sentez yöntemleri çok pahalı ve çevreye zararlı işlemlerdir. Çeşitli morfoloji ve şekillere sahip nanopartiküller, küçük boyutlarının avantajlarından dolayı biyosentez çalışmalarında sıklıkla kullanılmaktadır. Biyosentezlenen nanopartiküller, çevre kirliliğinin önlenmesi ve ekonomik olması gibi nedenlerle büyük önem kazanmaktadır. Zirkonyum dioksit nanopartikülleri (ZrO₂ NP'ler) özellikle diş kaplamalarında ve fotokatalitik uygulamalarda öne çıkmaktadır. Bu çalışma ile ilk kez zirkonyum dioksit nanopartikülleri biyolojik olarak *Streptomyces sp. HC1* suşu kullanılarak üretilmiştir. Biyo-sentezlenmiş ZrO₂ NP'leri, farklı yöntemler ve cihazlarla karakterize edildi. Daha sonra nanopartiküllerin biyoaktiviteleri, özellikle antimikrobiyal ve antibiyofilm üzerinde çalışıldı. Sonuçlar, zirkonyum dioksit nanopartiküllerin etkili antimikrobiyal etkisini ve ayrıca etkili antibiyofilm etkisini doğruladı. *Streptomyces sp. HC1*'den ZrO₂ nanoparçacıklarının biyolojik sentezi ve bu nanopartiküllerin biyoaktivitesinin belirlenmesi ilk kez bu çalışmada rapor edilmiştir.

Anahtar Kelimeler: zirkonyum nanopartikül, biyosentez, antimikrobiyal, antibiyofilm, *Streptomyces sp. HC1*

*Corresponding Author: gozdekosarsoy@hacettepe.edu.tr
Gözde KOŞARSOY AĞÇELİ, <https://orcid.org/0000-0001-8318-8990>
Hamideh HAMMAMCHİ, <https://orcid.org/0000-0002-2025-3828>
Nilüfer CİHANGİR, <https://orcid.org/0000-0002-0830-635X>
Zümriye AKSU, <https://orcid.org/0000-0002-2812-5345>

1. Introduction

Nanotechnology plays an increasingly significant role in many major technologies of the new millennium [1–3]. Nanoparticles as a result of their unique properties; It has widespread usage areas such as chemistry, biotechnology, agriculture, communication, defense, electronics, energy, environmental remediation, heavy industries, materials science, medicine, microbiology, optics, and various engineering fields [4]. Nanoparticles are used as carriers in growth factors, genes and some drugs. In in vitro and in Vivo imaging, nanoparticles act as cellular labels [5].

Zirconium (Zr) is a transition metal element of the titanium family in the periodic table [6]. Zirconia (ZrO_2) is one of the important materials used in the industry because of its high melting point, high mechanical properties, low thermal conductivity and high ionic conductivity [7–9]. ZrO_2 is transparent in the visible; it has high refractive index and bandgap values, good adhesion to substrates (glass, ceramics, silicon, polycor, and sapphire), thermal stability, and corrosion resistance [10]. Zirconia (ZrO_2) is a ceramic material with a number of interesting and useful properties [11]. Zirconium nanoparticles are used in different syntheses due to their various assets such as exceptional fracture toughness, high tensile strength and hardness [12]. Zirconium dioxide nanoparticles act as an important catalyst in medicine thanks to their wide optical, electrical, thermal and chemical properties. It is also used for dental fillings and dental crowns [13, 14]. In recent year, ZrO_2 nanoparticles are widely used in oxygen sensor, fuel cell, transparent optical devices, and fire retarding materials. In separation chromatography used to determine the absorbent properties of proteins in living creatures and various dyes, zirconium nanoparticles can act as supporting surfaces [15]. They are used in thermal barrier coatings in jet turbines and diesel engines to allow doing operation at higher temperatures [16, 17].

Currently, nanoscale metals are synthesized by chemical methods, which have undesirable effects such as environmental pollution, large energy consumption and potential health problems [18]. Green synthesis is more beneficial than conventional chemical synthesis because it costs less, reduces pollution and improves environmental and human health safety [19]. Biological synthesis of metal oxide nanoparticles is gaining importance day by day. Toxic substances formed during nanoparticle production are eliminated by biological synthesis. This method provides great advantage over physical and chemical synthesis as it is environmentally friendly, cost effective and can be scaled easily on a large scale [20]. An alternative environmentally benign bottom-up biosynthetic approach using microbes is being proposed in this report. From last few years, green bottom-up approaches using microorganisms have been successfully applied for the synthesis of nanocrystals of metal and metal oxides [21, 22]. Biosynthesis of nanoparticles has always been of great interest as an alternate to energy-intensive chemical methods [23, 24].

In recent years, different physical and chemical syntheses have been used for zirconium nanoparticles. Hydrothermal techniques, thermal decomposition, microwave plasma, sol-gel methods and laser ablation are among the newly developed techniques [25–29]. Zirconium (IV) alkoxides used in sol-gel method to synthesize zirconium dioxide nanoparticles cause high toxicity and high cost, making it difficult to control the homogeneity of different components [30]. Natural and environmentally friendly materials (eg reducing agents) are used in green synthesis. Some eco-friendly materials can also be used as final sealants and dispersants, which not only reduces energy consumption but also avoids the use of toxic and harmful reagents [31, 32]. At present, green synthesis mainly uses microorganisms (fungi, bacteria and algae) or extracts from the leaves, flowers, roots, bark, fruits and seeds of various plants. [33, 34]. The cost is reduced because the biological synthesis of nanoparticles requires low pH, temperature and pressure. The production of large-scale nanoparticles in the desired size and shape can be accomplished with a large amount of extracellular enzymes synthesized. Thus, the whole process can be environmentally friendly and cost-effective [35].

Bacteria, fungi, viruses, plants can biologically synthesize different metal nanoparticles (titanium, gold, silver, iron, zirconium etc.). The metal ion reduction abilities of these organisms are of great importance for nanoparticle synthesis. The production of different metal nanoparticles of some bacteria has been demonstrated by various studies. For example, *Desulfuromonas acetoxidans*, *Shewanella* spp. and *Magnetospirillum magnetotacticum* can synthesize iron oxide, *Serratia* and *Rhodobacter* can synthesize copper and cadmium sulfate, and *Escherichia coli* have the ability to produce cadmium nanoparticles. [35–39]. Deniz et al., in their study in 2019, successfully produced silver nanoparticles using the cytoplasmic fluids of *Coriolus versicolor* [40]. The rapid growth of bacteria under different temperature, pH and pressure conditions provides suitability for the synthesis of ZrO₂ nanoparticles [41]. Suriyaraj et al. synthesized ZrO₂ nanoparticles using an extremophilic bacterium, *Acinetobacter* sp., in their study in 2019 [42]. Ahmed et al. have recently synthesized zirconium nanoparticles with *Enterobacter* sp., which they isolated from paddy soils [43].

Here, we report the synthesis of ZrO₂ nanoparticles using soil bacterium *Streptomyces* sp. HC1. The biosynthesized zirconia nanoparticles were extensively characterized through and their antimicrobial and antibiofilm activity were evaluated against various pathogenic microorganisms.

2. Material and methods

2.1. Materials and microorganism

The microorganism culture of *Streptomyces* sp. HC1 was obtained from Hacettepe University Biotechnology Department, Turkey. Potassium hexafluorozirconate (K₂ZrF₆) and types of culture medium were purchased from Sigma-Aldrich and Merck.

2.2. Bacterial culture and zirconia nanoparticle biosynthesis

Streptomyces sp. HC1. mycelium or spores were inoculated 100 mL of LB medium in a 250 mL Erlenmeyer flask and incubated at 25°C, pH 9 with shaking at 200 rpm for 72 hours. The cultures taken after incubation were mixed with 10^{-3} M 100 mL K_2ZrF_6 (pH 3.6) solution, and the mixture suspension was incubated at 200 rpm for 24 hours [44]. Complex formed after adequate time of stirring was collected by centrifugation at 10000 rpm for 10 minutes. Separated complex was dried in oven at 40°C for 24 h. The sample was calcinated in muffle furnace at 450°C 3 hours to get zirconia NPs. Control experiments were performed with uninoculated media and K_2ZrF_6 solution to check the role of bacteria in the NP synthesis.

Ambient conditions were optimized for pH and zirconium concentration in order to obtain high efficiency nanoparticles. Results were measured with Zeta sizer.

2.3. Characterization of Zirconia NPs

Morphology and size dispersion of the zirconia NPs were documented by scanning electron microscopy (SEM) (Quanta 400F Field Emission). FTIR analysis was performed to confirm functional biomolecules related to zirconia nanoparticles. FTIR spectra were carried out a JASCO FT-IR 600 Spectrometer in the wavenumber region of 4000-400 cm^{-1} under nitrogen gas. All data manipulations were done by using JASCO Spectra Manager Software. The crystal form of zirconia nanoparticles was investigated by X-ray diffraction (XRD) (Rigaku Ultima-IV). Cu $K\alpha$ radiation with a wavelength of 1.54056 Å was used for the x-ray source. The zirconium nanoparticles were scanned in a 2θ range from 0° to 80° with 2° /min rate continuously with an accelerating voltage of 40 kV. Moreover, surface roughness of zirconia nanoparticle samples is measured by Veeco MultiMode V AFM with contact mode on 5 μ m x 5 μ m surface area. The average particle size and particle size distribution were measured using the Zeta-3000 HS Zetasizer(Malvern).

2.4. Antimicrobial effect

The antimicrobial effect of the zirconium nanoparticles were measured against Gram negative bacterium *E.coli* ATCC 35218, Gram positive bacterium *Staphylococcus aureus* ATCC 29213, yeast *Candida albicans* ATCC 10231 and mold *A. niger* ATCC6275 analyzed by the well diffusion method. Bacteria were inoculated into nutrient broth (Sigma–Aldrich, USA) and incubated at 37°C for 24 hours. Fungi were inoculated into sabouraud dextrose broth (Sigma–Aldrich, USA) and incubated at 30°C for 48 hours. The bacteria were inoculated on mueller hinton agar (Sigma–Aldrich, USA.), while fungal strains were inoculated on sabouraud dextrose agar (SDA, Merck). Agar plate was punched with a sterile cork borer of 5 mm size. 20 μ L ZrO_2 NPs poured with micropipette in the bore. *E.coli* and *S.aureus* incubated at 37°C, 48 hours. *C.albicans* and *Aspergillus niger* cultures incubated at 30°C, 48 hours.

2.5. Antibiofilm activities

Biofilm removal or disruption assay was evaluated using microtiter plate assay as previously described. The antibiofilm effect of the biologically synthesized zirconium dioxide nanoparticles was determined using *P. aeruginosa* ATCC 27853. After a 24-hour incubation at 37°C in LB agar, *Pseudomonas aeruginosa* ATCC 27853 cultures were prepared at a turbidity of 0.5 McFarland (10^8 CFU / mL: Colony Forming Unit / milliliter). The prepared cultures were taken into tubes containing 2% glucose tryptic soy broth (TSB) and incubated for 24 hours at 37°C. At the end of the incubation period, 1: 100 dilution of the cultures taken from TSB was made. 200µl of the diluted cultures were taken with sterile pipettes and added to 96-well microplates containing different concentrations (20 µL, 100 µL, 200 µL, 500 µL) of ZrO₂ NPs. 3 wells were used for each strain. TSB with 2% glucose without bacteria was used as a negative control of biofilm production. After the microplates were prepared, they were incubated at 37° C for 24 hours. At the end of the incubation period, the liquid medium in the microplates was poured and the wells were washed 3 times with distilled water. 200 µL of 2% crystal violet was added to each well and added. It was incubated for 30 minutes at room temperature. After 30 minutes, the wells were washed 3 times with distilled water and placed on the blotter paper and dried. 200 µL of ethanol:acetic acid (95: 5) was added to the wells that were sure to dry, and it was left for 10 minutes and the paint was dissolved. The biofilm waved on the wells was measured by spectrophotometer at 540 nm.

3. Results and discussion

Microorganisms produce some specific enzymes extracellularly, such as reductase, which are responsible for the enzymatic biological reduction of Zr⁴⁺ ions. According to the underlying mechanism of biological synthesis, the production of zirconium nanoparticles can be attributed to the redox of nicotinamide adenine dinucleotide (NAD⁺/NADH), which provides electrons for reduction of Zr⁴⁺ ions during nucleation [43].

The production of microorganisms for ZrO₂ NP synthesis was carried out on Nutrient Broth broth under optimum conditions, and 25 mL of the sample was transferred to a 75 mL sterile broth. After incubation, the cultures were mixed with 10⁻³ M 100 mL K₂ZrF₆ (pH 3.6) solution, adjusted to pH 5, 5.5, 6, 6.5 and 7 and incubated at 200 rpm for 24 hours again. The results were evaluated with zeta sizer.

As a result of the measurement, it has been determined that the optimum pH value of zirconium nanoparticle production environment for *Streptomyces* sp. HC1 is pH 6 (Fig.1). At this pH, the average size of nanoparticles was measured lower than other pH values.

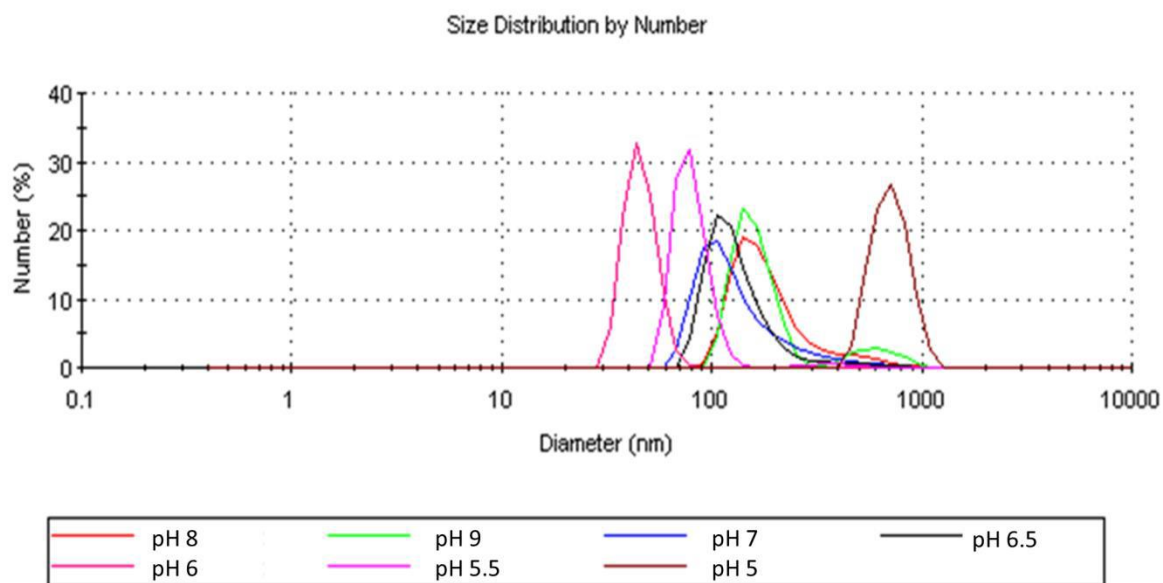


Fig.1. Size distribution of ZrO₂ nanoparticles synthesized under different pH conditions.

K₂ZrF₆: culture ratio was also evaluated in optimization of ZrO₂ nanoparticle production. It has been observed that zirconium nanoparticles have several effects on size distributions, and they fall below 10 nm with nanoparticle produced in 30:10 ratio (Fig.2).

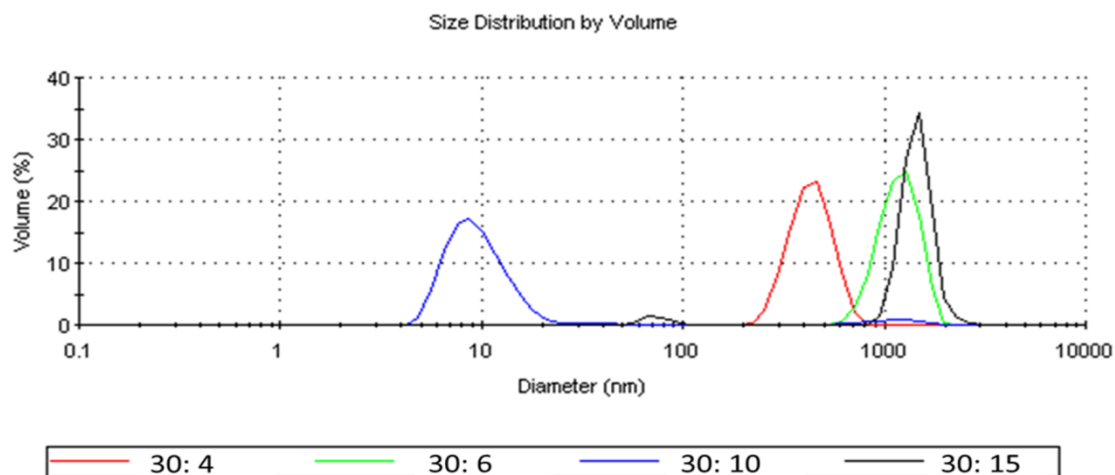


Fig.2. Size distribution graph of ZrO₂ nanoparticles by *Streptomyces* sp. HC1 with different K₂ZrF₆: culture concentrations.

3.1. Characterization of Zirconia Nanoparticles

Fig. 3. shows the FTIR spectra of the zirconia nanoparticles from *Streptomyces* sp. HC1. Since all samples are subjected to calcination, FTIR analysis is performed and the intensity of the above peaks is very small. Appearance of absorption band in the FTIR spectrum of the zirconia NP at 3420.36 cm⁻¹, was corresponds to the -OH bonds. At 1646.22 cm⁻¹, a weak band was

assigned to bending vibration of physically adsorbed H₂O [45]. Peaks between 961.30 and 1112.18 cm⁻¹ show the structure of Zr - O binding bands characteristic of the tetragonal phase of zirconium [45]. The FTIR spectra of ZrO₂ nanoparticles produced by Microwave Assisted Method in the 2019 study of Asha et al. also show similarities with the biosynthesis ZrO₂ performed in our study [46].

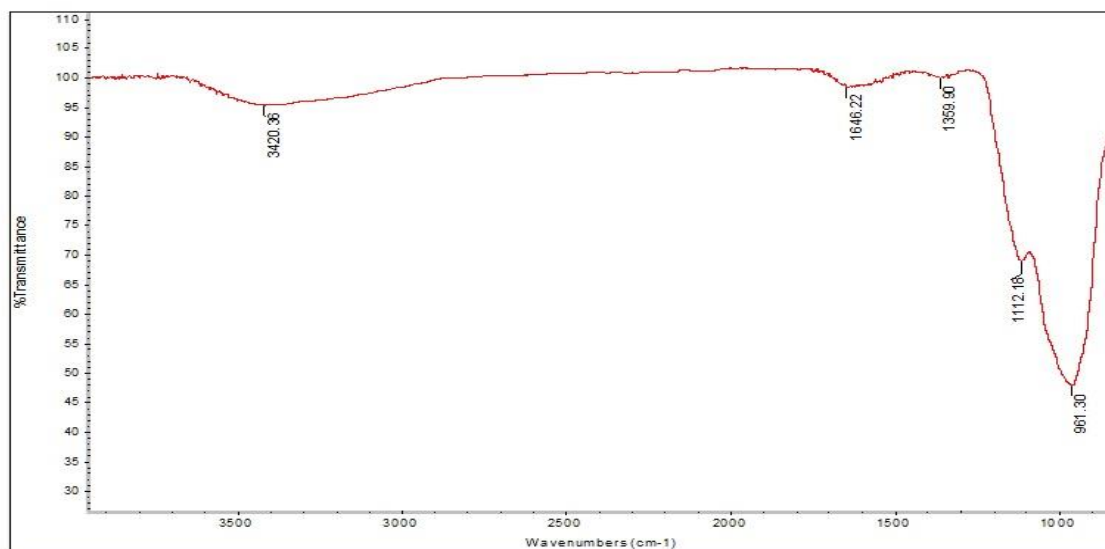


Fig. 3. FTIR spectra of the zirconium oxide nanoparticles synthesized by *Streptomyces sp. HC1*.

The XRD result of the Zirconia NPs produced with *Streptomyces sp. HC1*. is on the Fig. 4. It indicated sturdy diffraction peaks at 2 θ values of 27.56°, 31.58°, 45.395°, and 59.42°. XRD database, the diffraction peak at 30° is indicate by tetragonal structure of ZrO₂ while the diffraction peak at 28° and 31.5° is indicate by monoclinic structure of ZrO₂ [47].

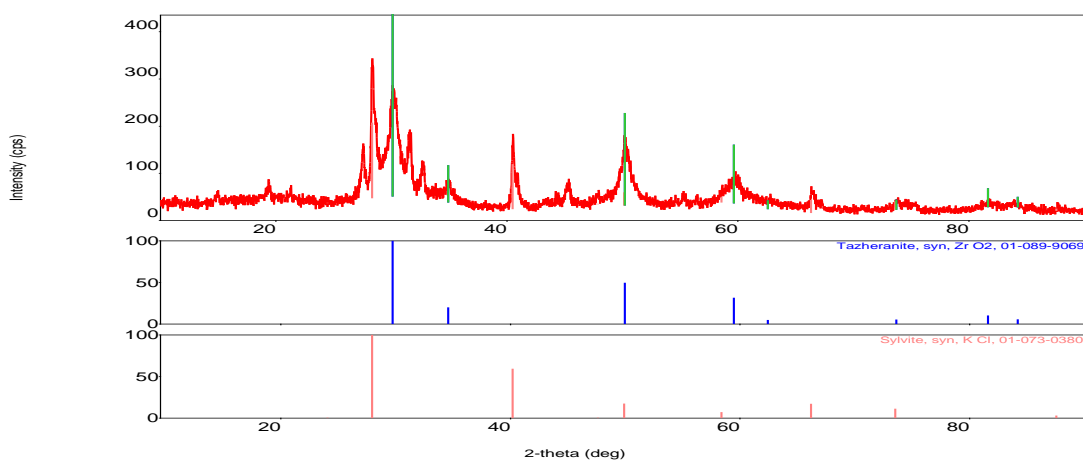


Fig.4. X-ray diffraction pattern of ZrO₂ synthesized by *Streptomyces sp. HC1*.

The average particle sizes of the synthesized zirconium nanoparticles were calculated using the Debye-Scherrer equation (1) given below [48, 49].

$$D = \frac{K \lambda}{\beta \cos \theta} \quad (\text{Eq.1})$$

D: average particle size, K: Scherrer constant (K) in the above formula accounts for the shape of the particle and is generally taken to have the value 0.9, λ : wavelength of light used for the diffraction 1.54060Å, β : full width at half maximum of the sharp peaks, θ : angle measured

Spherical and short-rod morphology of ZrO₂ nanoparticles has been confirmed from SEM imaging (Fig. 5.) Owing to aggregating/overlapping of smaller nanoparticles there are some larger particles that the average crystalline size could be 10 nm. The image clearly showed that the average zirconium oxide nanoparticles size could be 12.07±4.19 nm. The average size of ZnO₂ nanoparticles synthesized from *Fusarium oxysporum* in 2004 by Bansal et al. was reported as 7.3±2.0 nm [44].

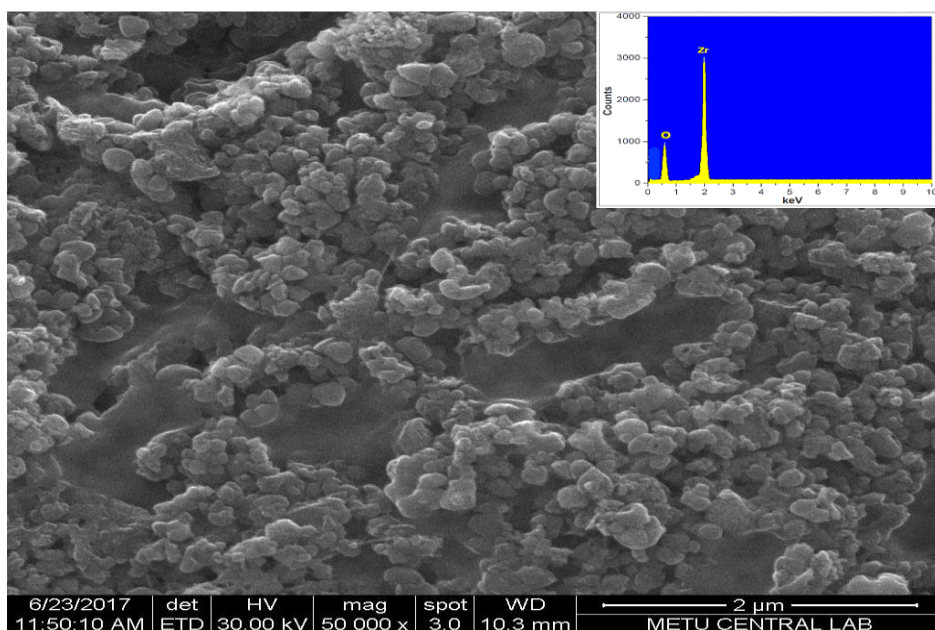


Fig. 5. SEM-EDX image of ZrO₂ nanoparticles by *Streptomyces* sp. HC1.

AFM characterization of nanostructured zirconium oxide is reported in Fig.6. Particle size dispersion of ZrO₂ nanoparticles was analyzed to be in the range of 9.5 to 18 nm. Substantially homogenous grooves were monitored in the 3-dimensional figure.

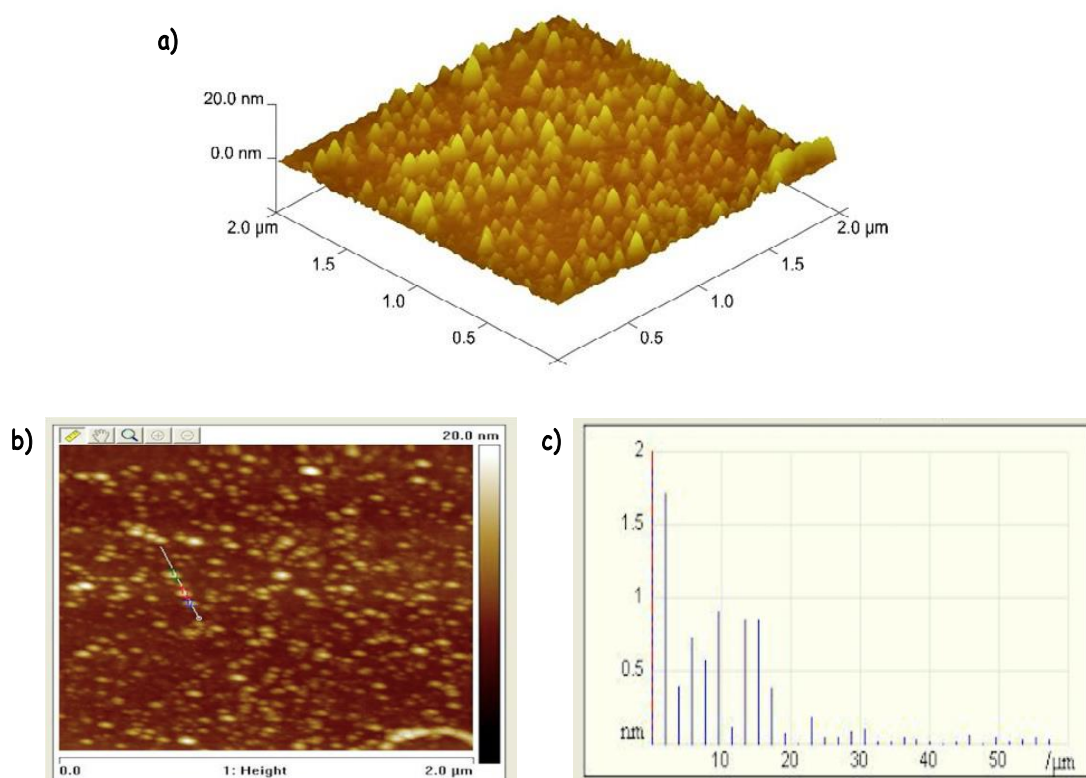


Fig. 6. AFM of zirconium oxide nanoparticles by *Streptomyces* sp. HC1. **a)** 3- dimensional image **b)** Sizes of three particles **c)** Particle size distribution curve

3.2. Antimicrobial effect of Zirconia NPs

Zirconia nanoparticles were tested for their antimicrobial efficacy against bacterial and fungal cultures by well diffusion method. The results showed that the zirconia NPs is more effective in *S. aureus* than *E. coli* and *C. albicans* (Table 1.) (Fig. 7.). In addition *Aspergillus niger* cultures were resistant zirconia NPs in this study.

Table 1. Antimicrobial effect of zirconia nanoparticles.

	Zone of Inhibition (mm)			
	<i>Escherichia coli</i>	<i>Staphylococcus aureus</i>	<i>Candida albicans</i>	<i>Aspergillus niger</i>
Zirconia NPs by <i>Streptomyces</i> sp. HC1	9.0 ± 0.07	11.0 ± 0.07	9.0 ± 0.07	-

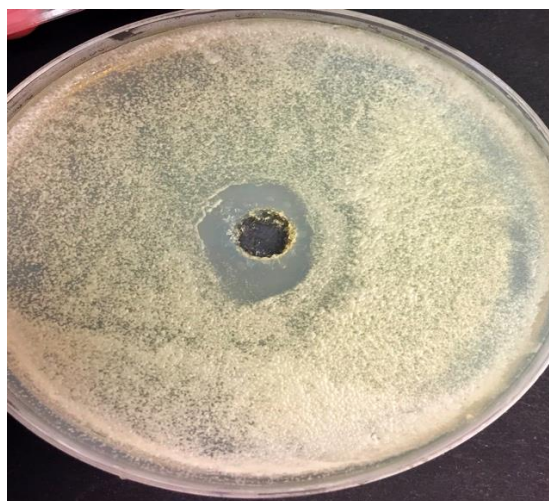


Fig.7. Antimicrobial effect of ZrO nanoparticles on *S.aureus*.

The antimicrobial effect of current studies were probably depending on many factors. Nanoparticles may react with the thiol group (- SH) in the bacterial cell wall, allowing the transport of nutrients through the cell wall, inactivate the protein and decrease the cell permeability and eventually causing the cellular death [50]. Recently, it has been demonstrated that metal oxide nanoparticles exhibit excellent biocidal and biostatic action against Gram positive and Gram negative bacteria [51]. Or may due to accumulation or deposition on the surface of *S. aureus* cells, disorganization of *E. coli* membranes, which increases membrane permeability leading to accumulation of NPs in the bacterial membrane and cytoplasmic regions of the cells [52].

3.3. Antibiofilm effect of Zirconia NPs

As a consequence, the maximum antibiofilm effect was for 500 μ L zirconia nanoparticles (Table 2.). About the antibiofilm properties of biologically synthesized zirconium oxide nanoparticles very few experiments have been done. Therefore, direct comparison of biofilm inhibition is difficult.

Table 2. Antibiofilm activities of zirconia NPs against *Pseudomonas aeruginosa*.

	Antibiofilm activities			
	20 μ L	100 μ L	200 μ L	500 μ L
Zirconia NPs by <i>Streptomyces</i> sp. HC1	Weak	Weak	Moderate	Strong

4. Conclusion

In addition to physical and chemical production, nanoparticles also have biological production. Biologically production is gaining importance day by day in terms of protecting the

environment and causing less harm to the environment. Nanoparticle production, which we realized in our study, is an example of biological production. Nanoparticle production, which we studied in the study, is an example of biological production. With this study, the zirconia nanoparticles were first biologically synthesized from *Streptomyces* sp. HC1 and these particles were confirmed to have antimicrobial and antibiofilm effects. *Streptomyces* sp. HC1 has been effectively used for the synthesis of zirconia nanoparticles. XRD analyzes of ZnO₂ nanoparticles obtained from *Streptomyces* sp. HC1 showed that the nanoparticles were synthesized with an average size of 12.07±4.19 nm. The antimicrobial effect of these ZnO₂ nanoparticles, which were synthesized by biosynthesis, against *Staphylococcus aureus* was found to be 11.0 ± 0.07 mm. ZnO₂ nanoparticles at a concentration of 500 µL showed a strong antibiofilm effect on *Pseudomonas aeruginosa*. This process for the biosynthesis of zirconia NPs is a green technology with no use of hazardous and toxic solvents or chemicals and hence is environment friendly.

References

- [1] Mandal, D., Bolander, M.E., Mukhopadhyay, D., Sarkar, G., Mukherjee, P. (2006) The use of microorganisms for the formation of metal nanoparticles and their application. *Appl. Microbiol. Biotechnol.*, 69, 485–492.
- [2] Dulta, K., Koşarsoy Ağçeli, G., Chauhan, P., Jasrotia, R., Chauhan, P.K. (2021) Ecofriendly Synthesis of Zinc Oxide Nanoparticles by *Carica papaya* Leaf Extract and Their Applications. *J Clust Sci.*, 33, 603–617.
- [3] Dulta, K., Koşarsoy Ağçeli, G., Chauhan, P., Jasrotia, R., Chauhan, P.K., Ighalo, J.O. (2022) Multifunctional CuO nanoparticles with enhanced photocatalytic dye degradation and antibacterial activity. *Sustain Environ Res* 32(1), 1–15.
- [4] Ighalo, J.O., Sagboye, P.A., Umenweke, G., Ajala, J.O., Omoarukhe, F.O., Adeyanju, C.A., Ogunniyi, S., Adeniyi, A.G. (2021) CuO Nanoparticles (CuO NPs) for Water Treatment: A Review of Recent Advances. *Environ Nanotechnology*, 15, 100443.
- [5] Kannan, S.K., Sundrarajan, M. (2015) Biosynthesis of Yttrium oxide nanoparticles using *Acalypha indica* leaf extract. *Bull Mater Sci.*, 38, 945–950.
- [6] Cazado, M.E., Goldberg, E., Togneri, M.A., Denis, A., Soba, A. (2021) A new irradiation growth model for Zr-based components of nuclear reactors for the DIONISIO code. *Nucl Eng Des.*, 373, 111009.
- [7] Sekulić, A., Furić, K., Stubičar, M. (1997) Raman study of phase transitions in pure and alloyed zirconia induced by ball-milling and a laser beam. In: *Journal of Molecular Structure*, 410-411, 275-279.
- [8] Ray, J.C., Saha, C.R., Pramanik, P. (2002) Stabilized nanoparticles of metastable ZrO₂ with Cr³⁺/Cr⁴⁺ cations: Preparation from a polymer precursor and the study of the thermal and structural properties. *J Eur Ceram Soc.*, 22(6), 851-862.

- [9] Peshev, P., Stambolova, I., Vassilev, S., Stefanov, P., Blaskov, V., Starbova, K., Starbov, N. (2003) Spray pyrolysis deposition of nanostructured zirconia thin films. *Mater Sci Eng B Solid-State Mater Adv Technol.*, 97 (1), 106-110.
- [10] Tran, V., Nguyen, D.T.C., Kumar, P.S., Din, A.T.M., Jalil, A.A., Vo, D.V.N. (2022) Green synthesis of ZrO₂ nanoparticles and nanocomposites for biomedical and environmental applications: a review. *Environ. Chem. Lett.*, 20, 1309–1331.
- [11] Zink, N., Emmerling, F., Häger, T., Panthöfer, M., Tahir, M.N., Kolb, U., Tremel, W. (2013) Low temperature synthesis of monodisperse nanoscaled ZrO₂ with a large specific surface area. *Dalt Trans.*, 42, 432-440.
- [12] Dong, Z., Yang, Q., Mei, M., Liu, L., Sun, J., Zhao, L., Zhou, C. (2018) Preparation and characterization of fluoride calcium silicate composites with multi-biofunction for clinical application in dentistry. *Compos Part B Eng.*, 143, 243-249.
- [13] Kim, J.S., Lee, D.H., Kang, S., Bae, D.S., Park, H.Y., Na, M.K. (2009) Synthesis and microstructure of zirconia nanopowders by glycothermal processing. *Trans Nonferrous Met Soc China (English Ed.)*, 19(1), 88-91.
- [14] Geethalakshmi, T.P., Hemalatha, J. (2012) Dielectric Studies on Nano Zirconium Dioxide Synthesized through Co-Precipitation Process. *Int J Mater Metall Eng.*, 6(4), 256-259.
- [15] Kumar, S., Bhanjana, G., Dilbaghi, N., Manuja, A. (2012) Comparative investigation of cellular response of nanoparticles. *Adv Mater Lett.*, 3(4), 345-349.
- [16] Reddy, B.M., Sreekanth, P.M., Yamada, Y., Kobayashi, T. (2005) Surface characterization and catalytic activity of sulfate-, molybdate- and tungstate-promoted Al₂O₃-ZrO₂ solid acid catalysts. *J Mol Catal A Chem.*, 227, 81-89.
- [17] Mueller, R., Jossen, R., Pratsinis, S.E., Watson, M., Kamal Akhtar, M. (2004) Zirconia Nanoparticles Made in Spray Flames at High Production Rates. *J Am Ceram Soc.*, 87(2), 197-202.
- [18] Pal, G., Rai, P., Pandey, A. (2019) Green Synthesis, Characterization and Applications of Nanoparticles, Ashutosh Kumar Shukla, Siavash Iravani, Green synthesis of nanoparticles: A greener approach for a cleaner future (1-26), Elsevier, United States.
- [19] Ying, S., Guan, Z., Ofoegbu, P.C., Clubb, P., Rico, C., He, F., Hong, J. (2022) Green synthesis of nanoparticles: Current developments and limitations. *Environ. Technol. Innov.*, 26, 102336.
- [20] Gardea-Torresdey, J.L., Parsons, J.G., Gomez, E., Peralta-Videa, J., Troiani, H.E., Santiago, P., Yacaman, M.J. (2002) Formation and Growth of Au Nanoparticles inside Live Alfalfa Plants. *Nano Lett.*, 2(4), 397–401.
- [21] Singh, A.V., Batuwangala, M., Mundra, R., Mehta, K., Patke, S., Falletta, E., Patil, R., Gade, W.N. (2014) Biom mineralized anisotropic gold microplate-macrophage

- interactions reveal frustrated phagocytosis-like phenomenon: A novel paclitaxel drug delivery vehicle. *ACS Appl Mater Interfaces.*, 6(16), 14679–14689.
- [22] V. Singh, A., Patil, R., Anand, A., Milani, P., Gade, W.N. (2010) Biological Synthesis of Copper Oxide Nano Particles Using *Escherichia coli*. *Curr Nanosci.*, 6(4), 365-369.
- [23] Parab, H., Shenoy, N., Kumar, S.A., Kumar, S.D., Reddy, A.V.R., (2016) One pot spontaneous green synthesis of gold nanoparticles using *Cocos nucifera* (coconut palm) coir extract. *J Mater Environ Sci.* 7(7), 2468-2481.
- [24] Aitenneite, H., Abboud, Y., Tanane, O., Solhy, A., Sebti, S., El Bouari, A., (2016) Rapid and green microwave-assisted synthesis of silver nanoparticles using aqueous *Phoenix dactylifera* L. (date palm) leaf extract and their catalytic activity for 4-Nitrophenol reduction. *J Mater Environ Sci.* 7(7), 2335-2339.
- [25] Tan, D., Teng, Y., Liu, Y., Zhuang, Y., Qiu, J. (2009) Preparation of zirconia nanoparticles by pulsed laser ablation in liquid. *Chem Lett.*, 38(11), 1102-1103.
- [26] Brossmann, U., Sagmeister, M., Pölt, P., Kothleitner, G., Letofsky-Papst, I., Szabó D, V., Würschum, R. (2007) Microwave plasma synthesis of nano-crystalline YSZ. *Phys Status Solidi - Rapid Res Lett.*, 1(3), 107-109.
- [27] Salavati-Niasari, M., Dadkhah, M., Davar, F. (2009) Pure cubic ZrO₂ nanoparticles by thermolysis of a new precursor. *Polyhedron.*, 28(14), 3005-3009.
- [28] Meetei, S.D., Singh, S.D. (2014) Hydrothermal synthesis and white light emission of cubic ZrO₂:Eu³⁺ nanocrystals. *J Alloys Compd.*, 587, 143-147.
- [29] Majedi, A., Davar, F., Abbasi, A. (2014) Sucrose-mediated sol-gel synthesis of nanosized pure and S-doped zirconia and its catalytic activity for the synthesis of acetyl salicylic acid. *J Ind Eng Chem.*, 20(6), 4215-4223.
- [30] Lin, C., Zhang, C., Lin, J. (2007) Phase transformation and photoluminescence properties of nanocrystalline ZrO₂ powders prepared via the pechini-type sol-gel process. *J Phys Chem C.*, 111(8), 3300–3307.
- [31] Devi, H.S., Boda, M.A., Shah, M.A., Parveen, S., Wani, A.H. (2019) Green synthesis of iron oxide nanoparticles using *Platanus orientalis* leaf extract for antifungal activity. *Green Process Synth.*, 8(1), 0145.
- [32] Can, M. (2020) Green gold nanoparticles from plant-derived materials: An overview of the reaction synthesis types, conditions, and applications. *Rev. Chem. Eng.*, 36(7), 145915309.
- [33] Vijay Kumar, P.P.N., Pammi, S.V.N., Kollu, P., Satyanarayana, K.V.V., Shameem, U. (2014) Green synthesis and characterization of silver nanoparticles using *Boerhaavia diffusa* plant extract and their anti bacterial activity. *Ind Crops Prod.*, 52, 562-566.
- [34] Leili, M., Fazlzadeh, M., Bhatnagar, A. (2018) Green synthesis of nano-zero-valent iron

- from Nettle and Thyme leaf extracts and their application for the removal of cephalexin antibiotic from aqueous solutions. *Environ Technol (United Kingdom)*, 39(9), 1158-1172.
- [35] Narayanan, K.B., Sakthivel, N. (2010) Biological synthesis of metal nanoparticles by microbes. *Adv. Colloid Interface Sci.*, 156 (1-2), 1-13.
- [36] Ash, A., Revati, K., Pandey, B.D. (2011) Microbial synthesis of iron-based nanomaterials - A review. *Bull. Mater. Sci.*, 34, 191–198.
- [37] Hasan, S.S., Singh, S., Parikh, R.Y., Dharne, M.S., Patole, M.S., Prasad, B.L.V., Shouche, Y.S. (2008) Bacterial synthesis of copper/copper oxide nanoparticles. *J Nanosci Nanotechnol.*, 8(6), 3191-6.
- [38] Huang, J., Lin, L., Li, Q., Sun, D., Wang, Y., Lu, Y., He, N., Yang, K., Yang, X., Wang, H., Wang, W., Lin, W. (2008) Continuous-flow biosynthesis of silver nanoparticles by lixivium of sundried cinnamomum camphora leaf in tubular microreactors. *Ind Eng Chem Res.*, 47 (16), 6081–6090.
- [39] Sweeney, R.Y., Mao, C., Gao, X., Burt, J.L., Belcher, A.M., Georgiou, G., Iverson, B.L. (2004) Bacterial biosynthesis of cadmium sulfide nanocrystals. *Chem Biol.*, 11(11), 1553-9.
- [40] Deniz, F., Adıgüzel, A.O., Mazmancı, M.A. (2019) The biosynthesis of silver nanoparticles with *Coriolus versicolor*. *Turkish J Eng.*, 3(2), 92-96.
- [41] Ram, S., Mitra, M., Shah, F., Tirkey, S.R., Mishra, S. (2020) Bacteria as an alternate biofactory for carotenoid production: A review of its applications, opportunities and challenges. *J. Funct. Foods*, 67, 103867.
- [42] Suriyaraj, S.P., Ramadoss, G., Chandraraj, K., Selvakumar, R. (2019) One pot facile green synthesis of crystalline bio-ZrO₂ nanoparticles using *Acinetobacter* sp. KCS11 under room temperature. *Mater Sci Eng C Mater Biol Appl.*, 105, 110021.
- [43] Ahmed, T., Ren, H., Noman, M., Shahid, M., Liu, M., Ali, M.A., Zhang, J., Tian, Y., Qi, X., Li, B. (2021) Green synthesis and characterization of zirconium oxide nanoparticles by using a native *Enterobacter* sp. and its antifungal activity against bayberry twig blight disease pathogen *Pestalotiopsis versicolor*. *NanoImpact.*, 21, 100281.
- [44] Bansal, V., Rautaray, D., Ahmad, A., Sastry, M. (2004) Biosynthesis of zirconia nanoparticles using the fungus *Fusarium oxysporum*. *J Mater Chem.*, 14 (22), 3303-3305.
- [45] Dwivedi, R., Maurya, A., Verma, A., Prasad, R., Bartwal, K.S. (2011) Microwave assisted sol-gel synthesis of tetragonal zirconia nanoparticles. *J Alloys Compd.*, 509 (24), 6848-6851.

- [46] Baby, Asha, S., Muthuraj, D., Kumar, E., Veeraputhiran, V. (2019) Synthesis and Characterization of ZrO₂ Nanoparticles using Microwave Assisted Method and Its Antimicrobial Activity. *J Nanosci Technol.*, 5(1), 642-644.
- [47] Lim, H.S., Ahmad, A., Hamzah, H. (2013) Synthesis of zirconium oxide nanoparticle by sol-gel technique. In: *AIP Conference Proceedings*, 1571, 812.
- [48] Lanje, A.S., Ningthoujam, R.S., Sharma, S.J., Pode, R.B., Vatsa, R.K., (2010) Luminescence properties of Sn_{1-x}Fe_xO₂ Nanoparticles. *Int J Nanotechnol.*, 7, 9-12.
- [49] Bokuniaeva, A.O., Vorokh, A.S. (2019) Estimation of particle size using the Debye equation and the Scherrer formula for polyphasic TiO₂ powder. In: *Journal of Physics: Conference Series*, Conf. Ser. 1410 012057.
- [50] Zhang, H., Chen, G. (2009) Potent antibacterial activities of Ag/TiO₂ nanocomposite powders synthesized by a one-pot sol-gel method. *Environ Sci Technol.*, 43, 8, 2905–2910.
- [51] M. Lopez Goerne, T. (2011) Study of Bacterial Sensitivity to Ag-TiO₂ Nanoparticles. *J Nanomed Nanotechnol.*, S5, 003.
- [52] Masoodiyeh, F., Karimi-Sabet, J., Khanchi, A.R., Mozdianfard, M.R. (2015) Zirconia nanoparticle synthesis in sub and supercritical water - particle morphology and chemical equilibria. *Powder Technol.*, 269, 461-469.

Electrochemical Behavior of CoO/Ag₂O/TiO₂ Ceramic and Composite Coated Selective Laser Manufactured 316L Stainless Steel

Tuba YETİM^{1*}

¹Erzurum Technical University, Faculty of Engineering and Architecture, Department of Chemical Engineering, Erzurum, Turkey

Received:03/02/2023, **Revised:** 27/02/2023, **Accepted:** 28/02/2023, **Published:** 30/03/2023

Abstract

In order to improve the corrosion resistance of 316L stainless steel manufactured by Selective Laser Melting (SLM) additive manufacturing, Ag₂O, CoO, and TiO₂ separately and Ag₂O/CoO/TiO₂ composite ceramic films were coated on the 316L surface by a sol-gel dip coating method. The structural properties of the uncoated and coated samples were characterized by XRD and SEM. The corrosion resistance for all samples was evaluated by potentiodynamic polarization and electrochemical impedance spectroscopy (EIS) tests in the simulated saliva fluid (SSF). According to the experimental results, quite dense, non-colonic, non-porous, compact, and between 30-40 µm thicknesses ceramic oxide films were formed successfully on the 316L sample surface. Also, all ceramic films increased the corrosion resistance of the 316L surface. The most corrosion-resistant surface was obtained at the Ag₂O/CoO/TiO₂ composite ceramic film-coated 316L surface.

Keywords: Additive manufacturing (SLM), 316L stainless steel, ceramic coating films, sol-gel dip coating, corrosion

CoO/Ag₂O/TiO₂ Seramik ve Kompozit ile Kaplanan Seçici Lazer ile Üretilmiş 316L Paslanmaz Çeliğin Elektrokimyasal Davranışı

Öz

Seçici lazer ergitme eklemeli üretim yöntemi ile üretilmiş 316L paslanmaz çeliğinin korozyon direncini artırmak için ayrı ayrı Ag₂O, CoO, ve TiO₂ ve Ag₂O/CoO/TiO₂ kompozit seramik film 316L yüzeyine sol-jel dip kaplama metodu ile kaplandı. Kaplanmış ve kaplanmamış numunelerin yapısal özellikleri XRD ve SEM ile karakterize edildi. Numunelerin tamamının korozyon direnci simüle edilmiş yapay tükürük sıvısı içerisinde potansiyodinamik polarizasyon ve elektrokimyasal empedans spektroskopisi (EIS) testleri değerlendirildi. Test sonuçlarına göre, oldukça yoğun, kolonsal ve porlu olmayan, kompakt ve 30-40 µm kalınlığında seramik oksit filmler 316L yüzeyinde oluşturuldu. Ayrıca bütün seramik filmler 316L yüzeyinin korozyon direncini artırdı. En yüksek korozyon dirençli yüzey Ag₂O/CoO/TiO₂ kompozit seramik film kaplı 316L yüzeyinde elde edildi.

Anahtar Kelimeler: Eklemeli imalat (SLM), 316L paslanmaz çelik, seramik kaplamalı filmler, sol-jel daldırma kaplama, korozyon

1. Introduction

Recently, the additive manufacturing method has become a very remarkable and popular production method used in the production of parts in many fields such as healthcare, aerospace, automobile manufacturing, and medical materials [1-5]. Additive manufacturing (AM) technology is based on the layer-by-layer deposition of materials in three-dimensional form. In this way, complex geometries can be produced at a low-cost [1, 6-11]. Among various AM technologies, selective laser melting (SLM) has been widely preferred in manufacturing used to produce Co-Cr-Mo, stainless steel, titanium, and its alloys [12-15]. In the SLM mechanism, a powder layer with a defined thickness is deposited on a movable base plate. Then, a precise laser beam scans the powder bed according to the slice data of a CAD model. Powder particles are melted quickly by the laser beam completely and the melt quickly solidifies to form a solid layer. After this, the piston moves down a defined distance, and the next powder layer is deposited. This process is repeated layer by layer until the production is completed. Finally, the non-sintered powder is removed, and the product is completed. The SLM factors such as the powder particle size and distribution, the thickness of the deposited powder layer, beam power and thickness, scanning rate, and distance between scanning points affect the quality of the final products [16-23].

316L stainless steel is widely used as biomaterials in the medical field because of its easy and low-cost manufacturing, good loading capacity, and excellent mechanical property [7,24-26]. However, it is difficult for 316L stainless steel to form a real chemical bond with human bone tissue due to its low biocompatibility, low bioactivity, and high modulus of elasticity [27-28]. On the other hand, the corrosion and wear resistance of 316L stainless steel is poor in vivo environment. It has been reported in some studies that the Cr³⁺ and Cr⁵⁺ cations can be released from the 316L stainless steel, and they diffuse to surrounding tissues, causing inflammation and necrosis of these tissues. This event ultimately leads to implantation failure due to corrosion and wear [27,7,29-30]. Therefore, surface treatments are applied to the 316L to overcome these problems. The surface modification technology of steel mainly includes thermal chemical reaction spraying, sol-gel, slurry, PVD, CVD, and plasma spray processes [27,31-33]. For surface treatment ceramic coatings are widely and effectively used to increase surface strength and corrosion resistance. Also, the sol-gel process is preferred for the production of protective ceramic films on the substrate. Due to its advantageous properties such as low equipment and production costs, controllable composition, low process temperature, well homogeneity, and no size limit advantage properties of sol-gel process, it is widely preferred use [34-37].

In this study, the 316L samples were produced by the SLM method. For surface treatment, the 316L samples were coated with Ag₂O, CoO, and TiO₂ separately and Ag₂O/CoO/TiO₂ composite ceramic structures by the sol-gel dip-coating method. After the coating process, the structural and corrosion behavior of the coated and uncoated samples were investigated. The aim of this study is to form the various ceramic structures on the SLM-manufactured 316L stainless steel (316L) and to increase the corrosion resistance of the 316L surface.

2. Materials and Methods

316L stainless steel (316L) specimens with the dimensions of 20 × 20 × 4 mm were produced by utilizing Laser Powder Bed Fusion additive manufacturing. The chemical composition of 316L powder is given in Table 1. Certified CL 20 ES 316L stainless steel powder was used in this study. The used powder was produced for medical purposes and it was indicated by the manufacturer that the average powder size was approximately 25 μm. Additive manufacturing operations were carried out using the MLab Cusing R Machine from Concept Laser, with 100W Ytterbium (Yb) fiber laser. Straight-line laser scans were utilized to melt each layer. The 316L specimen was produced in a nitrogen environment. The production parameters recipe for 316L stainless steel, which was determined and recommended by the manufacturer of the device, was used in the following values by keeping the parameters constant. The process parameters for SLM were; a laser power of 40 W, a scanning speed of 400 mm/s, parallel scanning of 100 μm, a layer thickness of 25 μm, and a scan rotation of 90°. Before the dip-coating process for surface treatment, the oxide layer existing on the surface of the 316L specimens was eliminated via polishing by SiC emery paper (80 to 1000 mesh grit). At the end of this preparation, specimens were polished with 0.3 μm alumina. Afterward, the specimens were cleaned ultrasonically in an ethanol bath. For the dip-coating by sol-gel process, the necessary ceramic coating solutions were prepared by using the silver nitrate (AgNO₃), cobalt II chloride hexahydrate (CoCl₂·6H₂O), titanium IV isopropoxide (TTIP), hydrazine hydrate (N₂H₄·H₂O), ammonium hydroxide (NH₄OH) and hydrochloric acid (HCl) chemicals obtained from Sigma-Aldrich and Merck and used any purification. All the ceramic film coating solutions were prepared at 0.5M of concentration. Each ceramic film coating solution was prepared as follows:

- Ag₂O ceramic film coating solution; The required mass amount of silver nitrate for 0.5 molar is dissolved in 100 milliliters of pure water. Ammonium hydroxide is added to the solution drop by drop until the pH reaches 12. This solution is mixed for about 2 hours with a magnetic stirrer. The solution is aged for 24 hours.
- CoO ceramic film coating solution; The required mass amount of cobalt II chloride hexahydrate for 0.5 molar is dissolved in 100 milliliters of pure water. 5 ml of hydrazine hydrate and the ammonium hydroxide is added to the solution drop by drop until the pH reaches 10. This solution is mixed for about 2 hours with a magnetic stirrer. The solution is aged for 24 hours.
- TiO₂ ceramic film coating solution; 74.7 ml pure water, and 8.8 ml HCl are mixed on a heated magnetic stirrer. When the temperature reaches 70°C 15.5 ml TTIP is added to the solution drop by drop. This solution is mixed for about 2 hours with a magnetic stirrer at that temperature. Then the solution is aged at room temperature for 24 hours.
- Ag₂O/CoO/TiO₂ composite ceramic film coating solution; For 0.5 molar of the composite solution, the required mass amount of silver nitrate, cobalt II chloride hexahydrate, and TTIP are used as equal amounts. They are dissolved in 100 milliliters of pure water. 5 ml of hydrazine hydrate and ammonium hydroxide is added to the solution drop by drop until the pH reaches 12. This solution is mixed for about 2 hours with a magnetic stirrer. The solution is aged for 24 hours.

After the preparation of coating solutions, the coating process was carried out by dip-coating method as follows. 316L substrate samples were immersed into the sol-gel solution at a constant speed of 10 cm.min⁻¹. The samples were kept in solution for 10 minutes. Then, they were removed from the solution at the same speed, and they were left to remove the excess solution from the sample for about 10 minutes. The dipping and removing processes were carried out in a vertical direction by the dip-coating device at room temperature. After that, they were dried in an oven at 100°C for 10 minutes. This process circle was repeated 3 times for a sample. Finally, the calcination was applied to the films on the coated sample surface with the thermal heat treatment furnace and it was open to the atmosphere. The calcination process was applied for 2 hours after the temperature reached the 500°C. This process steps were repeated for all coating samples. After the coating process, the samples were analyzed for determining the film structure and the electrochemical behavior of the samples.

Table 1. Chemical Composition (%W) of 316L Stainless Steel Powder

Cr	Ni	Mo	P	Mn	Si	C	S	Fe
16.5-18.5	10-13	2-2.5	0-0.045	0-2	0-1	0-0.03	0-0.03	Balanced

To analyze the structural properties, XRD measurements were carried out by using an XRD-GNR-Explorer operated at 40 kV and 30 mA Cu K α 1 ($\lambda=1.540 \text{ \AA}$) source diffractometer with 2θ scale from 10° to 100°. Cross-section and corroded surface images were also examined by Scanning electron microscope (SEM FEI-Quanta 250). Corrosion properties of untreated and coated samples were performed by a Gamry Series G750 potentiostat/galvanostat. For determining the corrosion behavior of all samples, simulated saliva fluid (SSF) was prepared at pH=6.5 to use in potentiodynamic polarization and Electrochemical Impedance Spectroscopy (EIS) tests. All corrosion measurements were conducted in simulated saliva fluid (SSF). The chemical composition of the SSF solution is shown in Table 2 [38-39]. Moreover, corrosion test results and data analyses were evaluated via Gamry Echem Analyst software. The electrochemical measurements were applied according to the three-compartment cell containing reference electrode (Ag/AgCl), counter electrode (graphite), and working electrode in 50 ml SSF solutions where 0.502 cm² surface area was exposed to corrosion. Open circuit potential (OCP), potentiodynamic polarization, and electrochemical impedance spectroscopy (EIS) measurements were conducted in all samples.

Table 2. Chemical Composition of Simulated Saliva Fluid (SSF)

Composition	Used amount (g/l)
Potassium chloride	0.720
Calcium chloride dihydrate	0.220
Sodium chloride	0.600
Potassium phosphate monobasic	0.680
Sodium phosphate dibasic	0.866 (dodecahydrate)
Potassium bicarbonate	1.500
Potassium thiocyanate	0.060
Citric Acid	0.030

3. Results and Discussion

3.1. Microstructural and morphological examinations

XRD pattern of untreated 316L, separately cobalt oxide, silver oxide, titanium oxide, and composite CoO/Ag₂O/TiO₂ coated samples are given in Figure 1. As expected, 316L stainless steel exhibited γ -austenite peaks with a face-centered-cubic (FCC) structure. It was observed that the leading peaks of γ -austenite were (111) and (200). In the case of the coated samples, XRD analysis showed that different oxide coating processes occurred successfully on the substrate. Although austenite peaks are still present from the substrate, it was seen that different metal oxides were formed according to the oxide coating type. It was determined that the rutile type TiO₂ structure was diffracted from the TiO₂ coatings. On the other hand, it is seen that CoO peaks are reflected in cobalt oxide coatings and also Ag₂O peaks in silver oxide coatings, as expected. In the triple composite coating, although formations of all three metal oxides were observed, it was determined that the dominant phase was TiO₂ because of its lower activation than others.

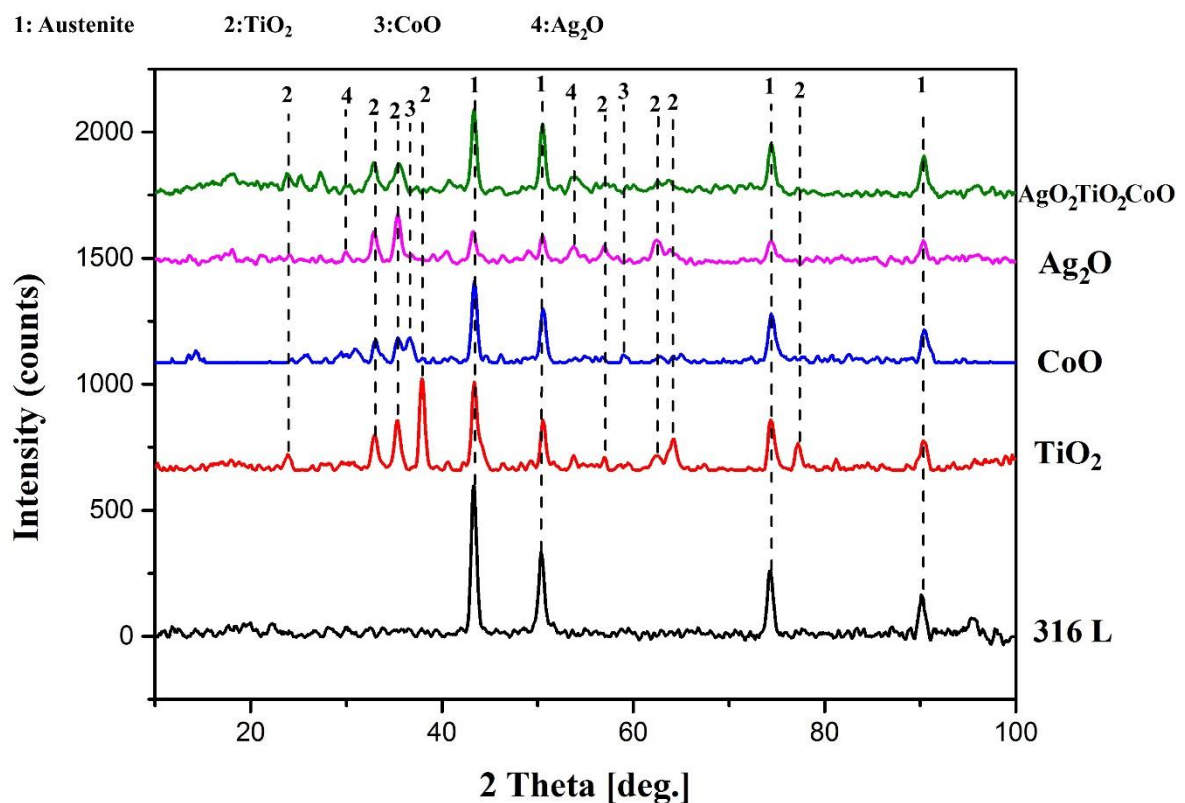


Figure 1. XRD pattern of untreated 316L, Ag₂O, CoO, TiO₂ and composite Ag₂O/CoO/TiO₂ coated samples

Figure 2 shows the cross-section SEM images of CoO, Ag₂O, TiO₂, and composite Ag₂O/CoO/TiO₂ coated samples. Similar morphological features were observed in all coated samples. As a whole, it was seen that the films were quite dense, non-colonic, non-porous, and

compact, and a very thin and rough texture was formed on the surface of these films (Figure 2a-d). All these metal oxide film thicknesses values were measured between 30-40 μm .

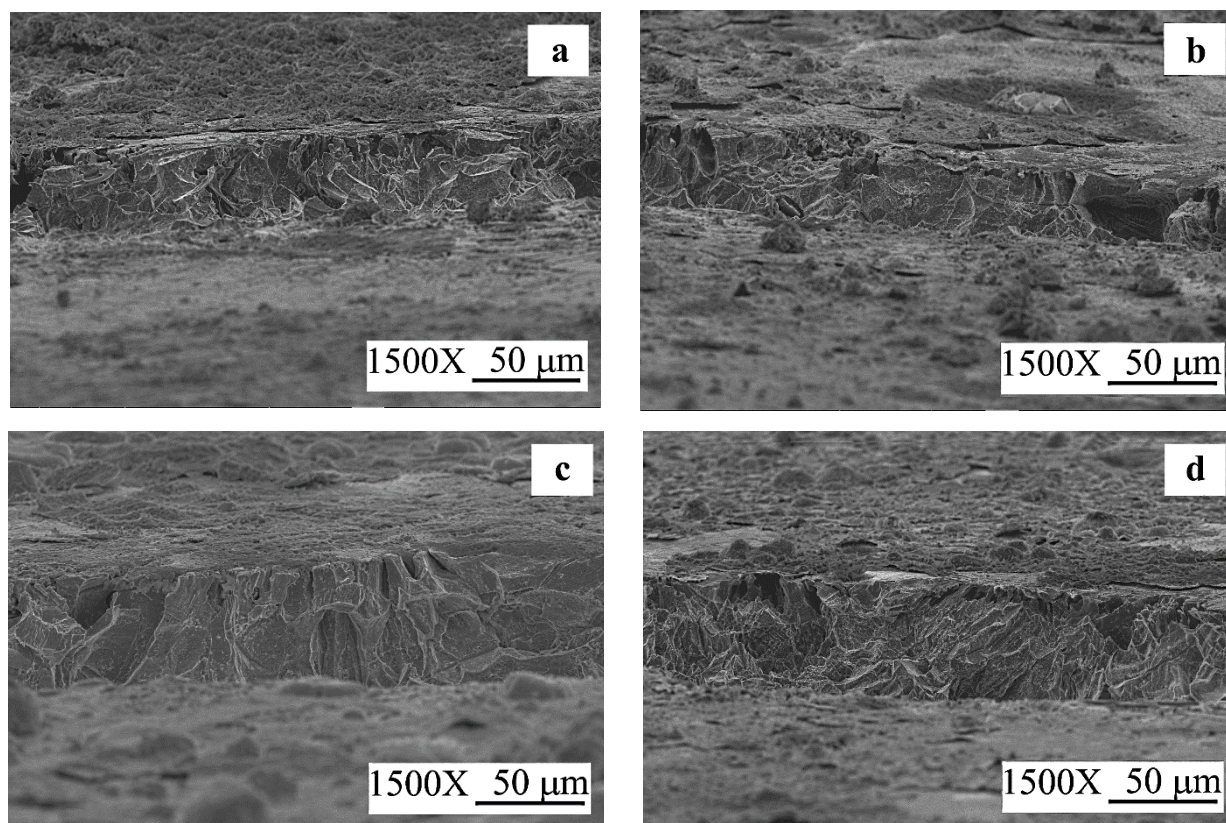


Figure 2. Cross-section SEM images of a) CoO, b) Ag₂O, c) TiO₂ and d) composite Ag₂O/CoO/TiO₂ coated samples

3.2. Electrochemical Behavior

Before the potentiodynamic and electrochemical impedance spectroscopy (EIS) tests, the open circuit potential (OCP) values were measured for determining the passivation behavior of both untreated and all ceramic-coated samples. Simulated saliva fluid was used during all electrochemical behavior-determining experiments. The sample to be analyzed was immersed in the simulated saliva fluid until obtaining a steady-state open circuit potential (OCP). It was repeated for all samples. This test was applied for 5000s and before this value, the potential difference was stable and reached a steady-state form for all samples. After equilibration, polarization was started by 0.5 mVs^{-1} rate from the potential range of -1.0 to $+2.0$ V vs OCP. When the anodic potentials reached over 2.0 V for all samples, the scanning processes were stopped. EIS measurements were carried out using AC signals at the OCP values of samples in the frequency range of 100000–0.01 Hz. The surface area of the corroded surfaces was 0.502 cm^2 and all data have been normalized according to the surface area.

The comparative potentiodynamic polarization curves (PDS) of the untreated and ceramic-coated samples and also some important corrosion parameters calculated from these curves are presented in Figure 3 and Table 3, respectively. From Figure 3, it was seen that the current remained constant as the potential increased at a zone which was called the passivation region.

Because of the forming a of passive oxide layer on the sample surface, it was encountered by this behavior. As a result of redox reactions in the corrosion mechanism, the metal immigrated into the electrolyte as cations. Then they reduced according to the redox reactions and the products collapsed on the sample surface. So that a passive layer forms on the anodic zone. This passive layer prevented the flow of current hence, the corrosion was prevented or slowed down. It was observed that as the increasing potential value, the current value increased. Also, this passive layer was broken and corrosion began again or continues rapidly after a period of time. This case was seen in the transpassive zone, and it occurred after the passive zone in Figure 3. Also, the protective efficiency P (%) of the samples can be estimated by Eq. (1):

$$P_i(\%) = [1 - (i_{\text{corr}}/i_{\text{corr}}^0)] \times 100$$

where I_{corr} and I_{corr}^0 are the corrosion current densities of the coated samples and substrate, respectively. The protective efficiency values of the Ag₂O, CoO, TiO₂, and Ag₂O/CoO/TiO₂ composite ceramic coatings were approximately 24.4%, 42.9%, 64.6%, and 88.9% respectively.

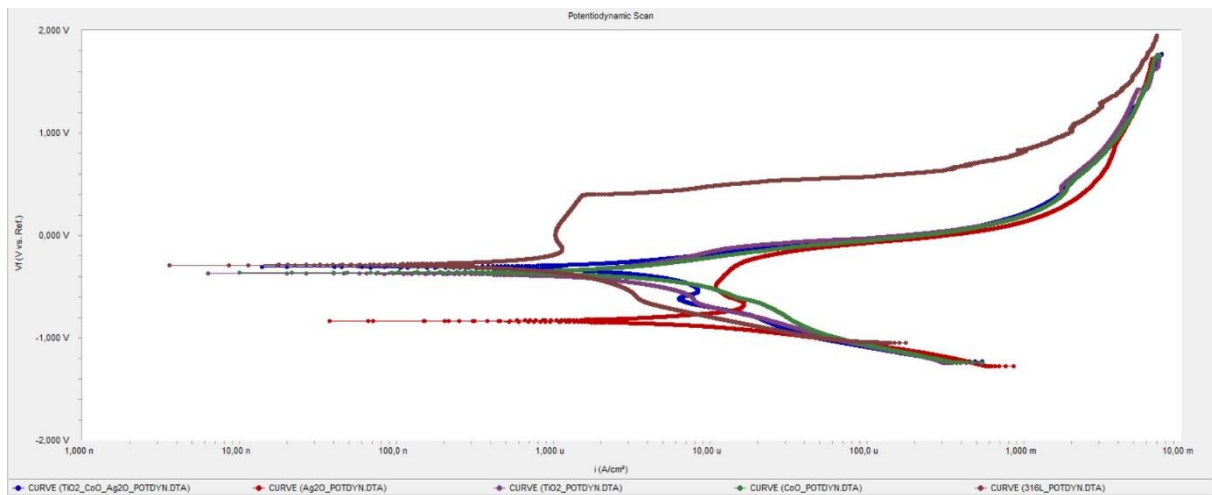


Figure 3. Potentiodynamic polarization curves of uncoated and ceramic-coated samples

Table 3. Corrosion values of all samples

	I_{corr} (mA/cm²)	E_{corr} (mV)	Corr.Rate (mpy)
316L	8.99 x10 ⁻³	-288	5.665
Ag₂O	6.80 x10 ⁻³	-835	4.283
CoO	5.13 x10 ⁻³	-360	3.230
TiO₂	3.18 x10 ⁻³	-372	2.007
Ag₂O/CoO/TiO₂	1.00 x10 ⁻³	-310	0.632

From the corrosion test results, it can be seen that the 316L, the untreated sample, had the most corrosion rate among all the analyzed samples. Also, its current density (I_{corr}) was the biggest value among the other samples, as expected. It means that the untreated and unprotected sample draws a large current or in other words, a large amount of current can pass into the untreated

sample. Thus the necessary electrons would be provided for the corrosion to continue. So the sample is heavily exposed to the corrosion process and the corrosion rate is determined as high, as seen in Table 3.

In Table 3, the corrosion rate and current density of untreated 316L are higher than the other samples, which means that the resistance is low. This is an expected result. However, the high E_{corr} value of 316L is not an expected result according to the above results. This unexpected result can be attributed to the production of 316L with SLM. It can be explained as in the following: It is known that the materials are produced layer by layer in selective additive manufacturing by laser melting with material powders. Although this method widens the range of geometry diversity of the materials to be produced and has many benefits, there are still many unresolved research questions, such as those involving inhomogeneity in material deposition or during the layer-by-layer fabrication of components, which leads to undesirable microstructures and excessive surface roughness [40] also, it is thought that the defects that may occur at the junction points of the layers without being aware of it during the production. Also these defects cause the formation of short circuits at the junction points of the layers can be thought as welding points. While there is resistance in other regions, the current can easily pass due to the much lower resistance in these junction points, so that the corrosion rate increases. It is known that in the short circuits systems higher current passes on the lower resistance at a constant potential source, usually. But in this corrosion analysis system the potential range was -1.0 to +2.0 V. So in these short circuit junction points, while there will be a very high current to flow, it is thought that the increase in the power consumed on the impedance, through the variable potential source, is not only met by the increase in the current, but also by the increase in the corrosion potential ($I=V/R$, $P=V.I=V^2/R$, P; power-watt, V; volt, I; current, R; resistance). [41-44] Another effective factor in this regard is that the materials produced by additive manufacturing have a highly porous structure. Again, due to this porosity, the current can find a way to create a short circuit [40]. Thus, higher corrosion current, potential and rate were obtained in the untreated 316L sample compared to other coatings.

It can be seen that the ceramic coating samples had better corrosion behavior than the untreated sample. With the ceramic-based coating of the material, the service life of the material will increase. While there will be a loss of approximately 5.7 milliinches per year from the uncoated sample, it was seen from the results of the study that this loss would decrease to approximately 0.6 milliinches per year in the ceramic coated sample that this was the best result among to the type of ceramic coatings. In other words, only the coating part of the coated sample will give the loss in 1 year of the untreated sample in 9.5 years. This means that the material loss in 1 year due to corrosion in the untreated sample is approximately 10.5 years in the ceramic film-coated sample, which gives the best results. This means that ceramic coatings increase the service life of the material by about 10.5 years.

When the ceramic coatings are considered in themselves, the difference in current density, resistance, and corrosion rates is thought to be related to two factors. The first of these is the structural properties of the film such as the thickness, roughness, integrity, and chemical content [5, 6, 34, 45-51]. The more homogeneous and compact the coatings are on the surface, the less

deformation could be mentioned. It has been determined that the corrosion resistance is better in coatings that its film thickness is sufficiently high and the film integrity is preserved, which means, there are no cracks or little cracks than the others are in the coating film. However, in non-homogeneous and non-compact structures, if there are cracks and places where the film is thin, it is highly possible that the corrosion will start from these areas. Also, it is highly possible that the electrolyte will leak into the coating film and the corrosion will increase. The other factor of corrosion resistance was thought to be the electronegativity of the element atoms forming the ceramic structure on the surface [52-54]. It was known that as electronegativity between atoms increases, the ionic bonding increases. From the corrosion test results, it was seen that the film resistances were close to each other. But with a little difference, the cobalt oxide film had less film resistance. This was attributed that it was related to its film structure at the surface of the film and it was thought to be due to it having little cracks on the film surface. But, these cracks don't reach the substrate surface. So that the electrolyte can't influence the substrate surface. Also, it had a high interface resistance between the film and the substrate (Table 4.). So in the total system resistance of CoO was high and its corrosion rate was less. On the other hand, the lowest corrosion rate and current density were observed in Ag₂O/CoO/TiO₂, and the highest resistance value was observed in TiO₂ at the interface between the film and the substrate (Table 4.). TiO₂ had the highest electronegativity difference in these three ceramic structures, and it had the highest resistance. The lowest electronegativity belongs to Ag₂O, which has the lowest resistance and the highest current density and corrosion rate. While Ag₂O/CoO/TiO₂ composite coating had the lowest corrosion rate, current density, and highest film resistance, it was expected to show the highest resistance at the interface too. However, TiO₂ coating showed the highest resistance at the interface. Since Ag₂O is also present in the Ag₂O/CoO/TiO₂ coating, the Ag₂O structure will be damaged the most. Therefore, the resistance decreased. However, since there will be more resistant TiO₂ or CoO film layers under the damaged Ag₂O layer, it is thought that no damage has occurred in the lower resistant layers, which may have prevented the flow of current and caused less corrosion compared to other coatings. It was thought that the electronegativity of the coatings at the interface was very relevant to releasing the ions, because of fewer ionic bonds. Also, it had a rougher and less homogeneous film structure than the other coated films (Figure 2.). Because of this roughness and non-homogeneous structure, although the resistance of the film surface is high, the electrolyte influenced the film and reached the interface of the film and the substrate, and at the end, it reached the surface of the substrate. So that in the total system, it was seen that the Ag₂O was less stable and it had a higher corrosion rate than the other coatings.

The electrochemical impedance spectroscopy (EIS) method is a very useful method to determine the corrosion behavior and the detailed electrochemical process occurring on the surface. Figures 4-7 show the Nyquist and Bode curves of untreated and coated samples after the EIS scanning. The diameter of the graphical semicircles in the Nyquist plane represents the polarization resistance of the test samples, and the larger cycle indicates a lower corrosion rate. [5, 49, 55-57]. As can be seen from the Nyquist curves in Figure 4. the formation of a semicircle with a lower radius of the untreated 316L compared to the ceramic-coated samples at low frequencies means that there is no protective layer on the surface of untreated 316L and that the corrosion resistance is low. It is seen from Figure 6. that the Nyquist curves of the ceramic-

coated samples are very close to each other. Also, they are in the way of forming a semi-circle to close, and while the diameters of these semi-circles increase the corrosion resistances increase too. It can be seen from the graph that the semicircular diameter of TiO₂ will be slightly higher than the others, and it can be said that the corrosion resistance is slightly higher than the others. It is known from the literature that, in Bode curves, the phase angle change in the low-frequency region shows the behavior of the metal; and the change of the phase angle in the high-frequency region, shows the strength of the film, and the size of the area under the Bode curves are related to the shielding efficiency of the film [58-62].

As seen in Bode curves (Figure 5. and 7), the uncoated 316L sample showed the lowest phase angle. Also, the least area under the Z_{mod}-frequency curve belongs to the uncoated 316L sample. The least phase angle and the lowest curve area meant poor corrosion behavior [56-58, 63-64]. Thus these results contributed to the worst corrosion behavior belonging to the uncoated 316L sample. In the phase angle-frequency curves in the low-frequency region, the phase angle, indicating the behavior of the metal, increased with TiO₂ and CoO ceramic coatings separately, while the phase angle in the high-frequency region, which indicated the surface film behavior, increased with Ag₂O ceramic-coating. This showed that the corrosion performance of ceramic coatings also varied according to the ceramic coating types. In Figure 7., it was seen that the areas under the Z_{mod}-frequency curves decreased rapidly with the increasing of the frequency, and they remained stable from mid-frequency to high frequencies. This meant that the ceramic coatings were resistant to corrosion behavior and protected the substrate material.

The equivalent circuit models for all samples and the obtained values of the circuit elements are shown in Figures 8, 9, and Table 4. The obtained simulated EIS fitting values were calculated with Gamry Echem Analyst software. The electronic components R_{sol}; the resistance of the electrolyte was simulated saliva fluid, R_{subs}; the charge transfer resistance in the interface, C_{subs}.; capacitance of the 316L substrate, R_{film}; the resistance of the ceramic film coatings, Q_{subs}.; the constant phase element (CPE) of the interface layer and substrate and Q_{film}.; the constant phase element (CPE) of the ceramic film coatings. Ceramic film coating resistance and charge transfer resistance are important parameters for evaluating the electrochemical behavior of the samples as mentioned in this section. Also, charge transfer resistance directly represents the corrosion rate in the interface between the layer and the substrate. It was seen from Table 4 that the EIS circuit fitting results supported the explanations about the corrosion behavior discussed in this section.

Table 4. EIS fitting parameters for uncoated and coated samples

	R _{sol} (Ω.cm ²)	R _{film} (Ω.cm ²)	R _{subs} (Ω.cm ²)	C _{subs} (F.cm ⁻²)	Q _{film}		Q _{subs}	
					Y ₀ (Ω.sec ⁿ cm ⁻²)	m x10 ⁻³	Y ₀ (Ω.sec ⁿ cm ⁻²)	n x10 ⁻³
316L	217.1	93.62	-	40.69x10 ⁻⁶	-	-	-	-
Ag₂O	348.7	156.5	9.218x10 ³	-	4.410x10 ⁻⁹	123.8	2.151x10 ⁻³	768.2
CoO	352.4	120.6	11.40x10 ³	-	1.840x10 ⁻⁹	79.39	852.610 ⁻⁶	786.3
TiO₂	442.0	149.7	13.01x10 ³	-	16.37x10 ⁻⁹	138.5	726.5x10 ⁻⁶	749.4
Ag₂O/CoO/TiO₂	202.6	258.7	8.569x10 ³	-	48.35x10 ⁻⁹	134.9	1.107x10 ⁻³	798.1

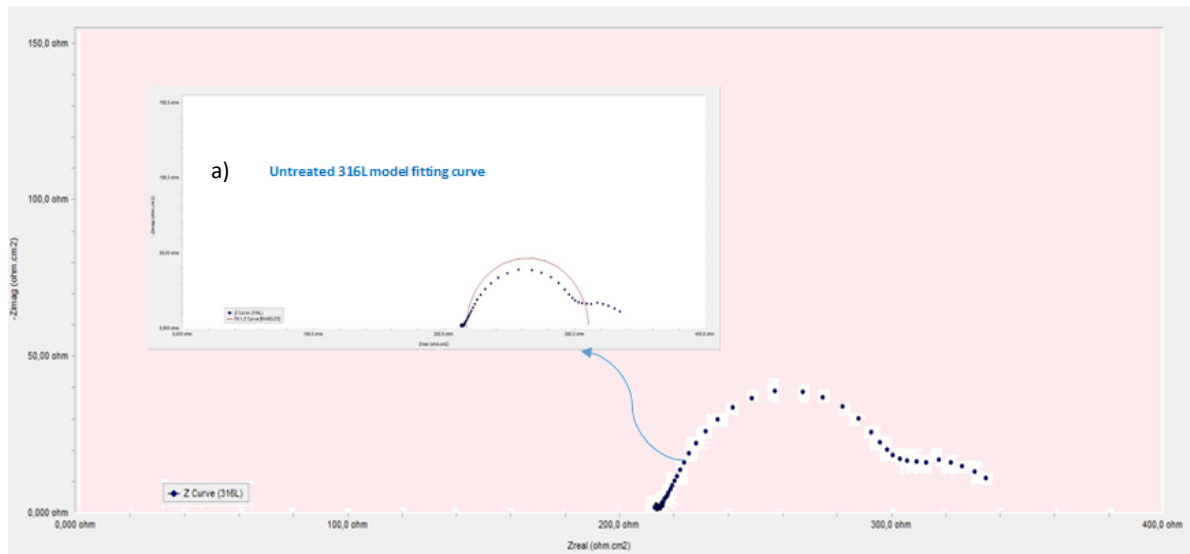


Figure 4. Nyquist curve of uncoated 316L sample a) model fit curve of uncoated 316L

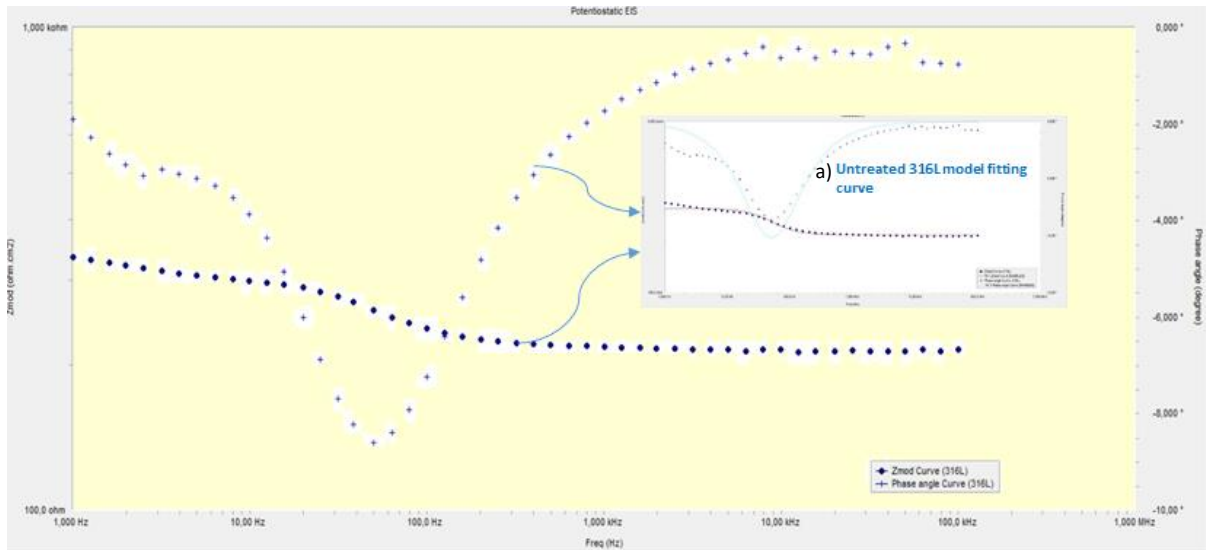


Figure 5. Bode curve of uncoated 316L sample a) model fit curves of uncoated 316L

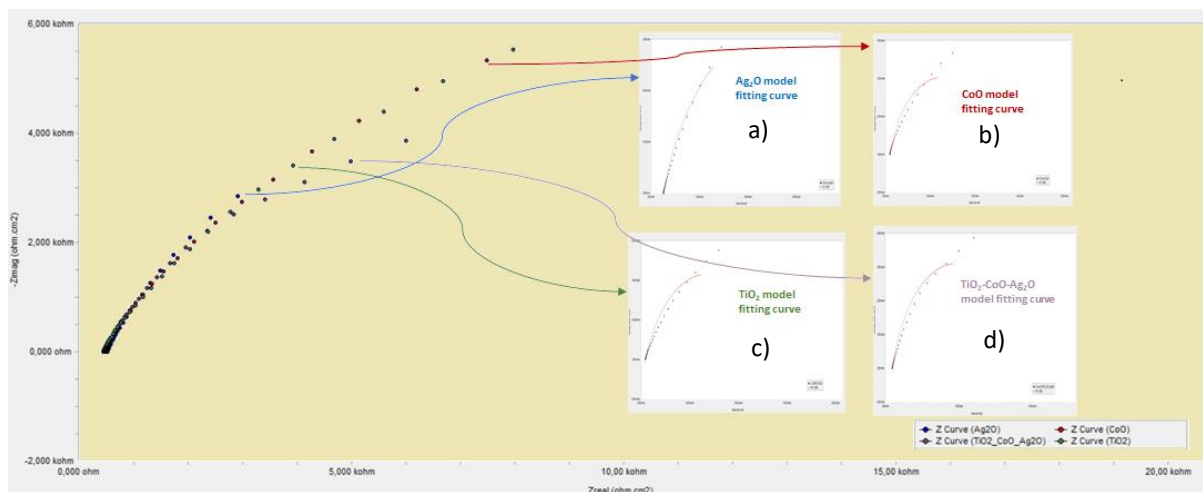


Figure 6. Nyquist curves of ceramic-coated samples a) model fit curve of Ag₂O ceramic-coating b) model fit curve of CoO ceramic-coating c) model fit curve of TiO₂ ceramic-coating d) model fit curve of TiO₂-CoO-Ag₂O ceramic-coating

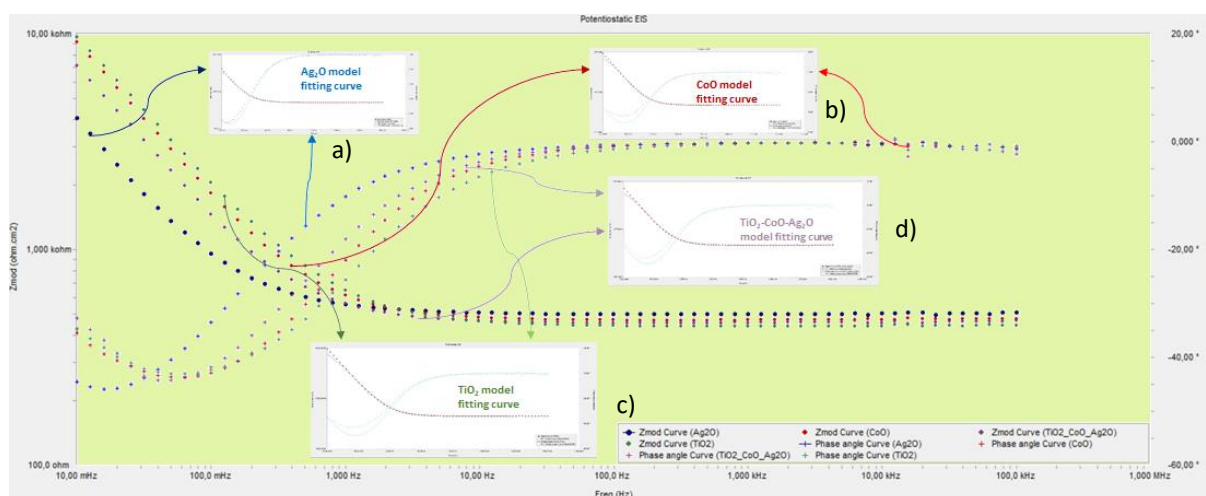


Figure 7. Bode curves of ceramic-coated samples a) model fit curve of Ag₂O ceramic-coating b) model fit curve of CoO ceramic-coating c) model fit curve of TiO₂ ceramic-coating d) model fit curve of TiO₂-CoO-Ag₂O ceramic-coating

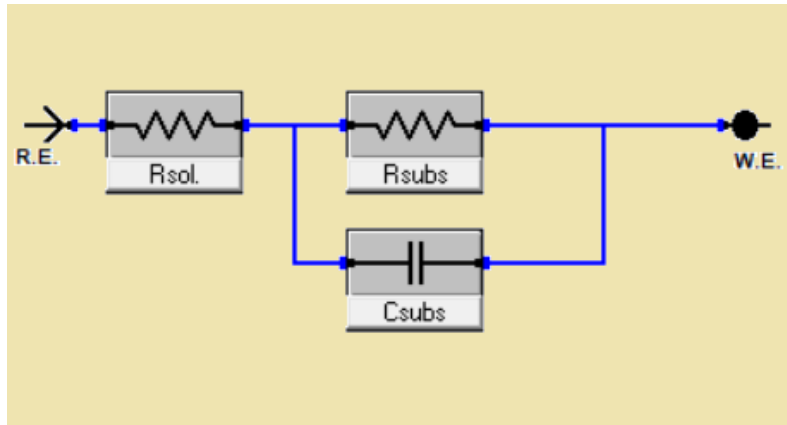


Figure 8. Equivalent circuit for (a) the uncoated 316L samples

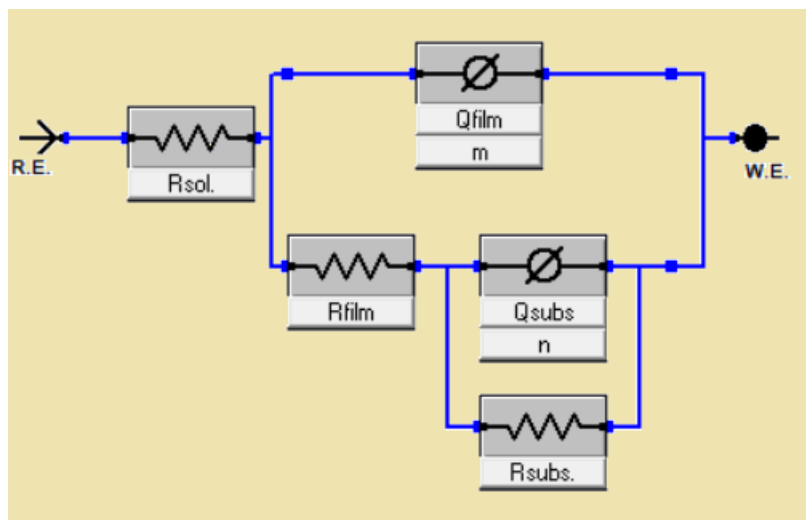


Figure 9. Equivalent circuit for the ceramic-coated samples.

4. Conclusion

In this study 316L stainless steel substrate was built by selective laser melting additive manufacturing method. To improve the corrosion behavior of 316L stainless steel, various ceramic film coatings were applied to the surface of the 316L. For this purpose Ag₂O, CoO, TiO₂, and the Ag₂O/CoO/ TiO₂ composite ceramic films were coated on the 316L sample surface by sol-gel dip-coating method. The structural and electrochemical properties of the coated ceramic films and the uncoated substrate were investigated. The following results were obtained;

- XRD analysis results showed that the different oxide coating processes occurred successfully on the substrate. 316L exhibited γ -austenite peaks (111) and (200) for uncoated samples and Ag₂O, CoO, and TiO₂ peaks were observed on the coated sample surfaces. Also, it was determined that TiO₂ oxide was rutile type according to the XRD peaks.
- Similar morphological features were observed in all coated samples from the SEM images. It was seen that the films were quite dense, non-colonic, non-porous, and compact, and a very thin and rough texture was formed on the surface of these films. However, it was observed that the quality of the surfaces of the films differed among themselves, depending on the fact that these properties were better.
- Potentiodynamic polarization and Electrochemical Impedance Spectroscopy (EIS) tests showed that the corrosion resistance of the ceramic film-coated samples displayed diversity with the various ceramic film coatings. But all ceramic film-coated samples had better corrosion behavior than the uncoated 316L sample. The uncoated 316L sample had the most corrosion rate among all the analyzed ceramic film-coated and uncoated samples.
- When the corrosion rates were compared, it was seen that the lowest corrosion rate belonged to the Ag₂O/CoO/ TiO₂ ceramic film-coated sample. According to the experiment results and the calculations it was seen that if this ceramic film coated on the 316L substrate surface, it would extend the service life of the substrate by approximately 10.5 years.
- The corrosion behavior of ceramic film-coated samples was compared to each other, and it was observed that Ag₂O showed the minimum corrosion resistance at the interface of the film and the substrate layer. But at the film surface, the minimum corrosion resistance was obtained at the CoO ceramic film-coated sample surface. These results were related to the electronegativity of the element atoms forming the ceramic film structures and also, the physical structure of the ceramic film surface.
- In the case of coated samples, the lowest corrosion rate was obtained at the Ag₂O/CoO/ TiO₂ ceramic composite film-coated sample, with both the dense, non-colonic, non-porous, and compact structure of the film and the positive effect of the electronegativity.

Ethics in Publishing

There are no ethical issues regarding the publication of this study.

References

- [1] Yao, D., Liu, X., Wang, J., Fan, W., Li, M., Fu, H., Zhang, H., Yang, X., Zou, Q., An, X., (2021) Numerical insights on the spreading of practical 316 L stainless steel powder in SLM additive manufacturing, *Powder Technology*, *390*, 197-208.
- [2] Wang, Y.F., Yu, C.F., Xing, L.L., Li, K.L., Chen J.H., Liu, W., Ma, J., Shen, Z.J., (2020) Grain structure and texture of the SLM single track, *J. Mater. Process. Technol.*, *281*, 116591.
- [3] Maconachie, T., Leary, M., Lozanovski, B., Zhang, X., Qian, M., Faruque, O., Brandt, M., (2019) SLM lattice structures: properties, performance, applications and challenges, *Mater. Des.*, *183*, 108137.
- [4] Samantaray, M., Thatoi, D.N., Sahoo, S., (2019) Modeling and optimization of process parameters for laser powder bed fusion of AlSi10Mg alloy, *Lasers Manufact. Mater. Process.*, *6*, 356–373.
- [5] Tekdir, H., Yetim, T., Yetim, A.F., (2021) Corrosion Properties of Ceramic-Based TiO₂ Films on Plasma Oxidized Ti6Al4V/316L Layered Implant Structured Manufactured by Selective Laser Melting, *J Bionic Eng.*, *18*, 944–957.
- [6] Tekdir, H., Yetim, A.F., (2021) Additive manufacturing of multiple layered materials (Ti6Al4V/316L) and improving their tribological properties with glow discharge surface modification, *Vacuum*, *184*, 109893.
- [7] Yetim, A. F., Yazici, M., (2014) Wear resistance and non-magnetic layer formation on 316L implant material with plasma nitriding, *J. Bionic Eng.*, *11* (4), 620-629.
- [8] Obadele, B.A., Andrews, A., Olubambi, P.A., Mathew, M.T., Pityana, S., (2015) Effect of ZrO₂ addition on the dry sliding wear behavior of laser clad Ti6Al4V alloy, *Wear*, *328* (329), 295-300.
- [9] Fernandes, A.C., (2006) Tribocorrosion behavior of plasma nitrided and plasma nitrided + oxidised Ti6Al4V alloy, *Surf. Coating. Technol.*, *200* (22), 6218-6224.
- [10] Zhu, Y., Zou, J., Yang, H., (2018) Wear performance of metal parts fabricated by selective laser melting: a literature review, *J. Zhejiang Univ. A*, *19*(2), 95-110.
- [11] Sing, S.L., Yeong, W.Y., Wiria, F.E., (2016) Selective laser melting of titanium alloy with 50wt% tantalum: microstructure and mechanical properties, *J. Alloys Compd.*, *660*, 461-470.
- [12] Song, C., Zhang, M., Yang, Y., Wang, D., Jia-kuo, Y., (2018) Morphology and properties of CoCrMo parts fabricated by selective laser melting, *Mater. Sci. Eng. A*, *713*, 206-213.
- [13] Simson, T., Emmel, A., Dwars, A., Böhm, J., (2017) Residual stress measurements on AISI 316L samples manufactured by selective laser melting, *Addit. Manuf.*, *17*, 183-189.

- [14] Mohammed, M.T., (2018) Mechanical properties of SLM-Titanium materials for biomedical applications: a review, *Mater. Today Proc.*, 5 (9), 17906-17913.
- [15] Agopovichev, A.V., Kokareva, V.V., Smelov, V.G., Sotov, A.V., (2016) Selective laser melting of titanium alloy: investigation of mechanical properties and microstructure, *IOP Conf. Ser. Mater. Sci. Eng.*, 156 (1).
- [16] Čapek, J., Machová, M., Fousová, M., Kubásek, J., Vojtěch, D., Fojt, J., Jablonská, E., Lipov, J., Ruml, T., (2016) Highly porous, low elastic modulus 316L stainless steel scaffold prepared by selective laser melting *Materials Science and Engineering C*, 69, 631-639.
- [17] Bremen, S., Meiners, W., Diatlov, A., (2012) *Laser. Technik. J.*, 9, 33–38.
- [18] Kruth, J., Froyen, P., Van, L., Vaerenbergh, J., (2004) *J. Mater. Process. Technol.*, 149, 616–622.
- [19] Laohaprapanon, A., Jeamwatthanachai, P., (2012) Wongcumchang, M., et al., *Mater. Manuf. Technol. II Pts 1 and 2*, 816–820.
- [20] Cherry, J.A., Davies, H.M., Mehmood, S., (2014) *Int. J. Adv. Manuf. Technol.*, 76, 869–879.
- [21] Yadroitsev, I., Krakhmalev, P., Yadroitsava, I., (2013) *J. Mater. Process. Technol.* 213, 606–613.
- [22] Li, R., Shi, Y., Wang, Z., (2010) Densification behavior of gas and water atomized 316L stainless steel powder during selective laser melting *Appl. Surf. Sci.*, 256, 4350–4356.
- [23] Li, R., Liu, J., Shi, Y., (2012) *Int. J. Adv. Manuf. Technol.*, 59, 1025–1035.
- [24] Tekdir, H., Yetim, T., Yetim, A.F., (2021) Corrosion Properties of Ceramic-Based TiO₂ Films on Plasma Oxidized Ti6Al4V/316L Layered Implant Structured Manufactured by Selective Laser Melting, *J Bionic Eng.*, 18, 944–957.
- [25] Bloyce, A., Qi, P.Y., Dong, H., Bell, T., (1998) Surface modification of titanium alloys for combined improvements in corrosion and wear resistance. *Surface and Coatings Technology*, 107, 125–132.
- [26] Bolzoni, L., Meléndez, I. M., Ruiz-Navas, E.M., Gordo, E., (2012) Microstructural evolution and mechanical properties of the Ti-6Al-4V alloy produced by vacuum hot-pressing. *Materials Science and Engineering A*, 546, 189–197.
- [27] Wu, G., Zhang, S., Wang, Y., Sun, M., Zhang, Q., Kovalenko, V., Yao, J., (2022) Porous ceramic coating formed on 316L by laser cladding combined plasma electrolytic oxidation for biomedical application, *Trans. Nonferrous Met. Soc. China*, 32, 2993–3004.
- [28] Yang, Z., Tu, Q., Maitz, M.F., Zhou, S., Wang, J., Huang, N., (2012) Direct thrombin inhibitor bivalirudin functionalized plasma polymerized allylamine coating for improved biocompatibility of vascular devices, *Biomaterials*, 33, 7959–7971.

- [29] Katta, P., Nalliyar, R., (2019) Corrosion resistance with selfhealing behavior and biocompatibility of Ce incorporated niobium oxide coated 316L SS for orthopedic applications, *Surface and Coatings Technology*, *375*, 715–726.
- [30] Garcia-Lobato, M.A., Mtz-Enriquez, A. I., Garcia, C.R., Velazquez-Manzanares, M., Avalosbelmontes, F., Ramos-Gonzalez, R., Garciacerda, L.A., (2019) Corrosion resistance and in vitro bioactivity of dense and porous titania coatings deposited on 316L SS by spraying method, *Applied Surface Science*, *484*, 975–980.
- [31] Moshref-Javadi, M., Edris, H., Shafyei, A., Salimi-Jazi H., Abdolvand, E., (2018) Evaluation of hydrogen permeation through standalone thermally sprayed coatings of AISI 316L stainless steel, *International Journal of Hydrogen Energy*, *43*, 4657–4670.
- [32] Ke-Dong, Z., Jian-Xin, D., Shu-Ting, L., Xiao-Ming, Y., (2016) Effect of micro/nano-textures and burnished MoS₂ addition on the tribological properties of PVD TiAlN coatings against AISI 316 stainless steel, *Surface and Coatings Technology*, *291*, 382–395.
- [33] Shu-Wei, G., Dong-Hai, X., Yu, L., Yan-Meng, G., Yan-Hui, L., (2020) Corrosion characterization of ZrO₂ and TiO₂ ceramic coatings via air plasma spraying on 316 stainless steel in oxygenated sub- and supercritical water, *The Journal of Supercritical Fluids*, *157*, 104716.
- [34] Çomaklı, O., Yazıcı, M., Kovacı, H., Yetim, T., Yetim, A.F., Çelik, A., (2018) Tribological and electrochemical properties of TiO₂ films produced on Cp-Ti by sol-gel and SILAR in bio-simulated environment, *Surf. Coat. Technol.*, *352*, 513-521.
- [35] Banerjee, D.A., Kessman, A.J., Cairns, D.R., Sierros, K.A., (2014) Tribology of silica nano-particle-reinforced, hydrophobic sol-gel composite coatings, *Surf. Coat. Technol.*, *260*, 214–219.
- [36] Mora, L.V., Naik, S., Paul, S., Dawson, R., Neville, A., Barker, R., (2017) Influence of silica nanoparticles on corrosion resistance of sol-gel based coatings on mild steel, *Surf. Coat. Technol.*, *324*, 368–375.
- [37] Çomaklı, O., Yazıcı, M., Yetim, T., Yetim, A.F., Çelik, A., (2017) The effects of aging time on the structural and electrochemical properties of composite coatings on CP-Ti substrate, *J. Bionic Eng.*, *14*, 532–539.
- [38] Margareth, R.C., Marques, Loebenberg, R., Almukainzi, M., (2011) Simulated Biological Fluids with Possible Application in Dissolution Testing *Dissolution Technologies*, August doi.org/10.14227/DT180311P15.
- [39] Duffo, G.S., Castillo E.Q., (2004) Development of an artificial saliva solution for studying the corrosion behavior of dental alloys. *Corrosion*, *6*, 594–602.
- [40] Pathak, S., Böhm, M., Kaufman, J., Kopeček, J., Zulić, S., Stránský, O., Shukla, A., Brajer, J., Beránek, L., Radhakrishnan, J., Rostohar, D., Mocek, T., (2023) Surface integrity of SLM manufactured meso-size gears in laser shock peening without coating, *Journal of Manufacturing Processes*, *85*, 764-773.

- [41] Arturo, G.R.M., Hugo, L.M.V., Rafael, G.H., Egberto, B.B., Antonio, G.S.J., (2015) Electrochemical Characterization of AISI 2205 Duplex Stainless Steel Welded Joints with Electromagnetic Interaction, *Procedia Materials Science*, 8, 950-958.
- [42] Gomes de Souza, D.D.B., Vilarinho, L.O., (2020) Influence of present phases in corrosion and mechanical behavior of UNS S31803 duplex stainless steel welded by conventional short circuit MIG/MAG process, *Journal of Materials Research and Technology*, 9, 11244-11254.
- [43] Araneda, A.A.B., Kappes, M.A., Rodríguez, M.A., Carranza, R.M., (2022) Pitting corrosion of Ni-Cr-Fe alloys at open circuit potential in chloride plus thiosulfate solutions, *Corrosion Science*, 198, 110121.
- [44] Wasekar, N.P., (2022) The influence of grain size and triple junctions on corrosion behavior of nanocrystalline Ni and Ni-W alloy, *Scripta Materialia*, 213, 114604
- [45] Yetim, T., Turalioglu, K., Taftali, M., Tekdir, H., Kovaci, H., Yetim, A.F., (2022) Synthesis and characterization of wear and corrosion resistant Ni-doped Al₂O₃ nanocomposite ceramic coatings by sol-gel method, *Surf. Coat. Technol.*, 444, 128659.
- [46] Çelik, A., Acar, M.T., Yetim, T., Kovacı, H., Yetim, A.F., (2020) Improving structural, tribological and electrochemical properties of Ti6Al4V alloy with B-doped TiO₂ thin films, *Tribology International*, 146, 106210.
- [47] Çeliker, M., (2019) Conicraly Bağ ve Ysz İçerikli Termal Bariyer Kaplamaların Elektrokimyasal Korozyon Davranışlarının İncelenmesi, Yüksek Lisans Tezi, Bartın.
- [48] Doğru, B. M., Yazıcı, B., (October, 06-09-2010)135 Poli(Pirol-Ko-O-Anisidin) Kaplı Alüminyumun %3,5 NaCl'deki Korozyon Davranışı, XII. International Corrosion Symposium, Eskişehir, Turkey.
- [49] Bozkurt, Y.B., Çelik, A., (2022) Tailoring biodegradation rate of AZ31 magnesium alloy *Electrochimica Acta*, 435, 141403.
- [50] Jihui, D.Z., Hu, W.W., (2022) Hydroxyapatite film prepared by hydrothermal method on layered double hydroxides coated Mg Alloy and its corrosion resistance, *Colloids and Surfaces A: Physicochemical and Engineering Aspects*, 647, 129075.
- [51] Husien, V., Haakmann, S.F., Brinkbaumer, J., Ulbricht, M., (2022) Comparison of the nucleation and growth of a phosphate conversion coating on Zn–Al and Zn–Al–Mg coatings under the influence of a corrosion inhibitor film, *Surface & Coatings Technology*, 451, 129044.
- [52] Wang, Y., Si, J., Si, Y., Shi, Z., (2023) Preparation and electrochemical corrosion performances of Zr-Ti-Ni-Cu-Be high-entropy bulk metallic glasses, *Materials Science & Engineering B*, 289, 116267.
- [53] Hernandez, R., Alma, B., Jose, D.M., Juan, G.P., Jose, M.O., Domínguez, M.E., Mujica, V., (2022) Experimental and theoretical study on the effectiveness of ionic liquids as corrosion inhibitors, *Computational and Theoretical Chemistry*, 1210, 113640.

- [54] Dong Wei, B., Tianyi, L., Longjun, Z., Yueming, C., Yonggang, F., Hai, Z., Weijian, L., Sun, Y.Y., (2023) Clarifying the effect of a small amount of Cr content on the corrosion of Ni-Mo steel in tropical marine atmospheric environment, *Corrosion Science*, *210*, 110813.
- [55] Turalioglu, K., Taftalı, M., Tekdir, H., Çomaklı, O., Yazıcı, M., Yetim, T., Yetim, A.F., (2021) The tribological and corrosion properties of anodized Ti6Al4V/316L bimetallic structures manufactured by additive manufacturing, *Surf. Coat. Technol.*, *405*, 126635.
- [56] Manazoğlu, M., (2013) Elektrokimyasal Yöntemle Nikelmolibden Alaşım Kaplamaların Üretimi ve Karakterizasyonu, Yüksek Lisans Tezi İstanbul.
- [57] Küstü, C., (2008) Asitli Ortamdaki Korozyona Karşı Schiff Bazı Temelli Bazı Yeni İnhibitörlerin Geliştirilmesi, Yüksek Lisans Tezi.
- [58] Duran, B., Çakmakçı, İ., Bereket, G., (06-09-2010) Bakır Üzerinde Pirol Ve N-Metil Pirolün Kopolimeri İle Çift Kaplamalarının Sentezi ve Korozyon Performanslarının Araştırılması, XII. International Corrosion Symposium, Eskişehir, Turkey.
- [59] Akbarinezhad, E., Faridi, H.R., (2008) *Surface Engineering*, *24*, 280-286.
- [60] Zhao, X., Wang, J., Wang, Y., Kong, T., Zhong, L. And Zhang, W., (2007) *Electrochemistry Communications*, *9*, 1394-1399.
- [61] Hirayama, R. and Haruyama, S., (1991) Electrochemical Impedance for Degraded Coated Steel Having Pores, *Corrosion*, *47*, 952-958.
- [62] Akbarinezhad, E., Bahremandi, M., Faridi, H.R., Rezaei, F., (1988) Another approach for ranking and evaluating organic paint coatings via electrochemical impedance spectroscopy, *Corrosion Science*, *51*, 356-363, 2009. 24.
- [63] Çoban, K., (2006) Ketonik Bazlı Reçinelerle Paslanmaz Çelik ve Bakırın Korozyonunun Önlenmesi, Yüksek Lisans Tezi.
- [64] Mutlu, R.N., Ateş, S., Mert, B.D., Yazıcı, B., (15-17 Ekim 2014) Sodyum Molibdat (Na₂MoO₄) Katkısının, 7075 Alüminyum Alaşımının Sülfürik Asit İçerisindeki Eloksal İşlemine ve Korozyon Davranışlarına Etkisi, 13. Uluslararası Korozyon Sempozyumu Bildiriler Kitabı, Fırat Üniversitesi, Elazığ, Türkiye.

Effects of Normal Load and Sliding Distance on the Dry Sliding Wear Characteristics of Invar-36 Superalloy

Yusuf KANCA^{1*}

¹Department of Mechanical Engineering, Faculty of Engineering, Hitit University, 19030, Çorum, Türkiye

Received: 14/02/2023, Revised: 23/03/2023, Accepted: 23/03/2023, Published: 30/03/2023

Abstract

In the present study, the wear and friction behavior of Fe-based Invar-36 superalloy was investigated against an alumina ball under various sliding distances (25, 50, 75 and 100 m) and normal loads (5, 15 and 25 N) using a ball-on-disk tribometer. The worn surfaces were characterized using scanning electron microscopy (SEM) equipped with energy dispersive X-ray spectroscopy (EDS) and 2D-profilometry. The experimental results show that the coefficient of friction (COF) of Invar-36 (0.37-0.51) significantly decreased with increasing normal load, with a minimum value at 25 N. On the other hand, a slight increase in friction coefficient was observed with increasing sliding distance. Moreover, the wear volume of Invar-36 (ranged from 2.63 to 157.17×10⁻³ mm³) was observed to increase with increasing normal load and sliding distance. The specific wear rate found a constant increase from 1.98-2.99×10⁻⁵ to 6.33-11.45×10⁻⁵ mm³/Nm at increasing normal loads. On the contrary, the wear rate was gradually reduced when the sliding distance was increased especially at higher applied loads, due to the densification process. In addition, the wear mechanism was complex, including oxidation, abrasion, and plastic deformation, became more intense as the normal load or the number of sliding cycles was increased.

Keywords: Invar-36 superalloy, Friction, Wear, Normal load, Sliding distance

Normal Yük ve Kayma Mesafesinin Invar-36 Süper Alaşımının Kuru Kaymalı Aşınma Özellikleri Üzerindeki Etkileri

Öz

Bu çalışmada, demir bazlı Invar-36 süper alaşımın aşınma ve sürtünme davranışı çeşitli kayma mesafeleri (25, 50, 75 ve 100 m) ve yükler (5, 15 ve 25 N) altında alümina top karşıt yüzeyi kullanılarak incelenmiştir. Aşınmış yüzeyler, enerji dağılımlı X-ışını spektroskopisi (EDS) ile donatılmış taramalı elektron mikroskobu (SEM) ve 2D-profilometri kullanılarak karakterize edilmiştir. Deneysel sonuçlar, Invar-36'nın sürtünme katsayısının (0,37-0,51) artan normal yük ile önemli ölçüde azaldığını göstermektedir ve en düşük değer 25 N'da elde edilmiştir. Buna karşın, artan kayma mesafesi ile sürtünme katsayısında çok az bir artış görülmüştür. Ayrıca, yapılan deneylerde 2,63-157,17×10⁻³ mm³ aralığında bulunan aşınma hacmi değerlerinin artan normal yük ve kayma mesafesi ile yükseldiği gözlenmiştir. Uygulanan yükün artmasıyla aşınma oranı 1,98-2,99×10⁻⁵'ten 6,33-11,45×10⁻⁵ mm³/Nm'ye çıkmıştır. Aksine, artan kayma mesafesi ile özellikle daha yüksek yükler altında yoğunlaştırma işlemi oluşması nedeniyle aşınma oranı kademeli olarak azalmıştır. Invar-36 yüzeyinde oksidasyon, abrazyon ve plastik deformasyon dahil olmak üzere çok farklı aşınma mekanizmaları oluşmuştur ve bu mekanizmalar artan normal yük veya kayma mesafesi ile daha yoğun hale gelmiştir.

Anahtar Kelimeler: Invar-36 süper alaşım, Sürtünme, Aşınma, Normal yük, Kayma mesafesi

1. Introduction

Invar-36 superalloy, as an iron-based iron-nickel alloy, has received wide attention in various applications such as precision measuring instruments, molding tools for aerospace and automotive industries [1-4]. This is because of the material's low coefficient of thermal expansion and high dimensional stability under the Curie temperature as well as its satisfactory chemical resistance [5]. However, the moderate tensile strength and surface hardness [6, 7] restrict the use of Invar-36 in load-bearing articulating applications, owing to its single phase austenite (γ -Fe) crystal structure.

A limited number of studies has been found in literature, investigating the wear and friction behavior of Invar-36. For instance, Kanca (2022) [8] examined the tribological performance of powder-pack borided Invar-36 surfaces in a reciprocating wear apparatus and found that the wear resistance significantly increased after the boriding process and increasing sliding distance caused a higher wear volume. Wang et al. (2023) [9] investigated the cryogenic friction and wear properties of Invar-36 superalloy with temperatures as low as $-196\text{ }^{\circ}\text{C}$ under the loads of 0.5-2 N in a rotatory type ball-on-disk tester. The researchers found the reduction in the wear rate and COF of Invar-36 under cryogenic conditions due to self-lubrication effect and lower stress generation on the contact surface. But, there is a lack of research data on Invar-36 alloy under a wide range of loading conditions (from low to high), which should be addressed to explore its tribological performance in more detail and estimate the life of this material under a wide range of loads.

The wear and friction performance of materials has been evaluated using different test parameters such as applied load, sliding distance and sliding speed. The test parameters are defined by considering the service conditions of devices and/or components. That is to say the tribological behavior of materials is significantly affected by the aforementioned test parameters. For instance, increasing applied load generally results in an increase in the wear volume while a decrease in friction coefficients. The lower friction coefficient is associated with the formation of a large number of wear debris and an increase in the surface roughness, which lead to a decrease in contact area between the articulating surfaces.

The present work investigates the tribological performance of Invar-36 alloy against alumina ceramic ball under dry conditions using a ball-on-disk tribometer at room temperature. All tests are carried out at sliding distances of 25, 50, 75 and 100 m and normal loads of 5, 15 and 25 N. This study provides the tribological data (friction coefficient, wear rate and wear mechanism) of Invar 36 alloy against alumina ball under different loads and sliding distances, and provides important experimental guidance for the material's potential to be used in various industries such as automotive and aerospace. The wear mechanisms are determined using a scanning electron microscopy (SEM) equipped with energy dispersive X-ray spectrometer (EDS) map analysis.

2. Materials and Methods

The chemical content of Fe-based Invar-36 superalloy used in the current study is provided in Table 1. Cylindrical samples (nominal diameter 25 mm, thickness 3.5 mm) were subjected to a conventional metallographic preparation process, composed of cold mounting, gradual sanding (320-600-800-1000-1200-2500 SiC) and polishing (1 μm diamond paste).

Table 1. Chemical content (wt.%) of Fe-based Invar-36 superalloy used in the current study.

Material	Fe	Ni	Mn	Si	C
Invar-36	Balance	36.55	0.25	0.16	0.02

The experiments were carried out in dry-sliding conditions on a customized ball-on-disk wear apparatus according to ASTM G-133. The Invar-36 discs were articulated against an alumina ball (diameter 6 mm) at room temperature at the loads of 5, 15 and 25 N and the sliding distances 25, 50, 75 and 100 m. All tests were performed at a stroke length of 5 mm and a sliding velocity of 20 mms^{-1} . The friction coefficient (COF) was calculated as the rate of frictional force (recorded during the wear experiment) to normal load. Mean COF values at the aforementioned sliding distances were calculated by averaging the 6-meter COF data before each specified sliding distance. A list of test parameters is provided in Table 2.

Table 2. Test conditions used for testing in ball-on-disk tribometer.

Test specimens	Upper: alumina ball ($\text{\O}6$ mm) Lower: Invar-36 disk ($\text{\O}25$ mm, 3.5 mm)
Stroke length	5 mm
Average sliding speed	20 mm/s
Applied load	5, 15 and 25 N
Sliding distance	25, 50, 75 and 100 m
Test temperature	Ambient

The wear volume (volume loss) was calculated from the wear track profiles obtained using a 2D profilometry (MarSurf M300, Germany), as previously described by Kanca, 2022 [8]. The wear rate (W) was then quantified as follows:

$$W = \Delta V / (FS) \quad (\text{Eq. 1})$$

Where ΔV : Wear track volume (mm^3), F: Test load (N) and S: Sliding distance (m).

The wear mechanism was examined using a scanning electron microscopy (SEM, Jeol JSM-7001F). Energy dispersive X-ray spectrometer (EDS) map analysis was performed with the same device to investigate the distribution of elements of the wear surfaces.

3. Results and Discussion

3.1. Friction and Wear Behavior

The friction and wear behavior of Invar-36 superalloy was evaluated under dry sliding conditions. Figure 1 demonstrates the coefficient of friction (COF) of Invar-36 superalloy against the alumina ball for the normal loads of 5, 15 and 25 N as a function of sliding distance. The COF of all tests found an initial sharp rise and drop state followed by a steady state. The COF rapidly increased to around 0.5 followed by decreasing to the levels of 0.25-0.33, classified as a running period, as defined in previous studies [10, 11]. Afterwards, the curve showed only a mild increase during the steady state, which can be attributed to the formation of a tribolayer suggested by Kuang et al. (2022) [12]. The steady COFs were found to decrease with increasing normal loads, which were 0.49-0.51, 0.37-0.40, and 0.33-0.35 under the normal loads of 5, 15, and 25 N, respectively.

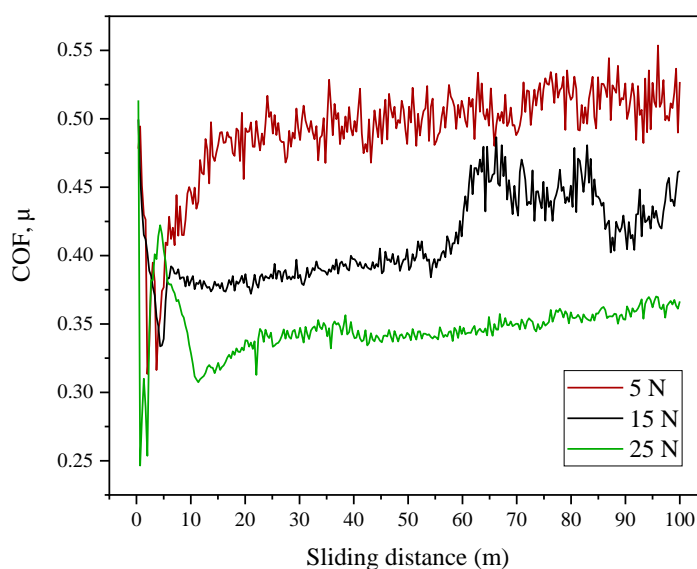


Figure 1. Coefficient of friction (μ) over sliding distance under the loads of 5, 15 and 25 N.

Figure 2 shows the mean COFs obtained from the articulation of Invar-36 surfaces as a function of sliding distance at the loads of 5, 15 and 25 N. The increase in the contact load caused a significant decrease in the COF for any given sliding distance. For instance, at the sliding distance of 25 m, the average friction coefficient was 0.50 under 5 N, which was found to be 0.46 with an 8% decrease as the load increased to 15 N, and 0.41 with a decrease of 18% at 25 N. Similar trend was observed at the sliding distances of 50, 75 and 100 m. Under increased loads there found to be an increase in the contact area between the articulating surfaces (see wear track width and depth values given in Table 3). Even so, it is stated by previous researchers [13, 14] that the increased concentration of wear debris between the two articulating materials at increasing loads leads to a decrease in the real contact area, which might result in the decrease in the COF at higher applied loads in the current work.

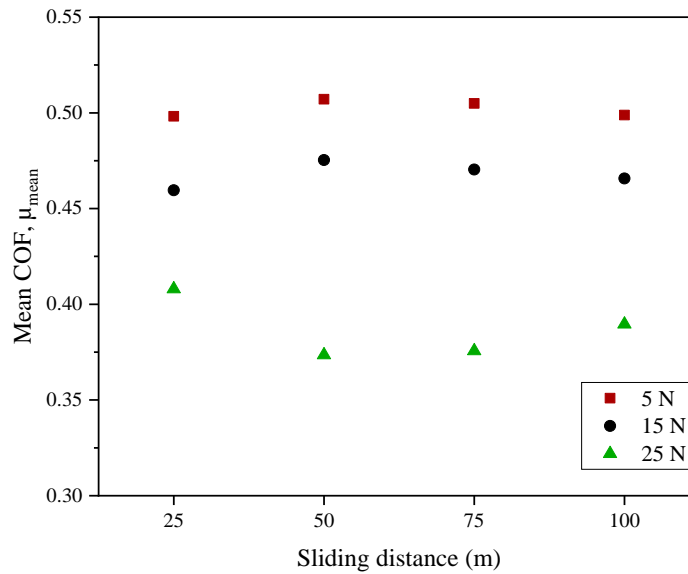


Figure 2. Mean coefficient of friction (μ_m) versus sliding distance at the loads of 5, 15 and 25 N.

After each wear test, 2D wear profiles across the wear tracks were obtained from the Invar-36 surfaces. Figure 3 shows typical wear profiles formed on the Invar-36 surfaces, obtained at the sliding distance of 50 m. The wear track widths and depths were found to increase with increasing normal load and sliding distance (Figure 3 and Table 3). Depending on the applied load and number of sliding cycle, the wear track width and depth values were ranged from 361.3 to 1115.3 μm and from 5.68 to 60.57 μm , respectively. When the normal load increased from 5 to 15 N, the wear track width increased by 98% (at the sliding distance of 25 m), 39% (at 50 m), 36% (at 75 m) and 35% (at 100 m). The increment was found to be 26-44% as the normal load was further increased to 25 N. Under a given normal load from the sliding distance of 25 to 100 m, the wear track width increased by 58% (at 5 N), 8% (at 15 N), and 12% (at 25 N). While, the wear track depth increased by 93% (at 5 N), 60% (at 15 N), and 67% (at 25 N).

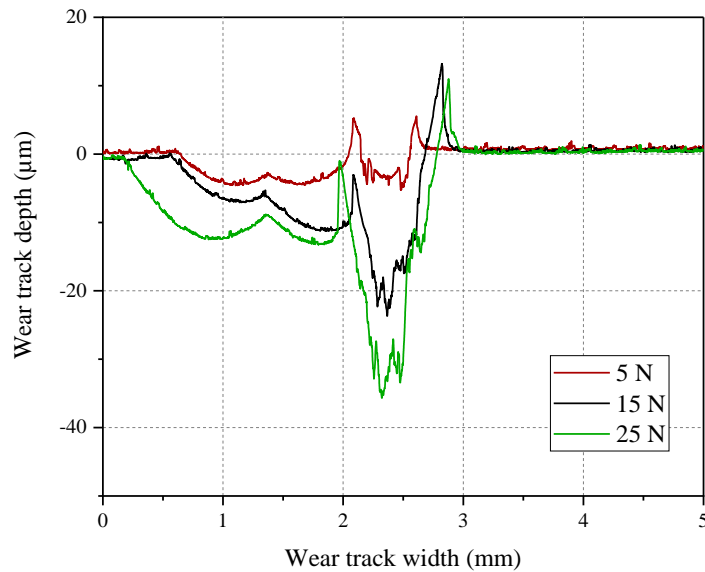


Figure 3. 2D wear track profiles of Invar-36 alloy, subjected to the tests at the sliding distance of 50 m under the loads of 5, 15 and 25 N.

Figure 4 shows the wear volume as a function of the sliding distance under the applied loads of 5, 15 and 25 N. The wear volume increased with the increase in the sliding distance and applied load. For instance, the wear volume increased by 1.5-fold (from 27.53×10^{-3} to $69.25 \times 10^{-3} \text{ mm}^3$) as the sliding distance increased from 25 to 100 m under the applied load of 15 N, and 10.9-fold (from 7.70×10^{-3} to $91.29 \times 10^{-3} \text{ mm}^3$) as the normal load increased from 5 to 25 N under the sliding distance of 50 m. The higher load and reciprocating cycle caused an intensive shear stress and plastic deformation at the articulating asperities and thereby a greater degree of wear volume on the Invar-36 surface. The wear volume was found to be $2.6 \times 10^{-3} \text{ mm}^3$, obtained at the lowest load and distance (5 N and 25 m). While, the most severe wear ($157.2 \times 10^{-3} \text{ mm}^3$) happened during the experiment conducted at the maximum applied load and sliding distance (25 N and 100 m). This finding is coincident with the mean surface roughness (R_a) observations (Table 3). The lowest R_a value ($0.353 \text{ } \mu\text{m}$) was obtained from the experiment performed at the normal load of 5 N and the sliding distance of 25 m while the highest R_a value ($1.953 \text{ } \mu\text{m}$) was obtained from the test conducted at the load of 25 N and the sliding distance of 100 m.

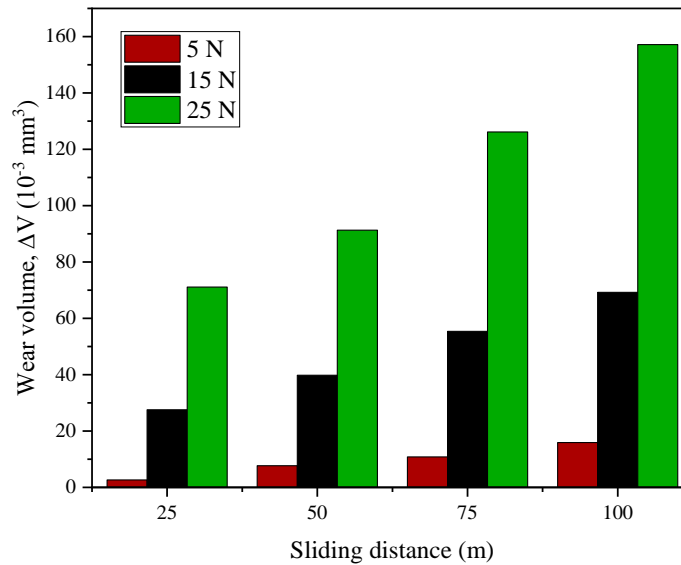


Figure 4. Wear volume of Invar-36 obtained after the articulation against the alumina ball at the loads of 5, 15 and 25 N and the sliding distances of 25, 50, 75 and 100 m.

Figure 5 shows the specific wear rate as a function of the sliding distance, obtained on the Invar-36 surfaces under the applied loads of 5, 15 and 25 N. When the normal load was increased from 5 to 25 N, the specific wear rate was observed to increase constantly from $1.98\text{-}2.99 \times 10^{-5}$ to $6.33\text{-}11.45 \times 10^{-5} \text{ mm}^3/\text{Nm}$. But, the results were diverse when the number of sliding cycle was increased. At the lowest applied load (5 N), the specific wear rate was increased by 46% (from 1.98×10^{-5} to $2.90 \times 10^{-5} \text{ mm}^3/\text{Nm}$) as the sliding distance was increased from 25 to 50 m, and remained around the same level at 75 m ($2.72 \times 10^{-5} \text{ mm}^3/\text{Nm}$) and 100 m ($2.99 \times 10^{-5} \text{ mm}^3/\text{Nm}$). At 15 and 25 N, on the other hand, the specific wear rate was reduced with the increase in the sliding distance and the reduction was more remarkable from the sliding distance of 25 to 50 m. The decrease in the wear rate even though the increase in the wear volume indicates a reduction in the wear intensity due to the densification process. The occurrence of wear intensity was reported by Kuang et al. (2022) [12] under elevated normal loads.

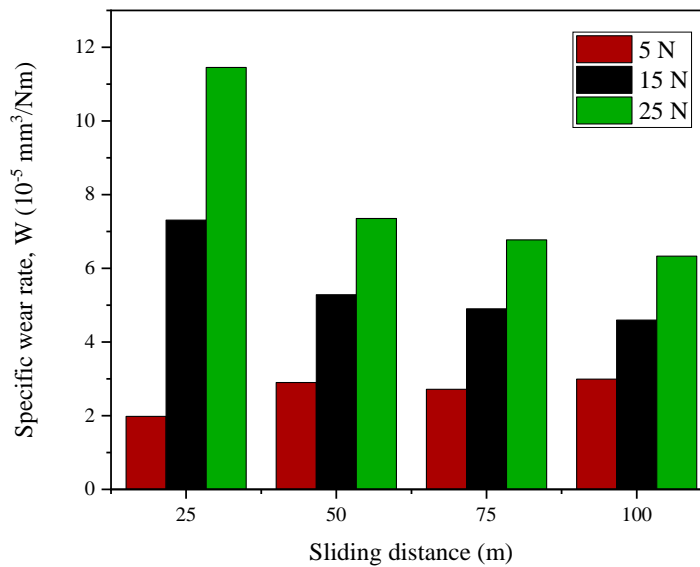


Figure 5. Specific wear rate of Invar-36 at the loads of 5, 15 and 25 N and the sliding distances of 25, 50, 75 and 100 m.

Table 3. Average surface roughness, mean COF, wear track width and depth, volume loss and wear rate of Invar-36 alloy, subjected to dry-sliding reciprocating wear tests under various loads and sliding distances.

Nomenclature	Ra (μm)	Mean COF	Wear track width (μm)	Wear track depth (μm)	Wear volume (10^{-3} mm^3)	Wear rate (10^{-5} mm^3/Nm)
25m-5N	0.353	0.498	361.3	5.68	2.63	1.98
25m-15N	0.924	0.460	716.4	18.84	27.53	7.31
25m-25N	1.753	0.408	993.2	36.25	71.10	11.45
50m-5N	0.562	0.507	526.3	6.79	7.69	2.90
50m-15N	1.066	0.475	729.2	24.47	39.79	5.28
50m-25N	1.285	0.374	936.1	37.42	91.29	7.35
75m-5N	0.681	0.505	568.0	11.78	10.81	2.72
75m-15N	1.037	0.470	774.3	26.69	55.37	4.90
75m-25N	0.830	0.376	975.8	41.97	126.13	6.77
100m-5N	0.669	0.499	571.0	10.97	15.89	2.99
100m-15N	0.756	0.466	772.7	30.05	69.25	4.60
100m-25N	1.953	0.390	1115.3	60.57	157.19	6.33

3.2. Surface Wear Analysis

Photographs, SEM and EDS mapping images of the wear scars obtained from the Invar-36 surfaces undergone a minimum (25m-5N), moderate (100m-5N) and maximum (100m-25N) wear deformation were shown in Figures 6-8. Micro-cracks perpendicular to the sliding direction were seen because of fatigue loading occurred during the wear tests, which indicates the occurrence of plastic deformation on the Invar-36 surface during the articulation. The plastic deformation was more evidence at increased sliding distances and normal loads. Moreover, SEM images obtained from the wear tracks showed micro-scratches parallel to the sliding direction, mainly caused by the plowing of the asperities on the Invar-36 surface. There also found to be the occurrence a large amount of wear debris during the wear test.

The EDS analysis was conducted to detect the oxidation behavior of the wear scars, as shown in Figures 6-8(d-e). There found to be iron (51.1-53.4 wt.%) and nickel (28.3-28.8 wt.%) on the wear tracks, which are available in the chemical composition of Invar-36 (Table 1). The presence of oxygen (17.7-20.2 wt.%) and aluminum (0.2-0.5 wt.%) should be noted, which indicates the oxidation of the surface and a small amount of elemental transfer from the abrasive ball. With the increase in the applied load, there observed to be an increase in oxygen levels due to the effect of increasing temperature and the increased wear of the abrasive ball which triggers the material transfer.

The SEM-EDS investigation on the wear tracks clearly shows that the mechanism of wear failure of Invar-36 alloy was complicated and occurred by the combination of abrasion, plastic deformation, and oxidation, acting simultaneously. The surfaces suffered severe wear when the tests were performed at higher applied loads and sliding distances, as evidenced by deeper and wider wear tracks (Figure 3 and Table 3). The wear track widths of 25m-5N, 100m-5N and 100m-25N were measured as 370.4, 570.3 and 1123.1 μm from the SEM images, respectively (Figures 6-8(b)). These values were consistent with those obtained from 2D profilometry (Figure 3 and Table 3).

Effects of Normal Load and Sliding Distance on the Dry Sliding Wear Characteristics of Invar-36 Superalloy

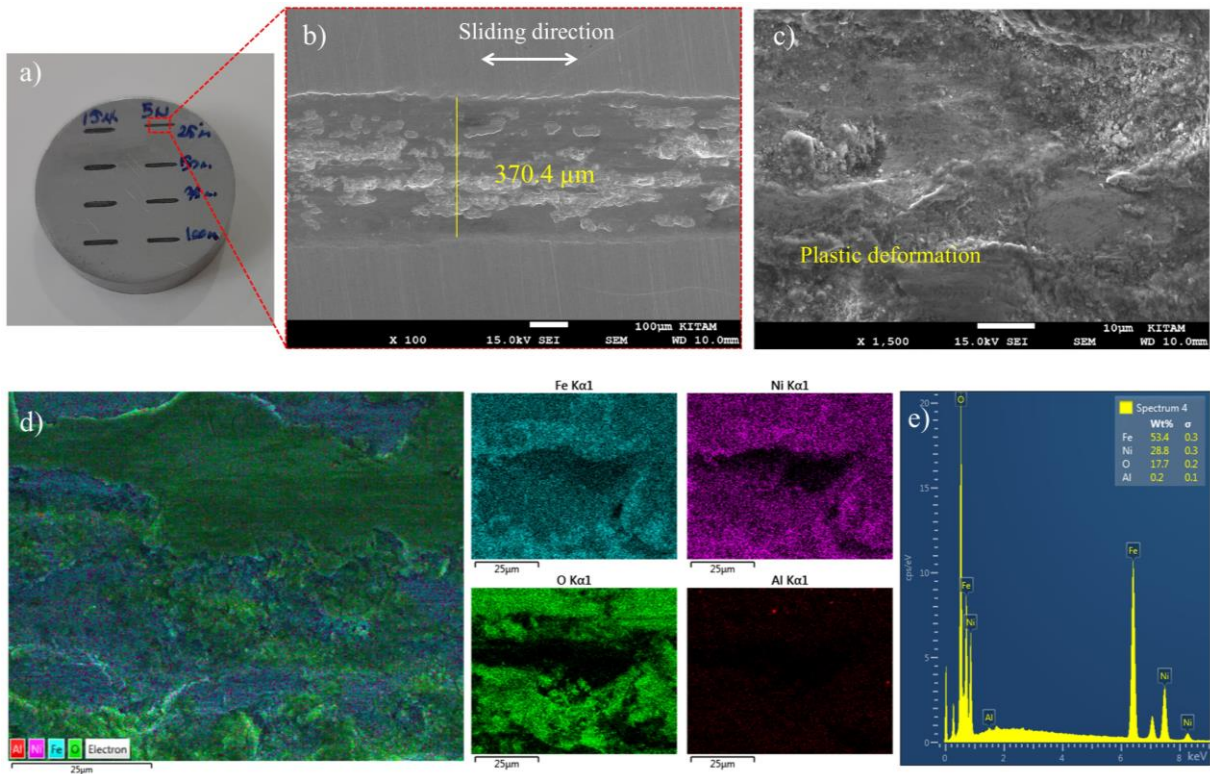


Figure 6. (a) A photograph, SEM images magnified by (b) $\times 100$ and (c) $\times 1500$, (d) EDS mapping and (e) EDS spectra of the worn surface obtained from the experiment performed at the sliding distance of 25 m and the load of 5 N.

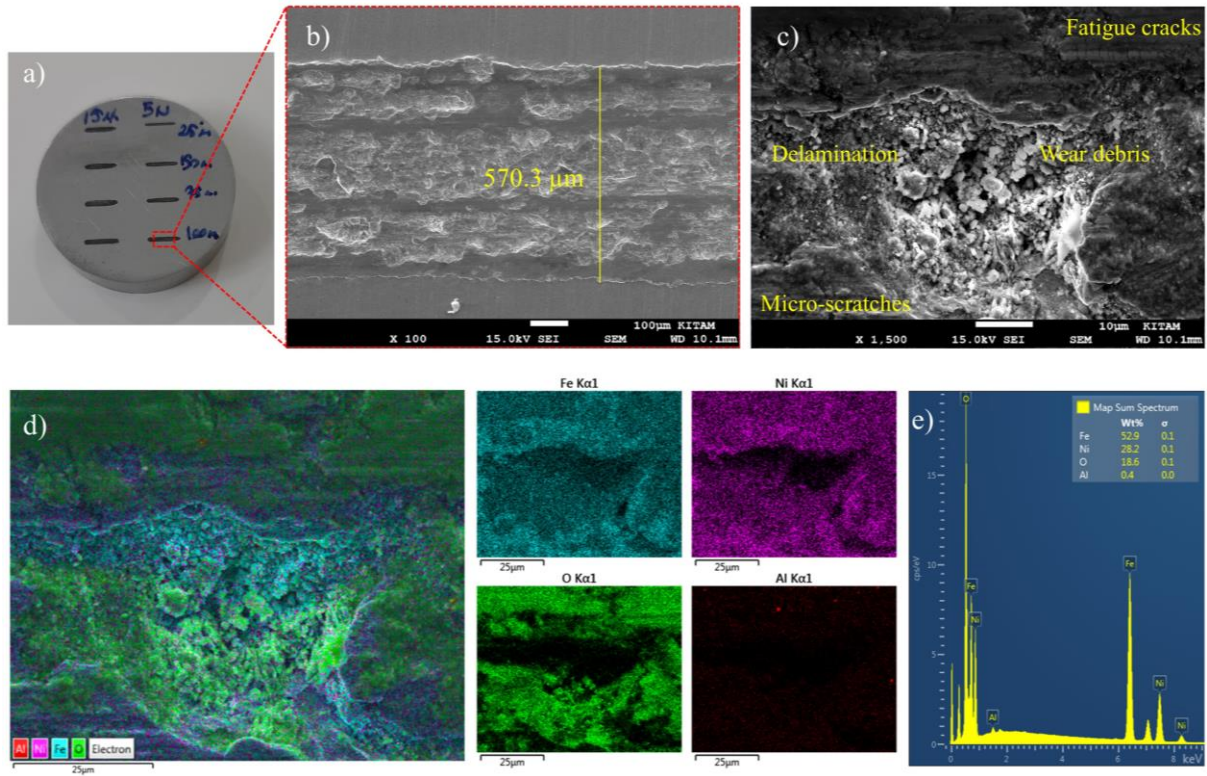


Figure 7. (a) A photograph, SEM images magnified by (b) $\times 100$ and (c) $\times 1500$, (d) EDS mapping and (e) EDS spectra of the worn surface obtained from the experiment performed at the sliding distance of 100 m and the load of 5 N.

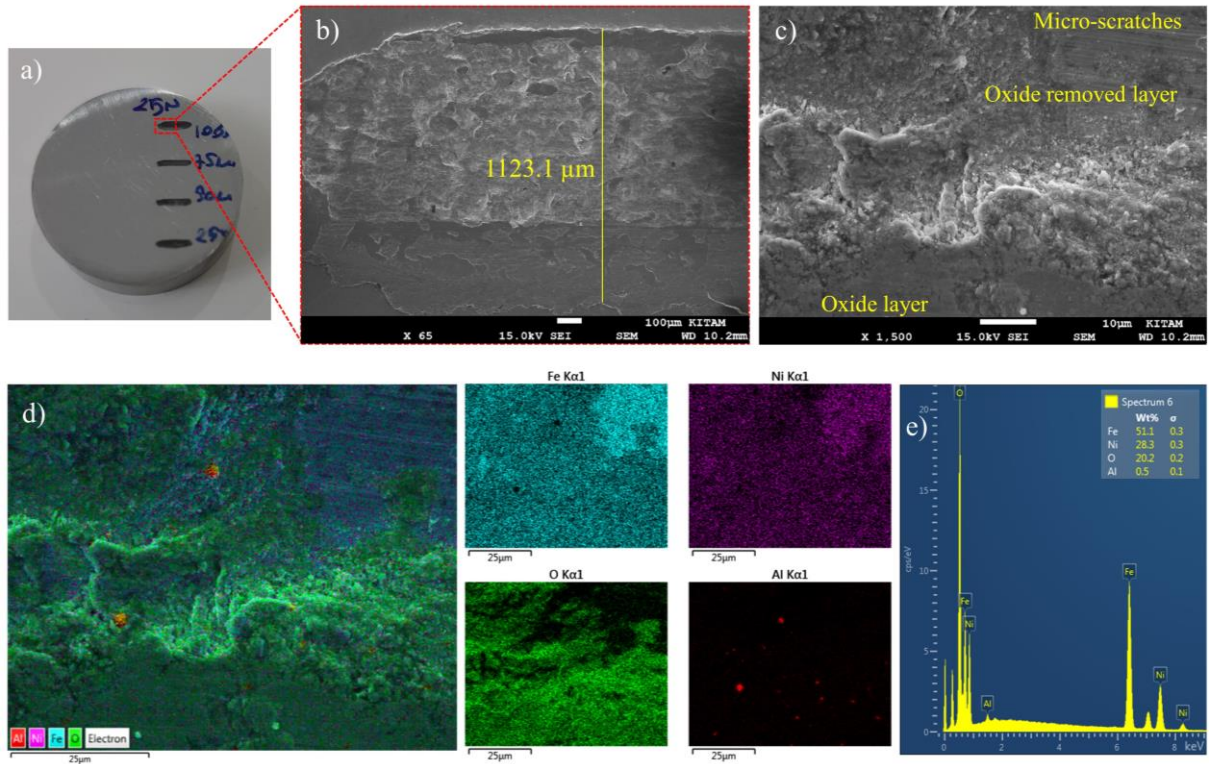


Figure 8. (a) A photograph, SEM images magnified by (b) $\times 100$ and (c) $\times 1500$, (d) EDS mapping and (e) EDS spectra of the worn surface obtained from the experiment performed at the sliding distance of 100 m and the load of 25 N.

4. Conclusions

In the current study, systematic dry sliding wear tests of Fe-based superalloy Invar-36 against alumina ball in a ball-on-disk tribometer using various parameters of sliding distance and normal load was conducted. The following conclusions can be drawn.

1. Both friction coefficient and specific wear rate of Invar-36 are strongly affected by the sliding parameters (the normal load and number of reciprocating cycles).
2. The friction coefficient of Invar-36 (0.37-0.51) was found to decrease with increasing applied load, with a minimum value at 25 N. On the other hand, only a slight increase in the COF was reported with increasing the number of reciprocating cycles.
3. The wear volume of Invar-36 was ranged from 2.63×10^{-3} to $157.17 \times 10^{-3} \text{ mm}^3$. The alloy exhibited higher wear volume at increased applied loads and the number of sliding cycles.
4. A constant increase in the wear rate (from $1.98\text{-}2.99 \times 10^{-5}$ to $6.33\text{-}11.45 \times 10^{-5} \text{ mm}^3/\text{Nm}$) was observed with the increase in the applied load. But, the wear rate was lowered when the sliding distance was increased especially at higher applied loads, due to the densification process.
5. The wear mechanism on the Invar-36 surfaces was complicated with the combination of oxidation, abrasion, and plastic deformation, which became more intense when the normal load or sliding distance was increased.

Ethics in Publishing

There are no ethical issues regarding the publication of this study.

Author Contributions

YK: Conceptualization, Methodology, Investigation, Resources, Formal analysis, Writing - original draft, Writing - review & editing.

References

- [1] Giolli, C., Turbil, M., Rizzi, G., Rosso, M., Scrivani, A., (2009) Wear resistance improvement of small dimension Invar massive molds for CFRP components, *Journal of thermal spray technology*, 18, 652-664.
- [2] Jasthi, B.K., Arbegast, W.J., Howard, S.M., (2009) Thermal expansion coefficient and mechanical properties of friction stir welded Invar (Fe-36%Ni), *Journal of materials engineering and performance*, 18, 925-934.
- [3] Yakout, M., Elbestawi, M.A., Veldhuis, S.C., (2018) A study of thermal expansion coefficients and microstructure during selective laser melting of Invar 36 and stainless steel 316L, *Additive manufacturing*, 24, 405-418.
- [4] Sahoo, A., Medicherla, V.R.R., (2021) Fe-Ni Invar alloys: A review, *Materials today: proceedings*, 43, 2242-2244
- [5] Wu, C., Guo, W., Li, R., Zhao, Y., Zhou, Q., (2020) Thermal effect on oxidation layer evolution and phase transformation in grinding of Fe-Ni super alloy, *Materials letters*, 275, 128072.
- [6] Wei, K., Yang, Q., Ling, B., Yang, X., Xie, H., Qu, Z., et al. (2020) Mechanical properties of Invar 36 alloy additively manufactured by selective laser melting, *Materials science and engineering: A*, 772, 138799.
- [7] Zheng, S., Sokoluk, M., Yao, G., de Rosa, I., Li, X., (2019) Fe–Ni Invar alloy reinforced by WC nanoparticles with high strength and low thermal expansion, *SN applied sciences*, 1:172.
- [8] Kanca, Y., (2022) Microstructural characterization and dry sliding wear behavior of boride layers grown on Invar-36 superalloy, *Surface and coatings technology*, 449, 128973
- [9] Wang, B., Guo, Y., Zhang, Z., Yi, X., Wang, D., (2023) Investigation of cryogenic friction and wear properties of Invar 36 alloy against Si₃N₄ ceramic balls, *Wear*, 518-519, 204648
- [10] Kanca, Y., Uçgun, M.C., Günen, A., (2022) Microstructural and tribological behavior of pack-borided Ni-based Hastelloy C-276 superalloy, *Metallurgical and materials transactions A*, 54, 671-687.

- [11] Deng, G., Tieu, A.K., Lan, X., Su, L., Wang, L., Zhu, Q., et al., (2020) Effects of normal load and velocity on the dry sliding tribological behaviour of CoCrFeNiMo0.2 high entropy alloy, *Tribology international*, 144, 106116.
- [12] Kuang, W., Qing, M., Wenfeng, D., Yanjun, Z., Biao, Z., Xuebing, W., et al, (2022) Fretting wear behaviour of machined layer of nickel-based superalloy produced by creep-feed profile grinding, *Chinese journal of aeronautics*, 35, 401-411.
- [13] Sarkar, A.D. (1980) *Friction and wear*. Academic Press.
- [14] Panagopoulos, C.N., Giannakopoulos, K.I., Saltas, V., (2003) Wear behavior of nickel superalloy, CMSX-186, *Materials letters*, 57, 4611-4616.

Evaluation of the Trophic Status of Karasu River (Erzincan, Türkiye) by Biodiversity Indices

Özden FAKIOĞLU¹, Özge ZENCİR TANIR^{2*}, Zeliha AKYÜZ¹, Muhammet Furkan TOPAL¹

¹Department of Basic Science, Fisheries Faculty, Atatürk University, Türkiye

²Department of Biology, Faculty of Arts and Sciences, Erzincan Binali Yıldırım University, Türkiye

Received:05/08/2022, **Revised:** 02/03/2023, **Accepted:** 06/03/2023, **Published:** 30/03/2023

Abstract

This study focuses on seasonal and temporal variations of the biodiversity and composition of the phytoplankton community in Karasu River. The phytoplankton and water samples were collected bimonthly from a depth of 0.5-8 m during the period from January 2019 to July 2019 from five stations. Four diversity indices (Shannon-Wiener, Simpson, Margalef and Menhinick) were studied. MINITAB 15 Software was used to interpret the relationship between the indices. Average water temperature, dissolved oxygen, pH and electrical conductivity values were measured as 19.43 °C, 7.9 mg L, 8.3 and 465 mS/cm, respectively. In this study, a total of 123 phytoplankton species were identified. Among these species, 106 species belonging to Bacillariophyta group, 10 species belonging to Chlorophyta group, 6 species belonging to Cyanobacteria group and 1 species belonging to Euglenophyta group were included. Throughout the study, Shannon-Wiener, Simpson Margalef, and Menhinick diversity indices were calculated as 1.83 H', 11.53, 5.12 and 0.83 and respectively. As a result of this study, phytoplankton diversity indices and ecological status assessment based on water quality were not found to be compatible. However, introducing reference conditions for different cities can increase the usability of the indices thus we recommend expanded further studies.

Keywords: Shannon-Wiener, biodiversity indices, phytoplankton, Karasu River

Karasu Nehri (Erzincan,Türkiye)'nin Trofik Durumunun Biyoçeşitlilik İndeksleriyle Değerlendirilmesi

Öz

Bu çalışma, Karasu Nehri'ndeki fitoplankton kompozisyonunun ve biyolojik çeşitliliğinin mevsimsel ve zamansal değişimlerine odaklanmıştır. Fitoplankton ve su örnekleri Ocak 2019-Temmuz 2019 döneminde iki ayda bir 0.5-8 m derinlikten beş istasyondan toplanmıştır. Dört çeşitlilik indeksi (Shannon-Wiener, Simpson, Margalef ve Menhinick) incelenmiştir. Endeksler arasındaki ilişkiyi yorumlamak için MINITAB 15 yazılımı kullanılmıştır. Ortalama su sıcaklığı, çözülmüş oksijen, pH ve iletkenlik değerleri sırasıyla 19.43 °C, 7.9 mg/L, 8.3 ve 465 mS/cm olarak ölçülmüştür. Bu çalışmada toplam 123 fitoplankton türü tespit edilmiştir. Bu türlerden Bacillariophyta grubuna ait 106 tür, Chlorophyta grubuna ait 10 tür, Cyanobacteri grubuna ait 6 tür ve Euglenophyta grubuna ait 1 tür teşhis edilmiştir. Çalışma boyunca Shannon-Wiener, Simpson Margalef ve Menhinick çeşitlilik indeksleri sırasıyla 1.83 H', 11.53, 5.12 ve 0.83 olarak hesaplanmıştır. Bu çalışma sonucunda fitoplankton çeşitlilik indeks değerleri ile Karasu Nehri'nin su kalitesine bağlı ekolojik durum değerlendirilmesi bir biri ile uyumlu olmadığı tespit edilmiştir. Ancak farklı şehirler için referans koşulların geliştirilmesi endekslerin kullanılabilirliğini artırabilir. Bu nedenle bu çalışmaların devam etmesini ve yaygınlaşmasını öneriyoruz.

Anahtar Kelimeler: Shannon-Wiener, biyolojik çeşitlilik indeksleri, fitoplankton, Karasu Nehri

*Corresponding Author: zencir06@hotmail.com

Özge ZENCİR TANIR, <https://orcid.org/0000-0002-2111-7019>

Özden FAKIOĞLU, <https://orcid.org/0000-0002-7193-2177>

Zeliha AKYÜZ, <https://orcid.org/0000-0002-2663-0161>

Muhammet Furkan TOPAL, <https://orcid.org/0000-0002-2408-8225>

1. Introduction

Türkiye has very important inland water resources with its streams and lakes covering an area of approximately 10000 km². The Eastern Anatolia Region has the highest lake and river potential in Turkey. Aras, Kura, Tigris, Euphrates and many streams and tributaries feeding these rivers are located in this region. Inland water resources have been declining gradually, especially in recent years, due to the impact of climate change, rapid population growth and pollution. In order to protect these resources, it is necessary to determine the physical, chemical and biological properties of these resources. In addition, it is important to take the restoration measures in cases where regular monitoring of fresh water resources is necessary in terms of the existence of these resources in the future.

Biological diversity can be expressed as the diversity of living communities that are in contact with each other. In other words, biodiversity encompasses all the genes in a region, the species that carry these genes, the ecosystems that host these species, and the events that connect them. In this context, diversity; is a very broad concept that includes the diversity of species, ecosystems and ecological events. Species diversity is the large number of species found in a particular region that includes all species [1, 2].

Among relatively intact streams ecosystems, primary productivity is directly related to flow patterns. Much of the increase in fluvial autotrophy is due to increased production of periphytic algae associated with widespread deposition of sedimentary surfaces and expansion of river folds and folded shallow subsurfaces. When stream ecosystems are disturbed, it increases algal biomass concentrations and potentially significantly increases primary productivity in this region [3].

Species diversity is an important key to our understanding of many systems. The structure and number of periphyton, macrophyte and plankton communities is an important factor in determining the pollution status of rivers. All freshwater algae are sensitive to changes in the water body. Phytoplankton communities are generally found in rivers associated with stagnant bodies of water (dam, lake, etc.) or in slow-flowing parts of rivers crossing large plains. The structure and abundance of phytoplankton communities are affected by the presence of light, temperature and nutrients in lakes, while flow and water velocity affect rivers [4].

The degree of diversity should be specified as a numerical value and diversity indices should be calculated in order to statistically compare the degree of diversity of different systems [5]. Shannon-Wiener, Simpson, Margalef, Menhinick, and McIntosh are the most widely used diversity indices to obtain information about species richness and distribution of individuals among species at stations [6].

There is constant substance inclusion in streams. For this reason, in addition to being under the influence of the basin through which the stream passes, environmental physical factors can sometimes be more effective than in lentic environments. In streams, where light can enter, there are autochthonous products, algae, algae and higher plants [7]. In order to understand the

efficiency of river systems, it is necessary to look at the planktonic richness of the environment and their qualitative and quantitative compositions [8].

Studies have shown that cyanobacteria respond favorably to higher phosphorus concentrations, lower nitrogen-to-phosphorus (N/P) ratios, longer residence time, and less turbulent conditions. In addition, many cyanobacteria can fix nitrogen (converting gaseous nitrogen to ammonia when nitrate is limited), this is expected to provide an advantage for cyanobacteria when nitrogen is limiting. Manier et al. (2021) [9] showed that phytoplankton communities in major rivers tended to transition from cyanobacteria predominant in the upper parts to diatoms predominant in the lower parts. This pattern is likely due to the fact that cyanobacteria lose their competitive advantage (ie access to light) during the turbulent and turbid conditions that prevail in the lower reaches of rivers.

This study focuses on seasonal and temporal variations of the biodiversity and composition of the phytoplankton community in Karasu River, which have not been adequately described yet. It was aimed to contribute to revealing the biodiversity and ecology of this aquatic ecosystem by adding knowledge to the phytoplankton composition and hydrobiology of the Karasu River.

2. Materials and Methods

2.1. Site description

As one of the main tributaries of the Euphrates River, the Karasu River flows from the Dumlu Mountains in the Erzurum Plain and is located in the eastern part of Turkey. It flows through the district of Aşkale and passes through the town of Mercan in the Karasu Valley in the province of Erzincan. It forms the Euphrates River joining the Murat River near the town of Keban. Its length to the Keban Dam Lake is 460 km [10]. This study contains Erzincan Provincial decomposition sections. The convenient stations and coordinates are given in Figure 1.



Figure 1. Location of the Karasu River and the sampling sites

2.2. Sampling and analysis

The phytoplankton samples were collected bimonthly from a depth of 0.5-8 m during the period from January 2019 to July 2019 from five stations. Water samples were taken with a nansen bottle in order to determine the phytoplankton density, species diversity and some water quality parameters at the selected sampling stations. The samples were filtered with 0.45 µm membrane filters and placed in polyethylene bottles.

Physico-chemical parameters including water temperature, pH, conductivity and dissolved oxygen (DO) were measured by a digital multiparameter (Model: YSI Plus) *in situ*.

The chlorophyll-a (630 nm, 645 nm and 665 nm), ammonia-nitrogen (410 nm), nitrite-nitrogen (523 nm), nitrate-nitrogen (410 nm), orthophosphate (720 nm) and total phosphorus (720 nm) were analyzed spectrophotometrically (Model: Beckman Coulter DU730 UV-Vis) [11].

The water samples were first dripped with 10 mL of Lugol's solution in the measuring tapes and kept overnight, then placed in the plankton counting circles (3 mL) and phytoplankton counts were made with the help of an inverted microscope according to the phytoplankton density [12]. Epilytic diatom samples were preserved in Lugol's solution [13]. The diatoms were boiled with equal volumes of nitric acid and sulfuric acid and the water samples were precipitated by dropping Lugol's solution, then fixed preparations were prepared with entellan after removing the acid by washing.

Phytoplankton identification was performed using sedimented water samples or samples taken with plankton scoops according to taxonomic literature [14, 15, 16, 17, 18, 19] under binocular microscope (100x and 400x magnification) [12].

2.3. Biodiversity indices

Four diversity indices (Shannon-Wiener, Simpson, Margalef and Menhinick) were calculated.

2.3.1. Shannon-Wiener diversity index (H')

This index is applied to biological systems which is derived from a mathematical formula by Shannon in 1948 [20]:

$$H' = -\sum_{i=1}^s p_i \log_e p_i, \quad p_i = n_i/n$$

Where s is the total number of species and p_i is the number of individuals belonging to i species (n_i) / total number of individuals (n) [21, 22, 23, 24].

2.3.2. Simpson diversity index (D)

$$1-D = [\sum n_i(n_i - 1)]/N(N-1)$$

Where n_i is the number of individuals belonging to i species and N is the total number of species [21, 22, 23, 24].

2.3.3. Margalef diversity index (D_{mg})

$$D_{mg} = S - 1 / \log N$$

Where S is the number of species and N signifies the number of individuals in a sample [24].

2.3.4. Menhinick diversity index (D_{mn})

$$D_{mn} = S / \sqrt{N}$$

Where S is the number of species and N signifies the number of individuals in a sample [25, 24].

2.4. Statistical analysis

Seasonal data of ammonia-nitrogen ($\text{NH}_3\text{-N}$), nitrite-nitrogen ($\text{NO}_2\text{-N}$), nitrate-nitrogen ($\text{NO}_3\text{-N}$), total phosphorus (TP), orthophosphate phosphorus ($\text{PO}_4\text{-P}$) and chlorophyll-a from sampling stations were analyzed by SPSS 20 using a three-factor Analysis of Variance (ANOVA) in factorial order. DUNCAN test was used to determine the significance level of the difference between groups. The relationship between the diversity indices was examined with the analysis of variance. MINITAB 15 Software was used to interpret the relationship between the indices.

3. Results

Water and plankton samples were taken from 5 stations which were conducted on the part of the Karasu River within the Erzincan Province. Average water temperature, dissolved oxygen, pH and electrical conductivity values were measured as 19.43 °C, 7.9 mg L, 8.3 and 465 mS/cm, respectively.

The variations of the total phosphorus, total orthophosphate, ammonia-nitrogen, nitrite-nitrogen and nitrate-nitrogen values depending on the month and stations were found to be statistically significant ($p < 0.05$). Average total phosphorus values in the river according to the stations were calculated as, 1.06±0.04 mg L, 0.47±0.03 mg L, 0.92±0.03 mg L, 0.32±0.02 mg L and 0.68±0.04 mg L, respectively. While the mean orthophosphate value was determined as 0.001±0.0 mg L, the highest value was found in the 2nd station (0.09±0.0 mg L) in January. Ammonia-nitrogen value was found between 1.56±0.0 mg L and 0.66±0.18 mg L throughout the study. The mean nitrite-nitrogen value in the river was determined according to the stations as 0.23±0.0 mg L, 0.20±0.0 mg L, 0.21±0.0 mg L, 0.17±0.0 mg L and 0.68±0.0 mg L, respectively. The highest value (0.71±0.0 mg L) in the river was detected at 4th station in October, and the lowest value (0.0±0.0 mg L) was detected at 3rd station in the same month. In this study, the mean chlorophyll-a value was calculated as 1.27±0.01 mg L. The lowest value

of chlorophyll-a (0.09 ± 0.03 mg L) was detected at the 1st station in January, and the highest value (4.91 ± 0.03 mg L) was detected at the 2nd station in August (Figure 2).

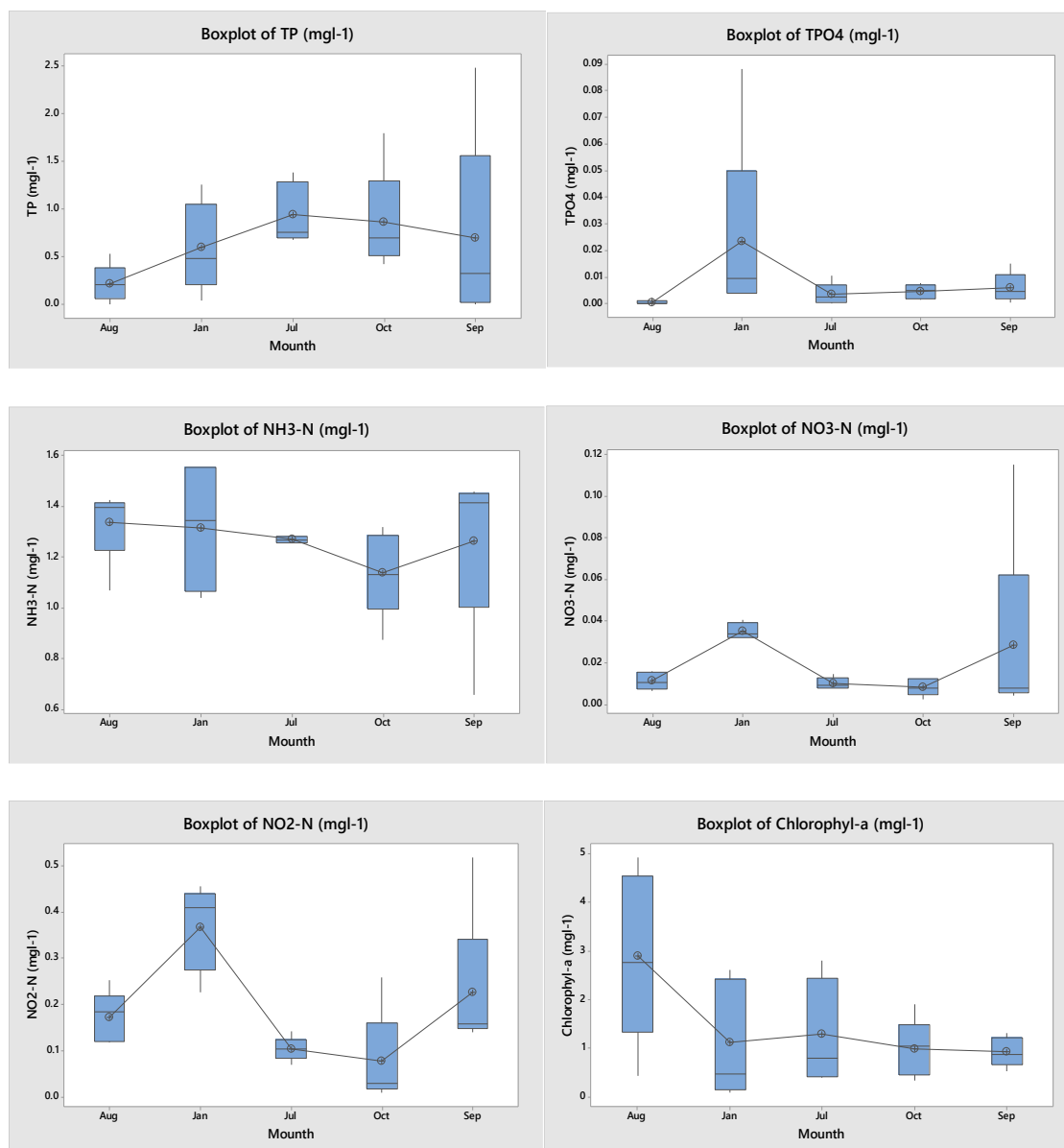


Figure 2. Change of total phosphorus, total orthophosphate, ammonia-nitrogen, nitrate-nitrogen, nitrate-nitrogen and chlorophyll-a values in Karasu River depending on months (n=4)

In this study, a total of 123 phytoplankton species were identified. Among these species, 106 species belonging to Bacillariophyta group, 10 species belonging to Chlorophyta group, 6 species belonging to Cyanobacteria group and 1 species belonging to Euglenophyta group were identified. The availability of the species detected in the Karasu River at the five stations is given in Table 1.

Table 1. Change of phytoplankton species on sampling stations in Karasu River

Species Names	St1	St2	St3	St4	St5
Bacillariophyta					
<i>Cocconeis placentula</i> Ehrenberg 1838	+	+	+	+	+
<i>C.placentula</i> var. <i>euglypta</i> (Ehrenberg) Grunow 1884	+	+	+	+	+
<i>Cymatopleura elliptica</i> (Brébisson) W. Smith 1851	+		+	+	+
<i>Cymbella affinis</i> Kützing 1844	+	+	+	+	+
<i>C.cymbiformis</i> C. Agardh 1830	+	+	+	+	+
<i>C.helvetica</i> Kützing 1844	+	+	+	+	+
<i>C.neoleptoceros</i> Krammer 2002				+	+
<i>Diatoma ehrenbergii</i> Kützing 1844	+	+	+	+	+
<i>D.vulgaris</i> Bory 1824	+	+	+	+	+
<i>Fragilaria capucina</i> Desmazières 1830	+		+	+	+
<i>Gomphonella olivacea</i> (Hornemann) Rabenhorst 1853	+	+	+	+	+
<i>G. augur</i> Ehrenberg 1841		+	+		+
<i>Melosira varians</i> C. Agardh 1827	+	+	+	+	+
<i>Navicula angusta</i> Grunow 1860	+	+	+	+	+
<i>N. bryophila</i> J.B. Petersen 1928	+	+	+	+	+
<i>Nitzschia dissipata</i> (Kützing) Rabenhorst 1860	+	+	+	+	+
<i>N. gracilis</i> Hantzsch 1860	+	+	+	+	+
<i>N. palea</i> (Kützing) W.Smith 1856		+		+	+
<i>Pantocsekiella ocellata</i> (Pantocsek) K.T. Kiss & Ács in Ács & al. 2016:	+		+	+	+
<i>Ulnaria ulna</i> (Nitzsch) Compère 2001	+	+	+	+	+
Chlorophyta					
<i>Acutodesmus raciborskii</i> (Woloszynska) Tsarenko & D.M. John 2011		+			+
<i>Lacunastrum gracillimum</i> (West & G.S. West) H.McManus in McManus & al. 2011			+	+	
<i>Monoraphidium contortum</i> (Thuret) Komárková-Legnerová in Fott 1969				+	+
<i>Pediastrum boryanum</i> var. <i>cornutum</i> (Raciborski) Sulek in Fott 1969	+	+			
<i>P. duplex</i> Meyen 1829		+	+		+
<i>Scenedesmus arcuatus</i> (Lemmermann) Lemmermann 1899	+	+		+	
<i>S. ellipticus</i> Corda 1835			+		
<i>Spirogyra decima</i> var. <i>laxa</i> Kützing 1855		+	+		
Cyanobacteria					
<i>Anabaena flosaquae</i> Brébisson ex Bornet & Flauhault 1886	+			+	
<i>Aphanizomenon gracile</i> Lemmermann 1907					+
<i>Micractinium quadrisetum</i> (Lemmermann) G.M. Smith 1916	+	+			
<i>Microcrocis irregularis</i> (Lagerheim) Geitler 1942	+	+			
<i>M. flosaquae</i> (Wittrock) Kirchner 1898					+
Euglenaphyta					
<i>Euglena acus</i> (O.F. Müller) Ehrenberg, 1830	+				

Throughout the study, Shannon-Wiener, Simpson, Margalef, and Menhinick diversity indexes were calculated as 1.86 H' , 11.53, 5.12 and 0.83 respectively (Table 2.)

Table 2. Shannon-Wiener, Simpson Margalef, and Menhinick diversity indices of the Karasu River

Grups	Count	Sum	Mean	Variance
Shannon-Wiener Diversity Index (H')	24	46.40	1.86	0.52
Simpson Diversity Index (D)	24	288.20	11.53	26.81
Margalef Diversity Index (D_{mg})	24	128.01	5.12	2.80
Menhinick Diversity Index (D_{mn})	24	20.76	0.83	0.08

ANOVA					
Grups	SS	df	MS	F	P-value
Shannon-Wiener Diversity Index (H')	12.38	24	1.39	3.82	0.018
Simpson Diversity Index (D)	643.41	24	88.21	3.86	0.018
Margalef Diversity Index (D_{mg})	67.09	24	6.72	1.68	0.194
Menhinick Diversity Index (D_{mn})	1.99	24	0.30	4.19	0.005

4. Discussion

In this study, some regional physical and chemical parameters of the Karasu River within the Erzincan Province were examined. The changes in total phosphorus, total orthophosphate, ammonia-nitrogen, nitrate-nitrogen and nitrite-nitrogen values depending on months and stations were found to be statistically significant ($p < 0.05$). The data on the phosphorus and nitrogen fractions in this study is important as it is the first for the part between the borders of Erzincan Province. In addition, the first data on phytoplankton communities were presented for the same region.

Biodiversity is the qualified dynamic of an ecological system [26]. The distribution of fish and phytoplankton communities in lakes shows spatial and temporal changes. The change in water quality also affects the species diversity of these creatures [27]. For this reason, some living things in aquatic ecosystems are used as bioindicator organisms. The use of bioindicators is

very important in evaluating the trophic level of lakes and rivers, as it shows the effects of environmental changes on the living group. In this study, although the number of species in the river is high, species indicating that the river is polluted were identified.

According to the Turkish Environmental Legislation [28], the river is in the I. quality class according to the water temperature and dissolved oxygen values, while it is in the III. class is in the quality class according to pH.

According to the Turkish Environmental Legislation [28], the Karasu River is classified as III. class by total phosphorus value, as class IV by nitrite-nitrogen and class I. by nitrate-nitrogen. This indicates show that there is a high level of organic pollution in the water. Eren and Kaya (2020) [29], in a study investigating the effect of Erzurum Wastewater Treatment Plant on the Karasu River, reported that although the BOD₅ and COD values in the effluent of the treatment plant were low, the BOD₅ and COD values measured in the river increased again, which may be due to agricultural and livestock activities in the surrounding area. Ammonia concentrations in natural waters are generally less than 0.1 mg/L. Concentrations higher than 30 mg/L can be found in wastewater [30]. In this study, the ammonia-nitrogen value was determined above 1 mg/L. This shows that organic pollution is mostly from agricultural activities.

Hilton et al. (2006) [31] reported that there was an increase in the growth of epiphytic and benthic algae in rivers with fast flow, while phytoplankton was dominant in rivers with slow flowing water. In a single sampling study conducted by Gürbüz and Ertuğrul (2003) [32] from the starting note of Karasu River, Bacillariophyta was found to be the most dominant group. *Cyclotella*, *Fragilaria*, *Synedra*, *Melosira*, *Nitzschia*, *Diatoma*, *Cymbelle*, *Ceratoneis* and *Chlorella* were reported as the most detected species. In this study, Bacillariophyta was determined as the most dominant group, while *Cocconeis placentula* var. *euglypta*, *Pantocsekiella ocellata* and *Craticula subminuscula* were the most detected species.

In the study carried out in the Karasu River, where the nutrients are not limiting and alkaline water features, it was reported that the *Cyclotella meneghiniana* was the dominant species [33]. In this study, the dominant species is *Cocconeis placentula*.

During this study, the lowest value of chlorophyll-a (0.09 ± 0.03 mg L) was calculated at the 1st station in January, and the highest value (4.91 ± 0.03 mg L) was calculated at the 2nd station in August. In the Melen River the chlorophyll-a value ranged between 0.009 and 0.64 mg L, and the phytoplankton abundance and biomass were low in winter months and high in late spring summer months like our study. It has been reported that the relationship between phytoplankton abundance, chlorophyll-a and temperature is important [34].

Based on the three diversity indices, the water quality was classified into four grades: no pollution ($D_{mg} > 5.0$ and $H' > 3.0$), light pollution ($5.0 > D_{mg} > 4.0$ and $3.0 > H' > 2.0$), moderate pollution ($4.0 > D_{mg} > 3.0$ and $2.0 > H' > 1.0$), and heavy pollution ($3.0 > D_{mg} > 0.0$ and $1.0 > H' > 0.0$) [35, 36]. While the Karasu River is determined as heavily polluted according to the Shannon-Weaver index, it is in the non-polluted area class according to the Margalef index. The classification of the river according to the Margalef index is in accordance

with the classification of the Turkish Environmental Legislation [28] according to the water temperature, dissolved oxygen and nitrate-nitrogen value. The classification of the river according to the Shannon-Weaver index is also compatible with the classification according to the pH, total phosphorus and nitrite-nitrogen values according to the Turkish Environmental Legislation [28].

Ding et al. (2021) [37] stated that the water quality parameters such as sediment and nutrient load significantly affect phytoplankton diversity patterns in Yellow River. However, Geoclimatic factors, such as water surface slope and annual mean precipitation and temperature, also provided non-negligible contributions to the variation in phytoplankton diversity indices. Therefore, in river ecosystems with a large geographical span and complex topography, phytoplankton diversity is not a suitable water quality indicator, although it can reflect habitat changes to a certain extent.

5. Conclusion

In the present study, the indece-based assessment of the Karasu River was differed. For this reason, the view that it requires the determination of the reference conditions used to control the extent of the change in wide-spread rivers and that all these processes need to be done in a large number of water bodies [38] is supported. As a result of this study, phytoplankton diversity indices is not a suitable water quality indicator. However, introducing reference conditions for different cities can increase the usability of the indices. For this reason, we recommend that these studies continue and expand. Furthermore, the presence of Cyanobacteria in natural environments is an important indicator of pollution, so it is recommended to monitor these systems regularly. Further study may be required to species richness as well as density of harmful species for evaluating the ecological quality status of the region.

Ethics in Publishing

There are no ethical issues regarding the publication of this study

Author Contributions

Özden FAKIOĞLU: Designing the study, analysis of water parameters, evaluation of results, statistical calculations, writing the article

Özge ZENCİR TANIR: Designing the study, evaluation of results, writing the article

Zeliha AKYÜZ: Analysis of water parameters, statistical calculations, writing the article

Muhammet Furkan TOPAL: Analysis of water parameters, statistical calculations, writing the article

Acknowledgment

This study was supported by the Erzincan Binali Yıldırım University Scientific Research Projects Coordination Unit (Project No. FBA-2019-634). We would like to thank Erzincan Binali Yıldırım University, Scientific Research Projects Unit for their financial support

References

- [1] Erten, S. (2004) Biodiversity as a rising value at the international level. Hacettepe University Faculty of Education Journal, 27:1-10.
- [2] Gülsoy, S., Özkan, K. (2008) Ecological importance of species diversity and some used indices. Süleyman Demirel University Faculty of Forestry Journal, Ser. A(1), 168-178.
- [3] Wetzel, R.G. (2001) Limnology, W.B. Saunders Company, No. DOE/EV/01599-235-Pt. 4; COO-1599-235-Pt. 4; COO-1599-234). Michigan State Univ., Hickory Corners (USA). WK Kellogg Biological Station London.
- [4] Allan, J.D. (1995) Stream ecology. The Netherlands: Kluwer Academic Publishers.
- [5] Odum, E.P., Barrett, G.W. (2005) Basic principles of ecology. In: Işık K, translation editor. Ankara: Palme Publishing, 598 (in Turkish)
- [6] Jorgensen, S.E., Costance, R., Xu, F.-L. (2005) Handbook of ecological indicators for assessment of ecosystem health. London, Taylor and Francis Group Edition.
- [7] Tanyolaç, J. (2000) Limnology (Freshwater Science). Cumhuriyet University, Faculty of Arts and Sciences, Department of Biology, Hatipoğlu Publishing House, Ankara (in Turkish)
- [8] Sönmez, A.Y., Hisar, O., Karataş, M., Arslan, G., Aras, M.S. (2008) Waters Information. Nobel Publication No: 1258, Science: 64, 1st Edition.
- [9] Manier, J.T., Haro, R.J., Houser, J.N., Strauss, E.A. (2021) Spatial and temporal dynamics of phytoplankton assemblages in the upper Mississippi River. River Research and Applications, 37(10), 1451-1462.
- [10] Saler, S., Bulut, H., Birici, N., Tepe, R., Alpaslan, K. (2015) Zooplankton of the Karasu River (Erzincan). Egirdir Faculty of Fisheries Journal, 11(1), 10-16.
- [11] Anonymous, (1995) Standard methods for the examination of water and wastewater. Washington: American Public Health Association (APHA).
- [12] Utermöhl, H. (1958) Zur Vervollkommnung der quantitativen phytoplankton-methodik, Mitteilungen der Internationale Vereinigung der theoretische und Angewandte. Limnologie, 5; 567-596.
- [13] Round, F.D. (1953) An Investigation of two benthic algal communities in Malham Tarn. Yorkshire. J. Ecol., 41; 174-197.
- [14] Cox, E.J. (1996) Identification of freshwater diatoms from live material. London: Chapman and Hall.

- [15] Hustedt, F. (1930) Bacillariophyta (Diatomeae), Heft 10. In: A. Pascher (Ed), Die Süßwasser –Flora Mitteleuropas, Verlag von Gustav Fisher, Jena, 466 p, Stuttgart.
- [16] Huber-Pestalozzi, G. (1942) Das Phytoplankton des Süßwassers, 2 Teil. Diatomeen. In: A. Thienemann (Ed), Die Binnengewasser, E. Schweizerbart'sche Verlagsbuchhandlung, 549 p., Stuttgart.
- [17] Huber-Pestalozzi, G. (1950) Das Phytoplankton des Süßwassers, 3 Teil. Cryptophyceen, Chloromonadien, Peridineen. In: A. Thienemann (Ed), Die Binnengewasser, E. Schweizerbart'sche Verlagsbuchhandlung, 310 p., Stuttgart
- [18] John, P.M., Whitton, B.A., Brook, A.J. (2002) The freshwater algal flora of the British Isles. Cambridge Univ. Press, Cambridge.
- [19] Lind, M.E., Brook, A.J. (1980) A key to the commoner desmids of the English Lake district. Freshwater Biol. Assoc. Publ., 123, Cumbria.
- [20] Türkmen, G., Kazancı, N. (2010) Applications of various biodiversity indices to benthic macroinvertebrate assemblages in streams of a national park in Turkey. Review of Hydrobiology, 111-125.
- [21] Hill, M.O. (1973) Diversity ve evenness: a unifying notation and its consequences. Ecology, 427-432.
- [22] Krebs. C.J. (1998) Ecological methodology. 2nd edition. Benjamin/Cummings, Menlo Park, California.
- [23] Kwak, T.J., Peterson, J.T. (2007) Community indices, parameters, and comparisons. in C.S. Guy and M.L. Brown, Editors. 677-763. Analysis and interpretation of freshwater fisheries data. American Fisheries Society, Bethesda, Maryland. ISBN-13: 978-1-888569-77-3.
- [24] James, B.K., Adejare, L.I. (2010) Nutrients and phytoplankton production dynamics of a tropical harbor in relation to water quality indices, J. Am. Sci, 261-275.
- [25] Menhinick, E.F. (1964) A Comparison of some species-individuals diversity indices applied to samples of field insects, Ecology, 859-861.
- [26] Cetinkaya, O. (2006) Exotic and native fish species inoculated or stocked in Turkish waters, their effects on aquaculture, fisheries, natural populations and aquatic ecosystems: a preliminary study for a database. I. Fishing and reservoir management symposium, 7-9 February (205-235), Antalya. (in Turkish).
- [27] Bobori, D.C., Salvarina, I. (2010) Seasonal variation of fish abundance and biomass in gillnet catches of an East Mediterranean lake: Lake Doirani. Journal of Environmental Biology, 31, 995-1000.

- [28] Anonymous, (2012). Water quality criteria according to classes of inland water resources according to Turkish Environmental Legislation, Regulation on Surface Water Quality Management. Part One. Ministry of Forestry and Water Management. Issue: 28483 Official Gazette. 26s. (in Turkish).
- [29] Eren, Z., Kaya, F. (2020) Biodiversity as a rising value at the international level. Hacettepe University Education Faculty Journal, 27, 1-10. (in Turkish).
- [30] Anonymous, (2004). Water Pollution Control Regulation. Ministry of Environment and Forestry. 1-55. Ankara (in Turkish)
- [31] Hilton, J. O'Hare M., Bowes, M.J., Jones, J.I. (2006) How green is my river: a new paradigm in eutrophication in rivers. *Sci. Total Environ*, 365, 66-83.
- [32] Gurbuz, H., Ertugrul, M. (2003) Determination of medium elements in algae of Karasu (Firat) River by EDXRF using an ²⁴¹Am excitation source. *Instrumentation Science & Technology*, 31(2), 189-196.
- [33] Gürbüz, H. (1990) A Research on the algae flora of the Karasu (Euphrates) River, Atatürk University Institute of Science and Technology (Unpublished Master's Thesis dissertation), 82.
- [34] Baykal, T., Açıkgöz, İ., Udoh, A.U., Yıldız, K. (2011) Seasonal variations in phytoplankton composition and biomass in a small lowland river – lake system (Melen River, Turkey). *Turk J. Biol.*, 35, 485-501.
- [35] Margalef, R. (1958) Information theory in biology. *General Systems Yearbook*, 3, 36-71.
- [36] Shannon, C.E. (1948) A mathematical theory of communication. *The Bell system technical journal*, 27(3), 379-423.
- [37] Ding, Y., Pan, B., Zhao, G., Sun, C., Han, X., Li, M. (2021) Geo-climatic factors weaken the effectiveness of phytoplankton diversity as a water quality indicator in a large sediment-laden river, *Science of The Total Environment*, 792, 148346.
- [38] Cetin, T. (2014) Biological quality elements according to the water framework directive: phytoplankton and phytobenthos. Unpublished expertise dissertation, T.C. Ministry of Forestry and Water Affairs, 144. Ankara. (in Turkish)

Unipotent and Unit-Regular Elements in Certain Subrings of $M_2(\mathbb{Z})$

Günseli GÜMÜŞEL^{1*} 

¹Atılım University, Faculty of Science and Literatures,
Ankara-TURKEY

Received: 02/12/2022, **Revised:** 16/01/2023, **Accepted:** 23/01/2023, **Published:** 31/03/2023

Abstract

We presented a simple and direct way to construct a unipotent unit and clean but not nil-clean element in a ring. New examples of unipotent/unit-regular elements that are not nil-clean are given. We also study the product of two idempotents/unit-regulars which are unit-regular. The studies are exemplified in two subrings of $M_2(\mathbb{Z})$.

Keywords: Idempotent Element, Nil-Clean Element, Nilpotent Element, Unit Element, Unit-Regular Element

$M_2(\mathbb{Z})$ Halkasının Belirli Alt Halkalarındaki Tek Kuvvetli ve Terslenir Düzenli Elemanlar

Öz

Bir halkada, bir sıfır güçlü terslenir ve temiz ama nil-temiz olmayan bir eleman oluşturmanın basit ve doğrudan bir yolunu sunduk. Nil-temiz olmayan sıfır güçlü/terslenir-düzenli elemanların yeni örnekleri verilmiştir. Ayrıca, terslenir-düzenli olan iki eşkare/birim-düzenli elemanların çarpımları da incelenmiştir. $M_2(\mathbb{Z})$ halkasının iki alt halkasında çalışmalar örneklendirilmiştir.

Anahtar Kelimeler: Eşkare Eleman, Nil-Temiz Eleman, Sıfır Güçlü Eleman, Terslenir Eleman, Terslenir-Düzenli Eleman.

1. Introduction

Vidinli Hüseyin Tevfik Pasha (1832-1901) was a famous Ottoman mathematician. He taught advanced algebra, high algebra, analytical geometry, differential, integral calculus, mechanics and astronomy at the Military Academy (*Harbiye Mektebi*) of the Ottoman Empire. What makes special his work *Linear Algebra*, written in English in 1882, is that he produced a completely original work at a time when it was tried to make progress in the sciences through translations and compilations in general.

Although his work seems to be dealing with real and complex numbers, one of the newest subjects of his time, he actually focused on three-dimensional algebras -not two dimensional- within the hypercomplex number system. In the background of this focus, pure quaternions which are a three-dimensional vector subspace of quaternions and a four-dimensional algebra have the purpose of repeating the mutation application in three-dimensional Euclidean geometry in two dimensions.

In short, Tevfik Pasa's *Linear Algebra* tries to spread the complex or virtual value system to three-dimensional space by making use of Argand's concept of a vector calculus.

Here we reconsider this problem by working on unipotent elements, unit-regular elements, nil-clean elements and clean elements based on the Tevfik Pasha's adaptation of linear algebra, which is one of the most important fundamental theories of modern mathematics. We present a simple and direct way to construct a unipotent unit and clean but not nil-clean element in the ring $\begin{pmatrix} \mathbb{Z} & \mathbb{Z} \\ s^2\mathbb{Z} & \mathbb{Z} \end{pmatrix}$ for every positive integer $s \geq 3$.

We show that the product of two unit-regolars in R_i is unit-regular if and only if the product of two idempotents in R_i is unit-regular where $R_1 := \begin{pmatrix} \mathbb{Z} & \mathbb{Z} \\ 4\mathbb{Z} & \mathbb{Z} \end{pmatrix}$ and $R_2 := \begin{pmatrix} \mathbb{Z} & \mathbb{Z} \\ s^2\mathbb{Z} & \mathbb{Z} \end{pmatrix}$ with $s \geq 3$. Because of this observation, we also obtain that the rings R_i ($i = 1,2$) are SSP if and only if product of two idempotents in R_i ($i = 1,2$) is unit-regular.

2. Preliminaries

Throughout, R is an associative ring with unity.

We write \mathbb{Z} is the ring of integers, $M_2(\mathbb{Z})$ is the 2×2 matrix ring over \mathbb{Z} whose identity is denoted by I_2 over R .

A ring R is called *clean* if each element of its can be written as the sum of a unit and an idempotent. Clean rings were introduced by W. K. Nicholson [7].

In [1], Andrica and Calugareanu found a counter example and gave a structure theorem which is nil-clean but not clean element in the matrix ring $M_2(\mathbb{Z})$. In [8] the authors considered this problem on the subring $\begin{pmatrix} \mathbb{Z} & \mathbb{Z} \\ s^2\mathbb{Z} & \mathbb{Z} \end{pmatrix}$ of $R := M_2(\mathbb{Z})$ instead of R since the subring $\begin{pmatrix} \mathbb{Z} & \mathbb{Z} \\ s^2\mathbb{Z} & \mathbb{Z} \end{pmatrix}$ contains much less clean elements than $M_2(\mathbb{Z})$, a huge advantage. The authors of [8] gave also

many counter-examples of unit-regular elements (an element in a ring is unit-regular if it is a product of an idempotent and a unit, and a ring is unit-regular if its every element is unit-regular) and nil-clean elements that are not clean in the ring $\begin{pmatrix} \mathbb{Z} & \mathbb{Z} \\ s^2\mathbb{Z} & \mathbb{Z} \end{pmatrix}$.

An element $a \in R$ in a ring is called *unipotent*, if $a - 1$ is nilpotent.

An element a in any ring R is said to *have (right) stable range 1* ($sr(a) = 1$) if $aR + bR = R$ (for any $b \in R$) implies that $a + br$ is a unit for some $r \in R$. We recall that if a is a unit-regular element in a ring R , then $sr(a) = 1$.

A ring R is said to being the *summand sum property (briefly SSP)* if the sum of two direct summands of R_R is also a direct summand of R ([5]). It is well known that $M_2(\mathbb{Z})$ is not SSP while \mathbb{Z} is an SSP ring.

3. Main Theorem and Proof

We begin recalling the following basic facts over the matrix ring $M_2(\mathbb{Z})$.

- The units in $M_2(\mathbb{Z})$ are the 2×2 matrices of $\det = \mp 1$.
- A non-trivial idempotent matrix in $M_2(\mathbb{Z})$ has *rank* 1.
- A nilpotent matrix in $M_2(\mathbb{Z})$ has the characteristic polynomial t^2 and so it has the trace which is equal to 1.

Lemma 3.1. ([1]) Let $s \in \mathbb{Z}$. Nontrivial idempotents and nilpotents in the ring $\begin{pmatrix} \mathbb{Z} & \mathbb{Z} \\ s\mathbb{Z} & \mathbb{Z} \end{pmatrix}$ are matrices $\begin{pmatrix} \alpha + 1 & u \\ sv & -\alpha \end{pmatrix}$ with $\alpha^2 + \alpha + suv = 0$ and $\begin{pmatrix} \beta & x \\ sy & -\beta \end{pmatrix}$ with $\beta^2 + sxy = 0$ respectively.

Proposition 3.2. For rings $R_1 = \begin{pmatrix} \mathbb{Z} & \mathbb{Z} \\ 4\mathbb{Z} & \mathbb{Z} \end{pmatrix}$ and $R_2 = \begin{pmatrix} \mathbb{Z} & \mathbb{Z} \\ s^2\mathbb{Z} & \mathbb{Z} \end{pmatrix}$ with $s \geq 3$ an even number, there exist no any invertible matrices U_i in R_i ($i = 1, 2$) such that $I_2 + U_i$ are invertible in R_i ($i = 1, 2$).

Proof: We only give proof for the ring R_1 . The other is similar.

Assume the contrary that there exists an invertible element $U_1 = \begin{pmatrix} a & b \\ 4c & d \end{pmatrix}$ in R_1 such that $\det(U_1) = ad - 4bc = \mp 1$. By the assumption, $I_2 + U_1$ must be also invertible in R_1 , i.e.,

$$I_2 + U_1 = \begin{pmatrix} 1 & 0 \\ 0 & 1 \end{pmatrix} + \begin{pmatrix} a & b \\ 4c & d \end{pmatrix} = \begin{pmatrix} a + 1 & b \\ 4c & d + 1 \end{pmatrix}$$

and $\det(I_2 + U_1) = (ad - 4bc) + (a + d + 1) = \mp 1$. Now we can proceed with the following cases.

Case 1. If $ad - 4bc = 1$, then $a + d = -1$ and $a + d = -3$.

Firstly, assume $a + d = -1$. Then $(-1 - d)d - 4bc = d + d^2 + 4bc = 1$. Since $4bc$ is an even number, the number $d + d^2 = d(d + 1)$ must be odd, a contradiction. If $a + d = -3$, we get $(-3 - d)d - 4bc = (3 + d)d + 4bc = -1$. Since $4bc$ is an even number, we get $d(d + 3)$ must be odd, a contradiction.

Case 2. If $ad - 4bc = -1$, then $a + d = -1$ and $a + d = 1$.

If we repeat the procedure of Case 1, we can obtain similar contradictions.

By [3, Corollary 3.3], $M_2(\mathbb{Z})$ is not UU (UR=1+NR) (i.e. $U(R) = 1 + N(R)$) since $I_2 + U_1$ in $M_2(\mathbb{Z})$ are not unipotent. ■

Theorem 3.3. There exist unipotent unit, clean matrices which are not nil-clean in $\begin{pmatrix} \mathbb{Z} & \mathbb{Z} \\ 4\mathbb{Z} & \mathbb{Z} \end{pmatrix}$

Proof: This is clear from Proposition 3.2. ■

Example 3.4. The matrix

$$A = \begin{pmatrix} -3 & -2 \\ 8 & 5 \end{pmatrix}$$

is a unipotent unit in $\begin{pmatrix} \mathbb{Z} & \mathbb{Z} \\ 4\mathbb{Z} & \mathbb{Z} \end{pmatrix}$ since $A - I_2 = \begin{pmatrix} -4 & -2 \\ 8 & 4 \end{pmatrix}$ is a nilpotent. As units are clean, the matrix A is clean but is not nil-clean in $\begin{pmatrix} \mathbb{Z} & \mathbb{Z} \\ 4\mathbb{Z} & \mathbb{Z} \end{pmatrix}$ by [8, Theorem 3.3].

Example 3.5. The matrix

$$A = \begin{pmatrix} s + 1 & 1 \\ -s^2 & -s + 1 \end{pmatrix}$$

is a unipotent unit in the ring $\begin{pmatrix} \mathbb{Z} & \mathbb{Z} \\ s^2\mathbb{Z} & \mathbb{Z} \end{pmatrix}$, where $s \geq 3$ is an even number since $I_2 - U = \begin{pmatrix} -s & -1 \\ s^2 & s \end{pmatrix}$ is a nilpotent matrix in $\begin{pmatrix} \mathbb{Z} & \mathbb{Z} \\ s^2\mathbb{Z} & \mathbb{Z} \end{pmatrix}$. As units are clean, the matrix A is clean but is not nil-clean in $\begin{pmatrix} \mathbb{Z} & \mathbb{Z} \\ s^2\mathbb{Z} & \mathbb{Z} \end{pmatrix}$ by [8, Theorem 3.4].

Lemma 3.6. ([6]) Let $s \in \mathbb{Z}$. Unit-regular elements in the ring $\begin{pmatrix} \mathbb{Z} & \mathbb{Z} \\ s\mathbb{Z} & \mathbb{Z} \end{pmatrix}$ are matrices

$$\begin{pmatrix} a & b \\ 0 & 0 \end{pmatrix} = \begin{pmatrix} 1 & u \\ 0 & 0 \end{pmatrix} \begin{pmatrix} x & y \\ sz & t \end{pmatrix},$$

where $E = \begin{pmatrix} 1 & u \\ 0 & 0 \end{pmatrix}$ is an idempotent and $U = \begin{pmatrix} x & y \\ sz & t \end{pmatrix}$ is a unit.

The following examples show that the product of two idempotents (or unit-regulars) in $R = \begin{pmatrix} \mathbb{Z} & \mathbb{Z} \\ 4\mathbb{Z} & \mathbb{Z} \end{pmatrix}$ need not be unit-regular, in general.

Example 3.7. Let $R = \begin{pmatrix} \mathbb{Z} & \mathbb{Z} \\ 4\mathbb{Z} & \mathbb{Z} \end{pmatrix}$. Consider the idempotents

$$E_1 = \begin{pmatrix} 1 & 0 \\ 4 & 0 \end{pmatrix} \text{ and } E_2 = \begin{pmatrix} 9 & 3 \\ -24 & -8 \end{pmatrix}$$

Then

$$E_1 E_2 = \begin{pmatrix} 9 & 3 \\ 36 & 0 \end{pmatrix}$$

is not unit-regular.

Example 3.8. Let $R = \begin{pmatrix} \mathbb{Z} & \mathbb{Z} \\ 4\mathbb{Z} & \mathbb{Z} \end{pmatrix}$. Consider the unit-regulars

$$A = \begin{pmatrix} 11 & 1 \\ 0 & 0 \end{pmatrix} = \begin{pmatrix} 1 & 0 \\ 0 & 0 \end{pmatrix} \begin{pmatrix} 11 & 1 \\ 32 & 3 \end{pmatrix}$$

and

$$B = \begin{pmatrix} 13 & 5 \\ 0 & 0 \end{pmatrix} = \begin{pmatrix} 1 & 0 \\ 0 & 0 \end{pmatrix} \begin{pmatrix} 13 & 5 \\ 8 & 3 \end{pmatrix}$$

in $\begin{pmatrix} \mathbb{Z} & \mathbb{Z} \\ 4\mathbb{Z} & \mathbb{Z} \end{pmatrix}$. Then

$$AB = \begin{pmatrix} 143 & 55 \\ 0 & 0 \end{pmatrix}$$

is not unit-regular. In fact, if

$$AB = \begin{pmatrix} 143 & 55 \\ 0 & 0 \end{pmatrix} = \begin{pmatrix} 1 & 0 \\ 0 & 0 \end{pmatrix} \begin{pmatrix} 143 & 55 \\ 4a & b \end{pmatrix}$$

then $220a - 143b = 11(20a - 13b)$ can not be -1 or 1 for any integers a and b .

The following examples show that the product of two idempotents (or unit-regulars) in $R = \begin{pmatrix} \mathbb{Z} & \mathbb{Z} \\ s^2\mathbb{Z} & \mathbb{Z} \end{pmatrix}$ need not be unit-regular, in general.

Example 3.9. Let $R = \begin{pmatrix} \mathbb{Z} & \mathbb{Z} \\ s^2\mathbb{Z} & \mathbb{Z} \end{pmatrix}$ with $s \geq 3$. Consider the idempotents

$$E_1 = \begin{pmatrix} 1 & 0 \\ 0 & 0 \end{pmatrix} \text{ and } E_2 = \begin{pmatrix} 1 & 0 \\ s^2 & 0 \end{pmatrix}$$

in R . Then

$$E_1 E_2 = \begin{pmatrix} 1 & 0 \\ 0 & 0 \end{pmatrix}$$

is not unit-regular.

Example 3.10. Let $R = \begin{pmatrix} \mathbb{Z} & \mathbb{Z} \\ s^2\mathbb{Z} & \mathbb{Z} \end{pmatrix}$ with $s \geq 3$. Consider the unit-regulars

$$A = \begin{pmatrix} 6 & 1 \\ 0 & 0 \end{pmatrix} = \begin{pmatrix} 1 & 0 \\ 0 & 0 \end{pmatrix} \begin{pmatrix} 6 & 1 \\ -25 & -4 \end{pmatrix}$$

and

$$B = \begin{pmatrix} 4 & 1 \\ 0 & 0 \end{pmatrix} = \begin{pmatrix} 1 & 0 \\ 0 & 0 \end{pmatrix} \begin{pmatrix} 4 & 1 \\ -9 & -2 \end{pmatrix}$$

in $\begin{pmatrix} \mathbb{Z} & \mathbb{Z} \\ s^2\mathbb{Z} & \mathbb{Z} \end{pmatrix}$. Then

$$AB = \begin{pmatrix} 24 & 6 \\ 0 & 0 \end{pmatrix}$$

is not unit-regular. In fact, if

$$AB = \begin{pmatrix} 24 & 6 \\ 0 & 0 \end{pmatrix} = \begin{pmatrix} 1 & 0 \\ 0 & 0 \end{pmatrix} \begin{pmatrix} 24 & 6 \\ s^2z & t \end{pmatrix}$$

then $24t - 6zs^2$ can not be -1 or 1 for any integers a and b .

Proposition 3.11. The following conditions are equivalent for the rings $R_1 := \begin{pmatrix} \mathbb{Z} & \mathbb{Z} \\ 4\mathbb{Z} & \mathbb{Z} \end{pmatrix}$ and $R_2 := \begin{pmatrix} \mathbb{Z} & \mathbb{Z} \\ s^2\mathbb{Z} & \mathbb{Z} \end{pmatrix}$ with $s \geq 3$:

- (1) The product of two unit-regulars in R_i ($i = 1, 2$) is unit-regular,
- (2) The product of two idempotents in R_i ($i = 1, 2$) is unit-regular.

Proof. We only give proof for the ring R_1 . The other is similar.

(1) \Rightarrow (2): Suppose that the product of two idempotents in R_1 is unit-regular. Let $A = E_1U_1$ and $B = E_2U_2$ be two unit-regular in R_1 , where $E_1, E_2 \in Id(R_1)$ and $U_1, U_2 \in U(R_1)$. It is easy to see that $U_1E_2U_1^{-1}$ is an idempotent and $AB = E_1(U_1E_2U_1^{-1})U_1U_2$. Put $E_3 := U_1E_2U_1^{-1}$. Then we conclude that

$$AB = E_1E_3U_1U_2$$

By the assumption, E_1E_3 is unit-regular and hence AB is unit-regular.

(2) \Rightarrow (1): It is clear. ■

Example 3.12. Let $R = \begin{pmatrix} \mathbb{Z} & \mathbb{Z} \\ 4\mathbb{Z} & \mathbb{Z} \end{pmatrix}$. Consider the idempotents

$$E_1 = \begin{pmatrix} 1 & 0 \\ 0 & 0 \end{pmatrix} \text{ and } E_2 = \begin{pmatrix} 9 & -18 \\ 4 & -8 \end{pmatrix}$$

in R . Then

$$E_1 E_2 = \begin{pmatrix} 9 & -18 \\ 0 & 0 \end{pmatrix}$$

is unit-regular. Let

$$A = \begin{pmatrix} 9 & 2 \\ 0 & 0 \end{pmatrix} = \begin{pmatrix} 1 & 0 \\ 0 & 0 \end{pmatrix} \begin{pmatrix} 9 & 2 \\ 4 & 1 \end{pmatrix}$$

and

$$B = \begin{pmatrix} 7 & 1 \\ 0 & 0 \end{pmatrix} = \begin{pmatrix} 1 & 0 \\ 0 & 0 \end{pmatrix} \begin{pmatrix} 7 & 1 \\ 8 & 1 \end{pmatrix}$$

Then AB is unit-regular. Since

$$AB = \begin{pmatrix} 63 & 9 \\ 0 & 0 \end{pmatrix} = \begin{pmatrix} 9 & -18 \\ 0 & 0 \end{pmatrix} \begin{pmatrix} 79 & 11 \\ 36 & 5 \end{pmatrix}$$

Example 3.13. In $R_2 = \begin{pmatrix} \mathbb{Z} & \mathbb{Z} \\ s^2\mathbb{Z} & \mathbb{Z} \end{pmatrix}$, consider the idempotents

$$E_1 = \begin{pmatrix} 1 & 0 \\ 0 & 0 \end{pmatrix} \text{ and } E_2 = \begin{pmatrix} -24 & -6 \\ 100 & 25 \end{pmatrix}.$$

Then

$$E_1 E_2 = \begin{pmatrix} -24 & -6 \\ 0 & 0 \end{pmatrix}$$

is unit-regular. Let

$$A = \begin{pmatrix} 6 & 1 \\ 0 & 0 \end{pmatrix} = \begin{pmatrix} 1 & 0 \\ 0 & 0 \end{pmatrix} \begin{pmatrix} 6 & 1 \\ -25 & -4 \end{pmatrix}$$

and

$$B = \begin{pmatrix} 11 & 2 \\ 0 & 0 \end{pmatrix} = \begin{pmatrix} 1 & 0 \\ 0 & 0 \end{pmatrix} \begin{pmatrix} 11 & 2 \\ 16 & 3 \end{pmatrix}$$

Then

$$AB = \begin{pmatrix} 66 & 12 \\ 0 & 0 \end{pmatrix} = \begin{pmatrix} -24 & -6 \\ 0 & 0 \end{pmatrix} \begin{pmatrix} 82 & 15 \\ -339 & -62 \end{pmatrix}$$

is unit-regular.

Corollary 3.14. The rings R_1 and R_2 are SSP if and only if the product of two unit-regulars in R_i ($i = 1, 2$) is unit-regular in R_i ($i = 1, 2$).

Proof. Assume the contrary that R_1 is SSP. Let E_1, E_2 be two idempotents in R_1 . Since R_1 is SSP, we get $(I_2 - E_1)R_1 + E_2R_1$ is a direct summand of R_1 , and so $E_1E_2R_1$ is a direct summand of R_1 . It follows that E_1E_2 is regular. Take $A = E_1E_2$ and $B \in R$ with $A = ABA$. Since all idempotents of R_1 have right stable range 1, we obtain that $sr(A) = 1$ by [4, Proposition 2]. Now, $AR_1 + (I_2 - AB)R_1 = R_1$. There exists C in R_1 such that $A + (I_2 - AB)C$ is a unit. Let U be a unit of R with $[A + (I_2 - AB)C]U = I_2$. Then, we have

$$E_1E_2 = A = ABA = AB[A + (I_2 - AB)C] = ABAUA = AUA$$

which implies that E_1E_2 is unit-regular.

For the converse, let E_1, E_2 be two idempotents of in R_1 . By the assumption (and hence from Proposition 3.11), we obtain that $(I_2 - E_1)E_2$ is unit-regular. Hence $(I_2 - E_1)E_2R_1$ is a direct summand of R_1 . Let I be a right ideal of R_1 such that $(I_2 - E_1)E_2R_1 \oplus I = R_1$. Then,

$$(I_2 - E_1)R_1 = (I_2 - E_1)E_2R_1 \oplus [(I_2 - E_1)R_1 \cap I]$$

In as much as $E_1R_1 + E_2R_1 = E_1R_1 \oplus (I_2 - E_1)E_2R_1$, we have

$$\begin{aligned} R_1 &= E_1R_1 \oplus (I_2 - E_1)E_2R_1 \oplus [(I_2 - E_1)R_1 \cap I] \\ &= (E_1R_1 + E_2R_1) \oplus [(I_2 - E_1)R_1 \cap I]. \end{aligned}$$

This shows that R_1 has SSP. ■

One can easily see that unit-regular elements can not be unipotents because of the structure in the rings $\begin{pmatrix} \mathbb{Z} & \mathbb{Z} \\ 4\mathbb{Z} & \mathbb{Z} \end{pmatrix}$ and $\begin{pmatrix} \mathbb{Z} & \mathbb{Z} \\ s^2\mathbb{Z} & \mathbb{Z} \end{pmatrix}$ with $s \geq 3$. The following gives us that there exists unit-regular elements which may be unipotents in these rings, but we don't know them, unfortunately.

Theorem 3.15. For rings R_1 and R_2 , there exist no any unit-regular matrices A_i in R_i ($i = 1, 2$) such that $I_2 + A_i$ are invertible in R_i ($i = 1, 2$).

Proof. We only give proof for the ring R_1 . The other is similar. Assume on contrary that there exists a unit-regular matrix A_1 in $R_1 = \begin{pmatrix} \mathbb{Z} & \mathbb{Z} \\ 4\mathbb{Z} & \mathbb{Z} \end{pmatrix}$ such that $I_2 + A_1$ are invertible in R_1 . In the general case, we consider the unit-regular element

$$A_1 = \begin{pmatrix} a & b \\ 0 & 0 \end{pmatrix} = \begin{pmatrix} 1 & 0 \\ 0 & 0 \end{pmatrix} \begin{pmatrix} x & y \\ 4z & t \end{pmatrix}$$

where $E = \begin{pmatrix} 1 & 0 \\ 0 & 0 \end{pmatrix}$ is an idempotent and $U = \begin{pmatrix} x & y \\ 4z & t \end{pmatrix}$ is a unit. By the assumption, $I_2 + A_1$ must be also invertible in R_1 , i.e.,

$$I_2 + A_1 = \begin{pmatrix} 1 & 0 \\ 0 & 1 \end{pmatrix} + \begin{pmatrix} a & b \\ 0 & 0 \end{pmatrix} = \begin{pmatrix} a+1 & b \\ 0 & 1 \end{pmatrix}$$

and $\det(I_2 + A_1) = a + 1 = \mp 1$. Now we can proceed with the following cases.

Case 1. If $a + 1 = 1$, then $a = 0$.

Hence $A_1 = \begin{pmatrix} a & b \\ 0 & 0 \end{pmatrix} = \begin{pmatrix} 0 & b \\ 0 & 0 \end{pmatrix}$ which is not a unit-regular element in R_1 .

Case 2. If $a + 1 = -1$, then $a = -2$.

Hence $A_1 = \begin{pmatrix} a & b \\ 0 & 0 \end{pmatrix} = \begin{pmatrix} -2 & b \\ 0 & 0 \end{pmatrix} = \begin{pmatrix} 1 & 0 \\ 0 & 1 \end{pmatrix} \begin{pmatrix} -2 & b \\ 4z & t \end{pmatrix}$, which gives us that $2t + 4bz$ should be ∓ 1 . Clearly, this equation has no integer solutions. ■

4. Conclusion

In this paper, we focus two subring of $M_2(\mathbb{Z})$. We give basic way to find not nil-clean elements which are unipotent and clean. We give examples of the product of two idempotent (unit-regulars) not be unit-regular in two subring of $M_2(\mathbb{Z})$.

Ethics in Publishing

There are no ethical issues regarding the publication of this study.

References

- [1] Andrica D., Călugăreanu G.G., (2014) A nil-clean 2×2 matrix over the integers which is not clean, J. Algebra, 13(6), 3115–3119. doi:[10.1142/S0219498814500091](https://doi.org/10.1142/S0219498814500091)
- [2] Călugăreanu, G., Lam, T.Y., (2015) Fine rings: A new class of simple rings, J. Algebra Appl., 15(9), 1650173-18 pages. doi:[10.1142/S0219498816501735](https://doi.org/10.1142/S0219498816501735)
- [3] Călugăreanu, G., (2015) UU rings, Carpathian J. Math., 31(2), 157-163. doi:[10.37193/CJM.2015.02.02](https://doi.org/10.37193/CJM.2015.02.02)
- [4] Călugăreanu, G., Pob, H.F. On stable range one matrices, Preprint
- [5] Garcia, J.L., (1989) Properties of direct summands of modules, Commun. Algebra, 17, 73–92. doi: [10.1080/00927878908823714](https://doi.org/10.1080/00927878908823714)
- [6] Khurana, D., Lam, T.Y., (2004) Clean matrices and unit-regular matrices, J. Algebra, 280, 683-698. doi:[10.1016/j.jalgebra.2004.04.019](https://doi.org/10.1016/j.jalgebra.2004.04.019)
- [7] Nicholson W. K., (1977) Lifting idempotents and exchange rings, Trans. Amer. Math. Soc., 229, 269-278. doi:[10.1090/S0002-9947-1977-0439876-2](https://doi.org/10.1090/S0002-9947-1977-0439876-2)
- [8] Wu, Y., Tang, G., Deng, G., Zhou, Y., (2019) Nil-clean and unit-regular elements in certain subrings of $M_2(\mathbb{Z})$, Czechoslovak Math. J., 69(1), 197-205. doi:[10.21136/CMJ.2018.0256-17](https://doi.org/10.21136/CMJ.2018.0256-17)

Corrigendum to “Numerical Solutions For Singularly Perturbed Nonlinear Reaction Diffusion Problems On The Piecewise Equidistant Mesh”

Hakkı DURU , Baransel GÜNEŞ *

Van Yüzüncü Yıl Üniversitesi, Fen Fakültesi, Matematik Bölümü, Van, Türkiye

Geliş / Received: 06/11/2018, Kabul / Accepted: 28/01/2019

Abstract

In this corrigendum, it is aimed to correct some typos of the paper entitled “Parçalı Düzgün Şebekede Singüler Pertürbe Özellikli Lineer Olmayan Reaksiyon Difüzyon Problemleri İçin Nümerik Çözümler” [Erzincan University Journal of Science and Technology, 12(1) (2019), 425-436].

Keywords: Differential equation, difference scheme, piecewise equidistant mesh, singular perturbation

Düzeltilme “Parçalı Düzgün Şebekede Singüler Pertürbe Özellikli Lineer Olmayan Reaksiyon Difüzyon Problemleri İçin Nümerik Çözümler”

Öz

Bu düzeltmede, “Parçalı Düzgün Şebekede Singüler Pertürbe Özellikli Lineer Olmayan Reaksiyon Difüzyon Problemleri İçin Nümerik Çözümler” [Erzincan University Journal of Science and Technology, 12(1) (2019), 425-436] başlıklı makaleye ait bazı yazım yanlışlarının giderilmesi amaçlanmıştır.

Anahtar Kelimeler: Diferansiyel denklem, fark şeması, parçalı düzgün şebeke, singular pertürbasyon

Yukarıda künyesi verilen makalenin aslı 24.03.2019 tarihinde yayınlanmıştır. Sayfa 431 ve sayfa 434’de bazı sembolik yazım yanlışları tespit edilmiştir [1]. Bu yanlışları giderme adına aşağıda bazı düzeltmelere yer verilmiştir:

Sayfa 431’de “4. Parçalı Düzgün Şebekede Fark Şemasının Kurulması” başlığı altında, bazı yerlerde \hbar_j olarak yazılan notasyon \hbar_i olmalıdır. Dolayısıyla,

$$\hbar_j^{-1} \int_{x_{i-1}}^{x_{i+1}} Lu\varphi_i dx = \hbar_j^{-1} \int_{x_{i-1}}^{x_{i+1}} (-\varepsilon^2 u'' + a(x)u(x))\varphi_i dx = \hbar_j^{-1} \int_{x_{i-1}}^{x_{i+1}} f(x, u)\varphi_i dx$$

ile verilen eşitlik

$$\hbar_i^{-1} \int_{x_{i-1}}^{x_{i+1}} Lu\varphi_i dx = \hbar_i^{-1} \int_{x_{i-1}}^{x_{i+1}} (-\varepsilon^2 u'' + a(x)u(x))\varphi_i dx = \hbar_i^{-1} \int_{x_{i-1}}^{x_{i+1}} f(x, u)\varphi_i dx$$

şeklinde ve $-\hbar_j^{-1} \int_{x_{i-1}}^{x_{i+1}} \varepsilon^2 u'' dx$ terimi de $-\hbar_i^{-1} \int_{x_{i-1}}^{x_{i+1}} \varepsilon^2 u'' dx$ biçiminde ifade edilmelidir. Ayrıca φ_i baz fonksiyonuna ilişkin problemlerde kullanılan $\varphi_j^{(1)}$ ve $\varphi_j^{(2)}$ ifadeleri $\varphi_i^{(1)}$ ve $\varphi_i^{(2)}$ olmalıdır. Yani, φ_i baz fonksiyonu

$$\begin{aligned} \varepsilon^2 \varphi_i^{(1)''} &= 0, \quad \varphi_i^{(1)}(x_i) = 1, \quad \varphi_i^{(1)}(x_{i-1}) = 0 \\ \varepsilon^2 \varphi_i^{(2)''} &= 0, \quad \varphi_i^{(2)}(x_i) = 1, \quad \varphi_i^{(2)}(x_{i+1}) = 0 \end{aligned}$$

problemlerinin çözümüdür.

Sayfa 434’de “5. Nümerik Örnek” başlığı altında A_i , B_i ve C_i katsayıları aşağıda belirtildiği biçimde yazılmalıdır:

$$\begin{aligned} A_i &= \frac{\varepsilon^2}{\hbar_i \hbar_i}, & B_i &= \frac{\varepsilon^2}{\hbar_i \hbar_{i+1}}, \\ C_i &= \varepsilon^2 \hbar_i^{-1} \left(\frac{1}{\hbar_i} + \frac{1}{\hbar_{i+1}} \right) + a_i - f_u(x_i, y_i^{(n-1)}) \end{aligned}$$

Kaynaklar

[1] Duru, H., Güneş B., 2019. Parçalı Düzgün Şebekede Singüler Pertürbe Özellikli Lineer Olmayan Reaksiyon Difüzyon Problemleri İçin Nümerik Çözümler, Erzincan University Journal of Science and Technology, 12 (1), 425-436.